Progress in Materials Science 93 (2018) 112–232

Contents lists available at ScienceDirect

Progress in Materials Science

journal homepage: www.elsevier.com/locate/pmatsci

Magnetocaloric effect: From materials research to refrigeration devices

V. Franco *, J.S. Blázquez, J.J. Ipus, J.Y. Law, L.M. Moreno-Ramírez, A. Conde

Dpto. Física de la Materia Condensada, ICMSE-CSIC, Universidad de Sevilla, P.O. Box 1065, 41080 Sevilla, Spain

ARTICLE INFO

Article history:
Received 6 April 2017
Received in revised form 25 October 2017
Accepted 26 October 2017
Available online 8 November 2017

Keywords:
Magnetocaloric effec
Magnetic refrigeration
Thermomagnetic properties

ABSTRACT

The magnetocaloric effect and its most straightforward application, magnetic refrigeration, are topics of current interest due to the potential improvement of energy efficiency of cooling and temperature control systems, in combination with other environmental benefits associated to a technology that does not rely on the compression/expansion of harmful gases. This review presents the fundamentals of the effect, the techniques for its measurement with consideration of possible artifacts found in the characterization of the samples, a comprehensive and comparative analysis of different magnetocaloric materials, as well as possible routes to improve their performance. An overview of the different magnetocaloric prototypes found in literature as well as alternative applications of the magnetocaloric effect for fundamental studies of phase transitions are also included.

Contents

* Corresponding author.
E-mail address: vfranco@us.es (V. Franco).

https://doi.org/10.1016/j.pmatsci.2017.10.005
0079-6425/

1. Introduction

Energy efficiency and sustainability are priority topics for most research funding agencies worldwide and are recurrent topics in different mass media. In fact, according to data from Laurence Livermore National Laboratory 61% of the estimated USA energy consumption in 2015 corresponds to rejected energy, while only the remaining 39% is actually employed in energy services. Values are comparable for other developed countries, like 63% rejected energy in 2011 in UK or Spain. These data indicate that it is not only necessary to focus on the primary energy source and avoid our dependence on non-renewable energy sources but also to dedicate large research efforts for improving the efficiency of energy conversion. In particular, most renewable energy sources have to be converted into electricity before their final use, and in USA 67% of the conversion process in 2015 resulted in wasted energy [1]. In many cases, magnetic materials play a relevant role in energy conversion into electricity. This constitutes a driving force for the improvement of magnetic materials for energy applications [2], with some current examples covered in a recent Viewpoint Set of Scripta Materialia [3].

Among the different final uses of energy in the residential and commercial sectors, refrigeration and air conditioning account for a relevant fraction of electricity use, with numbers varying from country to country due to their different climate. Recent data from EIA [4] estimate that 87% of USA households are furnished with air-conditioners and ~114 million units account for an annual energy demand of 186 billion kWh of electricity. There is no doubt that our way of life relies on our capability of cooling food and controlling the temperature of our living and working environments. If developing countries adopt similar trends in cooling habits, there can be a 50-fold increase in the demand of air conditioners [5]. In the European Union, heating and cooling in buildings and industry account for half of the EU's energy consumption and in order to fulfil the EU's climate and energy goals, the heating and cooling sector must drastically reduce their energy consumption and cut their use of fossil fuels [6]. Magnetic refrigeration can play a relevant role in this effort to improve the energy efficiency of temperature and climate control. It is expected that these refrigerators based on magnetocaloric effect (MCE) will be energetically more efficient than the current ones based on the compression and expansion of gasses.

In fact, magnetic refrigeration is a timely topic of research. The discovery of magnetic materials that exhibit a remarkable change in their temperature when they are adiabatically magnetized close to room temperature [7] has produced a surge in the number of publications on MCE in the last two decades. Simultaneously, as these materials enable the possibility of designing magnetic refrigerators with operation temperatures close to room temperature, there has been a noticeable increase in the development of magnetic refrigerator prototypes [8]. This scientific and technological interest is mainly

due to the environmental friendliness of magnetic refrigeration, which is energetically more efficient than the conventional refrigerator devices and does not require the use of ozone depleting or greenhouse effect related gasses. Room temperature magnetic refrigeration had been just a promise since Brown designed and built the first successful magnetic refrigerator prototype [9], with devices restricted to research laboratories. However, the situation has begun to change, as a domestic appliance of a wine cooler based on this principle of operation, developed by Haier, Astronautics Corporation of America and BASF, was presented in 2015 edition of the Las Vegas Consumer Electronics Show (CES2015) [10].

As this is a topic that encompasses material science and current trends in technology, we are convinced that a comprehensive overview, which analyzes materials properties in combination with the main characteristics of the models representing them and the basic operation principles of the devices, will facilitate the search of better materials with enhanced applicability. This will also enable technologists to have the tools for appropriate material selection and implementation of the appropriate models of materials properties for their simulations.

We will start this review with an overview of the thermodynamics associated to the MCE and its different thermodynamic cycles that can be used in magnetic refrigeration, since these two aspects justify the strategies used in the search for new materials. Subsequently, the experimental characterization techniques will be presented, making a distinction between those that directly measure the adiabatic temperature change or the isothermal magnetic entropy change, and those that infer these properties from indirect measurements. In this aspect, it is extremely important to clarify and, to some extent, quantify the different artifacts that can appear during the measurement procedure and analysis of the results. Such information relating the attributions of these artifacts allows experimentalists to reconcile the results obtained from direct and indirect techniques. In addition, it is important to know the different models that can represent these properties and this will be presented as two main types: first principles modeling and thermodynamic models. The revision of current magnetocaloric materials will be categorized into their microstructures and compositions. There could be a third classification criterion based on the order of the phase transition but it would not be compatible with compositional classification because minor stoichiometric changes in the materials might alter the nature of their phase transitions. Crystalline and amorphous materials will be considered independently as their properties differ in a great extent even qualitatively. Within these families, we will also classify the materials as rare earth containing and rare earth free, in agreement with the current concerns to avoid the use of strategic materials in energy-related applications. It will also be shown that materials fabrication and processing techniques, which enable the presence of multiple phases, refinement of the microstructure or alteration in the stoichiometry of the phases, will result in different, sometimes optimized, magnetocaloric properties. Next, it is worth dedicating a part of the review to present an alternative application of the magnetocaloric characterization of materials. This includes performing fundamental studies regarding the phase transitions involved, determining critical exponents and establishing the order of the phase transition even in cases for which purely magnetic methods are not applicable. The last part of the review will be devoted to the main application of the magnetocaloric effect, which has been the reason for its enormous interest nowadays: magnetic refrigeration. A comparison of existing refrigerator prototypes is presented placing the current materials' research in a proper context: devices need good magnetocaloric materials and magnetocaloric research would not have attained its current level without the possibility of implementing magnetic refrigerators. Conclusions and future outlook are then presented.

There have been previous review papers on magnetocalorics [2,8,11–21]. Some of them dealt with a specific aspect of the topic (theoretical models, prototypes, operation temperature close to room temperatures, etc.); others focus on specific types of materials. In particular, a recent book focuses mostly on magnetocaloric energy conversion and the principle of operation of different devices [22], which makes a difference with previous books, more dedicated to materials science [23]. We will refer to these reviews when appropriate. However, for the sake of completeness we will compile the main information of the different families of magnetocaloric materials, models and methods in the present review.

2. Thermodynamics of the magnetocaloric effect

Although books on magnetocaloric effect already include in introduction on thermodynamics [22,23], it is necessary to include in this review a brief description of thermodynamic relations and how to define the magnetocaloric response of a material from them. In addition, the different figures of merit that allow us to compare materials performance have to be defined, as they will be used throughout this review. This chapter ends with a succinct description of the different thermodynamic cycles that can be used in magnetic refrigerator devices, as those will ultimately control the way in which materials are used.

2.1. Thermodynamic relations

The magnetic effect is introduced in thermodynamic systems via the performed magnetic work, using the principles of energy conservation:

$$\mathrm{d}U = đQ - đW \tag{1}$$

where U, Q and W are the internal energy, the heat flux and the performed work, respectively (đ denotes that the heat flux and work are not state functions). In a quasistatic process, the different work terms are expressed as functions of different intensive magnitudes, Y_i, and its extensive counterpart, X_i, in the form of:

$$đW = \sum_i \pm Y_i dX_i \tag{2}$$

where the index i indicates the various types of work performed on the system. For example, mechanical work is expressed as $đW_{mec} = pdV$ (where p is pressure and V is volume) and magnetic work, $đW_{mag} = -\mu_0 H dm$ (where H is magnetic field, μ_0 is the free-space magnetic permeability and m is the magnetic moment). Considering a quasistatic heat flux ($đQ = TdS$, where T is temperature and S is entropy) in a closed system, the energy conservation principle can be expressed as:

$$dU = TdS - pdV + \mu_0 H dm \tag{3}$$

where the internal energy is a function of entropy, volume and magnetic moment: $U(S, V, m)$. Legendre transformations can be used to obtain different thermodynamic potentials as a function of other parameters. Normally, the experimental studies are performed at constant pressure while varying the temperature and the magnetic field, leading to Gibbs free energy as the most useful potential:

$$G(T, p, H) = U - TS + pV - m\mu_0 H \tag{4}$$

and its differential form:

$$dG = Vdp - SdT - m\mu_0 dH. \tag{5}$$

From this equation, entropy and magnetic moment can be obtained as:

$$S = -\left(\frac{\partial G}{\partial T}\right)_{p,H} \tag{6}$$

$$m = -\frac{1}{\mu_0}\left(\frac{\partial G}{\partial H}\right)_{p,T}. \tag{7}$$

The equality in the second derivate (Maxwell relations) gives the following relation:

$$\left(\frac{\partial S}{\partial H}\right)_{p,T} = \mu_0\left(\frac{\partial m}{\partial T}\right)_{p,H}. \tag{8}$$

This thermodynamic introduction can be further extended to obtain an analytical expression for MCE, which is defined as the reversible temperature change produced upon a magnetic field change in an adiabatic process. Hence, if we express the entropy as a function of magnetic field and temperature:

$$dS = \left(\frac{\partial S}{\partial T}\right)_{p,H} dT + \left(\frac{\partial S}{\partial H}\right)_{p,T} dH \tag{9}$$

and considering $dS = 0$, we get:

$$dT = -\mu_0\left[\left(\frac{\partial S}{\partial T}\right)_{p,H}\right]^{-1}\left(\frac{\partial S}{\partial H}\right)_{p,T} dH. \tag{10}$$

From the definition of the heat capacity (C) at a constant magnitude x (in our case $x = p, H$):

$$C_x = \left(\frac{đQ}{dT}\right)_x = T\left(\frac{dS}{dT}\right)_x \tag{11}$$

and combined with the Maxwell relation (8), we obtain:

$$dT = -\mu_0\frac{T}{C_{p,H}}\left(\frac{\partial m}{\partial T}\right)_{p,H} dH \tag{12}$$

while the total temperature change due to a magnetic field change is:

$$\Delta T_{ad} = -\mu_0\int_{H_I}^{H_F}\frac{T}{C_{p,H}}\left(\frac{\partial m}{\partial T}\right)_{p,H} dH \tag{13}$$

where H_F and H_I are the final and initial magnetic fields, respectively. Although it might seem that the temperature change of the sample might depend on its total magnetic moment, we have to notice that heat capacity is also an extensive variable, which eliminates the dependence of ΔT_{ad} on the size of the sample. In addition, MCE is also commonly characterized as the magnetic entropy change due to magnetic field change in an isothermal process ($dT = 0$). Then (9) takes the form of:

$$dS = \left(\frac{\partial S}{\partial H}\right)_{p,T} dH = \mu_0 \left(\frac{\partial m}{\partial T}\right)_{p,H} dH \tag{14}$$

where the total magnetic entropy change due to a magnetic field change is expressed as:

$$\Delta S_M = \mu_0 \int_{H_I}^{H_F} \left(\frac{\partial m}{\partial T}\right)_{p,H} dH \tag{15}$$

where the sign of the derivative determines the sign of ΔS_M. The case in which ΔS_M is negative is known as direct MCE while if it is positive it is denoted as inverse MCE.

Furthermore, magnetocaloric magnitudes can be correlated to heat capacity (11) by expressing the total entropy at a constant magnetic field as:

$$S_H(T) = S_0 + \int_0^T \frac{C_{p,H}}{T} dT \tag{16}$$

where S_0 is the zero entropy term. From this, the magnetocaloric magnitudes are obtained as [24,25]:

$$\Delta S_M(T, \Delta H) = [S_{H_F}(T) - S_{H_I}(T)]_T \tag{17}$$

$$\Delta T_{ad}(T, \Delta H) = [T_{H_F}(S) - T_{H_I}(S)]_S \tag{18}$$

wherein the entropy curves have to be inverted as $T_H(S)$ to calculate the adiabatic temperature change.

It can be observed in the previous expressions of MCE (Eqs. (13) and (15)) that its maximum appears when an abrupt change of magnetization exist, i.e. the region of interest will be close to a phase transition, either of first or second order type, which implies a change in the magnetic moment.

2.2. Figures of merit of the magnetocaloric effect

In order to find magnetocaloric materials with optimal properties, we need to define the figures of merit used for the comparison. The most intuitive one is the adiabatic temperature change, ΔT_{ad}, which is the temperature change of the material upon the adiabatic application of magnetic field, Eq. (13). However, magnetic entropy change, ΔS_M, Eq. (15) is easier to determine though less straightforward than the former magnitude.

The amount of heat that can be transferred between the cold and hot reservoirs, namely refrigerant capacity (*RC*) [26] (or relative cooling power by other authors, *RCP*) is defined as:

$$RC(H) = \int_{T_{cold}}^{T_{hot}} \Delta S_M(T, H)\ dT \tag{19}$$

where T_{cold} and T_{hot} are the temperatures of the reservoirs. Different approximations in the calculation of the integral give rise to the diverse definitions of *RC* available in the literature [27,28]. One typical approximation is that the temperature span between the reservoirs corresponds to the full width at half maximum (FWHM) of the peak, which could lead to numerous problems. For example, for extremely broad but short peaks their corresponding *RC* values would be large despite that such a shallow peak cannot be used for practical applications. If the peak magnitude of the adiabatic temperature change or the magnetic entropy change are too small, their *RC* would have no meaning from the practical point of view regardless of its practical definition. RC_{FWHM} approximates the integral by the product of the peak entropy change, ΔS_M^{pk}, times the full width at half maximum, δT_{FWHM}; RC_{Area} corresponds to the calculation of the area under the curve; and RC_{WP} corresponds to the area of the largest rectangle, which can be inscribed under the curve [26]. In cases when hysteretic losses are relevant and that will make the material heat up, a net *RC* upon the subtraction of these losses is required [28].

In addition, there are other figures of merit proposed for magnetocaloric materials, whereby magnetocaloric magnitudes are referred to the materials' cost [29]. One very recent suggestion is the coefficient of refrigerant performance, *CRP*, which compares the net work in a reversible cycle with the positive work on the refrigerant [30]. This implies a ratio of the reversible refrigerant capacity divided by the magnetic work performed on the magnetic refrigerant, which requires the knowledge of the magnetization curve at the transition temperature. Though this metric is highly advantageous since it removes the effect of hysteresis and it is adimensional, it is usually not possible to calculate it from literature data as the experimental magnetization curves are less commonly included in publications (or not with large enough resolution). Therefore, unlike *RC*, which can be mostly calculated from literature values, *CRP* requires additional measurements in order to evaluate it. Hence, this review covers material comparisons based on the typical magnitudes of ΔS_M^{pk}, ΔT_{ad} and *RC*, and not *CRP*.

2.3. Thermodynamic cycles

In general, a magnetic refrigerator uses a magnetocaloric material to absorb the heat of a low temperature load (cold exchanger) and discharges heat to a high temperature sink (hot exchanger). In turn, the load is cooled with repetitive cycles of these processes. These refrigerators usually consist of a working material (magnetocaloric), a variable magnetic field

generator system, hot and cold heat exchangers and a heat transfer system (using fluid or gas). Moreover, a regenerator can be included in the device. A regenerator is a thermal device that transfer heat between the different parts of the cycle, increasing the temperature span of the refrigerator. The regenerator alternatively absorbs and releases heat from/to the heat transfer fluid during different stages of the process. The regenerator is an important component of magnetic refrigerators devices due to the low temperature change of the MCE with respect to the conventional gas systems.

The refrigerators operate using the combination of various thermodynamic processes such as adiabatic, isothermal and isofield magnetizations. Consequently, the principal cycles used in a magnetic refrigerator include the Carnot, Ericsson, Brayton or AMR (active magnetic regenerator) cycles.

2.3.1. Carnot cycle

The Carnot cycle is the paradigmatic cycle for magnetic refrigeration as its processes involve the magnitudes used to characterize the MCE of the material (ΔS_M and ΔT_{ad}). In addition, it is the most efficient cycle working between two thermal sources. The cycle consists of two adiabatic and two isothermal processes (represented in Fig. 1a). While ramping to the maximum applied magnetic field, two processes occur (1 → 2): at (1), the temperature of the magnetic refrigerant increases from T_{cold} to T_{hot} under adiabatic conditions and subsequently at (2), the material isothermally exchanges heat with the high temperature sink, $Q_{hot} = T_{hot}\Delta S_M(T_{hot})$. Next, the field is decreased to its initial value, leading to a decreased temperature in the material (from T_{hot} to T_{cold}) during an adiabatic process at (3) and then a following heat absorption from the low temperature load at (4), $Q_{cold} = T_{cold}\Delta S_M(T_{cold})$.

In addition, the coefficient of performance (COP), i.e. the ratio between the refrigeration capacity,$\dot{Q}_{cold}$, and the power input, $\dot{W}$, (heat lifted/work done), when expressed in the Carnot cycle corresponds to:

$$\mathrm{COP}_{\mathrm{Carnot}} = \frac{T_{cold}}{T_{hot} - T_{cold}}. \tag{20}$$

The efficiency (η) of a refrigerator is defined as the ratio of its COP to the Carnot COP.

2.3.2. Ericsson cycle

The Ericsson cycle consists of two isothermal and two isofield processes (represented in Fig. 1b). During the isofield processes, heat regeneration is required. At (1), the magnetocaloric material is subjected to an increased magnetic field isothermally whereby its heat is discharged to the high temperature sink. Then at constant high field at (2), the sample is cooled down to T_{cold} by the heat absorption of the regenerator. Subsequently at (3), the material is demagnetized isothermally, absorbing heat from the load. Finally, the regenerator discharges heat to the material at (4), increasing the temperature of the material and closing the cycle.

For an ideal Ericsson cycle, if ΔS_M is a constant value ($S_H(T)$ curves are parallel), the performance of the cycle is optimal (the second law of thermodynamics is fulfilled as an equality and the maximum efficiency is attained).

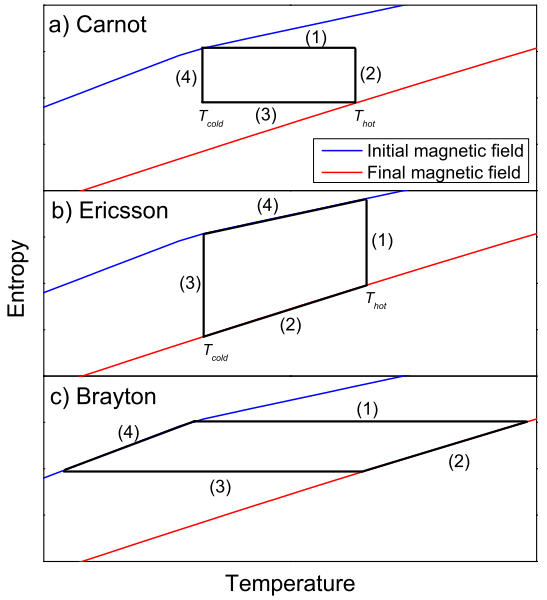

Fig. 1. *S-T* diagram representing the different Carnot, Ericsson and Brayton thermodynamic cycles used in a magnetic refrigerator.

2.3.3. Brayton cycle

The Brayton cycle consists of two adiabatic and two isofield processes (represented in Fig. 1c). Under adiabatic conditions at (1), a temperature change of the material is induced by varying the magnetic field. Subsequently, at constant magnetic field in (2), the material placed in contact with thermal fluid decreases its temperature (further cooling is achieved using a regenerator though it is unnecessary). Then, the magnetocaloric material is demagnetized adiabatically at (3), leading to a decrease in its temperature. Subsequently at constant low field at (4), the temperature of the material increases while the material is in contact with the thermal fluid (4). The Brayton cycle has a lower refrigeration capacity but larger heat rejection in comparison to Ericsson cycle.

2.3.4. AMR (Active Magnetic Regenerator) cycle

In an AMR cycle, the magnetocaloric material operates as both the refrigerant and regenerator. The AMR cycle was introduced by Steyert [31] and with the exception of the Carnot cycle, is the most efficient one for magnetic refrigeration at room temperature. The transfer fluid is required to pass through the magnetocaloric material acting as a regenerator. The AMR cycle consists of two adiabatic and two isofield processes (during which the heat regeneration occurs). The material is placed in contact at the two extreme ends of the cold and hot exchangers at T_{cold} and T_{hot}, respectively. In the beginning, the transfer fluid is at the cold side at T_{cold} and as the material is adiabatically magnetized, its temperature at the cold side increases to $T_{cold} + \Delta T_{cold}$ while in the hot side to $T_{hot} + \Delta T_{hot}$. Next, the fluid flows through the material, increasing its temperature from T_{cold} to $T_{hot} + \Delta T_{hot}$ (hotter than the high temperature sink). Then, at the hot side, the fluid discharges heat to the sink decreasing temperature to T_{hot}. Subsequently, when the material is adiabatically demagnetized, its temperature decreases to $T_{cold} - \Delta T_{cold}$ at the cold side and to $T_{hot} - \Delta T_{hot}$ at the hot side. Then, as the fluid passes through the material, its temperature reduces from T_{hot} to $T_{cold} - \Delta T_{cold}$ (lower than the temperature of the cold load). The fluid then absorbs heat from the cold load, increasing its temperature up to T_{cold} (closing the cycle).

3. Experimental methods for the characterization of the magnetocaloric effect

Typically, the characterization of MCE parameters are classified as direct and indirect methods according to how the parameters are obtained. One straightforward example of direct characterization techniques is a temperature sensor on the magnetocaloric material that is subjected to a magnetic field change, which directly determines the ΔT_{ad} of the sample. Contrastingly, indirect characterization methods require heat capacity and/or magnetization measurements data to determine ΔT_{ad} of the magnetocaloric material. Today, the indirect techniques are employed more commonly than the direct characterization methods, and one possible reason could be calorimeters and magnetometers are more commonly available in many laboratories (as compared to instrumentations measuring MCE parameters). However, the direct methods offer advantageous solutions to understand the performance of the magnetocaloric material, such as dynamic magnetocaloric properties of the material, namely dependence of $\Delta T_{ad}(T, H)$ on magnetic field change rate, which can only be obtained from the direct measurements. Furthermore, the challenges of accurately determining MCE in materials undergoing the first-order magnetic phase transition using indirect techniques still persist today. Current reported experimental apparatus, which characterized MCE parameters directly or indirectly, are discussed in the following pages.

3.1. Direct measurements

As indicated above, attractive candidates for promising magnetocaloric materials today are among those exhibiting first order magnetostructural transitions (FOPT) at transition temperatures near room temperatures. Their transition temperatures are field-dependent, hence leading to the possibility of inducing the transition by varying the magnetic fields, which produced large MCE properties (commonly termed as giant MCE). Nevertheless, the magnetostructural transitions are typically accompanied by magnetic and thermal hysteresis, raising reservations about their effective performances. Due to this hysteresis, the practice to appropriately determine the ΔS_M of FOPT materials from their magnetization data had raised many disagreements in regards to the equations used for computation as well as the way to perform the isothermal magnetization measurements (for further details, the reader is referred to the following section on indirect measurements). Therefore, the direct MCE measurements of such GMCE materials could serve as a better alternative to the open challenges in evaluating their material performances, for e.g. considering their dynamic properties and hysteretic influences.

The measurement of ΔT_{ad} had been recommended to offer a direct performance evaluation of magnetocaloric materials, instead of ΔS_M because the latter is an indirect and non-measurable parameter that only roughly estimates a quantitative MCE value [32]. Several types of experimental apparatus to directly measure ΔT_{ad} had been custom-built, and are typically classified depending on the procedure to apply the variable magnetic field to the sample (pulsed magnetic fields or static magnetic fields combined with moving samples), as well as the method for measuring the temperature change (either contact or non-contact, like the thermoacoustic method). The reader is referred to [23] for an overview of the most traditional methods.

Moreover, a commercial equipment for direct ΔT_{ad} measurements, named Magnetocaloric Measuring Setup (MMS), is available today and was also presented by Spichkin et al. (see Refs. [33,34]). The setup comprises of a Halbach permanent magnet field source (up to 1.7 T), ΔT measuring system, the measuring and control systems of both temperature and

magnetic field, measuring insert (to hold the specimen), cryogenic Dewar and control computer. This allows the characterization of the dynamic mode of ΔT_{ad}, in addition to performing multi-cycling of the measurements during the periodic variation of the magnetic field, in order to mimic the protocol followed in real practical magnetic refrigerators. One of the challenges for measuring with this type of setup is the necessity of having a large thermal mass of the sample in comparison to the sample holder. In the case of low mass samples, like melt-spun ribbons, recalibration with a standard, with a similar shape, could be needed [35].

Another concern in the performance evaluation of magnetocaloric materials arises when they are applied in practical magnetic refrigerators and subjected to accumulative cycles of ΔH, which operates in alternating (AC) magnetic fields. As the efficiencies of the refrigerators improve by increasing the working cycle frequency, this leads to alarming concerns regarding the field frequency dependence of MCE as well as the evolution of heat exchange process. The latter could be resolved by increasing the surface area of the magnetocaloric refrigerant material (i.e. thin films or ribbons) to optimize the heat transfer with the heat exchange fluid. However, the requirement of a dynamic characterization of the magnetocaloric properties remains. An experimental setup to directly measure ΔT_{ad} in modulating small amplitude magnetic fields was developed, with the aim to rectify the conventional laborious measurements like using high power inputs from large magnetic fields as well as the challenges of accurately characterizing samples with small size and mass [36]. The configuration enabled ΔT_{ad} detection using a lock-in amplifier and in small AC magnetic field generated by an electromagnet (up to 500 Oe and a frequency of 0.2–2 Hz). The authors then further developed another instrumental design to measure MCE in AC fields of frequencies up to 50 Hz, in order to investigate the AC field-frequency dependence of MCE [37]. This was attained by a custom-built alternating magnetic field source consisting of a set of four permanent magnets (0.62 T each) fixed onto a disk, which then, when rotated via stepper motor, generated AC magnetic fields with a relatively high frequency (up to 50 Hz).

As the influence of cyclic ΔH in experimental MCE data offers vital information about the material performance, it is important to evaluate that of FOPT materials, reason being their MCE can be larger during the first application of ΔH (or when characterized in quasistatic conditions) in comparison to the corresponding values measured in further runs of ΔH. For this reason, Skokov et al. developed a custom-built device to directly characterize the ΔT_{ad} of FOPT materials, with experimental protocols considering both the cyclic field dependence and temperature dependence of ΔT_{ad} [38]. The device configuration included Halbach-cylinder-configured permanent magnets (up to 1.93 T), type-T thermocouple directly in contact with the specimen and a passive adiabatic screen to minimize the radiative heat exchange between the specimen and holder. Dynamical studies of FOPT materials such as LaFeSi-based, Heusler type (Ni-Mn-In, Ni-Mn-In-Co), characterized by this setup had been reported [38,39]. These directly measured ΔT_{ad} results of Ni-Mn-In when combined with the zero-field entropy curve, enabled the determination of a large reversible ΔS_M in a fast mode (this is not possible by conventional standard calorimetric measurements alone). The cyclic field dependence of ΔT_{ad} in LaFeSi-type magnetocaloric alloys, characterized using this setup and experimental protocol, had reported a ~17% reduction in ΔT_{ad} upon field cycling.

Furthermore, apparatus designs to directly measure ΔT_{ad} in pulsed high magnetic fields (up to 55 T) with surface modifications to the test specimens were also reported [40,41]. Kohama et al. experimentally characterize C_P and ΔT_{ad} in 250 millisecond pulsed magnetic fields (up to 50 T from their report in ref. [40]) using an own-built calorimeter cell that comprised of a deposited NiCr-film (~10 nm thick) heater on one side of the sample and bare-chip resistive thermometers. The authors reported that the film indicated slight temperature and magnetic field dependences unlike thermometers: its measured magnetoresistance was 0.1% up to 45 T, which is 50× smaller than that of the resistive thermometer. They also used a high effective impedance system to generate a constant AC current during the pulse and a four-contact AC method with a digital lock-in system for the characterization of resistance of the thermometer and ΔT_{ad} of $Sr_3Cr_2O_8$ samples but proposed that the film deposited heater is less appropriate for metallic samples due to their high conductivities. In contrast, Kihara et al. fabricated a resistive film thermometer (a patterned Au_xGe_{1-x} alloy film of 100 nm thick) directly on the surface of the sample to measure its ΔT_{ad} in pulse magnetic fields up to 55 T, which could minimize the C_P of the sensor and maximize the thermal conductance between the sample and the sensor [41]. The tunable temperature dependence of resistivity of the film thermometer by its alloy composition enabled an adjustable sensitivity depending on the desired temperature range for measurements. A CaF_2 layer (150 nm thick) was developed, using vacuum evaporation technique, to electrically isolate the film thermometer from the sample. The resistance measurement of the film thermometer was performed using the standard DC four-probe practice or AC technique at 50 Hz using a digital lock-in with a time constant of 20 μs.

As previously mentioned, to prevent that the thermal mass of the temperature sensor (incorporated in many MCE measurement setups) could limit the applicability for high frequency measurements, non-contact ΔT_{ad} measurement methods were then implemented. Such instrumentation lowers the time constant of ΔT_{ad} characterization as well as improves the accuracy of the measurements [42,43]. One example, using the magneto-modulation technique (at >50 Hz and non-contact thermal radiation detection by HgCdTe-infrared detector), could perform highly sensitive low magnetic field ΔT_{ad} measurements of magnetocaloric micro- and thin-film specimens of FOPT (metamagnetic La-Fe-Co-Si) and SOPT materials [43]. Temperature-dependent measurements of the magnetocaloric peak in thin films were performed, presenting different magnetic field-dependences of the peak shapes that could be analytically expressed as interpolations between H_{ext}^2-behavior (low magnetic fields) and $H_{ext}^{2/3}$-behavior (high magnetic fields).

Recently, a non-contact direct ΔT_{ad} measurement instrumentation, which operated based on the mirage effect (an optical beam deflection technique used in photothermal spectroscopy to measure thermal diffusivity and the thermo-optical

absorption spectrum of materials) was developed to characterize the response of magnetocaloric materials to fast magnetic field pulses that represent high frequency operating conditions [44]. Using this setup to characterize for the direct ΔT_{ad} of Fe_2P-based compounds reveals that they exhibit excellent dynamic response and magnetocaloric properties, enabling their applicability. Its protocol adopts a simple and versatile measurement method as well as short measuring time, extending its applications to characterize low mass samples (i.e. ribbons, foils and thin films) with similar heat capacities as the sensors. Furthermore, the reduced measurement time constant to less than one millisecond enabled that the material's response under extreme operating conditions (1 T at a frequency of about 150 Hz) could be measured, which was a reported breakthrough.

In addition, direct MCE measurements were also extended to the characterization of ΔS_M, not only ΔT_{ad} experiments, of magnetocaloric materials using calorimetric techniques. Differential scanning calorimeter (DSC) is proposed as an appropriate study of FOPT as they directly measure the heat flux and that enabled the determination of latent heat of the transition [45]. Direct ΔS_M determination in field-induced transition had been evaluated from the calorimetric measurement curves of a purpose-built DSC which is maintained at a constant temperature during the sweeping of the magnetic field [45]. This was attained due to the induction of FOPT upon increasing the magnetic field whilst fixing the temperature of the calorimeter at above that of the peak of the transition ($H = 0$) [46]. The calorimeter operates under an applied field of up to 5 T for a temperature range of 10–300 K. In addition, this technique is based on employing differentially connected configuration of Peltier cells as heat flux sensors and its overall design could adapt to any cryostat equipped with a superconducting magnet. Adapted from this design, another custom-built calorimeter was developed, which was reported to directly characterize $\Delta S_{\mathrm{Isothermal}}$ for comparing to the barocaloric effect properties of Ni-Mn-In materials (a shape-memory alloy with FOPT) [46]. In contrast to the previously mentioned version, this device design could be placed within the poles of electromagnet, operates under magnetic fields up to 1 T and temperature control range of 200–350 K.

Another Peltier calorimetric technique, exploiting active use of Peltier heat, was also reported to directly characterize ΔS_M using an electromagnet as the magnetic field source (up to 2.3 T) [47]. In this case, the power-type Peltier cells were arranged in a sandwich configuration to actively function as heat pump and heat flow sensor, enabling measurements recorded using a digital feedback control. The authors reported that the measured entropy change as a function of magnetic field at the critical transition temperatures of a FOPT material revealed superposition of two contributions, one associated with the latent heat of the FOPT (which is hysteretic) and another with the conventional MCE of the phases without hysteresis. This active use of Peltier cells in calorimeters to perform direct MCE measurements avoided the unfavorable introduction of time delays by the sample from the passive techniques. However, the former is still limited by the time constants of the measuring cells, leading the authors to construct another design to investigate the dynamics of the symmetric differential arrangement of Peltier cells with theoretical heat flux diffusion models in the calorimeter [48]. Hence, a symmetric arrangement was used for the advanced setup. In this case, two types of Peltier cells were utilized: miniaturized ones for measuring heat flux while power-type cells for temperature regulation. The setup is capable of characterizing for specific C_P under constant magnetic field and ΔS_M induced by the variable magnetic field below room temperature. The authors demonstrated that their developed models, through this calorimeter setup, could enable kinetic corrections on the influence of time constants of the measuring cells, from the agreement of ΔS_M results obtained from the direct isothermal measurements and from the integration of measured C_P data. Another rather similar setup was reported by Nielsen et al. [49]. The modifications include using Halbach-type magnets as magnetic field source and fully automated systematic resetting function of the thermal and magnetic histories of the sample for measurements.

Another calorimetric technique for direct ΔS_M and ΔT_{ad} measurements using own-built adiabatic calorimetry instrumentation had been reported [48]. The setup included specially designed cryocooler from Cryogenic Limited and modified commercial adiabatic calorimeters (from Termis Ltd.) to directly characterize C_p, ΔS_M and ΔT_{ad} at magnetic fields (up to 9 T). Taking into consideration the influences of thermal and magnetic histories of the magnetic samples (especially FOPT materials), the authors developed appropriate experimental measurement protocols during increasing and decreasing the magnetic fields respectively. This led them to attain consistent ΔS_M results for a given sample, exhibiting FOPT with hysteresis, obtained from different techniques (direct measurements and indirect determination from magnetization and C_p measurements). As a result, this could address the open questions regarding the peak values of ΔS_M (computed from magnetization data) larger than the corresponding values calculated from C_p or direct thermal measurements for the same sample [50,51]. Moreover, the same characterization protocols were demonstrated to be also applicable to direct ΔT_{ad} measurements of FOPT materials using the same calorimeter, giving consistent ΔT_{ad} results that were determined directly or computed indirectly from C_p data. The materials studied using this adiabatic calorimetry instrumentation include Gd, Gd-Si-Ge-based materials, Mn-Co-As and Ni-Co-Mn-Sn alloys [51–54].

3.2. Indirect measurements

In general, indirect methods of MCE determination involved using magnetization data to calculate $\Delta S_M(T, H)$ and C_P data to compute $\Delta T_{ad}(T, H)$ and $\Delta S_M(T, H)$. As mentioned earlier and in many review papers associated to MCE, the calculation of $\Delta S_M(T, H)$ using one of the Maxwells relations, strictly speaking, is only applicable to SOPT cases due to the infinite term of $\partial M/\partial T$ at FOPT. Hence, ΔS_M of the latter could be determined using the Clausius-Clapeyron equation instead. However, the large artifacts found in the determination of ΔS_M from magnetization data of FOPT materials are not due to this divergence

but to the phase coexistence that takes place while the transition is taking place. The indirect characterization of MCE is performed using magnetometers and calorimeters as experimental techniques.

Magnetometry, which is readily accessible in numerous laboratories, has been the most common method used to map out *M(H, T)* of magnetocaloric samples to indirectly determine $\Delta S_M(T, H)$. The *M(H, T)* measurements are typically time consuming, especially in the case of FOPT. Thus, a conventional vibrating sample magnetometer (VSM) is well suited to perform these tedious measurements within the range applicable for room temperature magnetocaloric devices ($\mu_0\Delta H$ = 0–2 T; ΔT = 200–350 K) as compared to using a helium-cooled superconducting magnet (though it could offer higher magnetic fields up to 10 T and wider temperature range down to few kelvins). In the VSM method, the vibration of the sample within the constant uniform magnetic field led to an induced voltage measured in the pickup coils, which is used to determine the magnetic moment of the sample. It is sensitive enough to characterize samples of small mass and volume (starting from less than one cubic millimeter) and of any shape (bulk, plates, fragments, powders, etc.) though care has to be taken in order to avoid artifacts emerging from the demagnetizing field in the sample [55]. In general, it measures bulk magnetization and yields specific magnetization when divided by sample mass, which then calculates ΔS_M per unit mass. In order to convert the results to magnetic entropy change per unit volume, the density of the sample should be known. This is a trivial problem for bulk alloys, but can pose some difficulties for powder samples, porous materials, etc. being the reason why most of the magnetocaloric literature quotes the values per unit mass.

Basically, there are two methods to perform *M(T, H)* measurements for MCE determination: (1) iso-field $M(T)$ measurement curves for different values of applied field, or (2) isothermal $M(H)$ measurement curves at different temperatures. For the first technique, $\partial M/\partial T$ from the experimental results could be numerically integrated to determine ΔS_M, while in the second method the integrated area between two magnetization isotherms is used to compute ΔS_M at intermediate temperature. A tradeoff should be found between the smoothness of the obtained ΔS_M curves (the larger the temperature step used in the experiments, the lower the noise introduced in the curves by numerical derivation) and the temperature resolution of the curves (a smaller temperature increment will produce denser curves).

Regarding the speed of measurement, it is typically faster to keep the temperature constant and sweep the magnetic field (method 2 above) than varying the temperature for different constant values of applied magnetic field (method 1). Therefore, if we only focus on speed, isothermal $M(H)$ curves would be the method of choice. This method will give appropriate results for materials with a SOPT with no further precaution. However, the coexistence of phases in FOPT imposes certain restrictions on the way that the isothermal curves should be measured [50,56] and the application of Maxwell relation to isothermal magnetization curves gives unphysical magnetic entropy change spikes unless the sample is properly prepared before each measurement. To avoid these spurious results, two different approaches can be followed: either measuring isofield magnetization curves or preparing the sample to be in a single-phase state before each isothermal measurement [57]. A detailed description of the measurement protocols can be found in a recently published application note [58], and an example of their application to LaPrFeSi in [59]. In summary, $M(T)$ measurements can give reliable results, while $M(H)$ measurements require to saturate the transformation by heating to a temperature well above/below the transition to make it complete in the presence/absence of magnetic field, prior to reaching the desired measuring temperature and acquiring the $M(H)$ curve. The presence or absence of applied field during this procedure of erasing the memory of the material (analogous to saturation before making a $M(H)$ hysteresis loop for conventional ferromagnets) depends on the nature of the transition. For example, if the transition shifts to higher temperatures upon the application of magnetic field, the erasing procedure should include stages of heating the sample in zero field or cooling it in high field. This is the case for LaFeSi-type alloys.

It is important to note that magnetocaloric materials, by definition, change their temperature when subjected to a variant magnetic field adiabatically. Therefore, artifacts might appear when the ramp rates of magnetic field are too fast [60,61].

As for calorimetric technique for indirect determination of MCE, $C_P(H)$ is needed to assess the performance of a magnetocaloric material, however most commercial calorimeters could only measure the temperature dependence of the specific heat in the absence of magnetic field for a given sample and adapting them to measure in magnetic fields can be sophisticated. Basically, there are two reported varieties of calorimeters measuring C_P for magnetocaloric assessment: heat pulse type (the temperature of the sample is measured upon a known amount of heat supplied for a definite time interval while a constant temperature of the calorimeter is maintained during the measurement) and scanning types (whereby the temperature of the calorimeter is continuously changed while measuring the heat flux between a thermal block and the sample). Most of these utilize two heat flow sensors so that one can behave as a reference and enable the calorimeter to work differentially, and are known as DSC, which are the current custom-built designs specifically for MCE measurements (due to their shorter measurement durations and better precision to characterize C_P near FOPT) [62]. Nonetheless, heat pulse calorimeters were typically used for MCE characterization (e.g. a completely automatic design rapidly measuring C_P within ~3–350 K up to 10 T was reported by Pecharsky et al. [63]) before a customized DSC, using Peltier cells as heat flow sensors, was demonstrated to obtain highly reproducible C_P data with high sensitivity [64]. Many devices which adopted a similar approach were developed and some examples were mentioned in previous section that directly characterize MCE (whereas the original idea in using Peltier cells as heat flow sensors in [64] performs measurements of C_P and an approximation of heat release accompanying a magnetization process). An example of a customized DSC based on Peltier elements as heat flow sensors was developed by Jeppesen et al., which could indirectly determine MCE [65]. It operated in a temperature range of 200–340 K up to 1.8 T, giving a signal/noise ratio of 10^2–10^3, and its configuration could be further used with other types of magnets (permanent magnets, superconducting coils) and in a wider temperature range.

A contrasting approach of a thin film nanocalorimeter based on a commercial microchip module (comprised of submicron silicon nitride membrane with a film-thermopile and a resistive film-heater) and AC calorimetry had been reported [66,67]. It was shown capable of measuring C_P of low-mass samples (micrograms) within 5–300 K up to 8 T.

Furthermore, it is worth mentioning that to calculate the total entropy of the material from heat capacity data, it is necessary to perform measurements at temperatures close to zero kelvin and to know the zero entropy term (see Eq. (16)). If the zero entropy term is assumed field independent, it has no influence on $\Delta S_M(T)$ and $\Delta T_{ad}(T)$ curves. On the other hand, the necessity to reach temperatures close to zero kelvin would preferably be avoided. It has been found that starting the measurement at certain temperature (relatively close to the transition temperature) the magnetocaloric magnitudes are the same as those starting from zero kelvin. This temperature is the same for both $\Delta S_M(T)$ and $\Delta T_{ad}(T)$ [68]. Furthermore, this had been theoretically studied using numerical calculations of the Bean and Rodbell model, and experimentally investigated applicable to SOPT materials, like Gd-Zn [68] and Gd [69], and FOPT materials, like $Gd_5Si_2Ge_2$ [69]. This proposed method of identifying the optimal start temperature is based on the requirement that magnetocaloric curves go to zero at their high temperature tails. In this way, when starting from this optimal temperature, the magnetocaloric curve is the same as that starting from 0 K, minimizing the error.

Both calorimetric and magnetic measurement techniques, when using the proper measurement protocols, are able to provide reliable values for the magnetocaloric characteristics of materials. The analysis of error propagation [24] indicates that, depending on the sample and on experimental conditions, there are circumstances in which heat capacity techniques can provide lower absolute errors than results obtained from magnetization measurements (e.g. for $ErAl_2$ in Ref. [24]), while other cases provide comparable values of the total error (e.g. Gd metal in the same reference). Therefore, for each experiment, the actual contributions to the errors in the magnetocaloric magnitudes should be determined.

3.3. Dynamic magnetocaloric effect

An important point to consider in the selection of a magnetocaloric material for its application in a real refrigerator device is its operation in cycles of cooling and heating, magnetization and demagnetization. Theoretical estimates of the frequency limit in the operations of these devices indicate values in the order of 100 Hz [70]. Although this frequency is much larger than the one used nowadays, it gives us a warning that even if the quasistatic characterization of materials is an important starting point, the ultimate comparison among magnetic refrigerants should be based on their cyclic and dynamic performances.

Unfortunately, most of the published literature focus on the quasistatic characterization of samples. In the case of indirect characterization methods, like those based on magnetization measurements, they are by definition quasistatic, as the whole set of $M(T,H)$ curves has to be acquired before calculating the magnetic entropy change. As previously mentioned for first order phase transitions, the incomplete transformation of phases would give rise to artifacts when determining ΔS_M, which prevents the direct realization of cycles. However, it has recently been shown that the cyclic response of the material can be extracted from the quasistatically determined $\Delta S_M(T)$ curves as the intersection of the heating and cooling curves [59].

For the direct measurement of adiabatic temperature change, the procedure to get its cyclic response is less complicated as the measurement protocol can mimic the cycles performed in the refrigerator device and directly measure the cyclic changes of temperature. They might be, however, smaller than those predicted for the whole transformation since the loops undergone by the material in a refrigerator device might not accomplish the complete transformation. Nevertheless, there are procedures to predict this amount of reduction of the performance metrics [59].

Another important parameter of the magnetocaloric materials for their eventual applications is the influence of the rate of magnetic field variation on their ΔS_M and ΔT_{ad} values. Experimentally, the most straightforward way to produce a fast variation of magnetic field is using pulsed facilities. In that way, sweep rates up to 1500 T/s can be achieved [44,71,72]. In the case of Heusler alloys, the analysis of the dynamic behavior reveals that the nucleation process of the emerging phase is rather slow as compared to the movement of the phase boundary, posing a limitation for cycles above 100 Hz [72]. However, for the typical frequencies used nowadays in magnetic refrigeration, dynamical effects do not seem to be of a concern.

4. Models of the magnetocaloric effect

Some of the new magnetocaloric materials found in the literature are discovered through a process of trial and error. In some cases, the search of materials was based on the crystallographic structure of phases, the magnitude of their magnetization, etc., and has led to an initial discovery of a promising material, which could be subsequently refined for better properties. However, as in many other branches of science, the exhaustive search approach for solving the problem usually leads to a limited success, when results are compared to the efforts (time, costs, etc.) required to identify new magnetocaloric materials. In order to find new potential magnetocaloric materials, it is necessary to understand the mechanisms of large MCE (or even small MCE) reported in already known alloys and compounds. The models developed for their magnetothermal responses can facilitate the discovery of modifications, which would even further enhance their performance. In addition, models developed for a known material can be useful for predicting its response under different excitation conditions. If the model is properly developed, the time hassle in validation experiments can be minimized as only selected excitation conditions should be measured; subsequently, the performance of a device could be predicted by using the model.

The classification of models used in this field of research can be made between thermodynamic models and first principle models. Thermodynamic models are less capable for the identification of new materials but are extremely useful to evaluate the response of known materials (and some compositional variations) under multitude of excitation conditions. Therefore, they are also suitable to be introduced in models of the performance of magnetic refrigerators. First principle models are generally more suitable to predict the behavior of unknown alloys and compounds, streamlining the search for new compositions but that requires a detailed knowledge of the possible phases that will be present in the material. In this section, we will outline the main characteristics of the most representative cases of both families of models.

4.1. Thermodynamic models

Thermodynamic models utilize macroscopic variables to describe the change of magnetization with field and temperature. In many cases, this is made via equations of state (EOS), which link the magnitudes M, H and T, and the variables that describe the material under study are identified by fitting the experimental measurements to those EOS. Alternatively, Preisach models have been developed to reproduce the hysteretic behavior of FOPT [73].

For SOPT, the EOS can be obtained from a power expansion of the thermodynamic potential following the formalism of Landau [74]. Depending on the number of terms that we keep in the power expansion, the description can be almost accurate including corrections to the first order mean field approximation. Another possibility is to use a heuristic approach to tailor a known EOS to the material by including additional features known to be fulfilled in it. An example of this type of EOS is that of Arrott-Noakes [75], wherein the critical behavior with exponents different from those of the mean field ones was incorporated:

$$H^{\frac{1}{\gamma}} = a(T - T_C)M^{\frac{1}{\gamma}} + bM^{\frac{1}{\beta}+\frac{1}{\gamma}} \tag{21}$$

where a and b are characteristic parameters of the material under study and β and γ are the critical exponents. In this way, we can control the universality class to which the material belongs. This EOS has been extensively used for the study of SOPT magnetocaloric materials [76–79] and was the initial basis on which the scaling of magnetocaloric response and its universal curve was founded [76,80]. The phenomenological construction of the universal curve, which was also extended to ΔT_{ad} [33], has been used to predict the behavior of samples in experimental conditions that were not available in the laboratory (for e.g. larger magnetic fields or temperatures not within the experimental limits of the device).

For FOPT materials, the most popular EOS in the field of magnetocaloric research is the one from Bean and Rodbell [81]. This was initially developed to study the first order transition in MnAs compound. Based on experimental results, the phenomenological dependence of the exchange interaction on the inter-atomic spacing was considered and was introduced into the dependence of critical temperature on the volume change. With a control parameter η, the order of the transition from SOPT ($0 \leq \eta < 1$) to FOPT ($\eta > 1$) can be modified. Recently, it has been shown that the case $\eta = 1$ corresponds to the tricritical point, i.e. to the separation of first and second order phase transitions, and the critical exponents coincide with those associated to that special point [82]. This model has been successfully applied to a variety of magnetocaloric materials beyond the original MnAs [83–86].

There are some limitations to be considered when using these models based on an EOS for describing the magnetocaloric response of materials. The main one is that the material must be in technical saturation as EOS relates state functions, which are dependent on the state of the system and not the route followed to achieve it. Therefore, if there is a multi-domain configuration (e.g. for small fields), the magnetization of the sample will depend on how its different domains are configured, which is dependent on the history of magnetization and temperature that the sample followed. Therefore, results obtained from the model of the magnetic entropy change under small fields has to be analyzed with precaution.

Moreover, thermomagnetic hysteresis of FOPT materials can be further characterized using FORC (first order reversal curves). It provides a comprehensive fingerprint of the M(T,H) curves under excitation conditions that are not limited to saturation loops although it cannot be considered as a thermodynamic model of the material under study. Once the FORC distribution is obtained, it can model the behavior of the material under different minor loops of temperature and field. In particular, there is a growing interest on the T-FORC (temperature-FORC) characterization of magnetocaloric materials [87] and its use to determine how the hysteretic behavior is affected by temperature and magnetic field.

4.2. First principle models

The use of first principles calculations of exchange coupling energies and magnetic moments of magnetocaloric materials has become a usual procedure in the study of first order phase transition materials [88–94].

In most cases, modelling is performed with a two-stage approach [90,95]. Firstly, first principles calculations, using Density Functional Theory, are used to predict the zero temperature properties of the material; subsequently, the obtained magnitudes are used as inputs in thermomagnetic models, such as the Bean & Rodbell model [81], to extract information about the values of magnetization at finite temperatures, magnetic entropy, magnetostructural transition temperatures, and MCE.

More recently, the disordered local moment formalism, which is a model for metals above their Curie temperatures [96], has been used to study the temperature dependent properties and MCE of different materials, like FeRh [97,98], Lanthanide intermetallics [99] and LaFeSi [100].

In general, a good agreement is found between the experimental results and the outcome of the models. However, it has to be considered that such models require a fair amount of details of the studied material, which somehow limits the predictive power to materials relatively similar to those previously analyzed.

5. Magnetocaloric materials

5.1. Crystalline materials

5.1.1. Rare earth (RE) containing crystalline materials

Magnetocaloric behavior of pure lanthanide elements can be found in the review paper on magnetocaloric materials published in 2000 by Gschneidner and Pecharsky [11]. Among them, Gd is the only pure metal with a Curie temperature close to room temperature. For intra-lanthanides we also suggest to visit that review paper [11]. Slight improvement of MCE response in Gd has been reported by small addition of Nb [101] or Fe [102].

Small additions of B to Gd in $Gd_{1-x}B_x$ (x = 0–0.07) preserved the parent hexagonal structure while slightly increasing the cell volume. For x = 0.02, the alloy displayed $\Delta S_M = -2.8$ J kg^{-1} K^{-1} ($\mu_0\Delta H$ = 1 T) at T_C = 298 K and retained a constant ΔS_M at higher B contents [103]. Unlike for arc-melted samples, in $Gd_{1-x}B_x$ melt spun ribbons, the formation of GdB_2 and Gd_2B_5 is prevented even for x = 0.20, keeping T_C constant but causing a continuous decrease of MCE properties with the increasing B content [104].

Earlier in 1997, Gschneidner et al. [105] studied $Gd_{1-x}C_x$ solid solutions, which exhibit hexagonal structure and displayed constant MCE values for minor C additions (up to x = 0.025) [106] and a slight increase of T_C. However, the crystallization of an impurity Gd_2C phase occurred, which had a T_C = 623 K and a rhombohedral $CdCl_2$-type structure. With higher C content, T_C increased while $|\Delta S_M|$ progressively decreased. Theoretical studies using Monte Carlo simulations [107] showed an agreement of increasing T_C for C additions only up to x = 0.09, but predicted higher values of magnetic entropy change, which could be ascribed to the presence of Gd_2C impurities observed experimentally [105,106]. Partial substitution of Dy for Gd in $Gd_{0.98-x}Dy_xC_{0.02}$ tuned T_C between 295 K and 275 K for x = 0 and x = 0.2 respectively [108].

H impurities in GdH_x (x from 0 to 0.15) slightly increased T_C and broadened the magnetic transition [109]. Within this compositional range, ΔT_{ad} decreased from 4.9 K to 4.3 K at 1.78 T as the hydrogen content increased. In addition, the hydrogenated samples exhibit an increased electrical resistivity, which is an additional advantage.

Additions of Mn [110] or In [111] to hexagonal Gd decreased T_C without significant effects on MCE. However, $GdMn_2$ phase was formed in $Gd_{1-x}Mn_x$, which amount increases as Mn content increases in the alloy for x = 0.05–0.2, while for $Gd_{1-y}In_y$, a solid solution free of impurities was obtained up to y = 0.04 [112].

Ga substitution in $Gd_{100-x}Ga_x$ also led to a decrease of T_C. Jayaraman et al. [113] produced $Gd_{100-x}Ga_x$ (x = 0, 5, 10, 15, and 20 at.%) by conventional melting as well as rapid quenching, and in both cases α-Gd and Gd_5Ga_3 phases were found.

Recently, Provenzano et al. [114] reported a clear enhancement in both *RC* and ΔS_M with 10 at.% substitution of Fe and Co for Gd. As Fe and Co are insoluble in Gd hexagonal phase, they are located at the grain boundaries of Gd grains, forming a $(Fe, Co)_2Gd$ phase, which exhibits a higher T_C than that of Gd.

Room temperature MCE has been also studied for other Gd-M binary compounds such as $Gd_{0.85}Y_{0.15}$, $Gd_{0.85}Tb_{0.15}$ (peak temperature of MCE decreases and $\Delta T_{ad} \sim 2$ K at 1 T) [115], $Gd_{0.75}Zn_{0.25}$ [115,116] systems. Partial substitution of Pr or Nd for Gd in $Gd_{1-x}RE_x$ ($x \leq 0.05$) shows equivalent, close to linear, decreases of T_C as x increased [117]. Composites of $Gd_{1-x}Ho_x$ alloys (x = 0, 0.09 and 0.20 with mass ratios 0.59, 0.17 and 0.24, respectively) have been recently proposed to optimize flat MCE response in the region between 265 and 293 K, adequate for Ericsson refrigeration cycle [118]. $Gd_{1-x}Y_x$ (x from 0 to 0.4) alloys produced by arc-melting, exhibit some Gd and Y residual phases. Y substitution in the studied range linearly reduces T_C of this SOPT from 296 to 196 K, whereas $|\Delta S_M|$ decreases from 5.43 to 4.24 J kg^{-1} K^{-1} for x = 0–0.4 at 3 T [119]. The summarized influential studies of various elemental additions on T_C and ΔS_M of hexagonal Gd is presented in Fig. 2.

Other results are focused on low dimensional systems such as nanocrystalline Gd [120], Gd/W thin film heterostructures [121] and Gd/Ti multilayers [122,123]. Ultrathin films of Dy [124] and Ho [125] show a strong enhancement of MCE for low field changes when the thickness of the film is below the helix period whereby the helical structure is not formed. Dy nanoparticles and coated Dy nanocapsules have been also studied [126]. Superparamagnetic behavior is observed due to the small particle size (3.6 nm, smaller than the helix period). $\Delta S_M > 2$ J kg^{-1} K^{-1} is obtained from 7.5 to 105 K when field changes from 1 to 5 T. Novel routes to process Gd can be found in the recent literature: films deposition [127] or upon subjected to severe plastic deformation [128]. Recently, Dudek et al. [129] proposed a different approach to enhance MCE using magneto-auxetic systems predicting that mechanical stimulus could lead to large magnetic entropy changes. Caloric and multicaloric effects have been recently revised by Crossley et al. [130], Starkov et al. [131], and, particularly in multiferroic systems, by Flerov et al. [132] and Balli et al. [133].

In this section, several rare earth containing families of materials, whose MCE have deserved the interest of the research community, will be described in the following order: Laves phases, $La[Fe(SiAl)]_{13}$ compounds, $Gd_5(Si,Ge)_4$ compounds, $ThCr_2Si_2$-type compounds, ferromagnetic Lanthanum manganites and other RE containing compounds. As a general rule, the different compounds described will be classified by their crystal structures. The different references collected in this review usually describe this characteristic of their studied samples. However, further information for RE containing intermetallics could be found in [134].

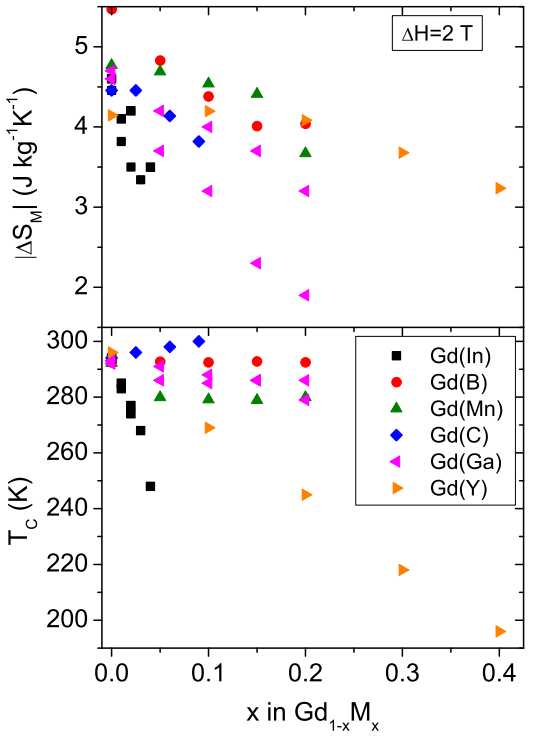

Fig. 2. Effect of the addition of some elements to hexagonal Gd on its T_C and ΔS_M. Data taken from [104,106,110–113,119]. For [106], [111] and [119], values of ΔS_M have been rescaled from $\mu_0\Delta H$ = 1 T to 2 T using the field dependence law with an exponent n = 0.67 [76].

5.1.1.1. Laves phases. Laves phases, named after the German crystallographer Fritz H. Laves [135], present a stoichiometry AB_2 with a structural configuration mainly due to a close packing structure of spherical atoms instead of chemical bonding. These phases crystallize in three types of structures [136]: cubic $MgCu_2$-type and hexagonal $MgZn_2$ and $MgNi_2$ structures (Fig. 3). The AB_2 intermetallic compounds with interesting magnetocaloric properties exhibit the cubic phase (space group *Fd*-3*m*), whereby *A* is a rare earth metal (including Sc and Y) and *B* mainly is a transition metal (other elements as Al, Ga, Ge, etc. can be found). However, there are other cases in which non-cubic Laves phases are reported to display MCE, such as ternary compounds of $Hf_{1-x}Ta_xFe_2$ [137,138], GdFeAl [139], DyCoAl [140] and DyFeAl ($-\Delta S_M$ = 6.4 J kg^{-1} K^{-1} at 130 K and 5 T and the critical exponents were determined) [141] whereby they crystallize in $MgZn_2$-type structure (space group $P6_3/mmc$). $Hf_{0.83}Ta_{0.17}Fe_2$ presents a FOPT and GMCE ($|\Delta S_M|$ = 18 J kg^{-1} K^{-1} at 1 T and 225 K), which are ascribed to AFM-FM transition [137]. However, this value is in contradiction with the results previously obtained by Herbst et al. at slightly lower fields [142] ($|\Delta S_M|$ = 1.5 J kg^{-1} K^{-1} at $\mu_0\Delta H$ = 0.9 T and 225 K). On the other hand, Diop et al. [143] reported an intermediate value for $Hf_{0.825}Ta_{0.175}Fe_2$ ~5 J kg^{-1} K^{-1} at $\mu_0\Delta H$ = 1 T but below 200 K, despite that the peak extends to higher temperatures at higher fields. Recent results [144] show that the presence of supercooled AFM and superheated FM states leads to unconventional thermal effects in $Hf_{0.82}Ta_{0.18}Fe_2$. Dong et al. studied partial substitution of Co for Fe [145] and Zr for Hf in (Hf, Ta)Fe_2 [146]. Both substitutions led to a decrease of the transition temperatures but Co reduces MCE, while Fe enhances it.

As shown in Fig. 3, RE atoms in the cubic $MgCu_2$-type structure form a diamond lattice while *B* atoms surround the RE atoms forming a tetrahedra. In those cases where transition metal is present, itinerant electron magnetism from TM can also occur in addition to the magnetic sublattice formed by RE. This phenomenon has been systematically studied for Co containing Laves phases. In $RECo_2$ compounds, the two magnetic sublattices either couple parallel for light RE or antiparallel for heavy RE. Therefore, Laves phases with Pr, Nd and Sm are ferromagnets (T_C = 40, 98 and 220 K respectively) while with Gd, Tb, Dy, Ho and Er are ferrimagnets (FiM) (T_C = 406, 231, 138, 78 and 32 K respectively) [147–151]. Moreover, FiM $HoCo_2$ (T_C = 78 K) and FM $NdCo_2$ (T_C = 98 K) undergo a spin reorientation transition, which is FOPT, at 16 and 42 K respectively [148]. Mudryk et al. [152], combining magnetic and in situ X-ray diffraction experiments, have recently shown that the magnetic moment of Co in $HoCo_2$ was reduced below its spin reorientation transition and its PM-FiM transition was assisted by itinerant electron metamagnetism.

Laves phases can present FOPT or SOPT. In the case that itinerant electron metamagnetic transition occurs in Laves phases, GMCE has been reported and a related review can be found in reference [153]. One example is $RECo_2$ system. Khmelevskyi and Mohn [154] developed a model predicting the order of the magnetic transition in $RECo_2$ using the lattice parameter by considering magnetovolume effects and spin fluctuations. For large lattice parameters (>0.722 nm), SOPT occurs as the Co atom carries a magnetic moment whereas for small lattice parameters (<0.705 nm), Co has no magnetic moment.

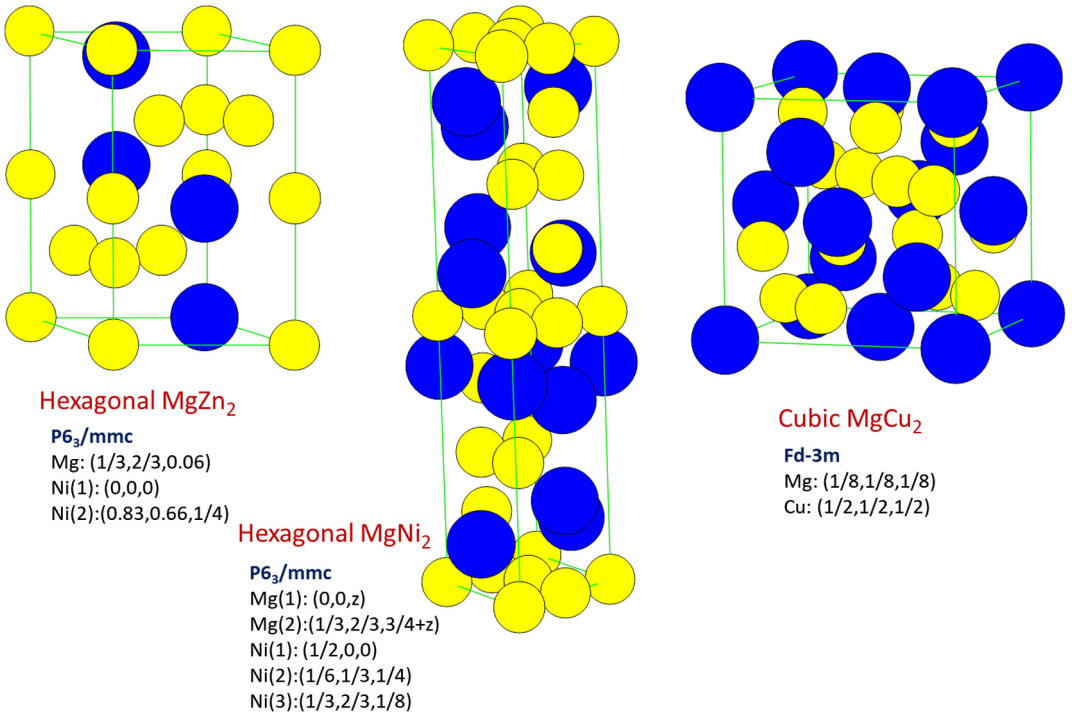

Fig. 3. Structure of the Laves phases presenting interesting MCE properties. Blue spheres correspond to Mg atoms.

Between those limits, itinerant electron metamagnetic transition (and thus FOPT) can be induced after the induction of magnetic moments in the transition metal sublattice from the molecular field of the RE sublattice. However, there are two exceptions in this series: $TbCo_2$ and $TmCo_2$. Both exhibit SOPT despite their corresponding lattice parameters (0.721 nm and 0.714 nm respectively) are within the theoretical limits of the model. In the case of $TbCo_2$, their high T_C (>200 K) can lead to spin fluctuations effects. In $TmCo_2$, $T_C = 4$ K but its molecular field is assumed to be very weak and insufficient to induce metamagnetism in the Co sublattice. In addition, there is a good agreement of the predictions of Khmelevskyi and Mohn with the experimental results of element substitutions and pressure application in $RECo_2$. E.g., element substitution leads to an increase of the lattice parameter in $RECo_2$, which tunes T_C to higher temperatures but at the expense of its FOPT. Similarly, pressure application reduces the cell volume and yields a decrease of transition temperatures [153]. Due to the interplay of magnetic transition and cell parameters, it is worth mentioning that lattice parameters of the different pseudo-binary alloys follows linearity or Vegard law (Fig. 4).

The first studies on MCE of Laves phases were reported by Nikitin and Tishin for $HoCo_2$ ($\Delta T_{ad} = 5$ K at $\mu_0\Delta H = 6$ T and T < 100 K) [155]. It is worth mentioning that although $|\Delta S_M|$ increases with ΔH in MCE materials with FOPT, it is mostly the broadening of the MCE peak that significantly enhances *RC*. On the other hand in SOPT materials, both their ΔS_M and

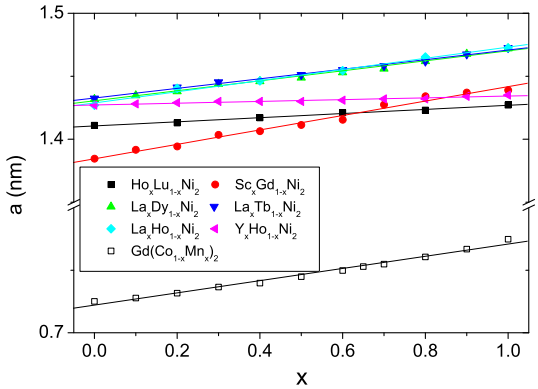

Fig. 4. Vegard law behavior for $Gd(Co,Mn)_2$ alloy series crystallizing in cubic Laves structure [187] and for several $RENi_2$ compounds crystallizing in a cubic superstructure of cubic Laves phase [192,198–200,202,1559].

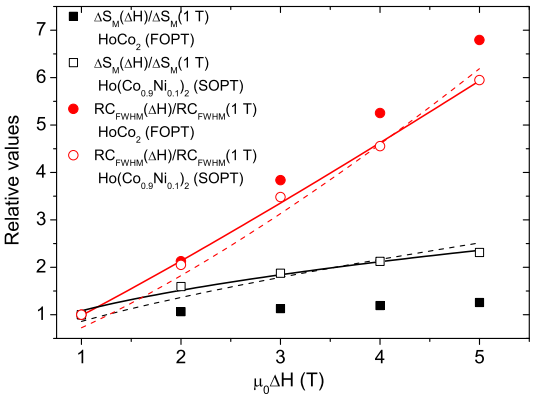

Fig. 5. Relative enhancement of ΔS_M and RC_{FWHM} for $HoCo_2$ Laves phase, with a FOPT, and $Ho(Co_{0.9}Ni_{0.1})_2$ Laves phase, with a SOPT, using the data of Ref. [156]. The solid lines correspond to the fitting of the SOPT data to power laws $\Delta S_M(H) = AH^n$ (n = 0.48 ± 0.04) and $RC_{FWHM} = BH^m$ (m = 1.12 ± 0.04), respectively. The dashed lines represent the same fitting using mean field values (n = 2/3 and m = 4/3).

RC clearly enhances with ΔH. This can be observed from the relative change of ΔS_M and RC_{FWHM} shown in Fig. 5, using the data from Ref. [156]. The universal curve describing the MCE behavior for SOPT has been successfully applied for several Laves phases undergoing such transition: $Tb(Co,Fe)_2$ [157,158], other $RECo_2$ [148] and $(Er,Dy)Al_2$ [159]. Von Ranke and co-workers, using molecular field approach and accounting for the influence of crystalline electrical field [160], reproduced the experimental MCE data of $REAl_2$ (RE = Dy and Er). Later they considered a Heisenberg Hamiltonian model to account for short range interactions [161] and Álvarez et al. [162] included the magnetic fluctuations in the analysis. The model was also extended to $RECo_2$ systems with FOPT, considering that the localized spins of RE ions are immersed in an effective subsystem of itinerant electrons from the 3d band of Co atoms [163]. In the frame of these models, they can reproduce the anomalous effect found in some Laves aluminide phases [164] and the change from FOPT to SOPT [165]. Hysteretic losses are ascribed to FOPT (see for example Ref. [166]).

In general, most of the Laves phases that are attractive for MCE exhibit transition temperatures below 100 K, while those with transition temperatures above 100 K typically comprises of Co as TM (although they could also display low transition temperatures). The relationship between $|\Delta S_M|$ and T_C (measured at $\mu_0\Delta H$ = 5 T) of this family of alloys is presented in Fig. 6. In addition, studies on pseudo-binary compounds are also reported for $(Ho,Tb)Co_2$ [167], $(Ho,Gd)Co_2$ [168], $(Er,Dy)Co_2$ [166,169,170], $(Er,Dy,Gd)Co_2$ [171], $(Er,Ho)Co_2$ [166], $(Ho,Dy)Co_2$ [172], $(Tb,Dy)Co_2$ [173], $(Tb,Dy,Er)Co_2$ [174], $(Tb,Ce)Co_2$ [175], and more recently for $(Tb,Er)Co_2$ and $(Tb,Ho)Co_2$ [176]. Transition temperatures in Laves family can be tuned to above 300 K. However, $|\Delta S_M|$ decreases exponentially with transition temperature, regardless the order of the transition, as shown in Fig. 6. As a general rule for this family, as the Curie temperature increases, FOPT changes to SOPT.

Minor partial substitutions of non-magnetic elements for Co in $DyCo_2$ or $GdCo_2$ were reported to shift transition temperatures to higher values as observed for $Dy(Co_{1-x}Al_x)_2$ [177], whereby its T_C increased from 143 K (x = 0) to 206 K (x = 0.1) and changing from FOPT for $x \leq 0.02$ to SOPT for $x \geq 0.04$. Another example is $Gd(Co,Al)_2$ [149], which T_C initially increased from 406 (x = 0) to 418 K for x = 0.05, then decreased to 357 K for x = 0.4, and its lattice parameters increased to above 0.7259 nm and exhibits SOPT. Results on $Dy(Co_{1-x}Ga_x)_2$ were also reported [178] which T_C increases up to 196 K for x = 0.2, although

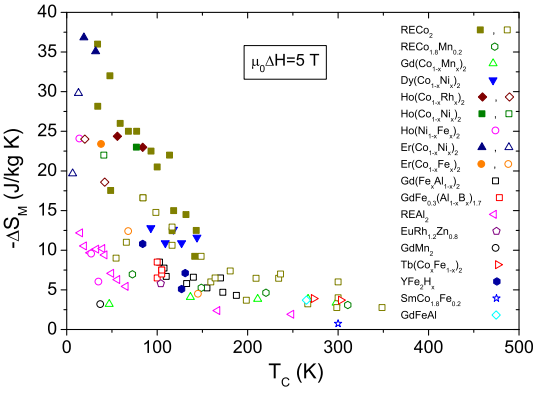

Fig. 6. Maximum magnetic entropy change as a function of the corresponding transition temperature for different Laves phases at $\mu_0\Delta H$ = 5 T. Solid circles correspond to FOPT and hollow circles correspond to SOPT. Data taken from [139,151,153,156,158,169,184,185,187,188,203–205,215,546,1560–1564].

some discrepancies are found with the data supplied by Singh et al. [153]. The latter authors also observed a decrease of T_C from 164 K to 154 K for x = 0.075 to x = 0.15 in $Dy(Co_{1-x}Si_x)_2$ [153]. However, higher Si concentrations weaken the magnetic interaction leading to a decrease in the Curie temperature. A table-like behavior has been recently reported in multiphase GdCoAl alloys, containing $GdCo_2$ phase [179]. The Al substitution for Co in $Ho(Co_{1-x}Al_x)_2$ Laves phase yields itinerant electron metamagnetism and positive magnetovolume effect at low Al concentration, increasing transition temperatures from 94 to 159 K as x increases from 0.01 to 0.1 [180]. $GdCo_xAl_{2-x}$ crystallizes in a mixture of $MgCu_2$- and $MgZn_2$-type phases but adopts a single phase transition at 77 K. With annealing, ΔS_M enhances but *RC* reduces [181].

Substitution of Fe for Co in $Dy(Co_{1-x}Fe_x)_2$ [182] and $(Tb,Dy,Ho)Co_{1.8}Fe_{0.2}$ [183] alloys changes FOPT to a SOPT despite their lattice parameters are within the defined limits of the model from Khmelevskyi and Mohn. However, Curie temperature is enhanced close to room temperature and thus the same argument explaining the second order character of the magnetic transition of $TbCo_2$ can be assumed for these Fe containing alloys. In the case of $Er(Co_{1-x}Fe_x)_2$ series [184], T_C increases from 32 K to 360 K for x = 0 to x = 0.2, with a significant decrease of MCE due to the change of the character of the transformation from a FOPT to a SOPT. Partial Fe substitution for Co in $Tb(Co_{1-x}Fe_x)_2$ [158] shifted the transition temperatures to room temperature and reduced $|\Delta S_M|$ from ~7 to ~4 J kg^{-1} K^{-1} ($\mu_0\Delta H$ = 5 T) when x increases from 0 to 0.1, despite resulting in a broader curve. In this case, a structural transition from *Fd*-3*m* to *R*-3*m* is coupled to the magnetic transformation [158]. Partial substitution of Co for Fe in $SmCo_2$ increases the Curie temperature. The spin reorientation transition reported for the Fe-free compound is not observed in $SmCo_{1.8}Fe_{0.2}$. Its maximum magnetic entropy change is modest at its Curie temperature of 300 K (ΔS_M = −0.20 J kg^{-1} K^{-1} at $\mu_0\Delta H$ = 1.5 T) [151]. Annealing the alloys led to 40% enhancement in the maximum entropy change but not in their refrigerant capacities.

Ni substitution for Co in $Dy(Co,Ni)_2$ [185] led to a decrease of Curie temperature, which is ascribed to the reduced magnetic exchange. Their lattice parameters were retained relatively constant. Progressive Ni substitution for Co in $Gd(Co,Ni)_2$ [186] lowered both the lattice parameter and Curie temperature, unlike the behavior earlier described for $RECo_2$ alloys. Partial substitution of Mn for Co has been also studied: e.g. $Gd(Co,Mn)_2$ [187] (its increased Mn content reduced T_C while $|\Delta S_M|$ slightly increased and SOPT was observed) and $RECo_{1.8}Mn_{0.2}$ [188] (it exhibits T_C = 140, 211 and 308 K for Dy, Ho and Tb, respectively, although $|\Delta S_M|$ decreases with Curie temperature, as generally observed in Fig. 6). Mn additions in off-stoichiometric $ErCo_2Mn_x$ [189] were reported changing the transition character from FOPT for x = 0 to SOPT. Moreover, when x increased from 0 to 0.6, the Curie temperature increased from 35 K to 212 K. However, a large amount of Th_6Mn_{23}-type impurity phase was observed for higher Mn additions. B additions in off-stoichiometric $DyCo_2B_x$ also change FOPT to SOPT and increase the transition temperatures [190]. The formation of vacancies in $Er_{1-x}Co_2$ leads to an increase of transition temperatures (from 32 to 46 K as x increases from 0 to 0.03) but at the expense of a reduced MCE response [191].

In the case of $RENi_2$ Laves phases, some deviation from the ideal $MgCu_2$-type structure is generally reported and most of them exhibit a cubic superstructure (space group *F*-43*m*), which unit cell is double of that of the original cubic Laves phase, and where there is a regular arrangement of vacancies of RE sites [192]. Recently, different $RENi_2$ alloys have been proposed to form composite materials to obtain table-like MCE responses [193]. Unlike for Laves phases containing Co, Mn or Fe, no magnetic moment is expected for Ni in these alloys despite a value of ~0.2 μ_B has been reported in $GdNi_2$ [194]. For Mn additions in off-stoichiometric $GdNi_2Mn_x$, $MgCu_2$ structure was retained at low x values but an additional phase with $PuNi_3$-type structure was formed at higher x values. However, the compositional limits differ from the results from Gerasimov et al. [195] and those of Aryal et al. [196]. Magnetic moment of Ni/Mn atoms increases from 1.5 to 3.2 μ_B as x increases from 0.5 to 1.5 and the best MCE properties observed among the series for non-mixed samples is $-\Delta S_M$ = 3.9 J kg^{-1} K^{-1} at ~175 K and RC_{FWHM} = 485 J/kg at 5 T [196]. The off-stoichiometric $TbNi_2Mn_x$ ($x \leq 1.10$) compound also crystallizes in the $MgCu_2$-type structure [197] and has a SOPT at 150 K, leading to $|\Delta S_M|$ = 3 J kg^{-1} K^{-1} at 5 T. Cwik et al. have studied several pseudo-binary Laves compounds including $Y_xHo_{1-x}Ni_2$ [198], $Lu_xHo_{1-x}Ni_2$ [199], $La_xHo_{1-x}Ni_2$ [200], $Sc_xHo_{1-x}Ni_2$ [201], $Tb_xLa_{1-x}Ni_2$ [202] and $Gd_xSc_{1-x}Ni_2$ [192]. Generally, their transition temperatures are very low and only those of $Gd_xSc_{1-x}Ni_2$ series are above 30 K. In the $Gd_xSc_{1-x}Ni_2$ series, Curie temperature decreases from 75.4 to 13.6 K as x decreases from 1 to 0.2 and MCE decreases with x (ΔT_{ad} decreases from 5.8 to 3.9 K at $\mu_0\Delta H$ = 4.2 T as x decreases from 1 to 0.7) [192].

For other Co-free Laves phases, their transition temperatures typically lie near to or even above 100 K. For example, the T_C of $Gd(Fe_x,Al_{1-x})_2$ [203] initially decreases from 175 K (x = 0) to 100 K (x = 0.15) then increases up to 190 K for x = 0.4 (its ΔS_M behaves inversely to T_C). However, for $GdFe_{0.3}(Al,B)_{1.7}$ [204] no significant effect on T_C was observed with respect to B-free alloy. Another example is $EuRh_{1.2}Zn_{0.8}$ [205] alloy, which exhibits a SOPT, lattice parameter of 0.76858 nm and ΔS_M = −7 J kg^{-1} K^{-1} at 7 T and T_C = 95 K. Partial substitutions of Ce for Gd in $Gd_{1-x}Ce_xAl_2$ reduce the Curie temperature from 163 K (x = 0) to 37 K (x = 0.75) and ΔS_M values followed an opposite trend to the general described one decreasing from 3.82 (x = 0) to 2.04 J kg^{-1} K^{-1} (x = 0.75) at 2 T [206]. Alho et al. [207] theoretically calculated the MCE response in $Gd_{1-x}Dy_xAl_2$ and found a reduction of T_C to ~65 K for x = 1 with a continuous increase of $|\Delta S_M|$ with Dy content although the simulated values are larger than experimental results. $REAl_2$ (RE = Pr and Nd) compounds order ferromagnetically at 32 K for Pr and 77 K for Nd, showing at 3 T a $-\Delta S_M$ = 10.2 and 3.74 J kg^{-1} K^{-1} respectively [208]. Recently Gil et al. [209] theoretically studied the anisotropic magnetocaloric effect in $HoAl_2$ at 20 K. They ascribed this MCE to the spontaneous spin reorientation transition from *[110]* to *[100]* direction axis as temperature increases. Other theoretical studies reported by Ribeiro et al. include $Er_{1-x}Tb_xAl_2$ [210] and $Tb_{1-x}Gd_xAl_2$ [211] alloy series. Partial substitution of Er for Pr in $Pr_{1-x}Er_xAl_2$ reduces the transition temperatures (and lattice parameter) and exhibit a maximum ΔT_{ad} = 5 K at 5 T for x = 0.95 [212]. Only $Pr_{0.6}Er_{0.4}Al_2$ alloy exhibits a sharp peak in the heat capacity experiments and even shows interesting magnetoresistance properties, and two MCE peaks at ~7 and 30 K [213].

In the case of giant magnetoresistive $HoCu_2$ with a Néel temperature at 10.5 K (SOPT) the alloy shows a large $\Delta S_M = -19.3$ J kg^{-1} K^{-1} at 5 T [214]. Gao et al. [215] studied the $TbMn_{1.8}Fe_{0.2}$ compound, which undergoes a SOPT of the Tb sublattice at 80 K with $\Delta S_M = -9.84$ J kg^{-1} K^{-1} and $\Delta T_{ad} = 3.5$ K at $\mu_0\Delta H = 5$ T. For $ErAl_{2-x}Fe_x$ series, although cubic Laves phase is found for the extreme compositions, $MgZn_2$-type structure is observed in the range $0.875 \leq x \leq 1.25$ [216]. For $x \sim 1.6$, T_C is tuned to near room temperature while a local maximum in $|\Delta S_M|$ is observed for $x \sim 1.2$ but not exceeding 3 J kg^{-1} K^{-1} for 2 T. More details on aluminides crystallizing in cubic Laves phase can be found in the review of Gschneidner and Pecharsky [11].

5.1.1.2. La[Fe(SiAl)]$_{13}$. Mixing of La and Fe does not form any intermetallic compound but their binary phase diagram shows an immiscible system. However, minor additions of Si or Al can yield the formation of a fcc $NaZn_{13}$-type structure (space group *Fm*-3*c*) containing 112 atoms per unit cell: 8 FeI, 96 FeII and 8 La positions, Si atoms are located in FeII sites [217] (e.g. see Fig. 1 in Ref. [218]). This intermetallic compound exhibits very interesting magnetic behavior and also GMCE, which was reported in 2001 by Hu et al. [219] for $LaFe_{11.4}Si_{1.6}$ ($-\Delta S_M \sim 20$ J kg^{-1} K^{-1} at 210 K and $RC_{FWHM} = 530$ J/kg at $\mu_0\Delta H = 5$ T). The GMCE was ascribed to an itinerant electron metamagnetic transition, which is FOPT. The phenomenology of the transition of this family of alloys and their corresponding MCE was reviewed in 2009 by Shen et al. [15]. For those alloys of this family with a FOPT, sharp volume shrinkage occurs as temperature increases above the magnetic transition without changing the symmetry. Moreover, several microstructural techniques, including X-ray [220], neutron diffraction [217,218] and Mössbauer spectroscopy [221–224], have shown the coexistence of two $NaZn_{13}$-type lattices in a ±2 K range around T_C [15]. Recent studies combining ab initio calculations and nuclear resonant inelastic x-ray scattering show that the changes in the vibrational density of states across this FOPT imply an anomalous magnetoelastic softening [225].

The itinerant electron metamagnetic transition can be lost upon increasing Si content or other compositional effects, which then lead to SOPT [12] reducing MCE but also implying negligible hysteresis losses. Typical curves of MCE for this family of alloys can be found in Ref. [226]. FOPT associated with lattice expansion implies large strains in the bulk samples that lead to their degradation after few cycles. Lyubina et al. [227,228] could overcome this problem by producing porous samples which could reduce grain boundaries. Although ~20% reduction in ΔT_{ad} is observed in the porous samples, both its thermal and magnetic hystereses are reduced compared to their bulk counterparts.

Fig. 7 shows the field dependence of the relative ΔS_M and RC_{FWHM} values of $LaFe_{11.8}Si_{1.2}$ (FOPT) and $LaFe_{11.2}Si_{1.8}$ (SOPT) from Ref. [226]. As previously shown for Laves phases, the increase of the maximum applied field does not enhance the relative ΔS_M of alloys that exhibit FOPT as much as it does for those with SOPT. However, the MCE peak significantly broadens with field, yielding a similar relative enhancement in *RC* for FOPT and SOPT. SOPT data can be better represented using the power law predictions from the universal curve analysis [229] than using mean field values. Nevertheless, De Medeiros and Oliveira [230] could find a good agreement of the experimental MCE data and calculations (using a microscopic model under mean field approach and a phenomenological consideration of the magnetovolume coupling) of $LaFe_{13-x}Si_x$ with FOPT.

The improvement of MCE in this family of alloys has drawn attention to two important factors: tuning transition temperatures to room temperature and enhancing the purity of phases.

In regards to tuning the transition for room temperature applications, several ways have been proposed: changing the Fe/Si ratio, partial substitution of Fe for Co or introducing interstitial elements (mainly H, although C, B and N have been also studied). Generally, when the transition temperatures shift to higher temperatures, a decrease of MCE could be accompanied. For example, as the Si/Fe ratio increases in $LaFe_{13-x}Si_x$, T_C increases from 190 to 240 K when x increases from 1.3 to 2.2, but $|\Delta S_M|$ at $\mu_0\Delta H = 5$ T decreases from 29 to below 10 J kg^{-1} K^{-1}, respectively, and the transition changes from FOPT to SOPT for compositions around $x \sim 1.6$ [231–234]. Moreover, MCE deteriorates as the magnetic moment of Fe atoms

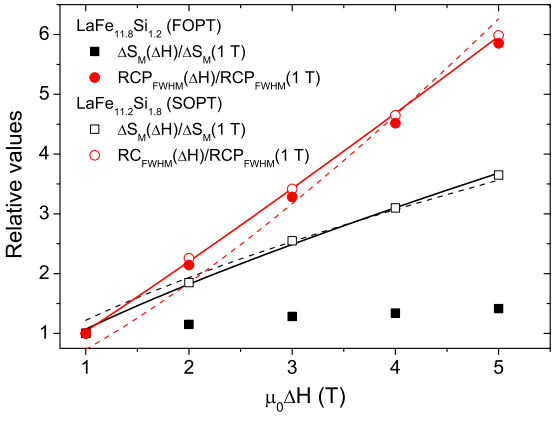

Fig. 7. Relative enhancement of ΔS_M and RC_{FWHM} for $LaFe_{13-x}Si_x$ phase, with a FOPT (x = 1.2) and a SOPT (x = 1.8) using the data of Ref. [226]. The solid lines correspond to the fitting of the SOPT data to power laws $\Delta S_M(H) = A \cdot H^n$ (n = 0.77 ± 0.03) and $RC_{FWHM} = B \cdot H^m$ (m = 1.087 ± 0.016), respectively. The dashed lines represent the same fitting using mean field values (n = 2/3 and m = 4/3).

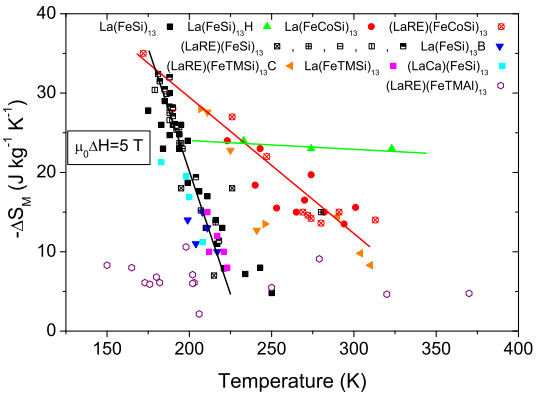

Fig. 8. Relationship between ΔS_M and T_C at $\mu_0\Delta H = 5$ T for several compositions of the La(Fe,Si)$_{13}$ family (data taken from [15,231,238,260,265,314,338,1565–1570]). Lines are guides to the eye to show the trend after changing the Fe/Si or RE/La ratio (black), Co content (red) and H (green).

decreases with increasing Si content. As the average magnetic moment of Fe in $LaFe_{13-x}Si_x$ compounds typically shows a linear behavior [231], the average magnetic moment of Fe atoms $\langle m_{Fe} \rangle$ can be estimated as:

$$\langle m_{\mathrm{Fe}} \rangle = \frac{31.1 - 5.2x}{13 - x}\mu_B. \tag{22}$$

On the other hand, Co substitution for Fe does not affect the magnetic moment and thus the Curie temperature can be shifted to higher temperatures in a more efficient way than decreasing Fe/Si ratio [231,234–236]. This behavior can be observed in Fig. 8 by comparing the black and red lines. However, the first order character of the transition converts to SOPT when the amount of Co substituting Fe increases. Conversely, when substituting Co for Si, α-Fe(Si,Co) phase is stabilized [237]. Regarding other transition metals substituted for Fe, Pathak et al. [238] studied 1 at.% Ni, Cu, Cr and V for Fe in La$(Fe_{0.99}X_{0.01})_{11.4}Si_{1.6}$, reporting a general deterioration of MCE. This MCE weakening is also confirmed from the recent results of minor substitutions of Cr, Mn, Co and Ni for Fe reported by Gercsi et al. [239]. They report that the magnetic moments of Cr and Mn couple in an antiparallel manner to that of Fe, which is not the case for Co and Ni whereby they form parallel coupling to Fe. However, they also observe that with V substitution for Fe, an 11 K increase in T_C with a significant decrease in hysteresis losses are observed. For partial substitutions of Mn for Fe [240–242], T_C decreases and the MCE peak broadens with increasing Mn content. Partial substitution of Cr for Fe also leads to a decrease in T_C, unlike partial Ni [242] or Cu [243] substitution for Fe.

Partial substitutions of RE for La has been studied for Ce [244–248], Nd [249,250], Pr [231,251–255], Gd [256] and Er [257]. Generally, the decrease in Curie temperature is compensated with an enhancement of MCE. Both ΔS_M and T_C are related following a similar behavior than that found in the ternary La(Fe,Si)$_{13}$ series. There is a roughly linear decrease of $|\Delta S_M|$ as T_C increases, regardless the FOPT or SOPT character of the transformation (see Fig. 8).

The substitution of Ce for La in $La_{1-y}Ce_y(Fe_{0.86}Si_{0.14})_{13}$ enables the change of SOPT (y = 0) to FOPT for y = 0.3, and consequently, MCE is clearly enhanced with a shift of about 30 K to lower temperatures [245]. For Nd substitutions (0 < y < 0.4 in $La_{1-y}Nd_y(Fe_{0.88}Si_{0.12})_{13}$), the lattice parameter linearly decreases with Nd concentration but its T_C does not change monotonically (between 205 and 215 K). Its $|\Delta S_M|$ is reduced from 13 to 10 J kg^{-1} K^{-1} at 5 T from y = 0 to 0.3, but the MCE peak broadens and leads to an enhancement of RC_{FWHM} (from 340 to 400 J/kg from y = 0 to 0.3) [249]. The influence of Pr substitutions is similar to those of Ce substitutions, whereby the Curie temperatures are shifted to lower values and enhanced $|\Delta S_M|$ is attained. A 37% increase in both $|\Delta S_M|$ and RC is reported in $La_{0.5}Pr_{0.5}(Fe_{0.88}Si_{0.12})_{13}$ compared to Pr-free alloy, whereas T_C decreases about 10 K [252]. Moreover, the lattice parameter decreases linearly with Pr content. Recently, Fujita et al. [258] reported that the hysteresis of La(FeSi)$_{13}$ compounds is reduced by controlling the Fermi level and magnetovolume effect with partial substitutions of Al and Pr. In $La_{0.7}Pr_{0.3}Fe_{11.4-x}Cr_xSi_{1.6}$ compound, the FOPT is preserved up to x = 0.34. When x = 0 increases to x = 0.06, $-\Delta S_M$(5 T) reduces from 17 J kg^{-1} K^{-1} (at 197 K) to 12 J kg^{-1} K^{-1} (at 180 K) and corresponding RC_{FWHM} decreases from 390 J/kg to 365 J/kg. At x = 0.34, $-\Delta S_M$(5 T) increases to 17.5 J kg^{-1} K^{-1} (at 195 K) and RC_{FWHM} also increases to 420 J/kg (with ΔT_{ad} = 8.4 K) [259]. Both α-Fe and LaFeSi impurities were observed. For Gd substitutions in $La_{0.80}Gd_{0.20}Fe_{11.4}Si_{1.6}$, ΔS_M(5 T) enhances (−21 J kg^{-1} K^{-1}) but with a lower Curie temperature (200 K), and also presents a RC_{FWHM} = 400 J/kg [256]. Similar to Nd substitutions, the substitution of Er in $La_{1-y}Er_yFe_{11.44}Si_{1.56}$ yields a reduction of the lattice parameter, converting FOPT to SOPT for y = 0.3 [257]. For y = 0.1, $|\Delta S_M|$ decreases 25% with respect to y = 0 despite retaining its FOPT character and a relatively constant Curie temperature. When Ca substitutes for La [260], the general relationship between ΔS_M and T_C is observed and $|\Delta S_M|$ decreases as T_C increases as it occurs for Fe/Si and La/RE series. Bao et al. [261] studied the viability of using La-Ce-Pr-Nd mischmetal instead of purified RE to produce $La_{0.7}(Ce,Pr,Nd)_{0.3}Fe_{11.6}Si_{1.4}$ and its hydrides (see below the effect of interstitials). Their main goal is the cost reduction of the starting materials in producing $NaZn_{13}$-phase with similar MCE parameters than those of $La_{0.7}Ce_{0.3}Fe_{11.6}Si_{1.4}$ system. However, a higher amount of LaFeSi

phase is observed in the alloy containing mischmetal. Large magnetic hysteresis of 56 J/kg, in $La_{0.5}Pr_{0.5}Fe_{11.4}Si_{1.6}$ compound ($|\Delta S_M|$ = 28.1 J kg^{-1} K^{-1} at 1.5 T and T_C = 186 K) decreases upon grounding to micrometric particles, whereas its thermal hysteresis (1 K for the bulk) is almost eliminated. Authors attribute the reduction of the hysteresis to the decrease of internal strains and improvement of heat transfer due to increase in surface to volume ratio [20].

The presence of interstitials in this family of alloys plays a particularly important role in compositional effects (sometimes appearing as the negative pressure effect), which generally increases Curie temperature. Among them, H is the most important but N, C and B have been studied too. Since 2002, hydrides are known to shift the FOPT to higher temperatures without depreciating ΔS_M after the works of Fujita et al. [262] and Chen et al. [263,264]. Several advantages were observed in hydrogenated samples with respect to H-free ones [265–267], such as smaller thermal hysteresis (~1 K [264,265]) and an enhanced ΔT_{ad} (7 K at $\mu_0\Delta H$ = 2 T [262] or 15.4 K at 5 T [268]) as the heat capacity remains almost unchanged [265]. Similar results have been found for hydrides of alloys with partial substitution of RE for La [252,267,269].

Neutron diffraction studies [217] conclude that H are located within the octahedron, formed by 2 La and 4 FeII (48f interstitials) as it occurs for C [270]. Recent in situ neutron studies describe the kinetics of H absorption in $LaFe_{11.44}Si_{1.56}C_x$ (x = 0 and 0.2) using Johnson-Mehl-Avrami-Kolmogorov theory, following the occupation of deuterium in 24d octahedral interstitial [271]. They found that C hinders H absorption, slowing down the kinetics and reducing 24d occupancy from ~0.04 to ~0.025. Mössbauer studies show a decrease of the magnetic moment in Mn doped alloys [272] and an increase in hyperfine field at 4.2 K after hydrogenation [223] without changes in the PM spectra. This concludes that an isotropic volume expansion due to the incorporation of H to the lattice is responsible for the large increase of T_C (from 195 to 330 K after 1.6 atoms of H per formula unit in $La(Fe_{0.88}Si_{0.12})_{13}$) and attributed to magnetovolume effect (which is typical of itinerant electron metamagnetic transitions). The kinetics of hydriding also has been recently studied by Wang et al. [273]. Jia et al. [274] found that partial substitution of Ce for La plays the opposite role to H interstitials although the crystallographic positions are completely different.

Hydrogenation process was studied by Wang et al. [275] as well as homogenization of hydrogenated samples [276], also studied by Ma et al. [277] and more recently by Wang et al. [273] (who studied the kinetics of hydrogen absorption and desorption) and Baumfeld et al. [278], who also found that the timescale of H diffusion in partially hydrogenated samples lies in the order of hours. H saturation could be obtained after 1 h at hydrogen-filling pressure of 65 bar in $LaFe_{11.44}Si_{156}$. To incorporate interstitial hydrogen to the alloy, Mandal et al. [279,280] successfully used reactive milling as an alternative route to the conventional annealing in hydrogen atmosphere. Lyubina et al. [281] have proposed electrolytic hydriding in the FM state (when the cell volume is ~1% larger and thus a higher diffusion of H is allowed) as an economic and safe procedure to produce hydrides, with the advantage of performing the experiments at low temperatures. Fujieda et al. [282] showed that high MCE values were retained when hydrogenation was performed on single phase systems. However, in inhomogeneous samples (with phase impurities) MCE reduces after hydriding due to the inhomogeneous distribution of H, which leads to a T_C distribution within the sample. Recently, Bez et al. [283] proposed a novel hydrogen-decrepitating-sintering-hydrogenation process, which consists of three steps: (1) a starting La-Fe-Si ingot is hydrogen-decrepitated at 423 K; (2) milled material is sintered at 1423 K; and (3) hydrogenating the sample during slow cooling from 773 K. They reduced the time duration of treatment from days to few hours.

However, the main drawback of these hydrides is instability [284]. Teixeira et al. [285] found that a small addition of C increases the temperature of hydrogen desorption from 460 K (C-free) to 540 K in samples with 0.2 atoms of C per formula unit. In this line, Zhao et al. [286] found a reduced rate of hydrogen absorption and release upon little C additions. Barcza et al. [287] reported that H-saturated samples remained stable while unsaturated hydrides are unstable close to their Curie temperatures and decompose into two types of samples (hydrogen rich and hydrogen poor phases), which adversely deteriorates MCE. To obtain stable hydrides with tunable Curie temperatures, they produced fully saturated $LaFe_{11.74-y}Mn_ySi_{1.26}H_z$ alloy series (z ~ 1.53, implying hydrogen saturation). Basso et al. [288] recently reported the deterioration of MCE with increasing Mn content but this is only noticed for samples with transitions below room temperature, while T_C can be tuned to ~300 K for x = 0.25 without noticeable effect on MCE. These results agree with the analyses of Bean-Rodbell model, which describe well the experimental results with FOPT (parameter η > 1 for x = 0.25) [289]. Similar qualitative results, using smaller η values, were also obtained by Piazzi et al. [290]. No isotope effect has been observed for this family of magnetocaloric materials [291].

Pressure application, in contrast to the effect of interstitials, leads to a decrease of the transition temperatures but while MCE enhances for hydrided samples, it deteriorates for H-free counterparts [292].

In the case of incorporating nitrogen into $La(FeSi)_{13}$ lattice, both their lattice parameter and T_C increase. However, the FOPT converts to SOPT in N-containing samples and significantly decreases MCE [293].

Using C interstitials in $LaFe_{11.6}Si_{1.4}C_x$ was proposed as an alternative to H by Chen et al. in 2003 [294], with the aim to develop a system of a higher chemical stability than hydrides. They found an increase of T_C from 195 to 250 K after adding 0.6 C atoms per formula unit. However, FOPT is only maintained for lower C content (x ~ 0.2) with a ~50% decrease in ΔS_M after x = 0.6, also in agreement with results reported by Teixeira et al. [285]. The presence of C interstitials in $La_{0.5}Pr_{0.5}Fe_{11.5}Si_{1.5}C_x$ [295] leads to an increase of both Curie temperature and lattice parameter as x increases from 0 to 0.3 with ~75% reduction of hysteresis losses. On the other hand, <15% reduction of $|\Delta S_M|$ (~30 J kg^{-1} K^{-1} for $\mu_0\Delta H$ = 5 T) is observed for x = 0.3 compared to C-free alloy. Although $LaFe_{11.2}Co_{0.7}Si_{1.1}C_x$ (x = 0.1–0.3) presents SOPT, the *RC* for these systems are larger than that of $Gd_5Ge_2Si_2$ exhibiting a FOPT [296]. Shen et al. [297] combined Co and C additions and obtained ΔS_M = −11.6 J kg^{-1} K^{-1} at 295 K and 5 T with negligible hysteresis since the transformation changes to SOPT.

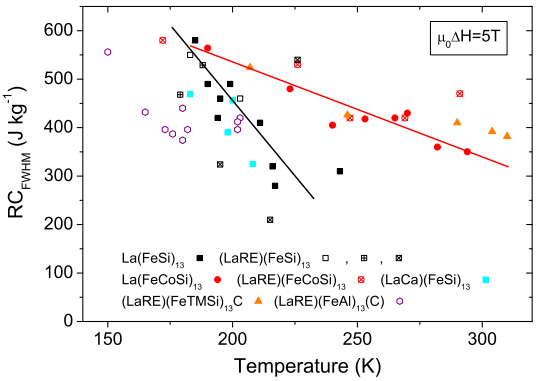

Fig. 9. Relationship between RC_{FWHM} and T_C at $\mu_0\Delta H$ = 5 T for several compositions of $LaFe_{13}$ family (data taken from [231,260,314,338,1566,1568,1571]). Lines are guides to the eye to show the trend upon changing the Fe/Si or RE/La ratio (black) and Co content (red).

B additions were also studied as elemental substitutions for Fe [298] and as additional element to occupy interstitial sites [299–301]. The former case leads to an increase of both Curie temperature and lattice parameter with B increase for a constant Si content, whereas thermal hysteresis (2 K for B-free samples) becomes negligible with B substitution. The latter case leads to an increase in T_C (7–8 K) and lattice parameter with a boron content of 0.1–0.5 in the formula unit. The B interstitials also reduce both thermal and magnetic hystereses.

Although there is a general decrease in $|\Delta S_M|$ with the transition temperatures, the MCE peak also generally broadens with increasing transition temperature. Thus, the reduction of *RC* with transition temperatures is smeared out with respect to that of ΔS_M in this family of alloys (Fig. 9).

$NaZn_{13}$-type structures with Al instead of Si was, in fact, firstly reported with MCE data among the $LaFe_{13}$ family of alloys [302,303]. $La(Fe_{0.98}Co_{0.02})_{11.7}Al_{1.3}$ exhibits a SOPT with $\Delta S_M = -11$ J kg^{-1} K^{-1} and T_C = 200 K at $\mu_0\Delta H$ = 5 T, which positively compares with the results of Gd. Studies on $La(Fe_xAl_{1-x})$ series ($0.86 \leq x \leq 0.89$) [304] show a gradual change from FM to weak AFM state. When Co substitutes for Fe, Curie temperatures increase for both Si- and Al-containing alloys [232]. Although MCE decreases with increasing Co content in the Si-containing $LaFe_{13}$ alloys (ascribed to the conversion of FOPT to SOPT), >100% enhancement of MCE is obtained in $La(Fe_{1-x}Co_x)Al_{1.6}$ for x = 0.04 and even remains unchanged with further increasing Co content (due to the increase in magnetic moment as deduced from the increase of hyperfine magnetic field [232]). In these aluminides, the effects of RE substitution for La (i.e. Pr and Nd) on their MCE, show that MCE enhances while Curie temperatures decrease with respect to the values of the parent system [305].

When interstitials are introduced to these Al-containing compounds, e.g. hydrogen additions, their T_C has the same behavior as those of the Si-containing alloys and furthermore ΔS_M are improved [306]. Carbon additions in Al-containing alloys also yield similar effects as those of Si containing alloys, in which T_C increases while $|\Delta S_M|$ slightly decreases as C content increases [221–223,307]. B additions in $LaFe_{11.5}Al_{11.5}B_x$ were studied by Zhang et al. [308] and Xu et al [307]. The original FOPT AFM-to-PM changes to SOPT FM-to-PM with B additions. For x = 0.1, 0.2 and 0.3, the alloys exhibit $-\Delta S_M$ = 7.64, 7.38 and 7.25 J kg^{-1} K^{-1} (3 T) at 178, 185 and 189 K respectively [308]. Other studies compare the effect of B and H interstitials in these systems [309].

As mentioned earlier, obtaining the single phase system in $LaFe_{13}$ alloys is another concern in the research community. Palstra et al. [310] studied the stabilization of $NaZn_{13}$-type phase in $LaFe_{13-x}Si_x$ ($1.3 \leq x \leq 2.6$) alloys after annealing 10 days at 1173 K but could only obtain single phased samples in the range of $1.56 \leq x \leq 2.47$. To exhibit FOPT, a lower Si content is essential. However, this causes difficulties to attain single phased $La(Fe,Si)_{13}$ samples and the formation of impurities, such as α-Fe phase (~5 wt.% is generally obtained after annealing considered as successful ones) and other La-rich phases like LaFeSi, still persists even after long durations of annealing at high temperatures (several days or even more than one month). This must be considered when comparing different results due to inhomogeneous compositions and, moreover, multiphase behavior rather than single phase behavior should be expected [311]. In the case of $LaFe_{13-x}Al_x$, the phase stability of $NaZn_{13}$ exhibits a wider compositional range ($1.0 \leq x \leq 7.0$) with $LaFe_4Al_8$ only formed for higher Al contents and α-Fe for lower Al concentrations [15].

To optimize the homogeneity of the samples, several procedures are followed: varying the compositions, optimizing the annealing temperatures, ultrafast cooling from the melt and high energy milling. For compositional variations, it is reported that RE partial substitutions for La in $(La,RE)Fe_{13-x}Si_x$ produces a single phase for x = 1.6 but not for lower x values when RE = Ce [312], and when RE = Nd, the phase fraction of α-Fe linearly decreases from 6.0 to 1.2 wt.% as x increases from 1.2 to 1.8. However, when RE = Gd in $(La,RE)Fe_{13-x}Si_x$, [256] the amount of α-Fe significantly decreases and the presence of LaFeSi is negligible for 0.2 Gd atoms per formula unit. With partial substitutions of Ca for La, the phase fraction of the La-rich impurity phase decreases while that of α-Fe phase increases instead [260]. Partial Co substitutions for Fe also lead to decreasing the amount of deleterious α-Fe phase [232,297] but the opposite is observed when substituting Co for Si [237]. A minor α-Fe phase in $La(Fe_{1-x}Mn_x)_{13}$ for x > 0.02 still persists even after annealing 30 days at 1300 K [240]. In fact, Mn substitutions

in both $La(FeSi)_{13}$ and their hydrides avoid the formation of co-existent phases. Composites with different Mn content provide a constant MCE extended over a large temperature span [313]. In addition, single phase also can be obtained by adding C interstitials in $La(Fe,Si)_{13}$ (for ~0.2 C atoms per formula unit) [285,314,315]. Furthermore, off-stoichiometric compositions (excess La concentration) also have been proposed as an effective way of reducing impurities [316–318]. A surplus of Fe in $La(Fe_x)_{11.6}Si_{1.4}$ shows that the amount of LaFeSi impurity phase depletes to nearly zero for x = 1.02 [319]. However, Lai et al. [320] reported that the order of transition changed in their off-stoichiometric samples when La/Fe ratio decreases and a larger amount of α-Fe(Si) type phase was formed compared to that of the stoichiometric composition. On the other hand, the phase fraction of LaFeSi significantly decreases with decreasing La/Fe ratio. It is worth noticing that off-stoichiometric compositions could appear due to the additions of excess La to compensate any losses upon arc-melting, as reported in [240]. On the other hand, the off-stoichiometric compositions with La excess are also reported to yield the $NaZn_{13}$-type phase and even La_5Si_3 phase, which does not significantly affect MCE [321,322].

Liu et al. made a systematic microstructural study of $LaFe_{11.8}Si_{1.2}$ and $LaFe_{11.6}Si_{1.4}$ alloys as a function of annealing temperatures and duration [323]. They suggest an intermediate phase with an eutectoid-type lamellae morphology previous to the formation of the $NaZn_{13}$-type phase. The optimum annealing temperatures differ between the two studied compositions, decreasing from 1373 K to 1323 K as Si content increases from 1.2 to 1.4 at per formula unit. The optimum annealing duration was found to be 7 days, in which ~90% of the desired phase could be formed. The minimum annealing duration explored was 1 day from this work. However, optimization has been also reported after high temperature annealing for short times: 91.4 vol.% of $NaZn_{13}$-type phase was reported to be formed in $LaFe_{11.6}Si_{1.4}$ alloy after annealing 1 h at 1573 K an arc melted sample with a matrix of 79.9 vol.% of α-Fe and 20.1 vol.% of LaFeSi phases in [324]. Kolat et al. [325] optimized the time duration of annealing the same composition at high temperature of 1473 K in the range from 5 min to 120 h and reported the formation of a single phase of $NaZn_{13}$ structure after annealing for 30 min. Xiang et al. [326] has studied the optimization of annealing conditions of $LaFe_{11.5}Si_{1.5}$ alloy within the range from 1223 K (5 h) to 1673 K (0.5 h) and found a significant amount of $NaZn_{13}$-type phase upon annealing at 1423 K. Within the temperature range from 1423 to 1573 K, the formation of α-Fe and LaFeSi phases rapidly decreases but LaFeSi phase with the presence of La_5Si_3 phase are detected upon annealing at higher temperatures, i.e. 1673 K. The optimum annealing conditions for this alloy were reported at 1523 K for 3–5 h. Better single phased samples are reported to be produced at ~1500 K, probably due to the formation of $NaZn_{13}$-type phase from the reactions between γ-Fe and La-rich phase [327].

Rapid quenching has being proposed for minimizing the annealing time durations because a better compositional homogenization of the sample is attained. Several studies on melt-spun ribbons [233,328–333], strip casting [334,335] or on melt-extraction [336] can be found in the literature. Liu et al. reported that an almost single phased systems in $La(Fe,Co)_{11.4}Si_{1.6}$ is obtained by annealing for 20 min at 1273 K [233]. They also found for as-quenched samples, an increased formation of $NaZn_{13}$-type phase with increasing Si content and wheel speed [329], in agreement with Lyubina et al. [331]. Moreover, melt-spun samples exhibit a significant reduction of magnetic and thermal hysteresis [330]. Hou et al. studied the microstructures [332] and magnetic domain structures [333] of both the wheel and air surfaces of the melt-spun ribbons. Copper mold casting method has been also found to reduce the optimum annealing duration from weeks to few hours [301]. In addition, high energy ball milling has been also used to decrease the annealing duration down to ~30 min to obtain monophasic systems [337,338]. Recently, Patissier and Paul-Boncour [339] used spark plasma sintering (30 min at 1473 K) for ball milled powder (without annealing) and achieved 89 wt.% of the $NaZn_{13}$-type structure. The presence of C from contamination is considered as the reason for their larger Curie temperatures as compared to those obtained from conventional annealing.

Mechanical stability of the system is also a drawback for this FOPT family leading to virgin effects [340]. However, Yuan et al. [341] observed irreversible microstructural changes (microcraks, etc.) even in $La(Fe_{0.94}Co_{0.06})_{11.8}Si_{1.2,}$ which exhibits SOPT, but only above 1000 cycles. A 10% deterioration in the MCE response was observed after 8000 cycles. Enhanced mechanical behavior has been attained by embedding the samples in soft materials, such as epoxy resin [342–345], polymer [346–348] or, more recently, in composites with a metallic amorphous [349] or tin matrices [350]. Also recently, Shao et al. [351] found that the presence of α-Fe(Co,Si) impurities contributes to enhancing the mechanical stability even with respect to polymer bonded samples. Core-shell $LaFe_{11.65}Si_{1.35}$/Cu spark plasma sintered powder with improved mechanical properties and corrosion resistance has been also reported [352]. Corrosion resistance has been studied for $La(Fe_{0.88}Si_{0.12})_{13}$ [353], $La(FeMnSi)_{13}$ [354], and $La(Fe,Co)_{13-x}Si_x$ series and compared to Gd [355]. Recent results show that corrosion resistance in these alloys enhances with partial substitutions of Co for Fe, and particularly C additions [356].

5.1.1.3. $Gd_5(Si,Ge)_4$ phases. In 1997, Pecharsky and Gschneidner [7] discovered that $Gd_5Si_2Ge_2$ intermetallic compound underwent a magnetostructural FOPT upon heating from orthorhombic Gd_5Si_4-type (space group *Pnma*) to monoclinic structure (space group $P2_1/a$). Both binary Gd_5Si_4 and Gd_5Ge_4 compounds (Gd_5Si_4- and Sm_5Ge_4-type structures respectively) exhibit orthorhombic structures. A representation of these three different structures can be found in Ref. [357]. Both orthorhombic structures have *Pnma* space group, but while dimers Ge-Ge bonds are present between the different slabs in Gd_5Si_4-type structure, they are absent in Sm_5Ge_4-type structure [357]. The two different structures can be distinguished from the different ratio of the lattice parameters. The discovery of $Gd_5Si_2Ge_2$ system was a key point in directing the research focus to room temperature magnetocaloric effect and several specific reviews devoted to the structure and properties of this particular system have been reported [358–361]. The magnetostructural transition is ascribed to the stabilization of monoclinic phase, which can be only achieved, for ternary $Gd_5(Si_xGe_{1-x})_4$ systems, for x ranging within $0.24 < x < 0.5$ [362]. However, the

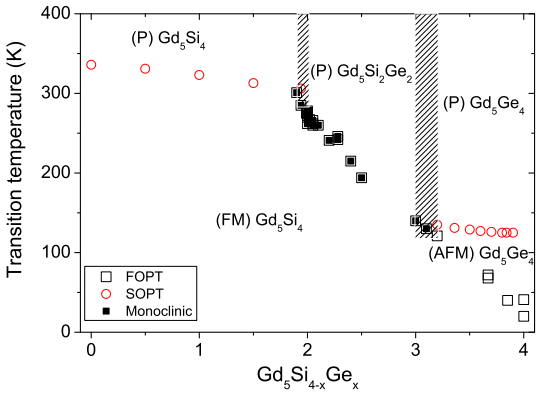

Fig. 10. Peak temperatures of MCE as a function of Ge content in $Gd_5Si_{4-x}Ge_2$ (data taken from [7,11,359,365,372,375,378,380,381,383,385,391,393,395,407,420,1572–1575]). For a more complete view of the different structural and magnetic transitions see [357].

equivalence between temperature and hydrostatic and chemical pressure is reported to affect the polymorphism of $Gd_5Si_2Ge_2$ system [363]. A recent phase diagram around $Gd_5Si_2Ge_2$ composition is supplied by Melikhov et al. [364].

The transformation would imply a sharp change in the magnetization (and thus a GMCE) when the critical temperature, $T_{Critical}$, (at which the free energies of both orthorhombic and monoclinic phases are equal) lies between the Curie temperatures of these two structures: $T_C^M < T_{Critical} < T_C^O$, where T_C^M is the Curie temperature of the monoclinic phase and T_C^O is that of the orthorhombic phase (Fig. 10). The GMCE should be enhanced as the difference between T_C^O and $T_{Critical}$ increases.

The magnetic properties of $Gd_5(Si_xGe_{1-x})_4$ system are composition dependent [357]. As Si content decreases, the Curie temperature of the simple ferromagnet linearly decreases from 335 K (x = 1) to 295 K (x ~ 0.5). This Si concentration agrees with the upper limit of Si content for the formation of monoclinic distortion in the parent orthorhombic Gd_5Si_4 structure, as mentioned earlier (ternary $Gd_5(Si_xGe_{1-x})_4$ systems for 0.24 < x < 0.5). At this stage, when the temperature decreases, the system initially orders ferromagnetically but with low net magnetic moment and, at lower temperatures, converts to another FM phase through a FOPT. The rate of the reduction of both transition temperatures, as Si content decreases, is faster than that of decreasing T_C for alloys with x > 0.5. For compositions below x = 0.24 (the lower compositional limit for stable monoclinic structure), orthorhombic structure forms again and the transition temperatures decrease, which yields a FiM system at ~125 K with a FOPT from FiM to FM state at lower temperatures. The transition temperature ascribed to this transformation also decreases as Si content decreases [365]. Si-free compound is AFM at temperatures below 130 K, which is also preserved at low fields down to ~2 K, while at higher magnetic fields above 1 T, a field induced structural transition occurs below 30 K [366].

Concerning MCE, the reference composition of this alloy family is $Gd_5Ge_2Si_2$, which was discovered by Pecharsky and Gschneidner in 1997 [7]. This system was reported with GMCE after the first GMCE material, FeRh alloy, and it exhibits a lower thermal hysteresis (~2–5 K) than that of the latter [367]. $Gd_5Ge_2Si_2$ shows $\Delta S_M = -18.5$ J kg^{-1} K^{-1} and $\Delta T_{ad} = 15$ K, both at 276 K at 5 T. MCE was evidently enhanced in Ge-enriched samples but their transition temperatures shift to lower values: $Gd_5(Ge_{1-x}Si_x)_4$ shows, at 5 T, $|\Delta S_M| \sim 70$ J kg^{-1} K^{-1} at $T_C \sim 150$ K, $RC_{FWHM} \sim 700$ J/kg for x = 0.25 while for x = 0.5 $|\Delta S_M| \sim 20$ J kg^{-1} K^{-1} at $T_C \sim 300$ K and $RC_{FWHM} \sim 500$ J/kg [365].

Theoretical models have been developed to describe the barocaloric and magnetocaloric effects of this compound. Melikhov et al. [368] used a phenomenological model, based on Jiles-Atherton theory (FM) and Curie Weiss law (PM), to describe its FOPT. Alvaranega et al. [369] considered the magnetic field dependence of the entropy of phonons in a Hamiltonian model and include Zeeman, magnetoelastic and exchange interactions. Pires et al. reviewed the exotic Griffiths-like phase appearing in $RE_5(Ge_{1-x}Si_x)_4$ compounds [370] using RE = Gd and Tb as examples. Von Moos et al. [371] developed a non-equilibrium Preisach-type model to study the hysteresis in $Gd_5Ge_2Si_2$ compound.

Fig. 11 shows the ΔS_M values of this alloy family as a function of the transition temperature at $\mu_0\Delta H = 5$ T. The maximum values considered in the figure are ~40 J kg^{-1} K^{-1}. Although values as high as 70 J kg^{-1} K^{-1} were reported in earlier publications, they were just observed at sharp peaks related to the inappropriate use of Maxwell relation for ΔS_M determination in these FOPT materials in the region of phase coexistence [372–375].

Compositional effects have been reported for $Gd_5Si_{1.985}Ge_{1.985}X_{0.03}$, whereby X = Fe, Ni, Co, Cu, Al, Ga or C, [376] and $Gd_5Si_2Ge_{1.9}X_{0.1}$, whereby X = Co, Cu, Ga, Mn, Al, Bi and Sn [377]. In general, their GMCE are eliminated and Curie temperatures are shifted to higher values (~300 K), except for minor amount of Ga substitution in which the GMCE is preserved till further increased Ga content whereby the former effects are resulted [376,378]. Analogously to Ga, small substitutions of Sn [379] retain FOPT and enhance both Curie temperature and MCE ($Gd_5Si_{1.935}Ge_{2.035}Sn_{0.03}$ exhibits a $T_C = 277$ K and a ΔS_M which is twice as large as that of $Gd_5Si_{1.95}Ge_{2.05}$ whose $T_C = 260$ K). Minor Pb substitutions for Ge and Si in $Gd_5Si_2Ge_2$, also preserve FOPT and thus GMCE [380]. Regarding hysteresis losses, they reduce significantly upon 0.1 addition per formula unit of Cu, Ga, Mn and Al [377] as previously observed for Fe [28]. However, 0.1 addition of Sn or Bi per formula unit has

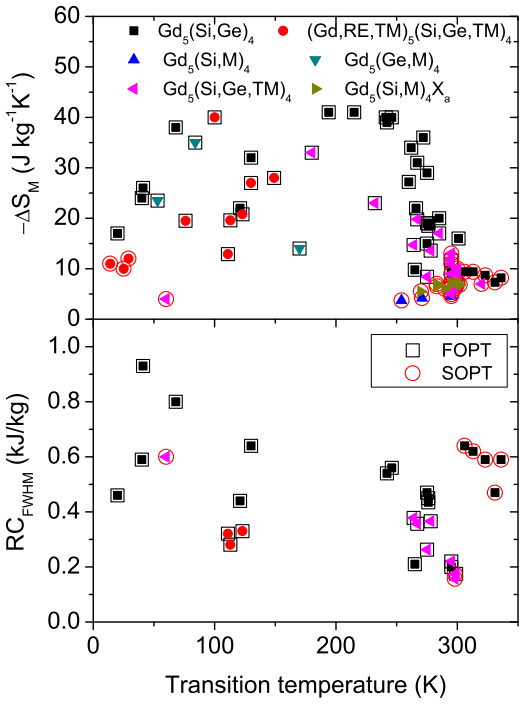

Fig. 11. The maximum ΔS_M (above) and RC_{FWHM} (below), both at $\mu_0\Delta H = 5$ T, as a function of transition temperatures for several compositions of the $Gd_5(Si,Ge)_4$ family (data taken from [7,11,28,359,365,372,376–378,383,384,390,391,393,395,414,419,433,1576–1585]).

a negligible effect on MCE and the associated hysteresis losses. Single phase was observed after substituting these two elements, unlike substituting other elements that form multiphase systems [377]. However, Li et al. succeeded in enhancing the MCE of $Gd_5Si_{1.95-x}Ge_{2.05-x}Sn_{2x}$ ($x \leq 0.05$) [381] and this is also confirmed by other studies [382]. It has been shown that little Mn content in $Gd_5Si_{2.05-x}Ge_{1.95-x}Mn_{2x}$ ($2x = 0$, 0.03 and 0.08) preserves monoclinic structure (with some 5:3 type impurity phase) and GMCE [383]. Similar effects are obtained with In substitution [384]. Partial substitutions of Nb in $Gd_5Si_{2-x}Ge_{2-x}Nb_{2x}$ alloys [385] are reported to beneficially increase Curie temperatures and MCE as x increases up to $x = 0.05$ ($\Delta S_M = -9.6$ J kg^{-1} K^{-1} at $T_C \sim 295$ K and $\mu_0\Delta H = 2$ T, which is a ~50% enhancement compared to Nb-free alloy), however, a low amount of detrimental Gd_5Si_3 phase has been found.

Fe substitution has been shown to be more effective in reducing hysteresis losses upon substitution for Ge than for Si in $Gd_5Ge_2Si_2$, being almost zero for $Gd_5Ge_{1.75}Si_2Fe_{0.25}$ [386]. Further increased amount of Fe substitution leads to destabilization of 5:4 stoichiometry and the appearance of 5:3 structures, which deteriorate MCE [387].

Complete substitution of Sb for Ge in $Gd_5Si_2Sb_2$ [388] leads to the formation of a ferromagnet, crystallizing in Sm_5Ge_4-type structure with $T_C = 240$ K, and with moderate MCE of $|\Delta S_M| < 5$ J kg^{-1} K^{-1} even at 7 T. One advantage in this material is the almost flat shape of the $\Delta S_M(T)$ curve, which could indicate a high *RC* but the reported data prevents further estimation. Similarly, in $Gd_5Si_{2.75}P_{1.25}$ alloy, orthorhombic Sm_5Ge_4-type structure is formed with a Curie transition at 177 K and $\Delta S_M = -7.8$ J kg^{-1} K^{-1} at $\mu_0\Delta H = 5$ T [389]. Chernyshov el al. [390] studied $Gd_5Ge_{4-x}Sb_x$ system and found the formation of $Tm_5Sb_2Si_2$-type phase (*Cmca* space group) for high Sb content but Sm_5Ge_4-type structure for $x = 0.7$ and 1, exhibiting FOPT and GMCE at ~40 K.

The additions of O to $Gd_5Si_{1.95}Ge_{2.05}$ deteriorate MCE in various ways [391]. Low oxygen content leads to the stabilization of orthorhombic phase and heterogeneous samples show a reduction of half of the MCE values, although having flat curves ($\Delta S_M \sim 7$ J kg^{-1} K^{-1} and $RC_{FWHM} > 420$ J/kg at $\mu_0\Delta H = 5$ T). At higher oxygen content, the alloy decomposes into 1:1 (CrB-type structure) (80–90%) and 5:3 (Mn_5Si_3-type structure) stoichiometries (~10%). Hydrogen additions also stabilize the orthorhombic phase but loses the GMCE even with its FOPT preserved after 0.1 atoms of H per formula unit [392]. The unit cell volume increases and T_C decreases as the Gd-Gd distance increases with the increase of H content [393].

Both purity and homogeneity play crucial roles in MCE [394]. The presence of untransformed orthorhombic phase and impurity phases deteriorates MCE, particularly, AFM hexagonal Gd_5Si_3 phase. Annealing at high temperatures leads to an evident enhancement of ΔS_M and ΔT_{ad} compared to those of arc-melted samples without post-annealing. This has been ascribed to the rearrangement of Ge and Si in their corresponding atomic sites of the monoclinic structure as well as the removal of retained polymorphic orthorhombic phase [395]. Generally, for rapid quenched systems, a higher cooling rate from the melt also enhances MCE [396,397]. Moreover, it is particularly worth mentioning that it is more beneficial to use highly pure Gd instead of commercial one [398,399] as the former leads to a clear enhancement of the MCE in $Gd_5Si_2Ge_2$ compound [395].

Several studies have been devoted to partial or complete substitution of other RE for Gd. Concerning the binary alloys, RE_5Si_4 (RE = Gd, Tb, Dy, Ho, Er) compounds are FM systems with Curie temperatures ranging from 336 K (for Gd) to 25 K (for Er) [400]. On the other hand, RE_5Ge_4 compounds are AFM systems with Néel temperatures ranging from 47 K (for Gd) to 25 K (for Er). The structure of $RE_5Si_{4-x}Ge_x$ systems depends on the Ge content: for high Ge content, orthorhombic structure exists from x = 4 to x ~ 1.3, 2.6, 3.2 and 2.9 when RE = Dy, Tb, Gd and Pr respectively; monoclinic structure exists from the former values down to x ~ 0.75, 1.3, 2.0 and 1.5 for RE = Dy, Tb, Gd and Pr respectively. Finally, orthorhombic structure is observed for RE = Dy, Tb, and Gd; and tetragonal Zr_5Si_4-type structure ($P4_12_12$ space group) for Pr [401]. In the case of RE = Nd, Magen et al. [402] stabilized monoclinic structure for x = 1.6 and Yang et al. [403] reported that as-cast samples, with x = 1.2 and 2, crystallize into a mixture of monoclinic and orthorhombic structures but crystallize into tetragonal Zr_5Si_4-type structure after annealing at 1273 K. For RE = Sm, the formation of orthorhombic phases is reported for Si- and Ge-rich compositions while that of monoclinic phase is reported for $Sm_5Si_2Ge_2$ compound [404].

Substitutions of Tb for Gd has been studied in $Gd_xTb_{5-x}Si_4$ in the complete range $0 \leq x \leq 5$ [400]. The volume of the unit cell linearly decreases (and density increases) with increasing Tb content while T_C linearly changes with Tb content from 346 K for Gd_5Si_4 to 223 K for Tb_5Si_4. On the other hand, ΔS_M does not significantly change (slightly enhanced from −8 to −9 J kg^{-1} K^{-1} at $\mu_0\Delta H$ = 5 T as T_C decreases) which is ascribed to exhibiting a SOPT. Morellón et al. [405] reported higher absolute values of ΔS_M of $Tb_5Si_xGe_{4-x}$ (x = 0, 2 and 4) for x = 4, whereby the alloy exhibits a SOPT. In the case of x = 0, Tb_5Ge_4 crystallizes in orthorhombic *Pnma* space group, and exhibits a complex canted AFM structure below 91 K and two peaks in its $\Delta S_M(T)$ curves, at 60 K and 95 K (−3.7 J kg^{-1} K^{-1} at $\mu_0\Delta H$ = 5 T). Similarly to Gd containing intermetallic, $Tb_5Si_2Ge_2$ crystallizes in monoclinic $P112_1/a$ space group and shows GMCE, which is ascribed to a magnetostructural FOPT with ΔS_M = −21.8 J kg^{-1} K^{-1} at ~110 K and $\mu_0\Delta H$ = 5 T. Thuy et al. [406] found that $Tb_5Si_3Ge_1$ compound exhibits monoclinic phase with a transition temperature of 215 K and ~50% decrease in $|\Delta S_M|$ with respect to that of $Tb_5Si_2Ge_2$. Lower values of $|\Delta S_M|$ reported by Thuy et al. with respect to those values reported by Morellón et al. could be due to the absence of post-annealing in Thuy's samples leading to the presence of tetragonal Tb(Si,Ge) impurity phase. Small partial substitution of Tb for Gd in $Gd_{5-x}Tb_xSi_{1.72}Ge_{2.28}$ [407] can preserve the first order magnetostructural character of the transition while T_C decreases and $|\Delta S_M|$ increases with increasing Tb content (up to ~25 J kg^{-1} K^{-1} at $\mu_0\Delta H$ = 2 T and T_C ~ 220 K). The preservation of magnetostructural FOPT in $Gd_{3.7}Tb_{1.3}Si_xGe_{4-x}$ (x = 1.72, 2 and 2.02) has been confirmed by Deng et al. [408], obtaining GMCE at the corresponding transition temperatures and further enhancing MCE after annealing. In $Tb_4GdSi_{2.035}Ge_{1.935}Mn_{0.03}$, FOPT is preserved at around 143 K (ΔS_M = −22.4 J kg^{-1} K^{-1} at 5 T) but besides the formation of monoclinic phase, impurity phases such as orthorhombic phase and Gd_5Si_3 type phase are also found [409].

Xie et al. [410] studied the effect of partial substitution of Dy for Gd in the pseudo-binary compound $Gd_{5-x}Dy_xSi_4$, which crystallizes in Sm_5Ge_4-type orthorhombic structure. A SOPT is observed and Curie temperature progressively decreases from 338 to 140 K (T_C of parent Gd_5Si_4 and Dy_5Si_4 binary compounds respectively). ΔS_M values of ~−2.5 J kg^{-1} K^{-1} ($\mu_0\Delta H$ = 0.95 T), very similar to that of pure Gd, are retained along the compositional series. In the pseudo-binary $Dy_5Si_{4-x}Ge_x$ compounds, the formation of monoclinic structure occurs for the compositional range around x = 1 [411]. For x = 0.5 and 1, two transition temperatures are observed, one at low temperature (~15 K for both) and the second one is a SOPT at 132 K for x = 0.5 but FOPT at 66 K for x = 1 (in agreement with the presence of monoclinic structure). However, the presence of the low temperature transition reduces MCE compared to that of the compound with Gd and shows similar transition temperatures [411]: ΔS_M = −9.6 and −21 J kg^{-1} K^{-1} (−32 at the spike) for x = 0.5 and 1 respectively at $\mu_0\Delta H$ = 5 T.

$Ho_5(Si_{0.8}Ge_{0.2})_4$ compound does not exhibit a FOPT although it crystallizes in the monoclinic structure at room temperature. This compound orders ferromagnetically at 50 K and exhibits a Griffiths phase like behavior between 50 and 100 K. Their MCE results are ΔS_M ~ −3 J kg^{-1} K^{-1} and RC_{FWHM} ~ 90 J/kg at 2 T [412]. Binary Ho_5Si_4 compound undergoes a SOPT from FM to PM state at 76 K and a spin reorientation transition at ~15 K. Their MCE results at ~76 K are ΔS_M = −14.8 J kg^{-1} K^{-1}, ΔT_{ad} = 6.1 K and RC_{FWHM} ~ 435 J/kg at $\mu_0\Delta H$ = 5 T [413].

When Er completely substitutes for Gd in $Er_5Si_xGe_{4-x}$ [414], the crystallization of monoclinic phase occurs in the range of $3.5 \leq x \leq 3.9$. Ordering temperatures are below 30 K and moderate MCE parameters are found ($|\Delta S_M| < 12$ J kg^{-1} K^{-1} at $\mu_0\Delta H$ = 5 T). In the case of partial substitution of Er for Gd in $Er_{5-x}Gd_xSi_4$ (x = 0.50 and 1.25) compounds, complex magnetic behavior was found [415]. Orthorhombic Gd_5Si_4-type structure is formed and the transition to monoclinic, found in Gd free compound at ~230 K, is suppressed. Linear increase of the three lattice parameters following Vegard law is found. Two transition temperatures are found: to AFM at relatively high temperatures (61 and 101 K for x = 0.1 and 0.25 respectively) and to FM at low temperatures (27 and 46 K for x = 0.5 and 1.25 respectively). ΔS_M at the high temperature transitions are ~−12 and −8 J kg^{-1} K^{-1} for x = 0.5 and 1.25 respectively.

Tm_5Ge_4 compound has been recently studied by Zou et al. [416] and it crystallizes in orthorhombic Sm_5Ge_4-type structure, being AFM with two transitions at 13 and 21 K.

The effects of light RE substitution for Gd in the MCE of $Gd_5Si_{4-x}Ge_x$ alloys have also been studied. In the case of $Ce_5Si_{4-x}Ge_x$ [417], its crystal structure is tetragonal Zr_5Si_4-type (space group $P4_12_12$) in the range of $0 \leq x < 2.15$, monoclinic $Gd_5Si_2Ge_2$-type structure at x ~ 2.2 and orthorhombic Sm_5Ge_4-type structure in the range of $2.4 < x \leq 4$. Unlike Gd compounds, the Ce_5Si_4 compound is AFM and the Ce_5Ge_4 compound, FM. The latter exhibits the maximum magnetic entropy change of the series (ΔS_M = −11.6 J kg^{-1} K^{-1} at T_C = 11.5 K and 5 T).

$Gd_{5-x}Pr_xSi_4$ (x = 0, 0.5, 0.75 and 1.0) [400] crystallizes in Gd_5Si_4-type orthorhombic structure and has a SOPT at the T_C. Their Curie temperatures, magnetic moments and $|\Delta S_M|$ decrease with increasing Pr content (T_C reduces from ~320 to

~290 K, magnetic moments decrease from 7.85 to 7.00 μ_B and $|\Delta S_M|$ lowers from 8.2 to 6.1 J kg^{-1} K^{-1} at $\mu_0\Delta H$ = 5 T as x increases from 0.5 to 1).

While Nd_5Si_4 and Nd_5Ge_4 crystallize in tetragonal Zr_5Si_4-type and Sm_5Ge_4-type structures respectively, monoclinic $Gd_5Si_2Ge_2$-type structure can be stabilized in $Nd_5Si_2Ge_2$ compound although phase coexistence occurs. The maximum $|\Delta S_M|$ value of the series is obtained at the FiM transition temperature of Ge-free compound, 71 K. However, recent results on partial substitution of Nd for Gd in $Gd_{5-x}Nd_xSi_2Ge_2$ (x = 0.05, 0.1 and 0.2) series, show that monoclinic phase only crystallizes for x = 0.05 whereas the other two compounds crystallize in Gd_5Si_4-type phase, changing from FOPT to SOPT for $x \geq 0.1$ [418]. Although transition temperature can be enhanced in orthorhombic Nd_5Si_3Ge up to 124 K, ~23% decrease in $|\Delta S_M|$ is observed [411].

Partial substitution of Y for Gd in $Gd_4Y_1Si_{1.9}Ge_{2.1}$ [419] preserves the monoclinic structure and reduces its ordering temperature to 149 K although the magnetic moment per Gd atom is enhanced to 7.87 μ_B compared to Y-free alloys. A FOPT from FM to PM state occurs at this temperature accompanied by a GMCE (ΔS_M = −28 J kg^{-1} K^{-1} at $\mu_0\Delta H$ = 5 T).

Small partial substitution of Zr for Gd in $Gd_{5-x}Zr_xSi_2Ge_2$ alloys was proposed to reduce the amount of detrimental AFM hexagonal Gd_5Si_3-type phase [420]. The amount of desired 5:4 type phase enhances with increasing Zr concentration, from 70% (x = 0) to 85% (x = 0.05). However, higher Zr additions led to a reduced fraction of 5:4 phase. Moreover, the presence of Zr changes 5:4 monoclinic structure (in Zr-free alloy) into a 5:4 orthorhombic one, thus converting FOPT to SOPT. Nevertheless, although $|\Delta S_M|$ decreases from 7.8 to 5.5 J kg^{-1} K^{-1} (2 T) from x = 0 to 0.05, a three-fold enhancement of RC_{FWHM} is attained (from ~50 to above 150 J/kg). For Zr-containing compounds, their Curie temperatures monotonically decrease from 292 to 272 K from x = 0.05 to x = 0.20.

The MCE of Re_5Sn_4 (RE = Tb, Dy, Ho, Er [421]) has been also studied and the alloys exhibit low transition temperatures (22, 15 and 8 K for the AFM-PM transition of the alloys with Dy, Ho and Er respectively). When RE = Tb in Re_5Sn_4, two magnetic transitions occur at 54 and 84 K ascribed to spin reorientation and FM-PM respectively. Their $\Delta S_M(T)$ curves show an inverse MCE behavior for all the studied samples at low temperatures and a direct MCE at higher temperatures. Their major phase adopts the Sm_5Ge_4-type structure (with an enhanced phase fraction after annealing) but up to 18 wt.% of RE_5Sn_3 and $RE_{11}Sn_{10}$ impurity phases were detected.

Application of pressure decreases the MCE of $Gd_5Si_2Ge_2$ and shifts their transition temperatures to higher values [422]. However, a significant broadening is reported, which resulted in >50% enhancement in *RC* for $Gd_5Ge_2Si_2$ prepared under the pressure application of 4.22 kbar [423]. For Tb_5Si_4 compound, the pressure application enhances its MCE [424] transforming from conventional MCE to a GMCE. However, the application of pressure induced a mixed phase in Gd_5Ge_4 compound [425], whereby its FM phase increases with pressure, resulting in higher transition temperatures. This is due to the progressive decrease of FOPT (AFM-FM) contribution to MCE while the contribution of SOPT (FM-PM) to MCE progressively increases.

Thin films of $Gd_5Si_{1.3}Ge_{2.7}$ show a broader FOPT ($|\Delta S_M|$ = 8.83 J kg^{-1} K^{-1} at 5 T), which reduces its magnetic hysteresis [426], while annealing significantly decreases its MCE response [427]. For multilayer systems [428], about 10% reduction of the onset field that is necessary to launch the metamagnetic transition in $Gd_5Si_{1.5}Ge_{2.5}$ was attained by evaporating thin layers of pure Fe (0.1–0.2 μm) on both polished faces of this alloy. Yue et al. [429] produced three component layers of $Gd_5Si_2Ge_2$/Gd/$Gd_5Si_{1.85}Ge_{2.15}$ and achieved a constant adiabatic temperature change in a wide temperature range from 240 to 310 K, which indicates that optimization could be attained by tailoring layer thickness. Thin films of Gd_5Si_4 (350 nm) protected with Pt developed by Hadimani et al. [430] show multiphase character (including Gd_5Si_4 and Gd_5Si_3) and their transitions lay close to those of the bulk system, which is not the case for ball milled powders despite same composition [431].

Ball milling of $Gd_5Si_2Ge_2$-type powder leads to a large decrease in $|\Delta S_M|$, MCE peak temperature and a broadening of the transition [432,433]. This is characteristic of the MCE of powdered samples produced after high energy milling. Trevizoli et al. [434] reported that pulverized bulk samples prior to compaction show that only slight changes to their MCE were observed with respect to those of the bulk counterparts. Short millings lead to various effects in $RE_5Si_{1.3}Ge_{2.7}$ systems, depending on RE = Gd or Tb. A ~35% decrease in the MCE of $RE_5Si_{1.3}Ge_{2.7}$ is observed for RE = Gd, while ~23% enhancement in MCE is obtained when RE = Tb [435].

New applications are also explored by embedding $Gd_5Si_2Ge_2$ particles in a piezoelectric polymer [436]. Upon applying a magnetic field, an electrical voltage is induced as a consequence of the strain induced due to the mechanical interaction between the magnetic and the piezoelectric phases.

5.1.1.4. RE-TM_2-X_2. These intermetallic compounds crystallize in the body-centered tetragonal $ThCr_2Si_2$-type structure (space group *I*4/*mmm*) formed by atomic layers stacked with a sequence of RE-X-TM-X-RE (X = Si, Ge or B and TM = transition metal, being Mn the only element carrying a magnetic moment). In Mn-containing RE-TM_2-X_2, its magnetic behavior is critically dependent on the Mn-Mn intralayer distance, d_{Mn-Mn}, leading to their complex magnetic phase diagrams. Therefore, different magnetic structures can be found concerning Mn-Mn interlayer (*ie*) and intralayer (*ia*) interactions [437]: I) FM exchange-coupled *ie* and AFM coupled *ia* (d_{Mn-Mn} > 0.287 nm for germanides) leading to a canted FM structure; II) both *ie* and *ia* AFM coupled, leading to a canted AFM structure (0.287 nm > d_{Mn-Mn} > 0.284 nm for germanides); III) AFM structure without canting occurring for lower values of d_{Mn-Mn} (d_{Mn-Mn} < 0.284 nm for germanides). Moreover, the interactions with RE moments would lead to more complex structures. One such example could be found in Fig. 1 of Ref. [437], whereby the transition concerning the ordering of RE moments appears at low temperatures, while at higher temperature multiple magnetic transitions and re-entrant ferromagnetism can be observed.

The MCE ascribed to this rich magnetic phenomenology has been studied and their reported results are shown in Figs. 12 and 13 ($|\Delta S_M|$ and ΔT_{ad} respectively). In general, MCE response (ΔT_{ad} and ΔS_M) decreases with increasing transition temperature and GMCE is observed below 50 K. MCE character can change from inverse to direct in a relative small temperature range as observed in $Sm_{1-x}Gd_xMn_2Ge_2$ [438,439] and $SmMn_2Ge_{2-y}Si_y$ although exhibiting modest results [440]. In this case, the largest MCE ($\Delta S_M = -3$ J kg^{-1} K^{-1} at $\mu_0\Delta H = 5$ T for y = 2) was obtained at the Sm ordering temperature (which increases from ~40 K to >100 K from y = 2 to 0). Furthermore, the application of pressure has a considerable effect tuning the transition temperatures of these systems and also increasing the stability range of the AFM order [441]. In addition, MCE ascribed to the low temperature transitions enhances with increasing pressure through the contraction of lattice parameters but no results were reported for the transitions occurring at room temperature.

$La_{0.5}Pr_{0.5}Mn_2Si_2$ compound [442] exhibits a crossover from inverse to direct MCE close to room temperature at ~250 K, with $|\Delta S_M| \sim 2$ J kg^{-1} K^{-1} at 220 K at $\mu_0\Delta H = 5$ T, while values above 280 K are not reported. Similar MCE curves are found for $La_{1-x}Ce_xMn_2Si_2$ [443] but explored in a wider temperature range. Their inverse MCE at low temperatures changes into direct MCE at room temperature, with $\Delta S_M \sim -3$ J kg^{-1} K^{-1} at $\mu_0\Delta H = 7$ T.

Fe substituted $LaMn_2Ge_2$ alloys are reported with $\Delta S_M = -1$ J kg^{-1} K^{-1} at $\mu_0\Delta H = 1.8$ T around room temperature and their transition temperatures decreasing with substituting Fe [444]. This is also included in the review paper by Brück et al. [445].

GMCE has been observed for $NdMn_2Ge_{0.4}Si_{1.6}$ ($\Delta S_M = -15$ J kg^{-1} K^{-1} at $\mu_0\Delta H = 5$ T) associated to a FOPT from AFM to FM state at 36 K [446]. $PrMn_{0.4}Fe_{0.6}Ge_2$ also shows a large MCE of $\Delta S_M \sim -11$ J kg^{-1} K^{-1} at 5 T for the ordering temperature of Pr at ~25 K, whereas a modest $|\Delta S_M|$ of ~1 J kg^{-1} K^{-1} (inverse MCE) was measured at the Néel transition at ~140 K (ascribed to interlayer Mn interaction) and at Curie transition (~165 K) with a crossover at 160 K [447]. MCE has been also studied for Nd $(Mn_{1-x}Fe_x)_2Ge_2$ (x = 0.1 and 0.2) compounds [448]. For x = 0.1, a weak transition at 33 K (Nd sublattice), a spin reorientation at 188 K and a Curie temperature of 290 K are observed. For x = 0.2, the compound exhibits a similar behavior as $SmMn_2Ge_2$, i.e. four magnetic transitions: Besides a weak ordering transition at ~33 K for the Nd sublattice, a FM behavior is also observed at low temperatures up to 95 K, which becomes AFM at temperatures up to 185 K. FM appears again at higher

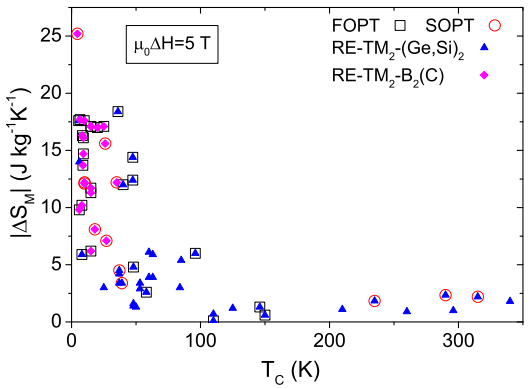

Fig. 12. Relationship between $|\Delta S_M|$ and transition temperatures of several compounds crystallizing in $ThCr_2Si_2$-type structure at $\mu_0\Delta H = 5$ T (data taken from [89,440,446–448,456–462,466,1586–1598]).

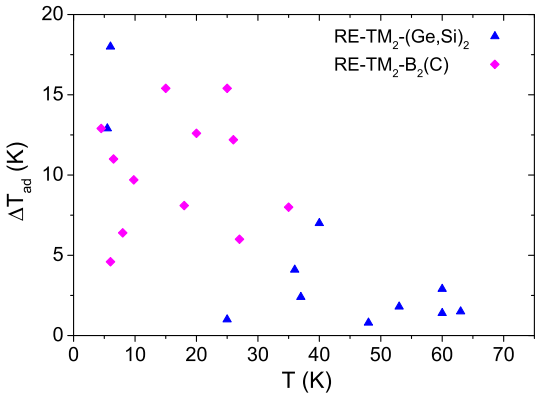

Fig. 13. Relationship between ΔT_{ad} and transition temperatures of several compounds with $ThCr_2Si_2$-type structure at $\mu_0\Delta H = 5$ T (data taken from [89,446,456,458–460,462,1586,1588,1589,1591,1594,1595]).

temperatures up to the Curie temperature (235 K). Modest MCE parameters are obtained: $\Delta S_M = -2.35$ and -1.84 J kg^{-1} K^{-1} (both at $\mu_0\Delta H = 5$ T) for x = 0.1 and 0.2 respectively. Similarly, for x = 0, the compound presents a spin reorientation at 208 K and a Curie temperature at 328 K with $\Delta S_M = -1.10$ J kg^{-1} K^{-1} at $\mu_0\Delta H = 2$ T [449]. Partial Cu substitution for Mn in $NdMn_{2-x}Cu_xSi_2$ ($x \leq 1$) yields higher FM ordering temperature of the Nd-sublattice (from 36 to 100 K), changing from FOPT to SOPT for $x \geq 0.6$, with a large reduction of MCE: $\Delta S_M = -27$ J kg^{-1} K^{-1} (x = 0) to 0.5 J kg^{-1} K^{-1} (x = 1), both at 5 T [450]. On the other hand, $NdMn_{1.7}Cr_{0.3}Si_2$ presents three magnetic transitions at 380 K (from PM to intralayer AFM), 320 K (to canted AFM) and 42 K (FOPT to canted FM). At this temperature, 42 K, it exhibits $-\Delta S_M = 15.9$ J kg^{-1} K^{-1} and $\Delta T_{ad} = 5$ K, both at 5 T [451]. $Nd_{0.2}Gd_{0.8}Mn_2Ge_2$ compound exhibits a transition from FiM to AFM at 262 K due to lattice contraction [452] and retained its AFM state down to 142 K. Moreover, a compensation temperature is observed at 82 K while an inverse MCE ($\Delta S_M = +0.68$ J kg^{-1} K^{-1} at $\mu_0\Delta H = 1$ T) is observed around 262 K and a direct (and larger) MCE around 142 K ($\Delta S_M = -0.81$ J kg^{-1} K^{-1} at $\mu_0\Delta H = 1$ T). $TmMn_2Si_2$ shows a large reversible MCE ($\Delta T_{ad} = 10.1$ K, $|\Delta S_M| = 22.7$ J kg^{-1} K^{-1} and $RC_{FWHM} = 250$ J/kg at 5 T) ascribed to a SOPT at 5.5 K [453]. In the case of $TbMn_2Si_2$ compound [454], two magnetic transitions are observed at higher temperatures (50 and 64 K respectively). While the former transition remains independent of the applied field, the latter shifts to higher temperatures. An estimated value of $\Delta T_{ad} = 7.5$ K was obtained using the specific heat at zero-field. Moreover, it exhibits $\Delta S_M = -16$ J kg^{-1} K^{-1} and $RC_{FWHM} = 396$ J/kg at 5 T due to the two successive FOPTs. Results are in agreement with those of Maji et al. [455], who also explain the significant exchange bias field observed at 5 K due to the presence of AFM and FM domains. Compounds with $ThCr_2Si_2$-type structure but without Mn content have also been studied: e. g. $ErRu_2Si_2$ (GMCE of $\Delta S_M = -20$ J kg^{-1} K^{-1} at $\mu_0\Delta H = 7$ T has been found at very low transition temperature of 5.5 K [456] associated to the field induced metamagnetic transition from AFM to FM state), and $GdRu_2Si_2$ ($\Delta S_M \sim -7$ J kg^{-1} K^{-1} at $\mu_0\Delta H = 7$ T and its transition temperature at ~45 K) [457].

Li and Nishimura [458] studied MCE of different RE-$(Ni,Co)_2B_2(C)$ borides, which also exhibit *I*/4*mmm* space group with $LuNi_2B_2C$-type structure. Some of these intermetallics exhibit a single second order FM to PM transition at low temperatures: e.g. $PrCo_2B_2$ ($\Delta S_M = -4.9$ J kg^{-1} K^{-1} (2 T) at $T_C = 18$ K [459]) and $NdCo_2B_2$ ($\Delta S_M = -4.5$ J kg^{-1} K^{-1} (2 T) at $T_C = 27$ K [460]). However, for $Dy_{0.9}Tm_{0.1}Ni_2B_2C$ [461], which is a superconductor below 4.5 K, it exhibits GMCE ascribed to field induced metamagnetic transition from AFM to FM state at T ~ 9.2 K with $\Delta S_M = -19.1$ J kg^{-1} K^{-1} (7 T). The same research group [462] has reported similar GMCE values for $GdCo_2B_2$, with $\Delta S_M = -21.5$ J kg^{-1} K^{-1} and $\Delta T_{ad} = 18.9$ K, both at ~25 K and $\mu_0\Delta H = 7$ T. Fe substitution in $ErNi_{2-x}Fe_xB_2C$ lowers the magnetic transition and reduces the hysteresis with respect to x = 0. In this series, inverse MCE is observed at low fields (ascribed to AFM behavior) but changes to direct MCE at higher fields. The ΔS_M reported for x = 0, 0.1 and 0.2 are -14.5, 12.7 and 10.6 J kg^{-1} K^{-1} (7 T) respectively [463]. Besides $ThCr_2Si_2$-type and $CeMg_2Si_2$-type (*P*4/*mmm* space group) phases, a new superstructure was observed for $NdMn_xCr_{2-x}Si_2C$ series [464], which shows a $\Delta S_M = -26.0$ J kg^{-1} K^{-1} at 5 T for x = 1.7. This corresponds to a 63% enhancement of MCE with respect to the interstitial-free composition described above [451].

$EuFe_2As_2$ exhibits a giant reversible anisotropic magnetocaloric response with a small hysteresis for a FOPT with $|\Delta S_M| = 14.6$ and 10.3 J kg^{-1} K^{-1} at 20 K and 5 T for in- and out-of-plane directions of the applied magnetic field respectively [465]. $DyNi_{2-x}TM_xB_2C$ (TM = Co and Cr; x = 0.1 and 0.2) shows that substitutions of Cr or Co for Ni decrease transition temperature and reduce magnetic hysteresis. Its AFM state at low temperature leads to an inverse MCE, which changes to direct MCE at high fields >2 T due to a field induced metamagnetic FOPT. Their $|\Delta S_M|$ values decrease with increasing x [466]. In addition, $RECu_2X_2$ (RE = Ho, Er; X = Si, Ge) systems with AFM-PM transition were also studied: e.g. $ErCu_2Si_2$ ($-\Delta S_M = 22.8$ J kg^{-1} K^{-1} at 2.5 K and 5 T [467]) and $HoRu_2Si_2$ ($-\Delta S_M = 9.11$ J kg^{-1} K^{-1} at 5 T and 19 K associated to a spin-flip metamagnetic transition [468]). Paramanik et al. [469] have recently proposed a method to generate magnetic field/temperature phase diagram for the latter compound based on the MCE response at the transitions.

5.1.1.5. Ferromagnetic Lanthanum Manganites. Manganites for magnetocaloric purposes are, in general, FM perovskite manganites, with the formula $La_{1-x-y}RE_xA_yMn_{1-z}TM_zO_3$ (where RE is a rare earth which partially or totally substitutes lanthanum, A is an element of IA or IIA group, with y ~ 0.3 and TM is a transition element, which partially substitutes Mn). Although the parent $LaMnO_3$ compound is semiconducting and orders antiferromagnetically at 150 K, ferromagnetism is observed after the formation of mixed valence in Mn ions via double exchange mechanism between Mn^{4+} and Mn^{3+}. Mixed valence can be achieved by several ways, such as partial substitution of a non-trivalent ion for rare earth, excess of oxygen [470] or La deficiency [471]. However, the magnetic phase diagrams of these lanthanum manganites as a function of the composition are relatively complicated. Taking $La_{1-x}Sr_xMnO_3$ as an example (found in Ref. [472]), at low temperatures, this system shows several states as x increases from 0 to 1: AFM with A-type phase (antiparallel planes), FM, again A-type AFM, AFM but C-type (antiparallel alignment of chains) and finally G-type AFM (antiparallel alignment of all magnetic neighbors). In $La_{1-x}Sr_xMnO_3$ series, upon cooling down from PM phase, a single SOPT to an ordered magnetic structure is attained, except for about $0.5 < x < 0.65$, whereby SOPT from PM to FM phase occurs prior to a FOPT from FM to AFM phase. For about $0.8 < x < 0.95$, the magnetic transition is coupled to a structural transition and thus FOPT occurs. In addition, as x increases from 0 to 1, the structures of PM phases also change from orthorhombic (two phases with space group *Pbnm* structures) to rhombohedric (*R*-3*c*), tetragonal (*I*4/*mcm*) and cubic (*Pm*-3*m*) [472]. Moreover, for about $0.5 < x < 0.65$, the FOPT from FM to AFM transition also implies a change from tetragonal to another orthorhombic structure (*Fmmm*).

Ferromagnetism is favored in metallic manganites due to the enhancement of double exchange interactions by electron transfer. However, the hopping integral gets null due to the antiparallel spins between neighboring Mn and thus AFM manganites are generally insulator systems [473]. Moreover, there are many types of magnetism observed for manganites

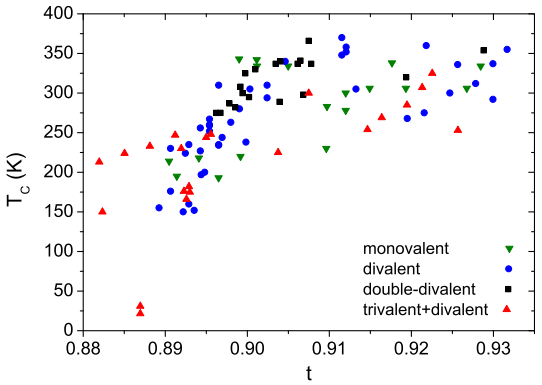

Fig. 14. Curie temperature as a function of the tolerance factor (t) for several manganite compounds with monovalent, divalent and trivalent substitution for La^{3+} (data taken from [474]).

including AFM insulators, FM insulators, AFM metals, glassy insulators, more complex canted magnetic structures and mixed phase states. The small differences among the possible ground states, which are due to competitions among different interactions, are the responsible for this wide variety of phenomenologies. These interactions are listed in Ref. [470]: crystal field splitting between e_g and t_{2g} electrons, kinetic energy of e_g electrons, Hund coupling between e_g and t_{2g} electrons, Jahn-Teller character of Mn^{3+} and Heisenberg magnetic coupling between nearest neighbors.

In the case of FM manganites, tailoring of Curie temperature in a wide range from ~150 to ~375 K can be obtained either upon substitution of a divalent ion (Ca^{2+}, Ba^{2+}, Sr^{2+}, Pb^{2+}, etc.) or a monovalent ion (Na^{1+}, K^{1+}, Ag^{1+}, Li^{1+}, etc.) for La^{3+} (see Table S5 of the Supplementary Material and e.g. [474] and references therein) or by an excess of oxygen [475]. In addition, the ground state of the manganites are affected by the average radii of the cations at the different sites. This can be tuned by partial substitution of La^{3+} by a trivalent rare earth, Y^{3+} or Bi^{3+}, or in La-free Pr or Nd manganites [474]. Fig. 14 shows the Curie temperatures of different manganites (data taken from [474]) as a function of the tolerance factor t, which is defined as:

$$t = \frac{\langle R_{La}\rangle + R_O}{\sqrt{2}(\langle R_{Mn}\rangle + R_O)} \tag{23}$$

where $\langle R_{La}\rangle$ is the average radii of La-site atoms, $\langle R_{Mn}\rangle$ is the average radii of Mn-site atoms and R_O is the radius of the O^{2-}. A correlation factor $r = 0.64$ is found, which is highly significant using statistical criteria for ~100 points. Moreover, deviations from the nominal stoichiometry in the experimental samples must also affect the data dispersion (e.g. charged vacancies will affect Mn^{4+} concentration).

Another possible method to tune T_C is via substitution of Mn by other element, generally TM but semimetals or metalloids can also be used. This generally leads to a deterioration of FM character as FM double exchange mechanism in Mn^{3+}-O^{2-}-Mn^{4+} groups competes with AFM superexchange mechanism when Mn is substituted by other transition metal. Fig. 15 shows the Curie temperatures of (La-A)-(Mn-TM)-O_3 as a function of TM content (where A is a divalent ion). Regarding TM substitutions for Mn in manganites, the tunable Curie temperature per 1 at.% substitution of TM is presented in Fig. 16. A similar T_C dependence was found by Ghosh et al. after substituting 5% of TM (from Cr to Zn) [476]. Conversely,

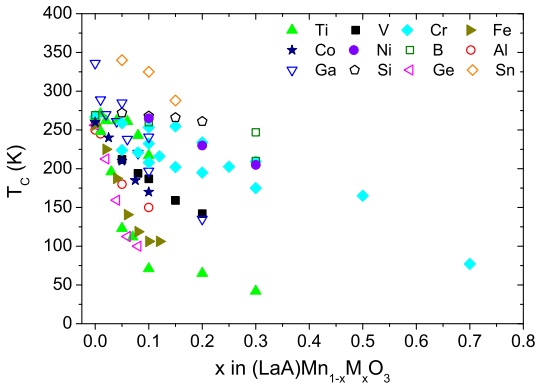

Fig. 15. Curie temperature dependence on the fraction of Mn substituted in manganites by TM element, with 67–70 at.% of La and A as a divalent ion (data taken from [1599–1609]).

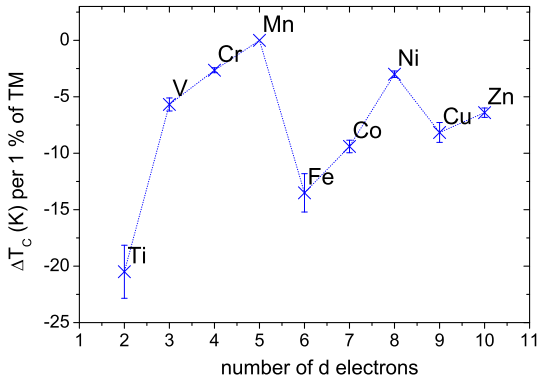

Fig. 16. Effect of different TM partial substitutions for Mn on the Curie temperatures of (La-A)-(Mn-TM)-O_3.

the results from Nisha et al. [477] using V substitution for Mn differ, showing an opposite behavior of increasing T_C with V content. However, the latter study reported multiphase character of their samples. Another exception to the generic rule of lowered Curie temperature with TM substitutions for Mn is found in $La_{0.7}Te_{0.3}Mn_{1-x}Co_xO_3$ series, in which Curie temperature increases from 160 to 220 K as x increases from 0 to 0.5 [478].

The first MCE studies of manganites appeared in 1996 [479–481]. Fig. 17 shows ΔS_M and RC_{FWHM} (1 T) estimated from the data supplied by Phan and Yu [474]. No significant correlation is found with the tolerance factor and thus with the Curie temperature. However, it is worth noticing that off-stoichiometric systems should affect the magnetic properties and could explain the dispersion of the data. Several factors apart from compositional changes can affect MCE: grain size [482–485], chemical order [486–489], sintering temperature [490–492] or pressure application [493–495]. For some compositions, the magnetic entropy change ascribed to the charge-ordered metamagnetic transition is also studied [496,497]. Field dependence of magnetocaloric properties in manganites have been studied [148,498–500] and SOPT systems exhibit the predicted power law dependence with the magnetic field change for ΔS_M and RC_{FWHM}, as shown in Fig. 18 using the data reported by [480]. Tricritical point is claimed as the explanation of the critical exponents found in $La_{0.7}Ca_{0.3}Mn_{0.91}Ni_{0.09}O_3$ [501] ($\Delta S_M = -7.1$ J kg^{-1} K^{-1} at 199.4 K and 4 T). Using the scaling law for the field dependence of ΔS_M, a very low exponent n = 0.55 is obtained and indicates the tricritical behavior. Recently, Abassi et al. [502] considered a phenomenological description of temperature dependence of magnetization for $La_{0.7}Ba_{0.1}Ca_{0.23}MnO_3$, which could nicely describe its MCE at SOPT. Phase

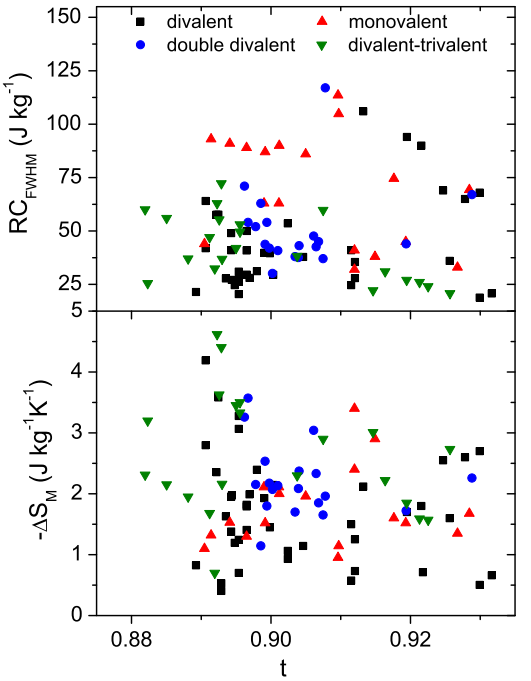

Fig. 17. Peak magnetic entropy change and refrigerant cooling power at 1 T as a function of the tolerance factor (data taken from [474]).

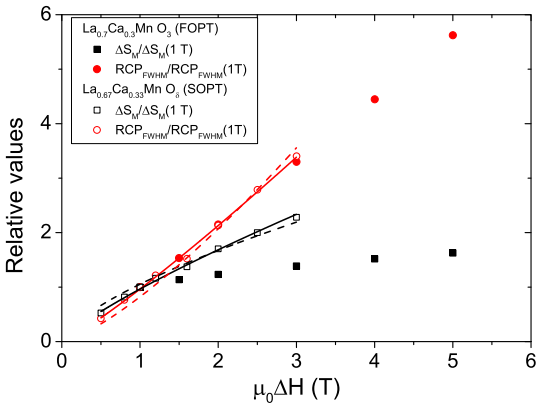

Fig. 18. Relative enhancement of ΔS_M and RC_{FWHM} for $La_{1-x}Ca_xMnO_z$ phase, with a FOPT (x = 0.3, z = 1 [505]) and a SOPT (x = 0.33, z = δ [480]). The solid lines correspond to the fitting of the SOPT data to power laws $\Delta S_M(H) = A \cdot H^n$ ($n = 0.80 \pm 0.02$) and $RC_{FWHM} = B \cdot H^m$ ($m = 1.14 \pm 0.03$), respectively. The dashed lines represent the same fitting using mean field values ($n = 2/3$ and $m = 4/3$).

coexistence (both orthorhombic phases with *Pnma* and *Fmmm* space groups) in $La_{0.5}Ca_{0.5-x}Sr_xMnO_3$ series ($0 \leq x \leq 0.5$) was studied using the field dependence of MCE [503]. The correlation of magnetocaloric and transport properties have also been pointed in doped manganites [504].

Higher $|\Delta S_M|$ values were reported for samples exhibiting a FOPT (e.g. 5.27 J kg^{-1} K^{-1} for 1.5 T in $La_{0.7}Ca_{0.3}MnO_3$ [505]). Recently, Bez et al. [506] tried to clarify the transformation character of $La_{0.67}Ca_{0.33}MnO_3$ compound with a systematic study of the presence of hysteresis using different measurement protocols. A FOPT was found but the experimental hysteresis is extrapolated to zero for an ideal infinitely slowly heating/cooling rate. Inhomogeneities and compositional variations affecting the transition temperatures are claimed to be responsible for this behavior. The close proximity of the Curie (263 K), and metal-insulator (265 K) transitions in $La_{0.7}Ca_{0.21}Ag_{0.09}MnO_3$ compound [507] yields a large MCE in this orthorhombic system, whereby $|\Delta S_M| = 4.8$ J kg^{-1} K^{-1} for 1 T. Unfortunately, the authors did not conduct experiments to determine the order of the transitions involved. Turcaud et al. [508] compare the experimental data of $La_{1-x}Ca_xMnO_3$ series with the predictions from Bean-Rodbell model, to quantify the effects of distributed transition temperatures and other inhomogeneities on the entropy change. A study of Ca deficiency in $La_{0.8}Ca_{0.2-x}MnO_3$ shows a transition from orthorhombic *Pnma* to rhombohedral *R*-3*c* structure, with increase of the unit cell volume and the transition temperature from 240 K (x = 0) to 260 K (x = 0.2) without ΔS_M significantly affected [509]. Quenched disorder yields changes from FOPT to SOPT in the so-called rounding process. This was observed for $La_{0.7}Ca_{0.3-x}Ba_xMnO_3$ series [510] with FOPT for x < 0.05 while SOPT for x > 0.075. Within these values, FOPT also changes to SOPT at magnetic fields above 4 T.

Low dimensionality manganites, such as nanoparticles and nanotubes produced by sol-gel technique [511–515], have recently received attention due to their broader MCE peaks. Their grain size reduction suppresses the long range order and instead aids the formation of metastable phases [516]. Das et al. [517] have recently transformed AFM bulk $La_{0.48}Ca_{0.52}MnO_3$ to a FM system, with an enhanced MCE response upon reducing the particle size to nanometer scale. The use of different substrates can also affect the transition temperatures in $Sm_{0.55}Sr_{0.45}MnO_3$ due to the strains in the lattice [518].

Composite systems of manganites and other oxides have also been proposed as candidates for magnetic refrigeration, with the general advantage of an extended temperature range for table-like MCE responses [519–533].

Although the studied compositions are generally (RE-A)-Mn-O_3 (A is a metal), some studies on (RE-A)$_3$-Mn_2-O_7 double perovskite manganites can be found [492,534–537]. Moreover, inverse and direct MCEs have been reported in $PrBaMn_2O_6$, which exhibits a tetragonal superlattice perovskite structure [538]. Balli et al. have recently characterized the MCE properties of a La_2MnNiO_6 monocrystal [539], using simulations from a mean field model. $LaSrMn_{2-x}Fe_xO_5$ ($0 \leq x \leq 0.5$) series has been studied and Fe substitution decreases Curie temperature (SOPT) from 365 K (x = 0) to 330 K (x = 0.5) ($-\Delta S_M = 0.75$ J kg^{-1} K^{-1} at 5 T for x = 0.2) [540]. In Mn- and RE-free double perovskite $Ba_2CrMo_{1-x}W_xO_6$ compound, similar values for MCE have been obtained: $\Delta S_M = -1.6$ J kg^{-1} K^{-1} at 285 K and $\mu_0\Delta H = 1$ T for x = 0.5 [541]. Recently, the giant anisotropy of the $HoMn_2O_5$ aids a large $\Delta S_M = -12.4$ J kg^{-1} K^{-1} by simply rotating the single crystal in a field of 7 T [542].

5.1.1.6. Y-Fe alloys. Y can be found in the literature among the RE elements. Therefore, the following discussion is placed in the sections concerning RE-containing alloys.

De Oliveira [543] reported the experimental results of pure Fe, Co and Ni, which reasonably fit with those of Nikitin et al. [544] and described the itinerant electron YFe_2 and YFe_3 systems. YFe_2 crystallizes in the cubic Laves phase ($MgCu_2$ type structure) [545] and has a magnetic ordering temperature of 540 K. Upon hydrogen additions, the cubic structure is not observed. For $YFe_2(H_{1-y}D_y)_{4.2}$, it crystallizes in a monoclinic structure below 340 K, with a strong isotope effect on its magnetic properties [546]. The MCE of $YFe_2D_{4.2}$ is $|\Delta S_M| > 10$ J kg^{-1} K^{-1} at $\mu_0\Delta H = 5$ T at temperatures between 90 and 110 K,

below the metamagnetic transition at 127 K. Hydrides of other Laves phases also present monoclinic structure, such as $HoMn_2H_x$ [547] but not in the case of $EuRh_2H_x$ [205] or YMn_2H_x and other $REMn_2H_6$ compounds [548].

YFe_3 crystallizes in $PuNi_3$-type structure [549] (space group *R*-3*m*) and exhibits a Curie temperature of 570 K. The magnetization of both compounds YFe_2 and YFe_3 emerges from Fe atoms. Slightly lower ΔS_M values are observed for the Fe-richest compound but, in both cases, are considered moderate MCE: between 0.4 and 0.5 J kg^{-1} K^{-1} at 1.58 T field change.

Y_2Fe_{17} crystallizes in Th_2Ni_{17}-type structure with a Curie temperature of 295 K and $\Delta S_M \sim -5$ J kg^{-1} K^{-1} at $\mu_0\Delta H = 5$ T [550]. Its melt-spun ribbons show higher Curie temperature of ~310 K, with $\Delta S_M = -1.6$ J kg^{-1} K^{-1} at $\mu_0\Delta H = 1$ T [551]. Recently, Karpenkov et al. [552] found a relatively linear correlation between the unit cell volume and transition temperatures for these rapidly quenched systems, which follows the trend reported for interstitially doped $Y_2Fe_{17}A_x$ (A = C, N) compounds. Moreover, their MCE seems to decrease with increasing ratio of the lattice parameter, c/a.

Wang et al. [553] reported $YFe_{9.5}Mo_{2.5}$ alloy undergoes a SOPT, showing a $\Delta S_M = -1.09$ J kg^{-1} K^{-1} at 275 K and 5 T and crystallizes in tetragonal $ThMn_{12}$-type structure (space group *I*4/*mmm*).

5.1.1.7. Molecular magnets. In addition to intermetallic compounds and alloys, some other complex systems have been also studied, such as organic molecules [554–557], Gd-complexes [558–562], or rare earth containing polymers [563–566]. In the case of molecular clusters [567–587], there is a mixture of rare-earth free and rare earth containing compositions, but we prefer to combine their description in a single section. These systems are generally proposed as refrigerants suitable for very low temperatures [588] to be an alternative to the use of the scarce helium-3 [589]. Evangelisti et al. [589,590] reviewed the magnetothermal properties of molecular magnets, including MCE. Optimization of these systems should require large spins and small anisotropies. Initially, systems based on Fe_8 and Mn_{12} clusters (with S = 10) [591] were studied but they exhibit a high anisotropy. Nearly anisotropic Cr_7Cd system ($T_C = 2$ K) shows modest MCE due to its low S = 3/2 [592]. Promising system should be based on Fe_{14} clusters with S = 25 but limited to very low temperatures ($T_C = 1.87$ K) [593]. MCE of these systems are competitive with, or even better than, those observed for Laves phases suitable below 10 K. Possibilities to extend to room temperature the thermal range of applicability of molecule based systems were opened after studies on Prussian blue analogues $CsNi^{II}[Cr^{III}(CN)_6]\cdot(H_2O)$ (FM ordering below ~90 K) and $Cr_3^{II}[Cr^{III}(CN)_6]_2\cdot 12(H_2O)$ (FiM ordering below ~230 K) with $|\Delta S_M| = 6.6$ and 0.93 J kg^{-1} K^{-1} respectively at 7 T [594].

5.1.1.8. Other rare earth containing crystalline compounds. This section will focus on those intermetallic compounds containing RE (but not belonging to any of the families described above) reported with MCE properties, and in particular, crystalline intermetallics and alloys. There is a plethora of RE-containing compounds besides the already-described families, which magnetic transitions have deserved the attention of the magnetocaloric scientific community. In order to establish a classification criteria, they will be described following a descending sequence of their RE content (at.%).

A peculiar case is the high entropy alloy only composed of five rare earth elements: $Gd_{20}Dy_{20}Er_{20}Ho_{20}Tb_{20}$ [595]. The alloy forms a single crystalline phase with HCP structure. For a smaller number of elements, multiple phases are formed, suggesting that phase formation is related to entropy, rather than atomic size, enthalpy, or electronegativity. The quinary alloy has a relatively large magnetic entropy change (8.6 J kg^{-1} K^{-1} at 186 K for an applied field of 5T) and a large refrigerant capacity (~630 J kg^{-1} for that same field) due to the broader phase transition emerging from the strong chemical disorder.

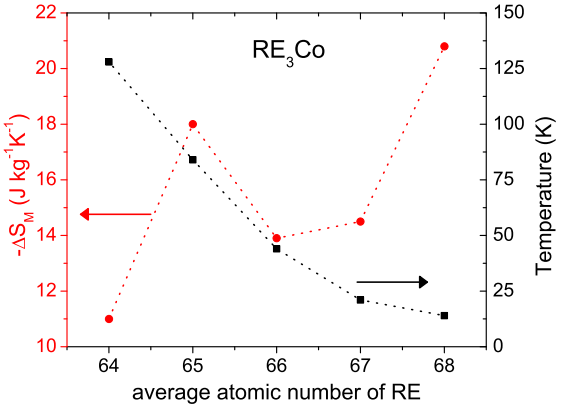

Fig. 19. Magnetic entropy change (at $\mu_0\Delta H = 5$ T) and transition temperature for RE_3Co compounds crystallizing in Fe_3C structure.

5.1.1.8.1. Compounds with 75 at.% of RE. Gd_3TM (TM = Co, Ni [596], Rh [597] and Ru [598]), Tb_3Co [599], Dy_3Co [600], Ho_3Co [601] and Er_3Co [602] crystallize in the orthorhombic cementite-like Fe_3C-type structure. The Néel temperatures are 128 and 99 K for Gd_3Co and Gd_3Ni, with $\Delta S_M \sim -11$ and -5 J kg^{-1} K^{-1} at $\mu_0\Delta H = 5$ T respectively. In the case of Gd_3Rh, its MCE peaks at 112 K ($\Delta S_M = -9.2$ J kg^{-1} K^{-1} at $\mu_0\Delta H = 5$ T) close to the ordering temperature of, presumably, a canted AFM system [597]. For Gd_3Ru compound, its GMCE is reported with $-\Delta S_M = 30$ J kg^{-1} K^{-1} and $\Delta T_{ad} = 5.7$ K (5 T) at around 59 K and $-\Delta S_M$ always above 5 J kg^{-1} K^{-1} in the temperature range from 40 to 90 K [598]. In the case of Tb_3Co compound, reports on its magnetic behavior differ: although two transition temperatures from FM to AFM state at 72 K and from AFM to PM state at 82 K were previously reported for Tb_3Co, Arrott plots indicate a SOPT from FM to PM state at 82 K [599] ($\Delta S_M = -18$ J kg^{-1} K^{-1} at 84 K and $\mu_0\Delta H = 5$ T). Dy_3Co shows two successive transformations: an AFM-AFM transition at 29 K and an AFM-PM transition at 44 K. Moreover, a field induced metamagnetic transformation occurs from AFM to FM below 44 K and its MCE changes from inverse to normal near the critical field. Its $-\Delta S_M = 13.9$ J kg^{-1} K^{-1} at around 44 K and $RC_{FWHM} \sim 600$ J/kg at 5 T are ascribed to the metamagnetic transition [600]. Rapid quenching preserves Fe_3C structure but $-\Delta S_M$ reduces to 6.5 J kg^{-1} K^{-1} and RC_{FWHM} to 364 J/kg (5 T) [603]. Ho_3Co also shows two successive magnetic transitions: from PM to AFM system at 21 K ($\Delta S_M = -14.5$ J kg^{-1} K^{-1} at 5 T) and a spin reorientation at lower temperature of 8.5 K [601]. Er_3Co undergoes a FM transition at 14 K, with $-\Delta S_M = 17$ J kg^{-1} K^{-1} at 5 T [602], though a higher value of $\sim$24.5 J kg^{-1} K^{-1} was reported by other authors [604]. Fig. 19 shows the influence of different types of RE in RE_3Co compounds on their ΔS_M and transition temperatures.

5.1.1.8.2. Compounds with 71 at.% of RE. Recent results on the MCE of compounds with the stoichiometry RE_5A_2, leading to this atomic fraction of RE, can be found for RE_5Pd_2 (RE = Dy [605] and Ho [606]) crystallizing in Dy_5Pd_2-type structure (space group *Fd*3*m*). In the case of Dy-containing compound, an inverse GMCE is observed at 3.5 K ($\Delta S_M = 29$ J kg^{-1} K^{-1} at $\mu_0\Delta H = 5$ T) and a large direct MCE at 60 K ($\Delta S_M = -8.3$ J kg^{-1} K^{-1} at $\mu_0\Delta H = 5$ T) [605]. In the case of Ho-containing compound, a maximum $-\Delta S_M = 15$ J kg^{-1} K^{-1} at $\mu_0\Delta H = 5$ T is observed at around 40 K. Both $|\Delta S_M|$ and the paramagnetic temperature increase with increasing Pd content in off-stoichiometric samples [606]. In partially substituted Ni for Pd samples, suppression of the MCE response resulted [607].

5.1.1.8.3. Compounds with 70 at.% of RE. The influence of compositional modification on the MCE of Gd_7Pd_3 alloys have been studied [608], wherein MCE decreases with decreasing crystal size [609]. They crystallize in hexagonal Th_7Fe_3-type structure (space group *P*6$_3$*mc*). Parent Gd_7Pd_3 compound [610] orders ferromagnetically above room temperature, 323 K, with $\Delta S_M = -6.5$ J kg^{-1} K^{-1} at $\mu_0\Delta H = 5$ T. The substitution of 1/3 of Ni for Pd retains the structure and shifts T_C to 310 K, whereas its $|\Delta S_M|$ reduces to 4.8 J kg^{-1} K^{-1} (5 T) [608]. Slightly higher values of $|\Delta S_M|$ were reported by Oboz et al. [611] but with a larger reduction in $T_C = 298$ K. In that study, $\Delta S_M \sim -7$ J kg^{-1} K^{-1} is reported at the maximum field of 7 T. These results have been recently confirmed by Talik et al. [612] and they also mention that the peak temperature of MCE decreases to 240 K for 2/3 Ni substitution for Pd. While ΔS_M is almost independent of Ni content, the FWHM significantly increases with increasing Ni content as there is a clear second maximum in $-\Delta S_M$ for Ni-containing compounds at $\sim$140 K. Partial Y substitution for Gd in $Gd_3Y_4Pd_3$ compound decreases Curie temperatures, maintaining its crystalline structure [613,614], whereas $\Delta S_M \sim -3$ J kg^{-1} K^{-1} (5 T) at 197 K [613]. More recently, the previous study was extended to single crystals of $Gd_{7-x}Y_xPd_3$ (x = 0–6) series [615] and reported that T_C decreases close to linearity as Y content increases, and $T_C = 0$ K when full Y substitution for Pd was extrapolated. Analogously, $|\Delta S_M|$ linearly decreases with Y content from $\sim$7 to $\sim$3 J kg^{-1} K^{-1} (7 T) as x increases from 0 to 6.

Gd_7Rh_3 also crystallizes in Th_7Fe_3-type structure and exhibits a Néel temperature at 140 K with $\Delta S_M = -5.7$ J kg^{-1} K^{-1} at $\mu_0\Delta H = 8$ T [616]. Amorphous Gd_7Ru_3 reported by Kumar et al. [617] shows two magnetic transitions at 58 and 34 K and a maximum $\Delta T_{ad} = 5$ K at 5 T.

5.1.1.8.4. Compounds with 67 at.% of RE. The RE_2In series with RE = Gd [618], Tb [619], Dy [620], Ho [621] and Er [622] crystallizes in hexagonal Ni_2In-type structure (space group *P*6$_3$/*mmc*). Dy- and Er-containing compounds present SOPT from FM to PM state at 130 and 46 K and an associated MCE characterized by $\Delta S_M = -9.2$ and -16 J kg^{-1} K^{-1}, respectively, at $\mu_0\Delta H =$ 5T. The other compounds exhibit two transformation temperatures: for RE = Ho, its spin reorientation occurs at 32 K and FM to PM at 85 K (SOPT), while for RE = Gd and Tb, their AFM to FM transformations occur at 105 and 45 K respectively, and a FM to PM (SOPT) at 190 and 165 K respectively. The MCE parameters at T_C are $\Delta S_M = -4.5$ J kg^{-1} K^{-1} at 4 T for Gd intermetallic and -6.6 and -11 J kg^{-1} K^{-1} at $\mu_0\Delta H = 5$ T for Tb and Ho intermetallics, respectively (see Fig. 20). 20 at.% substitution of Al, Ga, Sn or Pb for In was studied by Tence et al. [623]. They found the Al and Ga substitution only affects significantly the FM-AFM transition at low temperatures. However, PM-FM transition shifts to higher temperatures after substitution of Sn or Pb. This substitution also affects the transition at lower temperatures. In the case of Al substitutions, no significant alteration to ΔS_M is observed as compared to the parent compound but Pb substitution reduces it to -3.5 J kg^{-1} K^{-1} at 4 T.

Gd_2Al crystallizes in the Co_2Si-type structure (*Pnma* space group). Co additions in Gd_2AlCo_x ($x \leq 0.6$) enhance MCE and also form Gd_3Al_2 minor phase (*P*4$_2$*nm* space group) for $x \leq 0.2$ and $Gd_{57.5}Co_{20}Al_{22.5}$ phase (*Pbam* space group) with higher Co content. Its $-\Delta S_M$, at around 50 K, increases from 6.5 to 7.9 J kg^{-1} K^{-1} at 5 T as x increases from 0 to 0.2 [624].

The MCE of several RE_6CoTe_2 compounds (RE from Gd to Er) [625] exhibiting Fe_2P-type structure (space group *P*-62*m*) has also been reported. All the studied phases show two transition temperatures: high temperature transitions at 220, 174, 125, 60 and 30 K, and low temperature transitions at 180, 52, 26, 22 and 14 K for Gd, Tb, Dy, Ho and Er respectively. For the Gd-containing compound, $\Delta S_M = -6.5$ and -4.5 J kg^{-1} K^{-1} (5 T) at 180 and 220 K respectively. Also crystallizing in Fe_2P-type structure, Gd_6FeBi_2 [626] shows a Curie temperature at $\sim$350 K with $\Delta S_M = -4.3$ J kg^{-1} K^{-1} at 5 T.

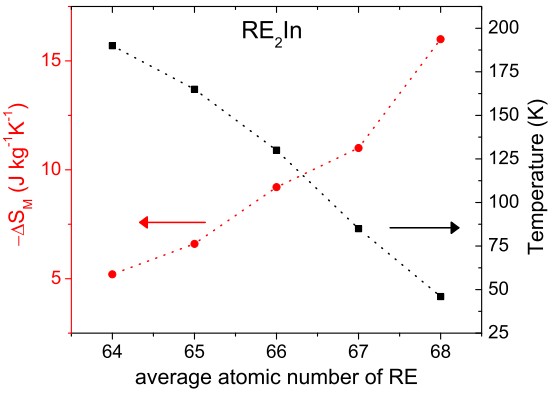

Fig. 20. Magnetic entropy change (at $\mu_0\Delta H = 5$ T) and transition temperature for RE_2In compounds crystallizing in Ni_2In structure.

A large reversible MCE is reported for Er_4NiCd compound ($\Delta S_M = -18.3$ J kg^{-1} K^{-1} for 5 T without hysteresis loss) [627], which crystallizes in Gd_4RhIn-type structure (space group *F*-43*m*) and antiferromagnetically orders at 5.9 K. For magnetic fields larger than 0.4 T, a metamagnetic transition occurs along with a Curie temperature at 7.5 K, indicating a rather unstable AFM ground state in this system. Eu_4PdMg shows a table-like MCE with $\Delta S_M = -5.5$ J kg^{-1} K^{-1} at 5 T from 20 K to 160 K, implying a large *RC* [628]. Also crystallizing in this structure, Tm_4AMg (A = Pd, Pt) compounds show a FM-PM transition at very low temperatures (6.0 and 4.5 K with $-\Delta S_M = 18.0$ and 16.5 J kg^{-1} K^{-1} at 5 T for Pd and Pt respectively). Many other compounds of this family are also discussed by Li et al. [629] in a recent review.

MCE was also studied for $Ho_{6-x}Er_xMnBi_2$ crystallizing in Zr_6CoAs_2-type structure (space group *P*-62*m*), decreasing transition temperatures from 201 to 98 K as x increases from 0 to 6 [630]. A SOPT is suggested with $|\Delta S_M|$ increasing from 5.0 to 10.6 J kg^{-1} K^{-1} at 5 T as x increases from 0 to 6. Crystallizing in the orthorhombic Ho_6Co_2Ga structure (space group *Immm*), $Dy_6Co_{2.5}Sn_{0.5}$ compound exhibits a metamagnetic transition below 42 K and presents an inverse MCE at ~13 K and a direct MCE at ~52 K [631].

GdScSi and GdScGe crystallize in CeScSi-type structure (space group *I*4/*mmm*) and show Curie temperatures above room temperature (around 350 K), with $\Delta S_M(2\text{ T}) = -1.34$ and -1.45 J kg^{-1} K^{-1} respectively [632].

5.1.1.8.5. Compounds with 63 at.% of RE. Gd_5CoSi_2 compound crystallizes in tetragonal structure, deriving from Cr_5B_3-type structure (space group *I*4/*mcm*), and is FM at temperatures below 168 K with $\Delta S_M \sim -9$ J kg^{-1} K^{-1} for $\mu_0\Delta H = 4.6$ T [633]. This structure is also observed in Nd_5Si_3 [634] and Pr_5Si_3 [635] compounds, which undergo SOPT at 112 and 47 K with $\Delta S_M = -5.0$ and -11.6 J kg^{-1} K^{-1}, respectively, at $\mu_0\Delta H = 5$ T. Derived from this structure, Mo_5SiB_2-type structure (*I*4/*mcm* space group) is found for RE_5Ir_2X (RE = Gd, Tb, Dy and Ho; X = Sn, Pb, Sb and Bi) [636]. In general, the transition temperatures decrease with increasing atomic number of the RE element. For Gd-containing compounds, $\Delta S_M \sim -7$ J kg^{-1} K^{-1} is observed at ~160 K and 5 T for Sn and Pb containing alloys but for Sb and Bi- containing alloys, they exhibit $\Delta S_M \sim -9$ J kg^{-1} K^{-1} at ~125 K and 5 T. Yuan et al. [637] studied $RE_5Ga_{3-x}TM_x$ (RE = Ho, Er; TM = Fe, Co), wherein its crystal structure changes from Mn_5Si_3-type to Cr_5B_3-type as TM content increases. They reported that $Ho_5Ga_{2.6}Co_{0.4}$ alloy (with Cr_5B_3-type structure) exhibits a $\Delta S_M \sim -12.7$ J kg^{-1} K^{-1} at 32.5 K and 5 T.

The binary Tb_5Si_3 compound, crystallizing in Mn_5Si_3-type structure (space group $P6_3/mcm$), undergoes a magnetic field induced transition and shows unusual positive magnetoresistance at very low temperatures [638]. Normal MCE is observed at the PM state (above 69 K) with a sign reversal of MCE in the ordered state. Their MCE results also indicate the existence of an inverse metamagnetism. Also crystallizing in the Mn_5Si_3-type phase, Pr_5Ge_3 compound exhibits AFM ordering at low temperature (18 K) but with competing FM interactions close to the transition temperature of 22.5 K with $\Delta S_M = -5.8$ J kg^{-1} K^{-1} at 7 T [639]. Nd_5Ge_3 compound shows a maximum in $-\Delta S(T)$ of ~5 J kg^{-1} K^{-1} at ~50 K and 7 T, which shifts to lower temperatures after ball milling [640]. The crystalline structure in $RE_5A_xSb_{3-x}$ (A = Si, Ge) changes to Yb_5Sb_3-type structure (space group *Pnma*) [641], showing multiple magnetic transitions for RE = Pr and Nd, while only a Pauly paramagnetic behavior for RE = La.

MCE of some compounds crystallizing in the Yb_5Sb_3-type structure (space group *Pnma*) has also been studied. Among them, Dy_5CoBi_2 exhibits a $\Delta S_M = -6.2$ J kg^{-1} K^{-1} and $\Delta T_{ad} = 2.2$ K at 38 K and 5 T [642], $Gd_5Ni_{0.96}Sb_{2.04}$ shows $\Delta S_M = -7.7$ J kg^{-1} K^{-1} at 112 K at 5 T and $Gd_5Ni_{0.71}Bi_{2.29}$ presents a $\Delta S_M = -5.6$ J kg^{-1} K^{-1} at 160 K at 5 T [643].

$(Gd_{12-x}Tb_x)Co_7$ ($0 \le x \le 8$) [644] crystallizes in monoclinic $Ho_{12}Co_7$-type structure (space group $P2_1/c$). When Tb content increases from 0 to 8 at.%, its Curie temperature decreases from 161 to 119 K and $|\Delta S_M|$ (SOPT) from 8.8 to 7.1 J kg^{-1} K^{-1} ($\mu_0\Delta H = 5$ T) respectively. For x = 0, its presence of a spin reorientation at 123 K yields a broader MCE peak with RC_{FWHM} ~ 650 J/kg. Among the $Ho_{12-x}Er_xCo_7$ series, composite samples with $Ho_{12}Co_7$ and $Ho_6Er_6Co_7$ optimize the width of the MCE response with $|\Delta S_M| = 16.7$ J kg^{-1} K^{-1} at 37.9 K and 5 T [645]. Fig. 21 shows the dependence of transition temperatures and $|\Delta S_M|$ on the atomic number of RE in these compounds (data taken from [645]). As the atomic number of RE increases, Curie temperature decreases while $|\Delta S_M|$ increases.

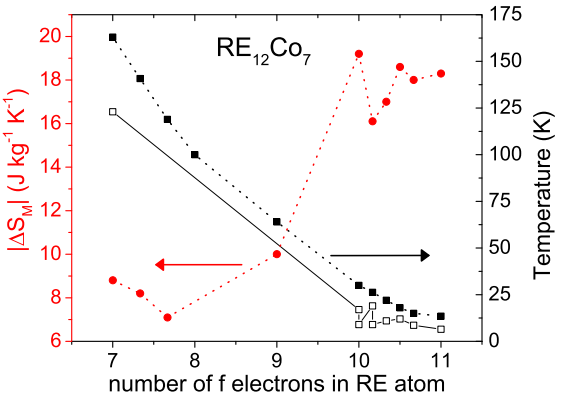

Fig. 21. Magnetic entropy change (at $\mu_0\Delta H = 5$ T) and transition temperatures for different $RE_{12}Co_7$ compounds (solid symbols represent those alloys with PM-FM transition and hollow ones for those with FM-AFM transition). Data adapted from [645].

5.1.1.8.6. Compounds with 60 at.% of RE. $(Gd_{1-x}X_x)_3Al_2$ series (X = Y, $0 \leq x \leq 0.3$ [646]; X = Dy, $0 \leq x \leq 0.5$ [647]) crystallizes in tetragonal Zr_3Al_2-type (space group $P4_2nm$). As X content increases, their lattice parameter and transition temperature decrease: from 284 K to 195 K when Y increases from 0 to 0.3 at.%, and to 215 K when Dy increases from 0 to 0.5 at.%. Their $|\Delta S_M|$ ascribed to SOPT also decreases with increasing x for Y-containing compound (from 2.3 to 1.8 J kg^{-1} K^{-1}, measured at $\mu_0\Delta H = 1$ T) but remains unchanged for Dy-containing compound. Also crystallizing in this structure (but with minor amounts of DyAl and $DyAl_3$ impurity phases) Dy_3Al_2 shows a PM-FM SOPT at 94 K and a spin reorientation at 69 K ($|\Delta S_M|$ = 12.1 and 5.2 J kg^{-1} K^{-1} respectively, at 5 T) [648]. Two transitions were also observed for Tb_3Al_2 compound: T_C = 190 K and a possible spin reorientation at 86 K [649]. It exhibits a $|\Delta S_M| > 12$ J kg^{-1} K^{-1} at 190 K and 5 T with $RC_{FWHM} >$ 600 J/kg.

RE_3Ni_2 compounds (RE = Ho and Er) crystallize in a rhomb-centered rhombohedral structure with space group *R*-3 and experience two successive transitions: SOPT from PM to FM state (at 36 K for Ho- and 17 K for Er-containing compounds) and spin reorientation transition (at 10 K for Ho- and ~12 K for Er-containing compounds). When RE = Ho, its $|\Delta S_M|$(5 T) = 21.7 J kg^{-1} K^{-1} while 19.5 J kg^{-1} K^{-1} for RE = Er [650].

$RE_{15}Si_9C$ compounds (RE = Gd, Tb and Dy) crystallize in $La_{15}Ge_9Fe$-type structure ($P6_3mc$ space group) that derives from Mn_5Si_3-type structure. They undergo a SOPT at 170, 130 and 70 K with $-\Delta S_M$ = 7.0, 11.8 and 12.9 J kg^{-1} K^{-1} and ΔT_{ad} = 5.06, 6.64 and 5.52 K at 7 T for RE = Gd, Tb and Dy, respectively [651]. The scaling law of the magnetic entropy change with applied field is also applicable in these systems.

5.1.1.8.7. Compounds with 57 at.% of RE. The $Gd_4(Bi_xSb_{1-x})_3$ series is FM, with T_C increasing from 266 K (x = 0) to 332 K (x = 1), and crystallizes in cubic anti-Th_3P_4-type structure (space group *I*-43*d*). For x = 0, $-\Delta S_M$ = 6.8 J kg^{-1} K^{-1} at $\mu_0\Delta H$ = 5 T and decreases with increasing x [652]. Monte Carlo simulations of Gd_4Sb_3 compound are in good agreement with their experimental data [653].

Gd_4Co_3 [654] and $(Gd_{0.9}Dy_{0.1})_4Co_3$ [655] ferrimagnets were assumed to crystallize in Ho_4Co_3-type structure (space group $P6_3/m$). The ordering transitions are at 220 K and 145 K for Dy-free and Dy-containing compounds respectively, with an enhanced ΔS_M value for the latter compound (−5.74 and −8.47 J kg^{-1} K^{-1} respectively, at $\mu_0\Delta H$ = 5 T). For Dy-free compound, the presence of a second magnetic transition at 163 K was initially ascribed to spin reorientation, resulting in a very broad MCE curve and $RC_{FWHM} \sim$ 800 J/kg, which is much higher than that (~500 J/kg) for Dy-containing compound. However, Tence et al. [656] claim that Gd_4Co_3 compound does not exist but a mixture of $Gd_{12}Co_7$ and $Gd_4Co_{\sim 3.23}$ is observed for this Gd/Co ratio. The latter $Gd_4Co_{\sim 3.23}$ phase, which exhibits the $P6_3/m$ space group, should be responsible for the high temperature transformation, whereas the FM transition of the $Gd_{12}Co_7$ impurity phase could be responsible for the low temperature transformation, which was previously ascribed to a spin-reorientation. A maximal ΔT_{ad} = 4.4 K at 4.5 T is reported for the mixture.

5.1.1.8.8. Compounds with 55 at.% of RE. This atomic fraction of RE corresponds to $Gd_5Si_2Ge_2$ family described earlier.

Hexagonal $Ce_6Ni_2Si_3$-type structure (space group $P6_3/m$) is exhibited by $RE_6Co_2Si_3$ compounds, whose Curie temperatures of 84.5 (RE = Nd), 187 (RE = Tb) [657] and 295 K (RE = Gd) [658] are reported. The MCE parameters associated with their SOPT are $-\Delta S_M$ = 5.3 (RE = Nd), 6.8 (RE = Tb) [657] and 6.3 J kg^{-1} K^{-1} at 5 T, for (RE = Gd), with a broad $\Delta S(T)$ peak (FWHM > 100 K and $RC_{FWHM} \sim$ 700 J/kg) for the latter [658]. For $RE_6Co_{1.67}Si_3$, minor changes in the stoichiometry retain its $Ce_6Ni_2Si_3$-type structure and SOPT character. Their MCE parameters at $\mu_0\Delta H$ = 5 T are: for RE = Pr, $-\Delta S_M$ = 6.9 J kg^{-1} K^{-1} and RC_{FWHM} = 262 J/kg at T_C = 48 K [659]; for RE = Tb, $-\Delta S_M$ = 7 J kg^{-1} K^{-1} and $RC_{FWHM} \sim$ 560 J/kg at T_C = 186 K[660]; for RE = Gd, $-\Delta S_M$ = 5.2 J kg^{-1} K^{-1} and RC_{FWHM} ~520 J/kg at T_C = 298 K [661]. Tb substitution for Dy in $RE_6Co_{1.67}Si_3$ series leads to decrease in T_C and $-\Delta S_M$ although *RC* increases [662]. When RE = Tb and Nd in $RE_6Co_{1.67}Si_3$, its magnetization behavior is found to be sensitive to the type of measurement protocol due to the strong magnetostructural coupling and/or magnetic frustration [663]. Partial substitution of Ge for Si in $Gd_6Co_{1.67}Si_{2.5}Ge_{0.5}$ yields a $\Delta S_M = -5.9$ J kg^{-1} K^{-1} (5 T) at T_C = 296 K,

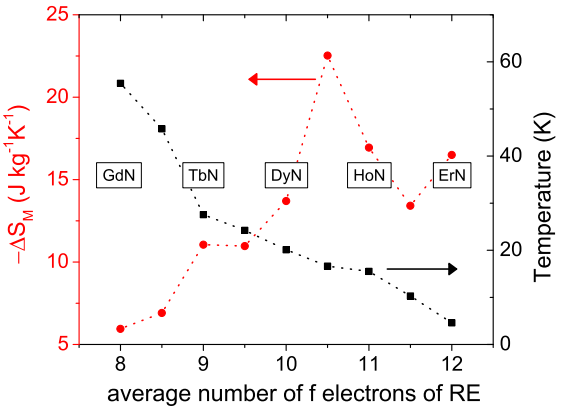

Fig. 22. Magnetic entropy change (at $\mu_0\Delta H = 2$ T) and transition temperature for different rare earth nitrides crystallizing in NaCl structure. Data adapted from [678].

with a broad MCE peak (FWHM ~ 100 K) [664]. $Gd_6Ni_{1.67}Si_3$ also crystallizes in $Ce_6Ni_2Si_3$-type structure but has higher Curie temperature of ~310 K [665]. Its MCE parameters are $\Delta S_M = -5.72$ J kg^{-1} K^{-1} and $\Delta T_{ad} \sim 6$ K at $\mu_0\Delta H = 4.8$ T. However, to obtain relatively single phased systems will further require annealing. $Gd_6Ni_2Si_3$ and $Gd_6Co_2Si_3$ were also studied by Pathak et al. [666] showing slightly different MCE values, wherein $-\Delta S_M(5\text{ T}) = 4.2$ and 5.3 J kg^{-1} K^{-1} at $T_C = 319$ and 298 K respectively. In addition, $Pr_6Co_2Si_3$ and $La_6Ni_2Si_3$, also crystallizing in this $Ce_6Ni_2Si_3$-type structure, display MCE parameters of: $-\Delta S_M(5\text{ T}) = 6.1$ and 0.1 J kg^{-1} K^{-1} at $T_C = 50$ and 7 K respectively. In the presence of a corrosive media (water flow), $Gd_6Co_{1.67}Si_3$ develops a passivated oxide layer ($Gd_2O_3 + SiO_2$) without affecting MCE [667]. Closely related to this structure, $Gd_6Co_{4.85}$ was reported as the only phase for Gd_4Co_3 stoichiometry [656,668] and it exhibits a single ordering temperature at 219 K with $\Delta S_M \sim -2.5$ J kg^{-1} K^{-1} (2 T) and $\Delta T_{ad} = 4.4$ K. Its transition occurring at 163 K is ascribed to impurities of the $Gd_{12}Co_7$ compound described above in the section corresponding to 63 at.% RE containing compounds.

5.1.1.8.9. Compounds with 52 at.% of RE. $Dy_{11}Si_4In_6$ crystallizes in $Sm_{11}Ge_4In_6$-type structure (space group *I*4/*mmm*), with a $|\Delta S_M|(9\text{ T}) = 16.5$ J kg^{-1} K^{-1} at $T_C = 52$ K (reduced to ~9 J kg^{-1} K^{-1} for 5 T) [669].

All $RE_{11}Ge_8In_2$ (RE = Gd-Tm) phases, with space group *I*4/*mmm*, experience a FM ordering at 84, 96, 76, 26, 24 and 10 K for Gd, Tb, Dy, Ho, Er and Tm respectively. In addition, their unit cell volume decreases with increasing atomic number of RE. For RE from Gd to Ho, their spin reorientation transitions occur below Curie temperatures. Their $-\Delta S_M$ (5 T) obtained around their SOPT are: 4.4 (RE = Gd), 6.3 (RE = Tb) and 10.6 J kg^{-1} K^{-1} (RE = Tm), which is the largest among the series [670].

5.1.1.8.10. Compounds with 50 at.% of RE. Mononitrides REN compounds (RE = Gd, Tb, Dy, Ho and Er) [671–673] exhibit SOPT at cryogenic temperatures between 7.5 (for ErN) [672] and 61.2 K (for GdN) [674]. Tunable transition temperatures of the nitrides of binary systems were also studied [674–678] as shown in Fig. 22. The $|\Delta S_M| \sim 30$ J kg^{-1} K^{-1} (5 T) and ΔT_{ad} = 8–10 K of ErN and HoN make these systems promising and competitive with the Laves phases for applications of hydrogen liquefying and other refrigeration demands at low temperatures. Moreover, rare earth nitrides are hydrogen inert systems with high thermal conductivity. They crystallize in a NaCl-type (*Fm*3*m* space group) structure and have higher RE packing densities than those of their corresponding hexagonal closed packed structures. Both their lattice parameters and transition temperatures linearly decrease with increasing atomic mass of the RE element. Recent studies on nanopowders of REN (RE = Tb, Dy and Ho [679]) [680] produced by plasma arc discharge, report that their high MCE values are retained at slightly lower PM-FM SOPT temperatures (35.7, 19.9 and14.2 K) than those produced via carbothermic reduction [671,675]. The presence of Ho_2O_3 impurities in HoN samples shifts the temperature of maximum MCE response to <5 K, which is below the explored range in Ref. [679].

EuO [681] also crystallizes in NaCl-type structure with a SOPT from FM to PM state at 67 K and exhibits high values of $|\Delta S_M| \sim 18$ J kg^{-1} K^{-1} and $\Delta T_{ad} \sim 7$ K at $\mu_0\Delta H = 5$ T. FM semiconductor EuS with this structure orders ferromagnetically at $T_C = 18$ K (SOPT) and has a $|\Delta S_M| = 37$ J kg^{-1} K^{-1}, $RC_{FWHM} = 782$ J/kg and $\Delta T_{ad} = 10.4$ K at $\mu_0\Delta H = 5$ T [682].

Also crystallizing in NaCl structure, DySb was reported as a promising material for low temperature refrigeration due to its small hysteresis and large values of ΔS_M [683]. DySb is an Ising antiferromagnet with Néel temperature ~9 K. The observed change in the sign of MCE is ascribed to a field induced metamagnetic FOPT from PM to FM state. An enhanced MCE is reported in their single crystals, which show highly anisotropic behavior [684].

CsCl-type structures (space group *Pm*3*m*) are found for TbZn [685], HoZn [686] and ErZn [686] compounds, wherein their MCE is affected by spontaneous and field induced spin reorientation transitions. Theoretical studies show a table-like behavior for TbZn and HoZn between their Curie (23 K) and reorientation transitions that are dependent on the field direction. GdZn, also crystallizing in CsCl-type structure, exhibits good MCE response, with $\Delta S_M = -3.5$ J kg^{-1} K^{-1} at $\mu_0\Delta H = 2$ T. Composites of Gd plus GdZn phases were prepared in a single production step and proposed to enhance oxidation resistance and

RC with table-like MCE response with $\Delta T_{ad} \sim 3.5$ K [687]. Other REZn (RE = Tm, Ho) compounds were reviewed by Li et al. [629] along with other stoichiometries of alloys containing metals with low boiling points. HoPd suffers a SOPT from PM to FM with $\Delta S_M \sim -20$ J kg^{-1} K^{-1} at 10 K and 5 T [688].

GdGa compound, crystallizing in orthorhombic CrB-type structure (space group *Cmcm*) exhibits a Curie transition at 183 K and a spin reorientation at ~100 K, with $\Delta S_M = -4.81$ J kg^{-1} K^{-1} for $\mu_0 \Delta H = 5$ T and $RC_{FWHM} = 576$ J/kg [689]. Zheng et al. [690] studied the $Gd_xEr_{1-x}Ga$ series, which compounds undergo a FM to PM transition followed by AFM to FM transition as temperature decreases. When x increases from 0 to 1, the low temperature transition increases from 15 to 66 K and the high temperature transition from 30 to 182 K. Differences are observed concerning low transition temperature for x = 1 but the high temperature one is in agreement with the results of Zhang et al. [689]. Table-like ΔS_M curves were observed for compounds with $0.1 \leq x \leq 0.4$. In addition, both PrGa and HoGa compounds crystallize in CrB-type structure. PrGa undergoes a FM to AFM transition at 27 K and a AFM to PM transition at 37 K, leading to an almost constant $-\Delta S_M \sim 10$ J kg^{-1} K^{-1} and $\Delta T_{ad} \sim 2.7$ K values from 29.5 to 37.5 K [691]. In the case of HoGa, a spin reorientation occurs at ~20 K and a SOPT from FM to PM state is found at 69 K, leading to a broad range of high $|\Delta S_M|$ values (7.8 J kg^{-1} K^{-1} at spin reorientation and 17.1 J kg^{-1} K^{-1} at the Curie transition at 5 T) [692]. SmNi also crystallizes in CrB-type structure and shows a $|\Delta S_M| \sim 2$ J kg^{-1} K^{-1} and $\Delta T_{ad} \sim 1.2$ K (5 T) at around 40 K [693]. ErSi also crystallizes in CrB-type structure and has a Néel temperature of 12.5 K, below which a field induced metamagnetic FOPT from AFM to FM state occurs with $\Delta S_M = -14.8$ J kg^{-1} K^{-1} (5 T) [694]. GdNi and its hydride $GdNiH_{3.2}$ also crystallize in CrB-type structure. Hydrogenation shifts the maximum of $\Delta S_M(T)$ curve from 75 to 10 K, without significantly affecting the maximum $|\Delta S_M| \sim 14$ J kg^{-1} K^{-1} (5 T) [695].

GdCu, crystallizing in FeB-type structure (*Pnma*), shows an enhancement of magnetic moment compared to that of pure Gd but their MCE values are modest ($\Delta S_M = -0.6$ J kg^{-1} K^{-1} at 5 T) and found at low temperatures in this AFM intermetallic with Néel temperature at 37 K [696]. Also crystallizing in this type of structure, CeSi compound is AFM with lower Néel temperature of 6.1 K. Its high MCE ($\Delta S_M = -13.7$ J kg^{-1} K^{-1} at 5 T without hysteresis loss) occurs ascribed to metamagnetic transition to FM under 0.4 T at 2 K [697].

HoAl undergoes an AFM to FM transition at 13 K and a FM to PM one at 20 K whereas ErAl changes from AFM to PM at 9 K, exhibiting $\Delta S_M(5\text{ T}) = -22.5$ and 16.4 J kg^{-1} K^{-1} respectively. Both compounds crystallize in orthorhombic DyAl-type structure (*Pbcm* space group), which is also present for other REAl intermetallics (e.g. the AFM compounds with RE = Gd, Tb and Dy, with Néel temperatures of 42, 72 and 20 K, respectively) [698].

The RE_3CoGe_2 series crystallizes in La_3NiGe_2-type structure (space group *Pnma*). For RE = Gd, the system undergoes a FiM transition at 150 K with a $\Delta S_M = -4.9$ J kg^{-1} K^{-1} (5 T) [699].

5.1.1.8.11. Compounds with 43 at.% of RE. Eu_3O_4 [700], crystallizing in orthorhombic $CaFe_2O_4$-type structure (*Pnam* space group), shows a metamagnetic transition from AFM to FM state at 5 K with high values of $\Delta S_M = -13.6$ J kg^{-1} K^{-1} (5 T) and $\Delta T_{ad} \sim 7$ K. Partial substitution of Eu for other lanthanide, such as Ho or Dy, preserves the structure and leads to promising MCE parameters at temperatures below 10 K: $\Delta S_M(8\text{ T}) = -30$ and -25 J kg^{-1} K^{-1} and $\Delta T_{ad} = 13$ and 16 K for $EuHo_2O_4$ and $EuDy_2O_4$ respectively [701].

RE_3NiSi_3 compounds (RE = Gd, Tb, Dy) crystallizing in Y_3NiSi_3-type structure (space group *Immm*), which is derived from Ta_3B_4-type, exhibit modest MCE [702].

5.1.1.8.12. Compounds with 40 at.% of RE. $Gd_2Ni_xCu_{2-x}Mg$ series crystallizes in the tetragonal Mo_2FeB_2-type structure (space group *P*4/*mbm*) and the Ni substitution for Cu significantly affects their magnetic properties and shows a linear decrease of the cell volume with Ni content. For x = 0.5, a temperature induced order to order transformation (SOPT) from FM to AFM phase occurs, while for x = 1, a FOPT metamagnetic transition with critical field of 0.8 T is found at 5 K. Reversible MCE is reported for both compounds: $-\Delta S_M(5\text{ T}) = 9.5$ (x = 0.5) and 11.4 J kg^{-1} K^{-1} (x = 1) at about 65 K [703].

Gd_2CoSi_2 and Gd_2CoGe_2 compounds crystallize in Sc_2CoSi_2-type structure (*C*2/*m* space group). They show $-\Delta S_M(5\text{ T}) = 3.0$ and 5.1 J kg^{-1} K^{-1} at Curie transition of 213 and 143 K for the compound with Si and Ge respectively [704]. In $Gd_2Co_{3-x}Si_x$ compounds, the La_2Ni_3-type structure (*Cmca* space group) is stabilized by partial substitution of Si for Co. Their T_C can be tuned from 280 to 338 K ($0.50 > x > 0.29$) and shows at 2 T a $\Delta S_M \sim -1.5$ J kg^{-1} K^{-1} and $\Delta T_{ad} \sim 1.3$ K at ~300 K [705]. RE_2TMSi_2 series (RE = Gd-Er and TM = Fe, Co) exhibits several transitions with several maxima of the magnetic entropy change (e.g. for RE = Er and TM = Co: $|\Delta S_M|(5\text{ T}) = 13.6$ and 8.4 J kg^{-1} K^{-1} at 32 and 12 K respectively) [706].

RE_2Co_2Al series crystallizes in W_2CoB_2-type structure (space group *Immm*). For RE = Tb and Dy compounds form 2:2:1 and 1:1:1 phases and show broad $\Delta S_M = -6.4$ J kg^{-1} K^{-1} (5 T) for RE = Tb (due to the Curie transitions of TbCoAl and Tb_2Co_2Al at 74 K and 102 K respectively), while for RE = Dy, its $\Delta S_M = -10.6$ J kg^{-1} K^{-1} (due to the T_C of Dy_2Co_2Al phase at 53 K, with negligible effect from DyCoAl phase with $T_C = 37$ K) [707]. Also crystallizing in W_2CoB_2-type structure, Dy_2Ni_2Sn compound is AFM below 43 K and its spin canting occurs below 28 K. Both transitions are FOPT as evidenced by clear thermal hysteresis and their ΔS_M changes from inverse (~2 J kg^{-1} K^{-1} (5 T) at 15 K) to direct MCE (~−4 J kg^{-1} K^{-1} (5 T) at 45 K) [708].

The tetragonal Mo_2B_2Fe-type structure (*P*4/*mbm* space group) is found in RE_2TM_2X compounds (X = Mg, Cd, Sn or In). RE_2Cu_2In shows PM-FM SOPT at 49.5, 30, 39.4 and 31.6 K and their $\Delta S_M(7\text{ T}) = -16.5$, 21.9, 18.4 and 18.2 J kg^{-1} K^{-1} for RE = Dy [709], Ho [710], Er and Tm [711] respectively. Their composite materials were proposed to exhibit enhanced table-like MCE response [711].

5.1.1.8.13. Compounds with 33 at.% of RE. The MCE of RE-containing compounds crystallizing in AB_2 stoichiometry, but different to the already-described Laves phases, have been also studied. The UGa_2 compound crystallizes in hexagonal AlB_2-type structure (space group *P*6/*mmm*) and minor partial substitution of Al for Ga enhances its maximum magnetic entropy change (ΔS_M(2 T) ~ −2 J kg^{-1} K^{-1} at T_C = 125 K) [712], which is not so significant for other elemental substitutions for Ga or pressure application [713]. The partial substitutions of Dy or Er for U gradually broaden and shift to lower temperatures the thermal range of the well defined transition observed for UGa_2 compound [714]. Also crystallizing in AlB_2-type structure, TbB_2 shows high $|\Delta S_M|$ and ΔT_{ad} values (5.2 J kg^{-1} K^{-1} –measured- and 14.7 K –estimated- at 2 T) at around a SOPT at 144 K [715]. The isostructural DyB_2 compound shows ΔS_M = −17 J kg^{-1} K^{-1} (5 T) ascribed to two successive transitions: spin-reorientation at 20 K and a FM to PM transition at 50 K [716]. Anisotropic MCE has been recently reported for RGa_2 (RE = Er and Ho) monocrystals [717]. Also crystallizing in AlB_2-type structure, RE_2CuSi_3 (RE = Pr and Gd) compounds experience two transitions: for Pr_2CuSi_3 and Gd_2CuSi_3, a PM to FM SOPT at 12 and 26 K respectively, and then a FM-spin glass transition at 6 and 7.5 K respectively [718]. RE_2PdSi_3 are isostructural to those compounds, with MCE reported for RE = Ho [719] and Gd, Dy and Er [719]: $|\Delta S_M|$(5 T) = 27.5, 11.8, 16.6 and 22 J kg^{-1} K^{-1} at transition temperatures of 10, 26, 10 and 9.5 K respectively. RE_2CoGa_3 (RE = Gd, Dy, Ho) compounds, crystallizing in RE_2RhSi_3-type structure (space group $P6_3/mmc$ or *P*-62*c* [720]) derived from AlB_2-type structure, experience a SOPT from PM to FM at 50, 17 and 10 K respectively, displaying $-\Delta S_M$(5 T) = 12.6, 10.8 and 13.8 J kg^{-1} K^{-1} for Gd, Dy and Ho respectively [721].

TbAgAl crystallizes in orthorhombic $CeCu_2$-type structure (space group *Imma*) and exhibits a complex magnetic behavior and ΔS_M(5 T) = −6.2 J kg^{-1} K^{-1} at 59 K [722]. RECuSi compounds (RE = Ho [723] and Dy [724]) crystallize in Ni_2In-type structure, with a field induced metamagnetic FOPT from AFM to FM state. For RE = Ho, ΔS_M(5 T) = −33.1 J kg^{-1} K^{-1} at T_N = 7 K [723] and −24.0 J kg^{-1} K^{-1} (5 T) at T_N = 10 K for RE = Dy [724]. TbH_δ hydrides ($\delta \sim 2$) crystallize in fcc CaF_2-type structure (space group *Fm*3*m*) and show two FOPT at low temperatures around 10–15 K with a $|\Delta S_M| \sim 10$ J kg^{-1} K^{-1} (9 T) [725,726]. Recently, Zhang et al. reviewed different RETMSi compounds [727], which are also summarized in Fig. 23.

The MCE properties of several intermetallic ternary compounds with stoichiometries 1:1:1 are recently reported in the literature. Concerning their crystal structure, we can find orthorhombic TiNiSi-type (space group *Pnma*), hexagonal ZrNiAl-type (space group *P*-62*m*) and tetragonal CeFeSi-type (space group *P*4/*nmm*) structures for these materials. GdNiGa and GdNiIn compounds [728] order ferromagnetically at 30.5 and 93.5 K, with ΔS_M(5 T) = −20.3 and −6.8 J kg^{-1} K^{-1} respectively. The former crystallizes in TiNiSi-type structure while the latter in ZrNiAl-type. Similar ternary Gd-X-Y alloys (X = Mn, Fe, Ni, Ru, Pd; Y = Al, In, Ge) have been studied [729,730] and reported with ΔS_M(5 T) = −10.6 (T = 57 K), −10.4 (T = 46 K), −4.6 (T = 90 K), −2.8 (T = 200 K), −0.7 J kg^{-1} K^{-1} (T = 274 K) and −6 J kg^{-1} K^{-1} (T = 70 K) for GdNiAl, GdPdAl, GdPdIn, GdFeAl, GdMnAl and GdRuGe, respectively. Later, some of the coauthors [731] reported corrected structures of $MgZn_2$ and $MgCu_2$-type for GdFeAl and GdMnAl respectively. $(Gd_{0.54}Er_{0.46})$NiAl, crystallizing in ZrNiAl-type structure was earlier proposed by Takeya et al. [732] as a suitable MCE material for Ericsson cycles due to its flat $\Delta S(T)$ curve between 15 and 40 K (ΔS_M(5.3 T) ~ −13 J kg^{-1} K^{-1} and $\Delta T_{ad} \sim 5$ K). RENiIn series (RE from Gd to Er) was studied by Zhang et al. [733] and

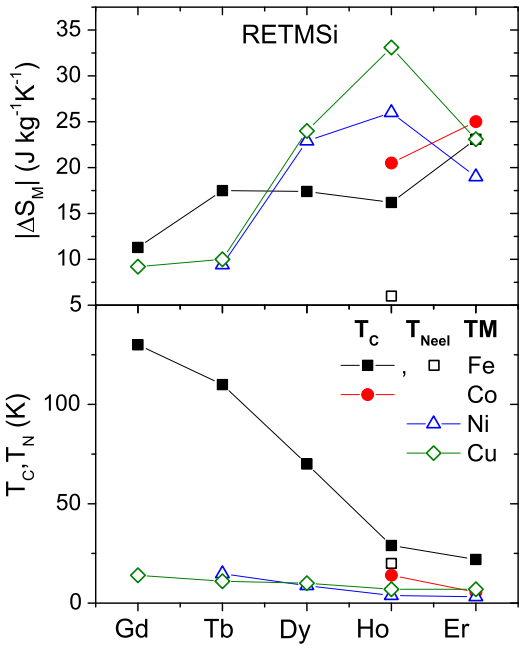

Fig. 23. Transition temperatures (Néel temperatures for hollow symbols and Curie temperatures for solid ones) and maximum magnetic entropy change at 5 T for different RETMSi compounds: black, Fe; red, Co; blue, Ni; and green, Cu. Data taken from [727].

they exhibit ZrNiAl-type structure. While Gd- and Er-containing RENiIn compounds show a single Curie transition (at 98 and 9 K respectively), Tb-, Dy- and Ho-containing compounds show two successive magnetic phase transitions (T_C at 71, 30 and 20 K and a transition from AFM to FM at 12, 14 and 7 K respectively). Their $-\Delta S_M$ (5 T) are 7.1, 5.3, 10.4, 21.7 and 15.1 J kg^{-1} K^{-1} for RE = Gd, Tb, Dy, Ho or Er in RENiIn compounds, respectively, at their corresponding T_C. Moreover, for RE = Tb and Dy, a field induced metamagnetic transition occurs from AFM to FM states. Partial Cu substitution for Ni in $HoNi_{1-x}Cu_xAl$ series changes the ordering nature of the ground state from mixed AFM/FM ($x \leq 0.1$) to AFM ($0.2 \leq x \leq 0.7$) and to FM ($x \geq 0.8$). In addition, a non-monotonous variation of MCE is observed along the series [734]. DyCuAl also crystallizes in ZrNiAl-type structure [735] with $\Delta S_M(5\,T) = -10.9$ J kg^{-1} K^{-1} at 28 K (SOPT). Likewise TbCuAl [736], HoCuAl [737] and ErCuAl [737] undergo SOPT at 52, 12 and 7 K with $\Delta S_M = -14.4$, -23.9 and -22.9 J kg^{-1} K^{-1} respectively. The influence of grain size on the MCE of DyCuAl have been studied and shows that a reduction of crystal size, from 90 nm to 38 nm, reduces T_C and also leads to a ~14% decrease in $|\Delta S_M|$ but ~11% enhancement in *RC* [738]. TbPdAl [739], also crystallizing in this structure, is a weak AFM structure and undergoes a field induced metamagnetic transition at 43 K from AFM to FM with a lower transition temperature at 22 K. Between the transition temperatures, 1/3 of the Tb magnetic moments are highly frustrated. The MCE of $Tb_{1-x}Y_xNiAl$ series shows no significant variation after partial substitution of Y for Tb ($\Delta S_M(2\,T) \sim -4$ J kg^{-1} K^{-1} at ~45 K) [740]. However for $TbNiAl_{1-y}In_y$ series, their ordering temperatures increase after complete substitution of In for Al and leads to a 50% decrease of $|\Delta S_M|$ [740]. Large anisotropic MCE effect has been observed for TbNiAl monocrystals [741]. UNiGa compound also crystallizes in ZrNiAl-type structure and undergoes two transformations: from PM to FiM at 38.4 K (normal MCE) and from FiM to AFM at 34.5 K (inverse MCE) at low fields [742]. However, at higher fields, its inverse MCE weakens ($\Delta S_M = -3.6$ J kg^{-1} K^{-1} at 37 K for 5 T) due to field induced metamagnetic phase transition.

As Cu content increases in $TmNi_{1-x}Cu_xAl$, its magnetic order transition reduces to below 2 K for $x \geq 0.3$. Large reversible MCE in these AFM systems are reported around ~4 K, whereby $-\Delta S_M(2\,T)$ increases from 5.5 (x = 0) to 17.2 J kg^{-1} K^{-1} (x = 1) [743].

REPdSn crystallizes in TiNiSi-type or Fe_2P-type structure depending on the type of RE, being both structures possible for RE = Ho [744]. Some compounds are AFM with a transition temperature ranging from 7.5 for RE = Ce to 23.5 K for RE = Tb. However, other compounds (RE = Pr, Tm) are PM at least down to liquid helium temperature. For RE = Sm, a Néel temperature of 14 K is found. On the other hand, REPdIn compounds crystallize in ZrNiAl-type structure. For RE = Gd in REPdIn, the compound is FM with $T_C = 102$ K [744]. SmPd(Sn,In) compounds exhibit modest MCE ($|\Delta S_M| < 0.1$ J kg^{-1} K^{-1} at 1 T) but MCE enhances one order of magnitude in $Sm_{1-x}Gd_xPdIn$ (x = 0.5 and 1) with transitions at 60 and 83 K, whereby $-\Delta S_M(7\,T) = 5.6$ and 6.2 J kg^{-1} K^{-1} respectively [744]. Also crystallizing in TiNiSi-type structure, REPtGa (RE = Dy, Ho and Er) orders antiferromagnetically at 15, 6.3 and 5 K ($|\Delta S_M| \sim 6$, 9 and 8 J kg^{-1} K^{-1}, and $RC_{FWHM} = 130$, 180 and 160 J/kg at 5 T) respectively [745].

Crystallizing in CeFeSi-type structure, HoTiGe and ErTiGe [746] undergo a field induced magnetic transition from AFM to PM state around their Néel temperatures (88 and 41 K respectively). While magnetic moments of Ho atoms are located along the c-axis, magnetic moments of Er atoms prefer to be perpendicularly aligned to c-axis. Its transformation is accompanied with hysteresis losses but no crystallographic changes are observed. Two peaks in their $\Delta S(T)$ curves are found at 20 and 90 K (-4.2 and -2.5 J kg^{-1} K^{-1} at 5 T). Fe additions to HoTiGe do not eliminate the hysteresis, unlike for $Gd_5Si_2Ge_2$ compound, but they enhance ΔS_M, in particular to temperatures below 15 K [747]. ErTiSi also crystallizes in CeFeSi-type structure and undergoes a field induced metamagnetic transition from AFM to FM state below Néel temperature ($\Delta S_M(5\,T) = -8.9$ J kg^{-1} K^{-1} at 46 K without hysteresis loss) [748]. HoFeSi compound (CeFeSi-type structure) shows two successive magnetic phase transitions (from PM to FM at 29 K and from FM to AFM or FiM at 20 K), leading to sequential inverse and normal MCE with $|\Delta S_M| = 7.1$ and 5.6 J kg^{-1} K^{-1} at the first and second transition respectively [749]. Multicomponent Gd-Ni-Al alloys ($Gd_{28}Ni_{24}Al_{48}$ and $Gd_{33}Ni_{13}Al_{54}$) with FM phases, such as $GdNiAl_2$, GdNiAl and $Gd(Al,Ni)_2$, exhibit ordering close to 40 K and show $|\Delta S_M|(5\,T) = 14.5$ J kg^{-1} K^{-1} [750]. $GdFe_{1-x}Co_xSi$ crystallizing in CeFeSi-type structure, was recently studied by Wlodarczyk et al. [751] and showed a minimum temperature for its phase transition at 70 K when x = 0.4 while for Co-free compound a maximum at 220 K is found (wherein $|\Delta S_M| = 10$ J kg^{-1} K^{-1} at 5 T)

Gupta et al. [752] have recently reviewed 1:1:1 stoichiometry concerning, among other properties, their MCE response. Fig. 24 uses the data from [752] distinguishing among the crystal structures and the type of ordered state (FM or AFM).

5.1.1.8.14. Compounds with 25 at.% of RE. Crystallizing in $PuNi_3$-type structure (space group *R*-3*m*), $Gd(Ni_{1-x}Fe_x)_3$ series [753] shows a wide range of Curie temperatures: when x increases from x = 0 (with spin reorientation at ~60 K) to 0.4, T_C increases from 115 K to 802 K and for x = 1, T_C reduces to 725 K. Compensation temperatures of these FiM systems increase from 575 K (x = 0.4) to 604 K (x = 1). For $x \leq 0.2$, $|\Delta S_M|(1\,T)$ (SOPT) decreases from 1.53 J kg^{-1} K^{-1} (x = 0) to 0.28 J kg^{-1} K^{-1} (x = 0.2). For $Gd(Ni_{1-x}Co_x)_3$ compounds ($x \leq 0.6$) [754] crystallizing in $PuNi_3$, their Curie temperatures range from 115 to 342 K for up to x = 0.6 ($T_C = 615$ K for $GdCo_3$). However, $|\Delta S_M|$ decreases to 0.27 J kg^{-1} K^{-1} (1 T) for x = 0.6.

Compounds of $Tb_{1-x}Y_xCoC_2$ series, with *Amm*2 space group, undergo a SOPT from PM to FM state and their T_C decreases from 28 to 18 K as x increases from 0 to 0.4. For x = 0.4, $|\Delta S_M| = 9.35$ J kg^{-1} K^{-1} at 20 K and 5 T [755].

The orthorhombic $CeNiSi_2$-type structure (*Cmcm* space group) [134] is found in many $RETMX_2$ compounds. It is related to the $ThCr_2Si_2$-type structure, and polyhedra enclosing a TM atom form layers (perpendicular to the longest axis) interconnected by Si-Si bonds in both structures. With the same *Cmcm* space group, the crystal structure Al_2CuMg is found for FM $GdNiAl_2$, which exhibits a SOPT at 28 K and $-\Delta S_M = 16.0$ J kg^{-1} K^{-1} (5 T) [756]. The MCE of $RECu_xGe_2$ compounds (RE = Ho or Er) crystallizing in $CeNiSi_2$-type structure has been recently reported [757] with $-\Delta S_M(5\,T) \sim 6$ J kg^{-1} K^{-1} at 10 K (RE = Ho and x = 0.33) and 10.5 J kg^{-1} K^{-1} at 5.5 K (RE = Er and x = 0.25). Another compound that crystallizes in this structure

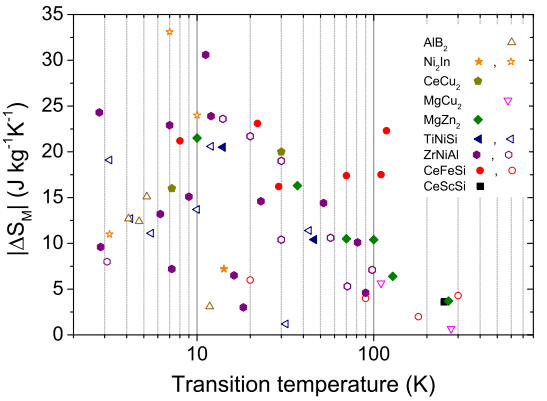

Fig. 24. Magnetic entropy change (at $\mu_0\Delta H = 5$ T) as a function of the transition temperature for several RETMX compounds grouped according to their crystal structures. Hollow symbols corresponds to AFM ground states and solid symbols to FM or FiM ground states. Data taken from [752].

is $TbNiGe_2$, which is AFM below 39 K and exhibits inverse MCE [758]. $REAgSn_2$ compounds (RE = Ho and Er) crystallize in a cubic phase (space group *Pm*3*m*) and also exhibit AFM ordering but with even lower MCE responses [759].

Recently, Jiang et al. [760] proposed $YbPt_2Sn$ as a metallic alternative to paramagnetic salts for demagnetization cooling from 2 to 0.2 K. This compound crystallizes in hexagonal $ZrPt_2Al$ type structure (*P6*$_3$/*mmc* space group). Substitution of In for Sn yields similar magnetic properties but the structure changes to a cubic $L2_1$ Heusler type structure [761].

5.1.1.8.15. Compounds with 22 at.% of RE. Dy_2Ni_7 and Ho_2Ni_7 compounds, crystallizing in the rhombohedral Gd_2Co_7-type structure (space group *R*-3*m*), exhibit two successive transformations from PM to FM state (81 and 65 K respectively) and a spin reorientation transition (35 and 25 K respectively). Both transitions being SOPT [762] show $\Delta S_M(5\,T) = -7.3$ and -12.5 J kg^{-1} K^{-1} at ~40 and ~25 K respectively. Hexagonal Nd_2Co_7 crystallizing in Ce_2Ni_7-type structure (space group *P*6$_3$/*mmc*) has a Curie temperature of 613 K but spin reorientation transitions appear around room temperature. Anisotropic MCE was observed for their monocrystals and a maximum $\Delta T_{ad}(1\,T) = 0.4$ K at 235 K and -0.44 K at 250 K is obtained when rotating the field perpendicular and parallel to the c-axis respectively [763].

$RE_2Cu_2O_5$ (RE = Tb-Lu and Y) cuprates are formed with RE atomic size smaller than Gd. They ordered AFM below 17.7, 9.5, 12.3, 25, 16.7 and 17.3 K from Tb to Lu and 10.5 K for RE = Y. In the case of Dy- and Ho-containing compounds, $|\Delta S_M|$ values are ~12 J kg^{-1} K^{-1} at 7 T [764].

5.1.1.8.16. Compounds with 21 at.% of RE. Lemoine et al. [765] have discussed the potential interest of RE_6Mn_{23} intermetallics (RE = Y, Nd, Sm, Gd, Tb, Dy, Ho, Er, Tm and Lu) for magnetic refrigeration. They crystallize in cubic Th_6Mn_{23}-type structure (space group *Fm*-3*m*). At high temperatures, Mn sublattice orders ferrimagnetically (at 505, 441, 456, 489, 457, 447, 445, 430, 411 and 398 K for RE = Y, Nd, Sm, Gd, Tb, Dy, Ho, Er, Tm and Lu respectively), whereas RE sublattice orders below 100 K. At this temperature, the $|\Delta S_M|(5\,T)$ are 0.34, 0.41, 0.36, 1.7, 2.5, 3.2, 5.2, 4.3, 5.2 and 0.46 J kg^{-1} K^{-1} respectively. In $Gd_6(Mn_{1-x}Fe_x)_{23}$, partial substitution of Fe for Mn decreases T_C from 489 to 176 K and increases $-\Delta S_M(5\,T)$ from 1.67 to 2.59 J kg^{-1} K^{-1} as x increases from 0 to 0.2 [766]. Partial substitution of Co for Mn decreases T_C to 118 K for x = 0.3 [767] and leads to wide but moderate MCE peaks in $Gd_6(Mn_{1-x}Co_x)_{23}$.

5.1.1.8.17. Compounds with 20 at.% of RE. This atomic fraction of RE corresponds to the $RETM_2X_2$ compounds, which crystallize in $ThCr_2Si_2$ structure described above.

The MCE in RE-containing titanate family has also received attention, such as $HoTiO_3$ whose $\Delta S_M = -11.6$ J kg^{-1} K^{-1} (5 T) ascribed to a SOPT occurring at 53 K [768], and $Er_2Ti_2O_7$ whose MCE peaks below 10 K [769]. However, attention has been particularly focused on $EuTiO_3$ system. Alho et al. [770] have studied the anisotropic magnetocaloric effect of this AFM system and no significant differences were reported between single crystals and polycrystalline samples, which exhibits huge $|\Delta S_M| = 49$ J kg^{-1} K^{-1} and $\Delta T_{ad} = 21$ K at 5.5 K and 7 T [771]. $Eu_{1-x}Ba_xTiO_3$ series ($0.1 \leq x \leq 0.9$) shows large $-\Delta S_M$ below 10 K (40 and 6.6 J kg^{-1} K^{-1} at 5 T for x = 0.1 and 0.9 respectively) [772]. Even larger values were obtained in partial substitution of Nb for Ti: $|\Delta S_M| = 51.3$ J kg^{-1} K^{-1} and $\Delta T_{ad} = 22$ K at ~10 K and 9 T [773]. Partial Cr substitution for Ti (below 10%) leads to a reduction of the MCE response without affecting the temperature of the maximum [774].

Theoretical calculations using Monte Carlo simulations and mean field model have been applied to the AFM perovskite-type $EuZrO_3$ compound [775] whose Néel temperature is about 4 K. A normal MCE of $\Delta T_{ad} = 15$–20 K at 2 T was calculated and an inverse MCE was predicted below 3.6 K at $\mu_0\Delta H = 1$ T. In the vanadate $HoVO_3$, several types of transformations occur: on cooling, SOPT from *Pbnm* orthorhombic to *Pb*11 monoclinic at 188 K, a Néel transition of the V sublattice at 110 K, a FOPT from monoclinic to orthorhombic at 40 K (accompanied by a reordering of V moments), a FM ordering of Ho moments at 15 K and a AFM ordering of the Ho moments at 4 K [776]. This yields a large $-\Delta S_M \sim 15$ J kg^{-1} K^{-1} (5 T) at ~15 K, with inverse MCE below 10 K for lower fields. In giant anisotropic $REFeO_3$ compounds, MCE can be even larger due to the rotation of

the field from b to c axis [777]: $-\Delta S_M$(5 T) = 17, 9 and 20 J kg^{-1} K^{-1} at 9, 17 and 7.5 K for Tb and Tm [778], and Dy [779], respectively. The MCE peak broadens with increasing fields. Ferroelectric $DyFe_{0.5}Cr_{0.5}O_3$ exhibits large MCE below 10 K [780]. Low temperature MCE was also studied for chromites such as $Dy_{0.7}RE_{0.3}CrO_3$ (RE = Y, Er and Ho) [781] and Gd_3CrO_3, which exhibits large $-\Delta S_M$ > 30 J kg^{-1} K^{-1} (4.4 T) below 5 K [782]. Ho ferro-chromites show values around 7 J kg^{-1} K^{-1} (7 T) but at a higher temperature of 20 K [783].

5.1.1.8.18. Compounds with 17 at.% of RE. $NdCo_5$ is a FM intermetallic that crystallizes in hexagonal $CaCu_5$-type structure (space group *P*6/*mmm*). There is a competition between Co (favoring c-axis orientation) and Nd (favoring planar orientation) sublattices in the magnetocrystalline anisotropy. For temperatures below 242 K, its magnetization lies in the basal plane [784] while at temperatures above 283 K, c-axis becomes the easy axis. Therefore, two spin reorientation transitions occur and a giant rotating MCE (ΔT_{ad} = 1.6 K at 1.3 T) has been reported at room temperature [785]. Partial substitutions of Al for Co or Dy for Nd in $Nd_{1-x}Dy_xCo_4Al$ (x = 0, 0.1), shift their transition temperatures to higher values and MCE close to room temperature. For x = 0, transitions occur at 299 and 311 K and their ΔS_M = 0.25 (inverse MCE) and −0.6 J kg^{-1} K^{-1} at $\mu_0\Delta H$ = 1 T respectively. For x = 0.1, their ΔS_M(1 T) = 0.15 J kg^{-1} K^{-1} (maximum inverse MCE at $\mu_0\Delta H$ = 0.7 T) and −0.6 J kg^{-1} K^{-1} at transitions of 305 and 317 K respectively [786]. Other elements (not Al) have been partially substituted for Co, such as Ga in $Dy_{1-x}Nd_xCo_4Ga$ [787], which also preserves $CaCu_5$-type structure [787]. Their Curie temperatures decrease from 498 to 410 K and spin-reorientation temperatures from 403 to 303 K as x increases from 0 to 1. The maximum entropy change are −0.91 J kg^{-1} K^{-1} (1.5 T) at 301 K for the spin-reorientation process. The $CaCu_5$-type compound $SmNi_5$ presents a PM-FM SOPT at 29 K with $|\Delta S_M|$ = 5.4 J kg^{-1} K^{-1} (5 T) [788]. In their work, Nouri et al. collected results from Coroian, who studied other $RENi_5$ compounds with $|\Delta S_M|$ = 0.6, 8.5, 11.3, 11.5, 15.7, 13.1 and 16.3 J kg^{-1} K^{-1} at 14, 8, 32, 23, 5, 12 and 9 K for RE = Pr, Nd, Gd, Tb, Ho, Dy and Er respectively [789]. This structure is also shown by $PrNi_{5-x}Co_x$ ($1.95 \leq x \leq 3$) series [790], which exhibits several transition temperatures: spin reorientations at ~150 K and FM to PM transition between ~60 K (x = 1.95) and ~537 K (x = 3) ($T_C \sim 900$ K for $PrCo_5$). Partial substitution of Nd in $Pr_{1-x}Nd_xCo_4Al$ compounds shifts the two spin reorientation transition temperatures from 170 and 186 K to room temperature: 276 and 294 K respectively. Its MCE changes from normal to inverse as x increases from 0 to 0.8 while the magnetic entropy change ascribed to the low temperature transition is enhanced compared to that at the high temperature one. Their broad MCE peaks yield $RC_{FWHM} \sim 30$ J/kg at 1 T [791]. $|\Delta S_M|$ remains below 0.3 J kg^{-1} K^{-1} at the Curie temperature for the studied series but that associated to the spin reorientation is enhanced for $x \sim 2.4$ (ΔS_M = −1.3 J kg^{-1} K^{-1} at $\mu_0\Delta H$ = 1 T). Direct MCE measurements of $HoCo_5$ single crystals show large influence of magnetic anisotropy on the sign and magnitude of MCE at temperatures close to a spin reorientation (SOPT) at ~180 K [792]. A second SOPT, also ascribed to spin reorientation, occurs at a lower temperature of 50 K. Between these two temperatures, a conical phase exists. $NdNi_4Si$ with SOPT occurring at very low temperature (T_C = 8 K) shows $|\Delta S_M| \sim 7.5$ J kg^{-1} K^{-1} at 5 T [793]. Theoretical studies of $DyNi_4Si$ [794], crystallizing in the YNi_4Si-type orthorhombic structure (space group *Cmmm*) derived from $CaCu_5$-type structure, predict a FM ordering at 19 K and $|\Delta S_M|$(14 T) = 15.6 J kg^{-1} K^{-1} at 22 K, which is in good agreement with experimental values extended to other RE = Ce, Gd, Tb and Dy [795]. $SmNi_3TMSi$ compounds (TM = Mn-Cu) [796,797] show FM ordering at 125, 190, 46, 17 and 12 K for TM = Mn, Fe, Co, Ni and Cu respectively, with modest ΔS_M values around the metamagnetic-like transition: the larger being −2.6 J kg^{-1} K^{-1} (5 T) at 65 K for Fe-containing compound [796].

Also belonging to $CaCu_5$-type crystals, $RENi_3TMSi$ compounds (RE = Gd and Tb; TM = Mn, Fe, Co and Cu) were studied by Morozkin et al. [798]. Maximum transition temperature was observed for TM = Fe compound but its MCE is moderate. The largest $|\Delta S_M|$(5 T) = 12.6 J kg^{-1} K^{-1} at 25 K was found for TM = Ni compound.

$RECo_3B_2$ compounds crystallize in hexagonal $CeCo_3B_2$-type structure (*P*6/*mmm* space group), which is derived from $CaCu_5$-type structure [799]. These compounds are PM at room temperature and at temperatures of 150–160 K their Co-Co sublattice undergoes a magnetic ordering transition, while further cooling leads to ordering of the RE-RE sublattice at 54, 47, 28 and 22 K for Gd, Sm, Tb and Dy respectively. Their MCE studied at the low temperature SOPT yields: ΔS_M = −5.0, −4.9 and −7.4 J kg^{-1} K^{-1} and ΔT_{ad} = 2.8, 4.0 and 6.4 K at 2 T for Gd- [800], Tb- [801] and Dy-compounds [799], respectively. Tolinski et al. [801] reported that the Dy containing compound exhibits ΔS_M = −17.5 J kg^{-1} K^{-1} and ΔT_{ad} = 14 K at 9 T. Other borides crystallizing with the same space group, exhibit Curie temperatures closer to room temperature: e.g. $CeCo_4B$ [802], a FiM compound which orders at 291 K (SOPT), shows ΔS_M = −0.36 J kg^{-1} K^{-1} (1 T); and $Ce_2GdCo_{11}B_4$, also FiM with T_C = 301 K (SOPT) displays ΔS_M = −0.31 J kg^{-1} K^{-1} (5 T) [803].

The effect of pressure and field on the MCE of $YbInCu_4$, which crystallizes in $AuBe_5$-type structure (space group *F*-43*m*), is reported with a maximum $|\Delta S_M|$ = 8.7 J kg^{-1} K^{-1} (7 T) at 6.6 kbar at 26 K near its Kondo temperature [804].

Midya et al. [805] studied the MCE of $RECrO_4$ (RE = Gd and Ho) compounds, which crystallize in $ZrSiO_4$-type structure (space group *I*4/*amd*) and show $|\Delta S_M|$(7 T) = 28 J kg^{-1} K^{-1} at 25 K for RE = Gd while 29 J kg^{-1} K^{-1} at 20 K for RE = Ho. Dong et al. studied $RECrO_4$ (RE = Gd and Er), which shows a PM-FM SOPT with $-\Delta S_M$(5 T) = 22.8 and 20.5 J kg^{-1} K^{-1} at 22 and 15 K respectively [806]. Their composite materials were proposed for refrigeration in the hydrogen liquefying temperature range. Recently, Palacios et al. [85] studied the MCE of $GdCrO_4$ attributed to the weak Gd-Cr interaction through which Cr^{5+} (FM ordered below 21.3 K) polarize the Gd^{3+} (ordered at 4.8 K). Midya et al. [807] also studied the MCE of $DyVO_4$, which is an AFM compound with Néel temperature at 3.5 K, and exhibits $|\Delta S_M|$ = 26 J kg^{-1} K^{-1} and ΔT_{ad} = 17 K at about 15 K and 8 T ascribed to a metamagnetic transition.

5.1.1.8.19. Compounds with 15 at.% of RE. Gadolinium gallium garnets (GGG), (e.g. $Gd_3Ga_5O_{12}$ with space group *Ia*3*d*) have been proposed for very low magnetic refrigeration, i.e. <20 K, but its temperature limit can be further increased by partial Fe substitution for Ga [808]. The MCE of these Fe substituted GGG agrees with the calculations for superparamagnetic materials and there is a close relationship between large MCE and strong geometrical magnetic frustration in these systems [809]. The MCE enhancement can be as large as one order of magnitude with respect to ideal paramagnets. However, when Gd substitutes for Dy or Ho, the MCE of Fe modified GGG is not improved although Dy and Ho have a larger orbital contribution to its magnetic moment [810]. The study of bulk and nanostructured gadolinium iron garnet shows a shift of transition temperature to lower values in nanostructured samples compared to bulk ones and a non-monotonous dependence of MCE with crystal size. For bulk samples, their MCE originated from their intrinsic magnetic frustration, whereas for nanostructured samples, surface spin disorder and particle blocking effects appear as additional factors [811]. Theoretical calculations for MCE of FiM iron garnets with Y and Dy have been performed in a wide temperature range from ∼0 to 600 K. The prediction of an inverse MCE associated to the compensation temperature (∼225 K) is in good agreement with experimental data [812].

A completely different family of samples is that of clathrates [813]. This term derives from the Latin "clathratus", which means "furnished with a lattice". Therefore, in this type of compounds, usually polyatomic, one component forms a cage structure that contains the other, which is normally a large metal atom. Clathrates are known for their outstanding thermoelectric properties. If the metal ion is Eu^{2+}, it has a large magnetic moment, making it interesting for the study of thermomagnetic properties. Actually, the combination of thermoelectric and magnetocaloric response in a single material can allow for new refrigeration technologies that combines the virtues of both thermoelectric and magnetocaloric refrigeration. Large MCE has been reported for $Eu_8Ga_{16}Ge_{30}$ clathrate compounds (and with partial Sr substitution for Eu) [814–817], which crystallize in two different complex structures: type I with space group *Pm*-3*n* and type VIII, space group *I*-43*m*. In these structures, Ga and Ge atoms form a network, which encloses Eu (and Sr) atoms. FM transitions occur at very low temperatures (13 K) and ascribed $\Delta S_M(3\,T) = -6$ and $-9.3\ J\ kg^{-1}\ K^{-1}$ are observed for types I and VIII [814]. Composite formed with clathrate and EuO, is found to exhibit a table-like MCE, which enhances *RC* [818]. Biswas et al. [819] reported that an enhanced MCE response of $Eu_8Ga_{16}Ge_{30}$ clathrates at lower temperatures is obtained by milling, which results in an almost constant $|\Delta S_M| \sim 5\ J\ kg^{-1}\ K^{-1}$ below 30 K. Other cage structures, whose MCE has deserved attention, are Wells-Dawson type $[Ni_6Gd_6P_6]$, with higher RE content ($|\Delta S_M| > 25\ J\ kg^{-1}\ K^{-1}$ at 3 K and 7 T) [820].

Slightly higher RE content is found in $Gd_3Co_{4+x}Al_{12-x}$ series, which crystallizes in $Gd_3Ru_4Al_{12}$-type structure (space group $P6_3/mmc$) with a FM ordering below 40 K with $-\Delta S_M = 3.28\ J\ kg^{-1}\ K^{-1}$ and $\Delta T_{ad} = 1.5$ K at 2 T [821].

5.1.1.8.20. Compounds with 14 at.% of RE. The reference lanthanum manganite compound previously described, $La_{0.7}Ca_{0.3}MnO_3$ presents this RE fraction. Besides this widely studied family, studies on $GdCu_6$, which orders antiferromagnetically at 16 K are also available [822]. This compound changes from inverse to normal MCE at an AFM-PM transition temperature, showing maximum $|\Delta S_M|(5\,T)$ as $\sim 0.5\ J\ kg^{-1}\ K^{-1}$ (at ∼15 K) and $\sim 0.6\ J\ kg^{-1}\ K^{-1}$ (at ∼20 K) for inverse and normal MCE respectively.

Belonging to the $RETM_4X_2$ series (X = Si, Ge, P, As), which crystallize in $ZrFe_4Si_2$-type phase, $ErCo_4Ge_2$ undergoes a PM-AFM SOPT at 2.6 K with $|\Delta S_M| = 11.7\ J\ kg^{-1}\ K^{-1}$ at 2 T [823].

5.1.1.8.21. Compounds with 12 at.% of RE. $Er_2Fe_{14}B$ compound crystallizes in a tetragonal structure with $P4_2/mnm$ space group and has been proposed as a refrigerant close to room temperature due to its spin reorientation transition at 322.8 K and $|\Delta S_M| = 0.735\ J\ kg^{-1}\ K^{-1}$ at 0.4 T [824]. The sign of the MCE is dependent on the direction of the applied magnetic field (along the a- or c-axis) [825].

5.1.1.8.22. Compounds with 11 at.% of RE. Besides preliminary results on intermetallics with RE_2X_{17} stoichiometry by Jin et al. [826], recent studies have focused on those that crystallize in two different structures: rhombohedral Th_2Zn_{17}-type (*R*-3*m*) and hexagonal Th_2Ni_{17}-type ($P6_3/mmc$). Nanometer sized ball milled powders of Pr_2Fe_{17} preserving Th_2Zn_{17}-type structure exhibit lower $|\Delta S_M|$ values ($4.5\ J\ kg^{-1}\ K^{-1}$ at $\mu_0\Delta H = 5$ T) than bulk counterparts [550] ($6.3\ J\ kg^{-1}\ K^{-1}$ at $\mu_0\Delta H = 5$ T) although *RC* of the former is enhanced due to the broadening of $\Delta S_M(T)$ curves and increasing of T_C from ∼290 to ∼300 K [827]. Some α-Fe impurities were found, which can be avoided for Pr content above 12 at.%. MCE was optimized in single phase $Pr_{13}Fe_{87}$ alloy [828]. Partial substitution of Al for Fe in Pr_2Fe_{17} compound, where Al preferentially occupies 6c positions, leads to a slight increase of the unit cell volume and T_C. ΔS_M decreases with Al content from 5.5 to $4.2\ J\ kg^{-1}\ K^{-1}$ (5 T) for x = 0 and 1 respectively [829]. Partial substitution of Mn for Fe in $Pr_2Fe_{17-x}Mn_x$ yields a non-monotonic change of the PM-FM SOPT temperature (283, 294 and 285 K for x = 0, 1 and 2 respectively) and ΔS_M (5.66, 5.77 and $4.31\ J\ kg^{-1}\ K^{-1}$ at 5 T for x = 0, 1 and 2 respectively) [830]. Bulk Nd_2Fe_{17} exhibits a single T_C at 339 K and upon ball milled, its Th_2Zn_{17}-type structure is preserved while its MCE broadens ($-\Delta S_M(1.5\,T) = 2.7\ J\ kg^{-1}\ K^{-1}$ for bulk and $\sim 2\ J\ kg^{-1}\ K^{-1}$ for ball milled powder) [831]. Two-phase amorphous-nanocrystalline $NdPrFe_{17}$ ribbons exhibit two close SOPT at 303 and 320 K, yielding an enhancement of refrigerant capacity [33]. Pseudo-binary $Ce_{2-x}RE_xFe_{17}$ compounds, with RE = Y (x = 1.2), Pr (x = 1.5) and Dy (x = 1.15), also crystallize in Th_2Zn_{17}-type structure and have been studied with the aim of tuning SOPT temperatures (253, 264 and 273 K for Y, Pr and Dy compounds respectively) [832]. $|\Delta S_M|$ and *RC* values decrease in the order of Pr > Y > Dy (5.3, 4.3 and $3.3\ J\ kg^{-1}\ K^{-1}$ respectively, at 5 T). $Ce_2Fe_{17-x}Mn_x$ ($x \leq 2$) series also crystallizes in Th_2Zn_{17}-type structure [833] and exhibits two magnetic transitions for $0 \leq x \leq 0.35$ and $1.3 \leq x \leq 2$: from FM to AFM state (decreasing from 94.4 to 22 K as x increases from 0 to 0.35 and increasing from 9 to 80 K as x increases from 1.3 to 2) and from AFM to PM state. However, for $0.5 \leq x \leq 1$, a single Néel transition is observed. Ascribed to the AFM-PM transformation (decreasing from 209 to 168 K as x increases from 0.35 to 2), $\Delta S_M \sim -3\ J\ kg^{-1}\ K^{-1}$ is obtained for low values of x, and for x = 2, 50% decrease in the absolute values is

observed. A distribution of Curie temperatures in mechanically alloyed RE_2Fe_{17} compounds (RE = Pr and Nd) broadens the temperature range of the MCE [834].

Hexagonal Th_2Ni_{17}-type structure (space group $P6_3/mmc$) is found for Tb_2Fe_{17} for which Mössbauer experiments show seven different Fe sites [835]. This compound exhibits a PM-FM SOPT at 412 K with $-\Delta S_M = 2.19$ J kg^{-1} K^{-1} and RC_{FWHM} = 88 J/kg at 1.5 T. Also crystallizing in Th_2Ni_{17}-type structure, Er_2Ni_{17} is FiM below 150 K, with a compensation temperature at 63 K at $\mu_0 H = 0.02$ T, which shifts to lower temperatures for higher fields. ΔS_M at the FiM-PM transition is about -0.7 J kg^{-1} K^{-1} at 5 T, with an inverse MCE around 60 K [836]. The $Lu_2Fe_{17-x}Mn_x$ ($0 \leq x \leq 2$) series also crystallizes in Th_2Ni_{17}-type structure (some α-Fe impurities were found) [837]. $Lu_2Fe_{17-x}Mn_x$ series with $x \leq 0.5$ exhibits a Néel temperature at ~278 K but transforms to FM state at a lower temperature (from 135 to 249 K as Mn content increases from 0 to 0.5). Alloys with $0.7 \leq x \leq 2$ are FM, with $T_C = 287$ K for x = 0.7. Their maximum $|\Delta S_M| = 3.6$ J kg^{-1} K^{-1} at $\mu_0 \Delta H = 5$ T is achieved at x = 0.7, where FOPT and SOPT merge.

Kuchin et al. [838] recently reviewed the MCE response of several $RE_2(Fe,Mn)_{17}$ (RE = Ce, Tm and Lu), hydrogenated Ce compounds, and off-stoichiometric RE = Tm compounds. Despite their different nature of magnetic transitions, $|\Delta S_M| \sim 3$ J kg^{-1} K^{-1} at $\mu_0 \Delta H = 5$ T at around 300 K. In the case of hydrogenated Ce compounds, the magnetic transition increases with H content.

5.1.1.8.23. Compounds with 10 at.% of RE or lower. $NdBaMn_2O_6$ exhibits a PM-FM SOPT at 290 K and a FM-AFM FOPT at 210 K. It presents normal and inverse MCE with $\Delta S_M = -2.5$ and 1.4 J kg^{-1} K^{-1} respectively [839].

New monoclinic $GdNi_8Si_3$ structure (space group $C2/c$) related to the tetragonal $BaCd_{11}$-type (space group $I4_1/amd$) was found for $RENi_8Si_3$ compounds (RE = Gd and Tb) [840]. These compounds order at ~3 K with $|\Delta S_M|$(14 T) = 19.8 and 12.1 J kg^{-1} K^{-1}, at 4 and 12 K for Gd and Tb compounds respectively.

Recently, it was shown that single crystals of $KEr(MoO_4)_2$ shows a MCE by simply rotating the crystal within the ab plane in a constant magnetic field ($|\Delta S_M| = 13$ J kg^{-1} K^{-1} at $\mu_0 H = 5$ T), which is quantitatively similar to that obtained after a 5 T field increase ($|\Delta S_M| = 14$ J kg^{-1} K^{-1}) [841].

HoB_{12} is a frustrated incommensurate amplitude-modulated AFM crystallizing in UB_{12}-type structure (Fm-3m space group). In the AFM region, a small inverse MCE is observed and, above the Néel temperature (7.4 K), ΔS_M scales close to the predicted behavior for an ideal paramagnet [842]. Crystallizing in $ThMn_{12}$-type structure (space group $I4/mmm$), $REFe_5Al_{17}$ compounds (RE = Gd and Dy) show several changes in the sign of the MCE, which is also observed in the magnetoresistance data [843]. Tetragonal phase with space group $P4/nmm$ is observed for $Gd_{3-x}Y_xCo_{29}Ge_4B_{10}$ compounds, whereby the Gd and Co atoms order ferrimagnetically. For Y-free compound $T_C = 212$ K, with a compensation point at 128 K and a moderate MCE at T_C of $\Delta S_M = -0.5$ J kg^{-1} K^{-1} is observed at 5 T. Partial Y substitution for Gd does not affect T_C but decreases the compensation temperature [844].

With a RE content about 7 at.%, $La(FeSi)_{13}$ family have been already described in previous sections.

FM $RuSr_2GdCu_2O_8$, a superconductor below 46 K, shows a GMCE at very low temperatures of ~4 K, characterized by $|\Delta S_M| = 15.5$ J kg^{-1} K^{-1} and $\Delta T_{ad} = 14$ K at 7 T [845]. At higher temperatures of ~145 K, other maximum is found with $|\Delta S_M| \sim 0.9$ J kg^{-1} K^{-1}.

Some boride compounds with transitions temperatures above 150 K have been studied. Metastable $NdFe_{12}B_6$ compound can be obtained from devitrification of amorphous alloys (besides ~20% of α-Fe phase) and exhibits an abrupt change in magnetization around its Curie temperature of ~220 K with $\Delta S_M = -8.4$ J kg^{-1} K^{-1} and $\Delta T_{ad} = 3.2$ K at $\mu_0 \Delta H = 1$ T [846]. This intermetallic crystallizes in hexagonal $SrNi_{12}B_6$-type (space group R-3m) with a high magnetic moment of 19.7 μ_B per formula unit. Mössbauer spectrometry results suggest a FOPT from FM to PM state responsible for the high MCE parameters [847]. The metastability of this compound can be overcome by alloying with the isostructural $NdCo_{12}B_6$ compound, which orders at 170 K. However, the first order character of the transition is lost, leading to moderate ΔS_M values (-1.4 J kg^{-1} K^{-1} at $\mu_0 \Delta H = 1$ T), which decrease with increasing Fe content. Nevertheless, refrigerant capacities are comparable to Co-free compound as the $\Delta S(T)$ curves become broader. Therefore, $Nd(Co_{1-x}Fe_x)_{12}B_6$ (x = 0, 0.05 and 0.1) can be obtained in the stable $SrNi_{12}B_6$-type structure by conventional casting and annealing methods with $\Delta S_M \sim -1.4$, -1.2 and -0.9 J kg^{-1} K^{-1} at 1 T and 175, 165 and 155 K for x = 0, 0.05 and 0.1, respectively [848]. Similarly, $PrFe_{12}B_6$ exhibits a FOPT at 200 K from FM to PM state accompanied by a lattice contraction, which leads to high MCE values (-11.7 J kg^{-1} K^{-1} for $\mu_0 \Delta H = 2$ T) [849].

As a summary of this section, Fig. 25 shows the plot of $|\Delta S_M|$ vs peak temperature for the described RE-containing compounds. In agreement with the description followed in this section, the different compounds are grouped according to their atomic fraction of RE. It can be observed that the behavior of the best values reported is very similar to those of Laves phases and $ThCr_2Si_2$-type structures.

5.1.2. Rare earth free crystalline materials

MCE has been studied for the three pure FM transition elements (Fe, Co and Ni) and their experimental results have a fairly good agreement using mean field approach in a Hamiltonian from Hubbard-like model describing itinerant electron systems [850]. Moreover, MCE studies ascribed to the superconductor transition of Nb [851–853] and In [854] can be also found to explore the parameters of the mixed state in these superconductors. However, majority of transition elements compounds are based on Mn. The main reason for considering Mn-containing compounds in the study of MCE is the large magnetic moment of the Mn atoms, which is the highest value among transition metals (up to 4μ_B in some intermetallics).

A previous review focused on Mn-containing systems was published by Brück et al. [445] including Heusler alloys, Mn(Fe,Co,Ni)(Si,Ge), $(Mn(Fe,Co))_5(Ge(Si,Sb)_3$, $(Fe,Mn)_3C$, $La(MnFe)_2Ge_2$ and arsenic-containing alloys. FM lanthanum manganites,

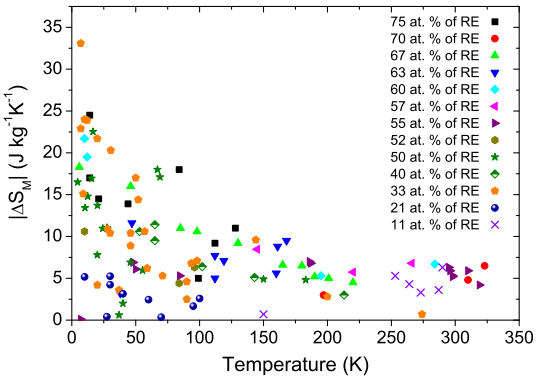

Fig. 25. Plot of $|\Delta S_M|$ at 5 T vs. peak temperature values for the different RE-containing compounds described above as a function of the atomic fraction of rare earth in their composition. Corresponding references can be found in the main text.

which constitute a big family among Mn-containing alloys were previously reviewed by Phan and Yu in 2007 [474] and in the present review they were already described in the section of RE-containing compounds. Curie temperatures and maximum entropy change at $\mu_0\Delta H = 1$ T (when literature data were only available for a different field, data were rescaled to 1 T using mean field parameters for those systems with SOPT) are plotted in Fig. 26 as a function of the magnetic moment per 3d atom.

In the following the main families of the RE-free compounds will be described.

5.1.2.1. Heusler alloys. Heusler alloys are named after the German scientist Friedrich Heusler, who in the early years of twentieth century discovered ferromagnetism in intermetallic compounds constituted by non-magnetic elements (Cu_2MnAl in 1903) [855]. Stoichiometric formula of these alloys is X_2YZ and they crystallize in $L2_1$ cubic structure (space group $Fm3m$). The crystallographic positions of the different elements are distinguished as shown in Fig. 27. X is a 3d element, generally Ni, although Fe, Co and Pt can be also found. *Y* atoms are responsible for the magnetism of the system (exchange interactions between *Y* and *X* atoms are also considered) and generally correspond to Mn (with a magnetic moment of $\sim$4 μ_B). Finally, several elements can be ascribed to *Z* atoms, being Ga, In, Sn and Sb the most interesting from the point of view of MCE. Recent reviews on the MCE of these systems can be found in Planes et al. [856,857], Buchelnikov et al. [858], Umetsu et al. [859] and Yu et al. [860]. Besides MCE, superelasticity, shape memory effect and magnetoresistance are found among the interesting properties exhibited by these systems. Generally, the different MCE studies of Heusler alloys are focused on FOPT martensitic transformations. However, many papers also supplied the MCE data corresponding to the SOPT austenitic Curie transition (see Table S6 of the Supplementary Material) and, recently Singh et al. [861] have reviewed the viability of this transition for MCE.

The feature leading to GMCE in these alloys is the existence of a structural transition from the high temperature austenitic phase to the low temperature martensitic phase, which for low *Z* concentration corresponds to the $L1_0$ tetragonal phase (space group $P4/mmm$) as shown in Fig. 28. In order to characterize this transition, four temperatures are considered. On cooling the sample, martensitic start temperature, M_s, corresponds to the temperature at which martensitic phase starts to form, while martensitic finish temperature, M_f, corresponds to the end of the transformation process. Analogously, on heating the sample from the martensitic phase, austenitic start temperature, A_s, corresponds to the onset of austenitic phase formation, while austenitic finish temperature, A_f, corresponds to the end of this process. As $M_s < A_f$ and $M_f < A_s$, a thermal hysteretic behavior of up to few tens of Kelvin is observed. However, martensitic transformation is quite complex and premartensitic transformations are reported to occur in some cases. Phase diagrams show the presence of several modulated phases at higher *Z* content as 5M (or 10M) and 7M (or 14M), where M refers to the monoclinic structure formed due to distortion. Thermal hysteresis could be narrowed when premartensitic (or intermartensitic) transition becomes close to basic martensite-austenite one [862]. These phase diagrams are generally represented as a function of the average number of electrons in the outer shell per atom, e/a (including 3d atoms for transition elements). Martensitic phase diagram, including intermartensitic transformation (from modulated to non-modulated phase) were recently studied by Dutta et al. [863] using an ab initio approach.

In off-stoichiometric $Ni_{2+x}Mn_{1-x}Ga$ alloys, Curie temperature and structural transition coincide in the compositional range $0.18 < x < 0.27$ [858] (corresponding to $7.635 < e/a < 7.7025$) and a FOPT magnetostructural transition occurs characterized by an evident thermal hysteresis. For $x < 0.18$, martensitic transformation occurs at temperatures lower than its Curie temperature. For $x > 0.27$, martensitic transformation occurs at temperatures higher than Curie temperature. For $x > 0.36$, ($e/a > 7.77$) secondary phases appear. Theoretical studies on the disorder in Mn and Ni sites effect on the magnetic moment of Mn-Ni-Ga alloys have been recently reported by D'Souza et al. [864]. In ternary alloys, transition temperature increases with e/a ratio (see line 1 in Fig. 28). However, if a transition element like Fe, Co or Cu is added, transition temperature decreases although e/a increases (see lines 2 and 3 in Fig. 28). On the other hand, partial substitution of Sn for Ga has no significant change in e/a but it has a clear effect on transition temperature (see line 4 in Fig. 28).

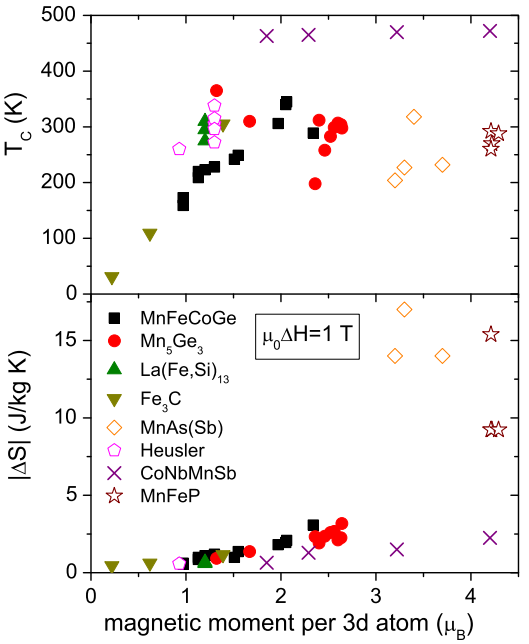

Fig. 26. Curie temperatures and maximum entropy change at 1 T as a function of the magnetic moment per 3d atom (see corresponding tables for references).

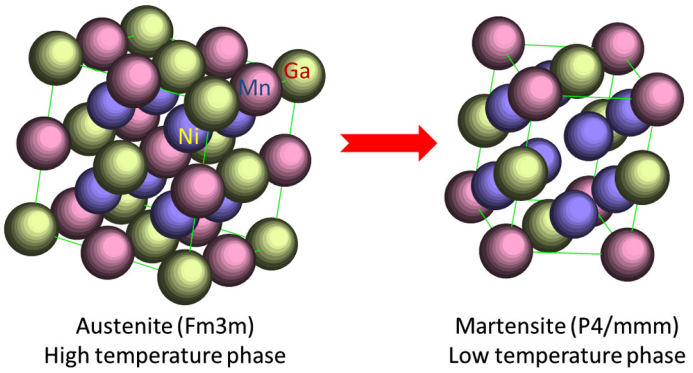

Fig. 27. Unit cells for $L2_1$ cubic austenitic (left) and $L1_0$ tetragonal martensitic (right) phases in Ni_2MnGa alloy.

First work on MCE of Heusler alloys appeared in 2000 and corresponds to Hu et al. [865]. They observed an inverse MCE at moderate fields ($\Delta S_M \sim +4$ J kg^{-1} K^{-1} at 0.9 T) ascribed to martensitic transformation (thermal hysteresis 10 K). Inverse MCE occurs as both phases are FM and the high temperature phase (austenite) exhibits a higher magnetization than that of low temperature one (martensite) at low fields due to the strong uniaxial magnetocrystalline anisotropy of martensitic phase [866]. However, for fields above 1 T, inverse MCE changes to direct MCE [867,868]. In the compositional region for which magnetostructural transformation occurs, GMCE is reported [869]. Zhou et al. [870,871] systematically studied the evolution of structural and magnetic transitions as well as MCE in off-stoichiometric ternary Ni_2MnGa alloys. Ni-rich alloys exhibit a lower Curie temperature and closer to room temperature than those of Mn-rich ones. Recently, Singh et al. [872] using neutron diffraction on Ni_2MnGa and $Ni_{1.75}Mn_{1.25}Ga$ systems show that the AFM interaction between the Mn atoms occupying inequivalent sites is the origin of inverse magnetocaloric effect. Fig. 29 shows the field dependence of the ΔS_M values for two examples: Ni_2MnGa and $Ni_2MnGa_{0.95}Sn_{0.05}$ adapted from [873].

Soon after the discovery of GMCE in Ni-Mn-Ga alloys, Marcos et al. [874,875] observed that MCE is directly related to magnetostructural coupling at the length scale of both magnetic and martensitic domains. This contribution is the dominant for those systems where Curie temperature and martensitic transition temperature are well separated (e/a $\sim$ 7.5) and yields a negative GMCE, whereas for alloys in which both temperatures become close (e/a $\sim$ 7.7), microscopic spin-phonon coupling becomes dominant and yields a positive GMCE. Pareti et al. [876] found a clear enhancement in ΔS_M (from -5 to

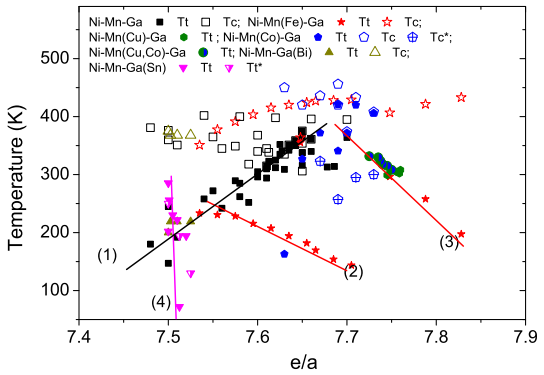

Fig. 28. Temperatures of martensitic transition (Tt), premartensitic transition (Tt*) and Curie temperatures of the austenitic phase (Tc) and martensitic phase (Tc*) as a function of the number of external electrons per atom (e/a) for ternary Ni-Mn-Ga alloys [870,871,875,878,999,1610–1614] and with Fe [992], Cu [888], Co [894], Cu and Co [891], Bi [896] and Sn [873,897]. Lines are guides to the eye showing the different trends. For number in parenthesis see text.

-20 J kg^{-1} K^{-1} at $\mu_0\Delta H = 1.6$ T) after increasing the Ni/Mn ratio to merge structural and magnetic transitions. For such alloy, Aliev et al. [877] used a statistical model of phase coexistence during martensitic transformation to describe the MCE of $Ni_{2.19}Mn_{0.81}Ga$ alloy. From a value of $\Delta T_{ad} = 1.2$ K at $\mu_0\Delta H = 2.6$ T and $T \sim 340$ K, they estimated a $|\Delta S_M| \sim 4.5$ J kg^{-1} K^{-1} at $\mu_0\Delta H = 1.5$ T, which is much lower than the value reported by Pareti et al. Moreover, the structural entropy change linearly increases from 9.1 to 15.6 J kg^{-1} K^{-1} as e/a increases from 7.48 to 7.66. Pasquale et al. [878] also found a strong discrepancy between very large $\Delta S_M = -86$ J kg^{-1} K^{-1} estimated from Maxwell relation and $\Delta T_{ad} = 2.2$ K at 5 T. Analysis using Clausius-Clapeyron equation reduces $|\Delta S_M|$ to $\sim$25 J kg^{-1} K^{-1} at 4 T. On the other hand, Duan et al. [879] considered both magnetic and lattice contributions of $Ni_{2.15}Mn_{0.85-x}Cu_xGa$ (x = 0.05 and 0.07) to its entropy change and compared the theoretical and experimental results, concluding that the main contribution to entropy change is magnetic. However, direct measurements of ΔT_{ad} ($\sim$1 K for $Ni_{2.19}Mn_{0.81}Ga$ at 2 T) showed to be one order of magnitude smaller than calculated values, which is ascribed to intrinsic factors of FOPT (exchange integrals of low and high temperature phases, thermal hysteresis and phase coexistence) although the rate of martensitic transformation is assumed to be fast enough to follow the field sweeps used [880]. In fact, the applicability of Maxwell relation to FOPT (implying phase coexistence) leads to artifacts affected by the integration method [881]. Zhang et al. [882] pointed that the use of Maxwell relation is correct for magnetic field values below the critical field. Khovailo et al. [880] also showed an irreversible character of ΔT_{ad} upon applying a magnetic field at a constant temperature when reached by cooling from $T > A_f$. The first application of the field can induce the formation of FM martensitic phase (contributing as an extra to the temperature change registered) but consequent removal of the magnetic field cannot induce the formation of austenitic phase (as martensitic phase is already stable) and thus a second cycle will show a reduced ΔT_{ad} as it occurs for $Ni_{2.19}Mn_{0.81}Ga$. The history dependence of MCE on the field and thermal sequence followed has been also pointed by Sasso et al. [883], whose conclusions agree with those of Khovaylo et al., assigning differences between field applied and field removed curves to the magnetostructural hysteresis. Porcary et al. [884] established the convergence of direct and indirect methods in the study of Ni(Co)-Mn-Ga alloy. In fact, there are many objections to using Heusler alloys as magnetic refrigerants due to the irreversible character of the magnetic field induced martensitic transformation and the large hysteresis found [885]. Hence, reducing hysteresis is the main goal, nowadays, prosecuted by researchers working in the MCE of Heusler.

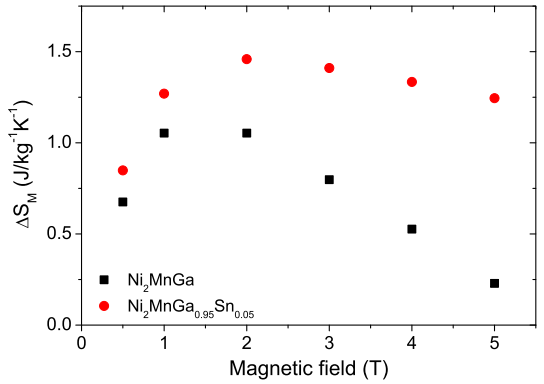

Fig. 29. Field dependence of ΔS_M for $Ni_2MnGa_{1-x}Sn_x$ (x = 0 and 0.05) alloys, adapted from [873].

Substitution of 1 at.% of Fe for Ni in $Ni_{55.5}Mn_{20}Ga_{24.5}$ increases Curie temperature and decreases martensitic transformation temperature [886]. Inverse MCE is observed at 0.5 T, changing to direct MCE at higher field changes. Partial substitutions of Co or Cu for Mn in stoichiometric Ni_2MnGa alloy [887,888] tune martensitic and Curie temperatures to coincide for $Ni_2Mn_{0.7}Co_{0.3}Ga$ and $Ni_2Mn_{0.75}Cu_{0.25}Ga$. The latter alloy exhibits a GMCE of $\Delta S_M(2\ T) = -17.6\ J\ kg^{-1}\ K^{-1}$ at 315 K and further studies showed that magnetostructural transition shifts to higher temperatures with increasing Mn deficiency in off-stoichiometric alloys while a nearly constant value of ΔS_M is observed [889]. As Cu substitution for Mn increases, magnetic transition decreases, delocalization of magnetism of Mn atoms increases and the chemical bond between Ni-Ga is reinforced, which increases the martensitic transition temperature [890]. Co substitution for Cu in $Ni_2Mn_{0.75}Cu_{0.25-x}Co_xGa$ ($0 \le x \le 0.05$) [891] progressively shifts FOPT to higher temperatures, maintaining GMCE ($\Delta S_M < \sim -50\ J\ kg^{-1}\ K^{-1}$ at $\mu_0\Delta H = 5T$). Magnetostructural transition temperature of $Ni_2Mn_{0.75}Cu_{0.25}Ga$ alloy could be tuned (preserving similar values of MCE) to lower temperatures in $Ni_2Mn_{0.71}Cu_{0.27}Fe_{0.02}Ga$ (~299 K) and to higher temperatures in $Ni_2Mn_{0.70}Cu_{0.30}Ga_{0.95}Ge_{0.05}$ (~316 K) [892]. Partial substitution of Co for Mn in $Ni_{2.15}Mn_{0.85-x}Co_xGa$ shows magnetostructural transition in the range $0.04 \le x \le 0.06$ [893]. As Co content increases, the transition temperature increases while $|\Delta S_M|$ decreases from a maximum of 14.2 $J\ kg^{-1}\ K^{-1}$ obtained for x = 0.04–7 $J\ kg^{-1}\ K^{-1}$ for x = 0.06 at $\mu_0\Delta H = 1.9$ T. When Co is substituted for Ni in Mn-rich/Ga-poor alloys, Curie temperature of the austenitic phase as well as the magnetization of this phase increase. This fact, along with a decrease of the Curie transition of the martensitic phase, leads to an inverse MCE [894]. Pathak et al. [895] studied the $Ni_{50-x}Co_xMn_{32-y}Fe_yGa_{18}$ alloy series (x = 0 and 8, and y = 0, 1 and 1.5) and found a maximum value of $\Delta S_M = +31\ J\ kg^{-1}\ K^{-1}$ for x = 8 and y = 2 alloy with a hysteresis loss of 40 J/kg.

Partial substitution of Bi for Ga in $Ni_2MnGa_{1-x}Bi_x$ ($x \le 0.05$) [896] leads to an increase of the martensitic transformation temperature and a decrease of the Curie temperature of the austenitic phase, without merging both temperatures in the explored compositional range. However, as it occurs for stoichiometric ternary alloy, MCE changes from inverse to normal with field while it decreases for Bi-containing alloys. Partial substitution of Sn for Ga in $Ni_{50}Mn_{25}Ga_{25-x}Sn_x$ alloys yields a decrease of martensitic temperature of 90 K as x increases from 0 to 2 at.% [897]. This decrease is out of the general trend found for increasing e/a above 7.5 (see Fig. 28). Moreover, 10% substitution of Sn for Ga in Ni_2MnGa alloy suppresses the martensitic transformation [873]. Partial substitution of Al for Ga has been reported without deleterious effect on MCE and can significantly reduce the cost of the alloy [898].

Addition of Gd in $Ni_{56}Mn_{18.8}Ga_{24.5}Gd_{0.7}$ [899] yields the formation of two phases, being the new one an intergranular phase rich in Gd. The intergranular phase was presumed to enhance the mechanical properties of these Heusler alloys. The enhanced mechanical behavior of Heusler alloys was also the reason to propose Ni-Fe-Ga systems [900].

As V content increases from 0 to 4 at.% in $Ni_{54}Mn_{21-x}V_xGa_{25}$, both martensitic and Curie temperatures decrease, with a higher rate of the former temperature, which leads to a separation of these two transitions. A 27% decrease in $|\Delta S_M|$ at the Curie temperature is observed as x increases from 0 to 4 [901].

Pressure effect on Ni-Mn-Ga alloys differs between Ni-rich and Mn-rich alloys [902]. In both cases, structural and magnetic transition temperatures increase with applied pressure. However, while the rate of increasing the transition temperatures is similar for both structural and magnetic transitions for the Ni-rich alloy (5.8 and 4.7 K/GPa, respectively), the structural transition temperature of Mn-rich alloy increases about three times faster than that of the magnetic one (17.0 and 6 K/GPa respectively), leading to a progressive overlapping of both transitions and thus enhancing MCE. Mandal et al. [903] also reported a large decrease of the magnetic hysteresis in samples submitted to 8 kbar of hydrostatic pressure. Comparison between the magnetocaloric and elastocaloric properties in Ni-Mn-Ga(Co) alloy series showed a similar relative cooling power after applying 0.8 T or 10 MPa [904].

In 2005, Krenke et al. [905] reported inverse GMCE in $Ni_{50}Mn_{37}Sn_{13}$ and, in 2006, Han et al. [906] reported inverse GMCE also for In-containing Heusler alloys. Later, in 2007, Khan et al. [907] and Du et al. [908] reported similar behavior for $Ni_{50}Mn_{37}Sb_{13}$. $Ni_2Mn_{1+x}Z_{1-x}$ alloys (Z = In, Sn, Sb) close to stoichiometric composition ($x < 0.3$) shows a cubic $L2_1$ austenitic phase and magnetic transition is typical FM-PM one preserving this austenitic phase. However, martensitic transformation is observed for alloys with a larger deviation from 2:1:1 stoichiometry. Unlike for Ga-containing Heusler alloys, AFM coupling between Mn atoms in these alloys is enhanced in the martensitic phase, leading to a metamagnetic transition from AFM to FM, which can be tailored to be a metamagnetostructural transition from AFM martensitic to FM austenitic phase. The presence of both inverse and normal MCE has been suggested as a mechanism of improved refrigeration cycle [909].

Values of the different temperatures as a function of e/a ratio are shown in Fig. 30 for several ternary and quaternary Ni-Mn-Sn systems.

Recent studies of the phase diagram of Ni-Mn-Sn Heusler alloys have been reported by Cakir et al. [910], including their intermartensitic transformations. As e/a increases in ternary Ni-Mn-Sn alloys, transition temperature linearly increases (~80 K per 0.1 increase in e/a) [911–913] (e.g. see lines corresponding to solid squares in Fig. 30). However, after partial substitution of transition elements, the general rule based on e/a is no longer fulfilled. In $Ni_{2+x}Mn_{1.4-x}Sn_{0.6}$ Heusler alloys, excess Ni has no monotonic effect on ΔS_M ascribed to the inverse MCE with maximum value at x = 0.12. However, *RC* increases continuously [914].

Studies have been done in tin-containing quaternary Heusler alloys with Co [915–921] or Fe [922–924]. The substitution of Co for Ni reduces the magnetostructural transformation temperature and increases the magnetic moment, and thus the Curie temperature of the austenitic phase. Co addition also slightly reduces thermal hysteresis [915,918] and martensitic transformation temperature but Curie temperature of the austenitic phase is reported to reduce [919,925], to slightly increase [926] or to be unaffected [927] depending on the alloy composition. Results on partial substitution of Fe for Mn

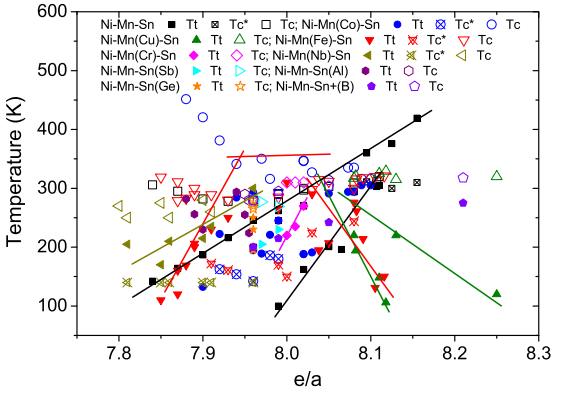

Fig. 30. Temperatures of martensitic transition (Tt) and magnetic transition temperatures of the austenitic phase (Tc) and martensitic phase (Tc*) as a function of the number of external electrons per atom (e/a) for ternary Ni-Mn-Sn alloys [911–913,1615,1616] and with Fe [915,922–924], Cu [919,925,926], Co [915–920,1617], Cr [928], Nb [929], Sb [930], In [1618], Ge [933], Al [931,932] and B [937]. Lines are guides to the eye showing the different trends described in the text.

differ between a continuous decrease of the martensitic transformation temperature (14 at.% of Sn) [922] and an increase of martensitic transformation temperature for low Fe substitution (~11 at.% Sn alloys) [923]. In both cases, Curie temperature of the austenitic phase increases and thermal hysteresis becomes broader. Ghosh et al. [924] studied Fe substitution for Ni or Mn for e/a < 8 and, in general, martensitic temperature increases with e/a. However, Curie temperature of both phases increases with Fe content, independently whether the substitution is for Mn or Ni.

Cr addition also leads to a decrease of the martensitic transformation but without significant effects on the Curie temperature of the austenitic phase [928]. Nb substitution for Ni yields a decrease of the martensitic transformation temperature and $|\Delta S_M|$, whereas Curie temperature of martensitic phase remains constant and that of the austenitic phase slightly decreases [929].

Substitution of non TM elements for Sn has also been explored, such as Sb [930], In [1040], Al [931,932], Ge [933,934] and Si [935]. In the case of Al and Ge, lattice contraction is responsible for the increase of the martensitic transformation temperature, which is in agreement with the observed increase of this temperature after applying hydrostatic pressure [936]. However, the addition of interstitial boron yields a lattice expansion and also shifts the martensitic transformation temperatures to higher values [937]. For $Ni_{48}Mn_{39.5}Sn_{12.5-x}Al_x$ (x = 0, 1, 2, 3) melt spun ribbons, martensitic transition temperature increases with Al content (~250, 275, 290 and 295 K for x = 0, 1, 2 and 3 respectively). While T_C of the austenite phase slightly decreases from 300 K to 296 K but that of the martensite phase is more affected by Al substitution (229, 215, 205 and 193 K respectively). Their MCE was studied above 200 K, presenting an inverse MCE at their structural transitions from PM martensite to FM austenite (ΔS_M(2 T) = +7.8, 5.7, 4.8 and 2.8 J kg^{-1} K^{-1} and RC_{FWHM}(2 T) = 56, 40, 32 and 18 J/kg) and a normal MCE at the austenite Curie transition ($-\Delta S_M$(2 T) = 1.8, 1.7, 1.5 and 0.9 J kg^{-1} K^{-1} and RC_{FWHM}(2 T) = 92, 53, 31 and 15 J/kg) [938]. Regarding Si substitution for Sn in $Ni_{48}Mn_{39}Sn_{13-x}Si_x$ Heusler alloys, a non-monotonic effect of pressure on MCE is reported although martensitic temperature increases with pressure [935]. Minor substitutions of Nb for Ni in $Ni_{45-x}Nb_xCo_5Mn_{40}Sn_{10}$ (x = 1 and 1.5) help to tune its martensitic temperature down to room temperature (68 K per at.% of

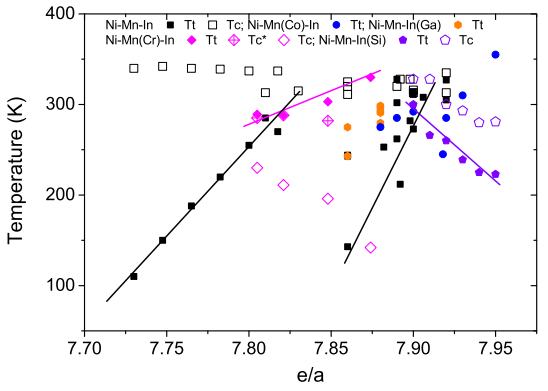

Fig. 31. Temperatures of martensitic transition (Tt) and magnetic transition temperatures of the austenitic phase (Tc) and martensitic phase (Tc*) as a function of the number of external electrons per atom (e/a) for ternary Ni-Mn-In alloys [993,1035,1619–1623] and with Co [942,976,979,1000,1624], Cr [944], Si [1625] and Ga [1626]. Lines are guides to the eye showing the different trends described in the text.

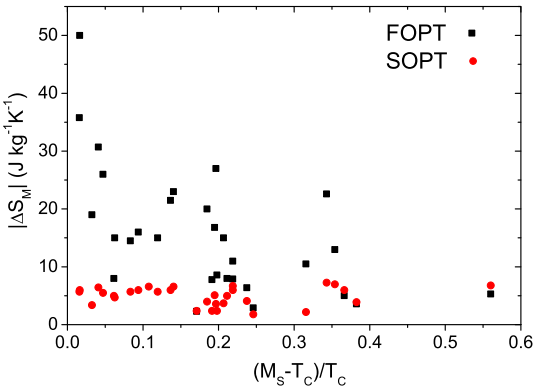

Fig. 32. Absolute values of the maximum adiabatic entropy changes at $\mu_0\Delta H$ = 5 T (data taken from Table S6 of the Supplementary Material) corresponding to the martensitic FOPT and the austenite Curie SOPT as a function of the relative difference between the austenitic T_C and the start martensitic transition temperatures.

Nb) and also reduce the Curie temperature of the austenite phase while retaining large values of magnetic entropy and low hysteresis [939].

Fig. 31 shows the transition temperatures of different Ni-Mn-In alloys as a function of e/a ratio. Their martensitic transformation temperature increases with e/a ratio, whereas slightly altering the Curie temperature of the austenitic phase.

Stern-Taulats et al. [940] proposed a relationship to correlate the caloric parameters and the temperature difference between the martensitic transformation temperature and austenitic Curie temperature in Ni-Mn-In with differing findings for barocaloric and magnetocaloric responses. Fig. 32 shows ΔS_M (5 T) of FOPT as a function of the relative temperature difference between the austenitic T_C and M_S (absolute values for the SOPTs are also shown) using the data shown in Table S6 of the Supplementary Material. As Stern-Taulats proposed, ΔS_M improves as the relative temperature difference reduces. The use of different experimental data from the literature could explain the dispersion of the data.

Different quaternary In-containing Heusler alloys have been recently studied by Dubenko et al. including additions of Si, B, Cu, Fe, Ag and Al [941]. Replacing Co for Ni decreases e/a ratio and transition temperature, which is a trend similar to that of ternary systems. For $Ni_{50-x}Co_xMn_{35}In_{15}$ alloys, martensitic transition is not observed at temperatures above 77 K for x > 2 [942]. In addition, the FOPT of this alloy series is close to the SOPT and significant changes in the MCE can be observed [943]. For Cr substitution in $Ni_{55}Mn_{33-x}Cr_xIn_{17}$ alloys [944], martensitic transformation does not follow a monotonous trend with the average e/a ratio due to the formation of precipitates affecting the Heusler phase composition. If the e/a ratio of this phase is considered, M_s increases with e/a. In the case of 2 at.% Cu additions in $Ni_{50}Mn_{34}In_{16}$, transition temperature shifted from 240 to 295 K [945]. The effects of the strength of magnetic exchange on MCE of this compound using Monte Carlo simulations has been studied by Sokolovskiy et al. [946]. Regarding substitutions for In, although Si and Sb increase e/a ratio, they lead to a decrease of transition temperature [947,948]. Pathak et al. [949] reported an enhancement of refrigerant capacity in $Ni_{50}Mn_{35}In_{15}$ alloy by substituting 1 at.% of Si, Ge or Al for In. In terms of ΔS_M, it enhances for Si- and Ge-containing samples as compared to that of the ternary alloy but not for Al-containing series, with a similar compositional dependence of the inverse MCE at FOPT and the normal MCE at the Curie temperature of the austenitic phase. $Ni_{50}Mn_{35}(In_{1-x}Cr_x)_{15}$ series ($0 \leq x \leq 0.1$) were studied by Quetz et al. [950], presenting a large $-\Delta S_M$ = 11 J kg^{-1} K^{-1} at 5 T at around 380 K for x = 0.02. For $Ni_{50}Mn_{35}In_{15}$, the substitution of small amount of B for In [951] yields large shifts of martensitic Curie and transition temperatures. Dubenko et al. [952] reported that for 1 at.% B, FOPT occurs at 320 K due to the transformation from FM martensitic phase to PM austenite and its direct characterization indicates a ΔT_{ad} = 1.5 K for $\mu_0\Delta H$ = 1.8 T. However, Pandey et al. [951] assign this transition to a FM-PM austenite transition, being the martensitic transformation around 240 K and the Curie transition of the martensite phase at ~200 K. Phase diagram at low fields shows that the effect of B is not monotonous and while T_C of austenite is almost insensitive to B content, for around 1 at.% of B substitution, martensitic transformation and Curie temperatures present a minimum and a maximum respectively [951]. For $Ni_{48}Mn_{39}In_{13-x}Ge_x$ (x = 1–3), partial Ge substitution for In changes the crystalline structure (e.g. $L2_1$ for $x \leq 2$ and modulated martensite for x = 3). When x increases from 1 to 3 at.%, its martensitic transformation increases from 220 K to 320 K. For $x \leq 2$, positive $\Delta S_M(5\,T) \sim 30$ J kg^{-1} K^{-1} occurs at 210 and 255 K while negative $\Delta S_M(5\,T) \sim -6$ J kg^{-1} K^{-1} at 280 and 275 K, whereas for x = 3 alloy, it shows a weak inverse MCE of ΔS_M = 4.8 J kg^{-1} K^{-1} at 320 K [953]. In addition, the martensitic transition temperature increases while the Curie temperature of the austenitic phase decreases with increasing Ge content. The atomic disorder in $Ni_{1.81}Co_{0.22}Mn_{1.46}In_{0.51}$ enhances ΔS_M but sharpens the MCE peak, resulting in an invariant refrigerant capacity [954].

Interstitial H additions to these Heusler alloys shift the martensitic transformation to lower temperatures [955]. This result agrees with the increase of the martensitic transformation after pressure application [956]. However, Pandey et al. [957] found in $Ni_{50}Mn_{35}In_{14.9}Ag_{0.1}$, instead of a decrease of the transformation temperature, a splitting of the MCE peak into two broader peaks after applying 6.6 kbar.

The initial reported MCE results of $Ni_{50}Mn_{37}Sb_{13}$ alloy differ between $\Delta S_M(5\ T) \sim 9$ [908] and $\sim 18\ J\ kg^{-1}\ K^{-1}$ [907]. They are analyzed using Maxwell relation and the samples were prepared in similar ways (arc-melting followed by annealing at 850 or 900 °C for one day) although Khan's samples were slowly cooled to room temperature while Du's samples were water-quenched. No comment about presence of impurities appears in any of these two papers. Martensitic transition temperature increases with e/a while Sb/Mn ratio changes [907,908] (e.g. trend line of 50 at.% Ni in Fig. 33), indicating a progressive increase as Sb content is reduced. However, when changing the Ni/Mn ratio, martensitic temperature slightly increases with e/a [958] (e.g. trend line of 12 at.% Sb in Fig. 33). The Curie temperature of the austenitic phase is relatively composition independent.

Partial Co substitution for Ni progressively decreases martensitic transition temperature but not significantly affecting the magnetic transitions of martensite and austenite phases [959,960]. Good MCE values at low fields (1 T) were obtained although thermal hysteresis increases after substitution [959]. For Co-containing Ni-Mn-Sb alloys, the effects of partial substitutions of Si and Ga [961] and Ge [962] for Sb have been also studied. For $Ni_{49-x}Cu_xMn_{39}Sb_{12}$, it shows an increasing trend of martensitic transition temperatures with e/a ratio but for partial substitution of Cu for Ni (assuming the typical e/a of 11 electrons per atom in Cu for the calculations), an inverse trend is observed, wherein M_s decreases from 340 to 257 K as x increases from 0 to 2 [963]. Likewise for $Ni_{50}Mn_{38-x}Fe_xSb_{12}$ alloys, a decrease of M_s with e/a is also observed [964].

The addition of interstitial boron in Sb-containing Heusler alloys increases the Curie temperature of the austenitic phase and decreases the martensitic transformation (from AFM martensite to FM austenite) [965], which gives a 30% enhancement in ΔS_M. As it is generally found, these results agree with those derived from pressure application, wherein M_s shifts to higher temperatures with increasing pressure [966].

Other Heusler alloy families have been a subject of study due to its MCE. Results on Ni-Mn-Ge were reported for temperatures around their SOPT [967] wherein T_C decreases with increasing Ni/Mn ratio. Mn-free systems can be also found in the literature, such as Ni-Fe-Ga [900,968–970], Ni-(Fe,Co)-Ga [971] and Co-Ni-Ga [972]. Ni-Fe-Ga was proposed as a more appropriate MCE material than Ni-Mn-Ga due to its better ductility. Its field dependence of MCE effect is similar to that of Ni-Mn-Ga and at low fields, it changes from inverse MCE to normal MCE. Addition of Co shifts transition temperature to higher values and helps to match Curie temperatures of martensite and austenite phases with the martensitic transformation. Moderate MCE values were reported: $\Delta S_M = -2.4\ J\ kg^{-1}\ K^{-1}$ at 360 K at 5 T [971]. On the other hand, $Co_{50}Ni_{22}Ga_{28}$ alloy was reported with higher MCE values: $\Delta S_M(5\ T) = -10.5\ J\ kg^{-1}\ K^{-1}$ at 313.5 K, ascribed to the martensitic transformation between FM martensite to FM austenite [972]. However, its sharp $\Delta S_M(T)$ curve (FWHM < 2 K) and the large thermal hysteresis of the martensitic transformation (~20 K) must be also considered. Vivas et al. [973] studied the effects of the number of valence electrons on the MCE of half-metal $Fe_2MnSi(Ga)$ alloys and found a phenomenological linear relationship between ΔS_M and this parameter.

As a summary, Fig. 34 shows the ΔS_M values at 5 T as a function of the transition temperatures of various Heusler alloys. For Ni_2MnGa, the magnetic moment of Mn atoms is 4 μ_B while that of Ni atoms is below 0.3 μ_B [871]. Accounting only the magnetic moment of Mn, a magnetic moment per formula unit of ~4 μ_B for Ni_2MnGa can be considered, while that of $Ni_2Mn_{1.4}X_{0.6}$ (X = In, Sn, Sb) should be considered ~5.6 μ_B. The latter yields a maximum magnetic entropy change, $\Delta S_M = R{\cdot}\mathrm{Ln}(2J+1)$, between 10 and 12 $J\ mol^{-1}K^{-1}$, which should correspond to 40–45 $J\ kg^{-1}\ K^{-1}$. However, several values exceeding this theoretical limit (see Table S6 of the Supplementary Material) were reported but they were obtained using Maxwell relation without employing an appropriate measurement protocol to avoid artifacts. Amaral and Amaral [974] have described how artificially high values of ΔS_M resulted from applying Maxwell relation to non-equilibrium states and when a mixture of phases exists in the analyzed range. Other authors also reported overestimated ΔS_M values from using Maxwell relation in comparison with those calculated using Clausius-Clapeyron equation [858,881,975]. However, Bourgault et al. found similar ΔS_M values computed from both equations [976] while Fabbrici et al. [894] obtained even lower $|\Delta S_M|$ values for

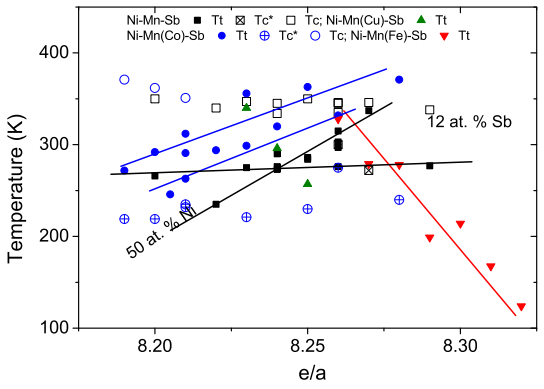

Fig. 33. Temperatures of martensitic transition (Tt) and magnetic transition temperatures of the austenitic phase (Tc) and martensitic phase (Tc*) as a function of the number of external electrons per atom (e/a) for ternary Ni-Mn-Sb alloys [907,908,958,1627] and with Co [959,960], Cu [963] and Fe [964]. Lines are guides to the eye showing the different trends.

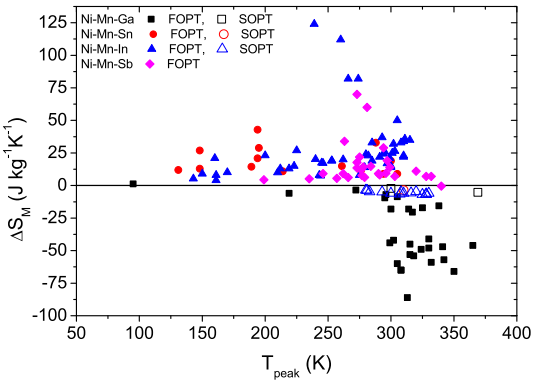

Fig. 34. ΔS_M values as a function of the peak temperatures for different Heusler alloys at 5 T. Data taken from Table S6 of the Supplementary Material.

$Ni_{50-y}Co_yMn_{30+x}Ga_{20-x}$ ($5 \leq y \leq 9$, $0 \leq x \leq 2$) with Maxwell relation than those obtained from Clausius-Clapeyron equation. Zhang et al. [882] pointed that Maxwell relation is valid for magnetic fields below the critical field. Nevertheless, although the presence of significant magnetoelastic interactions would explain these extraordinarily large ΔS_M values [977], the distinctive shapes of these $\Delta S_M(T)$ curves are with sharp peaks of FWHM < 3 K (a general feature in the present cases), which reduces the refrigerant capacity of the system. On the other hand, Caballero-Flores et al. [978] analyzing Ni-Mn-Ga samples, explained that smaller ΔT_{ad} values of samples with FOPT when compared to those of SOPT (assuming them with same magnetic entropy change), are due to their latent heat.

In fact, purely magnetic contribution is even neglected in some models: e.g. that of Recarte et al. [979] which describes the transformation in Ni-Mn-In-Co alloy and the influence of the field dependence of the martensitic temperatures on the measurements of magnetic entropy change. They assumed two constant entropy values for each phase: martensite and austenite. Therefore, the maximum achievable value of the magnetic entropy change would correspond to the structural one. For a field H, when heating the alloy, its martensitic transformation occurs between $A_s(H)$ and $A_f(H)$ temperatures and Recarte et al. assume a linear change of the entropy between the values of the martensite and the austenite phases within the temperature interval of A_s and A_f. With increasing H, the transition temperatures would ideally shift to lower values (stabilization of the austenitic phase) and ΔS would correspond to the difference between the entropy at certain field H_1 and that at zero field. Therefore, if $A_f(H_1) < A_s(0)$, the maximum ΔS_M allowed ($\Delta S_M = S$(austenite)-S(martensite)) could be obtained in the thermal range $A_f(H_1) < T < A_s(0)$. In this range, austenite phase is stable at H_1 but upon removing the field, martensite phase becomes the only stable phase and a complete transformation is induced. This is observed from the plateau in its $\Delta S(T)$ curve and ΔS_M is expected to be field-independent for fields above H_2, which corresponds to $A_f(H_2) = A_s(0)$. For lower fields, there is no thermal range at which a complete transition can be induced and the achieved ΔS_M is only a fraction of the structural entropy change. Borgault et al. [980], studying $Ni_{45.5}Co_{4.5}Mn_{37}In_{13}$ single crystals, extended this approximation using field dependence calorimetric data, by considering two new factors: decrease of entropy of the FM austenitic phase as field increases and a smeared transformation instead of an abrupt FOPT.

Recently, it has been proposed to unify both driving factors of the martensitic transition (magnetic field, H, and temperature, T) as a single effective temperature (T^*) to describe its hysteresis. This T^* is correlated to the actual temperature and the applied magnetic field, expressed as $T^* = T + a(T) \cdot H$, where the temperature dependent parameter a is related to the difference of the magnetization between martensitic and austenitic phases and to the entropy change during the martensitic transformation [981]. This study assumes an equivalent effect of both driving factors: temperature and field. However, Diestel et al. [982], studying thin films of Ni-Mn-Ga-Co, pointed a different character of field and temperature on the nucleation and growth mechanisms due to the vector and scalar character of those two magnitudes, respectively.

Gottschall et al. [72] reported that nucleation is a slower phenomenon than growth process, being hindered for fast field sweep (limitation for cycle cooling operation beyond 100 Hz). For a similar alloy composition, Stonaha et al. [983] characterized the microstructures using inelastic neutron scattering and found an unexpectedly large increase in the phonon entropy when heating at temperatures ranging from below to above the Curie temperature.

The total entropy change ascribed to the martensitic transformation is found to exponentially decay with the difference (Δ) between the austenitic Curie and the martensitic transformation temperatures: from ~45 to 5 J kg^{-1} K^{-1} as Δ increases from 0 to 150 K [984]. Ab initio studies on the MCE of Heusler alloys can be found in [946,985–990] and other thermodynamic models are developed to describe the GMCE of Heusler alloys [991].

As FOPT materials, Heusler alloys exhibit both thermal and magnetic hystereses, which are undesirable for applications. In general, there is no clear dependence of thermal hysteresis with MCE results, as observed from Fig. 35, which shows the difference between final austenite temperature and start martensite temperature for several Heusler compositions (collected from Table S6 of the Supplementary Material). However, in Ni_2(Mn,Fe)Ga alloy series, thermal hysteresis increases with Fe content [992]. In addition, Hu et al. [993] found thermal hysteresis below 2 K for $Ni_{51}Mn_{49-x}In_x$ (x = 15.6, 16 and 16.2), with

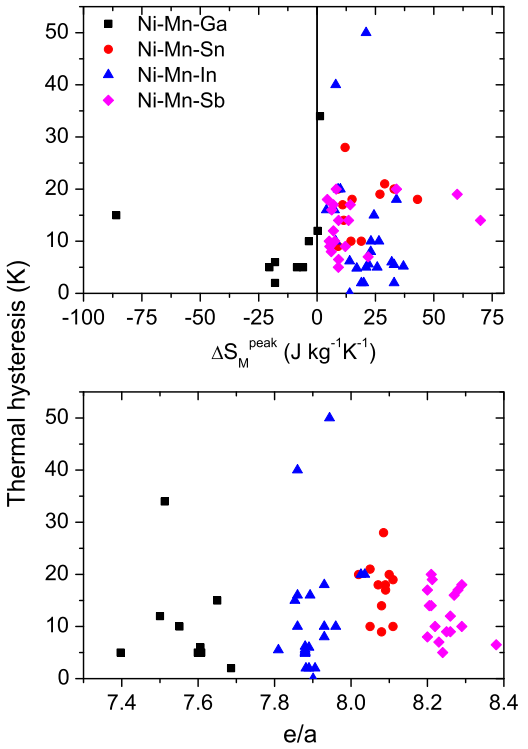

Fig. 35. Thermal hysteresis as a function of ΔS_M (5 T) and e/a for different Heusler compositions taken from Table S6 of the Supplementary Material.

ΔS_M up to 33 J kg^{-1} K^{-1}. For x = 16 and 16.2, the rate of transformation temperature reduces between 3 and 4 K/T, while for x = 15.6, its transition temperature is not significantly affected by field. Similarly, low thermal hysteresis are reported for $Ni_{55}Mn_{19.6}Ga_{25.4}$ melt-spun ribbons, with also low hysteresis losses [994] and $Ni_{43}Mn_{42}Co_4Sn_{11}$ ribbons [18]. Thermal hysteresis can be drastically reduced if the geometric compatibility between martensite and austenite phases is achieved [995]. This can be summarized in two conditions: no volume change during transformation and the direct compatibility between the austenitic phase and a single variant of martensite phase. Following these ideas, Srivastava et al. [918] studied $Ni_{45}Co_5Mn_{40}Sn_{10}$ alloy and reported a thermal hysteresis of 6 K. For $Ni_{45.7}Mn_{36.6}In_{13.5}Co_{4.2}$ alloy, Gottschall et al. [996] reported a high $\Delta T_{ad}(2\,T) = -8$ K but it is irreversible while the reversible value is −3 K. It was also found that minor loops lead to reduced hysteresis because the remnant untransformed phase upon incomplete transformation avoids the slow nucleation phenomenon. Recently, Franco et al. [87] proposed the FORC analysis of these minor loops as a new method to further analyze the magnetostructural transformation.

Metallic foams also have been proposed to reduce the thermal hysteresis of Ni-Mn-Ga alloys, for which, additionally, an enhancement of MCE is observed [997]. However, the behavior of $Ni_{43}Co_7Mn_{39}Sn_{11}$ foams is almost identical to that of their as-atomized powder [998].

Virgin effects, i.e. irreversibility between the first curve obtained and the following ones, have been observed by different authors [880,999–1006] and are ascribed to the field-induced arrest of the austenitic phase. This indicates the important role of the measurement protocol [39,1007] affecting the magnitude and sign of ΔS_M [54] or differences in the ΔS_M values derived from heating and cooling experiments [1008]. Therefore, in order to erase the thermal history of the sample in the case of a PM martensitic phase changing to a FM austenitic one, the sample must be cooled down at zero field below M_f before heating to the selected temperature to perform the isothermal field change measurement to really check the change from a starting pure martensite [883]. In some compositions, austenitic phase can be also arrested at high fields [1009,1010]. Khovaylo et al. [1011] and Booth et al. [1012], performing repetitive cycles, show a decrease of MCE ascribed to the presence of a remnant fraction of untransformed phase. Dincer et al. [926] studied the effect of irreversibility on MCE by comparing continuous and non-continuous heating experiments of (Ni,Cu)-Mn-Sn alloys. The influence of long thermal cycling on martensitic transformation was reported by Kokorin et al. [1013] with an enhanced field shift of the transformation temperatures (from 17 to 10 K/T) during 1000 cycles at magnetic fields of 1.1 T.

On the other hand, energy losses due to magnetic hysteresis are found ascribed to irreversibility of the magnetization curves at temperatures around the magnetostructural transformation. In order to consider the different data available ascribed to different field changes, a relative hysteresis loss with respect to RC_{FWHM} (both magnitudes at the same magnetic field change) have been calculated. This calculated percentage when presented as functions of e/a, ΔS_M (5 T) and the FWHM

of the $\Delta S_M(T)$ peak respectively, shows that hysteresis losses roughly decrease with increasing FWHM (the sharper the MCE peak, the higher the hysteresis losses) but increases with increasing $|\Delta S_M|$ (see Fig. 36).

In order to enhance the sample quality of Heusler alloys, it is worth noticing that martensitic transformation is highly dependent on quenching [1014,1015] and postquenching annealing [1016–1020], whereby both affect the atomic ordering. This is particularly important for these samples which are highly sensitive to tiny compositional changes [943] and thus to heterogeneities in the atomic distribution. In addition, their MCE is also affected by the texture in the samples [1021–1025], particularly during stress assisted thermal cycles [1026].

In 2008, melt-spinning technique was proposed by Hernando et al. [1027] as a way to produce Heusler alloys with enhanced homogeneity, reduced annealing time and lowered amount of undesirable impurity phases. Ga-containing Heusler melt-spun ribbons exhibit a diminished thermal hysteresis of ~2 K [994] and also reduced hysteresis losses (~2 J/kg) [1028]. However, for Ni-Mn(Co)-In, a lower thermal hysteresis for bulk samples than that for ribbons was reported [1029]. Recently, Zhang et al. reported a large enhancement of both ΔS_M (~40%) and ΔT_{ad} (~15%) for $Ni_{43}Mn_{46}Sn_{11}$ melt spun ribbons compared to the bulk counterpart [1030]. In general, rapid quenching techniques enable a better homogeneity, smaller crystal size (which stabilizes the cubic austenite) and the presence of disorder. Post-annealing of ribbons leads to crystal growth, compositional homogenization and ordering, generally increasing the martensitic and Curie temperatures. Other recent studies on MCE of melt-spun Heusler alloys can be found in the literature [927,942,984,1028,1031–1041].

Ball milling was also used to produce Heusler alloys or to induce mechanical stresses to the alloys [1038]. Varzaneh et al. produced $Ni_{47}Mn_{40}Sn_{13}$ alloy via mechanical alloying of pure powders, and reported results comparable to those obtained by arc-melting or rapid quenching techniques [1042]. Ni-Mn-Ga powders produced by spark erosion [1043] were reported with $|\Delta S_M| \sim 2\ J\ kg^{-1}\ K^{-1}$ (2 T) about 363 K, which is in agreement with the Curie transition of austenitic phase although its martensitic transformation was detected at 313 K from calorimetry. Singh et al. show that martensitic phase becomes stabilized in crushed powders due to the induced residual stresses [1044].

MCE in Heusler systems of reduced dimensions has been recently reviewed by Khovaylo et al. [1045]. In general, their MCE are reduced compared to those of their bulk counterparts. Different factors are considered as possible ones to explain this: spin canting, presence of a distribution of transition temperatures and suppression of the magnetic moment at interfaces. The fabrication of $Ni_{50.95}Mn_{25.45}Ga_{23.6}$ as microwires [1046] stabilizes the tetragonal martensitic phase, with an easy axis along the wire direction and a Curie temperature of 315 K. Their MCE corresponds to a SOPT, with $\Delta S_M = -0.7\ J\ kg^{-1}\ K^{-1}$ (3 T) at around room temperature. With Cu additions in $Ni_{48.8}Mn_{26.7}Ga_{20.8}Cu_{3.7}$ microwires, larger $\Delta S_M = -8.3\ J\ kg^{-1}\ K^{-1}$ (5 T)

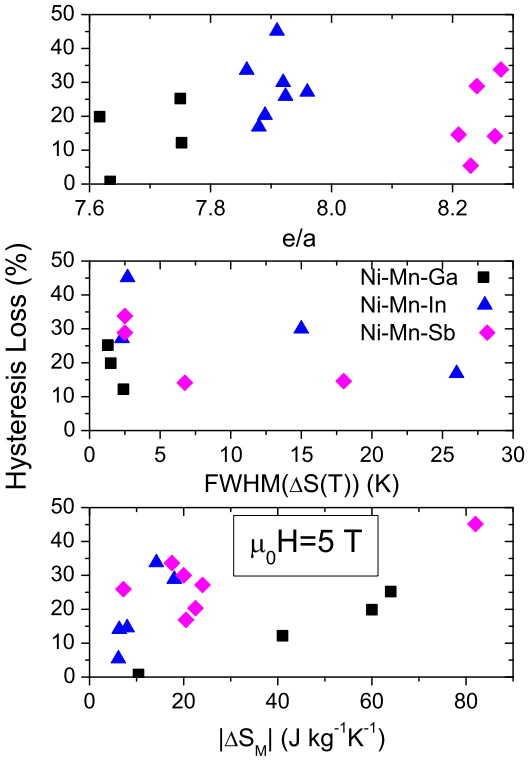

Fig. 36. Hysteresis losses for Ni-Mn-X (X = Ga, Sn, In, Sb) as a function of the number of electrons per atom (top), the full width at half maximum of the MCE peak (middle) and the maximum value of the magnetic entropy change (bottom). Data taken from [888,889,891,907,949,958,964,994,1034,1621,1624,1628–1631].

was obtained, for which the martensitic and Curie transitions overlap at 359 K and FM martensite directly transforms to PM austenite [1047].

Ni-Mn-Ga thin films with coincidence of martensitic and magnetic transitions enable the implementation in very small devices ($\Delta S_M = -8.5$ J kg^{-1} K^{-1} at 6 T and 346 K) [882,1003,1048,1049]. The transformations in thin film samples are affected by film thickness, whereby in Ni-Mn-In, it is ascribed to increasing grain sizes with film thickness [1050]: while samples with film thickness smaller than 90 nm do not show martensitic transformation, a FOPT is observed for thicknesses above 153 nm. Similarly, this occurs for Ni-Mn-Sn thin films on various types of substrates, which retains an untransformed layer of austenite [1051]. This layer is reduced when better compatibility between the martensite and the austenite is attained, which also lowers hysteresis. For Ni-Mn-Sb thin films with thickness of 800 nm, the partial substitution of Al for Sb increases both martensitic transformation temperature and the maximum magnetic entropy change, as reported by Akkera et al. [1052]. However, Barman et al. [1053], although agree that MCE enhances with increasing Al content, found that the martensitic temperature decreases with increasing Al content. It is worth noticing that, for Barman's samples, grain size decreases as Al content increases and no martensitic transformation is reported for samples with grain size below 100 nm. Dutta et al. [1054] recently studied the effect of strains on the MCE of Ni-Mn-Ga/Ni-Mn-Sn bilayers, which exhibit combined direct and inverse MCE. GMCE was found for $Ni_{41}Co_{10.4}Mn_{34.8}Al_{13.8}$ films, with $\Delta S_M = 17.5$ J kg^{-1} K^{-1} at 5 T, ascribed to the transformation from 14M modulated weakly magnetic martensite to FM austenite, which is detected at ~340 K on cooling and ~380 on heating [1055]. Combination of magnetocaloric Heusler thin films with ferroelectric thin films have been recently proposed for multicaloric applications [1056].

5.1.2.2. Mn(Fe,Co,Ni)(Si,Ge). Similar to Heusler alloys, MnCoGe compound undergoes a martensitic transformation from orthorhombic TiNiSi-type (space group *Pnma*) to hexagonal Ni_2In-type structure (space group $P6_3/mmc$) at 650 K. The lattice parameters of the two phases are correlated as: $a_{TiNiSi} = c_{Ni2In}$, $b_{TiNiSi} = a_{Ni2In}$ and $c_{TiNiSi} = \sqrt{3}a_{Ni2In}$, leading to the volume correlation: $V_{TiNiSi} = 2V_{Ni2In}$. Moreover, it shows a FOPT at 334 K, which implies a reduced unit cell volume of the orthorhombic volume cell [1057]. The sharp $M(T)$ decrease ascribed to this FOPT in off-stoichiometric $MnCo_{0.95}Ge_{1.14}$ compound yields interesting ΔS_M values (-6.4 J kg^{-1} K^{-1} for 1 T at 331 K) as reported by Fang et al. [1057]. For $Mn_{0.975}Co_{0.975}Ge_{1.05}$, its Curie temperature decreases with excess Ge and depends on sample preparation while $|\Delta S_M|$ is not significantly affected (1 J kg^{-1} K^{-1} at 1.5 T) [1058]. The ab-initio calculations for off-stoichiometric $MnCo_{1-x}Ge$ alloys predict that, for $x > 0.08$, its TiNiSi structure changes to Ni_2In [1059] with a large volume change (3.9%). Experimental validation of Fang et al. [1060] reported for $x < 0.06$ mainly TiNiSi structure whereas Ni_2In-type dominates at higher Ge concentration. They also reported ΔS_M about -2 J kg^{-1} K^{-1} at $\mu_0\Delta H = 1$ T for these compositions which Curie temperatures can be tailored around room temperature. For TM-deficient $Mn_{1-x}Co_{1-x}Ge$ series, magnetostructural transition is achieved in the range $0.015 < x < 0.025$ [1061]. For Mn-poor $Mn_{1-x}CoGe$ alloys ($x \leq 0.05$), magnetostructural transition from PM Ni_2In phase to FM TiNiSi phase can be induced and its $-\Delta S_M > 25$ J kg^{-1} K^{-1} (5 T) at 290 K for $x = 0.035$ [1062]. On the other hand, the relative Mn enrichment over Co in $Mn_{1+x}Co_{1-x}Ge$ alloys yields a progressive decrease of transition temperatures with x, giving a maximum $-\Delta S_M = 2.8$ J kg^{-1} K^{-1} (1.2 T) at 331 K [1063]. Similarly, FOPT was observed in Mn-enriched $MnCo_{0.95}Ge_{0.97}$ (with $\Delta T_{ad} \sim 1.5$ K at 282 K and 1.9 T) although SOPT is reported for $MnCo_{0.95}Ge_{0.95}$ (with $\Delta T_{ad} \sim 1.5$ K at ~330 K and 1.9 T) and $MnCo_{0.95}Ge$ compounds (with $\Delta T_{ad} \sim 0.9$ K at ~285 K and 1.9 T) [1064]. Large thermal and magnetic hystereses were found for $MnCo_{0.95}Ge_{0.97}$, indicating the alloy behavior is highly dependent on its thermal history.

Compositional tailoring of the structural change between Ni_2In and TiNiSi type phases has been reported. Previously in 2006, Lin et al. [1065] studied the $MnFe_{1-x}Co_xGe$ series, whereby the hexagonal phase characteristic of MnFeGe extends up to $x < 0.8$ while the orthorhombic phase characteristic of MnCoGe extends down to $x > 0.85$, and reported a continuous increase of T_C from ~150 to ~350 K, regardless of its crystalline structure. For $x = 0.8$, a maximum absolute magnetic entropy change of 9 J kg^{-1} K^{-1} (5 T) at $T_C = 289$ K is observed, for which the magnetic moment is maximum (4.69 μ_B/f.u.). However, traces of Ni_2In-type impurities were found [445]. For $CoMnGe_{0.945}Ga_{0.055}$, a FOPT occurs at 305 K, giving a GMCE of $-\Delta S_M(5\text{ T}) = 29.6$ J kg^{-1} K^{-1} and $\Delta T_{ad}(2\text{ T}) = 6.5$ K [1066]. For $MnCo_{1-x}In_xGe$ compounds, the partial substitution of Co for In can yield overlapping between martensitic transformation and Curie temperatures, which results in a magnetostructural coupling with a large ΔS_M for $x = 0.015$ [1067].

MnNiGe is a single spiral AFM with a Néel temperature of 346 K, which crystallizes in TiNiSi-type structure at room temperature and transforms into Ni_2In-type structure (with volume change -1.6%) at 470 K. Off-stoichiometry in $Mn_{1.9-x}Ni_xGe$ compounds [1068] reduces their structural transition temperatures below the Curie temperature of the Ni_2In type phase and produces two MCE peaks: an inverse magnetocaloric peak (for $x = 0.85$, $\Delta S_M = +5$ (1 T) and +27 J kg^{-1} K^{-1} (5 T) at about 135 K) ascribed to a FOPT metamagnetic structural transformation from AFM TiNiSi to FM Ni_2In structure, and a direct magnetocaloric peak ($\Delta S_M = -2$ (1 T) and -6.5 J kg^{-1} K^{-1} (5 T) at 205 K) ascribed to the SOPT Curie transition of the Ni_2In-type phase. Annealing of polycrystalline $MnNiGe_{1.05}$ melt-spun ribbons yields a sharpening of MCE peak with an enhanced $|\Delta S_M|$ and higher transition temperatures [1069]. For $MnNi_xCo_{1-x}Ge_{1.05}$ alloys with excess Ge, an inverse MCE below 200 K ($\Delta S = +1.9$ J kg^{-1} K^{-1} at 1 T) ascribed to the transition from AFM TiNiSi-type to FM Ni_2In-type structure is observed [1070]. For $x \sim 0.05$ in $MnNi_{1-x}Co_xGe_{1.05}$ series, structural transition from TiNiSi to Ni_2In-type phases and magnetic transition from PM to FM Ni_2In phase are obtained [1070]. $MnNi_{1-x}Co_xGe$ alloys with higher Co substitution ($x = 0.38$ and 0.40) [1071], exhibit both inverse and normal MCE, in a relative small thermal span, around the structural and magnetic transformations respectively. When Fe partially substitutes for Ni, the structural transformation temperatures decrease whereas the Curie temperatures are less significantly affected. The MCE curves of $MnNi_{0.75}Fe_{0.25}Ge$ show overlapped inverse and direct

curves, with maximum extremes of +1.5 J kg^{-1} K^{-1} (1 T) at 175 K and −1.2 J kg^{-1} K^{-1} (1 T) at 210 K [1072]. Magnetostructural coupling between martensite transformation and PM to FM states in Fe substituted MnNiGe alloys is discussed [1073]. When Fe substitutes for Mn or Ni in MnNiGe alloys, structural transition decreases below the magnetic transition of the low temperature phase and converts AFM (Fe-free parent compound) to FM, yielding a FM martensite to PM austenite transition upon heating the sample and GMCE ($MnNi_{0.77}Fe_{0.23}Ge$: $|\Delta S_M|$(5 T) ~ 18 J kg^{-1} K^{-1} at ~265 K; $Mn_{0.82}Fe_{0.18}NiGe$: $|\Delta S_M|$(5 T) ~ 30 J kg^{-1} K^{-1} at 205 K). For $Mn_{0.93}Cr_{0.07}NiGe_{1.05}$, a broad $-\Delta S_M$ peak of ~7 J kg^{-1} K^{-1} (5 T) at around ~350 K is found, whereas an inverse MCE is observed at $\mu_0 H$ = 1 T [950]. In addition, a larger $-\Delta S_M$ value with sharper peak is observed at 365 K.

Partial substitution of Co for Al in $MnCo_{1-x}Al_xGe$ [1074] yields a crystal structure of hexagonal Ni_2In-type for x > 0.03. Its Curie temperature can be tuned between 286 and 347 K by changing the Co/Al ratio and the maximum magnetic entropy change achieved in the studied series is 1.52 J kg^{-1} K^{-1} (1.5 T) at 310 K for x = 0.08. When Al is substituted in $MnNiGe_{1-x}Al_x$ compounds, a FOPT magnetostructural transition at ~190 K is observed for x ~ 0.09 with $|\Delta S_M|$ = 17.6 J kg^{-1} K^{-1} at 5 T [1075]. $MnCo_{1-x}V_xGe$ alloys crystallize in Ni_2Ti-type structure for x > 0.02 and are reported that increasing V content leads to a reduction of Curie temperature (e.g. for x = 0.06, $|\Delta S_M|$(1.5 T) = 3.9 J kg^{-1} K^{-1} at 265 K) [1076]. However, when Mn instead of Co substitutes for V in $Mn_{1-x}V_xCoGe$, thermal hysteresis decreases yielding large MCE at room temperature (for $Mn_{0.98}V_{0.02}CoGe$, $|\Delta S_M|$(1.2 T) = 9.5 J kg^{-1} K^{-1}) [1077]. For $Mn_{1-x}Cr_xCoGe$, when x = 0.11, structural and magnetic transitions coincide, and induce a single FOPT from FM to PM at 322 K [1078]. In addition, for $0.04 \leq x \leq 0.25$, the first order character of the transition is retained with large $-\Delta S_M$ values (e.g. 28.5 J kg^{-1} K^{-1} (5 T) at 322 K for x = 0.04) but for x = 0 and x = 0.27, SOPTs with much lower values of $-\Delta S_M$ are observed. Both substitution of Cr and hydrostatic pressure application in these systems shift their Curie temperatures to lower values [1079], showing a correlation between the effects of chemical and external pressures in this family of alloys.

Partial substitution of Sn for Ge in $CoMnGe_{1-x}Sn_x$ (x between 0.04 and 0.055) leads to a magnetostructural transition with $|\Delta S_M|$ = 4.5 J kg^{-1} K^{-1} but accompanied by large thermal hysteresis of ~20 K [1080]. Sandeman et al. [1081] studied the magnetocaloric effect ascribed to the metamagnetic transition of $CoMnSi_{1-x}Ge_x$ compounds ($x \leq 0.3$) with TiNiSi-type structure. Their FOPT shift to lower temperatures with increasing Ge concentration while their SOPT, ascribed to the Curie temperature (T_C ~ 390 K for x = 0), tune to higher temperatures. Previous reported values for the transition temperatures are broadly dispersed, which indicates that they are highly sensitive to sample preparation. The single phase CoMnSi compound presents ΔS_M ~ 6 J kg^{-1} K^{-1} and ΔT ~ 1.5 K ascribed to the metamagnetic transition at $\mu_0 \Delta H$ = 5 T. Zhang et al. [1082] found that the metamagnetic transition of $CoMnSi_{0.88}Ge_{0.12}$ is highly field-sensitive, leading to large inverse MCE of ΔS_M(2 T) > 6 J kg^{-1} K^{-1} at 185 K but with large magnetic and thermal hystereses. Interstitial B additions to MnCoGe yield GMCE near room temperature (e.g. for $MnCoGeB_{0.02}$, ΔS_M(5 T) = −47.3 J kg^{-1} K^{-1} at T = 287 K but with a thermal hysteresis of 14 K) [1083]. A magnetostructural FOPT is obtained after coincidence of the structural TiNiSi to Ni_2In transition with the FM to PM one. Annealing of $Mn_{1-x}Cu_xCoGe$ melt-spun ribbons leads to a magnetostructural transformation and an enhanced MCE (e.g. for x = 0.02, ΔS_M(1 T) = 7.2 J kg^{-1} K^{-1} at 286 K) [1084]. $MnV_{0.02}CoGe_{0.99}$ ribbons, with a single Ni_2In-type phase, were prepared using melt-spinning by Ma et al. [1085], presenting a SOPT at 252 K with $-\Delta S_M$(1 T) = 0.9 J kg^{-1} K^{-1} and RC_{FWHM}(1 T) = 36 J/kg.

The behavior of this alloy family can be generally described with MCE as a function of the average number of electrons in the outer shell per atom, e/a (including 3d atoms for transition elements), which was previously used to describe Heusler alloys. This is illustrated in Fig. 37 for several compounds. The maximum $|\Delta S_M|$ values are obtained for those e/a values leading to coincide the structural and magnetic transitions.

Moreover, some RE-TM-Ge compounds also exhibit TiNiSi structure with large magnetic moments above 4 μ_B but, in general, with transition temperatures well below room temperature. See some examples in the section *Compounds with 33 at.% of RE* described earlier.

5.1.2.3. $(Mn,Fe,Co)_5(Ge,Si,Sb)_3$. In 2002, Songlin et al. studied the $Mn_{5-x}Fe_xSi_3$ ($0 \leq x \leq 5$) [1086] and $Mn_{5-x}Ge_{3-x}Sb_x$ ($0 \leq x \leq 0.3$) [1087] series, both crystallizing in the hexagonal Mn_5Si_3-type structure (space group $P6_3/mcm$). For the former series, Mn_5Si_3 compound is an AFM system which experiences two FOPT (from AFM to AFM at 66 K and AFM to PM at 99 K). Inverse MCE is observed below the first transition while direct MCE is observed at higher temperatures [1088]. However, Fe_5Si_3 compound is FM up to 373 K. The maximum $|\Delta S_M|$ value as well as the maximum magnetic moments observed in the compounds of the Mn/Fe series were found for x = 4, which undergoes a Curie transition from FM to PM ($|\Delta S_M|$ ~ 2 J kg^{-1} K^{-1} at 305 K and 2 T). The AFM character of the alloy ($x \leq 2$) changes to FM one ($x \geq 4$) as Fe content increases. However, some discrepancies can be found in the literature. For $Mn_2Fe_3Si_3$ compound, while Songlin et al. [1086] found FM behavior with a Curie temperature at about 175 K, Candini et al. [1089] reported an AFM behavior with Néel temperature at 150 K. This reflects the magnetic character of the system is highly dependent on the bondings between transition metals, and possibly on the Fe and Mn occupancies of the 4d and 6g sites. Recently, Wu et al. [1090] reported that B additions to Fe_4MnSi_3 increase the lattice parameters while preserving the crystal structure, leading to the assumption of B addition to occupy interstitial positions. As a result, their Curie temperature increases but not their ΔS_M. The MCE of hexagonal $MnFe_4Si_3$ single crystals, with ordering transition at ~300 K, shows anisotropy with ΔS_M ~ 2.5 J kg^{-1} K^{-1} (5 T) for the field applied along *[100]* direction while 1.25 J kg^{-1} K^{-1} for the field applied along *[001]* direction [1091]. Studies on the density of phonon states were performed to correlate MCE and lattice dynamics, resulting an influence limited to long wavelength contributions [1092].

Regarding $Mn_{5-x}Ge_{3-x}Sb_x$ series, Mn_5Ge_3 alloy is FM with Curie transition at 296 K. The ascribed absolute value of $|\Delta S_M|$ ~ 9 J kg^{-1} K^{-1} at 5 T is comparable to that of Gd [1087]. Partial substitution of Sb for Ge retains its FM order while increasing

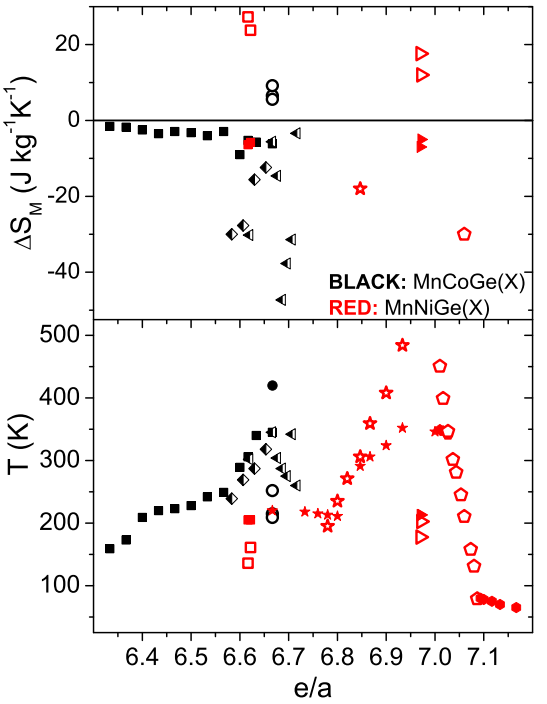

Fig. 37. Magnetic entropy change (5 T) and transition temperatures of MnCoGe [1065,1078,1081,1083] and MnNiGe alloy families [1068,1073,1075] as a function of their outer electrons per atom (e/a). Solid symbols represent SOPTs whereas hollow symbols represent magnetostructural or metamagnetic FOPTs. Half-filled symbols correspond to a first order Curie transition.

T_C about 50 K per Ge atomic substitution for Sb in the formula unit. For x = 0.3, ~40% decrease in ΔS_M while <10% reduction in *RC* is observed since the MCE peak becomes wider upon Sb substitution. Partial Fe substitution for Mn in $(Mn_{0.9}Fe_{0.1})_5Ge_3$ leads to enhancement of both ΔS_M and *RC* [1093]. Unlike the influence of Sb additions on the MCE of $Mn_{5-x}Ge_{3-x}Sb_x$, Si [1094,1095] and Ga [1096,1097] substitutions lead to a decrease of Curie temperatures. Partial substitution of Al and Sn have been also studied [1096]. Recently, Tolinski et al. [1098] found that mechanical milling of Mn_5Ge_3 reduces its MCE ($\Delta S_M \sim -4$ J kg^{-1} K^{-1}, T_C = 297.4 K and ΔT_{ad} = 1.8 K at 2 T).

Zhao et al. [1099] reported the increase of T_C (~250 K) for $Mn_{5-x}Sn_{3-x}Ga_x$ series with Ga content. Although its magnetic moment increases as compared to Ga-free alloy, their $|\Delta S_M|$ values are moderate (<1 J kg^{-1} K^{-1} at $\mu_0\Delta H$ = 2 T). Similar results are obtained for ball milled $(Mn_{1-x}Fe_x)_5Sn_3$ series (ΔS_M = 0.87 J kg^{-1} K^{-1} at $\mu_0\Delta H$ = 1.5 T), with a flat curve in a wide temperature range [1100], probably due to inhomogeneities inherent to the production process.

Some RE-containing alloys also exhibit the Mn_5Si_3-type phase and were already discussed in the section *Compounds with 63 at.% of RE*.

5.1.2.4. MnAs alloys. Although Kuhrt et al. [1101] reported MCE results for MnAs(P) as early as in 1985 (with ΔT_{ad} = 0.2 K at 0.65 T and 300 K accompanied by thermal hysteresis of ~10 K), the reason for the rise in studying this family can be found in the work of Wada et al. [1102], which reported in 2001 its GMCE ascribed to a FOPT from FM to PM in MnAs alloy with (ΔS_M = −30 J kg^{-1} K^{-1} and ΔT_{ad} = 13 K at 5 T and 318 K). The FOPT observed in the MnAs compound is ascribed to a magnetostructural transition of FM hexagonal NiAs-type structure (space group $P6_3/mmc$) to PM orthorhombic MnP-type structure (space group *Pnma*), which could be described as a kind of soft mode transition with large reduction in the modulus of compression and stress at T_C [1103]. The relationships among the lattice parameters of these two structures can be found in [1104]. In addition, a SOPT occurs at higher temperature of 378 K, which corresponds to a reversal transition from MnP to NiAs-type phase [1102,1105]. In general, arsenic-containing alloys attractive for MCE, can be grouped into two different families: alloys derived from MnAs compound and compounds crystallizing in Fe_2P-type structure. The former alloy family is described under this section while the latter will be discussed in the following section.

The FOPT of MnAs sharpens for monocrystalline samples and slightly shifts to lower temperatures (315.5 K), whereas its SOPT decreases to 391 K [1106]. Excess Mn in $Mn_{1+\delta}As$ compounds leads to linearly decreases of both the magnetic moment and the Curie temperature with δ as: μ = (3.55–2.78δ) μ_B/f.u. and T_C = (577–900δ) K respectively [1105]. Unusual attenuation of surface acoustic waves has been recently observed in magnetocaloric/piezoelectric MnAs/GaAs hybrid thin films, showing a weak dependence on the film thickness [1107].

Partial Sb substitution for As in $MnAs_{1-x}Sb_x$ effectively reduces both transition temperatures (e.g. 280 K in $MnAs_{0.9}Sb_{0.1}$) and thermal hysteresis (from 6 to <1 K for x = 0–0.1), although the system remains in NiAs-type structure and transformation apparently becomes a SOPT for above 10 at.% Sb [445]. For $0.125 \leq x \leq 0.25$, a good agreement between theoretical calculations and experimental measurements is found, while larger deviations are observed for x = 0.3, whereby a prominent MCE reduction is observed [1108]. Recently, Trassinelli et al. [1109] reported that the thermal hysteresis in MnAs thin films is suppressed by the induced defects from ion bombardment, which facilitate nucleation during the FOPT process.

A relatively linear correlation of the pressure application to $MnAs_{1-x}Sb_x$ and their transition temperatures has been reported with a rate of ~ -10 K/kbar (higher rate in Sb-free samples) [1110]. Shock compaction of $MnAs_{1-x}Sb_x$ (x = 0.068 and 0.073) decreases their MCE properties in FOPT although the outstanding MCE values ($\Delta S_M(1\ T) = -28\ J\ kg^{-1}\ K^{-1}$ for x = 0.073) are recovered after annealing at 1073 K for a week. However, Curie temperature changes compared to that of the starting powder [1102,1111–1116]. Recently, Rocco et al. [1117] studied the influence of pressure and chemical doping (to resemble negative pressure) on magnetic phases of $Mn_{1-x}Fe_xAs$ series ($x \leq 0.018$) and supplied a magnetic phase diagram of this compound under pressure conditions. They found that Fe doping only produces structural deformation and AFM orthorhombic phase coexists with FM hexagonal phase for the highest pressure studied below the critical temperature.

Besides Sb substitution for As [1102,1111–1116], other compositional tailoring have been studied. Si substitution for As in $MnAs_{1-x}Si_x$ ($x \leq 0.09$) series is reported to reduce thermal hysteresis (almost zero for x = 0.09), which is due to the transformation from FOPT to SOPT. Moreover, transition temperature increases with higher Si concentration (from 270 to 302 K for x = 0.03–0.09 [1118], although these values are below that of Si-free alloy [1102]), while maintaining high $|\Delta S_M|$ values (>10 J kg^{-1} K^{-1} at 5 T and >5 J kg^{-1} K^{-1} at 2 T). These $MnAs_{1-x}Si_x$ samples were prepared by ball milling and subsequently annealed but, unfortunately, a reference Si-free sample was not prepared in the study for comparison. Interstitial N additions to these Si-containing alloys yields a reduction in T_C and a slight MCE enhancement [1119]. Severe lattice distortions produced by addition of interstitial C in MnAsC alloys lead to a decrease of T_C with optimum $|\Delta S_M| > 22\ J\ kg^{-1}\ K^{-1}$ for $MnAsC_{0.03}$ [1120]. Substitution of P for As reduces the hysteresis and retains high $|\Delta S_M|$ (For $MnAs_{0.994}P_{0.006}$, $|\Delta S_M| = 11.3\ J\ kg^{-1}\ K^{-1}$ at 2 T and 294.5 K with thermal hysteresis of 4 K) [1121]. Large microstrains in $MnAs_{0.97}P_{0.03}$ due to ball milling, suppress the orthorhombic-hexagonal FOPT and promotes a helimagnetic state at low temperatures. These factors lead to a decrease of hysteresis but also to their MCE [1122]. Mitsiuk et al. [1123] studied the MCE of P substituted alloys at a high field change of 14 T ($|\Delta S_M| \sim 40\ J\ kg^{-1}\ K^{-1}$) and pointed that the structural instability is due to the anomalous expansion-compression between 350 and 250 K.

Besides As substitution, compositional tailoring by Mn substitution can be also found in the literature. Fe substitution for Mn in $Mn_{1-x}Fe_xAs$ decreases the transition temperature with an enhanced thermal hysteresis from 10 to 30 K as x increases from 0 to 0.015 [1124] unlike for Fe additions in $Gd_5Si_2Ge_2$ family [28]. Balli et al. [1125] showed that the combined substitution of V and Ti for Mn, retains the high $|\Delta S_M|$ values of $\sim$30 J kg^{-1} K^{-1} while tuning T_C from 318 to 266 K (for MnAs and $Mn_{0.9}Ti_{0.05}V_{0.05}As$ respectively). No monotonous trend for $|\Delta S_M|$ is reported for $Mn_{1-x}Al_xAs$, alloys with Al substituted for Mn but an evident decrease in MCE is observed for the x = 0.03 alloy, although thermal hysteresis persists in this alloy [1126]. Cu substitution for Mn does not significantly affects the transition temperature but increases thermal hysteresis while reducing the unit cell volume as compared to MnAs alloy ($|\Delta S_M| \sim 20$–$30\ J\ kg^{-1}\ K^{-1}$) [1127]. Xu et al. [1128] grew $Mn_{1-x}Co_xAs$ epitaxed films on GaAs and found a double $|\Delta S_M|$ value for 0.24% Co. The Cr substitution for Mn in $Mn_{1-x}Cr_xAs$ reduces transition temperature (e.g. 267 K for x = 0.01) and enhances MCE by reducing thermal hysteresis (e. g. 5 K for x = 0.01) [1129]. For ball milled $Mn_{0.95}Cr_{0.05}As$ alloy, it exhibits two FOPT: a combined magnetostructural transition from PM MnP-type phase to FM NiAs-type phase at 234 K ($\Delta S(T) = -5.28\ J\ kg^{-1}\ K^{-1}$, at 213 K and 5 T) and from FM NiAs-type phase to helimagnetic (H_a-type) MnP-type phase at 159 K (inverse MCE with $\Delta S(T) = 6.06\ J\ kg^{-1}\ K^{-1}$, at 163 K and 5 T) [1130]. For $Mn_{0.92}Ba_{0.08}As$ thin films grown on Al_2O_3 (0001) substrate, its T_C increases up to 350 K and exhibits high $|\Delta S_M|$ values [1131].

Colossal MCE phenomenon (magnetic entropy change far beyond the theoretical magnetic limit) was also reported in several papers [1124,1127,1132,1133] and some explanation was attempted to ascribe this colossal behavior to magnetovolume coupling [1124,1133–1136]. However, the use of Landau theory shows that the so-called colossal MCE could be an artifact derived from the estimation of ΔS_M when not accounting for the irreversibility and the mixed-phase regime typical of FOPTs [50,56,974,1137–1139]. Balli et al. [1140] also questioned the use of Maxwell relation to obtain ΔS_M data, in agreement with the work by Bratko et al. [1141]. It is worth pointing that Wada et al. [1102] already described the spikes in ΔS_M reaching $-40\ J\ kg^{-1}\ K^{-1}$ could probably be artifacts, as observed in their results. Therefore, the maximum values obtained at such spikes reported are neglected in this section. Niemann et al. [1142] describe the inapplicability of Maxwell relation to quantify MCE, when magnetic induced reorientation occurs (e.g. variants in magnetic shape memory alloys or domain structure in hard magnetic systems). They disagree to use Maxwell relation even when the measurement protocol proposed by Caron et al. [57] is used (to avoid artifact colossal MCE peaks) as it can yield spurious non-reversible MCE peaks.

5.1.2.5. MnFe(P,As) alloys. The compounds belonging to the other As-containing alloy family with interesting MCE properties crystallize in the hexagonal Fe_2P-type structure (space group *P*-62*m*). A recent review on these materials can be found in [1143]. Tegus et al. [1144] reported in 2002 the GMCE for $MnFeP_{0.45}As_{0.55}$, for which a magnetostructural FOPT occurs ($\Delta S_M = -14.5$ and $-18\ J\ kg^{-1}\ K^{-1}$ at 2 and 5 T respectively, and with thermal hysteresis below 1K at about 300 K). Recently, direct ΔT_{ad} measurements of $\sim$2.5 K were reported under millisecond pulse field by Cugini et al. [44]. In stoichiometric compounds, Mn and Fe occupy specific sites (3g and 3f respectively), whereas P and As are statistically distributed over 2c and 1b sites. The unit cell volume decreases with field and a metamagnetic transition from PM to FM is induced just above

Curie temperature [1145]. Ab initio studies have been performed to determine the preferential occupancy of Mn to the 3g site in $(Fe_{1-x}Mn_x)_2P_{1-y}Si_y$ doped compounds [1146]. Transition temperatures can be also tuned by varying Mn/Fe ratio (e.g. transition temperature decreases with increasing Mn content in $Mn_{2-x}Fe_xP_{0.5}As_{0.5}$ series with $|\Delta S_M|(2\ T) > 15\ J\ kg^{-1}\ K^{-1}$ for $x \geq 0.8$ [1147] and AFM phase stabilizes for x = 0.5–0.6 as observed from Mössbauer spectroscopy [1148]) or As/P ratio (T_C can be tuned between 168 and 332 K for As/P ratios of 3/1 and 13/7 respectively [1088]) without losing its GMCE. The phase diagram of $MnFeP_{1-x}As_x$ can be found in [1149], with an AFM phase for x < 0.35 and a magnetic triple point FM-AFM-PM at 210 K.

Recent results from Szymczak et al. [1150] showed that, for $Mn_{2-x}Fe_xP_{0.5}As_{0.5}$, while for x = 1, a single FOPT from PM to FM occurs at 275 K, for x = 0.7 this is splitted into two transitions: SOPT from PM to FM at 190 K and FM-AFM at 90 K. Tailoring Mn/Fe ratio in MnFe(P,As) alloys can also diminish thermal hysteresis below 1 K but transforms FOPT into a SOPT. For $Mn_xFe_{1.95-x}As_{0.5}P_{0.5}$ series, their Arrott plots indicate that the magnetoelastic FOPT obtained for x < 1.4 changes to a SOPT with increasing x and, although a stable hexagonal Fe_2P phase appears for $x \leq 0.8$, a magnetostructural transformation between FM hexagonal phase and a body centered orthorhombic phase (space group *Imm*2) occurs for higher x values [1151]. Small changes in the crystallographic order imply significant modifications to the magnetic order in these compounds [1152], which highlight the importance of sample preparation. Particularly, samples quenched in water exhibit lower hysteresis and enhanced MCE [1153]. Tegus et al. [1154] studied TM substitution in compositions close to $MnFeP_{0.5}As_{0.5}$ for MCE optimization, whereby Cr and Co substitutions for Fe reduce their transition temperatures. Contrarily, 10 at.% Mn substitution for Fe enhances MCE while not significantly affecting the transition temperature. On the other hand, 10 at.% substitution of Fe for Mn yields an increase of transition temperatures in these Fe-enriched samples. Gribanov et al. [1147] extended the study to Mn-rich composition in $Mn_{2-x}Fe_xP_{0.5}As_{0.5}$ and found a continuous decrease of transition temperatures as x decreases and that FM phase disappears when x = 0.5. Maximum $|\Delta S_M|$ values $>20\ J\ kg^{-1}\ K^{-1}$ (5 T) at 225 K were obtained for x = 0.9, while reduced about one half when x = 0.6. Recently, Balli et al. [1155] have studied the complex magnetic behavior exhibited by MnRhAs single crystals: metamagnetic AFM to FM transition at 158 K, SOPT from FM to another AFM state at 196 K and finally PM state occurs above 238 K. The former transition yields an inverse MCE of $\Delta S_M = 3\ J\ kg^{-1}\ K^{-1}$ at 1 T, while the second transition corresponds to a weaker direct MCE response ($\Delta S_M = -2.3\ J\ kg^{-1}\ K^{-1}$ at 5 T).

The presence of As in this promising alloy family, as well as the previously described one, should be considered an important drawback due to its inconvenient toxic nature especially for domestic appliances. Therefore, this prompted the search of substituting other elements (P, Si and Ge) for As in MnFe(P,As) alloys. Although GMCE could be preserved in As-free alloys, thermal hysteresis is generally increased.

Partial or complete substitution of Ge for As in $MnFeP_{0.5}As_{0.5-x}Ge_x$ does not change the Fe_2P-type structure but progressively increases T_C (up to 570 K in As-free sample). However, minor substitution of Ge for As converts the character of the transition to second order, implying a weakening of MCE (e.g. $MnFeP_{0.5}As_{0.44}Ge_{0.06,}$ ~50% decrease in $|\Delta S_M|$ is obtained compared to that of $MnFeP_{0.5}As_{0.5}$) [1156]. In the P- and Mn-enriched series, i.e. $Mn_{1.1}Fe_{0.9}P_{0.7}As_{0.3-x}Ge_x$ ($0 \leq x \leq 0.3$), T_C increases with x from 150 to 380 K, while field-induced FOPT is lost for x > 0.15 [1157]. For Mn-rich $Mn_{1.1}Fe_{0.9}P_{1-x}Ge_x$ ($0.20 \leq x \leq 0.23$) [1158,1159] and $Mn_{1.2}Fe_{0.8}P_{1-x}Ge_x$ (x = 0.22) series [1160], complete substitution of P and Ge for As preserves their GMCE ($|\Delta S_M| > 30\ J\ kg^{-1}\ K^{-1}$ for 5 T). The excess Mn atoms preferentially locate at 3f sites and affect the magnetic moment, hysteresis and critical field to induce the PM to FM transition [1161]. In both cases, Curie transition temperature increases with Ge content although the unit cell volume increases only in a certain x range [1159]. Liu et al. [1162] highlight the phase fraction of the transformed phases as a relevant parameter to describe $|\Delta S_M|$ values (It is worth mentioning that coexisting phases lead to artifacts in MCE curves, as described in the previous sections). With melt spinning, the initial good MCE results of ball milled $Mn_{1.1}Fe_{0.9}P_{0.76}Ge_{0.24}$ samples are further enhanced due to the improvement of compositional homogenization [1163]. Mössbauer results showed the coexistence of FM and PM phases in a temperature range of 50 K around T_C for $Mn_{1.1}Fe_{0.9}P_{1-x}Ge_x$ compounds, with 0.19 < x < 0.26, [1159]. For $Mn_{2-y}Fe_yP_{0.75}Ge_{0.25}$ series, thermal hysteresis could be reduced while preserving high MCE responses, by tuning Fe/Mn and optimizing the annealing conditions [1164]. The compositional limit of FOPT is y = 0.8 and its $\Delta S_M = -20\ J\ kg^{-1}\ K^{-1}$ at 2 T with negligible hysteresis. Spark plasma sintered $Mn_{1.1}Fe_{0.9}P_{0.8}Ge_{0.2}$ is reported with large $|\Delta S_M|$ values close to $50\ J\ kg^{-1}\ K^{-1}$ at 5 T ($\Delta T_{ad} = 1.2$ K at 1.5 T) at 253 K but accompanied by thermal hysteresis of about 15 K [1165]. In addition, higher hysteresis were reported in spark plasma sintered $MnFeP_{0.89-x}Si_xGe_{0.11}$ compounds ($0.14 \leq x \leq 0.26$) [1166]. The inhomogeneous distribution of Ge could affect the behavior of such compositions, whereby neutron diffraction studies found different Ge contents in coexisting FM and PM phases [1167]. Optimal thermal annealing treatment is reported to enhance homogenization, leading to the MCE enhancement and a decrease in thermal hysteresis [1168]. Chen et al. [1169] proposed that the crossover from SOPT to FOPT in $Mn_{1.1}Fe_{0.9}P_{1-x}Ge_x$ is related to the lattice parameter of its parent phase. They used Landau theory along with Bean-Rodbell theory to describe the transformation process in this series [1170]. They have further optimized the *RC* of $Mn_{1.1}Fe_{0.9}P_{1-x}Ge_x$ by preparing nanostructured $Mn_{1.1}Fe_{0.9}P_{0.79}Ge_{0.21,}$ which exhibits MCE of $\Delta S_M = -26.4\ J\ kg^{-1}\ K^{-1}$ at 281.5 K and 5 T and $RC_{FWHM} = 1138$ J/kg [1171]. Al doping in these systems retains the Fe_2P-type structure and MCE but affects the unit cell volume (increases with Al content) and reduces thermal hysteresis [1172]. Ru substitution in $MnFeP_{0.8}Ge_{0.2}$ and $Mn_{1.2}Fe_{0.8}P_{0.5}Si_{0.5}$ reduces thermal hysteresis from 10 K to 2–3 K, while preserving a sharp magnetic transition [1173].

Partial Si substitution for As in $MnFeP_{0.5}As_{0.5-x}Si_x$ ($0 \leq x \leq 0.3$) retains the Fe_2P-type structure and GMCE, which is ascribed to a field induced FOPT ($|\Delta S_M| = 32\ J\ kg^{-1}\ K^{-1}$ at 2 T and 294 K) without a monotonous trend of T_C with x [1174]. Complete substitutions of P and Si for As in $MnFeP_{1-x}Si_x$ compounds successfully lead to the formation of hexagonal

Fe_2P-type structure in the compositional range $0.28 \leq x \leq 0.64$, whereas orthorhombic Co_2P-type structure (space group *Pnma)* is formed for smaller Si content [1175]. For $0.28 < x < 0.48$, a secondary Fe_2MnSi phase (space group *Fm*3*m*) is detected, whose phase fraction increases with Si content. Large MCE values although accompanied with large thermal hysteresis, are reported for x = 0.5 ($\Delta S_M = -30$ J kg^{-1} K^{-1} at T_C = 300 K and $\mu_0\Delta H$ = 2 T and thermal hysteresis >20 K). The phase diagrams of this system show that the single-phased regions for Fe_2P and Co_2P phases are limited to $0.24 \leq x \leq 0.50$ and $x \leq 0.15$ respectively [1176]. Virgin effects due to irreversible structural changes are reported [1177]. Li et al. [1178] ascribed this virgin effect to partial chemical disordered structure (as it occurs for As containing compounds, Mn atoms preferentially occupy 3g sites [1179]). When the PM state of $MnFeP_{0.75}Si_{0.25}$ transforms to FM state, it results in the formation of an intermediate metastable AFM state, whereby AFM/FM ratio can be controlled by modifying the kinetics of atomic diffusion [1180]. Off-stoichiometric $Mn_xFe_{1.95-x}P_{0.50}Si_{0.50}$ compounds exhibit a gradual change from SOPT to FOPT as Mn/Fe ratio increases [1151]. Recently, Bartok et al. [1181] prepared off-stoichiometric $Mn_{1.3}Fe_{0.65}P_{0.5}Si_{0.5}$ compound via different techniques to produce bulk and spark plasma sintered powdered samples. The isothermal magnetization of powdered samples shows a smoother transition than those of bulk ones, which show a staircase shape. Latent heat measurements have been recently proposed to estimate MCE, assuming proportionality between this magnitude and the magnetic entropy change [1182]. For $Mn_{1.2}Fe_{0.75-x}Ni_xP_{0.5}Si_{0.5}$ and $Mn_{1.2}Fe_{0.8-x}Ru_xP_{0.5}Si_{0.5,}$ minor partial substitutions of Ru or Ni for Fe retain good MCE responses, while decreasing the transition temperatures and hysteresis [1183].

GMCE was maintained upon combined substitutions of Si and Ge for As in $MnFe(P_{0.89-x}Si_x)Ge_{0.11}$ (e.g. $|\Delta S_M|$(2 T) = 16 J kg^{-1} K^{-1} at 292 K for x = 0.26). Nevertheless, an increase of thermal hysteresis >15 K is observed together with virgin curve effects [1184,1185]. However, when Ge or Si partially substitute for P, T_C linearly increases with Ge content while it significantly varies in a non-linear dependence in Si substituted samples. T_C is suggested to be related to lattice parameters *a* and *c*: the larger *a* and smaller *c*, the higher T_C [1186]. In $MnFeP_{0.5}Ge_{0.5-x}Si_x$ compounds with Fe_2P-type structure, T_C increases from 300 to 548 K as x decreases from 0.45 to 0.1 [1187]. X-ray circular magnetic dichroism experiments (L_3 Mn edge) performed on these As-free samples evidence magnetic field dependence spectra, indicating a modification of the electronic levels of Mn above the Fermi level during the field induced FOPT [1188]. However, this result disagrees with those obtained for $Mn_{1.1}Fe_{0.9}P_{0.45}As_{0.55,}$ which exhibits unaltered electronic configuration of both Fe and Mn [1189]. On the other hand, first principle studies conclude that the competing exchange interactions between the different pairs of TM atoms are responsible for the large MCE ascribed to the field induced FOPT [1190]. Tailoring Mn/Fe ratio of As-free $Mn_{2-x}Fe_xP_{0.6}Ge_{0.15}Si_{0.25}$ compounds ($0.7 \leq x \leq 1$) was explored by Wang et al. [1191], whereby, for x = 0.7 and 0.8 compounds, the conversion of FOPT to SOPT is observed to reduce MCE and transition temperatures. The character of the transition in these compounds is analyzed by the scaling law of the entropy change [229] while the analysis from Arrott plots is not as straightforward [1192]. Addition of B to $MnFeP_{0.63}Ge_{0.12}Si_{0.25}B_x$ ($0 \leq x \leq 0.03$) produces no significant effects on MCE but a continuous increase in T_C (from 300 to 347 K) along with a decrease in thermal hysteresis (from 20 to 6 K) [1193]. However, Guillou et al. [1194] show that B substitution for Si or P changes FOPT to SOPT. They [1195] analyzed the characteristics to improve MCE in FOPT materials indicating that although latent heat should be sufficiently high to ensure a large ΔS_M, it must be limited to avoid a reduction in ΔT_{ad}. Hence, they proposed minor additions of B in MnFe(P,Si) compounds and found a highly reversible ΔT_{ad} = 2.8 K and $\Delta S_M = -9.8$ J kg^{-1} K^{-1} at 1 T and 280 K, with minimum hysteresis for $MnFe_{0.95}P_{0.595}B_{0.075}Si_{0.33}$, which poises this alloy family very promising and competitive to hydrogenated $La(FeSi)_{13}$ compounds. Both of these systems exhibit common advantages, such as not using critical and toxic elements, but Guillou et al. [1195] claim the former exhibits better mechanical stability. Recent X-ray absorption experiments show large changes in the K-edge of phosphorous in $MnFe_{0.95}P_{0.66-x}Si_{0.34}B_x$, which carries a small magnetic moment in the FM state [1196]. Recent results report a similar evolution of the magnetic moments of Mn and Fe through the transition, which contradicts theoretical predictions of quenched Fe moments [1197]. The cyclability [1198] and mechanical stability [1199] of these MnFe(P,Si,B) systems are also investigated. Enhancement of mechanical stability upon B doping and TM substitution was also recently reported by Roy et al. [1200]. In addition, mechanical stability can be also enhanced by interstitial N [1201].

The application of pressure affects the transition temperatures differently for different compositions of this alloy family. Moreover, the dependence is not related to the volume change but to the anisotropic evolution of the lattice parameters [1202]. The magnetostructural character of the transition implies an important role of the interactions [1079]. Transition temperature and its thermal hysteresis is thus related with the microstructural parameters of the Fe_2P. Fig. 38 shows these two parameters as a function of both the unit cell volume and the ratio between the lattice parameters of the hexagonal phase. Finally, regarding this family of alloys, the presence of impurity phases, such as Mn_2O_3 and Fe_2MnSi should be taken into account when comparing different data.

With a similar composition to that of the previous compounds, $(Co_{0.35}Mn_{0.65})_2P$ crystallizes in Co_2P-type structure and exhibits a FOPT (AFM to FM) at 240 K and a SOPT (FM to PM) at 320 K. Ascribed to this SOPT transition, $\Delta S_M = -2.3$ J kg^{-1} K^{-1} at 5 T [1203]. In addition, Fe and Ni partial substitution to this compound have been recently studied [1204]. The effects of B addition and varying Mn/Co ratio on the MCE of MnCoP can be found in Ref. [1205].

5.1.2.6. Mn antiperovskites. In 2003, two different groups independently reported the MCE characterization of the cubic antiperovskite Mn_3GaC compound (space group *Pm*3*m*) [1206,1207], whose cubic cell consists of a formula unit with a lattice parameter of 3.98 Å as shown in Fig. 39. Assuming the Ga atom is located at the corner of the cell, the three Mn atoms sit at the center of the faces while C atom is positioned at the center of the cubic cell.

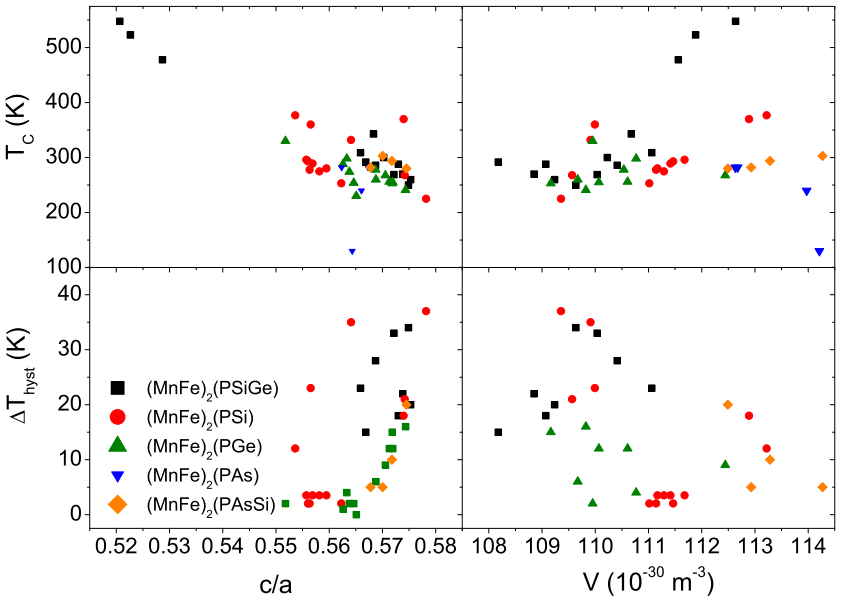

Fig. 38. Magnetic transition temperature and thermal hysteresis of FeMnP(AsSiGe) compounds as a function of the ratio between the lattice parameters a/c (left) and its unit cell volume (right). Data from [1153,1159,1164,1166–1168,1174,1175,1184,1187,1632].

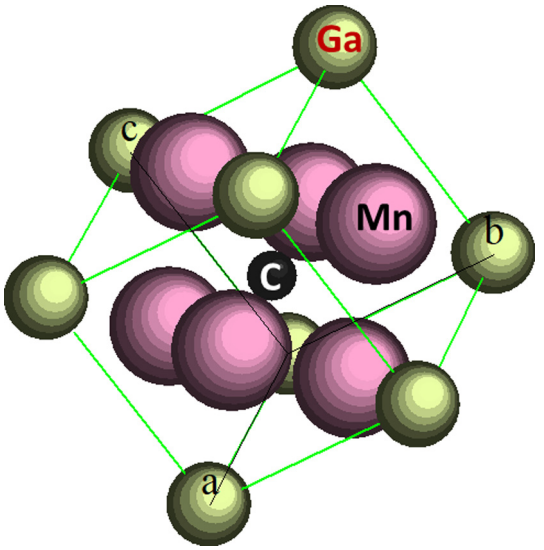

Fig. 39. Unit cell of Mn_3GaC compound.

These compounds are also attractive for their giant magnetoresistance among other properties [1208]. Upon heating, Mn_3GaC undergoes a FOPT from AFM to a canted FM, without symmetry change but with a volume change of −0.46% at about 160 K, followed by a SOPT at 164 K, with an ascribed inverse GMCE. A SOPT from FM to PM phase is observed at 250 K [1209]. Yu et al. [1206] reported a small thermal hysteresis of 2 K for the FOPT wherein $\Delta S_M = 13$ J kg^{-1} K^{-1}, which is almost field-independent (from 1 to 5 T) except that its peak broadens and shifts to lower temperatures (i.e. relatively constant ΔS_M within a temperature range of about 30 K at 5 T). In agreement with these results, Tohei et al. [1207] estimated from entropy measurements $\Delta S_M = 15$ J kg^{-1} K^{-1} and $\Delta T_{ad}(2\,\mathrm{T}) = -5.4$ K for Mn_3GaC at ∼160 K, which were later confirmed by direct MCE measurements [1210]. The X-ray magnetic circular dichroism studies, performed at the excitation energy range from 2p to 3d Mn levels, show that electronic changes near the Fermi level occur at the FOPT of this compound [1211]. Although ΔS_M spikes were reported [1212], they were probably due to artifacts as observed for other compositions. Cakir and Acet [1213] studied the reversibility of MCE by direct measurements observing only a 10% decrease in ΔT_{ad} from the virgin curve to the subsequent application/removing magnetic field cycles (2.8 K change is measured at 3 T). In Mn

antiperovskite compound, the field sweep rate of 700 mT/s is shown to preserve its GMCE but the FOPT is incomplete when using a fast rate of 1000 T/s [1214].

The MCE of $Mn_{3+x}Ga_{1-x}C$ series at the Curie transition was also studied, which reported that this transition shifts to higher temperatures from 250 to 323.5 K when x increases from 0 to 0.08 [1215]. In addition, $|\Delta S_M|$ decreases from ~2.5 to 1 J kg^{-1} K^{-1} (for a field of 4.5 T) for increasing x from 0 to 0.08, while RC_{FWHM} (in J/cm^3 units) increases up to x = 0.07. For Mn_3GaC_x (x = 0.8, 1.0 and 1.05), an increase in C content is concluded to convert the system from a FM metal (x = 0.8) into an AFM semiconductor (x = 1.05) [1216].

With partial Co substitution for Mn, its AFM to FM transition shifts to lower temperatures while MCE parameters are preserved, presenting a wide thermal range of 60–160 K [1217]. Partial Ni substitution for Mn in $Mn_{3-x}Ni_xGaC$ weakens AFM interaction, which then favors the magnetic field induced transition to the canted FM state, the AFM phase being suppressed for x = 0.1 [1218]. As x increases, the transition temperatures of AFM to canted FM as well as those from canted FM to FM phase shift to lower temperatures, whereas Curie temperature increases. In addition, its absolute ΔS_M value decreases as x increases. Carbon deficiency in $Mn_3GaC_{1-\delta}$ enhances the FM character at low temperatures leading to the absence of AFM phase [1219]. The MCE observed in this case is typically SOPT with $|\Delta S_M|$ = 3.7 J kg^{-1} K^{-1} (5 T) at a T_C = 295 K [1212].

For $Mn_3GaC_{0.85}N_{0.15}$, its FOPT is displaced to higher temperatures of 180 K and with almost negligible hysteresis by the partial substitution of N for C, which enhances its AFM character (ΔS_M = +8 J kg^{-1} K^{-1} at 4 T and ΔT_{ad} = 2.8 K at 5 T) [1220]. FM domains above FOPT are recently found absent based on polarization studies [1221]. Antiperovskite $Mn_3Cu_{0.89}N_{0.96}$ shows a ΔS_M = 13.5 J kg^{-1} K^{-1} (5 T) at 150 K, with RC_{FWHM} = 39 J/kg ascribed to a magnetostructural change from tetragonal to cubic [19].

Partial substitution of Al for Ga in $Mn_3Ga_{1-x}Al_xC$ ($0 \leq x \leq 0.15$) produces an increase in T_C from 250 to 312 K. Although saturation magnetization increases with Al content, $|\Delta S_M|$ lowers while the MCE peak broadens [1222]. Ga-free Mn_3AlC compound shows a SOPT at 287 K with the following MCE parameters at 4 T: $\Delta S_M = -3$ J kg^{-1} K^{-1}, RC_{FWHM} = 300 J/kg and ΔT_{ad} = 1.5 K at 285 K [1223].

Partial substitution of Ge for Ga in $Mn_3Ga_{1-x}Ge_xC$ (x = 0, 0.1 and 0.2) [1224] increases the FOPT temperature but reduces the Curie temperature. When >71 at.% Sn partially substitutes for Ga, the alloys display conventional MCE (ΔS_M(7 T) ~ −2.5 and −8 J kg^{-1} K^{-1} at 200 and 280 K for 71 and 100 at.% Sn substitution respectively). However, for Sn substitution below 55%, inverse MCE is preserved although the magnitude of the MCE decreases with Sn content: for 0, 20, 41 and 55% of Sn substitution for Ga, ΔS_M(7 T) ~ 15, 11, 8 and 4 J kg^{-1} K^{-1}, at ~165, 140, 145 and 150 K respectively [1225]. In comparison to Mn_3GaC compound (6.25 g/cm^3), Mn_3SnC compound, which exhibits a higher density (7.78 g/cm^3), experiences a FOPT close to room temperature ($|\Delta S_M|$ = 17 J kg^{-1} K^{-1} at 5 T and 279 K) from FiM to PM state. In addition, a thermal hysteresis of 2.5 K and a reduced unit cell volume (−0.1%), smaller than that of Mn_3GaC compound, were observed [1226]. Abrupt changes in the Seebeck and Hall coefficients near T_C, indicate a modification of the density of states near the Fermi level. In off-stoichiometric $Mn_{3+x}Sn_{1-x}C$, the Curie temperature initially decreases with x for $x \leq 0.1$, for which the transition changes from FOPT to SOPT. Then, Curie temperature increases with x. Their MCE continuously decreases with increasing x [1227].

In $Mn_{3-x}Fe_xSnC$ series, partial substitution of Fe for Mn decreases both Curie temperature (well correlated to the lattice parameter) and $|\Delta S_M|$. However, FWHM increases with x, being the optimum RC_{FWHM} for x = 0.05 [1228]. In addition, the effects of partial Co substitution for Sn on MCE of $Mn_3Sn_{1-x}Co_xC$ has been also reported [1229].

Antiperovskite Mn_3SbN crystallizes in a tetragonal structure at room temperature (*P*4/*mmm* space group) and shows a FOPT from FiM to PM phase at 353 K, which is associated with a structural change from tetragonal to cubic phase. MCE shows a sharp peak around this transformation temperature (FWHM ~3 K and $|\Delta S_M| \sim 7$ J kg^{-1} K^{-1} at 5 T) [1230]. Similarly, a weak FOPT from PM-FiM accompanied by a cubic to tetragonal structural transformation is found in $CuNMn_3$ compound at 141 K, with a $|\Delta S_M|$ = 3.49 J kg^{-1} K^{-1} at 2 T [1231].

5.1.2.7. FeRh alloys. FeRh deserves particularly attention as it was the first intermetallic reported with GMCE close to room temperature in early 90s of the last century with a maximum $-\Delta T_{ad}$ as high as 13 K (2 T) at 305 K for quenched $Fe_{49}Rh_{51}$ [1232]. However, this value reduces to only 4 K and the temperature of the peak shifted to 325 K upon annealing [1233].

The $Fe_{100-x}Rh_x$ compound crystallizes in an ordered α′ CsCl-type structure (space group *Pm*3*m*) in a wide compositional range [1234]. The formation of its AFM phase occurs for equiatomic composition (from ~49% to ~56%, which is also known as the α″ phase). From α″ phase, a FOPT from AFM to FM state (α′ phase) can be induced with an associated 1 vol.% increase [1235] (about 350 K for stoichiometric FeRh). The FM phase undergoes a typical SOPT with Curie temperature at 675 K for FeRh [367]. Ascribed to the FOPT, $Fe_{48}Rh_{52}$ shows an inverse GMCE of ΔS_M = +12 J kg^{-1} K^{-1} (5 T) at T ~ 300 K with RC_{FWHM} ~ 500 J/kg [1235]. However, this is accompanied with a thermal hysteresis about 10 K and significant virgin curves effects [1233]. However, Annazarov et al. proposed the development of heat pumps using stress-induced AFM-FM transition (orders of 1 GPa) [1236,1237] or magnetic field-induced (orders of 2 T) [1238]. Manekar and Roy [1235] described a refrigeration protocol for FeRh to achieved a reversible cycle: prior to increasing the adiabatic field, an initial field increasing and decreasing cycle at hot temperature should be performed isothermally [1184]. Recent results of subjecting $Fe_{49}Rh_{51}$ alloy to two-step cycling of the field (maximum 1.9 T) show ΔT_{ad} = 9.2 K prior to a large ΔT_{ad} = 6.2 K in the final step due to thermal hysteresis [1239]. Stern-Taulats et al. [1240] further investigated the cyclic dependence of MCE by increasing to ten cycles and found a good MCE reproducibility. Moreover, they also show the giant barocaloric effect in this system [1241]. Liu et al. [1242] have recently proposed a method to overcome the irreversibility of these systems by using a combined magnetic-electric stimulus, and attained 96% reduction of losses.

Theoretical studies based on Monte Carlo simulations [1243,1244] and density functional theory calculations [1245,1246] highlight that the magnetic moment of Rh atoms plays an important role to stabilize FM phase (~1 μ_B in FM phase and null in AFM phase). The main contribution to the entropy change is of electronic nature [1247]: a reduction of the carrier density by one order of magnitude in the AFM state compared to FM state, observed from Hall-effect measurements [1248]. Zverev et al. [98] have recently reported both theoretical and experimental investigations on the influence of defects and inhomogeneities on the MCE of $Fe_{50.4}Rh_{49.6}$.

MCE studies of pseudobinary Fe-Rh alloys with small additions of other metals, such as Pd [1249] and Ni [1250], show a reduction of transition temperatures compared to the binary alloy. On the other hand, Pt [1251,1252] and Ir [1251] substitutions shift the transition temperatures to higher values, however, to our knowledge, no MCE studies have been performed on these alloys.

In the case of $FeRh_{1-x}Pd_x$ alloy [1249], the transition temperature decreases from 325 to 154 K and ΔS_M decreases from ~14 to 6 J kg^{-1} K^{-1} at $\mu_0\Delta H = 2$ T, whereas thermal hysteresis increases from 10 to 43 K for x = 0–0.08. Although ΔS_M decreases with increasing x, for x = 0.08, its full width at half maximum of the MCE peak is about twice of that of x = 0. Moreover, although ΔS_M almost saturates for $\mu_0\Delta H \geq 2$ T, the MCE peak broadens linearly with field, from FWHM ~ 10 K to 80 K when the field increases from 1 to 7 T. For $FeRh_{0.45}Pd_{0.55}$, 1% volume change is predicted [1253]. $Fe(Rh_{1-x}A_x)$ (A = Cu, Pd) and $(Fe_{1-x}Ni_x)Rh$ (0 < x < 0.06), which were produced via arc-melting and subsequent annealing, present increased *RC* in the ternary alloys (as compared to that of binary alloys) although ΔS_M decreases [1250]. When slight amounts of Ni partially substitute for Fe in Fe-Ni-Rh, over 50% increase in MCE, in terms of *RC*, was already obtained for $Fe_{0.975}Ni_{0.025}Rh$. Although, ΔS_M decreases to 9 J kg^{-1} K^{-1} at 5 T and 260 K, the full width at half maximum reaches 80 K [1254].

For $Fe_{0.45}Mn_{0.55}Rh$, a large volume change of 3.6% in the AFM (CuAu-I type) to FM (CsCl-type) transition with a magnetic moment per formula unit of 4.5 μ_B is predicted [1253].

5.1.2.8. Fe_2P alloys. Fe_2P orders ferromagnetically below 214 K and is the prototypical phase for the homonymous structure type (space group *P*-62*m*) found in MnFe(P,As) family with GMCE [1255]. Fe is located in two different sites with different magnetic moments: 2.2 μ_B is found for Fe atoms in 3g pyramidal site (five P neighbors) and 0.6 μ_B for Fe atoms in 3f tetrahedral sites (four P neighbors). The small negative moment of P yields a total magnetic moment per formula unit of 2.7 μ_B in Fe_2P. The FM to PM transition in Fe_2P is a magnetoelastic FOPT, which implies a small volume shrinkage of 0.04% despite preserving the hexagonal symmetry. Both the elastic and magnetic transitions are displaced to higher temperatures with the application of an external magnetic field. Hudl et al. [1256] recently described the H-T phase diagrams of this system considering the influence of the direction of the applied field.

Regarding MCE properties, pure Fe_2P shows a $-\Delta S_M = 2$ J kg^{-1} K^{-1} at about 220 K and $\mu_0\Delta H = 1.3$ T [1257], which also agrees with recent results reported for polycrystalline ($-\Delta S_M > 4$ J kg^{-1} K^{-1} for 5 T) and monocrystalline samples ($-\Delta S_M$ obtained are much larger when subjected to field applied perpendicular to the c-axis) [1255]. Theoretical studies based on Landau theory and a magnetovolume coupling term agree with experimental data [1258].

Partial substitution of Ru for Fe in $Fe_{1.85}Ru_{0.15}P$ [1259] increases transition temperatures up to 240 K, although $|\Delta S_M|$ decreases to 1.2 J kg^{-1} K^{-1} ($\mu_0\Delta H = 1.3$ T) and its crystal symmetry changes from hexagonal to orthorhombic (Co_2P-type structure). However, for larger Rh content in $Fe_{1.75}Rh_{0.25}P$ [1259], the hexagonal symmetry is retained while increasing transition temperature up to 315 K. For this compound, $\Delta S_M = -1.2$ J kg^{-1} K^{-1} at $\mu_0\Delta H = 1.3$ T.

In $(Fe_{1-x}Ni_x)_2P$ series, Ni atoms are only located at 3f sites [1260] and for x = 0.025, Curie temperature increases up to 313 K. However, for x = 0.1 no significant increase of T_C is observed. The maximum $-\Delta S_M$ among the series is found for x = 0.025 (2.6 J kg^{-1} K^{-1} at 3 T) [1261]. In addition, its transition temperature is pressure-independent and 0.3% increase in the lattice volume is observed during FM to PM transition [1260].

Delczeg-Czirjak et al. [1262] using first principle studies, found that B, Si and As dopants in Fe_2P lead to an increase in T_C. The hexagonal phase is preserved in $Fe_2P_{1-x}M_x$ for x < 0.15 (M = B), x ≤ 0.25 (M = Si) and x ≤ 0.65 (M = As). In addition, the Monte Carlo simulations of FeCrAs compound crystallizing in Fe_2P-type structure, show table-like $\Delta S_M(T)$ curves [1263].

5.1.2.9. Fe-transition metals compounds. Fe nanocrystals embedded in Cu matrix have been reported with small MCE values at the blocking temperature and the Curie temperature of its interfacial FeCu phase [1264].

Fe_xPt_{100-x} (x = 78–88) alloys exhibit a structural transition from γ phase to α phase induced by cooling or by applying a magnetic field near the transition [1265]. A GMCE of $|\Delta S_M| > 30$ J kg^{-1} K^{-1} (5 T) at ~250 K reported for x = 79 is ascribed to a huge negative thermal expansion occurring at the transition (26.2%). The thermal hysteresis observed in the magnetization curve of this system, which is hundreds of Kelvins, is a clear drawback. The formation of Fe_3Pt phase for x < 78 leads to disappearance of this thermal hysteresis.

Recarte et al. [1266] studied the martensitic transformations occurring in $Fe_{70}Pd_{30}$ alloys and found a reversible transformation occurs at 290 K upon cooling (from face centered cubic to face centered tetragonal) and an irreversible transformation at 216 K (from face centered tetragonal to body centered tetragonal). They used MCE to study the magnetoelastic coupling of the alloys. With increasing magnetic field, MCE changes from inverse to direct MCE. At the transition temperature of the reversible martensitic transformation, the inverse MCE shows a maximum value of ΔS_M = ~0.015 J/kg at 0.1 T. For $Fe_{68.4}Pd_{30.6}Mn$ alloy ($|\Delta S_M| = 1.2$ J kg^{-1} K^{-1} at ~290 K and 6 T), partial substitution of 1 at.% Mn for Fe inhibits the irreversible martensitic transformation found in $Fe_{70}Pd_{30}$ alloys at 216 K, although it appears again for 2.5 at.% of Mn substitution for Fe [1267]. Prida et al. [1268] studied the SOPT occurring at 550 K for melt-spun $Fe_{73.2}Pd_{26.8}$, which results

in a $\Delta S_M = -1.04$ J kg^{-1} K^{-1} at 1.5 T. This SOPT is well described using the scaling law of field dependence of the MCE proposed by Franco et al. [76].

Ipus et al. [1269] produced γ-FeNi phase in $(Fe_{70}Ni_{30})_{89}Zr_7B_4$ alloy after ball milling and subsequent annealing at 973 K. Its MCE parameters ascribed to the SOPT from FM to PM state, are $\Delta S_M = 0.182$ J kg^{-1} K^{-1} (0.5 T) with a broad peak at 342 K. This phase was also obtained upon milling FeNi and its T_C can be tuned by controlling oxidation [1270]. Mo addition in milled $(Fe_{0.7}Ni_{0.3})_{100-x}Mo_x$ (x = 3, 4) also stabilizes the fcc γ-FeNi phase and shows RC_{FWHM} = 440 and 432 J/kg (5 T) for x = 3 and 4 respectively [1271]. The 8 at.% Mn addition in ball milled $(Fe_{0.7}Ni_{0.3})_{92}Mn_8$ reduces T_C from 443 (Mn-free alloy) to ∼375 K (α phase) and further to ∼335 K (γ phase which stabilizes after annealing) [1272]. Broad MCE peaks of $\Delta S_M \sim -1.5$ J kg^{-1} K^{-1} and $RC_{FWHM} \sim 500$ J/kg for 5 T are observed. Addition of B to milled FeNi samples in $(Fe_{0.7}Ni_{0.3})_{89}B_{11}$ yields a progressive increase of γ phase fractions with increasing milling time [1273]. Its $\Delta S_M \sim -2$ J kg^{-1} K^{-1} and large $RC_{FWHM} \sim 640$ J/kg at 5 T are calculated. In addition, the multiple phase coexistence can further enhance RC_{FWHM} [1274]. Austenite γ-$Fe_{49}Ni_{29}Cr_{22}$ shows a PM-FM SOPT at 125.5 K with a $\Delta S_M = -1.8$ J kg^{-1} K^{-1} at 5 T [1275].

High entropy $FeCoCr_xNi$ ($0.85 \leq x \leq 1.15$) alloys were also studied [1276]. T_C increases from ∼50 K for x = 1.15 to ∼200 K for x = 0.85. In addition, cold rolling broadens the MCE peak, showing a $\Delta S_M = -0.35$ J kg^{-1} K^{-1} at 2 T. Zhong et al. [1277] studied the MCE of $Fe_{50}Mn_{15-x}Co_xNi_{35}$ alloys produced by arc-melting. When x increases from 0 to 5, T_C increases from 237 to 342 K. A relatively constant $\Delta S_M \sim -2.5$ J kg^{-1} K^{-1} at 5 T is obtained for the studied series. $NiFeCoCrPd_x$ ($x \leq 0.5$) series, with a tunable SOPT from 100 K to above room temperature, shows $|\Delta S_M| < 1$ J kg^{-1} K^{-1} at 5 T [1278].

5.1.2.10. Other rare earth free crystalline compounds. Tan et al. [1279] have recently prepared $AlFe_2B_2$ compound, which crystallizes in a orthorhombic lattice (space group *Cmmm*) by forming slabs of Fe_2B_2 chains separated by Al layers. They pointed several advantages for this composition: only earth-abundant elements are used and good MCE properties ($\Delta S_M = -7.7$ J kg^{-1} K^{-1} and $\Delta T_{ad} \sim 3$ K at 307 K and RC_{FWHM} = 162 J/kg at 5 T). Further studies on this system can be found in the recent literature [1280,1281]. The PM-FM transition at 282 K disappears after Mn or Cr completely substitute for Fe [1282] despite retaining the structure. Partial Mn substitution for Fe leads to a reduction of the maximum magnetic entropy change and its temperature peak [1283].

Recently, Kaeswurm et al. [1284] studied the MCE of cementite (space group *Pnma*) at its T_C = 475 K, which exhibits a $\Delta S_M = -3.07$ J kg^{-1} K^{-1} and $\Delta T_{ad} = 1.76$ K at 2 T. Partial substitution of Mn for Fe in Fe_3C cementite [445] allows for tunable T_C below and above room temperature and also preserves the orthorhombic Fe_3C structure while its MCE remains low: $\Delta S_M = -1.39$ J kg^{-1} K^{-1} (5 T) at 305 K for $(Fe_{0.9}Mn_{0.1})_3C$. Mn-free $(FeCr)_3C$ cementite-type was also reported with a $\Delta S_M = -0.9$ J kg^{-1} K^{-1} at $\mu_0\Delta H = 1$ T [1285].

Zhang et al. [1286] explored the complete compositional range in the Heusler $Fe_2MnSi_{1-x}Ge_x$ series. The crystallization of the amorphous phase produced by milling leads to the formation of a metastable D03 phase (space group *Fm*3*m*) for $x \leq 0.5$, tuning the Curie temperature closer to room temperature (for x = 0 and x = 0.5, T_C = 243 and 260 K respectively) than that of $D0_{19}$ phase (space group $P6_3/mmc$; for x = 0.6 and 1, T_C = 355 and >400 K respectively). ΔS_M value of −1.5 J kg^{-1} K^{-1} at 5 T at the corresponding Curie temperature is reported for $Fe_2MnSi_{0.5}Ge_{0.5}$ alloy.

Mn_3Sn_2 compound crystallizes in Ni_3Sn_2-type structure (space group *Pnma*) below 753 K. Its anomalous MCE is due to the presence of two successive magnetic transitions: at 262 K (from PM to FM) and at 227 K (from FM to FM), assumed of second order character. Hence, its $\Delta S_M(T)$ curves exhibit two maxima centered at the two transition temperatures and of similar magnitude ($\Delta S_M \sim -3.3$ J kg^{-1} K^{-1} at $\mu_0\Delta H = 5$ T), leading to a broad curve and thus RC_{FWHM} > 300 J/kg [1287]. Recently, the same group has reported a third anomaly at 197 K, ascribed to the formation of a weak AFM interaction in this compound [1288].

$Mn_{1.9}Co_{0.1}Sb$ compound crystallizing in tetragonal Cu_2Sb-type structure, with *P*4/*nmm* space group, derives from the simple FiM Mn_2Sb. In Co added intermetallic, FOPT from AFM to FiM occurs and shows a $\Delta S_M = 5$ J kg^{-1} K^{-1} (1 T) at 165 K [1289]. On the other hand, CoMnSb crystallizes in *F*-43*m* space group and shows a high $|\Delta S_M| = 2.06$ J kg^{-1} K^{-1} (0.9 T) at a SOPT with T_C = 471 K [1290]. Annealing at higher temperatures leads to broadening of the MCE peak at the expense of decreasing $|\Delta S_M|$ [1291]. Partial substitution of Nb for Mn in Co-Nb-Mn-Sb slightly lowers T_C but more significantly reduces MCE ($\Delta T_C \sim 10$ K with a 75% decrease in $|\Delta S_M|$ for $CoNb_{0.6}Mn_{0.4}Sb$) [1292]. $Mn_{2-x}Cr_xSb_{1-y}In_y$ compounds show a AFM-FiM FOPT at 306 K with a $|\Delta S_M| \sim 5$ J kg^{-1} K^{-1} and $\Delta T_{ad} = 1.75$ K at 5 T, for a composition of x = 0.13 and y = 0.05 [1293]. Partial substitution of In for Sb is studied in the aim of suppressing the MnSb impurity phase.

Mn_5PB_2 crystallizes in a tetragonal structure, with space group *I*4/*mcm*, and experiences a SOPT from FM to PM at 302 K with a $\Delta S_M \sim -5$ J kg^{-1} K^{-1} (5 T) in the presence of some Mn_2P impurities [1294].

$(Mn_{0.83}Fe_{0.17})_{3.25}Ge$ compound is reported with an inverse MCE and a high ΔS_M of +11.6 J kg^{-1} K^{-1} (7 T) at 93 K, which is attributed to its field induced metamagnetic FOPT from collinear AFM to triangular AFM phase [1295]. This hexagonal compound undergoes a Néel transition to the PM state at 240 K.

The MCE of spinel compounds has been also studied. Non-magnetic substitution in Mn/Zn ferrites has been shown to be an effective way to tune the peak temperature of MCE without significant losses in MCE [1296]. $Ni_{1-x}Zn_xFe_2O_4$ ferrite shows SOPT [1297], with a continuous decrease of T_C from 845 to 302 K as x increases from 0 to 0.7. At 2.5 T, the maximum $|\Delta S_M| = 1.39$ J kg^{-1} K^{-1} is observed for x = 0.3 (T_C = 664 K) while the maximum RC_{FWHM} = 161 J/kg is attained for x = 0.5 (T_C = 481 K). Ball milling of $ZnFe_2O_4$ yields flat $\Delta S_M(T)$ curves (∼0.25 J kg^{-1} K^{-1} at 3 T from 100 to 300 K with RC_{FWHM} > 75 J/kg) [1298]. However, deposited nanosized $CoFe_2O_4$ prepared by sol-gel technique, exhibits an inverse MCE of $\Delta S_M = +0.25$ J kg^{-1} K^{-1} at 210 K and 1.3 T [1299]. Spinel vanadate MnV_2O_4 becomes FiM at 57 K (SOPT) although a structural phase transition occurs in the vicinity, which is at 53 K. Its GMCE of $|\Delta S_M| = 24$ J kg^{-1} K^{-1} (4 T) and $\Delta T_{ad} \sim 3$ K (2 T) is ascribed to the combined con-

tributions of spin entropy change plus the orbital entropy change induced in V^{3+} ions [1300]. However, it is worth noting that Maxwell analysis is used for this MCE determination and the maximum is sharp. Small substitution of Zn for V yields to a better decoupling of the two transitions [1301]. With 2.5% substitution of Al for V, smaller $\Delta S_M = -8.2$ J kg^{-1} K^{-1} and ΔT_{ad} = 2.6 K at T_C = 59.6 K (4 T) are obtained but with enhanced RC_{FWHM} = 177 J/kg as compared to Al-free compound [1302]. The critical exponents for Al-containing compound are consistent with mean field theory unlike for MnV_2O_4 compound [1303]. Partial Fe substitution for Mn in $Mn_{1-x}Fe_xV_2O_4$ broadens the MCE peak and aids *RC* enhancement [1304]. Sulfospinel $CdCr_2S_4$ with SOPT at a Curie temperature of 87 K, shows $\Delta S_M = -7$ J kg^{-1} K^{-1} and ΔT_{ad} = 2.6 K at 5 T [1305] due to spin-lattice coupling, as proved by electron paramagnetic resonance experiments [1306]. Minor partial substitutions of Cu or Fe for Cd retain the second order character of the transition, whereas T_C increases to 119 K for $Cd_{0.7}Fe_{0.3}Cr_2S_4$. However, $|\Delta S_M|$ is reduced to ~5 J kg^{-1} K^{-1} [1307]. For $CuCr_2Se_4$ [1308] and $CuCr_2Te_4$ [1309] spinels, with T_C = 430 and 330 K and $\Delta S_M = -0.7$ and -0.6 J kg^{-1} K^{-1} (1 T) respectively, scaling laws of ΔS_M and RC_{FWHM} are reported to be applicable and show critical exponents typical for a 3D-Heisenberg model. Lower T_C values are found for $CdCr_2Se_4$ (~130 K) and $HgCr_2Se_4$ (113 K) alloys [1310], which both exhibit the same $\Delta S_M = -1.5$ J kg^{-1} K^{-1} at 1.5 T. Mean field exponent was proposed for the field dependence of the MCE for these systems.

There are also some works reported on the MCE of CrO_2. Zhang et al. [1311] observed $\Delta S_M \sim -5$ J kg^{-1} K^{-1} (1.5 T) at 390 K for 400 nm sized CrO_2 particles but the response decreases for smaller particles. Smaller ΔS_M values with a broader T_C distribution were observed for CrO_2 films on TiO_2 substrate, leading to higher *RC* [1312]. Recently, partial substitution of O for F has been shown to effectively reduce the Curie temperature to room temperature [1313].

Zhong et al. [1314] studied several RE-free double perovskite systems, such as $Ba_2Fe_{1+x}Mo_{1-x}O_6$ [1315,1316], $Sr_2FeMo_{1-x}W_xO_6$ [1315], followed by other authors studying $Ba_2CrMo_{1-x}W_xO_6$ [541] and $Ba_2Fe_{1-x}Cr_xMoO_6$ [1317]. In $Ba_2Fe_{1+x}Mo_{1-x}O_6$ series, two contrary effects yield an almost unchanged T_C: large superexchange Fe-O-Fe interactions for x > 0 and reduced number of itinerant electrons (3 and 5 electrons per Fe and Mo respectively) [1315]. Although $|\Delta S_M|$ reduces from 1.54 to 1.2 J kg^{-1} K^{-1} (1 T) at ~335 K as x increases from 0 to 0.3, the peak becomes broader (FWHM from 20 to 30 K). Partial substitution of W for Mo reduces the Curie temperature to 285 K and, with 50 at.% W substitution, slight enhancement in MCE is attained: $|\Delta S_M|$ increases from 1.25 to 1.6 J kg^{-1} K^{-1} (1 T) [541]. T_C can also be tuned to room temperature with partial Cr substitution in $Ba_2Fe_{1-x}Cr_xMoO_6$ cubic perovskite series. However, its MCE decreases with increasing Cr content: for x = 0 and 1, $|\Delta S_M|$(1 T) = 2.08 and 0.65 J kg^{-1} K^{-1} at 340 and 310 K respectively [1317]. The MCE studies of $Li_{4-x}Ti_{5-2x}Fe_{3x}O_{12}$ system shows that the transition temperature of its SOPT is highly compositional dependent on x. However, the system shows moderate MCE of $|\Delta S_M| \sim 1$ J kg^{-1} K^{-1} at 5 T [1318].

High entropy alloys composed of transition metal elements of the family FeCoNiCuX, with X = Mn, Ag, Pt, and Mo have been proposed as a way of tuning transition temperature of the alloys with the hope of enhancing their magnetocaloric response for near-room-temperature applications [1319]. The distribution of exchange interactions intrinsic to these materials provoke a broad magnetic entropy change peak. However, in the current state of the art, the enhancement of the refrigerant capacity comes with the price of a small magnetic entropy change. This is in contrast with the rare earth high entropy alloys presented in Section 5.1.1.8, where an increased refrigerant capacity was achieved while keeping a large magnetic entropy change peak [595].

Recently, $Cs_2NaAl_{1-x}Cr_xF_6$ elpasolites (space group *R*-3*m*) were proposed for very low temperature cooling as they exhibit large MCE at 3 K: e.g. for x = 0.62, $|\Delta S_M| \sim 11$ J kg^{-1} K^{-1} and ΔT_{ad} = 8 K at 5 T [1320].

A more exotic type of magnetocaloric material is graphene, in which oscillatory behavior of the magnetic entropy change and adiabatic temperature change as a function of the applied magnetic field has been predicted [1321]. This oscillating behavior is intrinsic to diamagnetic materials [1322] and it emerges from the crossing of the Landau levels through the Fermi energy. In graphene, the value of the magnetocaloric effect is three orders of magnitude larger than for other two dimensional non-relativistic diamagnetic materials. This oscillating behavior has been the basis for a magnetocaloric cycle with six stages [1323], which is being proposed for low temperature magnetic refrigeration.

5.2. Amorphous materials

Among the advantages of amorphous materials as compared to their crystalline counterparts, compositional tailoring, low eddy current losses, low hysteresis losses and corrosion resistance can be listed. Amorphous alloys with attractive MCE undergo SOPT at their magnetic ordering temperatures. They are classified into two families: RE-based alloys (mainly Gd-based) and TM-based alloys (mainly Fe-based). Fig. 40 shows the various data of these alloys found in the literature and estimated at $\mu_0\Delta H$ = 1 T using the exponential laws for the field dependence of ΔS_M and RC_{FWHM} [80] (using mean field values for the critical exponents of 2/3 and 4/3 respectively [80]). The MCE of crystalline Gd, which is the reference material for MCE and particularly for SOPT materials, is also included.

Both alloy families exhibit dissimilar behavior. RE-based amorphous alloys show transition temperatures extending from cryogenic temperatures to close to room temperature but not beyond that of crystalline Gd. On the other hand, the transition temperatures of TM-based alloys extended from above 100 K to clearly above room temperature. In general, with increasing peak temperatures, $|\Delta S_M|$ decreases for RE-based alloys, whereas relatively increases for TM-based alloys. For amorphous alloys with similar transition temperatures to that of Gd, $|\Delta S_M|$ is clearly lower than that of Gd but it is not the case when comparing RC_{FWHM} of these systems. This is due to the highly disordered structure of amorphous systems, which smears out the magnetic transition and consequently, broadens the MCE peak.

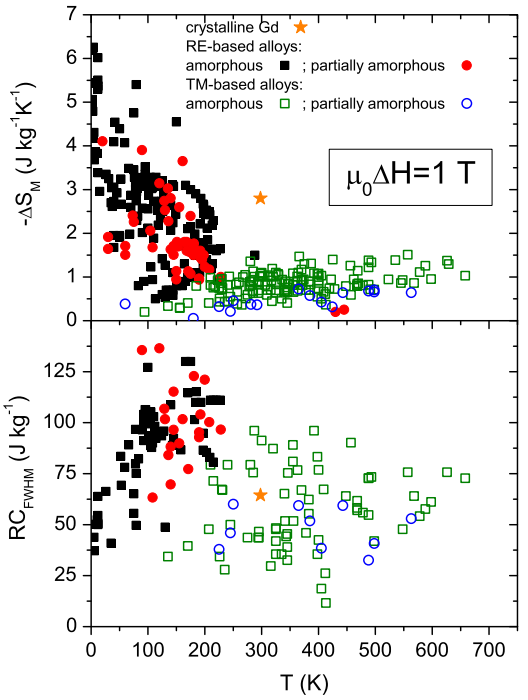

Fig. 40. Magnetic entropy change at peak and refrigerant capacity as a function of peak temperature for RE-based amorphous (solid black squares) and partially amorphous (solid red circles) alloys as well as for TM-based amorphous (hollow green squares) and partially amorphous (hollow blue circles) alloys. Corresponding references are collected in Table S7 of the Supplementary Material.

The partially amorphous RE-based and TM-based samples also show dissimilar behaviors. In the case of Gd-based amorphous alloys, the crystalline phases that appear as products of primary crystallization (or as crystalline products of rapid quenching) exhibit transition temperatures close to those of their amorphous systems (i.e. hexagonal Gd crystals). Nevertheless, the formation of α-Fe crystallites with a Curie temperature above 1000 K in Fe-based alloys is detrimental to room temperature MCE ascribed to the magnetic transition of the amorphous phase. Although the microstructures of both systems are similar (i.e. crystallites embedded in an amorphous matrix), the difference in their behaviors is due to the differences in the transition temperatures of both phases formed within the composites [1324,1325].

5.2.1. Rare earth based amorphous materials

Besides the review of Gschneidner and Pecharsky [11], reviews on different properties of bulk metallic glasses, including their MCE can be found in [1326,1327]. Binary alloys of Gd can show ΔS_M values similar to that of hexagonal Gd but with reduced T_C (see Fig. 41). On the other hand, these alloys exhibit broader transitions, resulting in enhanced *RC* compared to that of pure Gd.

Fig. 42 shows the Curie temperature and maximum magnetic entropy change at 5 T as a function of the average atomic number of the RE for different amorphous alloys. It is clear that the maximum transition temperatures are obtained for Gd-containing amorphous alloys. This temperature is generally well below that of hexagonal Gd, however, amorphous GdCo [1328–1330], GdCoB [1330], GdCoMn [1331], GdCoSi [1329], GdFe [1332], GdFeAl [1333,1334] and GdFeAlSi [1335] can show T_C above 200 K. Moreover, MCE peak temperatures of partially crystalline GdY and GdZn [115] can also exceed 200 K. Amorphous $Gd_{65}Mn_{35-x}Si_x$ (x = 5 and 10) ribbons show $-\Delta S_M = 4.6$ and 4.7 J kg^{-1} K^{-1} and $RC_{FWHM} = 625$ and 660 J/kg at ~230 K (5 T) for x = 5 and 10 respectively. Nanocrystallization sharpens the peak and shifts it to higher temperatures without affecting ΔS_M [1336]. On the other hand, amorphous/nanocrystalline $GdAl_2$ milled powder exhibits a table-like peak from 30 to 165 K, with enhancement of MCE below 30 K due to the presence of superparamagnetic particles [1337]. Although the higher temperatures are among these RE = Gd systems (see Fig. 42), partially amorphous $Nd_{45}Fe_{30}Co_{15}Al_{10}$ alloys have been recently shown to have a peak entropy change (moderate $\Delta S_M \sim -0.25$ J kg^{-1} K^{-1} for 1 T) at high temperature (430–445 K) [1338]. Previously, the maximum peak temperature for RE-based amorphous alloy was reported by Foldeaki et al. [1332] as $T_C = 288$ K for $Gd_{70}Fe_{30}$ amorphous ribbons, obtained by rapid quenching, which exhibit $\Delta S_M = -1.50$ J kg^{-1} K^{-1} at 1 T. Recently, Zhang et al. systematically studied the MCE of heavy RE-based metallic glasses in the series of $(RE^{(1)}_{1-x}RE^{(2)}_x)_{55}Al_{27.5}Co_{17.5}$, whereby $RE^{(i)}$ = Gd, Er or Ho, and x = 0, 0.3, 0.5, 0.7 and 1 [1339]. Their T_C can be tuned between 8 and 93 K and a relative linear correlation is observed between the absolute value of ΔS_M and $T_C^{-2/3}$. Higher Curie temperature is reported for $Gd_{55}Al_{20}Co_{20}Ni_5$ bulk metallic glass, with $-\Delta S_M = 9.8$ J kg^{-1} K^{-1} and $\Delta T_{ad} = 4.74$ K at 5 T and 105 K [1340].

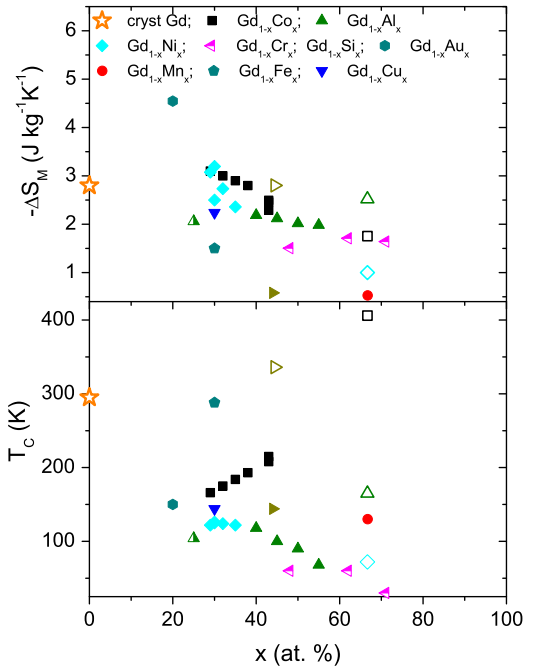

Fig. 41. Curie temperatures and ΔS_M values (1 T) of some binary Gd-based amorphous alloys (see Table S7 of the Supplementary Material for references). Solid symbols correspond to fully amorphous alloys, half-filled symbols correspond to partially amorphous alloys and hollow symbols correspond to fully crystalline alloys.

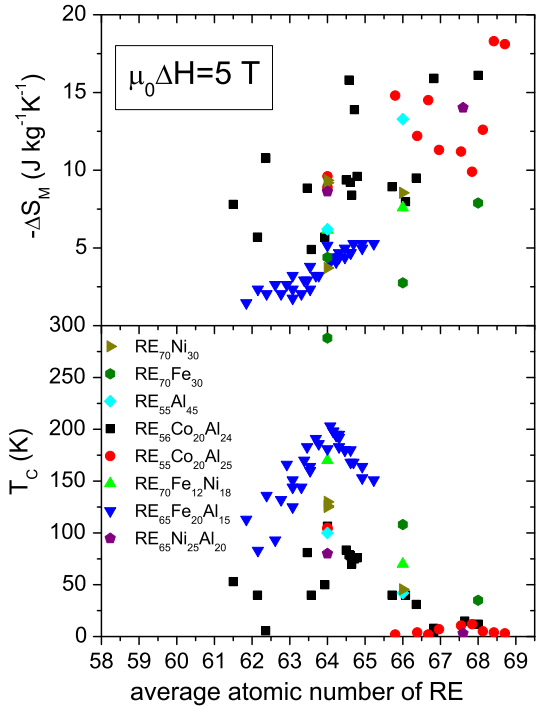

Fig. 42. Curie temperatures and ΔS_M values (5 T) of some RE-based amorphous/partially amorphous alloys as a function of average atomic number of RE (see Table S7 of the Supplementary Material for references).

Recently, Liu et al. [1341] reported table-like MCE response of amorphous $Gd_{50}Co_{45}Fe_5$ close to room temperature (ΔS_M = 3.8 J kg^{-1} K^{-1} at 289 K and 5 T).

Amorphous samples can be produced by different routes, typically by fast cooling (e.g. melt-spinning or suction casting) or by mechanical methods (mechanical grinding or alloying). Amorphous GdNiAl produced by ball milling [1342] exhibits a 25% smaller $|\Delta S_M|$ than that observed for rapidly quenched samples [1343] with no significant change in the FWHM ~ 55 K.

The MCE of amorphous micro-fibers and microwires were studied for $Gd_{55}Al_{25}Co_{20}$ (ΔS_M = −9.7 J kg^{-1} K^{-1} and RC_{FWHM} = 870 J/kg at 5 T and 100 K [1344]), $Gd_{68}Ni_{32}$ (ΔS_M = −4.5 J kg^{-1} K^{-1} at 122 K and 3 T) and $Gd_{53}Al_{24}Co_{20}Zr_3$ (ΔS_M = −7 J kg^{-1} K^{-1} at 97 K and 3 T) [1345].

The group of von Ranke performed different theoretical studies to describe the MCE of amorphous systems: e.g. $Er_{80}Au_{20}$ [1346] (Handrich-Kaneyoshi model is applied to this case), REAg and GdCuAl systems [1347], and other binary Dy-TM compounds [1348].

5.2.2. Transition metal based amorphous materials

To reduce materials cost, much interest is focused on RE-free compositions, which necessarily led to MCE investigations of TM-based amorphous alloys. These materials were previously studied due to their soft magnetic properties, which are related to absent magnetocrystalline anisotropy. Therefore, a large number of works on characterizing the compositional dependence of the magnetic properties of these systems can be found in the literature [1349]. Unlike RE-based amorphous alloys, TM-based amorphous systems exhibit a general increase of $|\Delta S_M|$ as transition temperature increases (as shown in Fig. 40). A review on the MCE of TM-based amorphous alloys can be found in [1350] for rapidly quenched systems and in [1351] for mechanically alloyed ones.

Maeda et al. in 1983 [1352] early studied the MCE of pseudobinary $(Fe_{1-x}Ni_x)_{90}Zr_{10}$ and $(Fe_{0.95}M_{0.05})Zr_{10}$ amorphous series and found that T_C increases with x up to 0.05 as well as with increasing atomic number of the M element (M = Al, Si, Ga, Ge and Sn). Almost constant $|\Delta S_M|$ values with less than 1% change is reported (~1.4 J kg^{-1} K^{-1} at 1.4 T assuming a density of 7.7 g/cm^3) among the different studied alloys. Maeda et al. also mentioned that the MCE behavior of these amorphous systems departs from the predictions of molecular field theory, which was later confirmed by Franco et al. [76].

The vast majority of studied TM-based compositions are Fe-based alloys and only a few examples on Co-based [1353,1354] and Pd-based [1355] alloys (the latter with significantly smaller MCE response) can be found in the literature. Among Fe-based alloys, those derived from $Fe_{90}Zr_{10}$ eutectic composition, or ternary and quaternary variations around eutectic composition $Fe_{80}B_{20}$ (including Cr, Mo, Nb or Mn) exhibit T_C close to room temperature. Fig. 43 shows the compositional dependence (Fe content) of ΔS_M and T_C for some Fe-Zr-M amorphous alloys. The Fe-based amorphous alloy exhibiting the largest MCE reported to date belongs to this Fe-Zr-M family with 4 at.% B and some partial substitution of Co and Ni for Fe. The results for some compositions of this series are also included in Fig. 43. The MCE of $Fe_{84-x}Ni_xZr_6B_{10}$ ($0 \leq x \leq 6$)

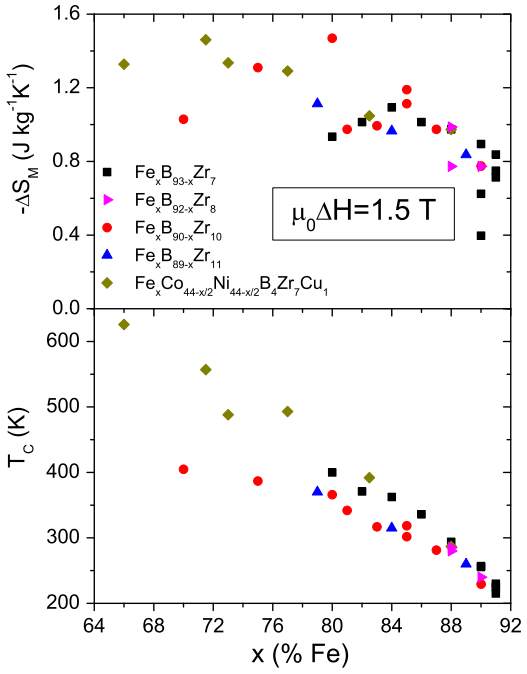

Fig. 43. Compositional dependence (Fe content) of the maximum absolute magnetic entropy change and transition temperature of Fe-Zr-M amorphous alloys at 1.5 T (see Table S7 of the Supplementary Material for references).

Nanoperm-type alloys is studied using the master-curve analysis, and also shows that Ni additions increase their T_C and MCE ($-\Delta S_M$ = 1.52 J kg^{-1} K^{-1} at ~480 K for 1.4 T) [1356].

Ball milled and mechanically alloyed TM-based amorphous alloys are also studied in addition to the earlier-discussed ultra-rapid quenched systems [432,433,1351,1357–1362]. The ribbon samples produced by the latter technique allows the assumption of a zero demagnetizing factor when the applied field direction is contained in the plane of the ribbon. However, for powder samples obtained from milling, a demagnetizing factor of 1/3 is a better approximation. In fact, if the demagnetizing factor is not considered, ΔS_M values are only slightly affected (~5%) but their field dependence completely departs from the predicted behavior, requiring a demagnetizing factor of 1/3 to properly account for the field dependence of this magnitude [1362]. Moreover, a broader Curie distribution in milled samples is observed due to compositional heterogeneities or strain distribution [1363].

Ball milling of amorphous $Fe_{75}Nb_{10}B_{15}$ melt-spun ribbons enlarges the metal-metal distance and thus enhances magnetization but $|\Delta S_M|$ is reduced, possibly due to a broader distribution of Curie temperatures after mechanical treatment [1361]. Compaction of these ball milled powders leads to different effects depending on the composition [1364], due to a general B enrichment of the amorphous phase upon annealing. In fact, B incorporation by milling is not trivial but this element remains as inclusions and is not completely incorporated to the matrix [1358]. This leads to clear differences between the MCE of B-containing compositions obtained via rapid quenching or ball milling [1362]. Besides B inclusions, remnant α-Fe type nanocrystals are generally found (though not clearly detected by some techniques: e. g. X-ray diffraction). Procedures to extract the information of the amorphous phase have been developed based on the power dependence of MCE with magnetic field [1365].

In general, for Fe-based amorphous alloys and unlike Gd-based amorphous ones, the presence of crystalline phases (due to quenched in crystallites or nucleated ones after partial crystallization) leads to a deterioration of MCE, as the Curie transitions of the crystalline phases are far beyond that of the amorphous phase [1365–1368]. Only few exceptions appear due to the formation of intermetallics with lower T_C [1360].

The MCE of $Fe_{49.7}Cr_{18}Mn_{1.9}Mo_{7.4}W_{1.6}B_{15.2}C_{3.8}Si_{2.4}$ gas atomized powders shows that amorphicity enhances with the reduction of particle size [1369]. $(Fe_{93}Zr_7)C_{0.11}$ alloys, which are prepared from carbon implantation of amorphous $Fe_{93}Zr_7$ (produced by magnetron sputtering) shows a MCE enhancement: $-\Delta S_M$ increases from 0.66 to 1.01 J kg^{-1} K^{-1} and RC_{FWHM} from 85 to 156 J/kg at 1.5 T as well as the Curie temperature increases from 160 to 311 K after C implantation [1370].

The tunable T_C by fine compositional modification of amorphous alloys favors the development of composite systems with table-like MCE responses [1325,1371–1373].

Furthermore, several works of Fe-based amorphous alloys with very high MCE values (using the terms of GMCE and even colossal MCE) can be found in the literature [1374–1378]. However, these results are also self-contradictory for the same alloy compositions in works reported by some of the coauthors (e.g. [1379]). Recent results reported conventional MCE behavior for these compositions and thus only these results are included in Table S7 of the Supplementary Material [1380].

To finish this section it should be helpful to position the different families in their way to be used in the main application of materials with MCE: magnetic refrigeration. As it will be shown in Section 8, first devices for low temperature applications used paramagnetic salts. Progressively GGG was also used. Nowadays, in addition to these two types of materials, Laves phases are also employed in the prototypes developed for the temperature range of hydrogen liquefaction, becoming the benchmark materials against which the new developed materials (such as molecular magnets or RE nitrides) are compared. The exponential decay of the magnetic entropy change observed in Laves phases as transition temperature increases (regardless of the order of the transition) is the typical behavior found for most of the RE-based systems, either crystalline or amorphous.

Concerning room temperature applications, the Gd and its alloys are by far, the most profusely used in the proposed devices. However, $La(Fe,Si)_{13}$-based systems (including hydrides) are becoming a usual material. Few refrigerators prototypes also use Lanthanum-manganites and $Gd_5(Si,Ge)_4$. The use of MnFePSi alloys in the prototype presented by Haier, Astronautics Corporation of America and BASF at the CES-Las Vegas in 2015 [10] opens a bright technological future for this kind of materials. The absence of Heusler alloys in the refrigeration devices should be ascribed to problems such as hysteresis and mechanical stability, leading to irreversibilities. These problems are nowadays under active research to look for solutions.

6. Enhancing the magnetocaloric effect through material processing techniques

Typically, the optimization of MCE is centered on the search for new alloys with enhanced performance and in particular to those exhibiting magnetism-structure coupling in FOPT, which gives rise to GMCE properties. Hence, a higher magnetic moment without modifying the phase transition is highly desired and even preferable if combined with a transition temperature near room temperature, which are usually not all easily attained in real cases. Moreover, material cost can play a significant role in the tradeoff between performance and cost, especially when the required elements of the strategic materials could only be extracted from few certain locations in the world, risking the ultimate success of any new technology subjected to the changes in geopolitical situation. Therefore, materials engineering approach (i.e. materials processing) could complement the former tradeoffs with a larger certainty of its success. For example, already-established compounds used as building blocks for composites, nanostructures, graded materials etc., could provide promising results in part due to the existing deep knowledge of the material's constituent phases. In this section, the materials processing methods currently used to

enhance MCE will be discussed while many earlier publications on the material selection for MCE and their related physical properties were reported and some mainly focused on the optimization of LaFeSi-related alloys, a type of GMCE material [2,12,18,19,1381,1382].

6.1. Multiphase materials and composites

An ideal material for Ericsson thermodynamic magnetic refrigeration cycles should exhibit a table-like MCE (i.e. a constant ΔS_M or ΔT_{ad} in the refrigeration temperature range), which could be achieved by either incorporating different phases or combining different tunable magnetic phase transitions in the same material [818,1325,1383,1384]. These methods could, in turn, optimize *RC* because the combined phases of tunable transition temperatures would broaden the MCE peak (provided that the magnitude of the peak value is not compensated). In particular, a theoretical ~90% *RC* enhancement in biphasic materials compared to their starting pure phases was reported when appropriate transition temperatures of phases and proportion of constituents were selected [1324]. Its main phase constituent should exhibit the largest transition temperature to maximize *RC* enhancement in the composite in comparison to that of the main phase. These results from the numerical calculations agree with the experimental measurements of a layered composite, which indicates MCE for moderate magnetic fields could be enhanced using this approach to design magnetic refrigerant materials that use the Ericsson cycle [1325]. Furthermore, multilayered composites were also used for the hydrogen liquefaction as well as active magnetic regenerators (AMR) [1325,1385,1386]. In addition, the optimization of the shape of the peak (to obtain a table-like MCE and to broaden the peak to enhance *RC)* is best obtained explicitly at applicable magnetic fields used in refrigerator devices, as the optimal phase proportion can change with field. A magnetocaloric nanocomposite of $La_{0.8}Ca_{0.2}MnO_3$(LCMO)/$La_{0.8}K_{0.2}MnO_3$(LKMO), with a mass fraction of 1:1, has been reported to display a table-like $\Delta S_M(T)$ curve with slightly lowered ΔS_M^{peak} and an *RC* enhancement of 33–35% compared to those of the components [533]. Very recently, a biphasic Gd + GdZn composite, developed in a single fabrication step by induction melting, was reported with an enhanced *RC* in comparison to single-phased Gd (11%) and GdZn (45%) respectively (see Fig. 44) [687]. GdZn, whose Curie temperature lies near room temperature and near that of Gd, could co-exist with the latter as a composite via varying the Gd:Zn ratio according to its phase diagram. The earlier theoretical studies also reveal the tunable MCE from the variant Gd + GdZn phase ratio, which enables them as highly effective MCE composite regenerator materials for a flexible choice of thermodynamic cycle [116].

6.2. Influence of fabrication techniques

6.2.1. Rapid solidification

Rapid solidification has been a popular choice to prepare many magnetocaloric alloys (either with FOPT or SOPT) since it is a well-known method to fabricate amorphous/nanocrystalline/polycrystalline materials with excellent composition homogeneity, controlled thickness catered for applications, good mechanical properties etc. For example, rapid solidification process in melt spinning or splat quenching uses a cooling rate of 10^4–10^7 Ks^{-1}, enabling one to easily obtain various microstructures, such as amorphous/polycrystalline states or a more complex microstructure of nanocrystallites in amorphous matrix. Another example: The resulted refined microstructures from higher cooling rates in rapid solidification help to shorten the duration for heat treatment, which is typically required for homogenization [1382]. The $La(Fe,Si)_{13}$ ribbons or flakes prepared by melt spinning only required a heat treatment duration of a few hours and resulted in a uniform microstructure and homogenous element distribution, in which the $NaZn_{13}$-type 1:13 phase in La–Fe–Si-based alloys (the origin of the GMCE in these materials) is not readily produced as a bulk material using conventional melting [1387]. Moreover, a bulk sample fabricated by conventional methods of 1:13 phase will entail a typical homogenization process at high temperatures of 1100 K for at least one week followed by quenching [323]. Another advantage includes the kilogram-scale

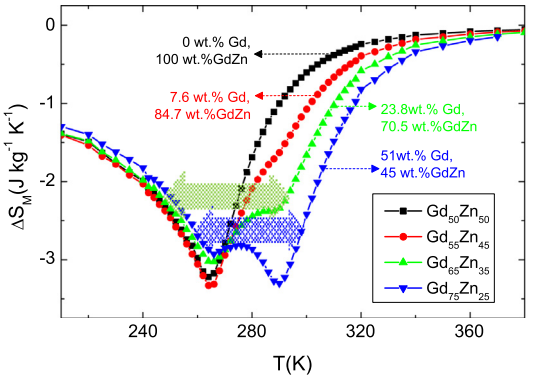

Fig. 44. Table-like MCE experimental results at $\mu_0\Delta H$ = 2 T observed in biphasic Gd + GdZn alloys with the extended temperature span as indicated by the arrows.

production of high performance magnetocaloric materials by strip casting [335]. It had also been reported that micro-sized spherical particles and wires, capable of good heat transfer under high operating frequency, were produced by rapid solidification [336,1388].

6.2.2. Powder metallurgy

Despite the above-mentioned advantages of rapidly solidified flakes and ribbons, they usually cannot be directly utilized in AMR and will need extra steps to form specific geometries, such as grinding them into fine powders as precursors for powder metallurgy. In addition, powder metallurgy processing has become an attractive fabrication method for magnetocaloric materials when Vacuumschmelze GmbH produced blocks of sintered La–Fe–Si-based alloys with this technique and furthermore it could be conveniently accompanied by solid-state sintering when preparing Fe_2P-type materials (another type of GMCE material) [1389]. In addition, mechanical alloying could address the challenges to melt toxic or volatile elements, such as P in Mn–Fe–P–(Ge, Si)–based materials.

6.2.3. Liquid reactive sintering and Thermal Decomposition and Recombination process

AMR refrigerants are typically required as thin plates of thickness well below 0.5 mm. However, machining the phase with a Curie temperature close to room temperature causes the formation of micro-cracks in the samples due to the local temperature gradients around the cutting tool [1390] and the large magnetovolume effect. In fact, microstructural characterization of a fully sintered $La(Fe,Si,Co)_{13}$ alloy reveals segregation of La-rich phase along the grain boundaries and the large thermal expansion of $NaZn_{13}$-type phase when above its T_C led to the formation of micro-cracks [1382]. This could be overcome by the thermally induced decomposition and recombination process (TDR), whereby decomposing the $La(Fe, Co, Si)_{13}$ phase into a lamellar structure of α-Fe and 1:1:1 phases, both of highly enhanced mechanical properties, allows easier machining [1382,1390]. The full recovery of $La(Fe, Co, Si)_{13}$ phase can be attained by annealing the cut decomposed thin plates at around 1323 K.

6.3. Nanostructures

Nanostructured magnetocaloric materials generally includes nanocrystalline materials, core-shell structures as well as nanoparticles, and they could be suitable for magnetic refrigeration of microfluidic reactors, electronic chips or other devices of small dimensions [18]. In addition, it has been demonstrated that nanostructuring can tune not only the quantitative response of a material but also its qualitative behavior, which can be completely dissimilar from that of its bulk counterpart [1391]. The magnetocaloric response of nanostructured materials will not only depend on the characteristics of the bulk material (the composition of the phase) but also highly dependent on other factors such as nanocrystallite size (and size distribution), nanoparticle concentration, interactions between particles, finite size scaling, anisotropy etc. Models accounting for these effects have been proposed [1391–1394]. For example, the magnetization of nanostructured magnetic materials with single-domain crystallites could rapidly vary (due to the dynamical freezing near blocking temperature, T_B) with a much larger magnetic response due to superparamagnetism [1394] and the authors also reported broadened ΔS_M extended over a wider temperature range near T_B in the nanostructured system.

6.3.1. Nanocrystalline materials

Nanocrystalline materials could be prepared by melt spinning using a lower cooling rate (lesser than that used for fabricating fully amorphous ribbons as mentioned earlier) and/or partial devitrification of an amorphous precursor. Nanocrystalline Nd_2Fe_{17} and Pr_2Fe_{17} powders milled for 10 h show ΔS_M^{peak} extended over a wider temperature span as compared to their bulk counterparts, which can aid to improve *RC* [1395]. Another example: Nanocrystalline FeSiBCuNb-type alloys exhibit superparamagnetic transition above the T_C of the residual amorphous phase (when the interactions between particles vanish) and this enables the tunable transition temperatures to even above room temperature, which is more useful than low temperature applications of superparamagnetic nanoparticles with enlarged magnetic moment (these are better magnetic refrigerants than paramagnetic materials) [1396–1398]. Moreover, superparamagnetic clusters could group together the spins, enabling the magnetic moments to be more easily aligned than those in paramagnetic systems [1399]. As a result, the entropy of the spins is more easily modified by the magnetic fields for certain ranges of the magnetic field, temperature and cluster size. However, in the case of superparamagnetic particles embedded in a residual amorphous matrix, the presence of Fe-rich nanocrystals in the amorphous matrix was later found to reduce MCE and *RC* due to the large separation between the transition temperatures of the different phases [1324,1325,1366,1400]. Very recently, $Gd_{(50+5x)}Al_{(30-5x)}Co_{20}$ microwires exhibiting amorphous/nanocrystalline phases produced by melt extraction, were reported to display larger *RC* values than those of GdAlCo-based alloys in the forms of bulk metallic glass or melt-spun ribbons [1401]. The authors attributed the enhanced *RC* values to the magnetic coupling between the amorphous and nanocrystalline phases (20 vol.% of ~10 nm nanocrystallites as observed by TEM).

6.3.2. Magnetocaloric nanoparticles

In the case of magnetocaloric nanoparticles, they could be prepared using various chemical synthesis techniques, mechanical milling [1269,1402], ion-exchange technique, spray pyrolysis [1403] and even on a large scale using plasma arch

discharge method [680]. The typical chemical synthesis methods reported include sol-gel [517,1404,1405], sol-gel based Pechini [511,1406], citric sol-gel [484,1407], glycine nitrate process [1403] and glycine-assisted combustion method [1408].

The reduced particle size of magnetic nanoparticles may not usually aid in large MCE but it could extend ΔS_M^{peak} over a larger temperature span [1409], which could sometimes increase *RC*. However, for the case of superparamagnetic nanoparticles, the effect of the particle size on MCE is reasonably evident. For example, $GdNi_5$ superparamagnetic nanoparticles exhibit larger $-\Delta S_M$ than that of $GdNi_5/Gd_2O_3$ nanocapsules ($\sim 4\times$ larger diameter), despite both fabricated in the same process using the arc-discharge technique [1410]. This is attributed to the superparamagnetic nanoparticles having a smaller magnetic anisotropy energy barrier due to their smaller particle size than the nanocapsules, which could impede the reversal of magnetic moment vector of nanoparticles during field variation. In addition, the transformation of antiferromagnetic behavior (in $La_{0.48}Ca_{0.52}MnO_3$ bulk state) to ferromagnetic via reducing the particle size dimension into nanometer scale has been recently reported [517]. The $La_{0.48}Ca_{0.52}MnO_3$ nanoparticles, synthesized by the conventional sol-gel method, show that their MCE and relative cooling power (*RCP*) systematically increase with smaller particle sizes. The authors also reported the *RCP* of a particle size sample of 45 nm is about 400% larger than that of the bulk counterpart. Another recent study on the MCE of $La_{0.7}Ca_{0.3}MnO_3$ nanoparticles prepared by reactive milling technique shows that larger grain sizes could decrease T_C and increase ΔS_M^{peak} [1411]. The authors report that the weakening of exchange interaction at the surfaces of smaller particles resulted in the decrease in saturation magnetization.

However, nanostructuring can also cause a decrease in MCE, in particular to materials that present a FOPT when in bulk form, due to the loss of the first-order character of the phase transition [1412]. A recent example would be the MCE report of $Sm_{0.6}Sr_{0.4}MnO_3$ nanotube and nanoparticles prepared by a sol-gel modified technique (Pechini) [511]. The nanostructured samples display broader $\Delta S_M(T)$ curves as compared to the bulk counterpart due to their extended widths of temperature range. However, their ΔS_M^{peak} were compensated due to the suppression of FOPT by nanostructuring. The authors reported that the nanotube sample (constituted of smaller nanoparticle size: 25 nm) exhibits an undesired M-shape $\Delta S_M(T)$ profile due to a uprising superparamagnetic behavior, which also indicates a threshold of nanostructuring, below which the advantage to make the transition wider is no longer valid.

Exceptional from the above, the effect associated with surface spin disorder in core-shell nanoparticles had been reported with a significant MCE [1413] despite being a second order phase transition, which could be studied using the techniques developed for Curie transitions [1414]. Another example is the system of isolated Gd_2O_3 nanoparticles embedded in the pores of a mesoporous silica matrix [1415], which recently reports extraordinarily large values of magnetic entropy change in the cryogenic temperature range, with the added advantage that the nanoparticles are not free standing but embedded in a matrix, which facilitates handling and possible technological applications.

One interesting point about magnetocaloric nanoparticles is that they extended the range of applications for magnetocaloric materials beyond magnetic refrigeration. Wang et al. developed magnetocaloric stimuli-responsive hydrogels of Fe_3O_4 colloidal nanocrystal clusters in poly(*N*-isopropylacrylamide) matrix loaded with dyed oil [1416]. Using MCE, they demonstrated controlled release of the incorporated hydrophobic molecules for each reversible shrinking-swelling cycle under AC magnetic field. The authors also suggested MCE offers advantages of remote control and precise selection, giving rise to further potential for practical engineering applications, like sensors, displays or controlled release for targeted medical therapy.

6.3.3. Nanostructured films (or thin films)

The materials' properties typically differ when the microstructure of the material alters, likewise when the microstructural dimensions reduced to nano-scale. Thus, nanostructured or thin films would exhibit different magnetocaloric properties than their bulk counterparts. As an example, the microstructure of the thin films of ferromagnetic shape memory alloys (which is dependent on alloy composition, film thickness, substrate temperature and post-deposition annealing) can strongly influence their characteristic phase transformation temperatures. This was experimentally observed in the magnetron-sputtered Ni-Mn-In, whereby the phase transformation temperatures were tuned to lower temperatures with decreasing film thickness [1050]. The authors also reported observing the completion of martensitic phase transformation in the thick film, in which its larger grain size reduced grain boundary density. In addition, there is another study on epitaxial Ni-Mn-Sn thin films on MgO (0 0 1) substrate fabricated by magnetron sputtering, which reports that the film thickness significantly affects the fraction of martensitic transformation, the transformation temperatures and the temperature range of transformation [1051]. The authors ascribed the former to the deferred transformation near the interface due to the rigid substrate, resulting in a residual layer of austenite at low temperatures, while the lower transformation temperatures and broadened martensitic transformation are presumably due to size effects. The films displayed an inverse MCE with a martensitic transition around 260 K, with comparable MCE values as those of bulk counterparts [1417].

Desautels et al. recently report that the formation of a FeCu interfacial phase in the nanostructured thin film of Cu matrix/Fe nanocrystallites, could control magnetic ordering temperature and MCE [1264]. The authors prepared the Fe/Cu thin films using a reactive ion beam deposition method, alternating the deposition of Fe (30 s or 60 s) then Cu (60 s) for five repeats (ten layers total). The intermix between the Fe nanocrystallites and deposited Cu was stimulated resulting in the formation of an interfacial FeCu phase. A larger *RCP* was observed for the sample with shorter deposit time of Fe, whereby the authors attributed to the overlap of the temperature ranges of the dynamical freezing (T_B) of Fe crystallite magnetizations and the spin fluctuations of FeCu alloy near T_C.

In addition, multilayers formed by layers with different composition (which exhibit a distribution of T_C) can improve the magnetic field responsiveness of magnetocaloric materials in the range of fields suitable for technological applications [123,1418]. In these cases, ΔS_M^{peak} correlates linearly to H in a broad temperature range close to the transition temperature, which is an enhancement with respect to the $H^{0.7}$ behavior typical of bulk materials.

6.3.4. Self-assembled nanostructures

Self-organized ferromagnetic nanowires embedded into highly ordered nanoporous anodic alumina templates have been found exhibiting a coexistence of conventional MCE together with inverse MCE (their sign and magnitude are controlled by the magnitude of the field) upon perpendicularly magnetized to their easy axes of magnetization [1391]. These results validate the numerical calculations that aim to establish the concept of tailoring magnetocaloric response via controlling the samplés microstructure. In contrast to previous results in which combined normal and inverse MCE was reported in other bulk magnetocaloric compounds with several different magnetic transitions [1419], the field-controlled combination of direct and inverse MCE arises due to the superparamagnetic transition of the nanowires and their peculiar anisotropy. This can lead to new possibilities to develop completely new applications of the materials.

Another example demonstrating that self-assembled nanostructures are promising for magnetic cooling near room temperature at low magnetic fields is illustrated in the enhanced magnetic phase transition temperature and MCE in the framework of interfacial coupling in self-assembled Mn_3O_4-$La_{0.7}Sr_{0.3}MnO_3$ nanocomposites [532]. The authors used a dual-target pulsed-laser deposition (PLD) technique to fabricate the growth of self-assembled nanostructures with varying amounts of Mn_3O_4 in the form of nanocrystals embedded in the $La_{0.7}Sr_{0.3}MnO_3$ matrix. The authors reported an enhanced ΔS_M^{peak} (the highest being similar to 130%) in the nanocomposite doped with low Mn_3O_4 content in comparison to that of pure $La_{0.7}Sr_{0.3}MnO_3$ thin film.

6.4. Special treatment conditions

The typical examples of special treatment conditions reported to contribute to enhanced MCE are hydrogenation and annealing, while porous/metal foam structuring improves the resistance to fatigue-cycling.

6.4.1. Hydrogenation

Hydrogenation is typically attained from conventionally annealing La(Fe,Si)$_{13}$–type compound in H-atmosphere at high pressures of 5 MPa, reactive milling in the presence of H_2, which could avoid the need of high pressures from the former technique, and electrolytic hydriding [223,264,265,279,281,532]. The FOPT and itinerant-electron metamagnetic (IEM) transitions (which contributes to the GMCE characteristic of La(Fe-Si)$_{13}$ alloy) were maintained with hydrogenation while significantly increasing T_C from ~195 K to near RT, which are desirable as RT magnetocaloric refrigerant. The effects of hydrogen absorption on the MCE of $La(Fe_{1-x}Si_x)_{13}H_y$ alloys were only significant at magnetic fields of 5 T, where $\Delta T_{ad}^{peak} = 12.6$ K for $y = 1.5$, which is about 50% larger than that for $y = 0$ ($\Delta T_{ad}^{peak} = 8.6K$) [265]. Otherwise, it is typically reported that hydrogenation treatment applied to this family of alloys increased T_C to RT without significantly altering MCE, even with full hydrogenation in reactive milling prior to a dehydrogenation process [330]. Partial dehydrogenation is a less optimal way to tune T_C. In the case of partially dehydrogenated $LaFe_{11.6}Si_{1.4}H_y$ alloys, two coexisting phases of different H concentration form prior to turning into one phase of single H content via thermal cycling but the two phases reinstate again upon storage near the T_C of the single phase [330]. Two distinct ΔS_M^{peak} were also reported in partially hydrided $LaFe_{11.6}Si_{1.4}H_y$ compounds prepared by electrochemical hydriding [281].

The hydrogenation of $LaFe_{11.57}Si_{1.43}$ into $LaFe_{11.57}Si_{1.43}H_{2.27}$ compound was also reported to display dramatic heating effect with time when subjected to a constant AC magnetic field and reached the ideal therapeutic range for hyperthermia treatment in less than a minute [1420]. It demonstrated unique self-regulated induction heating effect near first-order T_C since its temperature was controlled at 320 K (within the therapeutic T_{range}) due to its abrupt reduction of spontaneous magnetization at the T_C of its FOPT. The authors also found that the $LaFe_{11.57}Si_{1.43}H_{2.27}$ compound exhibits high estimated values of specific adsorption rate (*SAR*), which are more than one order magnitude larger than conventional Fe oxide-based materials observed under the same conditions. Moreover, its self-regulated heating effect within therapeutic temperature range with excellent SAR value made it stood out exceptional from the conventional superparamagnetic or ferromagnetic materials of relatively high SAR values.

6.4.2. Annealing

In the case of annealing method, grain size typically increases upon annealing and this is also reported in post-annealed $Ni_{41.98}Mn_{42.97}V_{2.08}Sn_{12.97}$ melt-spun ribbons [1421]. In addition, a decrease in lattice constants, enhanced exchange bias effect and increased martensitic transformation temperatures are observed. Large ΔS_M^{peak} of 41.6 J kg^{-1} K^{-1} ($\mu_0\Delta H$ = 30 T) near the martensitic transformation temperature was reported. On the other hand, annealing is an essential step in preparing $NaZn_{13}$-type La(Fe,Si)$_{13}$-based compounds because the 1:13 phase is difficult to be directly attained. The typical annealing process requires high temperatures for more than one week and followed by rapid quenching. Recently, an optimized annealing profile (1323 K for 24 h) has been studied for non-stoichiometric La(Fe,Co,Si)$_{13}$ composition, i.e. $La_{1.7}Fe_{11}Co_{0.8}Si_{1.2}$,

and this alloy displayed a large ΔS_M^{peak} of 7.5 J kg^{-1} K^{-1} ($\mu_0\Delta H$ = 2 T) at 271 K and a reversible magnetic phase transition with zero hysteresis [322]. The authors also reported a complex phase combination, which consisted of La(Fe,Co,Si)$_{13}$, La_5Si_3, La(Fe,Co)Si, α-Fe and La oxide phases, as compared to the stoichiometric La(Fe,Co,Si)$_{13}$ alloy.

Recently, it has been reported that increasing annealing temperatures can effectively tune MCE of $La_{0.7}Ba_{0.3}MnO_3/xTiO_2$ system (x = 0.04, 0.06), in which up to 24% increase of *RCP* could be observed by increasing the annealing temperature from 600 °C to 800 °C [527]. The authors attributed the enhanced *RCP* to the TiO_2 distribution in the doped composites, which alters the resistance of the grain boundaries affecting magnetization pinning.

6.4.3. Porous/metal foam structuring

In addition to the two above-mentioned techniques, porous/metal foam structures have been considered for enhancing the resistance to fatigue-cycling, showing potential to improve the lifetime of the material. Lyubina et al. report that by introducing porosity, the internal constraints imposed by grain boundaries could be removed, resulting in a desirable decrease of hysteresis in the field- and thermally induced magnetic phase transitions [227]. In addition, a distinct enhancement in mechanical stability during cycling was attained, leading to a fully reversible MCE despite having a lower ΔT_{ad}^{peak} than that of the bulk alloy. The authors suggested that the ideal porous materials to sharpen the transition and enhance MCE should comprise of single-crystalline particles with a uniform size distribution, based on their observations of the evolution of para- to ferromagnetic transition from magneto-optic Kerr microscopy. They also added that the magnetic and mechanical properties could be further improved through the fabrication of foams [227] and by embedding magnetic coolant particles in an elastic matrix [227].

7. Fundamental studies in magnetism using magnetocaloric characterization

Nowadays, a large majority of MCE research papers focus on the characterization of materials' properties, and the design and evaluation of possible magnetic refrigeration devices. However, in early times of this field, magnetocaloric characterization was considered a useful tool to enhance the knowledge that we had about phase transitions [1422,1423]. This fundamental aspect of magnetocaloric research was never completely forgotten but regained recent attention with the emergence of new methods for determining critical exponents or the order of phase transitions.

7.1. Critical phenomena

It has been demonstrated that the magnetocaloric magnitudes of materials with a SOPT, in the proximity of the critical region, follow power laws of the field of the type $magnitude \propto H^{\text{exponent}}$, with exponents that are related to the critical exponents of the material [80,1424] (Table 1). Therefore, it is possible to extract the values of these critical exponents by studying the field dependence of MCE. For simple cases, like a purely SOPT material wherein a single magnetic phase exists, the critical exponents obtained from the conventional Kouvel-Fisher method [1425] and those attained from the field dependence of MCE show a good agreement [1424]. However, for more complex cases, the conventional methods are not applicable, e.g. when there are several phase transitions coexisting in the same material. Nevertheless, it has been demonstrated that the scaling of MCE is capable of providing accurate values of the critical exponents even for these more complicated situations [1426].

For SOPT materials, a phenomenological construction of a universal curve was proposed [76]. This implied the possible identification of curve shape onto which all rescaled experimental data of that studied material should collapse without the prior knowledge of its critical exponents or EOS. The practical applications of this phenomenological universal curve ranges from the extrapolation of experimental data for fields and temperatures less commonly accessible in laboratories [1427] to the prediction of MCE responses of different alloys from series of materials with similar values of critical exponents, provided that a limited number of data points of those other alloys are known [1427]. The method is also applicable to addressing the noise in the measurements, which also allows the enhancement of data resolution recorded for low field [80]. In brief, the construction of the phenomenological universal curve involves: (1) normalizing each magnetic entropy change curve (each calculated for a certain value of the field) with respect to their own peak, (2) identifying the field

Table 1
Exponents controlling the field dependence of different magnitudes related to MCE ($magnitude \propto H^{exponent}$).

Magnitude	Exponent
$T_{pk} - T_C$ (not mean field)	$1/\Delta$
$T_{pk} - T_C$ (mean field)	0
$\Delta S_M(T = T_c)$	$1 + 1/\delta\,(1 - 1/\beta) = (1 - \alpha)/\Delta$
ΔS_M^{pk}	$1 + 1/\delta\,(1 - 1/\beta) = (1 - \alpha)/\Delta$
RC_{Area} or RC_{FWHM}	$1 + 1/\delta$

dependent reference temperatures (T_r) that provide a specific value of the normalized curve (which typically ranges between 0.5 and 0.7), and (3) rescaling the temperature axes of these curves as $\theta = (T - T_C)/(T_r - T_C)$.

The phenomenological construction was later theoretically justified by using scaling relations [229] and extended to the adiabatic temperature change of magnetocaloric materials [33]. It is important to note that both the universal scaling of MCE and the determination of critical exponents using MCE are restricted to the critical region of the material, i.e. for temperatures that are relatively close to the transition temperature and fields that are not too large [1428]. A detailed investigation on the applicability limits of scaling in magnetocaloric materials [1429] shows that the usual experimental conditions of fields up to 10 T are still appropriate for this type of studies. This is supported by numerous papers in which scaling is observed in many different materials by different authors [78,500,1278,1309,1430–1437]. It is also worth noticing that the demagnetizing field experienced by experimental samples, as well as the various coexisting phases in materials or the distribution of Curie temperature of the phases due to sample inhomogeneity might alter the field dependence of magnetocaloric magnitudes [55,1363,1438–1440].

7.2. Analysis of the order of phase transitions

While there were previous methods, based on only magnetic measurements, to determine the order of a thermomagnetic phase transition like the Banerjee criterion [1441], there were cases reporting that the reliability of this criterion was not appropriate as it predicted a SOPT behavior while calorimetric measurements indicated the transition was of the first order type [147]. On the other hand, the use of the universal curve enabled the demonstration, by using purely thermomagnetic data, that $DyCo_2$ undergoes a SOPT, in agreement with its calorimetric data [148]. The basis of procedure is that SOPT should collapse onto a universal curve when the magnitudes are properly rescaled, while this is not valid for FOPT. The validity of the phenomenological universal curve method, in comparison to the Banerjee criterion, is due to the latter imposing a specific EOS for the material to study the nature of its phase transition, while the method proposed by Franco et al. [80] does not rely on any EOS. Recent theoretical studies indicate that the scaling of MCE is valid, in the proximity of the critical region, for both SOPT materials and for those at the tricritical point [82].

Besides the frequent topics of MCE research (like the search for new magnetocaloric materials and, more recently, the determination of critical exponents via the scaling of MCE), there are also similar research fields with minimal magnetocaloric characterization, which could be because either these materials are less appropriate as potential refrigerants or that their main properties were not directly related to thermomagnetic properties. One of such examples is the field of skyrmions. It has recently been shown that the population of skyrmions in MnSi as a function of field can be determined from the analysis of the scaling of MCE [1442]. This compound exhibits helimagnetic order and an additional skyrmion phase for a range of magnetic field and temperature. The deviations from universal scaling allowed the authors to determine that the maximum concentration of skyrmion vortices took place for a temperature of 28.5 K and a field of 1.6 kOe.

8. Refrigerator devices

Magnetic refrigerators based on MCE are basically composed by three elements: the magnetic field source, the magnetocaloric material (the regenerator is formed by this magnetocaloric material along with the bed that contains it) and the heat exchange system.

In 2015, Kitanovski et al. [22] published an excellent book addressing the main engineering aspects and problems of magnetic refrigeration, including a deep description of the magnetic sources, heat transfer fluids and the corresponding heat transfer mechanisms, mainly for room temperature magnetocaloric applications. In this section, we briefly describe the main parameters to be considered in magnetic refrigerators as well as a comprehensive list of devices based on the magnetocaloric effect for a broad temperature range, including cryogenic temperatures.

There are several ways of performing magnetization/demagnetization of the MCE materials and that usually define the type of magnetic refrigerator: static, when the magnetic field intensity varies with time (e.g. powered by an AC current source); rotary, when the magnetic field source (or the regenerator) moves circularly around the regenerator (or the magnetic source); and reciprocating, when the magnetic field source or the MCE material performs a linear motion to create a variable magnetic field on the material. Different types of magnets are utilized for the magnetic field source, namely: superconducting magnets for low temperature applications while arrays of permanent magnets are preferred nowadays for room temperature devices.

Regarding the MCE materials used in the devices, gadolinium gallium garnet, $Gd_3Ga_5O_{12,}$ has been extensively used in the development of magnetic refrigerators working at cryogenic temperatures, with a more recent appearance of Laves phases, while Gd metal has been considered the reference material for those operating close to room temperature. In the recent years, room temperature devices also frequently tend to include $La(Fe,Si)_{13}$ type materials.

Heat is continuously stored and released in the heat exchangers, with a heat transfer fluid to transport the heat between exchangers. He gas is commonly used as heat transfer fluid to reach low temperatures for He or H_2 liquefaction or even lower temperatures, while water, with some antifreeze additives, is generally used in the development of room temperature prototypes. Liquid nitrogen can be found for applications at intermediate temperatures (O_2 or air liquefaction) or as an additional step for cryogenic temperatures.

In this section, we will categorize devices into two groups, depending if they are developed for cryogenic or room temperature applications. Prototypes will be presented in a chronological order.

8.1. Low temperature devices

In 1953, Collins et al. built a reciprocating adiabatic demagnetization refrigerator (ADR), whereby its magnetic material composed of two separate paramagnetic salt samples (Iron-Ammonium-Alum). The upper sample was initially magnetized by a magnetic field of 0.185 T, which was supplied by a permanent magnet. Next, this cold sample was moved out of the magnetic field and then kept in thermal contact with the lower sample until a thermal equilibrium between both samples was attained, and subsequently the cycle was started again. The authors reported a minimum temperature of 0.73 K for this device [1443].

In 1976, Rosenblum et al. presented a device based on that reported by Collins in 1953. In the new design, a magnetic field of 0.35 T was supplied by an alternate superconducting solenoid in its center gap, where a cylinder filled with $CeMn_{1.5}(NO_3)_6$ $12H_2O$ and Au powders were placed. Experimental results showed that this device attained a minimum temperature of around 10 mK [1444].

In 1977, Pratt et al. developed a rotary refrigerator using adiabatic demagnetization cooling. $Gd_2(SO_4)_38H_2O$ powders were used as the magnetic refrigerant material and were compacted to fill the rim of a wheel (wherein they were to be placed), which would be rotated through the high and low magnetic field regions generated by two permanent magnets. For a wheel operation frequency of 0.5 Hz, a cooling power of 150 mW and a minimum temperature of 2.1 K were obtained [1445].

In 1978, Steyert presented a rotary magnetic refrigerator, which employed a superconducting magnet to supply a constant magnetic field of 5 T and a paramagnetic Gd compound as the working material, which was placed on the surface of a wheel. As the wheel rotates, part of it moves into the region where the field is applied. Using He gas as a heat transfer fluid, a cooling power of $\sim$1 kW was measured with a working temperature of around 2 K [1446].

In 1979, Barclay presented a reciprocating magnetic refrigerator. This device, operating in a temperature range from 4.2 to 2.2 K, could only perform two cycles at a frequency of 0.016 Hz, showing a cooling power of 52 mW [1447].

A year later, Barclay developed a rotary type magnetic refrigerator operating under Carnot cycle. $DyPO_4$ single crystal was used as the working material, rotating inside the gap of a couple of coils, which generated a constant magnetic field of 7 T. The movement of the crystal was performed in such a way that its c-axis rotated perpendicularly to the direction of the magnetic field to perform the magnetization/demagnetization processes of the working material. He gas was used as the heat transfer fluid to transfer the heat between the reservoirs. This device was experimentally shown working within a temperature range of 20–4 K and generated a cooling power between 1 mW to 1W, depending on its operational frequency (e.g. 1 W of cooling power could be obtained with a frequency of about 2 Hz) [1448].

In 1981, Delpuec et al. presented a reciprocating magnetic refrigerator, in which $HoPO_4$, $Gd_2(SO_4)_3$ and $Gd_3Ga_5O_{12}$ were used as the magnetocaloric working materials. The magnetocaloric refrigerant moves in and out of a superconducting magnet, which gives a magnetic field of 5 T. Both the working material and magnet were immersed in liquid He, which acts as a refrigerant for the magnet and as a heat transfer fluid. When $HoPO_4$ was used as the working material, experimental results showed that for an operational frequency of 0.3 Hz, a temperature difference of 2.1 K and a cooling power of 0.12 W were obtained, reaching a temperature of 1.98 K. In the case of $Gd_2(SO_4)_3$, a working temperature of 2.1 K with a cooling power of 0.36 W were observed, reaching a temperature of 1.67 K. For $Gd_3Ga_5O_{12}$, a temperature of 1.8 K with a cooling power of 1.2 W were measured for an operation frequency of 0.95 Hz [1449].

In 1984, a Carnot type magnetic refrigerator was presented by Numazawa et al. In this device, $Gd_3Ga_5O_{12}$ single crystal in a cylindrical shape was located in the center gap of a superconducting magnet, whereby the magnetization/demagnetization of the working material was due to the switching on/off the magnetic field. He gas was used as the heat transfer fluid to carry the heat between the material and the heat exchange system. The working material reached temperatures below 4.2 K, thus, it was used for liquefaction of He [1450].

In 1985, Matsumoto et al. presented a reciprocating magnetic refrigerator operating under Carnot cycle. A superconducting magnet, supplying a magnetic field of 5 T, was operated in switch on - off mode to magnetize and demagnetize the magnetocaloric material. Two pieces of $DyAl_{2.2}$ were used as the magnetocaloric material and He gas as the heat transfer fluid. Experimental results showed that this device could provide a working temperature in the range from 77 K to 20 K [1451].

In the same year, Nakagome et al. developed a magnetic refrigerator using a cylinder working material, which could be formed by $Gd_3Ga_5O_{12}$, Er-Ni alloy, $Dy_3Al_5O_{12}$, $Gd_3Al_5O_{12}$, $GdPO_4$ or $Dy_2Ti_2O_7$ compounds. Its magnetic field was applied by superconducting coils powered by AC current source, which magnetize and demagnetize the working material placed in the center gap of the coils. Using He gas as the heat transfer fluid, this device allows the liquefaction of He [1452].

In addition, a magnetic refrigerator operating under Carnot cycle was developed in 1985. In this device of Hakuraku et al., a superconducting magnet with a maximum magnetic field of 3T was operated by switching on and off with a frequency of 0.3 Hz. Using $Gd_3Ga_5O_{12}$ as the working material, a cooling power of 0.6 W was obtained with a temperature of 1.8 K [1453].

Barclay et al. presented a rotary magnetic refrigerator working under Carnot cycle in the same year. $Gd_3Ga_5O_{12}$ placed on the rim of a wheel rotates through the gap of superconducting Helmholtz solenoids, and He gas was used as the heat transfer fluid in the hot and cold ends of the wheel. Tests were performed for applied magnetic fields of 4 and 5.6 T over the working

material rotating at a frequency of 0.08 Hz. Results showed a cooling power of ~0.9 and ~1.2 W, reaching a temperature below 4.2 K [1454].

In 1986, a rotary magnetic refrigerator operating under Carnot cycle was presented by Hakuraku et al. The working material consisted of 12 pieces of $Gd_3Ga_5O_{12}$ placed surrounding the rotor. A superconducting magnet was used to apply a magnetic field of 3 T into the bore where the working material rotates. Operating with a frequency of 0.4 Hz, a cooling power of 1.79 W was obtained, reaching a temperature of 1.8 K [1455].

In the same year, Hakuraku et al. presented a rotary magnetic refrigerator, working under Carnot cycle, wherein 8 disks of $Gd_3Ga_5O_{12}$ were placed equidistant on a cylinder. The cylinder was located inside of three superconducting Helmholtz coils, which generate a constant magnetic field of 2.94 T and rotate around the cylinder with the working material. Operating with a frequency of 0.2 Hz a cooling power of 1.5 W was obtained, reaching a minimum temperature of 1.9 K [1456].

Researchers from Massachusetts Institute of Technology presented a Carnot type magnetic refrigerator in 1986. The regenerator was formed by a set of parallel plates of $Gd_3Ga_5O_{12}$ in a cylindrical configuration and located in the bore of the magnet system, which consisted of a superconducting solenoid operating in AC mode. He gas was used as the heat transfer fluid driving heat between the heat exchangers and the regenerator. Test performed varying the magnetic field between 1 and 4 T showed a cooling power of 0.40 W, reaching a temperature of 3.9 K [1457].

Also in 1986, Nakagome et al. developed a reciprocating magnetic refrigerator which used $Gd_3Ga_5O_{12}$ single crystal in a cylindrical shape as the regenerator. It was moved in and out of the center gap of a superconducting magnet, which supplied a magnetic field of 4.5 T. Using He gas as the heat transfer fluid, experimental results showed a cooling power of 0.95 W under an operational frequency of 0.38 Hz, reaching a temperature below 4.2 K [1458].

In 1988, Nakagome et al. presented a rotary magnetic refrigerator which operated under a reverse Carnot cycle. Fourteen monocrystals of $Gd_3Ga_5O_{12}$, the working material, were contained in a disk that rotates in the gap of a superconducting magnet (a magnetic field gradient between 4.5 and 1.1 T was generated within the gap where the disk rotates). With an operation frequency of ~0.01 Hz, experimental results showed that the device developed a cooling power of 0.12 W in the working temperature range from 11.5 to 4.2 K [1459].

In 1991, Kuzmin et al. built a rotary Carnot type magnetic refrigerator. This device was formed by a superconducting solenoid and the working material in the shape of cylinder in the center of the gap. A $DyAlO_3$ monocrystal was used as the working material, which rotates from its b axis to the c axis. This motion of the monocrystal enabled its magnetization and demagnetization depending on the instantaneous orientation of the easy magnetization axis. Tests performed showed that this device worked within a temperature range of 20 and 4.2 K [1460].

In 1992, Filin et al. presented a static type magnetic refrigerator operating under Carnot cycle. The device consisted of a $Gd_3Ga_5O_{12}$ monocrystal as the working material, which was placed in the bore of pulsed superconducting magnet, and He gas as the heat transfer fluid. Experimental results showed that the device worked in the temperature range of 4.2–1.8 K [1461].

In the same year, DeGregoria et al. presented a reciprocating magnetic refrigerator operating under Brayton cycle. Its magnetic system consisted of a superconducting solenoid which could move in a reciprocating mode. The regenerator was formed by two beds filled with $Er_XGd_{1-X}Al_2$ particles with a cold heat exchanger placed between them and placed in the gap of the solenoid. He or N_2 gas were used as the heat transfer fluid depending on the working temperature range of the device. Tests were performed for different magnetic fields and results showed that the device reached a minimum temperature of around 4 K which gave the maximum temperature change of around 2 K for an applied magnetic field of 7 T [1462].

In 1994, Bezaguet et al. developed a magnetic refrigerator operating in a quasi Carnot cycle between 4.5 and 1.8 K. $Gd_3Ga_5O_{12}$ single crystal was used as the working material and its magnetization/demagnetization process was performed by a superconducting magnet which supplied a magnetic field of 3.5 T. Liquid He was used as the heat transfer fluid. Estimations showed that this device could allow a cooling power of about 25 W [1463].

In the same year, Jeong et al. presented a Carnot type tandem magnetic refrigerator. This device consisted of two magnetic systems, each filled with $Gd_3Ga_5O_{12}$ particles, which constitute the working material. A superconducting magnet supplied a magnetic field varying between 0.4 and 2.8 T in the bore where the working material was placed. Helium-3 gas was used as the heat transfer fluid carrying the heat between the heat exchangers through the working material. For switching the magnetic field with a frequency of 0.4 Hz, a cooling power of 12 mW per each magnetic system, reaching a temperature of 1.8 K were reported [1464].

In 1995, Zimm et al. presented a reciprocating active magnetic regenerator (AMR) refrigerator. The regenerator was composed by two beds filled with ErNi and was moved in and out of a superconducting solenoid, which supplied a constant magnetic field of 3 T. He gas, below 0.3 atm of pressure, was used as the heat transfer fluid of this device. Experimental tests showed a maximum cooling power of 1.6 W at 3.5 K [1465].

In the same year, Kashani et al. developed a Carnot type magnetic refrigerator, which used two flat pieces of $Gd_3Ga_5O_{12}$ separated by a small gap, as its working material. When the material was isothermally magnetized by a magnetic field of 6.5 T, the gap was filled with He gas from the high temperature heat-end, and when the material was isothermally demagnetized the gap was filled with liquid He from the cold-end. Experimental results showed a maximum cooling power of 30 mW operating from 9.6 to 1.8 K [1466,1467].

Also in 1995, Satoh et al. developed a magnetic refrigerator, which used Pb and $ErNi_{0.9}Co_{0.1}$ as the working materials, and obtained a cooling power of 1.5 W for a working temperature of 4.2 K [1468].

In 1996, Zimm et al. reported a design similar to that described above [1465] but using $GdNi_2$ particles instead of ErNi to fill both beds and a larger magnetic field of 7 T. A temperature span of 38 K was obtained [1469].

In 1996, Ohira et al. presented a magnetic refrigerator operating under Carnot cycle in which a cylindrical $Gd_3Ga_5O_{12}$ monocrystal was used as the working material and a Gifford-McMahon refrigerator as a hot reservoir. When the working material was isothermally magnetized with an applied field of 8 T, the material was then placed in thermal contact with the hot reservoir, and when the material was isothermally demagnetized, it was taken out from the reservoir. Experimental results showed that the device developed a cooling power of 0.21 W at a temperature of 20 K, when operated at a frequency of 0.002 Hz [1470].

In 1998, Hall and Barclay presented a rotary AMR refrigerator, wherein its regenerator consisted of a ring filled with the magnetocaloric material. A superconducting magnet supplied a constant magnetic field and He gas was used as its heat transfer fluid. During the rotation of the ring, only one part of it enters the region where the field is applied. Calculations showed that the device was capable of producing efficiencies of around 60% for a temperature span from 100 to 300 K [1471].

In 2000, Yayama et al. developed a static magnetic refrigerator operating under Brayton cycle and working along a conventional gas cooling cycle. ErNi alloy was used as its working material and a superconducting magnet powered by AC current source was used to produce a maximum magnetic field of 5 T. He gas was used as heat transfer fluid to transport the heat between the exchanger and as gas for the conventional cycle. The device showed an enhanced cooling power with respect to the single gas cooling apparatus, obtaining 0.36 W and reaching a temperature of 4 K. Finally the authors proposed to change its magnetic source to a mobile array of permanent magnets for room temperature devices [1472].

In 2001, Mullard Space Science Laboratory from UK developed an ADR for ultra low temperatures. This device consisted of: a paramagnetic material which was located in the bore of the magnet; the magnetic field source that can be formed by an array of permanent magnets or a superconducting magnet; a heat switch which cooled the paramagnetic material and extracted heat from the paramagnetic material before demagnetization; and a cold bath which provided the temperature for operation. The operation process of the ADR starts with the isothermal application of the magnetic field, followed by the adiabatic reduction of the magnetic field to attain a lower temperature. The next step involves the isothermal demagnetization of the material. Finally, the paramagnetic material absorbs heat to reach the conditions of the initial stage. This device realizes a double ADR, thus the process consisted of two-step cooling, in fact the first ADR acts as lower bath temperature and cools the second ADR. Tests performed with double ADR showed that the device allowed refrigeration in the temperature range from 4 to 0.01 K [1473].

In 2006, Yamiya et al. presented a magnetic refrigerator device for H_2 liquefaction operating under Carnot cycle. A superconducting magnet was used to apply a magnetic field of 6 T to a vertically moving working material (DyGaAl alloy) at a frequency of 0.71 Hz. H_2 gas was used as the heat transfer fluid and the results showed a maximum cooling power of 37.4 W attained for this device [1474].

In 2008, Numazawa et al. presented a reciprocating magnetic refrigerator for H_2 liquefaction. Its regenerator was formed by $Dy_{2.4}Gd_{0.6}Al_5O_{12}$ sheets, filling the interior of a non-magnetic cylinder, which moves in and out of the superconducting magnet (6 T) and H_2 gas was used as the heat transfer fluid. Tests performed with a frequency of ~0.02 Hz show a cooling power of 0.3 W for a working temperature between 77 and 20 K [1475].

In 2009, Matsumoto et al. reported a reciprocating magnetic regenerator, based on the device presented by Numazawa in 2008, but the precooling refrigerator was changed by an AMR refrigerator in the new device [1476].

In 2013 Numazawa et al. presented a reciprocating device for nitrogen liquefaction. In this device the regenerator was formed by three beds, each one filled with three magnetocaloric materials with different Curie temperatures ($Gd_5(Ga_{1-X}Fe_X)O_{12}$, $HoAl_2$ and $DyAl_2$). He gas was used as heat transfer fluid. Experimental results showed a range of working temperature from 77 to 20 K [1477].

Also in 2013, Kim et al. presented a two-step magnetic refrigerator. The regenerator consisted of two beds filled with different magnetocaloric materials. The first bed was filled with $GdNi_2$ and $Dy_{0.85}Er_{0.15}Al_2$ while the second with $Dy_{0.5}Er_{0.5}Al_2$ and $Gd_{0.1}Dy_{0.9}Al_2$ particles. Each bed was located inside a superconducting magnet operated in AC mode, which supplied a magnetic field peak of 4 T with a frequency of 0.1 Hz, each magnet. Experimental results showed that this device reached a temperature of 24 K [1478].

Additional devices working at cryogenic temperatures are collected in Table S8 of the Supplementary Material.

8.2. Devices working close to room temperature

The first person to use Gd element to build a laboratory scale device for magnetic refrigeration was Brown in 1976 [9,1479]. This reciprocating device used 0.175 kg of Gd disks separated by fine wires, and a mixture of water and ethyl alcohol as heat transfer fluid. The magnetocaloric material moved in and out of the gap of a superconducting magnet, which allowed an alternating magnetic field of maximum value of 7 T. A maximum temperature span of 47 K was obtained after fifty cycles of operation.

In 1978, after Brown's prototype, Steyert proposed the principle of the active magnetic regeneration, AMR. He presented a rotary device, in which Gd was placed on the rim of a wheel, rotating in and out of the magnetic source. Working with a frequency of 1 Hz, this device reached a temperature span of 14 K [1446,1480].

In 1987, Kirol and Dacus presented a design of rotary heat pump that was built using 125 coaxial disks of Gd, forming a cylinder with a mass of 0.270 kg. A magnetic field of 0.9 T produced by an array of permanent magnets of Fe-Nd-B, was used to get a working temperature span of 11 K while operating in an Ericsson type magnetic cycle [8,1481].

Green et al. in 1990 reported the construction of a reciprocating magnetic refrigerator using beds of Gd and Tb as the AMR and nitrogen gas as the heat transfer fluid. A superconducting magnet was used to apply a maximum magnetic field of 7 T and, with very low frequency, a temperature span of around 24 K was obtained after operating for several hundreds of cycles [1482].

New progresses in this field were reported in 1997, when Zimm et al. presented a reciprocating magnetic refrigerator that used Gd spheres as the magnetocaloric material, placed on beds. This device consisted of a superconducting magnet, which allowed for a maximum magnetic field of 5 T, and operated over 18 months without significant problems, indicating an improvement in the design as compared to earlier devices, which were only typically tested for few days. This equipment was able to produce a maximum cooling power of 600 W with a temperature span of 10 K [1483,1484]. Almost one year later, an enhancement in the performance of the device was reported, obtaining a larger temperature span of 38 K for a maximum applied magnetic field of 5 T despite a lower cooling power of 100 W [14].

In 2000, Bohigas et al. reported the development of a rotary magnetic refrigerator, which used permanent magnets as the magnetic field source. In this design, Gd ribbons were placed on the surface of a plastic wheel, which rotated around the pole pieces of the magnet at very low frequencies (between 0.06 and 0.8 Hz) and olive oil was utilized as the heat transfer fluid. In the optimal arrangements, the permanent magnets allowed for a maximum magnetic field of 0.9 T, leading to a maximum temperature span of 5 K [1485].

In the same year, Chubu Electric and Toshiba Company presented a reciprocating magnetic refrigerator, which employed Gd spheres forming beds as the magnetocaloric material and a superconducting magnet for a magnetic field of 4 T. The maximum cooling power obtained was 100 W with a temperature span of 21 K [1486].

In 2001, a new reciprocating device was presented by Rowe and Barkley from University of Victoria. It was composed of a superconducting solenoid, which generated a maximum magnetic field of 2 T, and AMR beds of layers of Gd and $Gd_{1-X}Tb_X$ alloys in the form of grains. This device was reported to generate a maximum temperature span of 14 K [1487].

In the same year, Astronautics Corporation of America developed a new rotating magnetic refrigerator, wherein its AMR was composed of three sets of beds filled with layers of Gd, Gd and $Gd_{94}Er_6$ alloy spheres (sizes between 0.25 and 0.5 mm) and only $La(Fe_{0.88}Si_{0.12})_{13}H_{1.0}$ particles in a wheel configuration. In this setup, the magnetocaloric material rotates through the gap of the magnetic source, which comprised of Fe-Nd-B permanent magnets yielding a maximum magnetic field of 1.5 T. Several tests using water with inhibitor as the heat transfer fluid showed a maximum temperature span of 18 and 24 K for a working frequency of 1 and 4 Hz respectively, generating a maximum refrigeration power of 50 W when only Gd layers were used. In the case of using Gd and Gd(Er) alloys, the temperature span and cooling power attained were 27 K and 25 W respectively. If the AMR consisted of solely La-Fe-Si-H intermetallics to fill the beds, lower values are expected. Finally was concluded that successive layers with different Curie temperatures were necessary to enhance the performance of the regenerator [1488–1490].

In 2002, a new superconducting regenerative magnetic refrigerator was presented by Blumenfeld et al. In this device, without moving parts, its magnetic field was supplied by an array of cryocooled coils, which allowed for a maximum magnetic field of 1.7 T. The regenerative bed was formed by Gd powder particles filling a cylinder, located inside of the coils, where the magnetic field was alternatively applied and removed. From the various tests performed, the best result showed a maximum temperature span of 15 K for cold and heat end temperatures of 293 and 308 K respectively [1491].

A group from Nanjing University in China also built a reciprocating magnetic refrigerator in the same year. The magnetocaloric material was placed in two beds, filled with Gd and Gd-Si-Ge or $Gd_5Si_{1.985}Ge_{1.985}Ga_{0.03}$ alloys in powder form, and the magnetic field was applied by an array of Halbach type magnets, which led to a magnetic field of 1.4 T. In this refrigerator, water was used as the heat transfer fluid. Results published show a maximum temperature span of 23 K when operating near room temperature around 298 K [8,1492].

In 2003, Tokyo Institute of Technology in collaboration with Chubu Electric Company developed a rotary magnetic refrigerator. The magnetocaloric refrigerant composed of four types of Gd-based alloys ($Gd_{0.91}Y_{0.09}$, $Gd_{0.84}Dy_{0.16}$, $Gd_{0.87}Dy_{0.13}$ and $Gd_{0.89}Dy_{0.11}$ with Curie temperatures: 277, 278, 280 and 283 K respectively) for a total of 1 kg of material. An array of Fe-Nd-B permanent magnets rotates around the magnetocaloric beds, supplying a variant magnetic field and a maximum intensity of 0.77 T. Using water as the heat transfer fluid, each bed was filled with these alloys positioned in an ascending order of their Curie temperatures to enhance the efficiency of the magnetocaloric beds. The experimental results showed a maximum cooling power and temperature span of 60 W and 8 K respectively, with a very low operation frequency of 0.4 Hz [1493].

In the same year, a group from Grenoble in France developed a reciprocating magnetic refrigerator. This prototype composed of an array of Halbach type permanent magnets (a maximum magnetic field of 0.8 T) and 0.230 kg of Gd sheets, piled to form the bed of magnetocaloric material, through which water was allowed to pass as heat transfer fluid. They reported a maximum cooling power of 8.8 W and a temperature span of 4 K, with an operation frequency of 0.5 Hz [1494,1495].

In 2004, groups from Universities of Victoria and Quebec, in Canada, developed a reciprocating magnetic refrigerator, which employed an array of permanent magnets as the magnetic field source for a maximum field intensity of 2 T. The regenerator consisted of two cylindrical beds filled under three different configurations: with 0.090 kg of Gd, 0.045 kg of Gd and 0.040 kg of $Gd_{0.74}Tb_{0.26}$ alloys and with 0.135 kg of Gd, $Gd_{0.74}Tb_{0.26}$ and $Gd_{0.85}Er_{0.15}$. In all cases, He gas was used as the heat transfer fluid. Experimental results reported a maximum temperature span of 16 K for the bed with Gd while

20 K for the bed of Gd and $Gd_{0.74}Tb_{0.26}$ alloy for an applied magnetic field of 2 T. For the beds composed of three materials and an applied magnetic field of 1.5 T, when the working temperatures were 301 and 299 K, the maximum temperature span of 37 and 44 K were obtained at the operational frequencies of 0.65 and 1 Hz, respectively. For an applied magnetic field of 2 T, the measured temperature spans were 46.8 and 51 K for frequencies of 0.65 and 1 Hz respectively [1496,1497].

The University of Quebec presented a reciprocating magnetic refrigeration device, using a superconducting magnet to supply a magnetic field of 2 T and its regenerator formed by a layered bed of Gd-Tb alloy. The reported experimental results showed a maximum temperature span of 14 K [1496].

In the same year, a group from Washington State University presented another reciprocating magnetic refrigerator. This equipment comprised of a bed of Gd powder as the magnetocaloric material and an array of permanent magnets, which provided a magnetic field of 2 T. The maximum temperature span reported was 5 K [1498].

In 2005, the company Cooltech Applications in France reported the construction of a rotary magnetic refrigerator, which composed of eight beds of magnetocaloric material inserted in a thermally isolated disc. An assembly of rotating Halbach type magnets of Fe-Nd-B alloy provided a magnetic field of 1.47 T in the air gap. Each bed was composed of fifteen sheets of Gd plates, with a total mass of 0.165 kg, where the heat exchanger fluid flowed between them. The experimental results showed that the maximum cooling capacity obtained ranged between 100 and 360 W depending on flow rate of the fluid [1499].

In the same year, scientists from Xi'an Jiaotong University in China developed a reciprocating magnetic refrigerator working at room temperature. A water cooled electromagnet was used to provide a maximum magnetic field of 2.18 T, and the AMR was built using Gd and $Gd_5Si_2Ge_2$ alloys. Experimental results performed at different temperature ranges and flowrates of the heat transfer fluid showed a maximum cooling power of 18.7 W [1500,1501].

Also in 2005, another reciprocating magnetic refrigerator was developed at the Graduate School of Engineering of the Hokkaido University. In this device, Gd was used as working material to fill the beds and distilled water as heat transfer fluid. The magnetic field was supplied by a permanent magnet with a maximum field of 2 T. At the operation frequency of ~0.2 Hz, a maximum temperature span of 10 K was reported [1502].

A magnetic refrigerator was presented by Kim et al. also in 2005. In this device, its regenerator was a block of $Gd_5(Si_2Ge_2)$ with a Si wafer containing microchannels for the flow of the heat transfer fluid. An electromagnet was used to apply a variably magnetic field with maximum value of 1.5 T and perform the magnetization/demagnetization process of the magnetocaloric material. Tests showed a maximum temperature change of 7 K for a temperature of 258 K was attained [1503].

In 2006, the Chinese Academy of Science developed a prototype with two cylindrical reciprocating active regenerative beds, which were filled with a total of 1.1674 kg of Gd particles. The magnetic field was supplied by an array of two permanent magnets, yielding a maximum magnetic field of 1.5 T. Several tests were performed by varying the operating frequency between 0.4 and 1.0 Hz, as well as the length of the piston that moved the exchange fluid (helium gas). Results show a maximum cooling power of 51.3 W and a temperature span of 18.2 K for a length of 0.11 m, while for a length of 0.20 m, values of 25.2 W and 11.0 K were reported [1504].

In the same year, Tokyo Institute of Technology and Chubu Electrics, performed an update of their device that was formerly developed in 2003. In the new rotary type refrigerator, besides an increase in the size of the equipment, eddy current losses were reduced, enhancing its cooling power. The applied magnetic field was also enhanced from 0.77 T to 1.1 T by changing the pole pieces for only one permanent magnet in V form. The magnetocaloric material used for the beds was retained like in the initial design (Gd) but the exchange fluid flowed in circumferential form in the new device instead of the former axial configuration. Tests performed on this device showed a maximum cooling power of 560 W [1505,1506].

Also in 2006, University of Applied Sciences of Western Switzerland developed a rotary magnetic refrigeration device for air conditioning technology. This equipment was presented in The World's Largest Industrial Fair at Hannover, Germany (2006), and they won the first prize of the Swiss Technology Award. It utilized air as the working fluid and a magnetic fluid with Gd particles as the magnetocaloric material to fill the bed, which was ring-shaped. This bed rotates inside the gap of a permanent magnet assembly, which provided a magnetic field of 0.8 T over half of the rotating ring, so the magnetic field was applied only on half of the bed [8,1507].

In the same year, Baotou Research Institute of Rare Earth in China presented a reciprocating magnetic refrigerator. The AMR bed was filled with particles of Gd (0.750 kg) and $LaFe_{10.97}Co_{0.78}Si_{1.05}B_{0.2}$ (0.200 kg) alloys and its magnetic field was supplied by an array of permanent magnets yielding a maximum field of 1.5 T. Using alkalescent water solution as the heat transfer fluid, a maximum temperature span of 5 K and a cooling power of 20 W upon 45 min of operation were obtained [1508,1509].

In 2007, a new rotary magnetic refrigerator was built by Astronautics Corporation of America. The device consisted of a base made of twelve static beds placed in the form of parallel disks filled with Gd as magnetocaloric material, with 0.946 kg of Gd per bed, and an array of rotating permanent magnets with a maximum applied magnetic field of 1.5 T. Tests performed, using water with inhibitors as heat transfer fluid and an operational frequency of 4 Hz, showed a maximum temperature span of 12 K with a cooling power of 220 W [1510].

Also in 2007, researchers from University of Victoria developed a rotary magnetic refrigerator to study different types of magnetic refrigerants in different configurations. This refrigerator consisted of an array of Fe-Nd-B permanent magnets: one external part of this array was static while another internal part could rotate, yielding a maximum magnetic field of 1.47 T. Water was used as the heat transfer fluid and its operational frequencies were between 0 and 4 Hz. Using cylindrical regen-

erators filled with Gd flakes and varying the operation frequency, the temperature span increases with frequency, reaching a maximum of 13.2 K [1511].

In 2007, Chelyabinsk State University built a rotational type magnetic refrigerator. The wheel containing Gd and NiMnGa alloys rotated with an operational frequency between 1 and 10 Hz, through the gap of the permanent magnet, which was formed by Fe-Nd-B pieces in a Fe yoke and supplied a magnetic field of 1 T. A cooling power of 40 W was predicted and presented [1512].

In the same year, Sichuan University in China designed a rotary magnetic refrigerator. Its regenerator consisted of a wheel divided in 36 sectors, wherein each was filled with 1 kg of Gd particles as the magnetocaloric material, and was allowed to rotate with a frequency between 0.1 and 0.7 Hz. Water was used as the heat transfer fluid and its magnet unit was a Halbach array of permanent magnets of Fe-Nd-B and Fe-Co-V, which supplied a maximum magnetic field of 1.5 T. This device provided a maximum temperature span of 11.5 K [1513].

In addition, Riso National Laboratory in Denmark developed a reciprocating magnetic refrigerator in the same year. An array of Gd plates was used as refrigerant, which could move into the gap of a ring-shaped Halbach type magnet (produced a maximum 1.2 T). For operation frequency below 1 Hz, a temperature span of ~9 K was predicted [1514].

INSA Institute and Cooltech Applications Company in France developed a rotary refrigerator prototype also in 2007. The device consisted of four static beds of Gd placed on a ring, water as the working fluid and a rotary array of permanent magnets, which applied a maximum field of 1.3 T [1515].

In 2008, researchers of Hokkaido University in Japan developed a reciprocating AMR equipment composed of two mobile permanent magnets, which led to a maximum magnetic field of 2 T in the middle of its gap, where the magnetocaloric material (a pack of 0.0334 kg Gd particles) was located during operation. This equipment was tested under different conditions using either air or water as the heat transfer fluid. Results show that for an optimal operation, a larger flow rate was needed for air than that used for water [8,1516].

Also in 2008, Bahl et al. developed a reciprocating AMR refrigerator. The regenerator consisted of a plastic cylinder, which contained parallel sheets of Gd and moved laterally in and out of the electromagnet (magnetic field of 1.4 T). The magnet was orientated with its magnetic field parallel to the plane of the Gd sheets. Several heat transfer fluids were used and results showed that for operation frequencies between 0.06 and 0.08 Hz, temperature spans of 6.9, 6.4, 6.2 and 6.0 K were measured for distilled water and ethanol, ethylene glycol, propylene glycol and olive oil respectively [1517].

In 2009, Hirano et al. built a reciprocating AMR device with a mobile bed containing particles of magnetocaloric material. The magnetic field was produced by an array of two opposing permanent magnets, which allowed for a maximum field of 2.3 T. The authors reported a temperature span of ~2 K when La-Fe-Si alloy was used [1518].

In the same year, South China University of Technology reported a reciprocating AMR system with its regenerator formed by two rectangular beds with a separation between them filled with Gd particles as the magnetocaloric material. An array of moving Fe-Nd-B permanent magnets led to a maximum magnetic field of 1.5 T in the center of the gap, where the two beds were located, performing a double regenerator cycle. Only theoretical studies on the dependence of the temperatures of hot and cool heat exchangers on the refrigeration power had been performed, showing that its cooling power decreased as the hot heat exchanger temperature increased [1519].

Cooltech Applications in France also built a reciprocating AMR in 2009. The prototype was formed by an array of 37 parallel plates of Gd, with a spacing between them to allow the flow of the passing heat transfer fluid and a Halbach type array of three Fe-Nd-B magnets, which supplied a maximum magnetic field between 0.8 and 1.1 T in the gap. Tests were performed varying the temperature of the heat and cool exchangers and showed that with an initial temperature of ~293 K, a temperature span of 16.1 K could be obtained [1520].

In the same year, researchers of Campinas State University in Brazil built a wheel-type AMR for a rotary magnetic refrigerator. The wheel, containing six beds filled with 0.160 kg Gd each, rotated inside the gap of the magnet but only half of it was inside the field region. The magnetic unit was an electromagnet, which supplied a magnetic field in the range of 0.24–2.30 T. Results of this device using ethyl alcohol as the heat transfer fluid show that the maximum temperature span obtained was 11 K upon about 20 min of operation at a frequency of 0.4–0.5 Hz [1521].

In 2009, Dupuis et al. developed a new reciprocating AMR to study the influence of demagnetizing factor and packing ratio of the magnetocaloric material, operational frequency, and flow rate of the exchanger fluids on the performance of the device. Gd plates were piled into a cylinder with its axis oriented parallel to the magnetic field. A Halbach array supplying a magnetic field of 0.8 T was moved to magnetize and demagnetize the magnetocaloric material. Results from the different tests showed that a maximum temperature span of 7.8 K was obtained with a heat transfer fluid flow rate of 3 ml/s [1522].

In the same year, Korea Advanced Institute of Science and Technology built a reciprocating magnetic refrigerator. Gd particles were used to form the bed that moved with a maximum frequency of 1 Hz in and out of the magnetic field area, which was generated by sixteen segments of permanent magnets in the shape of a cylinder, yielding a magnetic field of 1.58 T in the center of the gap. A maximum temperature span of 16 K was reported when using He gas as the heat transfer fluid [1523].

Adopted from their previous prototype, RISO DTU in Denmark developed a new device in 2009 by changing the regenerator. The bed was formed by parallel plates of $La_{0.67}Ca_{0.33-x}Sr_xMnO_3$ ($0 \leq x \leq 0.33$), whereby the size of the regenerator could be modified and the heat exchange fluid was a mixture of water and ethanol [1524].

Also in 2009, University of Applied Sciences of Western Switzerland built a reciprocating equipment to characterize different magnetocaloric materials. The magnetic field was supplied by Fe-Nd-B permanent magnets, which led to a maximum

field of 2 T in the air gap. The magnetocaloric material was placed into a holder, which was displaced in and out of the magnetic field region. Pulsed air was used as a heat transfer fluid. $LaFe_{11}Co_{0.9}Si_{1.1}$ and Gd were used to test the equipment measuring the temperature change on the magnetocaloric material under adiabatic and non-adiabatic conditions and showed that the device could determine the temperature change of the tested materials for different applied magnetic fields [1525].

Furthermore, University of Genoa in Italy presented a linear reciprocating magnetic refrigerator in the same year. Its magnetic field was supplied by an array in a crossed form of ten Fe-Nd-B magnets surrounded by a soft magnetic material, which led to a field of 1.55 T in the air gap. Two regenerators, each filled with 0.400 kg of Gd particles, were attached to a plastic shuttle for moving them in and out of the magnetic field region. A mixture of water and ethanol was employed as the heat transfer fluid with a maximum operative frequency of 0.2 Hz. Preliminary results showed a maximum temperature span of around 5.0 K and a degradation of the performance with increasing frequencies [1526,1527].

In 2009, Tura and Rowe improved their initial rotary prototype that was developed two years ago. In this new device, its regenerator was filled with 0.055 kg of Gd particles and its cold and hot end exchangers were modified to reduce dead volume. Tests performed showed a temperature span of 29 K, which was larger than that obtained from the previous device [1528].

University of Ljubljana in Slovenia developed a rotary magnetic refrigerator in 2009. This device consisted of a regenerator cylinder with 34 beds filled with ~0.600 kg Gd plates and operated at frequencies up to 4 Hz. The cylinder, which consisted of a stationary Fe soft magnetic alloy core, rotates inside a structure of a set of four permanents magnets. With the geometry of the two magnetic circuits, a magnetic field in the range of 0.05–0.98 T was attained in the air gap. Theoretical studies on this device predicted a temperature span of approximately 7 K [1529].

In 2010, Trevizoli et al. developed a reciprocating device with static AMR. The magnetic field was provided by a Halbach array of Fe-Nd-B permanent magnets, which led to a maximum field of 1.65 T in the air gap. This Halbach array moved linearly to magnetize and demagnetize the AMR during the cycle. The AMR consisted of an array of twenty-eight parallel sheets of Gd (total mass of 0.1954 kg) with a space between them for the flow of the heat transfer fluid. Initial results showed a temperature span of 4.4 K and a cooling power of 3.9 W [1530].

In the following year, researchers from Korea Advanced Institute of Science and Technology presented a reciprocating AMR with its regenerator consisting of a stainless steel tube filled with 0.021 kg of Gd particles, which moved in and out of the applied field region. The magnetic field was supplied by a hollow cylindrical array of permanent magnets, Halbach array, which generated a magnetic field of 1.5 T in the center of the gap, where the generator moved. He gas was used as the heat transfer fluid. Experimental results showed a maximum temperature span of 14 K [1531].

In the same year, Balli et al. built a reciprocating magnetic refrigeration device intended for industrial application. It consisted of two static Fe-Nd-B permanent magnets, which supplied a maximum magnetic field of 1.45 T in the space between them. Two mobile regenerators were used and each one was divided into two parts, which were separated by 0.030 m. This division of the regenerator was done to compensate the forces appearing in the regenerator when it entered into the magnetic field region. Each of these parts was made of 0.200 kg of Gd parallel sheets, using a total mass of 0.800 kg of magnetocaloric material. Experimental results showed a cooling power between 80–100 W and a temperature span of 20 K for an operational frequency of 0.5 Hz [1532].

In the same year, Tura et al. also presented a rotary AMR device, which used Gd as magnetocaloric material. Its magnetic field was supplied by a cylindrical nested Halbach array. In this configuration only the inner magnets in the array rotated, varying the magnetic field in the center gap, which led to a maximum magnetic field of 1.47 T. A static bed filled with 0.110 kg of Gd particles was placed in the gap of the Halbach array and a mixture of water and glycol was employed as the heat transfer fluid. Its experimental results showed a maximum temperature span of 29 K [1533].

In addition, Technical University of Denmark presented a reciprocating AMR in 2011. Its magnetic field was supplied by an array of permanent magnets in a Halbach cylinder type, with a maximum magnetic field of 1.03 T in the gap. The regenerator comprised of a bed filled with parallel plates of magnetocaloric material and it was moved vertically in and out of the field region, using a mixture of water and 25% vehicle antifreeze liquid as the heat transfer fluid. Tests were performed using three types of magnetocaloric materials. When Gd was used, a temperature span of around 10 K was measured. In the case of $La(Fe,Co,Si)_{13}$ compound, a temperature span of around 7 K was obtained. However, when two $La(Fe,Co,Si)_{13}$ compounds of different Curie temperatures were used, a temperature span of ~10 K was observed. On the other hand, tests using ceramic $La_{0.67}Ca_{0.26}Sr_{0.07}Mn_{1.05}O_3$ in the device, yielded a maximum temperature span of around 5 K [1386].

In 2012, Park et al. from Korea Advanced Institute of Science and Technology built a new reciprocating AMR refrigerator, which utilized a static Halbach array of permanent magnets to provide a maximum magnetic field of 1.4 T in its center gap. Its regenerator was formed by two beds containing 0.186 kg of Gd particles (with the cold heat exchanger placed between the beds) and moved in and out of the magnet. Tests using deionized water as the heat transfer fluid were performed, showing a maximum temperature span of 26.8 K and cooling power of 33 W [1534].

In the same year, researchers from Technical University of Denmark reported the construction of a rotary AMR device with its regenerator made of a nylon ring, which was divided into 24 separate beds. Gd particles were used as the magnetocaloric material to fill the beds and a mixture of deionized water and ethylene glycol was used as heat transfer fluid. The regenerator rotated in the gap of two cylindrical permanent magnets array. In this configuration, there were four regions with a high magnetic field of around 1.24 T and four others with low field close to zero. Experimental results with a variant fluid flow rate showed a maximum temperature span of around 20 K and a cooling power of 200 W for an operational frequency of around 2 Hz [1535].

In 2013, researchers from University of Victoria in Canada modified the magnet design of their rotary AMR device that was formerly built in 2007. The new magnet design comprised of a Halbach array of three concentric cylinders. Each of these cylinders was formed by twelve segments of permanent magnets in a configuration, whereby the internal cylinder was static, while the other two moved in opposite directions to create a sinusoidal magnetic field with a peak value of around 1.6 T. Tests performed using 0.650 kg of Gd and a operation frequency of 0.8 Hz, yielded a maximum temperature span of 33 K with a cooling power of 50 W [1536].

In the same year, Korean Advanced Institute of Science and Technology presented a named tandem reciprocating device. Its magnetic field was provided by a Halbach configuration with six segments of Fe-Nd-B permanent magnets located within an Fe yoke, to increase the magnetic field in the center gap, giving a maximum of 1.41 T in the direction where the regenerator moves. The regenerator plates were composed of two AMR beds filled with Gd particles, which were connected to the same cold end heat exchanger. Experimental results indicated a temperature span of 20 K with a cooling power of 2 W when using water as the heat transfer fluid [1537].

Also in 2013, the Chinese Academy of Science presented a new device, which utilized a combination of AMR refrigeration and Stirling regenerative refrigeration cycles. The magnetic field was supplied by an array of two hollow Halbach cylinders, each composed of sixteen segments of permanent magnets. The Halbach cylinders were configured in a manner that one was inside the other and the inner magnet rotated, providing a variable magnetic field from 0 to 1.5 T. The regenerator, located inside the rotating magnet, was a stainless steel tube filled with Gd sheets. Two cycles were tested for this regenerator: a Stirling cycle and an AMR refrigeration cycle. Tests performed with He gas as the heat transfer fluid and at operating frequency of 1.5 Hz, showed a temperature span of 14.9 K and 7.9 K for a cooling power of 6 W and 10 W respectively [1538].

Romero-Gómez et al also reported the construction of a reciprocating AMR refrigerator in 2013. In this device, the magnetic field source was formed by a set of twenty pieces of permanent magnets (Fe-Nd-B) placed in the extremes to close a C-shaped Fe yoke. This configuration of the magnet supplies a constant magnetic field of 1.015 T in the air gap, where the regenerator is moved. The regenerator was formed by two separated beds filled of parallel Gd sheets, piled with its plane perpendicular to the direction of the magnetic field. Distilled water was used as the heat transfer fluid and the operational frequency was varied between 0.15 and 0.25 Hz. Performed tests showed a maximum temperature span of 3.5 K and a cooling power of 3 W [1539].

In 2014, Aprea et al. from University of Salerno in Italy presented a rotary AMR equipment. Its magnet design consisted of four pieces of permanent magnets configured in two parallel semicircles, which supplied a maximum magnetic field of 1.25 T and rotated to magnetize/demagnetize the regenerators. The device utilized 1.20 kg of Gd particles distributed into 8 static beds, which were positioned at 45 degrees and fixed to an aluminium ring, and distilled water as its heat transfer fluid. Operating at a frequency of 0.5 Hz, the maximum temperature span measured was 13.5 K [1540].

In 2015, Technical University of Denmark presented a new rotary AMR prototype. In this device, its regenerator was placed in between two concentric cylindrical magnets and was formed by two concentric non-magnetic steel cylinders. Eleven beds were placed between the two cylinders in a periodic sequence of Gd, $Gd_{97.5}Y_{2.5}$, $Gd_{95}Y_5$ and $Gd_{90}Y_{10}$ particles. One of the two cylindrical magnets was a soft magnetic Fe-based alloy, which was located within the regenerator cylinder, while the other one surrounding the regenerator, was formed by two arrays of six blocks of Fe-Nd-B connected by Fe yokes. The last magnet could rotate creating a maximum magnetic field of ~1.2 T in the region where the regenerator was located. Using a mixture of demineralized water and ethyline glycol as the heat transfer fluid and at an operational frequency between 0 and 4 Hz, a maximum temperature span of 10.2 K and a cooling power of 103 W were obtained [1541].

In 2016, Institute of Non Ferrous Metals in Poland presented a magnetic refrigerator with a reciprocating magnetic field source. This source consisted of an array of four Fe-Nd-B permanent magnets placed in a C-shape structure of a soft magnetic Fe-based alloy, which supplied 0.8 T in the gap. It was allowed to move laterally in between two regenerators. These two regenerators were formed by parallel sheets of Gd and a liquid with a specific heat of about 4000 J kg^{-1} K^{-1} was employed as the heat transfer fluid. Experiments performed with an operational frequency of 0.5 Hz showed an adiabatic temperature change of 2.5 K [1542].

In the same year, researchers from Federal University of Santa Catarina in Brazil and Technical University of Denmark presented a rotary magnetic refrigerator, wherein it utilized a stationary ring shaped regenerator that was formed by eight pairs of beds, all filled with 1.7 kg of Gd particles and located surrounding the rotary magnetic source. This comprised of a two poles rotor-stator magnetic assembly formed by an array of Fe-Nd-B permanent magnet pieces, producing a maximum magnetic field of ~1.5 T. Experimental tests showed that for an operational frequency of 0.8 Hz, a cooling power of 80.4 W and a temperature span of 7.1 K was attained using a mixture of ethylene glycol and distilled water as the heat transfer fluid [1543].

Also in 2016, Abdelmessih et al. developed a magnetic cooling apparatus employing $Gd_5Si_2Ge_2$ alloy as its regenerator and an array of permanent magnets supplying a maximum field of 1 T, to magnetize/demagnetize the magnetocaloric material. Experimental results showed a maximum temperature change of 2.3 K for this device [1544].

In the same year, Benedict et al. presented a rotary AMR refrigerator. In this device, the regenerator was formed by two cylindrical beds filled with Gd particles and each bed was placed inside a Halbach array magnet. The magnet consisted of a pair of cylindrical magnets, which were formed by ten pieces of Fe-Nd-B permanent magnet, and could be independently rotated supplying a magnetic field between 0.05 and 1.5 T into the gap area where the regenerator was placed. Tests performed on this device were done with a maximum operational frequency of 2 Hz and using a mixture of water and ethylene glycol as the heat transfer fluid. Results showed a maximum temperature span of 21 K [1545].

Other devices working around room temperature for which some characteristics are available are collected in Table S8 of the Supplementary Material.

8.3. General considerations about system design

Any new technology that is being developed has to overcome limitations before reaching the market. The competition with already stablished systems, optimized for longer periods of time, poses several questions about the feasibility of the new technology. In the case of magnetic refrigeration, general questions arise about field application and moving parts (or fluids).

With respect to the application of magnetic field, as the magnetic entropy change and adiabatic temperature change both scale with the applied magnetic field in a non-linear way [33,76], it is natural to consider that the larger the field the larger the performance of the device. Currently, fields of the order of ~2 T can be applied using permanent magnets. For larger fields, superconducting magnets would be needed, increasing the cost of use of the refrigerator. While superconductor based devices seem unacceptable for home appliances, they might find their niche of application in central cooling plants.

Variable magnetic fields constitute an intrinsic requirement of magnetic refrigeration. This can be produced by mechanical movement of the permanent magnet or rotation of a set of halbach cylinders. Sample reciprocation is also possible, although it implies more technical challenges. Alternatively, studies on anisotropic magnetocaloric effect suggest that the rotation of the magnetocaloric material inside a constant magnetic field could be a way of inducing temperature changes [1546–1548].

Heat transfer from the magnetocaloric material to the refrigerator content or to the environment would, in principle, need heat transfer fluids or, alternatively, mechanical movement of the sample to put it in contact with the thermal reservoirs [1549]. This is seen as another apparent bottleneck for developing the technology, as it is one of the intrinsic limitations for increasing the frequency of operation [70]. New approaches considering thermal diodes could notably improve heat transfer and, therefore, the coefficient of performance of the devices [1550].

8.4. Other caloric refrigeration technologies

Although the focus of this review paper is magnetocaloric materials and their application in refrigerator devices, it is important to mention that there are other technologies based on other "caloric" effects, i.e. reversible temperature changes of the material produced by external fields. Among them, the most relevant nowadays are mechanocaloric (either elastocaloric or barocaloric), electrocaloric and magnetocaloric technologies. This generalization is currently attracting a lot of attention in the research literature, with a very recent example of an special issue of Journal of Physics D: Applied Physics (volume 50, 2017), edited by Mañosa and Planes, which covers many of the current approaches to generalize the magnetic field excitation to other fields like electrical or mechanical. A relatively recent review on caloric effects was published by Moya [1551].

The application of mechanical excitation to a material might cause elastocaloric and barocaloric effects, depending if the stress is applied in one direction or isotropically, respectively. In fact, the concept of elastocaloric effect was first described in 1805 [1552] and, over time, the concept and its thermodynamical interpretation [1553] were generalized to predict other caloric effects, like the magnetocaloric effect. For a very recent review on mechanocaloric materials the reader can consult [1554].

Electrocaloric effect consists in the reversible temperature change of a material under the application of an electric field. There is a broad variety of materials exhibiting this effect, ranging from perovskites to polymer films. An overview of this field of research can be found in [1555].

A comparison between different caloric refrigeration devices can be found in recent literature [22,1556]. A particularly interesting approach includes SMA foils in a demonstrator that incorporates mechanical work recovery [1557], as this design is compatible with the implementation of micro-cooling devices.

Among all caloric refrigeration technologies, the most technologically developed at this moment is magnetocaloric, followed by mechanocaloric. It is expected, however, that each of these three caloric effects will find its own market niche, depending on the desired operation conditions of the device and the intrinsic limitations of the technology [1556,1558].

9. Conclusions and future outlook

Magnetic refrigeration is an active field of research, with relevant activity both in the search of new magnetocaloric materials as well as in the application of these materials into magnetic refrigeration devices.

On the materials research side, one of the mainstream lines is the discovery of new phases with significant magnetocaloric response. At the same time, the application of materials engineering techniques to modify the microstructure of the samples, the combination of different phases to develop composites, etc. are helping researchers to understand the role of the different physical magnitudes in order to optimize the applicability of the materials, or to eliminate some of the limitations which seemed to be inherent to some of the phases.

The design of magnetic refrigeration devices has also experienced a big transition, from laboratory prototypes to the exhibition of pre-commercial systems at large industrial fairs in the recent years. The most used materials in the most recent refrigerator prototypes are Laves phases for low temperature applications and Gd (and its compounds), $La(FeSi)_{13}$ type phases and MnFePSi type phases for room temperature applications.

As shown in the previous sections, there are other materials that exhibit large magnetocaloric response, but they are not applied in magnetic refrigerator devices yet because of their large hysteresis or slow kinetics of the transformation. These detrimental factors could eventually be ameliorated by proper processing of the samples or by a clever combination of temperature and external field excitation during the refrigeration cycle.

In our opinion, the interface between these two interconnected fields of research, materials and devices, will give the most relevant results in the near future. The optimization of magnetocaloric materials in order to enhance their dynamic response and reduce their hysteresis will allow them to be incorporated into refrigerator devices, which are intrinsically cyclic in their operation.

From a more fundamental point of view, magnetocaloric characterization has been proven to be a reliable method for the determination of the characteristics of the phase transition that originates the phenomenon. Fundamental studies of the hysteresis of the materials will allow developing models for a comprehensive description of the magnetic refrigerant of devices under normal operating conditions, improving the optimization of the design. Techniques like FORC, broadly used in the characterization of magnetic hysteresis in permanent magnets, are being introduced into magnetocaloric research to analyze the thermal hysteresis of the materials. In addition, the new techniques for determining critical exponents, the order of phase transitions and the identification of the tricritical point separating first and second order phase transitions using magnetocaloric methods are being applied in the broader scope of the general characterization of magnetic materials.

At the same time, the successful application of the magnetocaloric effect in magnetic refrigerators has established the seed for the study of other caloric phenomena (like elasto-caloric, electro-caloric, etc.) and this will probably lead to alternative technologies for refrigeration.

Acknowledgements

This work was supported by the Spanish MINECO (project MAT2013-45165-P), AEI/FEDER-UE (project MAT-2016-77265-R) and the PAI of the Regional Government of Andalucía. L.M. Moreno-Ramírez acknowledges a FPU fellowship from the Spanish MECD.

Appendix A. Supplementary material

Supplementary data associated with this article can be found, in the online version, at https://doi.org/10.1016/j.pmatsci.2017.10.005.

References

[1] Energy Flow Charts. Laurence Livermore National Laboratory. <https://flowcharts.llnl.gov/commodities/energy>.
[2] Gutfleisch O, Willard MA, Bruck E, Chen CH, Sankar SG, Liu JP. Magnetic materials and devices for the 21st Century: stronger, lighter, and more energy efficient. Adv Mater 2011;23:821–42.
[3] Gutfleisch O, Franco V. Preface to the viewpoint set on: magnetic materials for energy. Scr Mater 2012;67:521–3.
[4] International Energy Outlook. U.S. Energy Information Administration; 2016. <http://www.eia.gov/outlooks/ieo>.
[5] Sivak M, Will AC. Put a chill on the global energy supply? Am Sci 2013;100:330.
[6] An EU Strategy on Heating and Cooling. European Commission; 2016. <https://ec.europa.eu/energy/sites/ener/files/documents/1_EN_ACT_part1_v14.pdf>.
[7] Pecharsky VK, Gschneidner KA. Giant magnetocaloric effect in Gd-5(Si2Ge2). Phys Rev Lett 1997;78:4494–7.
[8] Yu BF, Liu M, Egolf PW, Kitanovski A. A review of magnetic refrigerator and heat pump prototypes built before the year 2010. Int J Refrig-Rev Int Froid 2010;33:1029–60.
[9] Brown GV. Magnetic heat pumping near room temperature. J Appl Phys 1976;47:3673.
[10] Premiere of cutting-edge cooling appliance at CES; 2015. <https://www.basf.com/en/company/news-and-media/news-releases/2015/01/p-15-100.html>.
[11] Gschneidner KA, Pecharsky VK. Magnetocaloric materials. Annu Rev Mater Sci 2000;30:387–429.
[12] Gschneidner KA, Pecharsky VK, Tsokol AO. Recent developments in magnetocaloric materials. Rep Prog Phys 2005;68:1479–539.
[13] Bruck E. Developments in magnetocaloric refrigeration. J Phys D-Appl Phys 2005;38:R381–91.
[14] Gschneidner KA, Pecharsky VK. Thirty years of near room temperature magnetic cooling: where we are today and future prospects. Int J Refrig-Rev Int Froid 2008;31:945–61.
[15] Shen BG, Sun JR, Hu FX, Zhang HW, Cheng ZH. Recent progress in exploring magnetocaloric materials. Adv Mater 2009;21:4545–64.
[16] de Oliveira NA, von Ranke PJ. Theoretical aspects of the magnetocaloric effect. Phys Rep-Rev Sec Phys Lett 2010;489:89–159.
[17] Nielsen KK, Tusek J, Engelbrecht K, Schopfer S, Kitanovski A, Bahl CRH, et al. Review on numerical modeling of active magnetic regenerators for room temperature applications. Int J Refrig-Rev Int Froid 2011;34:603–16.
[18] Franco V, Blázquez JS, Ingale B, Conde A. The magnetocaloric effect and magnetic refrigeration near room temperature: materials and models. Annu Rev Mater Res 2012;42:305–42.
[19] Smith A, Bahl CRH, Bjork R, Engelbrecht K, Nielsen KK, Pryds N. Materials challenges for high performance magnetocaloric refrigeration devices. Adv Energy Mater 2012;2:1288–318.
[20] Gomez JR, Garcia RF, Carril JC, Gomez MR. A review of room temperature linear reciprocating magnetic refrigerators. Renew Sust Energ Rev 2013;21:1–12.
[21] Brown JS, Domanski PA. Review of alternative cooling technologies. Appl Therm Eng 2014;64:252–62.
[22] Kitanovski A, Tušek J, Tomc U, Plaznik U, Ožbolt M, Poredoš A. Magnetocaloric energy conversion. Springer International Publishing; 2015.

[23] Tishin AM, Spichkin YI. The magnetocaloric effect and its applications. Bristol: Institute of Physics Publishing; 2003.
[24] Pecharsky VK, Gschneidner KA. Magnetocaloric effect from indirect measurements: magnetization and heat capacity. J Appl Phys 1999;86:565–75.
[25] Pecharsky V, Gschneidner K, Pecharsky A, Tishin A. Thermodynamics of the magnetocaloric effect. Phys Rev B 2001;64:144406.
[26] Wood ME, Potter WH. General-analysis of magnetic refrigeration and its optimization using a new concept - maximization of refrigerant capacity. Cryogenics 1985;25:667–83.
[27] Gschneidner Jr KA, Pecharsky VK, Pecharsky AO, Zimm CB. Recent developments in magnetic refrigeration. Mater Sci Forum 1999;315–317:69–76.
[28] Provenzano V, Shapiro AJ, Shull RD. Reduction of hysteresis losses in the magnetic refrigerant Gd5Ge2Si2 by the addition of iron. Nature 2004;429:853–7.
[29] Ucar H, Ipus JJ, Franco V, McHenry ME, Laughlin DE. Overview of amorphous and nanocrystalline magnetocaloric materials operating near room temperature. Jom 2012;64:782–8.
[30] Bruck E, Yibole H, Zhang L. A universal metric for ferroic energy materials. Philos Trans R Soc A-Math Phys Eng Sci 2016;374:20150303.
[31] Steyert WA. Stirling-cycle rotating magnetic refrigerators and heat engines for use near room-temperature. J Appl Phys 1978;49:1216–26.
[32] Tishin AM, Spichkin YI, Zverev VI, Egolf PW. A review and new perspectives for the magnetocaloric effect: new materials and local heating and cooling inside the human body. Int J Refrig-Rev Int Froid 2016;68:177–86.
[33] Franco V, Conde A, Romero-Enrique JM, Spichkin YI, Zverev VI, Tishin AM. Field dependence of the adiabatic temperature change in second order phase transition materials: application to Gd. J Appl Phys 2009;106:103911.
[34] Liu J, Gottschall T, Skokov KP, Moore JD, Gutfleisch O. Giant magnetocaloric effect driven by structural transitions. Nat Mater 2012;11:620–6.
[35] Law JY, Franco V, Ramanujan RV. Direct magnetocaloric measurements of Fe-B-Cr-X (X = La, Ce) amorphous ribbons. J Appl Phys 2011;110:023907.
[36] Aliev AM, Batdalov AB, Kalitka VS. Magnetocaloric properties of manganites in alternating magnetic fields. Jetp Lett 2010;90:663–6.
[37] Aliev AM, Batdalov AB, Khanov LN, Koledov VV, Shavrov VG, Tereshina IS, et al. Magnetocaloric effect in some magnetic materials in alternating magnetic fields up to 22 Hz. J Alloys Comp 2016;676:601–5.
[38] Skokov KP, Muller KH, Moore JD, Liu J, Karpenkov AY, Krautz M, et al. Influence of thermal hysteresis and field cycling on the magnetocaloric effect in LaFe11.6Si1.4. J Alloys Comp 2013;552:310–7.
[39] Gottschall T, Skokov KP, Burriel R, Gutfleisch O. On the S(T) diagram of magnetocaloric materials with first-order transition: kinetic and cyclic effects of Heusler alloys. Acta Mater 2016;107:1–8.
[40] Kohama Y, Marcenat C, Klein T, Jaime M. AC measurement of heat capacity and magnetocaloric effect for pulsed magnetic fields. Rev Sci Instrum 2010;81:104902.
[41] Kihara T, Kohama Y, Hashimoto Y, Katsumoto S, Tokunaga M. Adiabatic measurements of magneto-caloric effects in pulsed high magnetic fields up to 55 T. Rev Sci Instrum 2013;84:074901.
[42] Cugini F, Porcari G, Solzi M. Non-contact direct measurement of the magnetocaloric effect in thin samples. Rev Sci Instrum 2014;85:074902.
[43] Döntgen J, Rudolph J, Gottschall T, Gutfleisch O, Salomon S, Ludwig A, et al. Temperature dependent low-field measurements of the magnetocaloric ΔT with sub-mK resolution in small volume and thin film samples. Appl Phys Lett 2015;106:032408.
[44] Cugini F, Porcari G, Viappiani C, Caron L, dos Santos AO, Cardoso LP, et al. Millisecond direct measurement of the magnetocaloric effect of a Fe2P-based compound by the mirage effect. Appl Phys Lett 2016;108:012407.
[45] Marcos J, Casanova F, Batlle X, Labarta A, Planes A, Manosa L. A high-sensitivity differential scanning calorimeter with magnetic field for magnetostructural transitions. Rev Sci Instrum 2003;74:4768–71.
[46] Casanova F, Labarta A, Batlle X, Perez-Reche FJ, Vives E, Manosa L, et al. Direct observation of the magnetic-field-induced entropy change in Gd-5(SixGe1-x)(4) giant magnetocaloric alloys. Appl Phys Lett 2005;86:262504.
[47] Basso V, Kupferling M, Sasso CP, Giudici L. A Peltier cell calorimeter for the direct measurement of the isothermal entropy change in magnetic materials. Rev Sci Instrum 2008;79:063907.
[48] Basso V, Sasso CP, Kupferling M. A Peltier cells differential calorimeter with kinetic correction for the measurement of c(p)(H, T) and Delta s(H, T) of magnetocaloric materials. Rev Sci Instrum 2010;81:113904.
[49] Nielsen KK, Bez HN, von Moos L, Bjork R, Eriksen D, Bahl CRH. Direct measurements of the magnetic entropy change. Rev Sci Instrum 2015;86:103903.
[50] Tocado L, Palacios E, Burriel R. Entropy determinations and magnetocaloric parameters in systems with first-order transitions: study of MnAs. J Appl Phys 2009;105:093918.
[51] Wang GF. Magnetic and calorimetric study of magnetocaloric effect in intermetallics exhibiting first-order magnetostructural transitions [Ph.D. Thesis]. Zaragoza (Spain): University of Zaragoza; 2012.
[52] Palacios E, Wang GF, Burriel R, Provenzano V, Shull RD. Direct measurement of the magnetocaloric effect in Gd5Si2Ge1.9Ga0.1. J Phys: Conf Ser 2010;200:092011.
[53] Wang GF, Palacios E, Coelho AA, Gama S, Burriel R. Comparative analysis of magnetic and caloric determinations of the magnetocaloric effect in Mn0.99Co0.01As. EPJ Web Conf 2014;75:04003.
[54] Palacios E, Bartolome J, Wang GF, Burriel R, Skokov K, Taskaev S, et al. Analysis of the magnetocaloric effect in heusler alloys: study of Ni50CoMn36Sn13 by calorimetric techniques. Entropy 2015;17:1236–52.
[55] Caballero-Flores R, Franco V, Conde A, Kiss LF. Influence of the demagnetizing field on the determination of the magnetocaloric effect from magnetization curves. J Appl Phys 2009;105:07A919.
[56] Carvalho AMG, Coelho AA, von Ranke PJ, Alves CS. The isothermal variation of the entropy (Delta S-T) may be miscalculated from magnetization isotherms in some cases: MnAs and Gd5Ge2Si2 compounds as examples. J Alloys Comp 2011;509:3452–6.
[57] Caron L, Ou ZQ, Nguyen TT, Thanh DTC, Tegus O, Bruck E. On the determination of the magnetic entropy change in materials with first-order transitions. J Magn Magn Mater 2009;321:3559–66.
[58] Franco V. Determination of the magnetic entropy change from magnetic measurements: the importance of the measurement protocol, http://www.lakeshore.com/products/Vibrating-Sample-Magnetometer/Pages/MCE.aspx. . Lake Shore Cryotronics; 2014.
[59] Kaeswurm B, Franco V, Skokov KP, Gutfleisch O. Assessment of the magnetocaloric effect in La, Pr(Fe, Si) under cycling. J Magn Magn Mater 2016;406:259–65.
[60] Moore JD, Morrison K, Sandeman KG, Katter M, Cohen LF. Reducing extrinsic hysteresis in first-order La(Fe Co, Si)(13) magnetocaloric systems. Appl Phys Lett 2009;95:252504.
[61] Hansen BR, Bahl CRH, Kuhn LT, Smith A, Gschneidner KA, Pecharsky VK. Consequences of the magnetocaloric effect on magnetometry measurements. J Appl Phys 2010;108:043923.
[62] Pecharsky VK, Gschneidner KA. Heat capacity near first order phase transitions and the magnetocaloric effect: an analysis of the errors, and a case study of Gd-5(Si2Ge2) and Dy. J Appl Phys 1999;86:6315–21.
[63] Pecharsky VK, Moorman JO, Gschneidner KA. A 3–350 K fast automatic small sample calorimeter. Rev Sci Instrum 1997;68:4196–207.
[64] Plackowski T, Wang YX, Junod A. Specific heat and magnetocaloric effect measurements using commercial heat-flow sensors. Rev Sci Instrum 2002;73:2755–65.
[65] Jeppesen S, Linderoth S, Pryds N, Kuhn LT, Jensen JB. Indirect measurement of the magnetocaloric effect using a novel differential scanning calorimeter with magnetic field. Rev Sci Instrum 2008;79:083901.
[66] Minakov AA, Roy SB, Bugoslavsky YV, Cohen LF. Thin-film alternating current nanocalorimeter for low temperatures and high magnetic fields. Rev Sci Instrum 2005;76.
[67] Morrison K, Bratko M, Turcaud J, Berenov A, Caplin AD, Cohen LF. A calorimetric method to detect a weak or distributed latent heat contribution at first order magnetic transitions. Rev Sci Instrum 2012;83:033901.

[68] Moreno-Ramírez LM, Blázquez JS, Law JY, Franco V, Conde A. Optimal temperature range for determining magnetocaloric magnitudes from heat capacity. J Phys D: Appl Phys 2016;49:495001.
[69] Moreno-Ramírez LM, Franco V, Conde A, Neves-Bez H, Mudryk Y, Pecharsky VK. Influence of the starting temperature of calorimetric measurements on the accuracy of determined magnetocaloric effect [submitted for publication].
[70] Kuz'min MD. Factors limiting the operation frequency of magnetic refrigerators. Appl Phys Lett 2007;90:251916.
[71] Ghorbani Zavareh M, Salazar Mejía C, Nayak AK, Skourski Y, Wosnitza J, Felser C, et al. Direct measurements of the magnetocaloric effect in pulsed magnetic fields: the example of the Heusler alloy Ni50Mn35In15. Appl Phys Lett 2015;106:071904.
[72] Gottschall T, Skokov KP, Scheibel F, Acet M, Zavareh MG, Skourski Y, et al. Dynamical effects of the martensitic transition in magnetocaloric heusler alloys from direct Delta T-ad measurements under different magnetic-field-sweep rates. Phys Rev Appl 2016;5:024013.
[73] Basso V, Bertotti G, LoBue M, Sasso CP. Theoretical approach to the magnetocaloric effect with hysteresis. J Magn Magn Mater 2005;290:654–7.
[74] Kuz'min MD. Landau-type parametrization of the equation of state of a ferromagnet. Phys Rev B 2008;77:184431.
[75] Arrott A, Noakes JE. Approximate equation of state for nickel near its critical temperature. Phys Rev Lett 1967;19:786–9.
[76] Franco V, Blazquez JS, Conde A. Field dependence of the magnetocaloric effect in materials with a second order phase transition: a master curve for the magnetic entropy change. Appl Phys Lett 2006;89:222512.
[77] Franco V, Conde A, Kiss LF. Magnetocaloric response of FeCrB amorphous alloys: predicting the magnetic entropy change from the Arrott-Noakes equation of state. J Appl Phys 2008;104:033903.
[78] Fan JY, Pi L, Zhang L, Tong W, Ling LS, Hong B, et al. Investigation of critical behavior in Pr0.55Sr0.45MnO3 by using the field dependence of magnetic entropy change. Appl Phys Lett 2011;98:072508.
[79] Zhang L, Ling LS, Fan JY, Li RW, Tan S, Zhang YH. 3D-Heisenberg ferromagnetic characteristics in CuCr2Se4. J Appl Phys 2011;109:113911.
[80] Franco V, Conde A. Scaling laws for the magnetocaloric effect in second order phase transitions: from physics to applications for the characterization of materials. Int J Refrig-Rev Int Froid 2010;33:465–73.
[81] Bean C, Rodbell D. Magnetic disorder as a first-order phase transformation. Phys Rev 1962;126:104–15.
[82] Romero-Muniz C, Franco V, Conde A. Two different critical regimes enclosed in the Bean-Rodbell model and their implications for the field dependence and universal scaling of the magnetocaloric effect. Phys Chem Chem Phys 2017;19:3582–95.
[83] Tegus O, Lin GX, Dagula W, Fuquan B, Zhang L, Bruck E, et al. A model description of the first-order phase transition in MnFeP1-xAsx. J Magn Magn Mater 2005;290:658–60.
[84] Balli M, Fruchart D, Gignoux D, Miraglia S, Hlil EK, Wolfers P. Modelling of the magnetocaloric effect in Gd1-xTbx and MnAs compounds. J Magn Magn Mater 2007;316:E558–61.
[85] Palacios E, Tomasi C, Saez-Puche R, Dos Santos-Garcia AJ, Fernandez-Martinez F, Burriel R. Effect of Gd polarization on the large magnetocaloric effect of GdCrO4 in a broad temperature range. Phys Rev B 2016;93:064420.
[86] Yahyaoui S, Khalfaoui M, Kallel S, Kallel N, Amaral JS, Ben Lamine A. Modeling the magnetic properties and magnetocaloric effect of La0.7Sr0.3Mn0.9Ti0.1O3. J Alloys Comp 2016;685:633–8.
[87] Franco V, Gottschall T, Skokov KP, Gutfleisch O. First-Order Reversal Curve (FORC) analysis of magnetocaloric Heusler-Type alloys. IEEE Magn Lett 2016;7:6602904.
[88] Harmon BN, Antonov VN. Electronic structure, optical, and magneto-optical properties of Gd-5(Si2Ge2) compound. J Appl Phys 2002;91:9815–20.
[89] Mihalik M, Vejpravova J, Rusz J, Divis M, Svoboda P, Sechovsky V. Anisotropic magnetic properties and specific-heat study of a TbFe2Si2 single crystal. Phys Rev B 2004;70:134405.
[90] Paudyal D, Pecharsky VK, Gschneidner KA, Harmon BN. Electron correlation effects on the magnetostructural transition and magnetocaloric effect in Gd5Si2Ge2. Phys Rev B 2006;73:144406.
[91] Buchelnikov VD, Sokolovskiy VV, Herper HC, Ebert H, Gruner ME, Taskaev SV, et al. First-principles and Monte Carlo study of magnetostructural transition and magnetocaloric properties of Ni2+xMn1-xGa. Phys Rev B 2010;81:094411.
[92] Entel P, Siewert M, Gruner ME, Chakrabarti A, Barman SR, Sokolovskiy VV, et al. Optimization of smart Heusler alloys from first principles. J Alloys Comp 2013;577:S107–12.
[93] Korotana R, Mallia G, Gercsi Z, Harrison NM. A hybrid-exchange density functional study of Ca-doped LaMnO3. J Appl Phys 2013;113:17A910.
[94] Li GJ, Eriksson O, Johansson B, Vitos L. Ab initio investigation of competing antiferromagnetic structures in low Si-content FeMn(PSi) alloy. J Phys-Condes Matter 2016;28:216002.
[95] Korotana RK, Mallia G, Fortunato NM, Amaral JS, Gercsi Z, Harrison NM. A combined thermodynamics and first principles study of the electronic, lattice and magnetic contributions to the magnetocaloric effect in La0.75Ca0.25MnO3. J Phys D-Appl Phys 2016;49:285001.
[96] Pindor AJ, Staunton J, Stocks GM, Winter H. Disordered local moment state of magnetic transition metals: a self-consistent KKR CPA calculation. J Phys F: Metal Phys 1983;13:979–89.
[97] Staunton JB, Banerjee R, Dias MdS, Deak A, Szunyogh L. Fluctuating local moments, itinerant electrons, and the magnetocaloric effect: compositional hypersensitivity of FeRh. Phys Rev B 2014;89:054427.
[98] Zverev VI, Saletsky AM, Gimaev RR, Tishin AM, Miyanaga T, Staunton JB. Influence of structural defects on the magnetocaloric effect in the vicinity of the first order magnetic transition in Fe50.4Rh49.6. Appl Phys Lett 2016;108:192405.
[99] Petit L, Paudyal D, Mudryk Y, Gschneidner Jr KA, Pecharsky VK, Luders M, et al. Complex magnetism of lanthanide intermetallics and the role of their valence electrons: ab initio theory and experiment. Phys Rev Lett 2015;115:207201.
[100] Fujita A. Relation between paramagnetic entropy and disordered local moment in La(Fe0.88Si0.12)(13) magnetocaloric compound. Apl Mater 2016;4:064108.
[101] Hou XL, Zhang P, Hu XH, Xu H, Ni JS, Zhou BX. Study on magnetocaloric effect of Gd0.95Nb0.05 alloys. Rare Metal Mater Eng 2010;39:126–8.
[102] Min JX, Zhong XC, Zheng ZG, Liu ZW, Zeng DC, Yu HY, et al. Large magnetocaloric effect and application features of Gd99.75Fe0.25 alloy. Rare Metal Mater Eng 2013;42:362–5.
[103] Wang DH, Huang SL, Han ZD, Su ZH, Wang Y, Du YW. The magnetic entropy changes in Gd1-xBx alloys. Solid State Commun 2004;131:97–9.
[104] Jayaraman TV, Koten MA, Shield JE. Near room temperature magnetocaloric properties of melt-spun Gd100-xBx (x=0, 5, 10, 15, and 20 at%) alloys. J Magn Magn Mater 2011;323:2037–41.
[105] GschneidnerJr KA, Pecharsky VK, Dennis B. Some observations on the Gd-rich side of the Gd-C system. J Alloys Comp 1997;260:107–10.
[106] Wang DH, Su ZH, Huang SL, Han Z, Zou WQ, Du YW. The magnetic entropy changes in Gd1-xCx alloys. J Alloys Comp 2005;387:6–8.
[107] Ma Y, Du A. Monte Carlo simulation of magnetic and magnetocaloric properties of binary alloy Gd1-xCx. J Magn Magn Mater 2009;321:L65–8.
[108] Chen YG, Wu JP, Mao SF, Zhang TB, Tang YB, Tu MJ. Magnetocaloric properties and solid solution strengthening of Gd-C and Gd-Dy-C alloys. J Alloys Comp 2006;422:21–4.
[109] Burkhanov GS, Kolchugina NB, Tereshina EA, Tereshina IS, Politova GA, Chzhan VB, et al. Magnetocaloric properties of distilled gadolinium: effects of structural inhomogeneity and hydrogen impurity. Appl Phys Lett 2014;104:242402.
[110] Jayaraman TV, Boone L, Shield JE. Near room temperature magnetic entropy changes in as-cast Gd100-xMnx (x = 0, 5, 10, 15, and 20 at.%) alloys. J Alloys Comp 2011;509:1411–7.
[111] Wang DH, Han ZD, Cao QQ, Huang SL, Zhang JR, Du YW. The reduced Curie temperature and magnetic entropy changes in Gd1-xInx alloys. J Alloys Comp 2005;396:22–4.
[112] Ren WJ, Li D, Liu W, Li J, Zhang ZD. Magnetic property and magnetocaloric effect of Gd(In) solid solutions. J Appl Phys 2008;103:07B323.
[113] Jayaraman TV, Boone L, Shield JE. Near room-temperature magnetocaloric properties of Gd-Ga alloys. J Magn Magn Mater 2014;363:201–9.
[114] Provenzano V, Shull RD, Kletetschka G, Stutzman PE. Gd90Co2.5Fe7.5 alloy displaying enhanced magnetocaloric properties. J Alloys Comp 2015;622:1061–7.

[115] Shao YZ, Zhang JX, Lai JKL, Shek CH. Magnetic entropy in nanocomposite binary gadolinium alloys. J Appl Phys 1996;80:76–80.
[116] Pecharsky VK, Gschneidner KA. Gd-Zn alloys as active magnetic regenerator materials for magnetic refrigeration. Cryocoolers 1999;10:629–37.
[117] Xiao SF, Chen YG. Magnetic properties and magnetic exchange interactions in Gd1-xREx (RE=Pr, Nd) alloys. J Rare Earths 2016;34:489–94.
[118] Xu ZC, Lin GX, Chen JC. A GdxHo1-x-based composite and its performance characteristics in a regenerative Ericsson refrigeration cycle. J Alloys Comp 2015;639:520–5.
[119] Perez ESL, Betancourt I, Paz JFH, Aquino JAM, Galindo JTE. Magnetocaloric effect in as-cast Gd1-xYx alloys with x=0.0, 0.1, 0.2, 0.3, 0.4. J Appl Phys 2014;115:17A910.
[120] Mathew SP, Kaul SN, Nigam AK, Probst AC, Birringer R. Magnetic irreversibility, spin-wave excitations and magnetocaloric effect in nanocrystalline Gadolinium. J Phys: Conference Series 2010;200:072047.
[121] Miller CW, Williams DV, Bingham NS, Srikanth H. Magnetocaloric effect in Gd/W thin film heterostructures. J Appl Phys 2010;107:09A903.
[122] Svalov AV, Vas'kovskiy VV, Balymov KG, Alonso J, Fdez-Gubieda ML, Kurlyandskaya GV. Magnetic properties and magnetic entropy change in Gd/Ti multilayers. IEEE Trans Magn 2014;50:4.
[123] Doblas D, Moreno-Ramírez LM, Franco V, Conde A, Svalov AV, Kurlyandskaya GV. Nanostructuring as a procedure to control the field dependence of the magnetocaloric effect. Mater Des 2017;114:214–9.
[124] Mello VD, Dantas AL, Carrico AS. Magnetocaloric effect of thin Dy films. Solid State Commun 2006;140:447–51.
[125] Medeiros FC, Mello VD, Dantas AL, Sales FHS, Carrico AS. Giant magnetocaloric effect of thin Ho films. J Appl Phys 2011;109:07A914.
[126] Liu XG, Or SW, Li B, Ou ZQ, Zhang L, Zhang Q, et al. Magnetic properties of Dy nanoparticles and Al2O3-coated Dy nanocapsules. J Nanopart Res 2011;13:1163–74.
[127] Shinde KP, Sinha BB, Oh SS, Kim HS, Ha HS, Baik SK, et al. Fabrication of Gd films by vacuum evaporation and its magnetocaloric properties. J Magn Magn Mater 2015;374:144–7.
[128] Taskaev S, Skokov K, Khovaylo V, Buchelnikov V, Pellenen A, Karpenkov D, et al. Effect of severe plastic deformation on the specific heat and magnetic properties of cold rolled Gd sheets. J Appl Phys 2015;117:5.
[129] Dudek MR, Wojciechowski KW, Grima JN, Caruana-Gauci R, Dudek KK. Colossal magnetocaloric effect in magnetoauxetic systems. Smart Mater Struct 2015;24:5.
[130] Crossley S, Mathur ND, Moya X. New developments in caloric materials for cooling applications. AIP Adv 2015;5:067153.
[131] Starkov AS, Starkov IA. Multicaloric effect in a solid: new aspects. J Exp Theor Phys 2014;119:258–63.
[132] Flerov IN, Mikhaleva EA, Gorev MV, Kartashev AV. Caloric and multicaloric effects in oxygen ferroics and multiferroics. Phys Solid State 2015;57:429–41.
[133] Balli M, Matte D, Jandl S, Fournier P, Gospodinov MM. Search for the magnetocaloric effect in multiferroics oxides. In: 6th Iir/Iif International conference on magnetic refrigeration (Thermag Vi). p. 47–8.
[134] Szytula A, Leciejewicz J. Hanbook of crystal structures and magnetic properties of rare earth intermetallics. Boca Raton, USA: CRC Press; 1993.
[135] Jagodzinski H. Fritz H. Laves. Obituary. Acta Crystall A 1979;35:343.
[136] Paufler P. Early work on Laves phases in East Germany. Intermetallics 2011;19:599–612.
[137] Huang SL, Wang DH, Han ZD, Su ZH, Tang SL, Du YW. Magnetic and magnetocaloric properties of quenched Hf1-xTaxFe2 materials. J Alloys Comp 2005;394:80–2.
[138] Han ZD, Wang DH, Huang SL, Su ZH, Tang SL, Du YW. Low-field magnetic entropy changes in Hf1-xTaxFe2. J Alloys Comp 2004;377:75–7.
[139] Dong QY, Shen BG, Chen J, Shen J, Zhang HW, Sun JR. Magnetic entropy change and refrigerant capacity in GdFeAl compound. J Appl Phys 2009;105:07A305.
[140] Chelvane JA, Das T, Mahato RN, Morozkin AV, Lamsal J, Yelon WB, et al. Magnetic structure and magnetic entropy change in the intermetallic compound DyCoAl. J Appl Phys 2010;107:09A906.
[141] Li LW, Huo DX, Qian ZH, Nishimura K. Study of the critical behaviour and magnetocaloric effect in DyFeAl. Intermetallics 2014;46:231–5.
[142] Herbst JF, Fuerst CD, McMichael RD. Structural, magnetic, and magnetocaloric properties of (Hf0.83Ta0.17)Fe-2+x materials. J Appl Phys 1996;79:5998–6000.
[143] Diop LVB, Kastil J, Isnard O, Arnold Z, Kamarad J. Magnetic and magnetocaloric properties of itinerant-electron system Hf1-xTaxFe2 (x=0.125 and 0.175). J Alloys Comp 2015;627:446–50.
[144] Bag P, Rawat R, Chaddah P, Babu PD, Siruguri V. Unconventional thermal effects across first-order magnetic transition in the Ta-doped HfFe2 intermetallic. Phys Rev B 2016;93:014416.
[145] Dong JD, Zhang MX, Liu J, Zhang PN, Yan A. Magnetic properties and magnetocaloric effect of Hf-Ta-Fe-(CO) alloys. Physica B 2015;476:171–4.
[146] Dong SY, Yang XZ, Chen JY, Shao Q, Qian B, Han ZD, et al. Large low-field magnetic entropy changes in as-cast Hf0.83-xZrxTa0.17Fe2 compounds. Physica B 2015;466:86–9.
[147] Herrero-Albillos J, Bartolome F, Garcia LM, Casanova F, Labarta A, Batlle X. Nature and entropy content of the ordering transitions in RCo2. Phys Rev B 2006;73:134410.
[148] Bonilla CM, Herrero-Albillos J, Bartolome F, Garcia LM, Parra-Borderias M, Franco V. Universal behavior for magnetic entropy change in magnetocaloric materials: an analysis on the nature of phase transitions. Phys Rev B 2010;81:224424.
[149] Gu ZF, Zhou B, Li JQ, Ao WQ, Cheng G, Zhao HC. Magnetocaloric effect of GdCo2-xAlx compounds. Solid State Commun 2007;141:548–50.
[150] Imai H, Wada H, Shiga M. Calorimetric study on magnetism of ERCO2. J Magn Magn Mater 1995;140:835–6.
[151] Burrola-Gandara LA, Grijalva-Castillo MC, Santillan-Rodriguez CR, Matutes-Aquino JA. Magnetocaloric effect in Sm-Co2-xFex alloys. J Appl Phys 2012;111:07A942.
[152] Mudryk Y, Paudyal D, Pathak AK, Pecharsky VK, Gschneidner KA. Balancing structural distortions via competing 4f and itinerant interactions: a case of polymorphism in magnetocaloric HoCo2. J Mater Chem C 2016;4:4521–31.
[153] Singh NK, Suresh KG, Nigam AK, Malik SK, Coelho AA, Gama S. Itinerant electron metamagnetism and magnetocaloric effect in RCo2-based Laves phase compounds. J Magn Magn Mater 2007;317:68–79.
[154] Khmelevskyi s, Mohn P. The order of the magnetic phase transitions in RCo2 (R = rare earth) intermetallic compounds. J Phys: Cond Matter 2000;12:9453–64.
[155] Nikitin SA, Tishin AM. Magnetocaloric effect in HoCo2 compound. Cryogenics 1991;31:166–7.
[156] Tohei T, Wada H. Change in the character of magnetocaloric effect with Ni substitution in Ho(Co1-xNix)(2). J Magn Magn Mater 2004;280:101–7.
[157] Dong QY, Zhang HW, Sun JR, Shen BG, Franco V. A phenomenological fitting curve for the magnetocaloric effect of materials with a second-order phase transition. J Appl Phys 2008;103:116101.
[158] Halder M, Yusuf SM, Mukadam MD, Shashikala K. Magnetocaloric effect and critical behavior near the paramagnetic to ferrimagnetic phase transition temperature in TbCo2-xFex. Phys Rev B 2010;81:174402.
[159] Franco V, Conde A, Pecharsky VK, Gschneidner KA. Field dependence of the magnetocaloric effect in Gd and (Er1-xDyx)Al-2: does a universal curve exist? Epl 2007;79:47009.
[160] von Ranke PJ, Pecharsky VK, Gschneidner KA. Influence of the crystalline electrical field on the magnetocaloric effect of DyAl2, ErAl2, and DyNi2. Phys Rev B 1998;58:12110–6.
[161] Nobrega EP, de Oliveira NA, von Ranke PJ, Troper A. Monte Carlo calculations of the magnetocaloric effect in RAl2 (R=Dy, Er). J Appl Phys 2006;99:08Q103.
[162] Alvarez P, Gorria P, Blanco JA. Influence of magnetic fluctuations in the magnetocaloric effect on rare-earth intermetallic compounds. Phys Rev B 2011;84:024412.

[163] de Oliveira NA, von Ranke PJ, Tovar Costa MV, Troper A. Magnetocaloric effect in the intermetallic compounds RCo2 (R=Dy, Ho, Er). Phys Rev B 2002;66:094402.
[164] Lima AL, Oliveira IS, Gomes AM, von Ranke PJ. Origin of anomalous magnetocaloric effect in (Dy1-zErz)Al-2 alloys. Phys Rev B 2002;65:172411.
[165] de Sousa VSR, Monteiro JCB, dos Reis RD, Medina AN, Gama S, von Ranke PJ, et al. Heat flow measurements and the order of the magnetic transition in (Dy, Gd)Co-2 solid solutions. J Alloys Comp 2012;513:615–9.
[166] Zhu YY, Asamoto K, Nishimura Y, Kouen T, Abe S, Matsumoto K, et al. Magnetocaloric effect of (Er(x)R(1-x))CO(2) (R = Ho, Dy) for magnetic refrigeration between 20 and 80 K. Cryogenics 2011;51:494–8.
[167] Balli M, Fruchart D, Gignoux D. A study of magnetism and magnetocaloric effect in Ho1-xTbxCo2 compounds. J Magn Magn Mater 2007;314:16–20.
[168] Balli M, Fruchart D, Gignoux D. The influence of gadolinium on magnetism and magnetocaloric properties of HoCo2 alloy. J Alloys Comp 2008;455:73–6.
[169] Balli M, Fruchart D, Gignoux D. Magnetic behaviour and experimental study of the magnetocaloric effect in the pseudobinary Laves phase Er1-xDyxCo2. J Alloys Comp 2011;509:3907–12.
[170] Cwik J, Palewski T, Nenkov K, Gutfleisch O, Klamut J. The influence of Er substitution on magnetic and magnetocaloric properties of Dy(1-x)Er(x)Co(2) solid solutions. Intermetallics 2011;19:1656–60.
[171] Cwik J, Palewski T, Nenkov K, Lyubina J, Gutfleisch O. Magnetic properties and magnetocaloric effect in (Dy(0.6)Er(0.4))(1-x)Gd(x)Co(2) multicomponent compounds. In: Spalek J, editor. Joint European magnetic symposia. Bristol: Iop Publishing Ltd; 2011. p. 012025.
[172] de Oliveira NA. Magnetocaloric effect in the pseudobinaries (Ho1-cRc)Co-2 (R = Er and Dy). Eur Phys J B 2008;65:207–12.
[173] Gu KM, Li JQ, Ao WQ, Jian YX, Tang JN. The magnetocaloric effect in (Dy, Tb)Co-2 alloys. J Alloys Comp 2007;441:39–42.
[174] Tereshina I, Politova G, Tereshina E, Nikitin S, Burkhanov G, Chistyakov O, et al. Magnetocaloric and magnetoelastic effects in (Tb0.45Dy0.55)(1-x)ErxCo2 multicomponent compounds. J Phys: Conference Series 2010;200:092012.
[175] Chen X, Zhuang YH. Magnetocaloric effect of (Tb1-xCex)Co-2 alloys in low magnetic field. J Rare Earths 2009;27:1027–30.
[176] de Oliveira NA, von Ranke PJ, Troper A. Magnetocaloric effect in (TbcR1-c)Co-2 (R = Er and Ho). J Alloys Comp 2015;618:386–9.
[177] Liu HD, Wang DH, Tang SL, Cao QQ, Tang T, Gu BX, et al. The magnetocaloric effect and magnetic phase transitions in Dy(Co1-xAlx)(2) compounds. J Alloys Comp 2002;346:314–9.
[178] Ao WQ, Li JQ, Liu FS, Jian YX. Magnetocaloric properties of DyCo2-xGax alloys. Solid State Commun 2007;141:219–22.
[179] Fu H, Ma Z, Zhang XJ, Wang DH, Teng BH, Balfour EA. Table-like magnetocaloric effect in the Gd-Co-Al alloys with multi-phase structure. Appl Phys Lett 2014;104:072401.
[180] Ivanova TI, Nikitin SA, Tskhadadze GA, Koshkid'ko YS, Suski W, Iwasieczko W, et al. Magnetic, transport and magnetocaloric properties in the Laves phase intermetallic Ho (Co1-xAlx)(2) compounds. J Alloys Comp 2014;592:271–6.
[181] Fu H, Hadimani RL, Ma Z, Wang MX, Teng BH, Jiles DC. Magnetocaloric effect in GdCoxAl2-x system for (0.15 <= x <= 1) compositions. J Appl Phys 2014;115:17A914.
[182] Han ZD, Hua ZH, Wang DH, Zhang CL, Gu BX, Du YW. Magnetic properties and magnetocaloric effect in Dy(Co1-xFex)(2) alloys. J Magn Magn Mater 2006;302:109–12.
[183] Tereshina IS, Politova GA, Tereshina EA, Burkhanov GS, Chistyakov OD, Nikitin SA. Magnetocaloric effect in (Tb, Dy, R)(Co, Fe)(2) (R = Ho, Er) multicomponent compounds. In: Takahashi M, Saito H, Yoshimura S, Takanashi K, Sahashi M, Tsunoda M, editors. 2nd International symposium on advanced magnetic materials and applications. Bristol: Iop Publishing Ltd; 2011. p. 012077.
[184] Liu XB, Altounian Z. Magnetocaloric effect in co-rich Er(Co1-xFex)(2) laves phase. J Appl Phys 2008;103:07B304.
[185] Balli M, Fruchart D, Gignoux D. Effect of Ni substitution on the magnetic and magnetocaloric properties of the Dy(Co1-xNix)(2) Laves phase. J Phys D-Appl Phys. 2007;40:7601–5.
[186] Li LW, Nishimura K, Tamei D, Mori K. Structure, transport properties and the magnetocaloric effect in Gd(Co1-xNix)(2) pseudobinary compounds. Solid State Commun 2008;145:427–31.
[187] Zhang JY, Luo J, Li JB, Liang JK, Wang YC, Ji LN, et al. Magnetocaloric effect of Gd(Co1-xMnx)(2) compounds. Solid State Commun 2007;143:541–4.
[188] Pathak AK, Dubenko I, Stadler S, Ali N. Magnetic, magnetocaloric, and magnetotransport properties of RCo1.8Mn0.2 (R = Er, Ho, Dy, and Tb) compounds. J Magn Magn Mater 2011;323:2436–40.
[189] Gerasimov EG, Mushnikov NV, Inishev AA, Terentev PB, Gaviko VS. Structure, magnetic and magnetothermal properties of the non-stoichiometric ErCo2Mnx alloys. J Alloys Comp 2016;680:359–65.
[190] Wang CL, Liu J, Mudryk Y, Gschneidner KA, Long Y, Pecharsky VK. The effect of boron doping on crystal structure, magnetic properties and magnetocaloric effect of DyCo2. J Magn Magn Mater 2016;405:122–8.
[191] Zou JD, Yan M, Yao JL. Manipulation of the magnetic properties in Er1-xCo2 compounds by atomic vacancies. J Alloys Comp 2015;632:30–6.
[192] Cwik J, Palewski T, Nenkov K, Warchulska J, Klamut J. Magnetic and magnetocaloric properties of Gd(1-x)Sc(x)Ni(2) solid solutions. J Magn Magn Mater 2012;324:677–82.
[193] Ibarra-Gaytán PJ, Sánchez Llamazares JL, Álvarez-Alonso P, Sánchez-Valdés CF, Gorria P, Blanco JA. Magnetic entropy table-like shape in RNi2 composites for cryogenic refrigeration. J Appl Phys 2015;117:17C116.
[194] Yano K, Tanaka Y, Matsumoto I, Umehara I, Sato K, Adachi H, et al. Detection of Ni magnetic moment in GdNi2 compound by magnetic Compton profile (MCP) method. J Phys: Cond Matter 2006;18:6891–5.
[195] Gerasimov EG, Mushnikov NV, Terentev PB, Gaviko VS, Inishev AA. Magnetic properties of the off-stoichiometric GdNi2Mnx alloys. J Alloys Comp 2013;571:132–7.
[196] Aryal A, Quetz A, Pandey S, Samanta T, Dubenko I, Mazumdar D, et al. Phase transitions and magnetocaloric and transport properties in off-stoichiometric GdNi2Mnx. J Appl Phys 2016;119:043905.
[197] Wang JL, Campbell SJ, Kennedy SJ, Zeng R, Dou SX, Wu GH. Critical magnetic transition in TbNi(2)Mn-magnetization and Mossbauer spectroscopy. J Phys-Cond Matter 2011;23:216002.
[198] Cwik J, Palewski T, Nenkov K, Tristan NV, Warchulska J, Burkhanova GS, et al. Some physical properties of YxHo1-xNi2 solid solutions. J Alloys Comp 2004;373:78–85.
[199] Cwik A, Palewski T, Nenkov K, Burkhanov GS, Chistyakov OD, Kolchugina N, et al. The effect of substitution of Lu for Ho on some physical properties of LuxHo1-xNi2 solid solutions. Physica B 2005;358:323–31.
[200] Cwik J, Palewski T, Nenkov K, Burkhanov GS. Magnetic, electrical, and thermodynamic properties of the LaxHo1-xNi2 solid solutions. J Alloys Comp 2005;399:7–13.
[201] Cwik J, Palewski T, Nenkov K, Burkhanov GS, Chistyakov OD, Warchulska J. The influence of Sc substitution on some physical properties of ScxHo1-xNi2 solid solutions. Phys Status Solidi B-Basic Solid State Phys 2005;242:1969–77.
[202] Cwik J, Palewski T, Nenkov K, Burkhanov GS, Chistyakov OD, Klamut J, et al. The effect of substitution of La for Tb on some physical properties of Tb1-xLaxNi2 solid solutions. J Alloys Comp 2008;460:41–6.
[203] Xiong DK, Li D, Liu W, Zhang ZD. Magnetocaloric effect of Gd(FexAl1-x)(2) compounds. Physica B 2005;369:273–7.
[204] Xiong DK, Li D, Ren WJ, Li J, Liu W, Zhang ZD. The influence of boron atoms on the magnetocaloric effect of Laves compounds Gd(Fe, Al)(2). J Alloys Comp 2006;413:7–10.
[205] Hermes W, Harmening T, Pottgen R. Ferromagnetism and magnetocaloric effect around 95 K in the Laves Phase EuRh1.2Zn0.8. Chem Mater 2009;21:3325–31.
[206] Gencer H, Izgi T, Kolat VS, Kaya AO, Atalay S. Magnetic and magnetocaloric properties of (Gd(1-x)Ce(x))Al(2) (x=0, 0.25, 0.5, 0.75) compounds. J Magn 2011;16:337–41.
[207] Alho BP, Ribeiro PO, Alvarenga TST, Carvalho AMG, Von Ranke PJ. Magnetocaloric effect in Gd(1-y)DyyAl2. Int J Refrig-Rev Int Froid 2014;37:297–302.

[208] Pathak AK, Paudyal D, Gschneidner KA, Pecharsky VK. Low temperature crystal structure and magnetic properties of RAl2. J Appl Phys 2014;115:17E109.
[209] Gil LA, Campoy JCP, Plaza EJR, de Souza MV. Conventional and anisotropic magnetic entropy change in HoAl2 ferromagnetic compound. J Magn Magn Mater 2016;409:45–9.
[210] Ribeiro PO, Alho BP, Alvarenga TST, Nobrega EP, de Sousa VSR, Carvalho AMG, et al. Theoretical investigations on magnetocaloric effect in Er1-yTbyAl2 series. J Magn Magn Mater 2015;379:112–6.
[211] Ribeiro PO, Alho BP, Alvarenga TST, Nobrega EP, Carvalho AMG, de Sousa VSR, et al. Theoretical investigations on the magnetocaloric and barocaloric effects in TbyGd(1-y)Al2 series. J Alloys Comp 2013;563:242–8.
[212] Pathak AK, Gschneidner KA, Pecharsky VK. The structural and magnetic properties of Pr1−xErxAl2. J Appl Phys 2015;117:17C107.
[213] Pathak AK, Gschneidner KA, Pecharsky VK. Negative to positive magnetoresistance and magnetocaloric effect in Pr0.6Er0.4Al2. J Alloys Comp 2015;621:411–4.
[214] Karmakar SK, Giri S, Majumdar S. Observation of large low temperature magnetocaloric effect in HoCu2. J Appl Phys 2015;117:193904.
[215] Gao T, Nishimura K, Li LW, Namiki T, Isikawa Y. Large magnetocaloric effect in Laves phase TbMn1.8Fe0.2 compound over a wide temperature range. J Alloys Comp 2012;530:26–9.
[216] Ćwik J, Koshkid'ko Y, Mikhailova A, Kolchugina N, Nenkov K, Hackamer A, et al. Magnetic properties and transformation of crystal structure in the ErFe2-ErAl2 system. J Appl Phys 2015;117:123912.
[217] Rosca M, Balli M, Fruchart D, Gignoux D, Hlil EK, Miraglia S, et al. Neutron diffraction study of LaFe11.31Si1.69 and LaFe11.31Si1.69H1.45 compounds. J Alloys Comp 2010;490:50–5.
[218] Wang FW, Wang GJ, Hu FX, Kurbakov A, Shen BG, Cheng ZH. Strong interplay between structure and magnetism in the giant magnetocaloric intermetallic compound LaFe11.4Si1.6: a neutron diffraction study. J Phys-Condes Matter 2003;15:5269–78.
[219] Hu FX, Shen BG, Sun JR, Cheng ZH, Rao GH, Zhang XX. Influence of negative lattice expansion and metamagnetic transition on magnetic entropy change in the compound LaFe11.4Si1.6. Appl Phys Lett 2001;78:3675–7.
[220] Ilyn M, Tishin AM, Hu F, Gao J, Sun JR, Shen BG. Magnetocaloric properties of the LaFe11.7Si1.3 and LaFe11.2Co0.7Si1.1 systems. J Magn Magn Mater 2005;290:712–4.
[221] Liu XB, Altounian Z, Ryan DH. Magnetocaloric enect in La(Fe0.88Al0.12)(13)Cx interstitial compounds. J Phys D-Appl Phys 2004;37:2469–74.
[222] Di NL, Cheng ZH, Li QA, Wang GJ, Kou ZQ, Ma X, et al. First-order magnetic phase transition in LaFe11.7Si1.3 studied using Mossbauer spectroscopy. Phys Rev B 2004;69:224411.
[223] Fujita A, Fujieda S, Fukamichi K. Influence of hydrogenation on the electronic structure and the itinerant-electron metamagnetic transition in strong magnetocaloric compound La(Fe0.88Si0.12)(13). J Magn Magn Mater 2009;321:3553–8.
[224] Wang JL, Campbell SJ, Kennedy SJ, Shamba P, Zeng R, Dou SX, et al. Magnetic transitions in LaFe13-x-yCoySix compounds. Hyperfine Interact 2014;226:405–13.
[225] Gruner ME, Keune W, Roldan Cuenya B, Weis C, Landers J, Makarov SI, et al. Element-resolved thermodynamics of magnetocaloric LaFe(13-x)Si(x). Phys Rev Lett 2015;114:057202.
[226] Gutfleisch O, Yan A, Muller KH. Large magnetocaloric effect in melt-spun LaFe13-xSix. J Appl Phys 2005;97:10M305.
[227] Lyubina J, Schafer R, Martin N, Schultz L, Gutfleisch O. Novel design of La(Fe, Si)(13) alloys towards high magnetic refrigeration performance. Adv Mater 2010;22:3735–9.
[228] Lyubina J. Recent advances in the microstructure design of materials for near room temperature magnetic cooling (invited). J Appl Phys 2011;109:07A902.
[229] Franco V, Conde A, Romero-Enrique JM, Blazquez JS. A universal curve for the magnetocaloric effect: an analysis based on scaling relations. J Phys-Condes Matter 2008;20:285207.
[230] de Medeiros LG, de Oliveira NA. Theoretical calculations of the magnetocaloric effect in La(FexSi1-x)(13). J Magn Magn Mater 2006;306:265–71.
[231] Jia L, Sun JR, Shen J, Dong QY, Zou JD, Gao B, et al. Magnetocaloric effects in the La(Fe, Si)(13) intermetallics doped by different elements. J Appl Phys 2009;105:07A924.
[232] Passamani EC, Larica C, Proveti JR, Takeuchi AY, Gomes AM, Ghivelder L. Magnetic and magnetocaloric properties of La(Fe, Co)(11.4)SP1.6 compounds (SP = Al or Si). J Magn Magn Mater 2007;312:65–71.
[233] Liu XB, Liu XD, Altounian Z. Phase formation and magnetocaloric effect in rapidly quenched La(Fe1-xCox)(11.4)Si-1.6. J Appl Phys 2005;98:113904.
[234] Hu FX, Gao J, Qian XL, Ilyn M, Tishin AM, Sun JR, et al. Magnetocaloric effect in itinerant electron metamagnetic systems La(Fe1-xCox)(11.9)Si-1.1. J Appl Phys 2005;97:10M303.
[235] Hu FX, Qian XL, Sun JR, Wang GJ, Zhang XX, Cheng ZH, et al. Magnetic entropy change and its temperature variation in compounds La(Fe1-xCox)(11.2)Si-1.8. J Appl Phys 2002;92:3620–3.
[236] Liu XB, Altounian Z. Effect of Co content on magnetic entropy change and structure of La(Fe1-xCox)(11.4)Si-1.6. J Magn Magn Mater 2003;264:209–13.
[237] Chen X, Chen YG, Tang YB, Xiao DQ. The system study of 1:13 phase formation, the magnetic transition adjustment, and magnetocaloric property in La(Fe, Co)(13-x)Si-x alloys. J Magn Magn Mater 2014;368:155–68.
[238] Pathak AK, Basnyat P, Dubenko I, Stadler S, Ali N. Influence of the small substitution of Z=Ni, Cu, Cr, V for Fe on the magnetic, magnetocaloric, and magnetoelastic properties of LaFe11.4Si1.6. J Magn Magn Mater 2010;322:692–7.
[239] Gercsi Z. Magnetic coupling in transition-metal–doped LaSiFe11.5 TM0.5 (TM=Cr, Mn, Co and Ni). EPL (Europhys Lett) 2015;110:47006.
[240] Wang F, Chen YF, Wang GJ, Shen BG. The effect of Mn substitution in LaFe11.7Si1.3 compound on the magnetic properties and magnetic entropy changes. J Phys D-Appl Phys 2003;36:1–3.
[241] Lin ZP, Li SD, Liu MM, Duh JG, Peng K, Mao XY. Magnetocaloric effect of La0.8Ce0.2Fe11.4-xMnxSi1.6 compounds. J Alloys Comp 2010;489:1–3.
[242] Fujieda S, Kawamoto N, Fujita A, Fukamichi K. Control of working temperature of large isothermal magnetic entropy change in La(FexTMySi1-x-y)(13) (TM = Cr, Mn, Ni) and La1-zCez(FexMnySi1-x-y)(13). Mater Trans 2006;47:482–5.
[243] Gao B, Hu FX, Wang J, Shen J, Sun JR, Shen BG. Influence of the substitution of Cu for Si on magnetic entropy change and hysteresis loss in LaFe11.7(Si1-xCux)(1.3) compounds. J Appl Phys 2009;105:07A916.
[244] Fujieda S, Fujita A, Fukamichi K. Enhancements of magnetocaloric effects in La(Fe0.90Si0.10)(13) and its hydride by partial substitution of Ce for La. Mater Trans 2004;45:3228–31.
[245] Fujieda S, Fujita A, Fukamichi K. Control of large magnetocaloric effects and hysteresis of La1-zCez(Fe0.86Si0.14)(13) compounds. IEEE Trans Magn 2005;41:2787–9.
[246] Fujieda S, Fujita A, Fukamichi K, Hirano N, Nagaya S. Large magnetocaloric effects enhanced by partial substitution of Ce for La in La(Fe0.88Si0.12)(13) compound. J Alloys Comp 2006;408:1165–8.
[247] Fujieda S, Fujita A, Kawamoto N, Fukamichi K. Strong magnetocaloric effects in La1-zCez(Fex-yMnySi1-x)(13) at low temperatures. Appl Phys Lett 2006;89:062504.
[248] Fujita A, Fujieda S, Fukamichi K. Changes in electronic states and magnetic free energy in La1-zCez(FexSi1-x)(13) magnetic refrigerants. J Phys D-Appl Phys 2011;44:064013.
[249] Anh DTK, Thuy NP, Duc NH, Nhien TT, Nong NV. Magnetism and magnetocaloric effect in La1-yNdy(Fe0.88Si0.12)(13) compounds. J Magn Magn Mater 2003;262:427–31.
[250] Mican S, Tetean R. Magnetic properties and magnetocaloric effect in La0.7Nd0.3Fe13-xSix compounds. J Solid State Chem 2012;187:238–43.
[251] Fujieda S, Fujita A, Fukamichi K. Reduction of hysteresis loss in itinerant-electron metamagnetic transition by partial substitution of Pr for La in La(FexSi1-x)(13). J Magn Magn Mater 2007;310:E1004–5.

[252] Fujieda S, Fujita A, Fukamichi K. Enhancement of magnetocaloric effects in La1-zPrz(Fe0.88Si0.12)(13) and their hydrides. J Appl Phys 2007;102:023907.
[253] Fu B, Long Y, Shi PJ, Bao B, Zhang M, Chang YQ, et al. Effect of praseodymium and cobalt substitution on magnetic properties and structures in La(Fe1-xSix)(13) compounds. J Rare Earths 2010;28:611–3.
[254] Ding MZ, Liu Z, Chen RJ, Yan AR. Magnetocaloric effect in NaZn13-type La(1-)PrxFe(11.44)Si(1.56) melt-spun ribbons. J Appl Phys 2010;107:09A952.
[255] Huang JH, Sun NK, Liu CL, Ge YM, Zhang T, Liu F, et al. Effect of particle size on the hysteretic behavior and magnetocaloric effect of La0.5Pr0.5Fe11.4Si1.6 compound. Acta Metall Sin-Engl Lett 2014;27:27–30.
[256] Demuner AS, Takeuchi AY, Passamani EC, Proveti JR, Larica C, Favre-Nicolin E, et al. Magnetocaloric properties of the (La-Gd)Fe11.4Si1.6 metamagnetic compound. J Magn Magn Mater 2009;321:1809–13.
[257] Balli M, Fruchart D, Gignoux D, Rosca M, Miraglia S. Magnetic and magnetocaloric properties of La1-xErxFe11.44Si1.56 compounds. J Magn Magn Mater 2007;313:43–6.
[258] Fujita A, Matsunami D, Yako H. Realization of small intrinsic hysteresis with large magnetic entropy change in La0.8Pr0.2(Fe0.88Si0.10Al0.02)(13) by controlling itinerant-electron characteristics. Appl Phys Lett 2014;104:122410.
[259] Din MFM, Wang JL, Studer AJ, Gu QF, Zeng R, Debnath JC, et al. Effects of Cr substitution on structural and magnetic properties in La0.7Pr0.3Fe11.4Si1.6 compound. J Appl Phys 2014;115:17A942.
[260] Zhang H, Long Y, Cao Q, Zou M, Gschneidner KA, Pecharsky VK. Effect of Ca on the microstructure and magnetocaloric effects in the La1-xCaxFe11.5Si1.5 compounds. J Alloys Comp 2011;509:3746–50.
[261] Bao LF, Hu FX, Chen L, Wang J, Sun JR, Shen BG. Magnetocaloric properties of La(Fe, Si)13-based material and its hydride prepared by industrial mischmetal. Appl Phys Lett 2012;101:162406.
[262] Fujita A, Fujieda S, Fukamichi K, Yamazaki Y, Iijima Y. Giant magnetic entropy change in hydrogenated La(Fe0.88Si0.12)(13)H-y compounds. Mater Trans 2002;43:1202–4.
[263] Chen YF, Wang F, Shen BG, Hu FX, Cheng ZH, Wang GJ, et al. Large magnetic entropy change near room temperature in the LaFe11.5Si1.5H1.3 interstitial compound. Chin Phys 2002;11:741–4.
[264] Chen YF, Wang F, Shen BG, Hu FX, Sun JR, Wang GJ, et al. Magnetic properties and magnetic entropy change of LaFe11.5Si1.5Hy interstitial compounds. J Phys-Condes Matter 2003;15:L161–7.
[265] Fujita A, Fujieda S, Hasegawa Y, Fukamichi K. Itinerant-electron metamagnetic transition and large magnetocaloric effects in La(FexSi1-x)(13) compounds and their hydrides. Phys Rev B 2003;67:104416.
[266] de Medeiros LG, de Oliveira NA. Magnetocaloric effect in La(FexSi1-x)(13) doped with hydrogen and under external pressure. J Alloys Comp 2006;424:41–5.
[267] Fujieda S, Fujita A, Fukamichi K. Large isothermal magnetic entropy change after hydrogen absorption into La0.5Pr0.5(Fe0.88Si0.12)(13). In: Chang YW, Kim NJ, Lee CS, editors. Advanced Materials Research, Advanced Materials and Processing. Stafa-Zurich: Trans Tech Publications Ltd; 2007. p. 577.
[268] Fujieda S, Fujita A, Fukamichi K. Large magnetocaloric effects in NaZn13-type La(FexSi1-x)(13) compounds and their hydrides composed of icosahedral clusters. Sci Technol Adv Mater 2003;4:339.
[269] Zhao JL, Shen J, Hu FX, Li YX, Sun JR, Shen BG. Reduction of magnetic hysteresis loss in La0.5Pr0.5Fe11.4Si1.6Hx hydrides with large magnetocaloric effects. J Appl Phys 2010;107:113911.
[270] Phejar M, Paul-Boncour V, Bessais L. Investigation on structural and magnetocaloric properties of LaFe13-xSix(H, C)(y) compounds. J Solid State Chem 2016;233:95–102.
[271] Hai X, Mayer C, Colin CV, Miraglia S. In-situ neutron investigation of hydrogen absorption kinetics in La(FexSi1-x)(13) magnetocaloric alloys for room-temperature refrigeration application. J Magn Magn Mater 2016;400:344–8.
[272] Makarov SI, Krautz M, Salamon S, Skokov K, Teixeira CS, Gutfleisch O, et al. Local electronic and magnetic properties of pure and Mn-containing magnetocaloric LaFe13−x Si x compounds inferred from Mössbauer spectroscopy and magnetometry. J Phys D: Appl Phys 2015;48:305006.
[273] Wang GF, Mu LJ, Zhang XF, Zhao ZR, Huang JH. Hydriding and dehydriding kinetics in magnetocaloric La(Fe, Si)(13) compounds. J Appl Phys 2014;115:143903.
[274] Jia L, Sun JR, Shen J, Gao B, Zhao TY, Zhang HW, et al. Influence of interstitial and substitutional atoms on the crystal structure of La(FeSi)(13). J Alloys Comp 2011;509:5804–9.
[275] Wang JW, Chen YG, Tang YB, Xiao SF, Liu T, Zhang EY. The hydrogenation behavior of LaFe11.44Si1.56 magnetic refrigerating alloy. J Alloys Comp 2009;485:313–5.
[276] Wang CL, Long Y, Ma T, Fu B, Ye RC, Chang YQ, et al. The hydrogen absorption properties and magnetocaloric effect of La0.8Ce0.2(Fe1-xMnx)(11.5)Si1.5Hy. J Appl Phys 2011;109:07A910.
[277] Ma T, Long Y, Liu R, Fu B, Zhang H, Ye RC, et al. Study on the homogeneity of hydrogenation for LaFe11.5Si1.5 intermetallic compound. Mater Lett 2010;64:2520–2.
[278] Baumfeld OL, Gercsi Z, Krautz M, Gutfleisch O, Sandeman KG. The dynamics of spontaneous hydrogen segregation in LaFe13-xSixHy. J Appl Phys 2014;115:203905.
[279] Mandal K, Gutfleisch O, Yan A, Handstein A, Muller KH. Effect of reactive milling in hydrogen on the magnetic and magnetocaloric properties of LaFe11.57Si1.43. J Magn Magn Mater 2005;290:673–5.
[280] Mandal K, Pal D, Gutfleisch O, Kerschl P, Muller KH. Magnetocaloric effect in reactively-milled LaFe11.57Si1.43Hy intermetallic compounds. J Appl Phys 2007;102:053906.
[281] Lyubina J, Hannemann U, Ryan MP, Cohen LF. Electrolytic hydriding of LaFe13-xSix alloys for energy efficient magnetic cooling. Adv Mater 2012;24:2042–6.
[282] Fujieda S, Fujita A, Fukamichi K, Suzuki S. Influence of homogenization of microstructual composition on hydrogen absorption into La(Fe(x)Si(1-x))(13) magnetic refrigerants. IEEE Trans Magn 2011;47:2459–62.
[283] Bez HN, Eggert BGF, Lozano JA, Bahl CRH, Barbosa JR, Teixeira CS, et al. Magnetocaloric effect and H gradient in bulk La(Fe, Si)(13)H-y magnetic refrigerants obtained by HDSH. J Magn Magn Mater 2015;386:125–8.
[284] Zheng HY, Tang YB, Chen YG, Wu JH, Wang HS, Xue XZ, et al. The high-temperature hydrogenation behavior of LaFe11.6Si1.4 and splitting of LaFe11.6Si1.4Hy magnetocaloric transition. J Alloys Comp 2015;646:124–8.
[285] Teixeira CS, Krautz M, Moore JD, Skokov K, Liu J, Wendhausen PAP, et al. Effect of carbon on magnetocaloric effect of LaFe11.6Si1.4 compounds and on the thermal stability of its hydrides. J Appl Phys 2012;111:07A927.
[286] Zhao JL, Shen J, Zhang H, Xu ZY, Wu JF, Hu FX, et al. Hydrogenating process and magnetocaloric effect in La0.7Pr0.3Fe11.5Si1.5C0.2Hx hydrides. J Alloys Comp 2012;520:277–80.
[287] Barcza A, Katter M, Zellmann V, Russek S, Jacobs S, Zimm C. Stability and magnetocaloric properties of sintered La(Fe, Mn, Si)(13)H(z) alloys. IEEE Trans Magn 2011;47:3391–4.
[288] Basso V, Kupferling M, Curcio C, Bennati C, Barzca A, Katter M, et al. Specific heat and entropy change at the first order phase transition of La(Fe-Mn-Si)(13)-H compounds. J Appl Phys 2015;118:6.
[289] Bez HN, Nielsen KK, Norby P, Smith A, Bahl CRH. Magneto-elastic coupling in La(Fe, Mn, Si)(13)Hy within the Bean-Rodbell model. AIP Adv. 2016;6:056217.
[290] Piazzi M, Bennati C, Curcio C, Kuepferling M, Basso V. Modeling specific heatandentropychangeinLa(Fe-Mn-Si)(13)-H compounds. J Magn Magn Mater 2016;400:349–55.

[291] Wang ZC, He LH, Cuevas F, Latroche M, Shen J, Wang FW. Hydrogenation, structure and magnetic properties of La(Fe0.91Si0.09)(13) hydrides and deuterides. Chin Phys B 2011;20:067502.
[292] Lyubina J, Nenkov K, Schultz L, Gutfleisch O. Multiple metamagnetic transitions in the magnetic refrigerant La(Fe, Si)(13)H-x. Phys Rev Lett 2008;101:177203.
[293] Balli M, Rosca M, Fruchart D, Gignoux D. Effect of interstitial nitrogen on magnetism and entropy change of LaFe11.7Si1.3 compound. J Magn Magn Mater 2009;321:123–5.
[294] Chen YF, Wang F, Shen BG, Wang GJ, Sun JR. Magnetism and magnetic entropy change of LaFe11.6Si1.4Cx (x=0-0.6) interstitial compounds. J Appl Phys 2003;93:1323–5.
[295] Shen J, Gao B, Zhang HW, Hu FX, Li YX, Sun JR, et al. Reduction of hysteresis loss and large magnetic entropy change in the NaZn13-type LaPrFeSiC interstitial compounds. Appl Phys Lett 2007;91:142504.
[296] Balli M, Fruchart D, Sari O, Huang JH, Rosca M. Refrigerant capacity and direct measurements of the magnetocaloric effect on LaFe11.2Co0.7Si1.1Cx materials. J Appl Phys 2010;107:09A933.
[297] Shen J, Zhao JL. Magnetocaloric effect in La0.5Pr0.5Fe11.5Si1.5 compounds with a combined addition of Co and C. J Appl Phys 2012;111:07A908.
[298] Shen J, Wang F, Zhao JL, Wu JF, Gong MQ, Hu FX, et al. Reduction in hysteresis losses and large magnetic entropy change in the B-doped La(Fe, Si)(13) compounds. J Appl Phys 2010;107:09A909.
[299] Xie SH, Li JQ, Zhuang YH. Influence of boron on the giant magnetocaloric effect of La(Fe0.9Si0.1)(13). J Magn Magn Mater 2007;311:589–93.
[300] Chen XA, Chen YG, Tang YB. Phase, structural, and magnetocaloric properties of high temperature annealed LaFe11.6Si1.4BX. J Alloys Comp 2011;509:2864–9.
[301] Lin ZP, Li SD, Liu M, Tsai SY, Duh JG, Liu MM, et al. The magnetic entropy change in La0.8Ce0.2Fe11.4Si1.6Bx compounds prepared by copper-mold casting. J Magn Magn Mater 2011;323:1741–4.
[302] Hu FX, Shen BG, Sun JR, Cheng ZH, Zhang XX. Magnetic entropy change in La(Fe0.98C0.02)(11.7)A(1)l(1.3). J Phys-Condes Matter 2000;12:L691–6.
[303] Wu JM, Li F, Cui LY, Tai LC. The magnetic entropy change properties of La(1-z)R(z)(Fe1-x-yCoxAly)(13) compounds. J Appl Phys 1996;79:982–7.
[304] Hu FX, Shen BG, Sun JR, Wang GJ, Gao J. Magnetic properties and magnetocaloric effect around phase boundary in La(FexAl1-x)(13) compounds. J Appl Phys 2007;101:09C525.
[305] Bao B, Huang P, Fu B, Shi P, Long Y, Chang YQ, et al. Enhancement of magnetocaloric effects in La0.8R0.2(Fe0.919Co0.081)(11.7) Al-1.3 (R = Pr, Nd) compounds. J Magn Magn Mater 2009;321:786–9.
[306] Zhao JL, Shen J, Shen BG, Hu FX, Sun JR. Enhancement of the magnetocaloric effect and magnetic transition temperature in LaFe11.5Al1.5 by hydrogenation. Solid State Commun 2010;150:2329–32.
[307] Xu L, Zhao JL, Zhang DK, Zhang HG, Yue M. The effects of interstitial atoms C and B on magnetic properties and magnetocaloric effect in LaFe11.5Al1.5 compound. J Alloys Comp 2015;651:8–11.
[308] Zhang DK, Zhao L, Zhang HG, Xu MF, Yue M. The magnetic properties and magnetocaloric effect in LaFe11.5Al1.5Bx compounds. J Alloys Comp 2014;591:143–6.
[309] Zhang DK, Zhao JL, Shen J, Zhang HG, Yue M. The effects of interstitial atoms H and B on magnetic properties and magnetocaloric effect in LaFe11.5Al1.5 compound. J Appl Phys 2014;115:183908.
[310] Palstra TTM, Mydosh J, Nieuwenhuys GJ, Buschow KHJ. Study of the critical behaviour of the magnetization and electrical resistivity in cubic La(Fe, Si) 13 compounds. J Magn Magn Mater 1983;36:290–6.
[311] Blazquez JS, Moreno-Ramirez LM, Ipus JJ, Kiss LF, Kaptas D, Kemeny T, et al. Effect of alpha-Fe impurities on the field dependence of magnetocaloric response in LaFe11.5Si1.5. J Alloys Comp 2015;646:101–5.
[312] Xu C, Li GD, Li XW, Wang LG. Itinerant-electron metamagnetic transition and giant magnetic entropy change in La0.8Ce0.2Fe11.4Si1.6 compound. Chin Sci Bull 2006;51:2046–9.
[313] Krautz M, Skokov K, Gottschall T, Teixeira CS, Waske A, Liu J, et al. Systematic investigation of Mn substituted La(Fe, Si)(13) alloys and their hydrides for room-temperature magnetocaloric application. J Alloys Comp 2014;598:27–32.
[314] Zhang H, Shen J, Xu ZY, Zheng XQ, Hu FX, Sun JR, et al. Simultaneous enhancements of Curie temperature and magnetocaloric effects in the La(1-x)Ce (x)Fe(11.5)Si(1.5)C(y) compounds. J Magn Magn Mater 2012;324:484–7.
[315] Zhang H, Shen BG, Xu ZY, Zheng XQ, Shen J, Hu FX, et al. Reduction of hysteresis loss and large magnetocaloric effect in the C- and H-doped La(Fe, Si) (13) compounds around room temperature. J Appl Phys 2012;111:07A909.
[316] Liu JJ, Bian BR, Han XH, Nie JW, Yan AR, Du J. Influence of H and extra La on magnetocaloric effect of La(0.5+x)Pr(0.5)Fe(11.4)Si(1.6) melt-spun ribbons. IEEE Trans Magn 2011;47:2478–81.
[317] Bao LH, Wei W, Fan WD, Tegus O. A novel preparation method and magnetic properties of NaZn13-type La(Fe, Si)(13) compounds. J Alloys Comp 2014;589:416–9.
[318] Fujita A, Nakayama Y, Kano M, Matsunami D. Improvement of low-field magnetic entropy change by increasing Fe concentration in solid-state reactive sintered La(FexSi1-x)(13). J Alloys Comp 2014;601:158–61.
[319] Chen X, Chen YG, Tang YB. Influence of iron on phase and magnetic property of the LaFe11.6Si1.4 compound. J Rare Earths 2011;29:354–8.
[320] Lai JW, Zheng ZG, Zhong XC, Montemayor R, Liu ZW, Zeng DC. Magnetocaloric effect of nonstoichiometric La1-xFe11.4+xSi1.6 alloys with first-order and second-order magnetic transitions. Intermetallics 2015;63:7–11.
[321] Zhang MX, Liu J, He C, Yan A. Novel microstructure and large magnetocaloric effect in La2Fe11Si2 magnetic refrigerant. Mater Lett 2014;134:87–90.
[322] Zhang ZT, He C, Zhang MX, Liu J. Influence of extra La and annealing temperature on microstructure and magnetocaloric properties of La-Fe-Co-Si alloys. Physica B 2015;476:167–70.
[323] Liu J, Krautz M, Skokov K, Woodcock TG, Gutfleisch O. Systematic study of the microstructure, entropy change and adiabatic temperature change in optimized La-Fe-Si alloys. Acta Mater 2011;59:3602–11.
[324] Liu T, Chen YG, Tang YB, Xiao SF, Zhang EY, Wang JW. Structure and magnetic properties of shortly high temperature annealing LaFe11.6Si1.4 compound. J Alloys Comp 2009;475:672–5.
[325] Kolat VS, Izgi T, Gencer H, Kaya AO, Bayri N, Atalay S. Production of LaFe11.4Si1.6 compound at high temperature with a very short annealing time. J Optoelectron Adv Mater 2009;11:1106–10.
[326] Xiang C, Chen YG, Tang YB. The effect of different temperature annealing on phase relation of LaFe(11.5)Si(1.5) and the magnetocaloric effects of La (0.8)Ce(0.2)Fe(11.5-x)Co(x)Si(1.5) alloys. J Magn Magn Mater 2011;323:3177–83.
[327] Zhang H, Bao B, Shi PJ, Fu B, Long Y, Chang YQ, et al. Phase formation with NaZn13 structure in metamagnetic La(Fe1-xCox)(11.9)Si-1.1 compounds. J Rare Earths 2008;26:727–30.
[328] Xie K, Song XP, Zhu YM, Lv WP, Sun ZB. Large magnetic entropy change in melt-spun LaFe11.5Si1.5 ribbons. J Phys D-Appl Phys 2004;37:3063–6.
[329] Liu XB, Liu XD, Altounian Z, Tu GH. Phase formation and structure in rapidly quenched La(Fe0.88Co0.12)(13-x)Si-x alloys. J Alloys Comp 2005;397:120–5.
[330] Lyubina J, Gutfleisch O, Kuz'min MD, Richter M. La(Fe, Si)(13)-based magnetic refrigerants obtained by novel processing routes. J Magn Magn Mater 2008;320:2252–8.
[331] Lyubina J, Gutfleisch O, Kuz'min MD, Richter M. La(Fe, Si)(13)-based magnetic refrigerants obtained by novel processing routes (vol 320, pg 2252, 2008). J Magn Magn Mater 2009;321:3571–7.
[332] Hou XL, Lampen-Kelley P, Xue Y, Liu CY, Xu H, Han N, et al. Formation mechanisms of NaZn13-type phase in giant magnetocaloric La-Fe-Si compounds during rapid solidification and annealing. J Alloys Comp 2015;646:503–11.
[333] Hou XL, Tian Y, Xue Y, Liu CY, Xia WX, Xu H, et al. Formation of tree-like and vortex magnetic domains of nanocrystalline alpha-(Fe, Si) in La-Fe-Si ribbons during rapid solidification and subsequent annealing. J Alloys Comp 2016;669:205–9.

[334] Zhang MX, Liu J, Zhang Y, Dong JD, Yan AR, Skokov KP, et al. Large entropy change, adiabatic temperature change, and small hysteresis in La(Fe, Mn)(11.6)Si-1.4 strip-cast flakes. J Magn Magn Mater 2015;377:90–4.
[335] Zhang M, Zhang Z, He C, Shao Y, Liu J, Yan A. Microstructure and magnetocaloric properties of $LaFe_{11.8-x}Co_xSi_{1.2}$ strip-cast flakes. IEEE Trans Magn 2015;51:2502404.
[336] Dong JD, Yan AR, Liu J. Microstructure and magnetocaloric properties of melt-extracted La-Fe-Si microwires. J Magn Magn Mater 2014;357:73–6.
[337] Phejar M, Paul-Boncour V, Bessais L. Structural and magnetic properties of magnetocaloric LaFe13-xSix compounds synthesized by high energy ball-milling. Intermetallics 2010;18:2301–7.
[338] Passamani EC, Takeuchi AY, Alves AL, Demuner AS, Favre-Nicolin E, Larica C, et al. Magnetocaloric properties of (La, RE)Fe11.4Si1.6 compounds (RE=Y, Gd). J Appl Phys 2007;102:093906.
[339] Patissier A, Paul-Boncour V. Fast synthesis of LaFe13-xSix magnetocaloric compounds by reactive Spark Plasma Sintering. J Alloys Comp 2015;645:143–50.
[340] Waske A, Giebeler L, Weise B, Funk A, Hinterstein M, Herklotz M, et al. Asymmetric first-order transition and interlocked particle state in magnetocaloric La(Fe, Si)(13). Phys Stat Solidi-Rapid Res Lett 2015;9:136–40.
[341] Yuan ZM, He J, Yang L, Xia ZJ, Zhao DL, You CY, et al. Influence of microstructural changes on magnetic refrigeration performance for La(Fe0.94Co0.06)(11.8)Si-1.2 alloys during magnetic field cycling. J Appl Phys 2015;117:4.
[342] Zhang H, Sun YJ, Niu E, Hu FX, Sun JR, Shen BG. Enhanced mechanical properties and large magnetocaloric effects in bonded La(Fe, Si)(13)-based magnetic refrigeration materials. Appl Phys Lett 2014;104:062407.
[343] Pulko B, Tusek J, Moore JD, Weise B, Skokov K, Mityashkin O, et al. Epoxy-bonded La-Fe-Co-Si magnetocaloric plates. J Magn Magn Mater 2015;375:65–73.
[344] Xia W, Huang JH, Sun NK, Lui CL, Ou ZQ, Song L. Influence of powder bonding on mechanical properties and magnetocaloric effects of La0.9Ce0.1(Fe, Mn)(11.7)Si1.3H1.8. J Alloys Comp 2015;635:124–8.
[345] Zhang H, Sun YJ, Li YW, Wu YY, Long Y, Shen J, et al. Mechanical properties and magnetocaloric effects in La(Fe, Si)(13) hydrides bonded with different epoxy resins. J Appl Phys 2015;117:4.
[346] Skokov KP, Karpenkov DY, Kuz'min MD, Radulov IA, Gottschall T, Kaeswurm B, et al. Heat exchangers made of polymer-bonded La(Fe, Si)(13). J Appl Phys 2014;115:17A941.
[347] Radulov IA, Skokov KP, Karpenkov DY, Gottschall T, Gutfleisch O. On the preparation of La(Fe, Mn, Si)(13)H-x polymer-composites with optimized magnetocaloric properties. J Magn Magn Mater 2015;396:228–36.
[348] Lanzarini J, Barriere T, Sahli M, Gelin JC, Dubrez A, Mayer C, et al. Thermoplastic filled with magnetocaloric powder. Mater Des 2015;87:1022–9.
[349] Krautz M, Funk A, Skokov KP, Gottschall T, Eckert J, Gutfleisch O, et al. A new type of La(Fe, Si)(13)-based magnetocaloric composite with amorphous metallic matrix. Scr Mater 2015;95:50–3.
[350] Zhang H, Liu J, Zhang MX, Shao YY, Li Y, Yan A. LaFe11.6Si1.4Hy/Sn magnetocaloric composites by hot pressing. Scr Mater 2016;120:58–61.
[351] Shao YY, Zhang MX, Luo HB, Yan A, Liu J. Enhanced thermal conductivity in off-stoichiometric La-(Fe, Co)-Si magnetocaloric alloys. Appl Phys Lett 2015;107:152403.
[352] You CY, Wang SP, Zhang J, Yang NN, Tian N. Improvement of magnetic hysteresis loss, corrosion resistance and compressive strength through spark plasma sintering magnetocaloric LaFe11.65Si1.35/Cu core-shell powders. AIP Adv 2016;6:055321.
[353] Fujieda S, Fukamichi K, Suzuki S. Suppression of aqueous corrosion of La(Fe0.88Si0.12)(13) by reducing dissolved oxygen concentration for high-performance magnetic refrigeration. J Alloys Comp 2014;600:67–70.
[354] Hu J, Guan L, Fu S, Sun YY, Long Y. Corrosion and latent heat in thermal cycles for La(Fe, Mn, Si)(13) magnetocaloric compounds. J Magn Magn Mater 2014;354:336–9.
[355] Forchelet J, Zamni L, El Alami SE, Hu J, Balli M, Sari O. Corrosion behavior of gadolinium and La-Fe-Co-Si compounds in various heat conducting fluids. Int J Refrig-Rev Int Froid 2014;37:307–13.
[356] Hu J, Zhang M, Long Y, Fu S, Wang HS, Zhong KX. Corrosion behavior and Delta S-T-c relation of LaFe13-x-yCoxSiyCz compounds near room temperature. J Magn Magn Mater 2015;377:368–72.
[357] Pecharsky AO, Gschneidner DA, Pecharsky VK, Schindler CE. The room temperature metastable/stable phase relationships in the pseudo-binary Gd5Si4-Gd5Ge4 system. J Alloys Comp 2002;338:126–35.
[358] Pecharsky VK, Gschneidner KA. Gd-5(SixGe1-x)(4): an extremum material. Adv Mater 2001;13:683–6.
[359] Pecharsky AO, Gschneidner KA, Pecharsky VK. The giant magnetocaloric effect between 190 and 300 K in the Gd5SixGe4-x alloys for 1.4 <= x <= 2.2. J Magn Magn Mater 2003;267:60–8.
[360] Pecharsky VK, Samolyuk GD, Antropov VP, Pecharsky AO, Gschneidner KA. The effect of varying the crystal structure on the magnetism, electronic structure and thermodynamics in the Gd-5(SixGe1-x)(4) system near x=0.5. J Solid State Chem 2003;171:57–68.
[361] Miller GJ. Complex rare-earth tetrelides, RE5(SixGe1-x)(4): new materials for magnetic refrigeration and a superb playground for solid state chemistry. Chem Soc Rev 2006;35:799–813.
[362] Pecharsky VK, Gschneidner KA, Mudryk Y, Paudyal D. Making the most of the magnetic and lattice entropy changes. J Magn Magn Mater 2009;321:3541–7.
[363] Mudryk Y, Lee Y, Vogt T, Gschneidner KA, Pecharsky VK. Polymorphism of Gd5Si2Ge2: the equivalence of temperature, magnetic field, and chemical and hydrostatic pressures. Phys Rev B 2005;71:174104.
[364] Melikhov Y, Hadimani RL, Raghunathan A. Gd-5(SixGe1-x)(4) system - updated phase diagram. J Magn Magn Mater 2015;395:143–6.
[365] Pecharsky VK, Gschneidner KA. Tunable magnetic regenerator alloys with a giant magnetocaloric effect for magnetic refrigeration from similar to 20 to similar to 290 K. Appl Phys Lett 1997;70:3299–301.
[366] Pecharsky VK, Holm AP, Gschneidner KA, Rink R. Massive magnetic-field-induced structural transformation in Gd5Ge4 and the nature of the giant magnetocaloric effect. Phys Rev Lett 2003;91:197204.
[367] Kouvel JS, Hartelius CC. Anomalous magnetic moments and transformations in the ordered FeRh. J Appl Phys 1962;33:1343–4.
[368] Melikhov Y, Hadimani RL, Raghunathan A. Phenomenological modelling of first order phase transitions in magnetic systems. J Appl Phys 2014;115:183902.
[369] Alvaranega TST, Alho BP, Nobrega EP, Ribeiro PO, Caldas A, de Sousa VSR, et al. Theoretical investigation on the barocaloric and magnetocaloric properties in the Gd5Si2Ge2 compound. J Appl Phys 2014;116:243908.
[370] Pires AL, Belo JH, Lopes AML, Gomes IT, Morellon L, Magen C, et al. Phase competitions behind the giant magnetic entropy variation: Gd5Si2Ge2 and Tb5Si2Ge2 case studies. Entropy 2014;16:3813–31.
[371] von Moos L, Bahl CRH, Nielsen KK, Engelbrecht K. The influence of hysteresis on the determination of the magnetocaloric effect in Gd5Si2Ge2. J Phys D: Appl Phys 2015;48:025005.
[372] Giguere A, Foldeaki M, Gopal BR, Chahine R, Bose TK, Frydman A, et al. Direct measurement of the "giant" adiabatic temperature change in Gd5Si2Ge2. Phys Rev Lett 1999;83:2262–5.
[373] Gschneidner KA, Pecharsky VK, Bruck E, Duijn HGM, Levin EM. Comment on "Direct measurement of the 'giant' adiabatic temperature change in Gd5Si2Ge2". Phys Rev Lett 2000;85:4190.
[374] Sun JR, Hu FX, Shen BG. Comment on "Direct measurement of the 'giant' adiabatic temperature change in Gd5Si2Ge2". Phys Rev Lett 2000;85:4191.
[375] Casanova F, Batlle X, Labarta A, Marcos J, Manosa L, Planes A. Entropy change and magnetocaloric effect in Gd-5(SixGe1-x)(4). Phys Rev B 2002;66:100401.
[376] Pecharsky VK, Gschneidner KA. Effect of alloying on the giant magnetocaloric effect of Gd-5(Si2Ge2). J Magn Magn Mater 1997;167:L179–84.

[377] Shull RD, Provenzano V, Shapiro AJ, Fu A, Lufaso MW, Karapetrova J, et al. The effects of small metal additions (Co, Cu, Ga, Mn, Al, Bi, Sn) on the magnetocaloric properties of the Gd5Ge2Si2 alloy. J Appl Phys 2006;99:08K908.
[378] Aksoy S, Yucel A, Elerman Y, Krenke T, Acet M, Moya X, et al. The influence of gallium on the magnetocaloric properties of Gd5Si2Ge2. J Alloys Comp 2008;460:94–8.
[379] Provenzano V, Zhang TB, Shapiro A, Chen YG, Shull RD. Magnetocaloric properties and structure of the Gd(5)Ge(1.8)Si(1.8)Sn(0.4)compund. IEEE Trans Magn 2008;44:3048–51.
[380] Zhuang YH, Li JQ, Huang WD, Sun WA, Ao WQ. Giant magnetocaloric effect enhanced by Pb-doping in Gd5Si2Ge2 compound. J Alloys Comp 2006;421:49–53.
[381] Li JQ, Sun WA, Jian YX, Zhuang YH, Huang WD, Liang JK. The giant magnetocaloric effect of Gd5Si1.95Ge2.05 enhanced by Sn doping. J Appl Phys 2006;100:073904.
[382] Aghababyan EV, Harutyunyan NP. Magnetocaloric effect of compounds in the Gd5Si2-xGe2-xSn2x system. J Contemp Phys-Armenian Acad Sci 2015;50:200–3.
[383] Yuzuak E, Dincer I, Elerman Y. Magnetocaloric properties of the Gd5Si2.05-xGe1.95-xMn2x compounds. J Rare Earths 2010;28:477–80.
[384] Yuzuak E, Dincer I, Elerman Y. Giant magnetocaloric effect in the Gd5Ge2.025Si1.925In0.05 compound. Chin Phys B 2010;19:037502.
[385] Prabahar K, Kumar DMR, Raja MM, Palit M, Chandrasekaran V. Solidification behaviour and microstructural correlations in magnetocaloric Gd-Si-Ge-Nb alloys. Mater Sci Eng B-Adv Funct Solid-State Mater 2010;172:294–9.
[386] Podmiljsak B, McGuiness P, Miklavic B, Rozman KZ, Kobe S. Magnetocaloric properties and nanoscale structure of Fe-doped Gd5Ge2Si2 alloys. J Appl Phys 2009;105:07A941.
[387] Podmiljsak B, Skulj I, Markoli B, Rozman KZ, McGuiness PJ, Kobe S. Microstructural changes in Fe-doped Gd5Si2Ge2. J Magn Magn Mater 2009;321:300–4.
[388] Nirmala R, Morozkin AV, Malik SK. Magnetocaloric effect in the intermetallic compound Gd5Si2Sb2. Europhys Lett 2005;72:652–7.
[389] Svitlyk V, Mozharivskyj Y. Magnetic transitions in the Gd5Si4-xPx (x=0.5, 0.75, 1.25) phases. Magnetocaloric effect of the Gd5Si2.75P1.25 phase. Solid State Sci 2009;11:1941–4.
[390] Chernyshov AS, Mudryk YS, Pecharsky VK, Gschneidner KA. Structural and magnetothermal properties of the Gd5SbxGe4-x system. J Appl Phys 2006;99:08Q102.
[391] Wu W, Tsokol AO, Gschneidner KA, Sampaio JA. Influence of oxygen on the giant magnetocaloric effect of Gd5Si1.95Ge2.05. J Alloys Comp 2005;403:118–23.
[392] Alves CS, Colucci CC, Gama S, Carvalho AMC, Coelho AA. Influence of hydrogen on the magnetic behaviour of Gd5Ge2Si2Hx, 0.1 <= x <= 2.5. J Magn Magn Mater 2004;272:2391–2.
[393] Carvalho AMG, Alves CS, Colucci CC, Bolanho MA, Coelho AA, Gama S, et al. Effect of hydrogen on the structural, magnetic and magnetocaloric properties of the Gd5Ge2.1Si1.9 compound. J Alloys Comp 2007;432:11–4.
[394] Belo JH, Pereira AM, Ventura J, Oliveira GNP, Araujo JP, Tavares PB, et al. Phase control studies in Gd5Si2Ge2 giant magnetocaloric compound. J Alloys Comp 2012;529:89–95.
[395] Pecharsky AO, Gschneidner KA, Pecharsky VK. The giant magnetocaloric effect of optimally prepared Gd5Si2Ge2. J Appl Phys 2003;93:4722–8.
[396] Yan A, Handstein A, Kerschl P, Nenkov K, Muller KH, Gutfleisch O. Effect of composition and cooling rate on the structure and magnetic entropy change in Gd5SixGe4-x. J Appl Phys 2004;95:7064–6.
[397] Lograsso TA, Schlagel DL, Pecharsky AO. Synthesis and characterization of single crystalline Gd-5(Si, Ge1-x)(4) by the Bridgman method. J Alloys Comp 2005;393:141–6.
[398] Gschneidner KA, Pecharsky VK. Magnetic refrigeration materials (invited). J Appl Phys 1999;85:5365–8.
[399] Fu H, Chen YG, Tu MJ, Zhang TB. Phase analysis of Gd-5(SixGe1-x)(4) alloys prepared from different purity Gd with x=0.475 and 0.43. Acta Mater 2005;53:2377–83.
[400] Spichkin YI, Pecharsky VK, Gschneidner KA. Preparation, crystal structure, magnetic and magnetothermal properties of (GdxR5-x)Si-4, where R=Pr and Tb, alloys. J Appl Phys 2001;89:1738–45.
[401] Yang HF, Rao GH, Liu GY, Ouyang ZW, Liu WF, Feng XM, et al. Crystal structure and magnetic properties of Pr5Si4-Ge-x(x) compounds. J Magn Magn Mater 2003;263:146–53.
[402] Magen C, Morellon L, Algarabel PA, Ibarra MR, Ritter C, Pecharsky AO, et al. Evidence for a coupled magnetic-crystallographic transformation in Nd-5(Si0.6Ge0.4)(4). Phys Rev B 2004;70:224429.
[403] Yang HF, Rao GH, Liu GY, Ouyang ZW, Liu WF, Feng XM, et al. Structure dependence of magnetic properties of Nd5Si4-xGex (x=1.2 and 2). Physica B 2003;325:293–9.
[404] Ahn K, Pecharsky VK, Gschneidner KA. Phase relationships, and the structural, magnetic, and thermodynamic properties in the Sm5SixGe4-x pseudobinary system. Phys Rev B 2007;76:014415.
[405] Morellon L, Magen C, Algarabel PA, Ibarra MR, Ritter C. Magnetocaloric effect in Tb-5(SixGe1-x)(4). Appl Phys Lett 2001;79:1318–20.
[406] Thuy NP, Nong NV, Hien NT, Tai LT, Vinh TQ, Thang PD, et al. Magnetic properties and magnetocaloric effect of Tb-5(SixGe1-x)(4) compounds. J Magn Magn Mater 2002;242:841–3.
[407] Deng JQ, Zhuang YH, Li JQ, Zhou KW. Magnetic phase transition and magnetocaloric effect in (Gd1-xTbx)(5)Si1.72Ge2.28 compounds. J Alloys Comp 2007;428:28–33.
[408] Deng JQ, Zhuang YH, Li JQ, Zhu QM. The magnetocaloric effect in (Gd0.74Tb0.26)(5)(SixGe1-x)(4) alloys. Mater Lett 2007;61:2359–61.
[409] Min JX, Zhong XC, Franco V, Tian HC, Liu ZW, Zheng ZG, et al. Structure, magnetic properties and giant magnetocaloric effect of Tb4Gd1Si2.035Ge1.935Mn0.03 alloy. Intermetallics 2015;57:68–72.
[410] Xie K, Sun ZB, Zhu YM, Yang S, Song XP. Magnetic entropy change in (Gd1-xDyx)Si-4 compounds. J Alloys Comp 2004;372:49–51.
[411] Gschneidner KA, Pecharsky VK, Pecharsky AO, Ivtchenko VV, Levin EM. The nonpareil R-5(SixGe1-x)(4) phases. J Alloys Comp 2000;303:214–22.
[412] Singh NK, Paudyal D, Mudryk Y, Pecharsky VK, Gschneidner KA. Magnetostructural properties of Ho(5)(Si(0.8)Ge(0.2))(4). Phys Rev B 2010;81:184414.
[413] Singh NK, Paudyal D, Pecharsky VK, Gschneidner KA. Magnetic and magnetothermodynamic properties of Ho5Si4. J Appl Phys 2010;107:09A921.
[414] Pecharsky AO, Gschneidner KA, Pecharsky VK, Schlagel DL, Lograsso TA. Phase relationships and structural, magnetic, and thermodynamic properties of alloys in the pseudobinary Er5Si4-Er5Ge4 system. Phys Rev B 2004;70:144419.
[415] Singh NK, Pecharsky VK, Gschneidner KA. Unusual magnetic properties of (Er1-xGdx)(5)Si-4 compounds. Phys Rev B 2008;77:054414.
[416] Zou JD, Yan M, Yao JL. The structural and magnetic properties of the compound Tm5Ge4. RSC Adv 2015;5:26850–5.
[417] Zhang H, Mudryk Y, Cao Q, Pecharsky VK, Gschneidner KA, Long Y. Phase relationships, and structural, magnetic, and magnetocaloric properties in the Ce5Si4-Ce5Ge4 system. J Appl Phys 2010;107:013909.
[418] Uthaman B, Raji GR, Thomas S, Suresh KG, Varma MR. Tuning the structural and magnetocaloric properties of Gd5Si2Ge2 with Nd substitution. J Appl Phys 2015;117:013910.
[419] Vecchini C, Moze O, Pecharsky AO, Pecharsky VK, Gschneidner KA, Bruck E, et al. Dynamic magnetic susceptibility of Gd5Si2Ge2 and Gd4YSi1.9Ge2.1. J Appl Phys 2004;95:7207–9.
[420] Prabahar K, Kumar DMR, Raja MM, Chandrasekaran V. Phase analysis and magnetocaloric properties of Zr substituted Gd-Si-Ge alloys. J Magn Magn Mater 2011;323:1755–9.
[421] Zhong XC, Zou M, Zhang H, Liu ZW, Zeng DC, Gschneidner KA, et al. Crystal structure and magnetic properties of R5Sn4 alloys, where R is Tb, Dy, Ho, and Er. J Appl Phys 2011;109:07A917.

[422] Carvalho AMG, Alves CS, de Campos A, Coelho AA, Gama S, Gandra FCG, et al. The magnetic and magnetocaloric properties of Gd5Ge2Si2 compound under hydrostatic pressure. J Appl Phys 2005;97:10M320.
[423] Zou JD. Magnetocaloric and barocaloric effects in a Gd5Si2Ge2 compound. Chin Phys B 2012;21:037503.
[424] Morellon L, Arnold Z, Magen C, Ritter C, Prokhnenko O, Skorokhod Y, et al. Pressure enhancement of the giant magnetocaloric effect in Tb5Si2Ge2. Phys Rev Lett 2004;93:137201.
[425] Arnold Z, Skorokhod Y, Kamarad J, Magen C, Algarabel PA. Pressure effect on phase transitions and magnetocaloric effect in Gd5Ge4. J Appl Phys 2009;105:07A934.
[426] Hadimani RL, Silva JHB, Pereira AM, Schlagel DL, Lograsso TA, Ren Y, et al. Gd5(Si, Ge)4 thin film displaying large magnetocaloric and strain effects due to magnetostructural transition. Appl Phys Lett 2015;106:032402.
[427] Pires AL, Belo JH, Gomes L, Hadimani RL, Jiles DC, Fernandes L, et al. Annealing influence on the magnetostructural transition in Gd5Si1.3Ge2.7 thin films. Mater Lett 2015;159:301–4.
[428] Lewis LH, Yu MH, Gambino RJ. Simple enhancement of the magnetocaloric effect in giant magnetocaloric materials. Appl Phys Lett 2003;83:515–7.
[429] Yue M, Zhang JX, Zeng H, Chen HL, Liu XB. Magnetocaloric effect in layer structural Gd-5(SixGe1-x)(4)/Gd composite material. J Appl Phys 2007;101:09C520.
[430] Hadimani RL, Mudryk Y, Prost TE, Pecharsky VK, Gschneidner KA, Jiles DC. Growth and characterization of Pt-protected Gd5Si4 thin films. J Appl Phys 2014;115:17C113.
[431] Hadimani RL, Gupta S, Harstad SM, Pecharsky VK, Jiles DC. Investigation of room temperature ferromagnetic nanoparticles of Gd_5Si_4. IEEE Trans Magn 2015;51:2504104.
[432] Rajkumar DM, Raja MM, Gopalan R, Chandrasekaran V. Magnetocaloric effect in high-energy ball-milled Gd5Si2Ge2 and Gd5Si2Ge2/Fe nanopowders. J Magn Magn Mater 2008;320:1479–84.
[433] Zhang TB, Provenzano V, Chen YG, Shull RD. Magnetic properties of a high energy ball-milled amorphous Gd5Si1.8Ge1.8Sn0.4 alloy. Solid State Commun 2008;147:107–10.
[434] Trevizoli PV, Alves CS, Mendes MAB, Carvalho AMG, Gama S. Powder metallurgy influences on the magnetic properties of Gd5.09Ge2.03Si1.88 alloy. J Magn Magn Mater 2008;320:1582–5.
[435] Pires AL, Belo JH, Turcaud J, Oliveira GNP, Araujo JP, Berenov A, et al. Influence of short time milling in R-5(Si, Ge)(4), R = Gd and Tb, magnetocaloric materials. Mater Des 2015;85:32–8.
[436] Ozaydin MF, Liang H. Multi-energy conversion of Gd-5 (SiGe2)-poly (vinylidene fluoride), a hybrid material. Appl Phys Lett 2014;105:062903.
[437] Wang JL, Campbell SJ, Studer AJ, Avdeev M, Zeng R, Dou SX. Magnetic phase transitions in Pr(1-x)LuxMn(2)Ge(2) compounds. J Phys-Condes Matter 2009;21:124217.
[438] Koyama K, Miura S, Okada H, Shigeoka T, Fujieda S, Fujita A, et al. Magnetocaloric and structural properties of SmMn2Ge2. J Alloys Comp 2006;408:118–21.
[439] Duraj M, Szytula A. Magnetic properties and magnetocaloric effect of R1-xRx ' Mn2Ge2 compounds. Acta Phys Pol A 2010;117:603–6.
[440] Kumar P, Suresh KG, Nigam AK, Malik SK. Magnetic, magnetothermal, and magnetotransport properties in SmMn2Si2-xGex compounds. J Appl Phys 2008;103:013909.
[441] Kumar P, Suresh KG, Nigam AK, Magnus A, Coelho AA, Gama S. Pressure-induced changes in the magnetic and magnetocaloric properties of RMn2Ge2 (R=Sm, Gd). Phys Rev B 2008;77:224427.
[442] Emre B, Aksoy S, Posth O, Acet M, Duman E, Lindner J, et al. Antiferromagnetic-ferromagnetic crossover in La0.5Pr0.5Mn2Si2 and its consequences on magnetoelastic and magnetocaloric properties. Phys Rev B 2008;78:144408.
[443] Emre B, Dincer I, Elerman Y. Magnetic and magnetocaloric results of magnetic field-induced transitions in La1-xCexMn2Si2 (x=0.35 and 0.45) compounds.. J Magn Magn Mater 2010;322:448–53.
[444] Zhang TB, Chen YG, Tang YB, Zhang EY, Tu MJ. Magnetocaloric effect in LaMn2-xFexGe2 at near room temperature. Phys Lett A 2006;354:462–5.
[445] Bruck E, Tegus O, Thanh DTC, Trung NT, Buschow KHJ. A review on Mn based materials for magnetic refrigeration: structure and properties. Int J Refrig-Rev Int Froid 2008;31:763–70.
[446] Wang JL, Campbell SJ, Cadogan JM, Studer AJ, Zeng R, Dou SX. Magnetocaloric effect in layered NdMn2Ge0.4Si1.6. Appl Phys Lett 2011;98:232509.
[447] Zeng R, Dou SX, Wang JL, Campbell SJ. Large magnetocaloric effect in re-entrant ferromagnet PrMn1.4Fe0.6Ge2. J Alloys Comp 2011;509:L119–23.
[448] Chen YQ, Luo J, Liang JK, Li JB, Rao GH. Magnetic properties and magnetocaloric effect of Nd(Mn1-xFex)(2)Ge-2 compounds. J Alloys Comp 2010;489:13–9.
[449] Kaya M, Rezaeivala M, Yuzuak E, Akturk S, Dincer I, Elerman Y. Effects of size reduction on the magnetic and magnetocaloric properties of NdMn2Ge2 nanoparticles prepared by high-energy ball milling. Phys Status Solidi B-Basic Solid State Phys 2015;252:192–7.
[450] Din MFM, Wang JL, Avdeev M, Gu QF, Zeng R, Campbell SJ, et al. Magnetic properties and magnetocaloric effect of NdMn2-xCuxSi2 compounds. J Appl Phys 2014;115:17A921.
[451] Md Din MF, Wang JL, Campbell SJ, Studer AJ, Avdeev M, Kennedy SJ, et al. Magnetic phase transitions and entropy change in layered NdMn1.7Cr0.3Si2. Appl Phys Lett 2014;104:042401.
[452] Kervan S, Kervan N, Ozturk A, Ozcelik B, Nane O. Magnetocaloric effect in re-entrant ferrimagnet Nd0.2Gd0.8Mn2Ge2 compound. Solid State Commun 2011;151:408–10.
[453] Li LW, Saensunon B, Hutchison WD, Huo DX, Nishimura K. Magnetic properties and large reversible magnetocaloric effect in TmMn2Si2. J Alloys Comp 2014;582:670–3.
[454] Li G, Wang J, Cheng Z, Ren Q, Fang C, Dou S. Large entropy change accompanying two successive magnetic phase transitions in TbMn2Si2 for magnetic refrigeration. Appl Phys Lett 2015;106:182405.
[455] Maji B, Ray MK, Suresh KG, Banerjee S. Large exchange bias and magnetocaloric effect in TbMn2Si2. J Appl Phys 2014;116:213913.
[456] Samanta T, Das I, Banerjee S. Giant magnetocaloric effect in antiferromagnetic ErRu2Si2 compound. Appl Phys Lett 2007;91:152506.
[457] Samanta T, Das I, Banerjee S. Comparative studies of magnetocaloric effect and magnetotransport behavior in GdRu2Si2 compound. J Appl Phys 2008;104:123901.
[458] Li LW, Nishimura K, Kadonaga M, Qian ZH, Huo DX. Giant magnetocaloric effect in antiferromagnetic borocarbide superconductor RNi(2)B(2)C (R = Dy, Ho, and Er) compounds. J Appl Phys 2011;110:043912.
[459] Li LW, Nishimura K. Magnetic properties and large reversible magnetocaloric effect in PrCo2B2 compound. J Appl Phys 2009;106:023903.
[460] Li LW, Nishimura K. Magnetic properties and magnetocaloric effect in NdCo2B2 compound. J Phys D-Appl Phys 2009;42:145003.
[461] Li LW, Nishimura K. Giant reversible magnetocaloric effect in antiferromagnetic superconductor Dy0.9Tm0.1Ni2B2C compound. Appl Phys Lett 2009;95:132505.
[462] Li LW, Nishimura K, Yamane H. Giant reversible magnetocaloric effect in antiferromagnetic GdCo2B2 compound. Appl Phys Lett 2009;94:102509.
[463] Zhang YK, Yang BJ. Effect of Fe substitution on magnetocaloric effect in metamagnetic boron-carbide ErNi2-xFexB2C compounds. J Alloys Comp 2014;610:540–3.
[464] Chen GF, Du QH, Yang WY, Lai YF, Yang JB, Wang CS, et al. The magnetic properties of NdMnxCr2-xSi2C ($0 < x < 2$). J Phys D-Appl Phys 2016;49:025001.
[465] Kim MS, Sung NH, Son Y, Ko MS, Cho BK. Giant reversible anisotropic magnetocaloric effect in an antiferromagnetic EuFe(2)As(2) single crystal. Appl Phys Lett 2011;98:172509.
[466] Li LW, Fan HB, Matsui S, Huo DX, Nishimura K. Magnetocaloric effect in metamagnetic borocarbide DyNi(2-x)A(x)B(2)C (A = Co and Cr) compounds. J Alloys Comp 2012;529:25–8.

[467] Mo Z-J, Shen J, Yan L-Q, Gao X-Q, Wang L-C, Tang C-C, et al. Magnetic properties and magnetocaloric effect in the RCu2Si2 and RCu2Ge2 (R = Ho, Er) compounds. J Appl Phys 2014;115:073905.
[468] Paramanik T, Das K, Samanta T, Das I. Observation of large magnetocaloric effect in HoRu2Si2. J Appl Phys 2014;115.
[469] Paramanik T, Das K, Samanta T, Das I. Generation of magnetic phase diagram of HoRu2Si2 using magnetocaloric effect. J Magn Magn Mater 2015;381:168–72.
[470] Dörr K. Ferromagnetic manganites: spin-polarized conduction versus competing interactions. J Phys D: Appl Phys 2006;39:R125–50.
[471] Wang ZM, Xu QY, Sun JZ, Pan JA, Zhang H. Room temperature magnetocaloric effect of La-deficient bulk perovskite manganite La0.7MnO3-delta. Physica B 2011;406:1436–40.
[472] Szewczyk A, Gutowska M, Dabrowski B. Specific heat and phase diagram of heavily doped La1-xSrxMnO3 (0.45 <= x <= 1.0). Phys Rev B 2005;72:224429.
[473] Sudheendra L, Moshnyaga V, Samwer K. Metal–insulator transition and colossal magnetoresistance: relevance of electron–lattice coupling and electronic phase separation. Contemp Phys 2007;48:349–64.
[474] Phan MH, Yu SC. Review of the magnetocaloric effect in manganite materials. J Magn Magn Mater 2007;308:325–40.
[475] Töpfer J, Goodenough JB. LaMnO3+d Revisited. J Solid State Chem 1997;130:117–28.
[476] Ghosh K, Ogale SB, Ramesh R, Greene RL, Venkatesan T, Gapchup KM, et al. Transition-element doping effects in La0.7Ca0.3MnO3. Phys Rev B 1999;59:533.
[477] Nisha P, Santhosh PN, Suresh KG, Pavithran C, Varma MR. Near room temperature magneto caloric effect in V doped La0.67Ca0.33MnO3 ceramics. J Alloys Comp 2009;478:566–71.
[478] Uthaman B, Anand KS, Rajan RK, Kyaw HH, Thomas S, Al-Harthi S, et al. Structural properties, magnetic interactions, magnetocaloric effect and critical behaviour of cobalt doped La0.7Te0.3MnO3. RSC Adv 2015;5:86144–55.
[479] Morelli DT, Mance AM, Mantese JV, Micheli AL. Magnetocaloric properties of doped lanthanum manganite film. J Appl Phys 1996;79:373.
[480] Zhang XX, Tejada J, Xin Y, Sun GF, Wong KW, Bohigas X. Magnetocaloric effect in La0.67Ca0.33MnOd and La0.60Y0.07Ca0.33MnOd bulk materials. Appl Phys Lett 1996;69:3596.
[481] Guo ZB, Zhang JR, Huang H, Ding WP, Du YW. Large magnetic entropy change in La0.75Ca0.25MnO3. Appl Phys Lett 1996;70:204.
[482] Zhang T, Fang YZ, Dressel M, Wang XP, Fang QF. Nanometer size effect on the structure and magnetic properties of high oxygen content ferromagnetic PrMnO[sub3+d] nanoparticles. J Appl Phys 2010;108:113901.
[483] Pękała M, Drozd V, Fagnard JF, Vanderbemden P, Ausloos M. Magnetocaloric effect in nano- and polycrystalline manganite La0.7Ca0.3MnO3. Appl Phys A-Mater Sci Process 2007;90:237–41.
[484] Pekala M, Drozd V, Fagnard JF, Vanderbemden P. Magnetocaloric effect in nano- and polycrystalline manganites La0.5Ca0.5MnO3. J Alloys Comp 2010;507:350–5.
[485] Tang W, Lu WJ, Luo X, Wang BS, Zhu XB, Song WH, et al. Size-induced changes of structural, magnetic and magnetocaloric properties of La0.7Ca0.2Ba0.1MnO3. Physica B 2010;405:2733–41.
[486] Hao CY, Zhao BC, Huang YA, Kuang GL, Sun YP. A-site-disorder-dependent magnetocaloric properties in the mono-valent-metal doped La0.7Ca0.3MnO3 manganites. J Alloys Comp 2011;509:5877–81.
[487] Ji Q, Lv B, Wang PF, Cai HL, Wu XS, Liu GH, et al. Effects of A-site cation disorder on structure and magnetocaloric properties in Y and Sr codoped La[sub 2/3]Ca[sub 1/3]MnO[sub 3] compounds. J Appl Phys 2009;105:07D713.
[488] Xie QY, Lv B, Wang PF, Song P, Wu XS. Evolution of A-site disorder-dependent structural and magnetic transport properties in La2/3-xEuxCa1/3-ySryMnO3. Mater Chem Phys 2009;114:636–43.
[489] Amaral JS, Tavares PB, Reis MS, Araujo JP, Mendonca TM, Amaral VS, et al. The effect of chemical distribution on the magnetocaloric effect: a case study in second-order phase transition manganites. J Non-Cryst Solids 2008;354:5301–3.
[490] Irmak AE, Coskun A, Tasarkuyu E, Akturk S, Unlu G, Samancioglu Y, et al. The influence of the sintering temperature on the structural and the magnetic properties of doped manganites: La0.95Ag0.05MnO3 and La0.75Ag0.25MnO3. J Magn Magn Mater 2010;322:945–51.
[491] Othmani S, Bejar M, Dhahri E, Hlil EK. The effect of the annealing temperature on the structural and magnetic properties of the manganites compounds. J Alloys Comp 2009;475:46–50.
[492] Tasarkuyu E, Coskun A, Irmak AE, Akturk S, Unlu G, Samancioglu Y, et al. Effect of high temperature sintering on the structural and the magnetic properties of La1.4Ca1.6Mn2O7. J Alloys Comp 2011;509:3717–22.
[493] Szymczak R, Kolano R, Kolano-Burian A, Pietosa J, Szymczak H. Cooling by adiabatic pressure application in La0.7Ca0.3MnO3 magnetocaloric effect material. J Magn Magn Mater 2010;322:1589–91.
[494] Thiyagarajan R, Esakki Muthu S, Mahendiran R, Arumugam S. Effect of hydrostatic pressure on magnetic and magnetocaloric properties of Mn-site doped perovskite manganites Pr0.6Ca0.4Mn0.96B0.04O3 (B=Co and Cr). J Appl Phys 2014;115:043905.
[495] Thiyagarajan R, Muthu SE, Manikandan K, Arumugam S. Effect of hydrostatic pressure on magnetic and magnetocaloric properties in La0.35Pr0.35Ca0.3Mn0.3. J Magn Magn Mater 2016;398:116–20.
[496] Bingham NS, Phan MH, Srikanth H, Torija MA, Leighton C. Magnetocaloric effect and refrigerant capacity in charge-ordered manganites. J Appl Phys 2009;106:023909.
[497] Karmakar S, Bose E, Taran S, Chaudhuri BK, Sun CP, Yang HD. Magnetocaloric effect in charge ordered Nd0.5Ca0.5MnO3 manganite. J Appl Phys 2008;103:023901.
[498] Bonilla CM, Bartolome F, Garcia LM, Parra-Borderias M, Herrero-Albillos J, Franco V. A new criterion to distinguish the order of magnetic transitions by means of magnetic measurements. J Appl Phys 2010;107:09E131.
[499] Dhahri A, Rhouma FIH, Mnefgui S, Dhahri J, Hlil EK. Room temperature critical behavior and magnetocaloric properties of La0.6Nd0.1(CaSr)(0.3)Mn0.9V0.1O3. Ceram Int 2014;40:459–64.
[500] Giri SK, Dasgupta P, Poddar A, Nath TK. Large magnetocaloric effect and critical behavior in Sm0.09Ca0.91MnO3 electron-doped nanomanganite. EPL 2014;105:47007.
[501] Phan TL, Tran QT, Thanh PQ, Yen PDH, Thanh TD, Yu SC. Critical behavior of La0.7Ca0.3Mn1-xNixO3 manganites exhibiting the crossover of first- and second-order phase transitions. Solid State Commun 2014;184:40–6.
[502] Abassi M, Mohamed Z, Dhahri J, Hlil EK. Theoretical investigations on the magnetocaloric and electrical properties of a perovskite manganite La0.67Ba0.1Ca0.23MnO3. Dalton Trans 2016;45:4736–46.
[503] Khondabi M, Ahmadvand H, Kameli P, Amirzadeh P, Salamati H, Dasgupta P, et al. Magnetocaloric and phase coexistence in La0.5Ca0.5-xSrxMnO3 manganites. J Appl Phys 2015;118:233908.
[504] Mohamed AA, Hernando B, Ahmed AM. Magnetocaloric-transport properties correlation in doped manganites. Solid State Commun 2016;233:15–7.
[505] Debnath JC, Zeng R, Kim JH, Dou SX. Giant magnetic entropy change in colossal magnetoresistance in La0.7Ca0.3MnO3 material in low field. J Appl Phys 2010;107:09A916.
[506] Bez HN, Nielsen KK, Smith A, Bahl CRH. A detailed study of the hysteresis in La0.67Ca0.33MnO3. J Magn Magn Mater 2016;416:429–33.
[507] Coskun A, Tasarkuyu E, Irmak AE, Akturk S. High magnetic entropy change in La0.70Ca0.21Ag0.09MnO3 compound. J Alloys Comp 2016;669:217–23.
[508] Turcaud JA, Pereira AM, Cohen LF. Publisher's Note: Quantifying the deleterious role of strong correlations inLa1−xCaxMnO3at the magnetocaloric transition [Phys. Rev. B91, 134410 (2015)]. Phys Rev B 2015;91:139902.
[509] Khlifi M, Dhahri E, Hlil EK. Magnetic, magnetocaloric, magnetotransport and magnetoresistance properties of calcium deficient manganites La0.8Ca0.2-x square xMnO3 post-annealed at 800 degrees C. J Alloys Comp 2014;587:771–7.
[510] Phan TL, Dang NT, Ho TA, Manh TV, Thanh TD, Jung CU, et al. First-to-second-order magnetic-phase transformation in La0.7Ca0.3-xBaxMnO3 exhibiting large magnetocaloric effect. J Alloys Comp 2016;657:818–34.

[511] Andrade VM, Pedro SS, Vivas RJC, Rocco DL, Reis MS, Campos APC, et al. Magnetocaloric functional properties of Sm0.6Sr0.4MnO3 manganite due to advanced nanostructured morphology. Mater Chem Phys 2016;172:20–5.
[512] Andrade VM, Vivas RJC, Pedro SS, Tedesco JCG, Rossi AL, Coelho AA, et al. Magnetic and magnetocaloric properties of La0.6Ca0.4MnO3 tunable by particle size and dimensionality. Acta Mater 2016;102:49–55.
[513] Anwar MS, Ahmed F, Koo BH. Dimensionality dependent magnetic and magnetocaloric response of La0.6Ca0.4MnO3 manganite. J Nanosci Nanotechnol 2014;14:8745–9.
[514] Kumaresavanji M, Sousa CT, Pires A, Pereira AM, Lopes AML, Araujo JP. Room temperature magnetocaloric effect and refrigerant capacitance in La0.7Sr0.3MnO3 nanotube arrays. Appl Phys Lett 2014;105:083110.
[515] Kumaresavanji M, Sousa CT, Pires A, Pereira AM, Lopes AML, Araujo JP. Magnetocaloric effect in La0.7Ca0.3MnO3 nanotube arrays with broad working temperature span. J Appl Phys 2015;117:104304.
[516] Quintero M, Passanante S, Irurzun I, Goijman D, Polla G. Grain size modification in the magnetocaloric and non-magnetocaloric transitions in La0.5Ca0.5MnO3 probed by direct and indirect methods. Appl Phys Lett 2014;105:152411.
[517] Das K, Das I. Giant enhancement of magnetocaloric effect at room temperature by the formation of nanoparticle of La0.48Ca0.52MnO3 compound. J Appl Phys 2016;119:093903.
[518] Giri SK, Dasgupta P, Poddar A, Sahoo RC, Paladhi D, Nath TK. Strain modulated large magnetocaloric effect in Sm0.55Sr0.45MnO3 epitaxial films. Appl Phys Lett 2015;106:023507.
[519] Bhatt RC, Awana VPS, Kishan H, Srivastava PC. Near room temperature magneto-transport (TCR & MR) and magnetocaloric effect in Pr2/3Sr1/3MnO3: Ag2O composite. J Alloys Comp 2015;619:151–6.
[520] Hussain I, Anwar MS, Lee SR, Koo BH. Effect of Zn on the Magnetic and Magnetocaloric Properties of (0.95)La0.7Ca0.3MnO3/(0.05)Mn1-x Zn (x) Fe2O4 Composites. J Supercond Nov Magn 2015;28:3323–8.
[521] Jerbi A, Krichene A, Chniba-Boudjada N, Boujelben W. Magnetic and magnetocaloric study of manganite compounds Pr(0.5)A(0.05)Sr(0.45)MnO(3) (A=Na and K) and composite. Physica B 2015;477:75–82.
[522] Marzouki-Ajmi A, Cheikrouhou-Koubaa W, Cheikhrouhou A. Magnetic and magnetocaloric study of polycrystalline (1-x) La0.65Ca0.35MnO3/xFe(2)O (3) composites. J Supercond Nov Magn 2015;28:103–8.
[523] Marzouki-Ajmi A, Cheikhrouhou-Koubaa W, Koubaa M, Cheikhrouhou A. Structural, magnetic and magnetocaloric study of polycrystalline (1-x) La0.65Ca0.35MnO3/xCr(2)O(3) composites. J Supercond Nov Magn 2015;28:1065–70.
[524] Mikhaleva E, Eremin E, Flerov I, Kartashev A, Sablina K, Mikhashenok N. Magnetization and magnetocaloric effect in La0.7Pb0.3MnO3 ceramics and 0.85(La0.7Pb0.3MnO3)-0.15(PbTiO3) composite. J Mater Res 2015;30:278–85.
[525] M'Nassri R. Enhanced refrigerant capacity and magnetic entropy nearly flattening in (La-2/3 Ba-1/3 MnO3)(1-x/)(La-2/3 Ba-1/3 MnO2.98)(x) Composite. J Supercond Nov Magn 2016;29:1879–85.
[526] Mohamed AA, Vega V, Ipatov M, Ahmed AM, Hernando B. Magnetoresistive and magnetocaloric response of manganite/insulator system. J Alloys Comp 2016;657:495–505.
[527] Mohamed A, Vega V, Ipatov M, Ahmed AM, Hernando B. Annealing temperature effect on magnetic and magnetocaloric properties of manganites. J Alloys Comp 2016;665:394–403.
[528] Nasri M, Khelifi J, Triki M, Dhahri E, Hlil EK. Impact of CuO phase on magnetocaloric and magnetotransport properties of La0.6Ca0.4MnO3 ceramic composites. J Alloys Comp 2016;678:427–33.
[529] Pekala M, Pekala K, Drozd V, Fagnard JF, Vanderbemden P. Effect of nanocrystalline structure on magnetocaloric effect in manganite composites (1/3) La0.7Ca0.3MnO3/(2/3)La0.8Sr0.2MnO3. J Alloys Comp 2015;629:98–104.
[530] Sellami-Jmal E, Regaieg Y, Cheikhrouhou-Koubaa W, Koubaa M, Cheikhrouhou A, Njah N. Magnetic and magnetocaloric properties of La0.65Ca0.35MnO3/La0.7Ca0.2Ba0.1MnO3 and La0.65Ca0.35MnO3/Pr0.5Sr0.5MnO3 composite manganites. J Supercond Nov Magn 2015;28:3121–6.
[531] Skini R, Khlifi M, Hlil EK. An efficient composite magnetocaloric material with a tunable temperature transition in K-deficient manganites. RSC Adv 2016;6:34271–9.
[532] Vandrangi SK, Yang JC, Zhu YM, Chin YY, Lin HJ, Chen CT, et al. Enhanced magnetocaloric effect driven by interfacial magnetic coupling in self-assembled Mn3O4-La0.7Sr0.3MnO3 nanocomposites. ACS Appl Mater Interfaces 2015;7:26504–11.
[533] Wang GF, Zhao ZR, Li HL, Zhang XF. Enhancement of refrigeration capacity and table-like magnetocaloric effect in La0.8Ca0.2MnO3/La0.8K0.2MnO3 nanocrystalline composite. Ceram Int 2015;41:9035–40.
[534] Han L, Chen CL. Magnetocaloric and colossal magnetoresistance effect in layered perovskite La1.4Sr1.6Mn2O7. J Mater Sci Technol 2010;26:234–6.
[535] Tetean R, Himcinschi C, Burzo E. Magnetic properties and magnetocaloric effect in La1.4-XRXCa1.6Mn2O7 compounds with R=Ho or Yb. J Optoelectron Adv Mater 2008;10:849–52.
[536] Wang AH, Liu Y, Zhang ZY, Long Y, Cao GH. Magnetic entropy change and colossal magnetoresistance effect in the layered perovskite La1.34Sr1.66Mn2O7. Solid State Commun 2004;130:293–6.
[537] Himcinschi C, Burzo E, Deville JP. Magnetic and magnetocaloric properties of La1.4-XYbXCa1.6Mn2O7. In: Baryakhtar VG, editor. European magnetic materials and applications. Zurich-Uetikon: Trans Tech Publications Ltd; 2001. p. 521–4.
[538] Aliev AM, Gamzatov AG, Batdalov AB, Kalitka VS, Kaul AR. Direct and inverse magnetocaloric effects in A-site ordered PrBaMn2O6 manganite. J Alloys Comp 2011;509:L165–7.
[539] Balli M, Fournier P, Jandl S, Gospodinov MM. A study of the phase transition and magnetocaloric effect in multiferroic La2MnNiO6 single crystals. J Appl Phys 2014;115:173904.
[540] Mohamed M, Rammeh N, Kabadou A, Dhahri E, Van der Lee A. Effect of the partial substitution of Fe on the magnetic properties of new brownmillerite oxides LaSrMn2-xFexO5 (0 <= x <= 0.5). J Magn Magn Mater 2014;361:44–9.
[541] Dhahri A, Dhahri J, Zemni S, Oumezzine M, Vincent H. Structural, magnetic and magnetocaloric effect in double perovskite Ba2CrMo1-xWxO6. J Alloys Comp 2006;420:15–9.
[542] Balli M, Jandl S, Fournier P, Gospodinov MM. Anisotropy-enhanced giant reversible rotating magnetocaloric effect in HoMn2O5 single crystals. Appl Phys Lett 2014;104:232402.
[543] de Oliveira N. Magnetocaloric effect in systems of itinerant electrons: application to Fe Co, Ni, YFe and YFe compounds. J Alloys Comp 2005;403:45–8.
[544] Nikitin SA, Talalaeva EV, Chernikova LA, Andreenko AS. Magnetocaloric effect in compounds of rare-earth metals with iron. Soviet Phys JETP-USSR 1974;38:1028–30.
[545] Buschow KHJ. Intermetallic compounds of rare-earth and 3d transition metals. Rep Prog Phys 1977;40:1179–256.
[546] Paul-Boncour V, Mazet T. Investigation of compounds for magnetocaloric applications: YFe2H4.2, YFe2D4.2, and Y0.5Tb0.5Fe2D4.2. J Appl Phys 2009;105:013914.
[547] Budziak A, Balanda M, Figiel H, Kolwicz-Chodak L, Tarnawski Z. Structural and magnetic transformations in HoMn(2)H(x) hydrides. In: Spalek J, editor. Joint European magnetic symposia. p. 012010.
[548] Klepka MT, Wolska A, Lawniczak-Jablonska K, Filipek SM, Sato R, Paul-Boncour V, et al. EXAFS and XRD investigation of crystal structure in Cr doped YMn2 deuterides. Radiat Phys Chem 2011;80:1019–25.
[549] Morariu m. Mossbauer effect on YFe3 compound. Solid State Commun 1974;15:1313–5.
[550] Mandal K, Yan A, Kerschl P, Handstein A, Gutfleisch O, Muller KH. The study of magnetocaloric effect in R2Fe17 (R = Y, Pr) alloys. J Phys D-Appl Phys 2004;37:2628–31.
[551] Fang YK, Chang CW, Yeh CC, Chang HW, Li W, Chang WC. Microstructure and magnetocaloric effect of melt-spun Y(2)Fe(17) ribbons. J Appl Phys 2008;103:07B302.

[552] Karpenkov DY, Skokov KP, Liu J, Karpenkov AY, Semenova EM, Airiyan EL, et al. Adiabatic temperature change of micro- and nanocrystalline Y2Fe17 heat-exchangers for magnetic cooling. J Alloys Comp 2016;668:40–5.
[553] Wang ZH, Geng DY, Li J, Liu W, Zhang ZD. Magnetic properties of YFe(12-x)Mo(x) compounds and magnetocaloric effect of YFe(9.5)Mo(2.5). J Magn Magn Mater 2010;322:3000–3.
[554] Karotsis G, Kennedy S, Teat SJ, Beavers CM, Fowler DA, Morales JJ, et al. Mn(4)(III)Ln(4)(III) Calix 4 arene clusters as enhanced magnetic coolers and molecular magnets. J Am Chem Soc 2010;132:12983–90.
[555] Langley SK, Chilton NF, Moubaraki B, Hooper T, Brechin EK, Evangelisti M, et al. Molecular coolers: the case for (Cu5Gd4III)-Gd-II. Chem Sci 2011;2:1166–9.
[556] Adhikary A, Jena HS, Konar S. A family of Fe3+ based double-stranded helicates showing a magnetocaloric effect, and Rhodamine B dye and DNA binding activities. Dalton Trans 2015;44:15531–43.
[557] Biswas S, Mondal AK, Konar S. Densely packed lanthanide cubane based 3D metal-organic frameworks for efficient magnetic refrigeration and slow magnetic relaxation. Inorg Chem 2016;55:2085–90.
[558] Guo FS, Leng JD, Liu JL, Meng ZS, Tong ML. Polynuclear and polymeric gadolinium acetate derivatives with large magnetocaloric effect. Inorg Chem 2012;51:405–13.
[559] Zheng YZ, Evangelisti M, Winpenny REP. Co-Gd phosphonate complexes as magnetic refrigerants. Chem Sci 2011;2:99–102.
[560] Pineda EM, Tuna F, Zheng YZ, Teat SJ, Winpenny REP, Schnack J, et al. Iron lanthanide phosphonate clusters: Fe(6)Ln(6)P(6) Wells-Dawson-like structures with D-3d symmetry. Inorg Chem 2014;53:3032–8.
[561] Sibille R, Didelot E, Mazet T, Malaman B, François M. Magnetocaloric effect in gadolinium-oxalate framework Gd2(C2O4)3(H2O)6·(0·6H2O). APL Mater 2014;2:124402.
[562] Tang XY, Zhong QX, Xu J, Li HQ, Xu SN, Cui XY, et al. Co(II)(4)Gd(III)(6) phosphonate grid and cage as molecular refrigerants. Inorg Chim Acta 2016;442:195–9.
[563] Lorusso G, Palacios MA, Nichol GS, Brechin EK, Roubeau O, Evangelisti M. Increasing the dimensionality of cryogenic molecular coolers: Gd-based polymers and metal-organic frameworks. Chem Commun 2012;48:7592–4.
[564] Ding LJ, Zhong Y, Fan SW, Zhu LY. The magnetocaloric effect with critical behavior of a periodic Anderson-like organic polymer. Phys Chem Chem Phys 2016;18:510–8.
[565] Liu SJ, Cao C, Xie CC, Zheng TF, Tong XL, Liao JS, et al. Tricarboxylate-based Gd-III coordination polymers exhibiting large magnetocaloric effects. Dalton Trans. 2016;45:9209–15.
[566] Qiu JZ, Chen YC, Wang LF, Li QW, Orendac M, Tong ML. The effect of magnetic coupling on magnetocaloric behaviour in two 3D Gd(III)-glycolate coordination polymers. Inorg Chem Front 2016;3:150–6.
[567] Peng JB, Zhang QC, Kong XJ, Ren YP, Long LS, Huang RB, et al. A 48-metal cluster exhibiting a large magnetocaloric effect. Angew Chem-Int Ed 2011;50:10649–52.
[568] Hooper TN, Schnack J, Piligkos S, Evangelisti M, Brechin EK. The importance of being exchanged: (Gd4M8II)-M-III(OH)(8)(L)(8)(O2CR)(8) (4+) clusters for magnetic refrigeration. Angew Chem-Int Ed 2012;51:4633–6.
[569] Florez JM, Vargas P, Garcia C. Thermal observables in coupled Cr7Ni molecular rings: role and quantification of spin-entanglement. J Appl Phys 2011;109:07B109.
[570] Chen YC, Guo FS, Liu JL, Leng JD, Vrabel P, Orendac M, et al. Switching of the magnetocaloric effect of Mn-II glycolate by water molecules. Chem-Eur J 2014;20:3029–35.
[571] Tian CB, Chen RP, He C, Li WJ, Wei Q, Zhang XD, et al. Reversible crystal-to-amorphous-to-crystal phase transition and a large magnetocaloric effect in a spongelike metal organic framework material. Chem Commun 2014;50:1915–7.
[572] Biswas S, Jena HS, Goswami S, Sanda S, Konar S. Synthesis and characterization of two lanthanide (Gd3+ and Dy3+)-based three-dimensional metal organic frameworks with squashed metallomacrocycle type building blocks and their magnetic, sorption, and fluorescence properties study. Cryst Growth Des 2014;14:1287–95.
[573] Adhikary A, Sheikh JA, Biswas S, Konar S. Synthesis, crystal structure and study of magnetocaloric effect and single molecular magnetic behaviour in discrete lanthanide complexes. Dalton Trans 2014;43:9334–43.
[574] Pasatoiu TD, Ghirri A, Madalan AM, Affronte M, Andruh M. Octanuclear Ni(4)(II)Ln(4)(III) complexes. Synthesis, crystal structures and magnetocaloric properties. Dalton Trans 2014;43:9136–42.
[575] Upadhyay A, Komatireddy N, Ghirri A, Tuna F, Langley SK, Srivastava AK, et al. Synthesis and magnetothermal properties of a ferromagnetically coupled Ni-II-Gd-III-Ni-II cluster. Dalton Trans 2014;43:259–66.
[576] Wang P, Shannigrahi S, Yakovlev NL, Hor TSA. Magnetocaloric effect of a series of remarkably isostructural intermetallic Ni(3)(II)Ln(III) cubane aggregates. Dalton Trans 2014;43:182–7.
[577] Xiong G, Xu H, Cui JZ, Wang QL, Zhao B. The multiple core-shell structure in Cu(24)Ln(6) cluster with magnetocaloric effect and slow magnetization relaxation. Dalton Trans 2014;43:5639–42.
[578] Wang K, Zou HH, Chen ZL, Zhang Z, Sun WY, Liang FP. A series of 3D metal organic frameworks based on 24-MC-6 metallacrown clusters: structure, magnetic and luminescence properties. Dalton Trans 2014;43:12989–95.
[579] Biswas S, Jena HS, Adhikary A, Konar S. Two isostructural 3D lanthanide coordination networks (Ln = Gd-3 Dy3+) with squashed cuboid-type nanoscopic cages showing significant cryogenic magnetic refrigeration and slow magnetic relaxation. Inorg Chem 2014;53:3926–8.
[580] Orendac M, Cizmar E, Orendacova A, Tkacova J, Kuchar J, Cernak J. Enhanced magnetocaloric effect in quasi-one-dimensional S = 1/2 Heisenberg antiferromagnet Cu(dmen)(2)(H2O) SiF6. J Alloys Comp 2014;586:34–8.
[581] Pelka R, Konieczny P, Zielinski PM, WasiutYnski T, Miyazaki Y, Inaba A, et al. Magnetocaloric effect in {Fe(pyrazole)(4) (2) Nb(CN)(8) center dot 4H(2) O}(n) molecular magnet. J Magn Magn Mater 2014;354:359–62.
[582] Alexandropoulos DI, Cunha-Silva L, Lorusso G, Evangelisti M, Tang JK, Stamatatos TC. Dodecanuclear 3d/4f-metal clusters with a 'Star of David' topology: single-molecule magnetism and magnetocaloric properties. Chem Commun 2016;52:1693–6.
[583] Balanda M, Pelka R, Fitta M, Laskowski L, Laskowska M. Relaxation and magnetocaloric effect in the Mn-12 molecular nanomagnet incorporated into mesoporous silica: a comparative study. RSC Adv 2016;6:49179–86.
[584] Kuang WW, Zhu LL, Li LC, Yang PP. Synthesis, crystal structure, and magnetic properties of a family of undecanuclear Cu(9)(II)Ln(2)(III) nanoclusters. Eur J Inorg Chem 2015:2245–53.
[585] Langley SK, Moubaraki B, Tomasi C, Evangelisti M, Brechin EK, Murray KS. Synthesis, structure, and magnetism of a family of heterometallic Cu(2)Ln (7) and Cu(4)Ln(12) (Ln = Gd, Tb, and Dy) complexes: the Gd analogues exhibiting a large magnetocaloric effect. Inorg Chem 2014;53:13154–61.
[586] Liu C-M, Zhang D-Q, Zhu D-B. Hexanuclear Ni(2)Ln(4) clusters exhibiting enhanced magnetocaloric effect and slow magnetic relaxation. RSC Adv 2014;4:53870–6.
[587] Pedersen KS, Lorusso G, Morales JJ, Weyhermuller T, Piligkos S, Singh SK, et al. Fluoride-bridged Gd-III M-3(III) (2) (M= Cr, Fe, Ga) molecular magnetic refrigerants. Angew Chem-Int Ed 2014;53:2394–7.
[588] Liu JL, Chen YC, Tong ML. Molecular design for cryogenic magnetic coolants. Chem Rec 2016;16:825–34.
[589] Evangelisti M, Brechin EK. Recipes for enhanced molecular cooling. Dalton Trans 2010;39:4672–6.
[590] Evangelisti M, Luis F, de Jongh LJ, Affronte M. Magnetothermal properties of molecule-based materials. J Mater Chem 2006;16:2534.
[591] Torres F, Hernandez JM, Bohigas X, Tejada J. Giant and time-dependent magnetocaloric effect in high-spin molecular magnets. Appl Phys Lett 2000;77:3248–50.
[592] Affronte M, Ghirri A, Carretta S, Amoretti G, Piligkos S, Timco GA, et al. Engineering molecular rings for magnetocaloric effect. Appl Phys Lett 2004;84:3468–70.

[593] Evangelisti M, Candini A, Ghirri A, Affronte M, Piligkos S, Brechin EK, et al. Molecular nanoclusters as magnetic refrigerants: the case of Fe-14 with very large spin ground-state. Polyhedron 2005;24:2573–8.
[594] Manuel E, Evangelisti M, Affronte M, Okubo M, Train C, Verdaguer M. Magnetocaloric effect in hexacyanochromate Prussian blue analogs. Phys Rev B 2006;73:172406.
[595] Yuan Y, Wu Y, Tong X, Zhang H, Wang H, Liu XJ, et al. Rare-earth high-entropy alloys with giant magnetocaloric effect. Acta Mater 2017;125:481–9.
[596] Tripathy SK, Suresh KG, Nigam AK. A comparative study of the magnetocaloric effect in Gd3Co and Gd3Ni. J Magn Magn Mater 2006;306:24–9.
[597] Kumar P, Suresh KG, Nigam AK. Magnetothermal effect in Gd3Rh. J Appl Phys 2011;109:07A909.
[598] Monteiro JCB, dos Reis RD, Gandra FG. The physical properties of Gd3Ru: a real candidate for a practical cryogenic refrigerator. Appl Phys Lett 2015;106:194106.
[599] Li B, Du J, Ren WJ, Hu WJ, Zhang Q, Li D, et al. Large reversible magnetocaloric effect in Tb3Co compound. Appl Phys Lett 2008;92:242504.
[600] Shen J, Zhao JL, Hu FX, Rao GH, Liu GY, Wu JF, et al. Magnetocaloric effect in antiferromagnetic Dy3Co compound. Appl Phys A-Mater Sci Process 2010;99:853–8.
[601] Shen J, Wu JF. Magnetocaloric effect and magnetic phase transition in Ho3Co. J Appl Phys 2011;109:07A931.
[602] Kumar P, Singh NK, Nayak AK, Haldar A, Suresh KG, Nigam AK. Large reversible magnetocaloric effect in Er3Co compound. J Appl Phys 2010;107:09A932.
[603] Sánchez Llamazares JL, Flores-Zúñiga H, Álvarez-Alonso P, Sánchez-Valdés CF, Lara Rodríguez GA, Fernández-Gubieda ML. Magnetocaloric properties of rapidly solidified Dy3Co alloy ribbons. J Appl Phys 2015;117:17A706.
[604] Shen J, Zhao JL, Hu FX, Wu JF, Sun JR, Shen BG. Order of magnetic transition and large magnetocaloric effect in Er3Co. Chin Phys B 2010;19:047502.
[605] Paramanik T, Samanta T, Ranganathan R, Das I. Magnetic and magnetocaloric properties of Dy5Pd2: role of magnetic irreversibility. RSC Adv 2015;5:47860–5.
[606] Toyoizumi S, Kitazawa H, Kawamura Y, Mamiya H, Terada N, Tamura R, et al. Sample dependence of giant magnetocaloric effect in a cluster-glass system Ho5Pd2. J Appl Phys 2015;117:17D101.
[607] Toyoizumi S, Kitazawa H, Morita K, Tamaki A. Iop. Magnetocaloric effect in a cluster-glass system Ho5Pd2-xNix. In: Tmu international symposium on new quantum phases emerging from novel crystal structure. Bristol: Iop Publishing Ltd; 2016. p. 012036.
[608] Canepa F, Cirafici S, Napoletano M, Merlo F. Magnetocaloric properties of Gd7Pd3 and related intermetallic compounds. IEEE Trans Magn 2002;38:3249–51.
[609] Talik E, Guzik A, Oboz M, Zajdel P, Ziolkowski G. Magnetocaloric and Hopkinson effects in slowly and rapidly cooled Gd7Pd3. Int J Mater Res 2016;107:3–12.
[610] Canepa F, Napoletano M, Cirafici S. Magnetocaloric effect in the intermetallic compound Gd7Pd3. Intermetallics 2002;10:731–4.
[611] Oboz M, Talik E, Kusz J, Winiarski A. Physical properties of Gd7NiPd2 single crystal. J Alloys Comp 2011;509:4478–83.
[612] Talik E, Guzik A, Oboz M, Kusz J, Zajdel P, Zubko M. Influence of nickel on the electronic structure and magnetic properties in Gd7Pd3-xNix. Philos Mag 2016;96:1073–92.
[613] Oboz M, Talik E, Kusz J, Hofmeister W. Magnetic and transport properties of Gd3Y4Pd3 single crystal. J Alloys Comp 2010;492:13–8.
[614] Talik E, Oboz M, Tran VH, Kusz J, Hofmeister W, Winiarski A. Magnetic properties of Gd4Y3Pd3 single crystal. J Cryst Growth 2010;312:1651–8.
[615] Talik E, Oboz M, Kusz J, Winiarski A, Hofmeister W. Magnetic and transport properties of Gd7-xYxPd3 (x=0-6) system. J Alloys Comp 2014;582:718–29.
[616] Sengupta K, Iyer KK, Sampathkumaran EV. Large magnetoresistance and magnetocaloric effect above 70 K in Gd2Co2Al, Gd2Co2Ga, and Gd7Rh3. Phys Rev B 2005;72:054422.
[617] Kumar P, Kumar R. Magnetocaloric effect and refrigeration cooling power in amorphous Gd7Ru3 alloys. AIP Adv 2015;5:077125.
[618] Bhattacharyya A, Giri S, Majumdar S. Field induced sign reversal of magnetocaloric effect in Gd2In. J Magn Magn Mater 2012;324:1239–41.
[619] Zhang Q, Cho JH, Du J, Yang F, Liu XG, Feng WJ, et al. Large reversible magnetocaloric effect in Tb2In. Solid State Commun 2009;149:396–9.
[620] Zhang Q, Liu XG, Yang F, Feng WJ, Zhao XG, Kang DJ, et al. Large reversible magnetocaloric effect in Dy2In. J Phys D-Appl Phys 2009;42:055011.
[621] Zhang Q, Cho JH, Li B, Hu WJ, Zhang ZD. Magnetocaloric effect in Ho2In over a wide temperature range. Appl Phys Lett 2009;94:182501.
[622] Zhang H, Shen BG, Xu ZY, Chen J, Shen J, Hu FX, et al. Large reversible magnetocaloric effect in Er2In compound. J Alloys Comp 2011;509:2602–5.
[623] Tence S, Chevalier B. Magnetic and magnetocaloric properties of Gd2In0.8X0.2 compounds (X=Al, Ga, Sn, Pb). J Magn Magn Mater 2016;399:46–50.
[624] Hadimani RL, Agurgo Balfour E, Dembele SN, Jiles DC. Enhancement of magnetocaloric effect in the Gd2Al phase by Co alloying. J Appl Phys 2014;116:183908.
[625] Morozkin AV, Mozharivskyj Y, Svitlyk V, Nirmala R, Isnard O, Manfrinetti P, et al. Magnetic properties of Fe2P-type R6CoTe2 compounds (R = Gd-Er). J Solid State Chem 2010;183:1314–25.
[626] Zhang JL, Shan GC, Zheng ZG, Shek CH. Structure and magnetic behaviors of Gd6FeBi2 compound. Intermetallics 2016;68:51–6.
[627] Hermes W, Rodewald UC, Pottgen R. Large reversible magnetocaloric effect due to a rather unstable antiferromagnetic ground state in Er4NiCd. J Appl Phys 2010;108:113919.
[628] Li L, Niehaus O, Kersting M, Pöttgen R. Reversible table-like magnetocaloric effect in Eu4PdMg over a very large temperature span. Appl Phys Lett 2014;104:092416.
[629] Li LW. Review of magnetic properties and magnetocaloric effect in the intermetallic compounds of rare earth with low boiling point metals. Chin Phys B 2016;25:037502.
[630] Wang F, Zhang J, Yuan FY, Cao Y, Gao CJ, Hao YM, et al. Magnetic properties and magnetocaloric effect in Ho6-xErxMnBi2 compounds. J Appl Phys 2010;107:09A918.
[631] Morozkin AV, Nirmala R, Malik SK. Magnetic and magnetocaloric properties of Ho6Co2Ga-type Dy6Co2.5Sn0.5 compound. J Magn Magn Mater 2015;378:174–7.
[632] Couillaud S, Gaudin E, Franco V, Conde A, Pottgen R, Heying B, et al. The magnetocaloric properties of GdScSi and GdScGe. Intermetallics 2011;19:1573–8.
[633] Mayer C, Gaudin E, Gorsse S, Chevalier B. The new ternary silicide Gd5CoSi2: structural, magnetic and magnetocaloric properties. J Solid State Chem 2011;184:325–30.
[634] Tian G, Du HL, Zhang Y, Xia YH, Wang CS, Han JZ, et al. Magnetic properties and magnetocaloric effect in Nd5Si3 compound. J Appl Phys 2010;107:09A917.
[635] Tian GA, Du HL, Zhang Y, Xia YH, Wang CS, Han JZ, et al. Large reversible magnetocaloric effect of light rare-earth intermetallic compound Pr5Si3. J Alloys Comp 2010;496:517–20.
[636] Schafer K, Schwickert C, Niehaus O, Winter F, Pottgen R. Magnetic properties of RE5Ir2X (RE = Y, Gd-Ho, X = Sn, Sb, Pb, Bi) and magnetocaloric characterization of Gd5Ir2X. Solid State Sci 2014;35:66–73.
[637] Yuan F, Morozkin AV, Mozharivskyj Y. Targeted structural changes and magnetic properties study in (Ho/Er)(5)Ga3-x(Co/Fe)(x). J Alloys Comp 2015;620:376–82.
[638] Mohapatra N, Das SD, Mukherjee K, Sampathkumaran EV. Isothermal magnetic entropy behavior in Tb(5)Si(3): sign reversal and non-monotonic variation with temperature, and implications. Solid State Commun 2011;151:1340–3.
[639] Nirmala R, Morozkin AV, Nigam AK, Lamsal J, Yelon WB, Isnard O, et al. Competing magnetic interactions in the intermetallic compounds Pr5Ge3 and Nd5Ge3. J Appl Phys 2011;109:07A716.
[640] Maji B, Suresh KG, Chen X, Ramanujan RV. Magnetic and magnetocaloric properties of ball milled Nd5Ge3. J Appl Phys 2012;111:073905.
[641] Bie H, Mar A. Rare-earth tetrel antimonidesRE5TtxSb3-x(RE= La-Nd;Tt= Si, Ge). Eur J Inorg Chem 2009;2009:3403–13.

[642] Morozkin AV, Mozharivskyj Y, Svitlyk V, Nirmala R, Malik SK. New ternary Yb5Sb3-type R5T1-x{Sb, Bi}(2+x) phases (R = Y, Dy, Ho, T = Co, Ru, Rh, Pd) and their magnetic properties. Intermetallics 2011;19:302–6.
[643] Svitlyk V, Fei F, Mozharivskyj Y. Gd5Ni0.96Sb2.04 and Gd5Ni0.71Bi2.29: crystal structure, magnetic properties and magnetocaloric effect. Structural transformation and magnetic properties of hexagonal Gd5Bi3. J Solid State Chem 2008;181:1080–6.
[644] Zheng ZG, Zhong XC, Yu HY, Liu ZW, Zeng DC. Magnetic phase transitions and magnetocaloric properties of (Gd(12-x)Tb(x))Co(7) alloys. J Appl Phys 2011;109:07A919.
[645] Zheng XQ, Zhang B, Li YQ, Wu H, Zhang H, Zhang JY, et al. Large magnetocaloric effect in Er12Co7 compound and the enhancement of delta T-FWHM by Ho-substitution. J Alloys Comp 2016;680:617–22.
[646] Shigeoka T, Fujiwara T, Kanto K, Zhang YH, Uwatoko Y. Novel magnetic behaviour of GdPd2Si2 single crystal. In: Ronning FBC, editor. International conference on strongly correlated electron systems. Bristol: Iop Publishing Ltd; 2011. p. 012121.
[647] Han ZD, Zhang P, Qian B, Jiang XF, Wang DH, Chen J, et al. Low-field magnetocaloric effect in (Gd1-xDyx)(3)Al-2 alloys. J Alloys Comp 2010;504:310–3.
[648] Li YW, Zhang H, Yan T, Long KW, Wang HS, Xue YJ, et al. Successive magnetic transitions and magnetocaloric effect in Dy3Al2 compound. J Alloys Comp 2015;651:278–82.
[649] Zhang H, Yang LH, Li JY, Wang Z, Niu E, Liu RM, et al. Magnetic properties and magnetocaloric effect in Tb3Al2 compound. J Alloys Comp 2014;615:406–9.
[650] Dong QY, Chen J, Shen J, Sun JR, Shen BG. Magnetic properties and magnetocaloric effects in R(3)Ni(2) (R = Ho and Er) compounds. Appl Phys Lett 2011;99:132504.
[651] Bhattacharyya A, Thamizhavel A, Dhar SK, Manfrinetti P. Magnetocaloric effect near the second order ferromagnetic transition in superstructure R15Si9C compounds (R = Gd, Tb and Dy). J Alloys Comp 2014;588:720–4.
[652] Niu XJ, Gschneidner KA, Pecharsky AO, Pecharsky VK. Crystallography, magnetic properties and magnetocaloric effect in Gd-4(BixSb1-x)(3) alloys. J Magn Magn Mater 2001;234:193–206.
[653] Nobrega EP, Alho BP, Gomes MB, von Ranke PJ, de Oliveira NA. Theoretical investigation on the magnetocaloric effect in the intermetallic Gd(4)Sb(3). J Alloys Comp 2011;509:8979–82.
[654] Mohapatra N, Iyer KK, Sampathkumaran EV. Large magnetocaloric effect and magnetoresistance behavior in Gd4Co3. Eur Phys J B 2008;63:451–4.
[655] Zhang Q, Li B, Zhao XG, Zhang ZD. Magnetic and reversible magnetocaloric properties of (Gd1-xDyx)(4)Co-3 ferrimagnets. J Appl Phys 2009;105:053902.
[656] Tence S, Gaudin E, Chevalier B. Around the composition Gd4Co3: Structural, magnetic and magnetocaloric properties of Gd6Co4.85(2). Intermetallics 2010;18:1216–21.
[657] Shen J, Li YX, Sun JR. Magnetic properties and magnetocaloric effects in R6Co2Si3 compounds with R=Nd and Tb. J Alloys Comp 2009;476:693–6.
[658] Shen J, Wu JF, Sun JR. Room-temperature large refrigerant capacity of Gd6Co2Si3. J Appl Phys 2009;106:083902.
[659] Shen J, Wang F, Li YX, Sun JR, Shen BG. Magnetocaloric effect in Pr6Co1.67Si3 compound. J Alloys Comp 2008;458:L6–8.
[660] Shen J, Wang F, Li YX, Sun JR, Shen BG. Magnetic properties and magnetocaloric effects in Tb6Co1.67Si3 compound. Chin Phys 2007;16:3853–7.
[661] Shen J, Li YX, Dong QY, Wang F, Sun JR. Magnetocaloric effect in Gd6Co1.67Si3 compound with a second-order phase transition. Chin Phys B 2008;17:2268–71.
[662] Zhao JL, Shen J, Li YX, Hu FX, Sun JR, Shen BG. Effect of Dy substitution on magnetic properties and magnetocaloric effects of Tb6Co1.67Si3 compounds. Chin Phys B 2010;19:047501.
[663] Haldar A, Singh NK, Suresh KG, Nigam AK. Metastable magnetization behavior of magnetocaloric R6Co1.67Si3 (R=Tb and Nd) compounds. Physica B 2010;405:3446–51.
[664] Shen J, Zhang H, Wu JF. Magnetic entropy change and large refrigerant capacity of Ce6Ni2Si3-type GdCoSiGe compound. Chin Phys B 2011;20:027501.
[665] Gaudin E, Tence S, Weill F, Fernandez JR, Chevalier B. Structural and magnetocaloric properties of the new ternary silicides Gd6M5/3Si3 with M = Co and Ni. Chem Mater 2008;20:2972–9.
[666] Pathak AK, Dubenko I, Stadler S, Ali N. Magnetic and magnetocaloric properties of Gd6X2Si3 (X = Ni, Co) and Ln(6)Co(2)Si(3) (Ln = Pr, La). J Appl Phys 2011;109:07A913.
[667] Chennabasappa M, Chevalier B, Lahaye M, Labrugere C, Toulemonde O. A core-shell phenomenon maintain the magnetocaloric properties of the ternary silicide Gd6Co1.67Si3 during water flux ageing. J Alloys Comp 2014;584:34–40.
[668] Zhang JL, Zheng ZG, Shan GC, Bobev S, Shek CH. Abnormal thermal expansion, multiple transitions, magnetocaloric effect, and electronic structure of Gd6Co4.85. J Appl Phys 2015;118:133903.
[669] Duraj D, Baran S, Jaworska-Golab T, Kalychak YM, Przewoznik J, Szytula A, et al. Magnetic properties of Dy11Si4In6. Acta Phys Pol A 2012;121:1118–20.
[670] Cheung YYJ, Svitlyk V, Mozharivskyj Y. Structure, magnetic and magnetocaloric properties of RE11Ge8In2 (RE = Gd-Tm). Intermetallics 2011;19:276–81.
[671] Yamamoto TA, Nakagawa T, Sako K, Arakawa T, Nitani H. Magnetocaloric effect of rare earth mono-nitrides, TbN and HoN. J Alloys Comp 2004;376:17–22.
[672] Nakagawa T, Arakawa T, Sako K, Tomioka N, Yamamoto TA, Kusunose T, et al. Magnetocaloric effects of ferromagnetic erbium mononitride. J Alloys Comp 2006;408:191–5.
[673] Nishio S, Nakagawa T, Arakawa T, Tomioka N, Yamamoto TA, Kusunose T, et al. Specific heat and thermal conductivity of HoN and ErN at cryogenic temperatures. J Appl Phys 2006;99:08K901.
[674] Nakagawa T, Sako K, Arakawa T, Tomioka N, Yamamoto TA, Kamiya K, et al. Magnetocaloric effects of binary rare earth mononitrides, GdxTb1-xN and TbxHo1-xN. J Alloys Comp 2006;408:187–90.
[675] Nakagawa T, Sako K, Arakawa T, Yamamoto TA. Magnetocaloric effect of mononitride containing gadolinium and dysprosium GdxDy1-xN. J Alloys Comp 2004;364:53–8.
[676] Hirayama Y, Tomioka N, Nishio S, Kusunose N, Nakagawa T, Kamiya K, et al. Magnetocaloric effect, specific heat and adiabatic temperature change of HoxEr1-xN (x=0.25, 0.5, 0.75). J Alloys Comp 2008;462:L12–5.
[677] von Ranke PJ, Alvarenga TST, Alho BP, Nobrega EP, Ribeiro PO, Carvalho AMG, et al. Spin reorientation and the magnetocaloric effect in HoyEr(1-y)N. J Appl Phys 2012;111:113916.
[678] Hirayama Y, Nakagawa T, Kusunose T, Yamamoto TA. Magnetocaloric effect of rare earth nitrides. IEEE Trans Magn 2008;44:2997–3000.
[679] Kim D, Ahn J, Sinha B, Kim J, Choi C. Novel route to prepare HoN nanoparticles for magnetic refrigerant in cryogenic temperature. Int J Hydrog Energy 2015;40:11465–9.
[680] Shinde KP, Jang SH, Kim JW, Kim DS, Ranot M, Chung KC. Magnetocaloric properties of TbN, DyN and HoN nanopowders prepared by the plasma arc discharge method. Dalton Trans 2015;44:20386–91.
[681] Ahn K, Pecharsky AO, Gschneidner KA, Pecharsky VK. Preparation, heat capacity, magnetic properties, and the magnetocaloric effect of EuO. J Appl Phys 2004;97:063901.
[682] Li DX, Yamamura T, Nimori S, Homma Y, Honda F, Haga Y, et al. Large reversible magnetocaloric effect in ferromagnetic semiconductor EuS. Solid State Commun 2014;193:6–10.
[683] Hu WJ, Du J, Li B, Zhang Q, Zhang ZD. Giant magnetocaloric effect in the Ising antiferromagnet DySb. Appl Phys Lett 2008;92:192505.
[684] Li DX, Nimori S, Shikama T. Giant and anisotropic magnetocaloric effect in antiferromagnetic single crystalline DySb. Solid State Commun 2010;150:1865–8.

[685] de Sousa VSR, Plaza EJR, von Ranke PJ. The influence of spontaneous and field induced spin reorientation transitions on the magnetocaloric properties in rare earth intermetallic compounds: application to TbZn. J Appl Phys 2010;107:103928.
[686] de Sousa VSR, von Ranke PJ, Gandra FCG. The influence of spontaneous and field-induced spin reorientation transitions on the magnetocaloric properties of HoZn and ErZn. J Appl Phys 2011;109:063904.
[687] Law JY, Moreno-Ramirez LM, Blazquez JS, Franco V, Conde A. Gd plus GdZn biphasic magnetic composites synthesized in a single preparation step: increasing refrigerant capacity without decreasing magnetic entropy change. J Alloys Comp 2016;675:244–7.
[688] Mo Z-J, Shen J, Gao X-Q, Liu Y, Wu J-F, Shen B-G, et al. Magnetic properties and magnetocaloric effects in HoPd intermetallic. Chin Phys B 2015;24:037503.
[689] Zhang JY, Luo J, Li JB, Liang JK, Wang YC, Ji LN, et al. Magnetic properties and magnetocaloric effect of GdGa compound. J Alloys Comp 2009;469:15–9.
[690] Zheng XQ, Chen J, Wang LC, Wu RR, Hu FX, Sun JR, et al. Magnetic properties and magnetocaloric effects of GdxEr1-xGa (0 <= x <= 1) compounds. J Appl Phys 2014;115:17A905.
[691] Zheng XQ, Chen J, Xu ZY, Mo ZJ, Hu FX, Sun JR, et al. Nearly constant magnetic entropy change and adiabatic temperature change in PrGa compound. J Appl Phys 2014;115:17A938.
[692] Chen J, Shen BG, Dong QY, Sun JR. Giant magnetocaloric effect in HoGa compound over a large temperature span. Solid State Commun 2010;150:157–9.
[693] Drulis H, Hackemer A, Zaleski A, Yaropolov YL, Nikitin SA, Verbetsky VN. The magnetocaloric effect and low temperature specific heat of SmNi. Solid State Commun 2011;151:1240–3.
[694] Xu ZY, Shen J, Zheng XQ, Zhang H. Magnetocaloric effect in ErSi compound. IEEE Trans Magn 2011;47:2470–3.
[695] Smarzhevskaya AI, Iwasieczko W, Verbetsky VN, Nikitin SA. New magnetocaloric material based on GdNiH3.2 hydride for application in cryogenic devices. Phys Stat Solidi C: Curr Topics Solid State Phys 2014;11(5–6):1102–5.
[696] Oboz M, Talik E, Winiarski A. Magnetocaloric effect in GdCu intermetallic compound. Cryst Res Technol 2012;47:341–6.
[697] Wang LC, Dong QY, Lu J, Shao XP, Mo ZJ, Xu ZY, et al. Low-temperature large magnetocaloric effect in the antiferromagnetic CeSi compound. J Alloys Comp 2014;587:10–3.
[698] Yang LH, Zhang H, Hu FX, Sun JR, Pan LQ, Shen BG. Magnetic and magnetocaloric properties of equiatomic alloys RAl (R = Ho and Er). J Alloys Comp 2014;596:58–62.
[699] Manfrinetti P, Morozkin AV, Isnard O, Wrubl F, Mozharivskyj Y, Svitlyk V. Magnetic ordering of novel La3NiGe2-type R3CoGe2 compounds (R = Pr, Nd, Sm, Gd-Dy). Intermetallics 2011;19:321–6.
[700] Ahn K, Pecharsky VK, Gischneidner KA. The magnetothermal behavior of mixed-valence Eu3O4. J Appl Phys 2009;106:043918.
[701] Midya A, Khan N, Bhoi D, Mandal P. Giant magnetocaloric effect in magnetically frustrated EuHo[sub 2]O[sub 4] and EuDy[sub 2]O[sub 4] compounds. Appl Phys Lett 2012;101:132415.
[702] Morozkin AV, Yapaskurt VO, Nirmala R, Malik SK, Quezado S, Yao JL, et al. Magnetic order of Y3NiSi3-type R3NiSi3 (R= Gd-DY) compounds. J Magn Magn Mater 2016;398:141–7.
[703] Linsinger S, Hermes W, Eul M, Pottgen R. The solid solution Gd2NixCu2-xMg: Large reversible magnetocaloric effect and a drastic change of the magnetism by substitution. J Appl Phys 2010;108:043903.
[704] Morozkin AV, Yao JL, Mozharivskyj Y. Magnetic properties and magnetocaloric effect of Sc(2)CoSi(2)-type Gd(2)CoSi(2) and Gd(2)CoGe(2) compounds. Intermetallics 2012;21:115–20.
[705] Tence S, Flores RC, Chable J, Gorsse S, Chevalier B, Gaudin E. Stabilization by Si substitution of the pseudobinary compound Gd-2(Co3-xSix) with magnetocaloric properties around room temperature. Inorg Chem 2014;53:6728–36.
[706] Morozkin AV, Knotko AV, Yapaskurt VO, Pani M, Nirmala R, Quezado S, et al. Magnetic ordering in Sc2CoSi2-type R2FeSi2 (R = Gd, Tb) and R2CoSi2 (R=Y, Gd-Er) compounds. J Magn Magn Mater 2016;413:97–107.
[707] Fu H, Zou M, Guo MS, Zheng Q, Zu XT. Structural, magnetic, and magnetothermal properties of R(2)Co(2)Al (R = Tb, and Dy) compounds. Mater Charact 2011;62:451–5.
[708] Karmakar SK, Giri S, Majumdar S. Investigation of magnetic and electrical transport properties of Dy2Ni2Sn. J Magn Magn Mater 2014;370:96–9.
[709] Zhang YK, Xu X, Yang Y, Hou L, Ren ZM, Li X, et al. Study of the magnetic phase transitions and magnetocaloric effect in Dy2Cu2In compound. J Alloys Comp 2016;667:130–3.
[710] Li LW, Yi YL, Su KP, Qi Y, Huo DX, Pottgen R. Magnetic properties and large magnetocaloric effect in Ho2Cu2In and Ho2Au2In compounds. J Mater Sci 2016;51:5421–6.
[711] Zhang YK, Yang Y, Xu X, Hou L, Ren ZM, Li X, et al. Large reversible magnetocaloric effect in RE2Cu2In (RE = Er and Tm) and enhanced refrigerant capacity in its composite materials. J Phys D-Appl Phys 2016;49:145002.
[712] da Silva LM, Gandra FG, Medina AN, dos Santos AO, Cardoso LP. Magnetization and specific heat in U1-xLaxGa2 and magnetocaloric effect in UGa2. J Appl Phys 2005;97:10A921.
[713] da Silva LM, dos Santos AO, Medina AN, Coelho AA, Cardoso LP, Gandra FG. A study of pressure and chemical substitution effects on the magnetocaloric properties of the ferromagnetic compound UGa2. J Phys-Condes Matter 2009;21:276001.
[714] da Silva LM, dos Santos AO, Gandra FG, Cardoso LP, Gama S. Magnetic and magnetocaloric properties on the U1-yRyGa2 (R=Er and Dy) compound. J Appl Phys 2008;103:07B308.
[715] Han Z, Li D, Meng H, Liu XH, Zhang ZD. Magnetocaloric effect in terbium diboride. J Alloys Comp 2010;498:118–20.
[716] Meng H, Li B, Han Z, Zhang YQ, Wang XW, Zhang ZD. Reversible magnetocaloric effect and refrigeration capacity enhanced by two successive magnetic transitions in DyB2. Sci China-Technol Sci 2012;55:501–4.
[717] dos Reis RD, da Silva LM, dos Santos AO, Medina AMN, Cardoso LP, Gandra FCG. Anisotropic magnetocaloric effect in ErGa2 and HoGa2 single-crystals. J Alloys Comp 2014;582:461–5.
[718] Wang F, Yuan FY, Wang JZ, Feng TF, Hu GQ. Conventional and inverse magnetocaloric effect in Pr2CuSi3 and Gd2CuSi3 compounds. J Alloys Comp 2014;592:63–6.
[719] Mo ZJ, Shen J, Yan LQ, Gao XQ, Tang CC, Wu JF, et al. A giant reversible magnetocaloric effect in Ho2PdSi3 compound. J Alloys Comp 2015;618:512–5.
[720] Bazela W, Wawrzynska E, Penc B, Stusser N, Szytula A, Zygmunt A. Magnetic structures of R2RhSi3 (R=Ho, Er) compounds. J Alloys Comp 2003;360:76–80.
[721] Wang LC, Cui L, Dong QY, Mo ZJ, Xu ZY, Hu FX, et al. Large magnetocaloric effect with a wide working temperature span in the R2CoGa3 (R = Gd, Dy, and Ho) compounds. J Appl Phys 2014;115:233913.
[722] Singh NK, Kumar P, Suresh KG, Nigam AK. Investigations on magnetic and magnetocaloric properties of the intermetallic compound TbAgAl. J Appl Phys 2009;105:023901.
[723] Chen J, Shen BG, Dong QY, Hu FX, Sun JR. Giant reversible magnetocaloric effect in metamagnetic HoCuSi compound. Appl Phys Lett 2010;96:152501.
[724] Chen J, Shen BG, Dong QY, Sun JR. Giant magnetic entropy change in antiferromagnetic DyCuSi compound. Solid State Commun 2010;150:1429–31.
[725] Drulis H, Hackemer A, Folcik L, Zaleski A. Magnetocaloric effect in terbium dihydrides: Heat capacity measurements. Solid State Commun 2010;150:164–7.
[726] Drulis H, Hackemer A, Folcik L. Magnetic properties of terbium dihydrides. Solid State Commun 2009;149:1266–8.
[727] Zhang H, Shen BG. Magnetocaloric effects in RT X intermetallic compounds (R = Gd-Tm, T = Fe-Cu and Pd, X = Al and Si). Chin Phys B 2015;24:127504.
[728] Canepa F, Napoletano M, Palenzona A, Merlo F, Cirafici S. Magnetocaloric properties of GdNiGa and GdNiIn intermetallic compounds. J Phys D-Appl Phys 1999;32:2721–5.
[729] Klimczak M, Talik E. Magnetocaloric effect of GdTX (T = Mn, Fe, Ni, Pd, X=Al, In) and GdFe6Al6 ternary compounds. J Phys: Conference Series 2010;200:092009.

[730] Schappacher FM, Rayaprol S, Pottgen R. Structure and magnetism of GdRuGe. Solid State Commun 2008;148:326–30.
[731] Oboz M, Talik E. Properties of the GdTX (T = Mn, Fe, Ni, Pd, X = Al, In) and GdFe6Al6 intermetallics. J Alloys Comp 2011;509:5441–6.
[732] Takeya H, Pecharsky VK, Gschneidner KA, Moorman JO. New-type of magnetocaloric effect - implications on low-temperature magnetic refrigeration using an ericsson cycle. Appl Phys Lett 1994;64:2739–41.
[733] Zhang H, Xu ZY, Zheng XQ, Shen J, Hu FX, Sun JR, et al. Magnetocaloric effects in RNiIn (R = Gd-Er) intermetallic compounds. J Appl Phys 2011;109:123926.
[734] Cui L, Wang LC, Dong QY, Liu FH, Mo ZJ, Zhang Y, et al. Effect of Cu doping on the magnetic and magnetocaloric properties in the HoNiAl intermetallic compound. J Alloys Comp 2015;622:24–8.
[735] Dong QY, Shen BG, Chen J, Shen J, Sun JR. Large reversible magnetocaloric effect in DyCuAl compound. J Appl Phys 2009;105:113902.
[736] Dong QY, Shen BG, Chen J, Shen J, Sun JR. Spin-glass behavior and magnetocaloric effect in melt-spun TbCuAl alloys. Solid State Commun 2011;151:112–5.
[737] Dong QY, Chen J, Shen J, Sun JR, Shen BG. Large magnetic entropy change and refrigerant capacity in rare-earth intermetallic RCuAl (R=Ho and Er) compounds. J Magn Magn Mater 2012;324:2676–8.
[738] Dong QY, Shen BG, He SL, Jiang HW, Zheng W, Sun JR. Effect of crystal grain dimension on the magnetic properties and magnetocaloric effects in DyCuAl compound. J Nanosci Nanotechnol 2012;12:1040–3.
[739] Shen J, Xu ZY, Zhang H, Zheng XQ, Wu JF, Hu FX, et al. Metamagnetic transition and magnetocaloric effect in antiferromagnetic TbPdAl compound. J Magn Magn Mater 2011;323:2949–52.
[740] Kastil J, Javorsky P, Klicpera M. Magnetocaloric effect of the Tb1-xYxNiAl and TbNiAl1-yIny Series. Acta Phys Pol A 2010;118:888–90.
[741] Kastil J, Javorsky P, Pospisil J. Anisotropic magnetocaloric effect in TbNiAl. J Alloys Comp 2011;509:5931–4.
[742] Mukadam MD, Yusuf SM. Magnetocaloric effect in UNiGa compound with the multiple magnetic phase transitions. Physica B 2010;405:686–9.
[743] Mo ZJ, Shen J, Chen GF, Yan LQ, Zheng XQ, Wu JF, et al. Evolution of magnetic properties and magnetocaloric effect in TmNi1-xCuxAl (x=0, 0.1, 0.3, 0.5, 0.7, 0.9, 1) compounds. J Appl Phys 2014;115:17A909.
[744] Bajorek A, Chelkowska G, Chrobak A, Sterkowicz B. Magnetism of selected ternary Sm compounds. J Alloys Comp 2011;509:2667–71.
[745] Franca ELT, dos Santos AO, Coelho AA, da Silva LM. Magnetocaloric effect of the ternary Dy, Ho and Er platinum gallides. J Magn Magn Mater 2016;401:1088–92.
[746] Prokes K, Tegus O, Bruck E, Klaasse JCP, de Boer FR, Buschow KHJ. Magnetic properties and magnetic structure of HoTiGe and ErTiGe. J Alloys Comp 2002;335:62–9.
[747] Provenzano V, Baumgold B, Shull RD, Shapiro AJ, Koyama K, Watanabe K, et al. Structure and magnetocaloric properties of the Fe-doped HoTiGe alloy. J Appl Phys 2006;99:08K906.
[748] Shen J, Zhao JL, Hu FX, Wu JF, Gong MQ, Li YX, et al. Magnetic properties and magnetocaloric effects in antiferromagnetic ErTiSi. J Appl Phys 2010;107:09A931.
[749] Zhang H, Sun YJ, Yang LH, Niu E, Wang HS, Hu FX, et al. Successive inverse and normal magnetocaloric effects in HoFeSi compound. J Appl Phys 2014;115:063901.
[750] Ma Z, Shang YF, Balfour EA, Fu H, Teng BH, Wang L, et al. Comparative study of the magnetocaloric effect in multiphase Gd-Ni-Al alloys: single peak versus table-like profile in magnetic entropy changes. J Alloys Comp 2016;680:268–72.
[751] Wlodarczyk P, Hawelek L, Zackiewicz P, Roy TR, Chrobak A, Kaminska M, et al. Characterization of magnetocaloric effect, magnetic ordering and electronic structure in the GdFe1-xCoxSi intermetallic compounds. Mater Chem Phys 2015;162:273–8.
[752] Gupta S, Suresh KG. Review on magnetic and related properties of RTX compounds. J Alloys Comp 2015;618:562–606.
[753] Bajorek A, Chrobak A, Chelkowska G, Kwiecien M. Influence of Fe substitution on the structure and magnetic properties in Gd(Ni1-xFex)(3) intermetallic compounds. J Alloys Comp 2009;485:6–12.
[754] Bajorek A, Chrobak A, Chelkowska G, Kwiecien-Grudziecka M. Magnetic properties and magnetocaloric effect in Gd(Ni1-xCox)(3) intermetallic compounds. J Alloys Comp 2010;494:22–7.
[755] Xie ZG, Li B, Li J, Geng DY, Zhang ZD. Tunable magnetocaloric effect around hydrogen liquefaction temperature in Tb1-xYxCoC2 compounds. Physica B 2010;405:2133–6.
[756] Dembele SN, Ma Z, Shang YF, Fu H, Balfour EA, Hadimani RL, et al. Large magnetocaloric effect of GdNiAl2 compound. J Magn Magn Mater 2015;391:191–4.
[757] Gao RL, Xu ZY, Wang LC, Dong QY, Zhang Y, Liu FH, et al. Magnetic properties and low-temperature large magnetocaloric effect in the antiferromagnetic HoCu0.33Ge2 and ErCu0.25Ge2 compounds. J Alloys Comp 2015;631:33–7.
[758] Gupta S, Suresh KG, Lukoyanov AV, Knyazev YV, Kuz'min YI. Magnetism, electronic structure and optical properties of TbNiGe2. J Alloys Comp 2016;664:120–4.
[759] Gupta S, Suresh KG, Lukoyanov AV, Knyazev YV, Kuz'min YI. Theoretical and experimental investigations on the magnetic and related properties of RAgSn2 (R=Ho, Er) compounds. J Mater Sci 2016;51:6341–7.
[760] Jang D, Gruner T, Steppke A, Mitsumoto K, Geibel C, Brando M. Large magnetocaloric effect and adiabatic demagnetization refrigeration with YbPt2Sn. Nat Commun 2015;6:8680.
[761] Gruner T, Jang D, Steppke A, Brando M, Ritter F, Krellner C, et al. Unusual weak magnetic exchange in two different structure types: YbPt2Sn and YbPt2In. J Phys Condens Matter 2014;26:485002.
[762] Bhattacharyya A, Giri S, Majumdar S. Successive magnetic transitions and low temperature magnetocaloric effect in RE2Ni7 (RE=Dy, Ho). J Magn Magn Mater 2011;323:1484–9.
[763] Ilyn M, Bartashevich MI, Andreev AV, Tereshina EA, Zhukova V, Zhukov A, et al. Magnetocaloric effect in single crystal Nd2Co7. J Appl Phys 2011;109:083932.
[764] Li LW, Wang J, Su KP, Huo DX, Qi Y. Magnetic properties and magnetocaloric effect in metamagnetic RE2Cu2O5 (RE = Dy and Ho) cuprates. J Alloys Comp 2016;658:500–4.
[765] Lemoine P, Verniere A, Mazet T, Malaman B. Magnetic and magnetocaloric properties of R(6)Mn(23) (R=Y, Nd, Sm, Gd-Tm, Lu) compounds. J Magn Magn Mater 2011;323:2690–5.
[766] Lemoine P, Ban V, Verniere A, Mazet T, Malaman B. Magnetocaloric properties of Gd-6(Mn1-xFex)(23) alloys (x <= 0.2). Solid State Commun 2010;150:1556–9.
[767] Lemoine P, Verniere A, Malaman B, Mazet T. Magnetic and magnetocaloric properties of Gd-6(Mn1-xCox)(23) compounds (x <= 0.3). J Alloys Comp 2016;680:612–6.
[768] Su YT, Sui Y, Cheng JG, Wang XJ, Wang Y, Liu WF, et al. Large reversible magnetocaloric effect in HoTiO(3) single crystal. J Appl Phys 2011;110:083912.
[769] Ben Amor N, Bejar M, Hussein M, Dhahri E, Valente MA, Hlil EK. Synthesis, Magnetic Properties, Magnetic Entropy and Arrot Plot of Antiferromagnetic Frustrated Er2Ti2O7 Compound. J Supercond Nov Magn 2012;25:1035–42.
[770] Alho BP, Carvalho AMG, von Ranke PJ. Anisotropic magnetocaloric effect in antiferromagnetic systems: application to EuTiO3. J Appl Phys 2014;116:113907.
[771] Midya A, Mandal P, Rubi K, Chen RF, Wang JS, Mahendiran R, et al. Large adiabatic temperature and magnetic entropy changes in EuTiO3. Phys Rev B 2016;93:094422.
[772] Rubi K, Kumar P, Maheswar Repaka DV, Chen R, Wang J-S, Mahendiran R. Giant magnetocaloric effect in magnetoelectric Eu1-xBaxTiO3. Appl Phys Lett 2014;104:032407.
[773] Roy S, Khan N, Mandal P. Giant low-field magnetocaloric effect in single-crystalline EuTi0.85Nb0.15O3. APL Mater 2016;4:026102.
[774] Mo ZJ, Hao ZH, Shen J, Li L, Wu JF, Hu FX, et al. Observation of giant magnetocaloric effect in EuTi1-xCrxO3. J Alloys Comp 2015;649:674–8.

[775] Alho BP, Nobrega EP, de Sousa VSR, Carvalho AMG, de Oliveira NA, von Ranke PJ. Theoretical investigation on the existence of inverse and direct magnetocaloric effect in perovskite EuZrO3. J Appl Phys 2011;109:083942.
[776] Balli M, Roberge B, Jandl S, Fournier P, Palstra TTM, Nugroho AA. Observation of large refrigerant capacity in the HoVO3 vanadate single crystal. J Appl Phys 2015;118:073903.
[777] Cao YM, Xiang ML, Zhao WY, Wang GH, Feng ZJ, Kang BJ, et al. Magnetic phase transition and giant anisotropic magnetic entropy change in TbFeO3 single crystal. J Appl Phys 2016;119:063904.
[778] Ke YJ, Zhang XQ, Ma Y, Cheng ZH. Anisotropic magnetic entropy change in RFeO3 single crystals(R = Tb, Tm, or Y). Sci Rep 2016;6:19775.
[779] Ke Y-J, Zhang X-Q, Ge H, Ma Y, Cheng Z-H. Low field induced giant anisotropic magnetocaloric effect in DyFeO3 single crystal. Chin Phys B 2015;24:037501.
[780] Yin LH, Yang J, Zhang RR, Dai JM, Song WH, Sun YP. Multiferroicity and magnetoelectric coupling enhanced large magnetocaloric effect in DyFe0.5Cr0.5O3. Appl Phys Lett 2014;104:032904.
[781] McDannald A, Jain M. Magnetocaloric properties of rare-earth substituted DyCrO3. J Appl Phys 2015;118:043904.
[782] Yin LH, Yang J, Kan XC, Song WH, Dai JM, Sun YP. Giant magnetocaloric effect and temperature induced magnetization jump in GdCrO3 single crystal. J Appl Phys 2015;117:133901.
[783] Yin SQ, Sharma V, McDannald A, Reboredo FA, Jain M. Magnetic and magnetocaloric properties of iron substituted holmium chromite and dysprosium chromite. RSC Adv 2016;6:9475–83.
[784] Ido H, Konno K, Cheng SF, Wallace WE, Sankar SG. Effect of al substitution on the magnetic-properties of RCo5 (R = rare-earth). J Appl Phys 1990;67:4638–40.
[785] Nikitin SA, Skokov KP, Koshkid'ko YS, Pastushenkov YG, Ivanova TI. Giant rotating magnetocaloric effect in the region of spin-reorientation transition in the NdCo5 single crystal. Phys Rev Lett 2010;105:137205.
[786] Ma SC, Wang DH, Zhang CL, Xuan HC, Li SD, Huang ZG, et al. The study of the magnetic and room-temperature magnetocaloric properties in spin-reorientation Nd1-xDyxCo4Al (x=0, 0.1) alloys. J Alloys Comp 2010;499:7–10.
[787] Ao WQ, Zhang WH, Li JQ, Yu YJ, Liu FS. Structural and magnetic properties of Dy(1-x)Nc(1-x)Co(4)Ga compounds. J Alloys Comp 2010;495:13–6.
[788] Nouri K, Jemmali M, Walha S, Zehani K, Ben Salah A, Bessais L. Structural, atomic Hirschfeld surface, magnetic and magnetocaloric properties of SmNi5 compound. J Alloys Comp 2016;672:440–8.
[789] Coroian N. Propriétés structurales et magnétiques de composés intermétalliques à base des terres rares, cobalt et silicium. Cluj-Napoca: Université Joseph Fourier, Grenoble et Université Babes-Bolyai; 2008.
[790] Rocco DL, Amaral JS, Leitao JV, Amaral VS, Reis MS, Das S, et al. High refrigerant capacity of PrNi5-xCox magnetic compounds exploiting its spin reorientation and magnetic transition over a wide temperature zone. J Phys D-Appl Phys 2009;42:055002.
[791] Ma SC, Wang DH, Zhong ZC, Shen LJ, Xuan HC, Cao QQ, et al. Effect of partial Nd-substitution on the magnetic and magnetocaloric properties in spin-reorientation PrCo(4)Al alloy. Eur Phys J B 2011;84:167–71.
[792] Skokov KP, Pastushenkov YG, Koshkid'ko YS, Shutz G, Goll D, Ivanova TI, et al. Magnetocaloric effect, magnetic domain structure and spin-reorientation transitions in HoCo5 single crystals. J Magn Magn Mater 2011;323:447–50.
[793] Falkowski M, Tolinski T, Kowalczyk A. Magnetocaloric effect in NdNi4Si compound. Acta Phys Pol A 2012;121:1290–2.
[794] Laghrissi A, Salmani E, Ez-Zahraouy H, Benyoussef A. Ab initio, theoretical and Monte Carlo approaches for the magnetocaloric effect in DyNi4Si. J Magn Magn Mater 2016;412:259–65.
[795] Morozkin AV, Nirmala R, Malik SK. Magnetism and magnetocaloric effect in YNi4Si-type RNi4Si (R=Ce, Gd, Tb and Dy) compounds. J Magn Magn Mater 2015;378:221–7.
[796] Yao JL, Yan X, Morozkin AV. Giant magnetic coercivity in CaCu5-type SmNi3TSi (T=Mn-Cu) solid solutions. J Solid State Chem 2015;232:213–20.
[797] Yao JL, Morozkin AV. Giant magnetic coercivity in orthorhombic YNi4Si-type SmNi4Si compound. J Solid State Chem 2015;230:249–53.
[798] Morozkin AV, Knotko AV, Yapaskurt VO, Yao JL, Yuan F, Mozharivskyj Y, et al. Magnetic properties of CaCu5-type RNi3TSi (R = Gd and Tb, T = Mn, Fe, Co and Cu) compounds. J Solid State Chem 2015;232:150–6.
[799] Li LW, Igawa H, Nishimura K, Huo DX. Study of the magnetic transition and large magnetocaloric effect in DyCo3B2 compound. J Appl Phys 2011;109:083901.
[800] Li LW, Nishimura K, Igawa H, Huo DX. Magnetic properties and magnetocaloric effect in GdCo3B2 compound. J Alloys Comp 2011;509:4198–200.
[801] Tolinski T, Falkowski M, Kowalczyk A, Synoradzki K. Magnetocaloric effect in the ternary DyCO3B2 compound. Solid State Sci 2011;13:1865–8.
[802] Gencer H, Kervan N, Gencer A, Gunes A, Atalay S. Magnetocaloric effect in CeCo4B compound. J Alloys Comp 2008;466:1–4.
[803] Kervan N, Kervan S, Sozeri H, Gencer A. Magnetic properties and magnetocaloric effect of Ce2GdCo11B4 boride. Mater Chem Phys 2009;116:586–8.
[804] Sharma ALL, Gomes AM, Mejia CS, Drymiotis FR, Carvalho AMG. Pressure tuning the magnetocaloric effect in valence transition compound YbInCu4. J Appl Phys 2010;108:083918.
[805] Midya A, Khan N, Bhoi D. Mandal p. 3d–4f spin interaction and field-induced metamagnetism in RCrO4 (R=Ho, Gd, Lu) compounds. J Appl Phys 2014;115:17E114.
[806] Dong QY, Ma Y, Ke YJ, Zhang XQ, Wang LC, Shen BG, et al. Ericsson-like giant magnetocaloric effect in GdCrO4-ErCrO4 composite oxides near liquid hydrogen temperature. Mater Lett 2015;161:669–73.
[807] Midya A, Khan N, Bhoi D, Mandal P. Giant magnetocaloric effect in antiferromagnetic DyVO4 compound. Physica B 2014;448:43–5.
[808] McMichael RD, Ritter JJ, Shull RD. Enhanced magnetocaloric effect in Gd3Ga5-xFexO12. J Appl Phys 1993;73:6946–8.
[809] Zhitomirsky ME. Enhanced magnetocaloric effect in frustrated magnets. Phys Rev B 2003;67:104421.
[810] Provenzano V, Li J, King T, Canavan E, Shirron P, DiPirro M, et al. Enhanced magnetocaloric effects in R-3(Ga1-xFex)(5)O-12 (R = Gd, Dy, Ho; 0 < x < 1) nanocomposites. J Magn Magn Mater 2003;266:185–93.
[811] Phan MH, Morales MB, Chinnasamy CN, Latha B, Harris VG, Srikanth H. Magnetocaloric effect in bulk and nanostructured Gd3Fe5O12 materials. J Phys D-Appl Phys 2009;42:115007.
[812] von Ranke PJ, Alho BP, Plaza EJR, Carvalho AMG, de Sousa VSR, de Oliveira NA. Theoretical investigation on the magnetocaloric effect in garnets R3Fe5O12 where (R=Y and Dy). J Appl Phys 2009;106:053914.
[813] Nolas GS, Slack GA, Schujman SB. Semiconductor clathrates: a phonon glass electron crystal material with potential for thermoelectric applications. In: Tritt TM, editor. Semiconductors and semimetals. Elsevier; 2001. p. 255–300.
[814] Srinath S, Gass J, Rebar DJ, Woods GT, Srikanth H, Nolas GS. Giant magnetocaloric effect in clathrates. J Appl Phys 2006;99:08K902.
[815] Phan MH, Woods GT, Chaturvedi A, Stefanoski S, Nolas GS, Srikanth H. Long-range ferromagnetism and giant magnetocaloric effect in type VIII Eu8Ga16Ge30 clathrates. Appl Phys Lett 2008;93:252505.
[816] Phan MH, Franco V, Chaturvedi A, Stefanoski S, Kirby H, Nolas GS, et al. Magnetocaloric effect and refrigerant capacity in Sr-doped Eu8Ga16Ge30 type-I clathrates. J Appl Phys 2010;107:09A910.
[817] Phan MH, Franco V, Chaturvedi A, Stefanoski S, Nolas GS, Srikanth H. Origin of the magnetic anomaly and tunneling effect of europium on the ferromagnetic ordering in Eu(8-x)Sr(x)Ga(16)Ge(30) (x=0,4) type-I clathrates. Phys Rev B 2011;84:054436.
[818] Chaturvedi A, Stefanoski S, Phan M-H, Nolas GS, Srikanth H. Table-like magnetocaloric effect and enhanced refrigerant capacity in Eu8Ga16Ge30-EuO composite materials. Appl Phys Lett 2011;99:162513.
[819] Biswas A, Chandra S, Stefanoski S, Blázquez JS, Ipus JJ, Conde A, et al. Enhanced cryogenic magnetocaloric effect in Eu8Ga16Ge30 clathrate nanocrystals. J Appl Phys 2015;117:033903.
[820] Zheng YZ, Evangelisti M, Winpenny REP. Large magnetocaloric effect in a Wells-Dawson type Ni6Gd6P6 cage. Angew Chem-Int Ed 2011;50:3692–5.
[821] Pasturel M, Nasri N, Gastebois J, Guizouarn T, Belgacem B, Ben Hassen R, et al. Magnetocaloric properties of a novel ferromagnet Gd3Co4+xAl12-x (x=0.50). Intermetallics 2015;60:28–32.

[822] Chattopadhyay MK, Arora P, Mondal P, Roy SB. Magnetic transitions and thermomagnetic properties of GdCu6. J Magn Magn Mater 2010;322:3142–7.
[823] Liu J, Pecharsky VK, Gschneidner KA. Metamagnetic transition and magnetothermal properties of ErCo4Ge2. J Appl Phys 2015;118:013904.
[824] Basso V, Sasso CP, Kupferling M, Skokov KP, Gutfleisch O. Er2Fe14B single crystal as magnetic refrigerant at the spin reorientation transition. J Appl Phys 2011;109:083910.
[825] Skokov KP, Pastushenkov YG, Nikitin SA, Fries M, Gutfleisch O. Rotational magnetocaloric effect in the Er2Fe14B single crystal. IEEE Trans Magn 2016;52:2500304.
[826] Jin SG, Liu LM, Wang YL, Chen BX. Research for room-temperature magnetic refrigerants in RXCE2-XFE17 series. J Appl Phys 1991;70:6275–6.
[827] Gorria P, Alvarez P, Marcos JS, Llamazares JLS, Perez MJ, Blanco JA. Crystal structure, magnetocaloric effect and magnetovolume anomalies in nanostructured Pr2Fe17. Acta Mater 2009;57:1724–33.
[828] Pawlik K, Skorvanek I, Kovac J, Pawlik P, Wyslocki JJ, Bodak OI. Phase structure and magnetocaloric effect in binary Pr-Fe alloys. J Magn Magn Mater 2006;304:E510–2.
[829] Guetari R, Bez R, Belhadj A, Zehani K, Bezergheanu A, Mliki N, et al. Influence of Al substitution on magnetocaloric effect of Pr2Fe17-xAlx. J Alloys Comp 2014;588:64–9.
[830] Zhong XC, Liu ZW, Zeng DC, Gschneidner KA, Pecharsky VK. Magnetocaloric effect of Pr2Fe17-x Mn (x) alloys. Rare Metals 2014;33:552–5.
[831] Alvarez P, Gorria P, Franco V, Marcos JS, Perez MJ, Llamazares JLS, et al. Nanocrystalline Nd2Fe17 synthesized by high-energy ball milling: crystal structure, microstructure and magnetic properties. J Phys-Condes Matter 2010;22:216005.
[832] Alvarez P, Gorria P, Llamazares JLS, Perez MJ, Franco V, Reiffers M, et al. Magnetic properties and magneto-caloric effect in pseudo-binary intermetallic (Ce, R)(2)Fe-17 compounds (R = Y, Pr and Dy). Intermetallics 2011;19:982–7.
[833] Kuchin AG, Iwasieczko W. Magnetocaloric effect in the Ce2Fe17-xMnx helical magnets. J Alloys Comp 2011;509:6763–7.
[834] Alvarez-Alonso P, Llamazares JLS, Sanchez-Valdes CF, Cuello GJ, Franco V, Gorria P, et al. On the broadening of the magnetic entropy change due to Curie temperature distribution. J Appl Phys 2014;115:17A929.
[835] Charfeddine S, Zehani K, Bessais L, Korchef A. Structural, magnetic, magneto-caloric and Mossbauer spectral study of Tb2Fe17 compound synthesized by arc melting. J Solid State Chem 2016;238:15–20.
[836] Banerjee D, Kumar P, Suresh KG, Nigam AK. Anomalous magnetic and magnetocaloric properties of Er2Ni17. J Phys D-Appl Phys 2007;40:2691–4.
[837] Kuchin AG, Iwasieczko W. Enhancement of the magnetocaloric effect in the Lu2Fe17-xMnx system. Solid State Commun 2010;150:1580–3.
[838] Kuchin AG, Iwasieczko W, Platonov SP. The magnetocaloric effect in R2Fe17 intermetallics with different types of magnetic phase transition. Low Temp Phys 2015;41:985–9.
[839] Zhang Q, Guillou F, Wahl A, Breard Y, Hardy V. Coexistence of inverse and normal magnetocaloric effect in A-site ordered NdBaMn2O6. Appl Phys Lett 2010;96:242506.
[840] Pani M, Morozkin AV, Yapaskurt VO, Provino A, Manfrinetti P, Nirmala R, et al. RNi8Si3 (R= Gd, Tb): novel ternary ordered derivatives of the BaCd11 type. J Solid State Chem 2016;233:397–406.
[841] Tkáč V, Orendáčová A, Čižmár E, Orendáč M, Feher A, Anders AG. Giant reversible rotating cryomagnetocaloric effect inKEr(MoO4)2induced by a crystal-field anisotropy. Phys Rev B 2015;92:024406.
[842] Snyman JL, Flachbart K, Gabani S, Reiffers M, Shitsevalova N, Siemensmeyer K, et al. Magnetocaloric effect in geometrically frustrated magnetic compound HoB12. Acta Phys Pol A 2010;118:873–4.
[843] Chandragiri V, Iyer KK, Sampathkumaran EV. Magnetic and magnetotransport behavior ofRFe5Al7(R=GdandDy): observation of reentrant inverse-magnetocaloric phenomenon and asymmetric magnetoresistance behavior. Phys Rev B 2015;92:7.
[844] Hill P, Dubenko I, Samanta T, Quetz A, Ali N. Magnetic and magnetocaloric properties of the new rare-earth-transition-metal intermetallic compound Gd3Co29Ge4B10. J Appl Phys 2012;111:07E333.
[845] Midya A, Mandal P. Giant magnetocaloric effect in ferromagnetic superconductor RuSr2GdCu2O8. J Appl Phys 2014;116:223905.
[846] Zhang CL, Wang DH, Han ZD, Tang SL, Gu BX, Du YW. Large magnetic entropy changes in NdFe12B6 compound. Appl Phys Lett 2006;89:122503.
[847] Huang YJ, Shi ZL, Zhang CL, Li SZ, Chen N, Han ZD, et al. Structural properties and Mossbauer spectra of metastable NdFe12B6. Mater Lett 2008;62:85–7.
[848] Zhang CL, Chen J, Wang TZ, Xie GX, Zhu C, Wang DH. The magnetocaloric effect in Nd(Co1-xFex)(12)B-6 alloys. Physica B 2011;406:2840–2.
[849] Wang F, Shen BG, Zhang JA, Sun JR, Meng FB, Li YX. Magnetic properties and magnetocaloric effect in compound PrFe12B6. Chin Phys B 2010;19:067501.
[850] de Oliveira NA. Magnetocaloric effect in systems of itinerant electrons: application to Fe Co, Ni, YFe2 and YFe3 compounds. J Alloys Comp 2005;403:45–8.
[851] Daniilidis ND, Dimitrov IK, Mitrovic VF, Elbaum C, Ling XS. Magnetocaloric studies of the peak effect in Nb. Phys Rev B 2007;75:174519.
[852] Ohtsuka T. Reversible magnetocaloric effect in superconducting niobium. Phys Lett 1965;17:194.
[853] Wasim SM, Grenier CG, Zebouni NH. Magnetocaloric effects and enthalpy in mixed state of superconducting niobium. Phys Lett 1965;19:165.
[854] Dong F, Graf MJ, Huber TE, Huber CI. Specific heat of superconducting indium in porous Vycor glass. Solid State Commun 1997;101:929–33.
[855] Graf T, Felser C, Parkin SSP. Simple rules for the understanding of Heusler compounds. Prog Solid State Chem 2011;39:1–50.
[856] Planes A, Manosa L, Acet M. Magnetocaloric effect and its relation to shape-memory properties in ferromagnetic Heusler alloys. J Phys-Condes Matter 2009;21:233201.
[857] Planes A, Stern-Taulats E, Castan T, Vives E, Manosa L, Saxena A. Caloric and multicaloric effects in shape memory alloys. Mater Today-Proc 2015;2:477–84.
[858] Buchelnikov VD, Sokolovskiy VV. Magnetocaloric effect in Ni-Mn-X (X = Ga, In, Sn, Sb) Heusler alloys. Phys Metals Metallogr 2011;112:633–65.
[859] Umetsu RY, Xu X, Kainuma R. NiMn-based metamagnetic shape memory alloys. Scr Mater 2016;116:1–6.
[860] Yu GH, Xu YL, Liu ZH, Qiu HM, Zhu ZY, Huang XP, et al. Recent progress in Heusler-type magnetic shape memory alloys. Rare Metals 2015;34:527–39.
[861] Singh S, Caron L, D'Souza SW, Fichtner T, Porcari G, Fabbrici S, et al. Large magnetization and reversible magnetocaloric effect at the second-order magnetic transition in heusler materials. Adv Mater 2016;28:3321–5.
[862] Kokorin VV, Konoplyuk SM, Perekos AE, Semenova YS. Martensitic transformation temperature hysteresis narrowing and magnetocaloric effect in ferromagnetic shape memory alloys Ni-Mn-Ga. J Magn Magn Mater 2009;321:782–5.
[863] Dutta B, Cakir A, Giacobbe C, Al-Zubi A, Hickel T, Acet M, et al. Ab initio prediction of martensitic and intermartensitic phase boundaries in Ni-Mn-Ga. Phys Rev Lett 2016;116:025503.
[864] D'Souza SW, Roy T, Barman SR, Chakrabarti A. Magnetic properties and electronic structure of Mn-Ni-Ga magnetic shape memory alloys. J Phys Condens Matter 2014;26:506001.
[865] Hu FX, Shen BG, Sun JR. Magnetic entropy change in Ni51.5Mn22.7Ga25.8 alloy. Appl Phys Lett 2000;76:3460–2.
[866] Fukuda T, Maeda H, Yasui M, Kakeshita T. Influence of magnetocrystalline anisotropy on martensitic transformation under magnetic field of single-crystalline Ni2MnGa. Scr Mater 2009;60:261–3.
[867] Hu FX, Sun JR, Wu GH, Shen BG. Magnetic entropy change in Ni50.1Mn20.7Ga29.6 single crystal. J Appl Phys 2001;90:5216–9.
[868] Hu FX, Shen BG, Sun JR, Wu GH. Large magnetic entropy change in a Heusler alloy Ni52.6Mn23.1Ga24.3 single crystal. Phys Rev B 2001;64:132412.
[869] Mandal K, Pal D, Scheerbaum N, Lyubina J, Gutfleisch O. Magnetocaloric effect in Ni-Mn-Ga alloys. IEEE Trans Magn 2008;44:2993–6.
[870] Zhou XZ, Li W, Kunkel HP, Williams G. Influence of the nature of the magnetic phase transition on the associated magnetocaloric effect in the Ni-Mn-Ga system. J Magn Magn Mater 2005;293:854–62.
[871] Zhou XZ, Kunkel H, Williams G, Zhang SH, Xue DH. Phase transitions and the magnetocaloric effect in Mn rich Ni-Mn-Ga Heusler alloys. J Magn Magn Mater 2006;305:372–6.

[872] Singh S, Esakki Muthu S, Senyshyn A, Rajput P, Suard E, Arumugam S, et al. Inverse magnetocaloric effect in Mn2NiGa and Mn1.75Ni1.25Ga magnetic shape memory alloys. Appl Phys Lett 2014;104:051905.
[873] Chatterjee S, Giri S, Majumdar S, De SK, Koledov VV. Effect of Sn doping on the martensitic and premartensitic transitions in Ni2MnGa. J Magn Magn Mater 2012;324:1891–6.
[874] Marcos J, Planes A, Manosa L, Casanova F, Batlle X, Labarta A, et al. Magnetic field induced entropy change and magnetoelasticity in Ni-Mn-Ga alloys. Phys Rev B 2002;66:224413.
[875] Marcos J, Manosa L, Planes A, Casanova F, Batlle X, Labarta A. Multiscale origin of the magnetocaloric effect in Ni-Mn-Ga shape-memory alloys. Phys Rev B 2003;68:094401.
[876] Pareti L, Solzi M, Albertini F, Paoluzi A. Giant entropy change at the co-occurrence of structural and magnetic transitions in the Ni2.19Mn0.81Ga Heusler alloy. Eur Phys J B 2003;32:303–7.
[877] Aliev A, Batdalov A, Bosko S, Buchelnikov V, Dikshtein I, Khovailo V, et al. Magnetocaloric effect and magnetization in a Ni-Mn-Ga Heusler alloy in the vicinity of magnetostructural transition. J Magn Magn Mater 2004;272:2040–2.
[878] Pasquale M, Sasso CP, Lewis LH, Giudici L, Lograsso T, Schlagel D. Magnetostructural transition and magnetocaloric effect in Ni55Mn20Ga25 single crystals. Phys Rev B 2005;72:094435.
[879] Duan JF, Long Y, Bao B, Zhang H, Ye RC, Chang YQ, et al. Experimental and theoretical investigations of the magnetocaloric effect of Ni2.15Mn0.85-xCuxGa (x=0.05,0.07) alloys. J Appl Phys 2008;103:063911.
[880] Khovaylo VV, Skokov KP, Koshkid'ko YS, Koledov VV, Shavrov VG, Buchelnikov VD, et al. Adiabatic temperature change at first-order magnetic phase transitions: Ni2.19Mn0.81Ga as a case study. Phys Rev B 2008;78:060403.
[881] Li Z, Jing C, Zhang HL, Cao SX, Zhang JC. Determination of the magnetocaloric effect associated with martensitic transition in Ni46Cu4Mn38Sn12 and Ni50CoMn34In15 Heusler alloys. Chin Phys B 2011;20:047502.
[882] Zhang YP, Hughes RA, Britten JF, Dube PA, Preston JS, Botton GA, et al. Magnetocaloric effect in Ni-Mn-Ga thin films under concurrent magnetostructural and Curie transitions. J Appl Phys 2011;110:013910.
[883] Sasso CP, Kuepferling M, Giudici L, Basso V, Pasquale M. Direct measurements of the entropy change and its history dependence in Ni-Mn-Ga alloys. J Appl Phys 2008;103:07B306.
[884] Porcari G, Cugini F, Fabbrici S, Pernechele C, Albertini F, Buzzi M, et al. Convergence of direct and indirect methods in the magnetocaloric study of first order transformations: the case of Ni-Co-Mn-Ga Heusler alloys. Phys Rev B 2012;86:104432.
[885] Khovaylo V. Inconvenient magnetocaloric effect in ferromagnetic shape memory alloys. J Alloys Comp 2013;577:S362–6.
[886] Duan JF, Huang P, Zhang H, Long Y, Wu GH, Ye RC, et al. Negative and positive magnetocaloric effect in Ni-Fe-Mn-Ga alloy. J Magn Magn Mater 2007;309:96–9.
[887] Gomes AM, Khan M, Stadler S, Ali N, Dubenko I, Takeuchi AY, et al. Magnetocaloric properties of the Ni2Mn1-x(Cu, Co)(x)Ga heusler alloys. J Appl Phys 2006;99:08Q106.
[888] Stadler S, Khan M, Mitchell J, Ali N, Gomes AM, Dubenko I, et al. Magnetocaloric properties of Ni2Mn1-xCuxGa. Appl Phys Lett 2006;88:192511.
[889] Gautam BR, Dubenko I, Mabon JC, Stadler S, Ali N. Effect of small changes in Mn concentration on phase transition temperatures and magnetic entropy variations in Ni2Mn0.75Cu0.25Ga Heusler alloys. J Alloys Comp 2009;472:35–9.
[890] Roy S, Blackburn E, Valvidares SM, Fitzsimmons MR, Vogel SC, Khan M, et al. Delocalization and hybridization enhance the magnetocaloric effect in Cu-doped Ni2MnGa. Phys Rev B 2009;79:235127.
[891] Khan M, Dubenko I, Stadler S, Ali N. Phase transitions and corresponding magnetic entropy changes in Ni2Mn0.75Cu0.25-xCoxGa Heusler alloys. J Appl Phys 2007;102:023901.
[892] Khan M, Stadler S, Ali N. Magnetocaloric properties of fe and ge doped Ni2Mn1-xCuxGa. J Appl Phys 2007;101:09C515.
[893] Bao B, Long Y, Duan JF, Shi PJ, Wu GH, Ye RC, et al. Phase transition processes and magnetocaloric effect in Ni2.15Mn0.85-xCoxGa alloys. J Appl Phys 2008;103:07B335.
[894] Fabbrici S, Kamarad J, Arnold Z, Casoli F, Paoluzi A, Bolzoni F, et al. From direct to inverse giant magnetocaloric effect in Co-doped NiMnGa multifunctional alloys. Acta Mater 2011;59:412–9.
[895] Pathak AK, Dubenko I, Karaca HE, Stadler S, Ali N. Large inverse magnetic entropy changes and magnetoresistance in the vicinity of a field-induced martensitic transformation in Ni50-xCoxMn32-yFeyGa18. Appl Phys Lett 2010;97:062505.
[896] Leitao JCV, Rocco DL, Amaral JS, Reis MD, Amaral VBS, Fernandes RP, et al. Influence of the magnetic anisotropy on the magnetic entropy change of Ni2Mn(Ga, Bi) memory shape alloy. IEEE Trans Magn 2008;44:3036–9.
[897] Gao ZY, Liu C, Wu D, Ma WJ, Zhang J, Cai W. Martensitic transformation and magnetocaloric properties of Sn doping Mn-Ni-Ga alloys. J Magn Magn Mater 2010;322:2488–92.
[898] Mejia CS, Gomes AM, de Oliveira LAS. A less expensive NiMnGa based Heusler alloy for magnetic refrigeration. J Appl Phys 2012;111:07A923.
[899] Zhang ZY, Long Y, Duan JF, Huang P, Wu GH, Chang YQ. Magnetocaloric effect of Ni56Mn18.8Ga24.5Gd0.7 alloy. J Rare Earths 2006;24:579–81.
[900] Recarte V, Perez-Landazabal JI, Gomez-Polo C, Cesari E, Dutkiewicz J. Magnetocaloric effect in Ni-Fe-Ga shape memory alloys. Appl Phys Lett 2006;88:1032503.
[901] Min SG, Zhang YD, Malkinski L, Yu SC, Lee KW, Kim YC. Magnetic entropy change of V substituted Ni-Mn-Ga Heusler alloy. J Appl Phys 2009;105:07A929.
[902] Albertini F, Kamarad J, Arnold Z, Pareti L, Villa E, Righi L. Pressure effects on the magnetocaloric properties of Ni-rich and Mn-rich Ni2MnGa alloys. J Magn Magn Mater 2007;316:364–7.
[903] Mandal K, Pal D, Scheerbaum N, Lyubina J, Gutfleisch O. Effect of pressure on the magnetocaloric properties of nickel-rich Ni-Mn-Ga Heusler alloys. J Appl Phys 2009;105:073509.
[904] Castillo-Villa PO, Soto-Parra DE, Matutes-Aquino JA, Ochoa-Gamboa RA, Planes A, Manosa L, et al. Caloric effects induced by magnetic and mechanical fields in a Ni50Mn25-xGa25Cox magnetic shape memory alloy. Phys Rev B 2011;83:174109.
[905] Krenke T, Duman E, Acet M, Wassermann EF, Moya X, Manosa L, et al. Inverse magnetocaloric effect in ferromagnetic Ni-Mn-Sn alloys. Nat Mater 2005;4:450–4.
[906] Han ZD, Wang DH, Zhang CL, Tang SL, Gu BX, Du YW. Large magnetic entropy changes in the Ni45.4Mn41.5In13.1 ferromagnetic shape memory alloy. Appl Phys Lett 2006;89:182507.
[907] Khan M, Ali N, Stadler S. Inverse magnetocaloric effect in ferromagnetic Ni50Mn37+xSb13-x Heusler alloys. J Appl Phys 2007;101:053919.
[908] Du J, Zheng Q, Ren WJ, Feng WJ, Liu XG, Zhang ZD. Magnetocaloric effect and magnetic-field-induced shape recovery effect at room temperature in ferromagnetic Heusler alloy Ni-Mn-Sb. J Phys D-Appl Phys 2007;40:5523–6.
[909] Titov I, Acet M, Farle M, González-Alonso D, Mañosa L, Planes A, et al. Hysteresis effects in the inverse magnetocaloric effect in martensitic Ni-Mn-In and Ni-Mn-Sn. J Appl Phys 2012;112:073914.
[910] Cakir A, Righi L, Albertini F, Acet M, Farle M. Intermartensitic transitions and phase stability in Ni50Mn50-xSnx Heusler alloys. Acta Mater 2015;99:140–9.
[911] Han ZD, Wang DH, Zhang CL, Xuan HC, Gu BX, Du YW. Low-field inverse magnetocaloric effect in Ni50-xMn39+xSn11 Heusler alloys. Appl Phys Lett 2007;90:042507.
[912] Xuan HC, Zheng YX, Ma SC, Cao QQ, Wang DH, Du YW. The martensitic transformation, magnetocaloric effect, and magnetoresistance in high-Mn content Mn47+xNi43-xSn10 ferromagnetic shape memory alloys. J Appl Phys 2010;108:103920.
[913] Ingale BD, Kuo YK, Ram S. Phase Transformation, Microstructure and Magnetocaloric Properties in Polycrystalline Bulk Ni(50)Mn(50-z)Sn(z) Alloys. IEEE Trans Magn 2011;47:3395–8.

[914] Ray MK, Bagani K, Banerjee S. Effect of excess Ni on martensitic transition, exchange bias and inverse magnetocaloric effect in Ni2+xMn1.4-xSn0.6 alloy. J Alloys Comp 2014;600:55–9.
[915] Krenke T, Duman E, Acet M, Moya X, Manosa L, Planes A. Effect of Co and Fe on the inverse magnetocaloric properties of Ni-Mn-Sn. J Appl Phys 2007;102:033903.
[916] Gao B, Hu FX, Shen J, Wang J, Sun JR, Shen BG. Field-induced structural transition and the related magnetic entropy change in Ni43Mn43Co3Sn11 alloy. J Magn Magn Mater 2009;321:2571–4.
[917] Liu HS, Zhang CL, Han ZD, Xuan HC, Wang DH, Du YW. The effect of Co doping on the magnetic entropy changes in Ni44-xCoxMn45Sn11 alloys. J Alloys Comp 2009;467:27–30.
[918] Srivastava V, Chen XA, James RD. Hysteresis and unusual magnetic properties in the singular Heusler alloy Ni45Co5Mn40Sn10. Appl Phys Lett 2010;97:014101.
[919] Das R, Sarma S, Perumal A, Srinivasan A. Effect of Co and Cu substitution on the magnetic entropy change in Ni46Mn43Sn11 alloy. J Appl Phys 2011;109:07A901.
[920] Han ZD, Chen J, Qian B, Zhang P, Jiang XF, Wang DH, et al. Phase diagram and magnetocaloric effect in Mn(2)Ni(1.64-x)Co(x)Sn(0.36) alloys. Scr Mater 2012;66:121–4.
[921] Yang LH, Zhang H, Hu FX, Sun JR, Pan LQ, Shen BG. Magnetocaloric effect and martensitic transition in Ni50Mn36-xCoxSn14. J Alloys Comp 2014;588:46–8.
[922] Passamani EC, Xavier F, Favre-Nicolin E, Larica C, Takeuchi AY, Castro IL, et al. Magnetic properties of NiMn-based Heusler alloys influenced by Fe atoms replacing Mn. J Appl Phys 2009;105:033919.
[923] Yan JL, Li ZZ, Chen X, Zhou KW, Shen SX, Zhou HB. Martensitic transition and magnetocaloric properties in Ni45Mn44-xFexSn11 alloys. J Alloys Comp 2010;506:516–9.
[924] Ghosh A, Mandal K. Effect of Fe substitution on the magnetic and magnetocaloric properties of Mn-rich Mn-Ni-Fe-Sn off-stoichiometric Heusler alloys. J Appl Phys 2015;117:093909.
[925] Gao B, Shen J, Hu FX, Wang J, Sun JR, Shen BG. Magnetic properties and magnetic entropy change in Heusler alloys Ni50Mn35-x Cu (x) Sn-15. Appl Phys A-Mater Sci Process 2009;97:443–7.
[926] Dincer I, Yuzuak E, Elerman Y. Influence of irreversibility on inverse magnetocaloric and magnetoresistance properties of the (Ni, Cu)(50)Mn36Sn14 alloys. J Alloys Comp 2010;506:508–12.
[927] Huu DT, Yen NH, Thanh PT, Mai NT, Thanh TD, Phan TL, et al. Magnetic, magnetocaloric and critical properties of Ni50-xCuxMn37Sn13 rapidly quenched ribbons. J Alloys Comp 2015;622:535–40.
[928] Zhang CL, Zou WQ, Xuan HC, Han ZD, Wang DH, Gu BX, et al. Giant low-field magnetic entropy changes in Ni45Mn44-xCrxSn11 ferromagnetic shape memory alloys. J Phys D-Appl Phys 2007;40:7287–90.
[929] Han ZD, Chen X, Zhang Y, Chen J, Qian B, Jiang XF, et al. Martensitic transformation and magnetocaloric effect in Mn-Ni-Nb-Sn shape memory alloys: the effect of 4d transition-metal doping. J Alloys Comp 2012;515:114–8.
[930] Xuan HC, Wang DH, Zhang CL, Han ZD, Liu HS, Gu BX, et al. The large low-field magnetic entropy changes in Ni43Mn46Sn11-xSbx alloys. Solid State Commun 2007;142:591–4.
[931] Chen J, Han ZD, Qian B, Zhang P, Wang DH, Du YW. The influence of Al substitution on the phase transitions and magnetocaloric effect in Ni43Mn46Sn11-xAlx alloys. J Magn Magn Mater 2011;323:248–51.
[932] Wang RL, Yan JB, Xu LS, Marchenkov VV, Chen SS, Tang SL, et al. Effect of Al doping on the martensitic transition and magnetic entropy change in Ni-Mn-Sn alloys. Solid State Commun 2011;151:1196–9.
[933] Han ZD, Wang DH, Zhang CL, Xuan HC, Zhang JR, Gu BX, et al. Effect of lattice contraction on martensitic transformation and magnetocaloric effect in Ge doped Ni-Mn-Sn alloys. Mater Sci Eng B-Adv Funct Solid-State Mater 2009;157:40–3.
[934] Xuan HC, Han PD, Wang DH, Du YW. The influence of Ge substitution on the magnetostucture transition and magnetocaloric effect of Mn-Ni-Sn-Ge alloys. J Alloys Comp 2014;582:369–73.
[935] Muthu SE, Kanagaraj M, Singh S, Sastry PU, Ravikumar G, Rao NVR, et al. Hydrostatic pressure effects on martensitic transition, magnetic and magnetocaloric effect in Si doped Ni-Mn-Sn Heusler alloys. J Alloys Comp 2014;584:175–9.
[936] Muthu SE, Rao NVR, Raja MM, Arumugam S, Matsubayasi K, Uwatoko Y. Hydrostatic pressure effect on the martensitic transition, magnetic, and magnetocaloric properties in Ni(50-x)Mn(37+x)Sn(13) Heusler alloys. J Appl Phys 2011;110:083902.
[937] Xuan HC, Wang DH, Zhang CL, Han ZD, Gu BX, Du YW. Boron's effect on martensitic transformation and magnetocaloric effect in Ni43Mn46Sn11Bx alloys. Appl Phys Lett 2008;92:102503.
[938] Czaja P, Maziarz W, Przewoznik J, Kapusta C, Hawelek L, Chrobak A, et al. Magnetocaloric properties and exchange bias effect in Al for Sn substituted Ni48Mn39.5Sn12.5 Heusler alloy ribbons. J Magn Magn Mater 2014;358:142–8.
[939] Emre B, Bruno NM, Yuce Emre S, Karaman I. Effect of niobium addition on the martensitic transformation and magnetocaloric effect in low hysteresis NiCoMnSn magnetic shape memory alloys. Appl Phys Lett 2014;105:231910.
[940] Stern-Taulats E, Planes A, Lloveras P, Barrio M, Tamarit J-L, Pramanick S, et al. Tailoring barocaloric and magnetocaloric properties in low-hysteresis magnetic shape memory alloys. Acta Mater 2015;96:324–32.
[941] Dubenko I, Quetz A, Pandey S, Aryal A, Eubank M, Rodionov I, et al. Multifunctional properties related to magnetostructural transitions in ternary and quaternary Heusler alloys. J Magn Magn Mater 2015;383:186–9.
[942] Guan W, Liu QR, Gao B, Yang S, Wang Y, Xu MW, et al. Large magnetocaloric effect at low magnetic field in Ni50-xCoxMn35In15 ribbons. J Appl Phys 2011;109:07A903.
[943] Gottschall T, Skokov KP, Benke D, Gruner ME, Gutfleisch O. Contradictory role of the magnetic contribution in inverse magnetocaloric Heusler materials. Phys Rev B 2016;93:184431.
[944] Sanchez-Alarcos V, Recarte V, Perez-Landazabal JI, Chapelon JR, Rodriguez-Velamazan JA. Structural and magnetic properties of Cr-doped Ni-Mn-In metamagnetic shape memory alloys. J Phys D-Appl Phys 2011;44:395001.
[945] Sharma VK, Chattopadhyay MK, Khandelwal A, Roy SB. Martensitic transition near room temperature and the temperature- and magnetic-field-induced multifunctional properties of Ni49CuMn34In16 alloy. Phys Rev B 2010;82:172411.
[946] Sokolovskiy VV, Buchelnikov VD, Khovaylo VV, Taskaev SV, Entel P. Tuning magnetic exchange interactions to enhance magnetocaloric effect in Ni50Mn34In16 Heusler alloy: Monte Carlo and ab initio studies. Int J Refrig-Rev Int Froid 2014;37:273–80.
[947] Liu ZH, Aksoy S, Acet M. Influence of Sb on the magnetic and magnetocaloric properties of ferromagnetic shape memory alloy NiMnIn. J Appl Phys 2009;105:033913.
[948] Zhao XG, Yang JL, Wang XW, Hsieh CC, Chang WC, Liu W, et al. Magnetocaloric and electrical properties in annealed Si-doped Ni-Mn-In Heusler alloy ribbons. IEEE Trans Magn 2011;47:2455–8.
[949] Pathak AK, Dubenko I, Mabon JC, Stadler S, Ali N. The effect of partial substitution of In by X = Si, Ge and Al on the crystal structure, magnetic properties and resistivity of Ni50Mn35In15 Heusler alloys. J Phys D-Appl Phys 2009;42:045004.
[950] Quetz A, Muchharla B, Samanta T, Dubenko I, Talapatra S, Stadler S, et al. Phase diagram and magnetocaloric effects in Ni50Mn35(In1-xCrx)(15) and (Mn1-xCrx)NiGe1.05 alloys. J Appl Phys 2014;115:17A922.
[951] Pandey S, Quetz A, Rodionov ID, Aryal A, Blinov MI, Titov IS, et al. Magnetic, transport, and magnetocaloric properties of boron doped Ni-Mn-In alloys. J Appl Phys 2015;117:183905.
[952] Dubenko I, Samanta T, Quetz A, Kazakov A, Rodionov I, Mettus D, et al. The comparison of direct and indirect methods for determining the magnetocaloric parameters in the Heusler alloy Ni50Mn34.8In14.2B. Appl Phys Lett 2012;100:192402.

[953] Zhao XG, Ning XK, Shih CW, Tong M, Chang WC, Liu W, et al. Martensitic transitions and magnetocaloric properties in Ni48Mn39In13-xGex (x=1–3) ribbons. IEEE Trans Magn 2014;50:2500404.
[954] Singh S, Glavatskyy I, Biswas C. The influence of quench atomic disorder on the magnetocaloric properties of Ni-Co-Mn-In alloys. J Alloys Comp 2014;601:108–11.
[955] Hu FX, Wang J, Chen L, Zhao JL, Sun JR, Shen BG. Effect of the introduction of H atoms on magnetic properties and magnetic entropy change in metamagnetic Heusler alloys Ni-Mn-In. Appl Phys Lett 2009;95:112503.
[956] Sharma VK, Chattopadhyay MK, Roy SB. The effect of external pressure on the magnetocaloric effect of Ni-Mn-In alloy. J Phys-Condes Matter. 2011;23:366001.
[957] Pandey S, Quetz A, Aryal A, Dubenko I, Samanta T, Mazumdar D, et al. The effects of substituting Ag for In on the magnetoresistance and magnetocaloric properties of Ni-Mn-In Heusler alloys. AIP Adv 2016;6:056213.
[958] Feng WJ, Du J, Li B, Hu WJ, Zhang ZD, Li XH, et al. Large low-field inverse magnetocaloric effect in Ni50-xMn38+xSb12 alloys. J Phys D-Appl Phys 2009;42:125003.
[959] Han ZD, Wang DH, Zhang CL, Xuan HC, Zhang JR, Gu BX, et al. The phase transitions, magnetocaloric effect, and magnetoresistance in Co doped Ni-Mn-Sb ferromagnetic shape memory alloys. J Appl Phys 2008;104:053906.
[960] Nayak AK, Suresh KG, Nigam AK. Giant inverse magnetocaloric effect near room temperature in Co substituted NiMnSb Heusler alloys. J Phys D-Appl Phys 2009;42:035009.
[961] Sahoo R, Nayak AK, Suresh KG, Nigam AK. Effect of Si and Ga substitutions on the magnetocaloric properties of NiCoMnSb quaternary Heusler alloys. J Appl Phys 2011;109:07A921.
[962] Sahoo R, Nayak AK, Suresh KG, Nigam AK. Structural, magnetic, magnetocaloric and magnetotransport properties in Ge doped Ni-Mn-Sb Heusler alloys. J Magn Magn Mater 2012;324:1267–71.
[963] Feng WJ, Zuo L, Li YB, Wang YD, Gao M, Fang GL. Abnormal e/a-dependence of T-M and large inverse magnetocaloric effect in Ni49-xCuxMn39Sb12 alloys. Mater Sci Eng B-Adv Funct Solid-State Mater 2011;176:621–5.
[964] Sahoo R, Nayak AK, Suresh KG, Nigam AK. Effect of Fe substitution on the magnetic, transport, thermal and magnetocaloric properties in Ni(50)Mn(38-x)Fe(x)Sb(12) Heusler alloys. J Appl Phys 2011;109:123904.
[965] Nong NV, Tai LT, Huy NT, Trung NT, Bahl CRH, Venkatesh R, et al. Structural, magnetic and magnetocaloric properties of Heusler alloys Ni(50)Mn(38)Sb(12) with boron addition. Mater Sci Eng B-Adv Funct Solid-State Mater 2011;176:1322–5.
[966] Nayak AK, Suresh KG, Nigam AK, Coelho AA, Gama S. Pressure induced magnetic and magnetocaloric properties in NiCoMnSb Heusler alloy. J Appl Phys 2009;106:053901.
[967] Si PZ, Liu JJ, Chen CQ, Wu Q, Jiao ZW, Ge HL. The effect of Ni-substitution on the magnetic properties of Ni2MnGe Heusler alloys. J Alloys Comp 2008;462:1–3.
[968] Recarte V, Perez-Landazabal JI, Gomez-Polo C, Sanchez-Alarcos V, Cesari E, Pons J. Vibrational and magnetic contributions to the entropy change associated with the martensitic transformation of Ni-Fe-Ga ferromagnetic shape memory alloys. J Phys-Condes Matter 2010;22:416001.
[969] Pal D, Mandal K. Magnetocaloric effect and magnetoresistance of Ni-Fe-Ga alloys. J Phys D-Appl Phys 2010;43:455002.
[970] Yu HJ, Fu H, Zeng ZM, Sun JX, Wang ZG, Zhou WL, et al. Phase transformations and magnetocaloric effect in NiFeGa ferromagnetic shape memory alloy. J Alloys Comp 2009;477:732–5.
[971] Liu J, Scheerbaum N, Hinz D, Gutfleisch O. A high-temperature coupling of martensitic and magnetic transformations and magnetic entropy change in Ni-Fe-Ga-Co alloys. Scr Mater 2008;59:1063–6.
[972] Fu H, Yu HJ, Teng BH, Zhang XY, Zu XT. Magnetic properties and magnetic entropy change of Co50Ni22Ga28 alloy. J Alloys Comp 2009;474:595–7.
[973] Vivas RJC, Pedro SS, Cruz C, Tedesco JCG, Coelho AA, Carvalho AMG, et al. Experimental evidences of enhanced magnetocaloric properties at room temperature and half-metallicity on Fe2MnSi-based Heusler alloys. Mater Chem Phys 2016;174:23–7.
[974] Amaral JS, Amaral VS. The effect of magnetic irreversibility on estimating the magnetocaloric effect from magnetization measurements. Appl Phys Lett 2009;94:042506.
[975] Buchelnikov VD, Sokolovskiy VV, Taskaev SV, Khovaylo VV, Aliev AA, Khanov LN, et al. Monte Carlo simulations of the magnetocaloric effect in magnetic Ni-Mn-X (X = Ga, In) Heusler alloys. J Phys D-Appl Phys 2011;44:064012.
[976] Bourgault D, Tillier J, Courtois P, Maillard D, Chaud X. Large inverse magnetocaloric effect in Ni45Co5Mn37.5In12.5 single crystal above 300 K. Appl Phys Lett 2010;96:132501.
[977] Mukherjee T, Michalski S, Skomski R, Sellmyer DJ, Binek C. Overcoming the spin-multiplicity limit of entropy by means of lattice degrees of freedom: a minimal model. Phys Rev B 2011;83:214413.
[978] Caballero-Flores R, Sanchez-Alarcos V, Recarte V, Perez-Landazabal JI, Gomez-Polo C. Latent heat contribution to the direct magnetocaloric effect in Ni-Mn-Ga shape memory alloys with coupled martensitic and magnetic transformations. J Phys D-Appl Phys 2016;49:205004.
[979] Recarte V, Perez-Landazabal JI, Kustov S, Cesari E. Entropy change linked to the magnetic field induced martensitic transformation in a Ni-Mn-In-Co shape memory alloy. J Appl Phys 2010;107:053501.
[980] Bourgault D, Porcar L, Rivoirard S, Courtois P, Hardy V. Entropy change of a Ni45.5Co4.5Mn37In13 single crystal studied by scanning calorimetry in high magnetic fields: Field dependence of the magnetocaloric effect. Appl Phys Lett 2015;107:092403.
[981] Blázquez JS, Franco V, Conde A, Gottschall T, Skokov KP, Gutfleisch O. A unified approach to describe the thermal and magnetic hysteresis in Heusler alloys. Appl Phys Lett 2016;109:122410.
[982] Diestel A, Niemann R, Schleicher B, Schwabe S, Schultz L, Fähler S. Field-temperature phase diagrams of freestanding and substrate-constrained epitaxial Ni-Mn-Ga-Co films for magnetocaloric applications. J Appl Phys 2015;118:023908.
[983] Stonaha PJ, Manley ME, Bruno NM, Karaman I, Arroyave R, Singh N, et al. Lattice vibrations boost demagnetization entropy in a shape-memory alloy. Phys Rev B 2015;92:140406.
[984] Aguilar-Ortiz CO, Soto-Parra D, Alvarez-Alonso P, Lazpita P, Salazar D, Castillo-Villa PO, et al. Influence of Fe doping and magnetic field on martensitic transition in Ni-Mn-Sn melt-spun ribbons. Acta Mater 2016;107:9–16.
[985] Buchelnikov VD, Sokolovskiy VV, Zagrebin MA, Klyuchnikova MA, Entel P. First-principles study of the structural and magnetic properties of the Ni45Co5Mn39Sn11 Heusler alloy. J Magn Magn Mater 2015;383:180–5.
[986] Entel P, Sokolovskiy VV, Buchelnikov VD, Ogura M, Gruner ME, Grunebohm A, et al. The metamagnetic behavior and giant inverse magnetocaloric effect in Ni-Co-Mn-(Ga, In, Sn) Heusler alloys. J Magn Magn Mater 2015;385:193–7.
[987] Goncalves JN, Amaral JS, Amaral VS. Magnetovolume effects in heusler compounds via first-principles calculations. IEEE Trans Magn 2014;50:1–4.
[988] Sokolovskiy V, Grunebohm A, Buchelnikov V, Entel P. Ab Initio and Monte Carlo approaches for the magnetocaloric effect in Co- and In-doped Ni-Mn-Ga Heusler alloys. Entropy 2014;16:4992–5019.
[989] Sokolovskiy VV, Pavlukhina O, Buchelnikov VD, Entel P. Monte Carlo and first-principles approaches for single crystal and polycrystalline Ni2MnGa Heusler alloys. J Phys D: Appl Phys 2014;47:425002.
[990] Sokolovskiy VV, Entel P, Buchelnikov VD, Gruner ME. Achieving large magnetocaloric effects in Co- and Cr-substituted Heusler alloys: predictions from first-principles and Monte Carlo studies. Phys Rev B 2015;91:220409.
[991] L'Vov VA, Kosogor A, Barandiaran JM, Chernenko VA. Theoretical description of magnetocaloric effect in the shape memory alloy exhibiting metamagnetic behavior. J Appl Phys 2016;119:013902.
[992] Liu ZH, Zhang M, Wang WQ, Wang WH, Chen JL, Wu GH, et al. Magnetic properties and martensitic transformation in quaternary Heusler alloy of NiMnFeGa. J Appl Phys 2002;92:5006.
[993] Hu FX, Wang J, Shen J, Gao B, Sun JR, Shen BG. Large magnetic entropy change with small thermal hysteresis near room temperature in metamagnetic alloys Ni51Mn49-xInx. J Appl Phys 2009;105:07A940.

[994] Rao NVR, Gopalan R, Chandrasekaran V, Suresh KG. Microstructure, magnetic properties and magnetocaloric effect in melt-spun Ni-Mn-Ga ribbons. J Alloys Comp 2009;478:59–62.
[995] Cui J, Chu YS, Famodu OO, Furuya Y, Hattrick-Simpers J, James RD, et al. Combinatorial search of thermoelastic shape-memory alloys with extremely small hysteresis width. Nat Mater 2006;5:286–90.
[996] Gottschall T, Skokov KP, Frincu B, Gutfleisch O. Large reversible magnetocaloric effect in Ni-Mn-In-Co. Appl Phys Lett 2015;106:021901.
[997] Sasso CP, Zheng PQ, Basso V, Mullner P, Dunand DC. Enhanced field induced martensitic phase transition and magnetocaloric effect in Ni55Mn20Ga25 metallic foams. Intermetallics 2011;19:952–6.
[998] Monroe JA, Cruz-Perez J, Yegin C, Karaman I, Geltmacher AB, Everett RK, et al. Magnetic response of porous NiCoMnSn metamagnetic shape memory alloys fabricated using solid-state replication. Scr Mater 2012;67:116–9.
[999] Pasquale M, Sasso CP, Lewis LH. Magnetic entropy in Ni2MnGa single crystals. J Appl Phys 2004;95:6918–20.
[1000] Liu J, Scheerbaum N, Lyubina J, Gutfleisch O. Reversibility of magnetostructural transition and associated magnetocaloric effect in Ni-Mn-In-Co. Appl Phys Lett. 2008;93:102512.
[1001] Chatterjee S, Giri S, Majumdar S, De SK. Giant magnetoresistance and large inverse magnetocaloric effect in Ni2Mn1.36Sn0.64 alloy. J Phys D-Appl Phys 2009;42:065001.
[1002] Khovaylo VV, Skokov KP, Gutfleisch O, Miki H, Takagi T, Kanomata T, et al. Peculiarities of the magnetocaloric properties in Ni-Mn-Sn ferromagnetic shape memory alloys. Phys Rev B 2010;81:214406.
[1003] Niemann R, Heczko O, Schultz L, Fahler S. Metamagnetic transitions and magnetocaloric effect in epitaxial Ni-Co-Mn-In films. Appl Phys Lett 2010;97:222507.
[1004] Dincer I, Yuzuak E, Elerman Y. The effect of the substitution of Cu for Ni on magnetoresistance and magnetocaloric properties of Ni50Mn34In16. J Alloys Comp 2011;509:794–9.
[1005] Basso V, Sasso CP, Skokov KP, Gutfleisch O, Khovaylo VV. Hysteresis and magnetocaloric effect at the magnetostructural phase transition of Ni-Mn-Ga and Ni-Mn-Co-Sn Heusler alloys. Phys Rev B 2012;85:014430.
[1006] Bennett LH, Provenzano V, Shull RD, Levin I, Della Torre E, Jin Y. Ferri- to ferro-magnetic transition in the martensitic phase of a Heusler alloy. J Alloys Comp 2012;525:34–8.
[1007] Ghosh A, Sen P, Mandal K. Measurement protocol dependent magnetocaloric properties in a Si-doped Mn-rich Mn-Ni-Sn-Si off-stoichiometric Heusler alloy. J Appl Phys 2016;119:183902.
[1008] Sarkar SK, Babu PD, Biswas A, Siruguri V, Krishnan M. Giant magnetocaloric effect from reverse martensitic transformation in Ni-Mn-Ga-Cu ferromagnetic shape memory alloys. J Alloys Comp 2016;670:281–8.
[1009] Pal D, Ghosh A, Mandal K. Large inverse magnetocaloric effect and magnetoresistance in nickel rich Ni52Mn34Sn14 Heusler alloy. J Magn Magn Mater 2014;360:183–7.
[1010] Salazar Mejía C, Ghorbani Zavareh M, Nayak AK, Skourski Y, Wosnitza J, Felser C, et al. Pulsed high-magnetic-field experiments: New insights into the magnetocaloric effect in Ni-Mn-In Heusler alloys. J Appl Phys 2015;117:17E710.
[1011] Khovaylo VV, Skokov KP, Gutfleisch O, Miki H, Kainuma R, Kanomata T. Reversibility and irreversibility of magnetocaloric effect in a metamagnetic shape memory alloy under cyclic action of a magnetic field. Appl Phys Lett 2010;97:052503.
[1012] Booth RA, Majetich SA. The magnetocaloric effect in thermally cycled polycrystalline Ni-Mn-Ga. J Appl Phys 2012;111:07A933.
[1013] Kokorin VV, Koledov VV, Shavrov VG, Konoplyuk SM, Thürer S, Troyanovsky DA, et al. Effect of thermal cycling on the martensitic transformation in Ni-Mn-In alloys. J Appl Phys 2014;116:103515.
[1014] Kalbfleisch AS, Matthews G, Jacques PJ. On the influence of the cooling rate on the martensitic transformation of Ni-Mn-Sn Heusler alloys. Scr Mater 2016;114:121–4.
[1015] Ma SC, Shih CW, Liu J, Yuan JH, Lee SY, Lee YI, et al. Wheel speed-dependent martensitic transformation and magnetocaloric effect in Ni-Co-Mn-Sn ferromagnetic shape memory alloy ribbons. Acta Mater 2015;90:292–302.
[1016] Agarwal S, Stern-Taulats E, Manosa L, Mukhopadhyay PK. Effect of low temperature annealing on magneto-caloric effect of Ni-Mn-Sn-Al ferromagnetic shape memory alloy. J Alloys Comp 2015;641:244–8.
[1017] Chen F, Liu WL, Shi YG, Mullner P. Influence of annealing on martensitic transformation and magnetic entropy change in Ni37.7Co12.7Mn40.8Sn8.8 magnetic shape memory alloy ribbon. J Magn Magn Mater 2015;377:137–41.
[1018] Crouïgneau G, Porcar L, Courtois P, Pairis S, Mossang E, Eyraud E, et al. Annealing effect on the magnetic induced austenite transformation in polycrystalline freestanding Ni-Co-Mn-In films produced by co-sputtering. J Appl Phys 2015;117:035302.
[1019] Czaja P, Fitta M, Przewoznik J, Maziarz W, Morgiel J, Czeppe T, et al. Effect of heat treatment on magnetostructural transformations and exchange bias in Heusler Ni48Mn39.5Sn9.5Al3 ribbons. Acta Mater 2016;103:30–45.
[1020] Wang W, Li HW, Ren J, Fu JX, Zhai QJ, Luo ZP, et al. Enhanced magnetocaloric properties in annealed Heusler Ni-Mn-Sn ribbons. J Magn Magn Mater 2015;374:153–6.
[1021] Czaja P, Chulist R, Szczerba MJ, Przewoznik J, Olejnik E, Chrobak A, et al. Magnetostructural transition and magnetocaloric effect in highly textured Ni-Mn-Sn alloy. J Appl Phys 2016;119:165102.
[1022] Li Z, Zhang YL, Xu K, Jing C. Large magnetocaloric effect related to martensitic transformation in Ni50Co2Mn33In15 textured alloy. Physica B 2015;476:179–82.
[1023] Sahoo R, Raj Kumar DM, Babu DA, Suresh KG, Raja MM. In-plane and out of plane magnetic properties in Ni46Co4Mn38Sb12 ribbons. J Appl Phys 2013;113:17A940.
[1024] Giri AK, Paterson BA, McLeod MV, Dennis CL, Majumdar BS, Cho KC, et al. Effect of crystallographic alignment on the magnetocaloric effect in alloys near the Ni2MnGa stoichiometry. J Appl Phys 2013;113:17A907.
[1025] Hernando B, Llamazares JLS, Prida VM, Baldomir D, Serantes D, Ilyn M, et al. Magnetocaloric effect in preferentially textured Mn50Ni40In10 melt spun ribbons. Appl Phys Lett 2009;94:222502.
[1026] McLeod MV, Giri AK, Paterson BA, Dennis CL, Zhou L, Vogel SC, et al. Magnetocaloric response of non-stoichiometric Ni2MnGa alloys and the influence of crystallographic texture. Acta Mater 2015;97:245–56.
[1027] Hernando B, Llamazares JLS, Santos JD, Prida VM, Baldomir D, Serantes D, et al. Magnetocaloric effect in melt spun Ni50.3Mn35.5Sn14.4 ribbons. Appl Phys Lett 2008;92:132507.
[1028] Li ZB, Llamazares JLS, Sanchez-Valdes CF, Zhang YD, Esling C, Zhao X, et al. Microstructure and magnetocaloric effect of melt-spun Ni52Mn26Ga22 ribbon. Appl Phys Lett 2012;100:174102.
[1029] Liu J, Woodcock TG, Scheerbaum N, Gutfleisch O. Influence of annealing on magnetic field-induced structural transformation and magnetocaloric effect in Ni-Mn-In-Co ribbons. Acta Mater 2009;57:4911–20.
[1030] Zhang Y, Zheng Q, Xia WX, Zhang J, Du J, Yan A. Enhanced large magnetic entropy change and adiabatic temperature change of Ni43Mn46Sn11 alloys by a rapid solidification method. Scr Mater 2015;104:41–4.
[1031] Aliev AM, Batdalov AB, Kamilov IK, Koledov VV, Shavrov VG, Buchelnikov VD, et al. Magnetocaloric effect in ribbon samples of Heusler alloys Ni-Mn-M (M=In, Sn). Appl Phys Lett 2010;97:212505.
[1032] Zhao XG, Hsieh CC, Lai JH, Cheng XJ, Chang WC, Cui WB, et al. Effects of annealing on the magnetic entropy change and exchange bias behavior in melt-spun Ni-Mn-In ribbons. Scr Mater 2010;63:250–3.
[1033] Rostamnejadi A, Venkatesan M, Kameli P, Salamati H, Coey JMD. Magnetocaloric effect in La(0.67)Sr(0.33)MnO(3) manganite above room temperature. J Magn Magn Mater 2011;323:2214–8.
[1034] Llamazares JL, Garcia C, Hernando B, Prida VM, Baldomir D, Serantes D, et al. Magnetocaloric properties of as-quenched Ni50.4Mn34.9In14.7 ferromagnetic shape memory alloy ribbons. Appl Phys A-Mater Sci Process 2011;103:1125–30.

[1035] Kumar DMR, Rao NVR, Raja MM, Rao DVS, Srinivas M, Muthu SE, et al. Structure, magneto-structural transitions and magnetocaloric properties in Ni(50-x)Mn(37+x)In(13) melt spun ribbons. J Magn Magn Mater 2012;324:26–32.
[1036] Llamazares JLS, Flores-Zuniga H, Sanchez-Valdes C, Ross CA, Garcia C. Refrigerant capacity of austenite in as-quenched and annealed Ni51.1Mn31.2In17.7 melt spun ribbons. J Appl Phys 2012;111:07A932.
[1037] Caballero-Flores R, Gonzalez-Legarreta L, Rosa WO, Sanchez T, Prida VM, Escoda L, et al. Magnetocaloric effect, magnetostructural and magnetic phase transformations in Ni50.3Mn36.5Sn13.2 Heusler alloy ribbons. J Alloys Comp 2015;629:332–42.
[1038] Czaja P, Przewoznik J, Fitta M, Balanda M, Chrobak A, Kania B, et al. Effect of ball milling and thermal treatment on exchange bias and magnetocaloric properties of Ni48Mn39.5Sn10.5Al2 ribbons. J Magn Magn Mater 2016;401:223–30.
[1039] Dey S, Singh S, Roy RK, Ghosh M, Mitra A, Panda AK. Influence of Mn incorporation for Ni on the magnetocaloric properties of rapidly solidified off-stoichiometric NiMnGa ribbons. J Magn Magn Mater 2016;397:342–6.
[1040] Gonzalez-Legarreta L, Gonzalez-Alonso D, Rosa WO, Caballero-Flores R, Sunol JJ, Gonzalez J, et al. Magnetostructural phase transition in off-stoichiometric Ni-Mn-In Heusler alloy ribbons with low In content. J Magn Magn Mater 2015;383:190–5.
[1041] Li HW, Feng ST, Ren J, Zhai QJ, Fu JX, Luo ZP, et al. Magnetostructural transitions in Mn-rich Heusler Mn-Ni-In melt-spun ribbons with enhanced magnetocaloric effect. J Magn Magn Mater 2015;391:17–21.
[1042] Varzaneh AG, Kameli P, Karimzadeh F, Aslibeiki B, Varvaro G, Salamati H. Magnetocaloric effect in Ni47Mn40Sn13 alloy prepared by mechanical alloying. J Alloys Comp 2014;598:6–10.
[1043] Tang YJ, Solomon VC, Smith DJ, Harper H, Berkowitz AE. Magnetocaloric effect in NiMnGa particles produced by spark erosion. J Appl Phys 2005;97:10M309.
[1044] Singh S, Kushwaha P, Scheibel F, Liermann H-P, Barman SR, Acet M, et al. Residual stress induced stabilization of martensite phase and its effect on the magnetostructural transition in Mn-rich Ni-Mn-In/Ga magnetic shape-memory alloys. Phys Rev B 2015;92:020105.
[1045] Khovaylo VV, Rodionova VV, Shevyrtalov SN, Novosad V. Magnetocaloric effect in "reduced" dimensions: thin films, ribbons, and microwires of Heusler alloys and related compounds. Phys Status Solidi B-Basic Solid State Phys 2014;251:2104–13.
[1046] Varga R, Ryba T, Vargova Z, Saksl K, Zhukova V, Zhukov A. Magnetic and structural properties of Ni-Mn-Ga Heusler-type microwires. Scr Mater 2011;65:703–6.
[1047] Zhang XX, Qian MF, Zhang Z, Wei LS, Geng L, Sun JF. Magnetostructural coupling and magnetocaloric effect in Ni-Mn-Ga-Cu microwires. Appl Phys Lett 2016;108:052401.
[1048] Recarte V, Perez-Landazabal JI, Sanchez-Alarcos V, Chernenko VA, Ohtsuka M. Magnetocaloric effect linked to the martensitic transformation in sputter-deposited Ni-Mn-Ga thin films. Appl Phys Lett 2009;95:141908.
[1049] Niemann R, Schultz L, Fahler S. Growth of sputter-deposited metamagnetic epitaxial Ni-Co-Mn-In films. J Appl Phys 2012;111:093909.
[1050] Akkera HS, Singh I, Kaur D. Martensitic phase transformation of magnetron sputtered nanostructured Ni-Mn-In ferromagnetic shape memory alloy thin films. J Alloys Comp 2015;642:53–62.
[1051] Teichert N, Auge A, Yuzuak E, Dincer I, Elerman Y, Krumme B, et al. Influence of film thickness and composition on the martensitic transformation in epitaxial Ni-Mn-Sn thin films. Acta Mater 2015;86:279–85.
[1052] Akkera HS, Choudhary N, Kaur D. Martensitic phase transformations and magnetocaloric effect in Al co-sputtered Ni-Mn-Sb alloy thin films. Mater Sci Eng B-Adv Funct Solid-State Mater 2015;198:113–9.
[1053] Barman R, Kaur D. Improved magnetocaloric effect in magnetron sputtered Ni-Mn-Sb-Al ferromagnetic shape memory alloy thin films. Vacuum 2015;120:22–6.
[1054] Dutta B, Hickel T, Neugebauer J, Behler C, Fahler S, Behler A, et al. Interplay of strain and interdiffusion in Heusler alloy bilayers. Phys Status Solidi-Rapid Res Lett 2015;9:321–5.
[1055] Teichert N, Kucza D, Yildirim O, Yuzuak E, Dincer I, Behler A, et al. Structure and giant inverse magnetocaloric effect of epitaxial Ni-Co-Mn-Al films. Phys Rev B 2015;91:184405.
[1056] Schleicher B, Niemann R, Diestel A, Hühne R, Schultz L, Fähler S. Epitaxial Ni-Mn-Ga-Co thin films on PMN-PT substrates for multicaloric applications. J Appl Phys 2015;118:053906.
[1057] Fang YK, Yeh CC, Chang CW, Chang WC, Zhu MG, Li W. Large low-field magnetocaloric effect in MnCo0.95Ge1.14 alloy. Scr Mater 2007;57:453–6.
[1058] Zhang E, Chen Y, Tang Y. The magnetic and magnetocaloric effect of (Mn0.5Co0.5)(65)Ge-35 alloy in low magnetic field. J Magn Magn Mater 2008;320:1671–4.
[1059] Wang J-T, Wang D-S, Chen C, Nashima O, Kanomata T, Mizuseki H, et al. Vacancy induced structural and magnetic transition in MnCo[sub 1−x]Ge. Appl Phys Lett 2006;89:262504.
[1060] Fang YK, Yeh JC, Chang WC, Li XM, Li W. Structures, magnetic properties, and magnetocaloric effect in MnCo1-xGe (0.02 <= x <= 0.2) compounds. J Magn Magn Mater 2009;321:3053–6.
[1061] Markin PE, Mushnikov NV. Magnetic Properties and Structural Transitions in (MnCo)(1-x)Ge. In: Perov N, editor. Magnetism and magnetic materials. Stafa-Zurich: Trans Tech Publications Ltd; 2009. p. 489–92.
[1062] Liu EK, Zhu W, Feng L, Chen JL, Wang WH, Wu GH, et al. Vacancy-tuned paramagnetic/ferromagnetic martensitic transformation in Mn-poor Mn1-xCoGe alloys. EPL 2010;91:17003.
[1063] Ma SC, Wang DH, Xuan HC, Shen LJ, Cao QQ, Du YW. Effects of the Mn/Co ratio on the magnetic transition and magnetocaloric properties of Mn(1+x)Co(1-x)Ge alloys. Chin Phys B 2011;20:087502.
[1064] Liu J, Skokov K, Gutfleisch O. Magnetostructural transition and adiabatic temperature change in Mn-Co-Ge magnetic refrigerants. Scr Mater 2012;66:642–5.
[1065] Lin S, Tegus O, Bruck E, Dagula W, Gortenmulder TJ, Buschow KHJ. Structural and magnetic properties of MnFe1-xCoxGe compounds. IEEE Trans Magn 2006;42:3776–8.
[1066] Dincer I, Yuzuak E, Durak G, Elerman Y. The magnetic and magnetocaloric properties of CoMnGe1-xGax alloys. J Alloys Comp 2014;588:332–6.
[1067] Wu RR, Bao LF, Hu FX, Wang J, Zheng XQ, Liu Y, et al. Effect of substitution of In for Co on magnetostructural coupling and magnetocaloric effect in MnCo1-xInxGe compounds. J Appl Phys 2014;115:17A911.
[1068] Zhang CL, Wang DH, Cao QQ, Han ZD, Xuan HC, Du YW. Magnetostructural phase transition and magnetocaloric effect in off-stoichiometric Mn1.9-xNixGe alloys. Appl Phys Lett 2008;93:122505.
[1069] Daniel-Perez G, Llamazares JLS, Quintana-Nedelcos A, Alvarez-Alonso P, Varga R, Chernenko V. Magnetostructural transition and magnetocaloric effect in MnNiGe1.05 melt-spun ribbons. J Appl Phys 2014;115:17A920.
[1070] Zhang CL, Wang DH, Cao QQ, Ma SC, Xuan HC, Du YW. The magnetostructural transformation and magnetocaloric effect in Co-doped MnNiGe1.05 alloys. J Phys D-Appl Phys 2010;43:205003.
[1071] Zhang CL, Chen J, Wang TZ, Xie GX, Zhu C, Wang DH. The magnetic phase transitions and magnetocaloric effect in MnNi(1-x)Co(x)Ge alloys. Solid State Commun 2011;151:1359–62.
[1072] Zhang CL, Wang DH, Chen J, Wang TZ, Xie GX, Zhu C. Magnetic phase transitions and magnetocaloric effect in the Fe-doped MnNiGe alloys. Chin Phys B 2011;20:097501.
[1073] Liu EK, Wang WH, Feng L, Zhu W, Li GJ, Chen JL, et al. Stable magnetostructural coupling with tunable magnetoresponsive effects in hexagonal ferromagnets. Nat Commun 2012;3:873.
[1074] Zhang WG, Tegus O, Wu YL, Yirgeltu, Yan HY, Lin S. Magnetocaloric effect in MnCo1-xAlxGe compounds. J Mater Sci Technol 2009;25:781–4.
[1075] Samanta T, Dubenko I, Quetz A, Temple S, Stadler S, Ali N. Magnetostructural phase transitions and magnetocaloric effects in MnNiGe1-xAlx. Appl Phys Lett 2012;100:052404.
[1076] Meng GH, Tegus O, Zhang WG, Song L, Huang JH. Structural and magnetic properties of MnCo1-xVxGe compounds. J Alloys Comp 2010;497:14–6.

[1077] Ma SC, Zheng YX, Xuan HC, Shen LJ, Cao QQ, Wang DH, et al. Large roomtemperature magnetocaloric effect with negligible magnetic hysteresis losses in Mn(1-x)V(x)CoGe alloys. J Magn Magn Mater 2012;324:135–9.
[1078] Trung NT, Biharie V, Zhang L, Caron L, Buschow KHJ, Bruck E. From single- to double-first-order magnetic phase transition in magnetocaloric Mn1-xCrxCoGe compounds. Appl Phys Lett 2010;96:162507.
[1079] Caron L, Trung NT, Bruck E. Pressure-tuned magnetocaloric effect in Mn(0.93)Cr(0.07)CoGe. Phys Rev B 2011;84:020414.
[1080] Hamer JBA, Daou R, Ozcan S, Mathur ND, Fray DJ, Sandeman KG. Phase diagram and magnetocaloric effect of CoMnGe1-xSnx alloys. J Magn Magn Mater 2009;321:3535–40.
[1081] Sandeman KG, Daou R, Ozcan S, Durrell JH, Mathur ND, Fray DJ. Negative magnetocaloric effect from highly sensitive metamagnetism in CoMnSi1-xGex. Phys Rev B 2006;74:224436.
[1082] Zhang CL, Wang DH, Cao QQ, Han ZD, Xuan HC, Du YW. Large magnetic entropy change and broad working temperature span in CoMnSi0.88Ge0.12 alloy. J Phys D-Appl Phys 2009;42:015007.
[1083] Trung NT, Zhang L, Caron L, Buschow KHJ, Bruck E. Giant magnetocaloric effects by tailoring the phase transitions. Appl Phys Lett 2010;96:172504.
[1084] Ma SC, Hou D, Shih CW, Wang JF, Lee YI, Chang WC, et al. Magnetostructural transformation and magnetocaloric effect in melt-spun and annealed Mni(1-x)Cu(x)CoGe ribbons. J Alloys Comp 2014;610:15–9.
[1085] Ma SC, Liu YH, Shih CW, Lee YI, Chang WC. Microstructure and magnetic properties in melt-spun MnV0.02CoGe0.99 ribbons. J Magn Magn Mater 2014;357:41–4.
[1086] Songlin, Dagula, Tegus O, Bruck E, Klaasse JCP, de Boer FR, et al. Magnetic phase transition and magnetocaloric effect in Mn5-xFexSi3. J Alloys Comp 2002;334:249–52.
[1087] Songlin, Dagula, Tegus O, Bruck E, de Boer FR, Buschow KHJ. Magnetic and magnetocaloric properties of Mn5Ge3-xSbx. J Alloys Comp 2002;337:269–71.
[1088] Tegus O, Bruck E, Zhang L, Dagula, Buschow KHJ, de Boer FR. Magnetic-phase transitions and magnetocaloric effects. Physica B 2002;319:174–92.
[1089] Candini A, Moze O, Kockelmann W, Cadogan JM, Bruck E, Tegus O. Revised magnetic phase diagram for FexMn5-xSi3 intermetallics. J Appl Phys 2004;95:6819–21.
[1090] Wu YL, Tegus O, Zhang WG, Yiriyoltu S, Mend B, Songlin. Magnetocaloric effects in Fe(4)MnSi(3)B(x) interstitial compounds. Acta Metall Sin-Engl Lett 2009;22:397–400.
[1091] Hering P, Friese K, Voigt J, Persson J, Aliouane N, Grzechnik A, et al. Structure, magnetism, and the magnetocaloric effect of MnFe4Si3 Single crystals and powder samples. Chem Mater 2015;27:7128–36.
[1092] Herlitschke M, Klobes B, Sergueev I, Hering P, Peron J, Hermann RP. Elasticity and magnetocaloric effect in MnFe4Si3. Phys Rev B 2016;93:094304.
[1093] Zhang Q, Du J, Li YB, Sun NK, Cui WB, Li D, et al. Magnetic properties and enhanced magnetic refrigeration in (Mn1-xFex)(5)Ge-3 compounds. J Appl Phys 2007;101:123911.
[1094] Zhao FQ, Dagula W, Tegus O, Buschow KHJ. Magnetic-entropy change in Mn5Ge3-xSix alloys. J Alloys Comp 2006;416:43–5.
[1095] Liu XB, Altounian Z. Magnetocaloric effect in Mn5Ge3-xSix pseudobinary compounds. J Appl Phys 2006;99:08Q101.
[1096] Liu XB, Shen BG. Magnetic properties and magnetocaloric effects of Mn5Ge2.7 M-0.3 (M = Ga, Al, Sn) compounds. Acta Phys Sin 2005;54:5884–9.
[1097] Liu XB, Zhang SY, Shen BG. Magnetic properties and magnetocaloric effects of Mn5Ge3-xGax. Chin Phys 2004;13:397–400.
[1098] Tolinski T, Synoradzki K. Specific heat and magnetocaloric effect of the Mn5Ge3 ferromagnet. Intermetallics 2014;47:1–5.
[1099] Zhao FQ, Dagula W, Tegus O, Gortenmulder TJ, Bruck E, Buschow KHJ. Magnetocaloric properties of Mn5Sn3-xGax alloys. IEEE Trans Magn 2005;41:3754–6.
[1100] Zhang P, Hou XL, Hu XH, Xu H, Ni JS, Zhou BX. Crystal structure and curie temperature of (Mn1-xFex)(5)Sn-3 alloy. Rare Metal Mater Eng 2010;39:549–51.
[1101] Kuhrt C, Schittny T, Barner K. Magnetic B-T phase-diagram of anion substituted MNAS - magnetocaloric experiments. Phys Status Solidi A-Appl Res 1985;91:105–13.
[1102] Wada H, Tanabe Y. Giant magnetocaloric effect of MnAs1-xSbx. Appl Phys Lett 2001;79:3302–4.
[1103] Zou JD, Wada H, Shen BG, Sun JR, Li W. Giant magnetocaloric effect and soft-mode magneto-structural phase transition in MnAs. EPL 2008;81:47002.
[1104] Franzen H, Haas C, Jellinek F. Phase transitions between NiAs- and MnP-type phases. Phys Rev B 1974;10:1248–51.
[1105] Morikawa T, Wada H, Kogure R, Hirosawa S. Effect of concentration deviation from stoichiometry on the magnetism of Mn1+delta As0.75Sb0.25. J Magn Magn Mater 2004;283:322–8.
[1106] de Campos A, Mota MA, Gama S, Coelho AA, White BD, da Luz MS, et al. Single crystal growth and characterization of MnAs. J Cryst Growth 2011;333:54–8.
[1107] Marangolo M, Karboul-Trojet W, Prieur JY, Etgens VH, Eddrief M, Becerra L, et al. Surface acoustic wave triggering of giant magnetocaloric effect in MnAs/GaAs devices. Appl Phys Lett 2014;105:162403.
[1108] de Campos A, da Luz MS, de Campos A, Coelho AA, Cardoso LP, dos Santos AO, et al. Investigations in MnAs1-xSbx: experimental validation of a new magnetocaloric composite. J Magn Magn Mater 2015;374:342–4.
[1109] Trassinelli M, Marangolo M, Eddrief M, Etgens VH, Gafton V, Hidki S, et al. Suppression of the thermal hysteresis in magnetocaloric MnAs thin film by highly charged ion bombardment. Appl Phys Lett 2014;104:081906.
[1110] Wada H, Matsuo S, Mitsuda A. Pressure dependence of magnetic entropy change and magnetic transition in MnAs1-xSbx. Phys Rev B 2009;79:092407.
[1111] Wada H, Taniguchi K, Tanabe Y. Extremely large magnetic entropy change of MnAs1-xSbx near room temperature. Mater Trans 2002;43:73–7.
[1112] Wada H, Morikawa T, Taniguchi K, Shibata T, Yamada Y, Akishige Y. Giant magnetocaloric effect of MnAs1-xSbx in the vicinity of first-order magnetic transition. Physica B 2003;328:114–6.
[1113] Morikawa T, Wada H. Effect of deviation from stoichiometry on magnetic and magnetocaloric properties in MnAs1-xSbx. J Magn Magn Mater 2004;272:E583–4.
[1114] Wada H, Funaba C, Asano T. Effects of heat treatment on the magnetic phase transition and magnetocaloric properties of Mn1+delta As1-xSbx. Mater Trans 2006;47:486–91.
[1115] Wada H, Asano T, Ilyn M, Tishin AM. Direct measurements of magnetocaloric effects of Mn1+delta As1-xSbx. J Magn Magn Mater 2007;310:2811–2.
[1116] Kim Y, Wada H, Lee Y, Itoh S. Magnetization, magnetic transition and magnetic entropy changes of bulk MnAs1-xSbx fabricated by underwater shock compaction. Mater Sci Eng B-Adv Funct Solid-State Mater 2010;167:114–8.
[1117] Rocco DL, de Campos A, Carvalho AMG, dos Santos AO, da Silva LM, Gama S, et al. Influence of chemical doping and hydrostatic pressure on the magnetic properties of Mn1-xFexAs magnetocaloric compounds. Phys Rev B 2016;93:054431.
[1118] Cui WB, Liu W, Liu XH, Guo S, Han Z, Zhao XG, et al. Magnetocaloric effects and reduced thermal hysteresis in Si-doped MnAs compounds. J Alloys Comp 2009;479:189–92.
[1119] Cui WB, Lv XK, Yang F, Yu Y, Skomski R, Zhao XG, et al. Interstitial-nitrogen effect on phase transition and magnetocaloric effect in Mn(As, Si) (invited). J Appl Phys 2010;107:09A938.
[1120] Cui WB, Liu W, Zhang Q, Li B, Liu XH, Yang F, et al. Carbon-doping effects on the metamagnetic transition and magnetocaloric effect in MnAsCx. J Magn Magn Mater 2010;322:2223–6.
[1121] Sun NK, Xu SN, Li D, Zhang ZD. Magnetocaloric effect and size-effect related thermal hysteresis reduction in MnAs(1-x)P(x) compounds. Phys Status Solidi A-Appl Mater 2011;208:1950–2.
[1122] Sun NK, Liu F, Gao YB, Cai ZQ, Du BS, Xu SN, et al. Effect of microstrain on the magnetism and magnetocaloric properties of MnAs0.97P0.03. Appl Phys Lett 2012;100:112407.

[1123] Mitsiuk VI, Govor GA, Budzynski M. Phase transitions and magnetocaloric effect in MnAs, MnAs0.99P0.01, and MnAs0.98P0.02 single crystals. Inorg Mater 2013;49:14–7.
[1124] De Campos A, Rocco DL, Carvalho AMG, Caron L, Coelho AA, Gama S, et al. Ambient pressure colossal magnetocaloric effect tuned by composition in Mn1-xFexAs. Nat Mater 2006;5:802–4.
[1125] Balli M, Fruchart D, Gignoux D, Dupuis C, Kedous-Lebouc A, Zach R. Giant magnetocaloric effect in Mn1-x(Ti0.5V0.5)(x)As: experiments and calculations. J Appl Phys 2008;103:103908.
[1126] Cui WB, Liu W, Liu XH, Guo S, Han Z, Zhao XG, et al. Beneficial effect of minor Al substitution on the magnetocaloric effect of Mn1-xAlxAs. Mater Lett 2009;63:595–7.
[1127] Rocco DL, de Campos A, Carvalho AMG, Caron L, Coelho AA, Gama S, et al. Ambient pressure colossal magnetocaloric effect in Mn1-xCuxAs compounds. Appl Phys Lett 2007;90:242507.
[1128] Xu PF, Nie SH, Meng KK, Wang SL, Chen L, Zhao JH. Co doping enhanced giant magnetocaloric effect in Mn1-xCoxAs films epitaxied on GaAs (001). Appl Phys Lett 2010;97:042502.
[1129] Sun NK, Cui WB, Li D, Geng DY, Yang F, Zhang ZD. Giant room-temperature magnetocaloric effect in Mn1-xCrxAs. Appl Phys Lett 2008;92:072504.
[1130] Sun NK, Xu SN, Gao YB, Ji TB, Li YB. Magnetism and magnetocaloric properties of Mn0.95Cr0.05As. Physica B 2011;406:2731–3.
[1131] Dung DD, Tuan DA, Thiet DV, Shin Y, Cho S. Giant magnetocaloric effect of Mn0.92Ba0.08As thin film grown on Al2O3(0001) substrate. J Appl Phys 2012;111:07C310.
[1132] Mejia CS, Gomes AM, Reis MS, Rocco DL. Fe/Cr substitution in MnAs compound: Increase in the relative cooling power. Appl Phys Lett 2011;98:102515.
[1133] Gama S, Coelho AA, de Campos A, Carvalho AMG, Gandra FCG, von Ranke PJ, et al. Pressure-induced colossal magnetocaloric effect in MnAs. Phys Rev Lett 2004;93:237202.
[1134] von Ranke PJ, de Oliveira NA, Mello C, Carvalho AMG, Gama S. Analytical model to understand the colossal magnetocaloric effect. Phys Rev B 2005;71:054410.
[1135] von Ranke PJ, Gama S, Coelho AA, de Campos A, Carvalho AMG, Gandra FCG, et al. Theoretical description of the colossal entropic magnetocaloric effect: Application to MnAs. Phys Rev B 2006;73:014415.
[1136] Plaza EJR, Campoy JCP. Magnetocaloric effect: Overcoming the magnetic limit. J Magn Magn Mater 2009;321:446–9.
[1137] Carvalho AMG, Coelho AA, Gama S, Gandra FCG, von Ranke PJ, de Oliveira NA. Investigation of the first-order metamagnetic transitions and the colossal magnetocaloric effect using a Landau expansion applied to MnAs compound. Eur Phys J B 2009;68:67–72.
[1138] Sharma ALL, Gama S, Coelho AA, de Campos A. Irreversibility in cooling and heating processes in the magnetocaloric MnAs and alloys. Appl Phys Lett 2008;93:261910.
[1139] Alho BP, de Oliveira NA, de Sousa VSR, Gama S, Coelho AA, Carvalho AMG, et al. Theoretical investigation on the magnetocaloric effect in MnAs using a microscopic model to describe the magnetic and thermal hysteresis. Solid State Commun 2012;152:951–4.
[1140] Balli M, Fruchart D, Gignoux D, Zach R. The, ‘‘colossal” magnetocaloric effect in Mn1-xFexAs: What are we really measuring? Appl Phys Lett 2009;95:072509.
[1141] Bratko M, Morrison K, de Campos A, Gama S, Cohen LF, Sandeman KG. History dependence of directly observed magnetocaloric effects in (Mn, Fe)As. Appl Phys Lett 2012;100:252409.
[1142] Niemann R, Heczko O, Schultz L, Fahler S. Inapplicability of the Maxwell relation for the quantification of caloric effects in anisotropic ferroic materials. Int J Refrig-Rev Int Froid 2014;37:281–8.
[1143] Tegus O, Bao LH, Song L. Phase transitions and magnetocaloric effects in intermetallic compounds MnFeX (X=P, As, Si, Ge). Chin Phys B 2013;22:037506.
[1144] Tegus O, Bruck E, Buschow KHJ, de Boer FR. Transition-metal-based magnetic refrigerants for room-temperature applications. Nature 2002;415:150–2.
[1145] Koyama K, Kanomata T, Matsukawa T, Watanabe K. Magnetic field effect on structural property of MnFeP0.5As0.5. Mater Trans 2005;46:1753–6.
[1146] Goraus J, Hawelek L, Wlodarczyk P. The effect of doping on magnetic properties of (Fe-1 (-) Mn-x(x))2P(1) (-) Si-y(y) series. Solid State Commun 2015;224:41–5.
[1147] Gribanov IF, Golovchan AV, Varyukhin DV, Val'kov VI, Kamenev VI, Sivachenko AP, et al. Magnetic and magnetocaloric properties of the alloys Mn2-xFexP0.5As0.5 (0 <= x <= 0.5). Low Temp Phys 2009;35:786–91.
[1148] Budzynski M, Valkov VI, Golovchan AV, Mitsiuk VI, Sivachenko AP, Surowiec Z, et al. Influence of Mn/Fe ratio on the magnetic properties of the Mn2-xFexP0.5As0.5, 0.5 <= x <= 1 alloys. Physica B 2014;452:37–41.
[1149] Hermann RP, Tegus O, Bruck E, Buschow KHJ, de Boer FR, Long GJ, et al. Mossbauer spectral study of the magnetocaloric FeMnP1-xAsx compounds. Phys Rev B 2004;70:214425.
[1150] Szymczak R, Nedelko N, Lewinska S, Zubov E, Sivachenko A, Gribanov I, et al. Comparison of magnetocaloric properties of the Mn2-xFexP0.5As0.5 (x=1.0 and 0.7) compounds. Solid State Sci 2014;36:29–34.
[1151] Dung NH, Zhang L, Ou ZQ, Bruck E. From first-order magneto-elastic to magneto-structural transition in (Mn, Fe)(1.95)P(0.50)Si(0.50) compounds. Appl Phys Lett 2011;99:092511.
[1152] Hudl M, Nordblad P, Bjorkman T, Eriksson O, Haggstrom L, Sahlberg M, et al. Order-disorder induced magnetic structures of FeMnP0.75Si0.25. Phys Rev B 2011;83:134420.
[1153] Geng YX, Tegus O, Bi LG. Magnetocaloric effects in Mn1.35Fe0.65P1-xSix compounds. Chin Phys B 2012;21:037504.
[1154] Tegus O, Bruck E, Li XW, Zhang L, Dagula W, de Boer FR, et al. Tuning of the magneto-caloric effects in MnFe(P, As) by substitution of elements. J Magn Magn Mater 2004;272:2389–90.
[1155] Balli M, Fruchart D, Zach R. Negative and conventional magnetocaloric effects of a MnRhAs single crystal. J Appl Phys 2014;115:203909.
[1156] Li XW, Tegus O, Zhang L, Dagula W, Bruck E, Buschow KHJ, et al. Magnetic properties of MnFeP0.5As0.5-xGex. IEEE Trans Magn 2003;39:3148–50.
[1157] Tegus O, Fuquan B, Dagula W, Zhang L, Bruck E, Si PZ, et al. Magnetic-entropy change in Mn1.1Fe0.9P0.7As0.3-xGex. J Alloys Comp 2005;396:6–9.
[1158] Dagula W, Tegus O, Fuquan B, Zhang L, Si PZ, Zhang M, et al. Magnetic-entropy change in Mn1.1Fe0.9P1-xGex compounds. IEEE Trans Magn 2005;41:2778–80.
[1159] Sougrati MT, Hermann RP, Grandjean F, Long GJ, Bruck E, Tegus O, et al. A structural, magnetic and Mossbauer spectral study of the magnetocaloric Mn1.1Fe0.9P1-xGex compounds. J Phys-Condes Matter 2008;20:475206.
[1160] Ou ZQ, Wang GF, Lin S, Tegus O, Bruck E, Buschow KJ. Magnetic properties and magnetocaloric effects in Mn1.2Fe0.8P1-xGex compounds. J Phys-Condes Matter 2006;18:11577–84.
[1161] Liu DM, Zhang ZL, Zhou SL, Huang QZ, Deng XJ, Yue M, et al. A pathway to optimize the properties of magnetocaloric Mn2-xFexP1-yGey for magnetic refrigeration. J Alloys Comp 2016;666:108–17.
[1162] Liu DM, Yue M, Zhang JX, McQueen TM, Lynn JW, Wang XL, et al. Origin and tuning of the magnetocaloric effect in the magnetic refrigerant Mn1.1Fe0.9(P0.8Ge0.2). Phys Rev B 2009;79:014435.
[1163] Yan A, Muller KH, Schultz L, Gutfleisch O. Magnetic entropy change in melt-spun MnFePGe (invited). J Appl Phys 2006;99:08K903.
[1164] Trung NT, Ou ZQ, Gortenmulder TJ, Tegus O, Buschow KHJ, Bruck E. Tunable thermal hysteresis in MnFe(P, Ge) compounds. Appl Phys Lett 2009;94:102513.
[1165] Yue M, Li ZQ, Wang XL, Liu DM, Zhang JX, Liu XB. Crystal structure and magnetic transition of MnFePGe compound prepared by spark plasma sintering. J Appl Phys 2009;105:07A915.
[1166] Yue M, Xu H, Zhao JL, Xu MF, Liu DM, Zhang JX. Structural, thermal, and magnetic properties of MnFePSiGe compounds prepared by spark plasma sintering method. J Magn Magn Mater 2013;335:114–7.

[1167] Liu LJ, Liu DM, Huang QZ, Zhang TL, Zhang L, Yue M, et al. Neutron diffraction study of the magnetic refrigerant Mn1.1Fe0.9P0.76Ge0.24. Powder Diffr 2010;25:S25–7.
[1168] Yue M, Li ZQ, Xu H, Huang QZ, Liu XB, Liu DM, et al. Effect of annealing on the structure and magnetic properties of Mn1.1Fe0.9P0.8Ge0.2 compound. J Appl Phys 2010;107:09A939.
[1169] Chen X, Repaka DVM, Ramanujan RV. Structural investigation of the crossover in the magnetic transition of Mn-Fe-P-Ge magnetocaloric powders. J Alloys Comp 2016;658:104–9.
[1170] Chen X, Ramanujan RV. The magnetic phase transition in Mn1.1Fe0.9P1−xGex magnetocaloric alloys. J Appl Phys 2015;117:063909.
[1171] Chen X, Ramanujan RV. Large magnetocaloric effect near room temperature in Mn-Fe-P-Ge nanostructured powders. J Alloys Comp 2015;652:393–9.
[1172] Liu DM, Zhang H, Wang SB, Xiao WQ, Zhang ZL, Tian N, et al. The effect of Al doping on the crystal structure and magnetocaloric behavior of Mn1.2Fe0.8P1-xGex compounds. J Alloys Comp 2015;633:120–6.
[1173] Wada H, Nakamura K, Katagiri K, Ohnishi T, Yamashita K, Matsushita A. Tuning the Curie temperature and thermal hysteresis of giant magnetocaloric (MnFe)(2)PX (X = Ge and Si) compounds by the Ru substitution. Jpn J Appl Phys 2014;53:063001.
[1174] Dagula W, Tegus O, Li XW, Song L, Bruck E, Thanh DTC, et al. Magnetic properties and magnetic-entropy change of MnFeP0.5As0.5-xSix(x=0-0.3) compounds. J Appl Phys 2006;99:08Q105.
[1175] Thanh DTC, Brueck E, Trung NT, Klaasse JCP, Buschow KHJ, Ou ZQ, et al. Structure, magnetism, and magnetocaloric properties of MnFeP1-xSix compounds. J Appl Phys 2008;103:07B318.
[1176] Hoglin V, Cedervall J, Andersson MS, Sarkar T, Hudl M, Nordblad P, et al. Phase diagram, structures and magnetism of the FeMnP1-xSix-system. RSC Adv 2015;5:8278–84.
[1177] Hoglin V, Cedervall J, Andersson MS, Sarkar T, Nordblad P, Sahlberg M. Irreversible structure change of the as prepared FeMnP1-xSix-structure on the initial cooling through the curie temperature. J Magn Magn Mater 2015;374:455–8.
[1178] Li GJ, Eriksson O, Johansson B, Vitos L. Thermodynamic-state and kinetic-process dependent dual ferromagnetic states in high-Si content FeMn(PSi) alloys. J Appl Phys 2015;118:213903.
[1179] Neish MJ, Oxley MP, Guo J, Sales BC, Allen LJ, Chisholm MF. Local observation of the site occupancy of Mn in a MnFePSi compound. Phys Rev Lett 2015;114:106101.
[1180] Li G, Li W, Schönecker S, Li X, Delczeg-Czirjak EK, Kvashnin YO, et al. Kinetic arrest induced antiferromagnetic order in hexagonal FeMnP0.75Si0.25 alloy. Appl Phys Lett 2014;105:262405.
[1181] Bartok A, Kustov M, Cohen LF, Pasko A, Zehani K, Bessais L, et al. Study of the first paramagnetic to ferromagnetic transition in as prepared samples of Mn-Fe-P-Si magnetocaloric compounds prepared by different synthesis routes. J Magn Magn Mater 2016;400:333–8.
[1182] Roy P, Uck EB, de Groot RA. Latent heat of the first-order magnetic transition of MnFeSi0.33P0.66. Phys Rev B 2016;93:165101.
[1183] Wada H, Takahara T, Katagiri K, Ohnishi T, Soejima K, Yamashita K. Recent progress of magnetocaloric effect and magnetic refrigerant materials of Mn compounds (invited). J Appl Phys 2015;117:172606.
[1184] Thanh DTC, Bruck E, Tegus O, Klaasse JCP, Gortenmulder TJ, Buschow KHJ. Magnetocaloric effect in MnFe(P, Si, Ge) compounds. J Appl Phys 2006;99:08Q107.
[1185] Zhang L, Moze O, Prokes K, Tegus O, Brucka E. Neutron diffraction study of history dependence in MnFeP0.6Si0.4. J Magn Magn Mater 2005;290:679–81.
[1186] Thanh DTC, Brueck E, Tegus O, Klaasse JCP, Buschow KHJ. Influence of Si and Ge on the magnetic phase transition and magnetocaloric properties of MnFe(P, Si, Ge). J Magn Magn Mater 2007;310:E1012–4.
[1187] Song L, Wang GF, Ou ZQ, Haschaolu O, Tegus O, Bruck E, et al. Magnetic properties and magnetocaloric effect of MnFeP0.5Ge0.5-xSix compounds. J Alloys Comp 2009;474:388–90.
[1188] Tsunekawa M, Imada S, Matsumoto A, Yamasaki A, Suga S, Schmid B, et al. Temperature and magnetic. eld dependence of the soft X-ray magnetic circular dichroism intensity for the Mn-L-3 edge of MnFeP0.78Ge0.22. J Magn Magn Mater 2007;310:E1010–1.
[1189] Takeda Y, Okane T, Ohkochi T, Fujimori S, Saitoh Y, Yamagami H, et al. Electronic states of magnetic refrigerator materials Mn0.9Fe1.1P0.55As0.45 using Soft X-ray magnetic circular dichroism. J Phys: Conference Series 2010;200:012199.
[1190] Liu XB, Altounian Z. A first-principles study on the magnetocaloric compound MnFeP2/3Si1/3. J Appl Phys 2009;105:07A902.
[1191] Wang GF, Zhao ZR, Song L, Tegus O. Peculiar influence of Mn/Fe ratio on the magnetic and magnetocaloric properties of Mn2-xFexP0.6Si0.25Ge0.15 compounds. J Alloys Comp 2013;554:208–13.
[1192] Wang GF, Zhao ZR, Zhang XF, Song L, Tegus O. Analysis of the first-order phase transition of (Mn, Fe)2(P, Si, Ge) using entropy change scaling. J Phys D: Appl Phys 2013;46:295001.
[1193] Wang DM, Song L, Wang YH, Zhang W, Bilige TO. Magnetocaloric effect in MnFeP0.63Ge0.12Si0.25Bx (x=0, 0.01, 0.02, 0.03) compounds. Acta Metall Sin 2011;47:344–8.
[1194] Guillou F, Yibole H, van Dijk NH, Bruck E. Effect of boron substitution on the ferromagnetic transition of MnFe0.95P2/3Si1/3. J Alloys Comp 2015;632:717–22.
[1195] Guillou F, Porcari G, Yibole H, van Dijk N, Bruck E. Taming the first-order transition in giant magnetocaloric materials. Adv Mater 2014;26:2671–5.
[1196] Guillou F, Ollefs K, Wilhelm F, Rogalev A, Yaresko AN, Yibole H, et al. Electronic and magnetic properties of phosphorus across the first-order ferromagnetic transition of (Mn, Fe)(2)(P, Si, B) giant magnetocaloric materials. Phys Rev B 2015;92:224427.
[1197] Yibole H, Guillou F, Caron L, Jiménez E, de Groot FMF, Roy P, et al. Moment evolution across the ferromagnetic phase transition of giant magnetocaloric(Mn, Fe)2(P, Si, B)compounds. Phys Rev B 2015;91:014429.
[1198] Guillou F, Yibole H, Porcari G, Zhang L, van Dijk NH, Brück E. Magnetocaloric effect, cyclability and coefficient of refrigerant performance in the MnFe (P, Si, B) system. J Appl Phys 2014;116:063903.
[1199] Guillou F, Yibole H, van Dijk NH, Zhang L, Hardy V, Bruck E. About the mechanical stability of MnFe(P, Si, B) giant-magnetocaloric materials. J Alloys Comp 2014;617:569–74.
[1200] Roy P, Torun E, de Groot RA. Effect of doping and elastic properties in (Mn, Fe)(2)(Si, P). Phys Rev B 2016;93:094110.
[1201] Thang NV, Miao XF, van Dijk NH, Bruck E. Structural and magnetocaloric properties of (Mn, Fe)(2)(P, Si) materials with added nitrogen. J Alloys Comp 2016;670:123–7.
[1202] Yabuta H, Umeo K, Takabatake T, Chen L, Uwatoko Y. Pressure effects on the first order transition in MnFe(P, As) and MnFe(P, Ge). J Magn Magn Mater 2007;310:1826–8.
[1203] Sun NK, Li D, Xu SN, Wang ZH, Zhang ZD. Room-temperature magnetocaloric effect in (Co0.35Mn0.65)(2)P compound. J Mater Sci Technol 2011;27:382–4.
[1204] Haj-Khlifa S, de Rango P, Fruchart D, Zach R. Crystal and magnetic effects of selected substitutions of Ni for Fe and for Co in the orthorhombic MnFe0.35Co0.65P compound. J Alloys Comp 2015;652:322–30.
[1205] Ma L, Guillou F, Yibole H, Miao XF, Lefering AJE, Rao GH, et al. Structural, magnetic and magnetocaloric properties of (Mn, Co)(2)(Si, P) compounds. J Alloys Comp 2015;625:95–100.
[1206] Yu MH, Lewis LH, Moodenbaugh AR. Large magnetic entropy change in the metallic antiperovskite Mn3GaC. J Appl Phys 2003;93:10128–30.
[1207] Tohei T, Wada H, Kanomata T. Negative magnetocaloric effect at the antiferromagnetic to ferromagnetic transition of Mn3GaC. J Appl Phys 2003;94:1800–2.
[1208] Tong P, Wang B-S, Sun Y-P. Mn-based antiperovskite functional materials: review of research. Chin Phys B 2013;22:067501.
[1209] Kanomata T, Kikuchi M, Kaneko T, Kamishima K, Bartashevich MI, Katori HA, et al. Field-induced magnetic transition of Mn3GaC. Solid State Commun 1997;101:811–4.

[1210] Burriel R, Tocado L, Palacios E, Tohei T, Wada H. Square-shape magnetocaloric effect in Mn3GaC. J Magn Magn Mater 2005;290:715–8.
[1211] Matsumoto A, Tsunekawa M, Suga S, Wada H, Muro T, Nakamura T, et al. Electronic and magnetic states of Mn2.97Co0.03GaC studied by soft X-ray photoemission and magnetic circular dichroism. Jpn J Appl Phys 2008;47:1567–9.
[1212] Yu MH, Lewis LH, Moodenbaugh AR. Assessment of the magnetic entropy change in the metallic antiperovskite Mn3GaC1-delta (delta=0, 0.22). J Magn Magn Mater 2006;299:317–26.
[1213] Cakir O, Acet M. Reversibility in the inverse magnetocaloric effect in Mn3GaC studied by direct adiabatic temperature-change measurements. Appl Phys Lett 2012;100:202404.
[1214] Scheibel F, Gottschall T, Skokov K, Gutfleisch O, Ghorbani-Zavareh M, Skourski Y, et al. Dependence of the inverse magnetocaloric effect on the field-change rate in Mn3GaC and its relationship to the kinetics of the phase transition. J Appl Phys 2015;117:233902.
[1215] Wang BS, Tong P, Sun YP, Zhu XB, Luo X, Li G, et al. Reversible room-temperature magnetocaloric effect with large temperature span in antiperovskite compounds Ga1-xCMn3+x (x=0, 0.06, 0.07, and 0.08). J Appl Phys 2009;105:083907.
[1216] Dias ET, Priolkar KR, Nigam AK. Effect of carbon content on magnetostructural properties of Mn3GaC. J Magn Magn Mater 2014;363:140–4.
[1217] Tohei T, Wada H, Kanomata T. Large magnetocaloric effect of Mn3-xCoxGaC. J Magn Magn Mater 2004;272:E585–6.
[1218] Wang BS, Tong P, Sun YP, Tang W, Li LJ, Zhu XB, et al. Structural, magnetic properties and magnetocaloric effect in Ni-doped antiperovskite compounds GaCMn3-xNix (0 <= x <= 0.10). Physica B 2010;405:2427–30.
[1219] Lewis LH, Yoder D, Moodenbaugh AR, Fischer DA, Yu MH. Magnetism and the defect state in the magnetocaloric antiperovskite Mn3GaC1-delta. J Phys-Condes Matter 2006;18:1677–86.
[1220] Cakir O, Acet M. Adiabatic temperature change around coinciding first and second order magnetic transitions in Mn3Ga(C0.85N0.15). J Magn Magn Mater 2013;344:207–10.
[1221] Cakr O, Acet M, Farle M, Wildes A. Magnetic correlations in the magnetocaloric materials Mn3GaC and Mn3GaC0.85N0.15 studied by neutron polarization analysis and neutron depolarization. J Phys-Condes Matter 2016;28:13LT02.
[1222] Wang BS, Li CC, Lin S, Lin JC, Li LJ, Tong P, et al. Magnetic properties and room-temperature magnetocaloric effect in the doped antipervoskite compounds Ga1-xAlxCMn3 (0 <= x <= 0.15). J Magn Magn Mater 2011;323:2017–22.
[1223] Wang BS, Lin JC, Tong P, Zhang L, Lu WJ, Zhu XB, et al. Structural, magnetic, electrical transport properties, and reversible room-temperature magnetocaloric effect in antipervoskite compound AlCMn3. J Appl Phys 2010;108:093925.
[1224] Shao Q, Lv Q, Yang XZ, Han ZD, Dong SY, Qian B, et al. Low-field magnetocaloric effect in antiperovskite Mn3Ga1-xGexC compounds. J Magn Magn Mater 2015;396:160–5.
[1225] Dias ET, Priolkar KR, Çakir Ö, Acet M, Nigam AK. Effect of composition on magnetocaloric properties of Mn3Ga(1−x)SnxC. J Appl Phys 2015;117:123901.
[1226] Wang BS, Tong P, Sun YP, Luo X, Zhu XB, Li G, et al. Large magnetic entropy change near room temperature in antiperovskite SnCMn3. EPL 2009;85:47004.
[1227] Wang BS, Lu WJ, Lin S, Lin JC, Tong P, Zhao BC, et al. Magnetic/structural diagram, chemical composition-dependent magnetocaloric effect in self-doped antipervoskite compounds Sn(1-x)CMn(3+x) (0 <= x <= 0.40). J Magn Magn Mater 2012;324:773–81.
[1228] Wang BS, Tong P, Sun YP, Tang W, Li LJ, Zhu XB, et al. Magnetism, magnetocaloric effect and positive magnetoresistance in Fe-doped antipervoskite compounds SnCMn3-xFex (x=0.05–0.20). J Magn Magn Mater 2010;322:163–8.
[1229] Yan J, Sun Y, Wang C, Shi ZX, Deng SH, Shi KW, et al. Effects of Co doping on the magnetic properties, entropy change, and magnetocaloric effect in Mn3Sn1-xCoxC1.1 compounds. Acta Phys Sin 2014;63:167502.
[1230] Sun Y, Guo Y-F, Tsujimoto Y, Wang X, Li J, Sathish CI, et al. Thermodynamic, electromagnetic, and lattice properties of antiperovskite Mn3SbN. Adv Condens Matter Phys 2013;286325.
[1231] Yang C, Tong P, Lin JC, Lin S, Cui DP, Wang BS, et al. Large magnetic entropy change associated with the weakly first-order paramagnetic to ferrimagnetic transition in antiperovskite manganese nitride CuNMn3. J Appl Phys 2014;116:033902.
[1232] Annaorazov MP, Asatryan KA, Myalikgulyev G, Nikitin SA, Tishin AM, Tyurin AL. Alloys of the Fe-Rh system as a new class of working material for magnetic refrigerators. Cryogenics 1992;32:867–72.
[1233] Nikitin SA, Myalikgulyev G, Tishin AM, Annaorazov MP, Asatryan KA, Tyurin AL. The magnetocaloric effect in FE49RH51 compound. Phys Lett A 1990;148:363–6.
[1234] Shirane G, Chen C, Flinn P, Nathans R. Mössbauer study of hyperfine fields and isomer shifts in the Fe-Rh alloys. Phys Rev 1963;131:183–90.
[1235] Manekar M, Roy SB. Reproducible room temperature giant magnetocaloric effect in Fe-Rh. J Phys D-Appl Phys 2008;41:192004.
[1236] Annaorazov MP, Nikitin SA, Tyurin AL, Akopyan SA, Myndyev RW. Heat pump cycles based on the AF-F transition in Fe-Rh alloys induced by tensile stress. Int J Refrig-Rev Int Froid 2002;25:1034–42.
[1237] Annaorazov MP. An analysis of the process of adiabatic inducement of the F-AF transition in FeRh by pressure. J Alloys Comp 2003;354:1–5.
[1238] Annaorazov MP, Unal M, Nikitin SA, Tyurin AL, Asatryan KA. Magnetocaloric heat-pump cycles based on the AF-F transition in Fe-Rh alloys. J Magn Magn Mater 2002;251:61–73.
[1239] Chirkova A, Skokov KP, Schultz L, Baranov NV, Gutfleisch O, Woodcock TG. Giant adiabatic temperature change in FeRh alloys evidenced by direct measurements under cyclic conditions. Acta Mater 2016;106:15–21.
[1240] Stern-Taulats E, Gracia-Condal A, Planes A, Lloveras P, Barrio M, Tamarit JL, et al. Reversible adiabatic temperature changes at the magnetocaloric and barocaloric effects in Fe49Rh51. Appl Phys Lett 2015;107:152409.
[1241] Stern-Taulats E, Planes A, Lloveras P, Barrio M, Tamarit J-L, Pramanick S, et al. Barocaloric and magnetocaloric effects inFe49Rh51. Phys Rev B 2014;89:214105.
[1242] Liu Y, Phillips LC, Mattana R, Bibes M, Barthelemy A, Dkhil B. Large reversible caloric effect in FeRh thin films via a dual-stimulus multicaloric cycle. Nat Commun 2016;7:11614.
[1243] Gruner ME, Hoffmann E, Entel P. Instability of the rhodium magnetic moment as the origin of the metamagnetic phase transition in alpha-FeRh. Phys Rev B 2003;67:064415.
[1244] Gruner ME, Entel P. Simulation of the (p, T) phase diagram of the temperature-driven metamagnet alpha-FeRh. Phase Trans 2005;78:209–17.
[1245] Gu RY, Antropov VP. Dominance of the spin-wave contribution to the magnetic phase transition in FeRh. Phys Rev B 2005;72:012403.
[1246] Sandratskii L, Mavropoulos P. Magnetic excitations and femtomagnetism of FeRh: a first-principles study. Phys Rev B 2011;83:174408.
[1247] Annaorazov MP, Nikitin SA, Tyurin AL, Asatryan KA, Dovletov AK. Anomalously high entropy change in FeRh alloy. J Appl Phys 1996;79:1689–95.
[1248] de Vries MA, Loving M, Mihai AP, Lewis LH, Heiman D, Marrows CH. Hall-effect characterization of the metamagnetic transition in FeRh. New J Phys 2013;15:013008.
[1249] Nishimura K, Nakazawa Y, Li L, Mori K. Magnetocaloric effect of Fe(Rh1-xPdx) alloys. Mater Trans 2008;49:1753–6.
[1250] Barua R, Jimenez-Villacorta F, Lewis LH. Towards tailoring the magnetocaloric response in FeRh-based ternary compounds. J Appl Phys 2014;115:17A903.
[1251] Kouvel JS. Unusual nature of the abrupt magnetic transition in FeRh and its pseudobinary variants. J Appl Phys 1966;37:1257–8.
[1252] Lu W, Nam NT, Suzuki T. First-order magnetic phase transition in FeRh-Pt thin films. J Appl Phys 2009;105:07A904.
[1253] Uebayashi K, Yamada H. Structure and magnetism of pseudo-binary ordered alloys Fe(Rh, Pd), Mn(Rh, Pd), (Fe, Mn)Rh and (Fe, Mn)Pd. J Magn Magn Mater 2007;310:1051–2.
[1254] Manekar M, Roy SB. Very large refrigerant capacity at room temperature with reproducible magnetocaloric effect in Fe0.975Ni0.025Rh. J Phys D-Appl Phys 2011;44:242001.
[1255] Caron L, Hudl M, Hoglin V, Dung NH, Gomez CP, Sahlberg M, et al. Magnetocrystalline anisotropy and the magnetocaloric effect in Fe2P. Phys Rev B 2013;88:094440.

[1256] Hudl M, Campanini D, Caron L, Höglin V, Sahlberg M, Nordblad P, et al. Thermodynamics around the first-order ferromagnetic phase transition ofFe2Psingle crystals. Phys Rev B 2014;90:144432.
[1257] Fruchart D, Allab F, Balli M, Gignoux D, Hlil EK, Koumina A, et al. On the magnetocaloric effect in d-metal pnictides. Physica A 2005;358:123–35.
[1258] Gruber C, Bedolla PO, Mohn P. Electronic structure and the magneto-caloric effect. J Phys-Condes Matter 2013;25:436002.
[1259] Wiendlocha B, Tobola J, Kaprzyk S, Zach R, Hlil EK, Fruchart D. Magnetocaloric properties of Fe2-xTxP (T = Ru and Rh) from electronic structure calculations and magnetization measurements. J Phys D-Appl Phys 2008;41:205007.
[1260] Zach R, Toboła J, Średniawa B, Kaprzyk S, Casado C, Bacmann M, et al. Magneto-elastic properties and electronic structure analysis of the (Fe1−xNix)2P system. J Alloys Comp 2004;383:322–7.
[1261] Balli M, Fruchart D, Gignoux D, Tobola J, Hlil EK, Wolfers P, et al. Magnetocaloric effect in ternary metal phosphides (Fe1-xNix)(2)P. J Magn Magn Mater 2007;316:358–60.
[1262] Delczeg-Czirjak EK, Gercsi Z, Bergqvist L, Eriksson O, Szunyogh L, Nordblad P, et al. Magnetic exchange interactions in B-, Si-, and As-doped Fe2P from first-principles theory. Phys Rev B 2012;85:224435.
[1263] Florez JM, Vargas P, Garcia C, Ross CA. Magnetic entropy change plateau in a geometrically frustrated layered system: FeCrAs-like iron-pnictide structure as a magnetocaloric prototype. J Phys Condens Matter 2013;25:226004.
[1264] Desautels RD, Shueh C, Lin KW, Freeland JW, van Lierop J. Dynamical freezing, magnetic ordering, and the magnetocaloric effect in nanostructured Fe/Cu thin films. Appl Phys Lett 2016;108:172410.
[1265] Rong CB, Liu JP. Temperature- and magnetic-field-induced phase transitions in Fe-rich FePt alloys. Appl Phys Lett 2007;90:222504.
[1266] Recarte V, Gomez-Polo C, Sanchez-Alarcos V, Perez-Landazabal JI. Magnetic study of the martensitic transformation in a Fe-Pd alloy. J Magn Magn Mater 2007;316:E614–7.
[1267] Sanchez-Alarcos V, Recarte V, Perez-Landazabal JI, Gonzalez MA, Rodriguez-Velamazan JA. Effect of Mn addition on the structural and magnetic properties of Fe-Pd ferromagnetic shape memory alloys. Acta Mater 2009;57:4224–32.
[1268] Prida VM, Franco V, Vega V, Sanchez-Llamazares JL, Sunol JJ, Conde A, et al. Magnetocaloric effect in melt-spun FePd ribbon alloy with second order phase transition. J Alloys Comp 2011;509:190–4.
[1269] Ipus JJ, Ucar H, McHenry ME. Near room temperature magnetocaloric response of an (FeNi)ZrB alloy. IEEE Trans Magn 2011;47:2494–7.
[1270] Ucar H, Ipus JJ, Laughlin DE, McHenry ME. Tuning the Curie temperature in gamma-FeNi nanoparticles for magnetocaloric applications by controlling the oxidation kinetics. J Appl Phys 2013;113:17A918.
[1271] Ucar H, Craven M, Laughlin DE, McHenry ME. Effect of Mo addition on structure and magnetocaloric effect in gamma-FeNi nanocrystals. J Electron Mater 2014;43:137–41.
[1272] Chaudhary V, Ramanujan RV. Magnetic and structural properties of high relative cooling power (Fe70Ni30)(92)Mn-8 magnetocaloric nanoparticles. J Phys D-Appl Phys 2015;48:305003.
[1273] Chaudhary V, Repaka DVM, Chaturvedi A, Sridhar I, Ramanujan RV. Magnetocaloric properties and critical behavior of high relative cooling power FeNiB nanoparticles. J Appl Phys 2014;116:163918.
[1274] Chaudhary V, Ramanujan RV. High relative cooling power in a multiphase magnetocaloric Fe-Ni-B alloy. IEEE Magn Lett 2015;6:6700104.
[1275] Mandal S, Panda J, Nath TK. Investigation of the critical behaviour and magnetocaloric effect in gamma-Fe49Ni29Cr22 disordered austenitic stainless steel alloy by using the field dependence of magnetic entropy change. J Alloys Comp 2015;653:453–9.
[1276] Lucas MS, Belyea D, Bauer C, Bryant N, Michel E, Turgut Z, et al. Thermomagnetic analysis of FeCoCrxNi alloys: magnetic entropy of high-entropy alloys. J Appl Phys 2013;113:17A923.
[1277] Zhong X, Tian H, Tang P, Liu Z, Zheng Z, Zeng D. Structure, magnetic properties and magnetocaloric effects of Fe50Mn15-x Co (x) Ni-35 alloys. Sci China-Phys Mech Astron 2014;57:437–41.
[1278] Belyea DD, Lucas MS, Michel E, Horwath J, Miller CW. Tunable magnetocaloric effect in transition metal alloys. Sci Rep 2015;5:15755.
[1279] Tan X, Chai P, Thompson CM, Shatruk M. Magnetocaloric effect in AlFe2B2: toward magnetic refrigerants from earth-abundant elements. J Am Chem Soc 2013;135:9553–7.
[1280] Cedervall J, Andersson MS, Sarkar T, Delczeg-Czirjak EK, Bergqvist L, Hansen TC, et al. Magnetic structure of the magnetocaloric compound AlFe2B2. J Alloys Comp 2016;664:784–91.
[1281] Lewis LH, Barua R, Lejeune B. Developing magnetofunctionality: coupled structural and magnetic phase transition in AlFe2B2. J Alloys Comp 2015;650:482–8.
[1282] Chai P, Stoian SA, Tan X, Dube PA, Shatruk M. Investigation of magnetic properties and electronic structure of layered-structure borides AlT2B2 (T=Fe, Mn, Cr) and AlFe2-xMnxB2. J Solid State Chem 2015;224:52–61.
[1283] Du Q, Chen G, Yang W, Wei J, Hua M, Du H, et al. Magnetic frustration and magnetocaloric effect in AlFe2-xMnxB2 (x=0-0.5) ribbons. J Phys D-Appl Phys 2015;48:335001.
[1284] Kaeswurm B, Friemert K, Guersoy M, Skokov KP, Gutfleisch O. Direct measurement of the magnetocaloric effect in cementite. J Magn Magn Mater 2016;410:105–8.
[1285] Zhao FQ, Tegus O, Fuquan B, Bruck E. Magnetic properties of Fe(3(1-x))Cr(3x)C alloys. Int J Miner Metall Mater 2009;16:314–6.
[1286] Zhang L, Bruck E, Tegus O, Buschow KHJ, de Boer FR. The crystallographic phases and magnetic properties of Fe2MnSi1-xGex. Physica B 2003;328:295–301.
[1287] Mazet T, Ihou-Mouko H, Malaman B. Mn3Sn2: a promising material for magnetic refrigeration. Appl Phys Lett 2006;89:022503.
[1288] Recour Q, Mazet T, Malaman B. Magnetocaloric properties of Mn(3)Sn(2) from heat capacity measurements. J Appl Phys 2009;105:033905.
[1289] Ma SC, Hou D, Gong YY, Wang LY, Huang YL, Zhong ZC, et al. Giant magnetocaloric and magnetoresistance effects in ferrimagnetic Mn1.9Co0.1Sb alloy. Appl Phys Lett 2014;104:022410.
[1290] Li SD, Liu MM, Huang ZG, Xu F, Zou WQ, Zhang FM, et al. CoMnSb: a magnetocaloric material with a large low-field magnetic entropy change at intermediate temperature. J Appl Phys 2006;99:063901.
[1291] Li SD, Yuan ZR, Lu LY, Liu MM, Huang ZG, Zhang FM, et al. Effect of annealing on the magnetic entropy change of CoMnSb alloy. Mater Sci Eng A-Struct Mater Prop Microstruct Process 2006;428:332–5.
[1292] Li SD, Liu MM, Yuan ZR, Lu LY, Zhang ZC, Lin YB, et al. Effect of Nb addition on the magnetic properties and magnetocaloric effect of CoMnSb alloy. J Alloys Comp 2007;427:15–7.
[1293] Tekgul A, Cakir O, Acet M, Farle M, Unal N. The structural, magnetic, and magnetocaloric properties of In-doped Mn2-xCrxSb. J Appl Phys 2015;118:153903.
[1294] Xie ZG, Geng DY, Zhang ZD. Reversible room-temperature magnetocaloric effect in Mn[sub 5]PB[sub 2]. Appl Phys Lett 2010;97:202504.
[1295] Du J, Cui WB, Zhang Q, Ma S, Xiong DK, Zhang ZD. Giant magnetocaloric effect in epsilon-(Mn0.83Fe0.17)(3.25)Ge antiferromagnet. Appl Phys Lett 2007;90:042510.
[1296] Mamiya H, Terada N, Furubayashi T, Suzuki HS, Kitazawa H. Influence of random substitution on magnetocaloric effect in a spinel ferrite. J Magn Magn Mater 2010;322:1561–4.
[1297] Anwar MS, Ahmed F, Koo BH. Enhanced relative cooling power of Ni1-xZnxFe2O4 (0.0 <= x <= 0.7) ferrites. Acta Mater 2014;71:100–7.
[1298] Gass J, Srikanth H, Kislov N, Srinivasan SS, Emirov Y. Magnetization and magnetocaloric effect in ball-milled zinc ferrite powder. J Appl Phys 2008;103:07B309.
[1299] Gopalan EV, Al-Omari IA, Kumar DS, Yoshida Y, Joy PA, Anantharaman MR. Inverse magnetocaloric effect in sol-gel derived nanosized cobalt ferrite. Appl Phys A-Mater Sci Process 2010;99:497–503.
[1300] Luo X, Sun YP, Hu L, Wang BS, Lu WJ, Zhu XB, et al. Observation of the large magnetocaloric effect in an orbital-spin-coupled system MnV(2)O(4). J Phys-Condes Matter 2009;21:436010.

[1301] Luo X, Sun YP, Lu WJ, Zhu XB, Yang ZR, Song WH. Observation of the large orbital entropy in Zn-doped orbital-spin-coupled system MnV2O4. Appl Phys Lett 2010;96:211903.
[1302] Luo X, Lu WJ, Huang ZH, Hu XB, Hu L, Zhu XB, et al. Large reversible magnetocaloric effect in spinel MnV2O4 with minimal Al substitution. J Magn Magn Mater 2012;324:766–9.
[1303] Fu YK, Luo X, Huang ZH, Hu L, Lu WJ, Zhao BC, et al. Critical behavior of spinel vanadate MnV1.95Al0.05O4. J Magn Magn Mater 2013;326:205–9.
[1304] Huang ZH, Luo X, Hu L, Tan SG, Liu Y, Yuan B, et al. Observation of the large magnetocaloric effect and suppression of orbital entropy change in Fe-doped MnV2O4. J Appl Phys 2014;115:034903.
[1305] Yan LQ, Shen J, Li YX, Wang FW, Jiang ZW, Hu FX, et al. Large magnetocaloric effect in spinel CdCr2S4. Appl Phys Lett 2007;90:262502.
[1306] Zhang L, Li L, Li RW, Fan JY, Ling LS, Tong W, et al. Spin-lattice coupling studied by magnetic entropy and EPR in the CdCr2S4 system. Solid State Commun 2010;150:2109–13.
[1307] Shen J, Yan LQ, Zhang J, Wang FW, Sun JR, Hu FX, et al. Magnetic properties and magnetic entropy change in spinels (Cd, M)Cr(2)S(4) with M=Cu or Fe. J Appl Phys 2008;103:07B315.
[1308] Zhang L, Fan JY, Tong W, Ling LS, Pi L, Zhang YH. Scaling of the magnetic entropy change in spinel selenide CuCr2Se4. Physica B 2012;407:3543–6.
[1309] Li RW, Zhang CJ, Zhang YH. Study of magnetic entropy and ESR in ferromagnet CuCr2Te4. J Magn Magn Mater 2012;324:3133–7.
[1310] Bebenin NG, Zainullina RI, Sukhorukov YP. Magnetocaloric effect and inhomogeneity of CdCr2Se4 and HgCr2Se4 single crystals. J Magn Magn Mater 2015;387:127–30.
[1311] Zhang XY, Chen YJ, Lu LY, Li ZY. A potential oxide for magnetic refrigeration application: CrO2 particles. J Phys-Condes Matter 2006;18:L559–66.
[1312] Jiang T, Xie L, Yao YP, Liu YK, Li XG. Large magnetocaloric effect in CrO2/TiO2 epitaxial films above room temperature. Mater Lett 2012;76:25–7.
[1313] Ren W, Li B, Liang W, Jin C, Zhang Z. Tunable magnetic transition and reversible magnetocaloric effects at room temperature in transition-metal-oxyfluorides CrO2-xFx. J Alloys Comp 2014;596:69–72.
[1314] Zhong W, Au C-T, Du Y-W. Review of magnetocaloric effect in perovskite-type oxides. Chin Phys B 2013;22:057501.
[1315] Zhong W, Tang NJ, Wu XL, Liu W, Chen W, Jiang HY, et al. Magnetocaloric effect above room temperature in the ordered double-perovskite Ba2Fe1+xMo1-xO6. J Magn Magn Mater 2004;282:151–5.
[1316] Zhong W, Wu XL, Tang NJ, Liu W, Chen W, Au CT, et al. Magnetocaloric effect in ordered double-perovskite Ba2FeMoO6 synthesized using wet chemistry. Eur Phys J B 2004;41:213–7.
[1317] El-Hagary M. Effect of partial substitution of Cr3+ for Fe3+ on magnetism, magnetocaloric effect and transport properties of Ba2FeMoO6 double perovskites. J Alloys Comp 2010;502:376–81.
[1318] Alvarez-Serrano I, Arillo MA, Lopez ML, Veiga ML, Pico C. Tunable ferrites as environmentally friendly materials for energy-efficient processes. Adv Mater 2011;23:5237–42.
[1319] Kurniawan M, Perrin A, Xu P, Keylin V, McHenry M. Curie temperature engineering in high entropy alloys for magnetocaloric applications. IEEE Magn Lett 2016;7:6105005.
[1320] Pedro SS, Tedesco JCG, Yokaichiya F, Brandao P, Gomes AM, Landsgesell S, et al. Cs2NaAl1-xCrxF6: a family of compounds presenting magnetocaloric effect. Phys Rev B 2014;90:064407.
[1321] Alisultanov ZZ, Paixão LS, Reis MS. Oscillating magnetocaloric effect of a multilayer graphene. Appl Phys Lett 2014;105:232406.
[1322] Reis MS. Oscillating magnetocaloric effect. Appl Phys Lett 2011;99:052511.
[1323] Reis MS. Magnetocaloric cycle with six stages: Possible application of graphene at low temperature. Appl Phys Lett 2015;107:102401.
[1324] Caballero-Flores R, Franco V, Conde A, Knipling KE, Willard MA. Optimization of the refrigerant capacity in multiphase magnetocaloric materials. Appl Phys Lett 2011;98:102505.
[1325] Paticopoulos SC, Caballero-Flores R, Franco V, Blazquez JS, Conde A, Knipling KE, et al. Enhancement of the magnetocaloric effect in composites: experimental validation. Solid State Commun 2012;152:1590–4.
[1326] Luo Q, Wang WH. Rare earth based bulk metallic glasses. J Non-Cryst Solids 2009;355:759–75.
[1327] Wang WH. Bulk metallic glasses with functional physical properties. Adv Mater 2009;21:4524–44.
[1328] Zhang JL, Zheng ZG, Cao WH, Shek CH. Magnetic behavior of Gd4Co3 metallic glass. J Magn Magn Mater 2013;326:157–61.
[1329] Zheng ZG, Zhong XC, Liu ZW, Zeng DC, Franco V, Zhang JL. Magnetocaloric effect and critical behavior of amorphous (Gd4Co3)(1-x)Si-x alloys. J Magn Magn Mater 2013;343:184–8.
[1330] Zhong XC, Gao BB, Liu ZW, Zheng ZG, Zeng DC. Amorphous and crystallized (Gd4Co3)(100-x)B-x alloys for magnetic refrigerants working in the vicinity of 200 K. J Alloys Comp 2013;553:152–6.
[1331] Zheng ZG, Zhong XC, Yu HY, Franco V, Liu ZW, Zeng DC. The magnetocaloric effect and critical behavior in amorphous Gd60Co40-xMnx alloys. J Appl Phys 2012;111:07A922.
[1332] Foldeaki M, Giguere A, Gopal BR, Chahine R, Bose TK, Liu XY, et al. Composition dependence of magnetic properties in amorphous rare-earth-metal-based alloys. J Magn Magn Mater 1997;174:295–308.
[1333] Fang YK, Chen HC, Hsieh CC, Chang HW, Zhao XG, Chang WC, et al. Structures and magnetocaloric effects of Gd65-xRExFe20Al15 (x=0-20; RE=Tb, Dy, Ho, and Er) ribbons. J Appl Phys 2011;109:07A933.
[1334] Zheng ZG, Zhong XC, Su KP, Yu HY, Liu ZW, Zeng DC. Magnetic properties and large magnetocaloric effects in amorphous Gd-Al-Fe alloys for magnetic refrigeration. Sci China-Phys Mech Astron 2011;54:1267–70.
[1335] Zhao XG, Lai JH, Hsieh CC, Fang YK, Chang WC, Zhang ZD. The influence of Si addition on the glass forming ability, magnetic and magnetocaloric properties of the Gd-Fe-Al glassy ribbons. J Appl Phys 2011;109:07A911.
[1336] Min JX, Zhong XC, Liu ZW, Zheng ZG, Zeng DC. Magnetic properties and magnetocaloric effects of Gd-Mn-Si ribbons in amorphous and crystalline states. J Alloys Comp 2014;606:50–4.
[1337] de Paula VG, da Silva LM, dos Santos AO, Lang R, Otubo L, Coelho AA, et al. Magnetocaloric effect and evidence of superparamagnetism in GdAl2 nanocrystallites: a magnetic-structural correlation. Phys Rev B 2016;93:094427.
[1338] Phan TL, Zhang YD, Dan NH, Thang DD, Thanh TD, Zhang P, et al. Ferromagnetic order in rapidly cooled Nd-Fe-Co-Al alloy ribbons. IEEE Trans Magn 2013;49:3375–8.
[1339] Zhang H, Li R, Zhang L, Zhang T. Tunable magnetic and magnetocaloric properties in heavy rare-earth based metallic glasses through the substitution of similar elements. J Appl Phys 2014;115:133903.
[1340] Xia L, Tang MB, Chan KC, Dong YD. Large magnetic entropy change and adiabatic temperature rise of a Gd55Al20Co20Ni5 bulk metallic glass. J Appl Phys 2014;115:223904.
[1341] Liu GL, Zhao DQ, Bai HY, Wang WH, Pan MX. Room temperature table-like magnetocaloric effect in amorphous Gd50Co45Fe5 ribbon. J Phys D-Appl Phys 2016;49:055004.
[1342] Chevalier B, Bobet JL, Marcos JS, Fernandez JR, Sal JCG. Magnetocaloric properties of amorphous GdNiAl obtained by mechanical grinding. Appl Phys A-Mater Sci Process 2005;80:601–6.
[1343] Si L, Ding J, Li Y, Yao B, Tan H. Magnetic properties and magnetic entropy change of amorphous and crystalline GdNiAl ribbons. Appl Phys A-Mater Sci Process 2002;75:535–9.
[1344] Shen H, Wang H, Liu J, Xing D, Qin F, Cao F, et al. Enhanced magnetocaloric and mechanical properties of melt-extracted Gd55Al25Co20 micro-fibers. J Alloys Comp 2014;603:167–71.
[1345] Biswas A, Yu YY, Bingham NS, Wang H, Qin FX, Sun JF, et al. Impact of structural disorder on the magnetic ordering and magnetocaloric response of amorphous Gd-based microwires. J Appl Phys 2014;115:17A318.
[1346] Costa SS, Roriz OAV, de O Silvano N, von Ranke PJ, Nobrega EP. Theoretical investigation on the magnetocaloric effect in amorphous Eu80Au20 system. J Magn Magn Mater 2016;414:78–81.

[1347] von Ranke PJ, Nobrega EP, Caldas A, Alho BP, Ribeiro PO, Alvarenga TST, et al. Theoretical investigations on magnetic entropy change in amorphous and crystalline systems: applications to RAg (R=Tb, Dy, Ho) and GdCuAl. J Magn Magn Mater 2014;369:34–9.
[1348] von Ranke PJ, Nobrega EP, Caldas A, Alho BP, Ribeiro PO, Alvarenga TST, et al. Calculations of the magnetic entropy change in amorphous through a microscopic anisotropic model: applications to Dy70Zr30 and DyCo3.4 alloys. J Appl Phys 2014;116:143903.
[1349] McHenry ME, Willard MA, Laughlin DE. Amorphous and nanocrystalline materials for applications as soft magnets. Progr Mater Sci 1999;44:291–433.
[1350] Franco V, Conde A. Magnetic refrigerants with continuous phase transitions: amorphous and nanostructured materials. Scr Mater 2012;67:594–9.
[1351] Blázquez JS, Ipus JJ, Moreno-Ramírez LM, Borrego JM, Lozano-Pérez S, Franco V, et al. Analysis of the magnetocaloric effect in powder samples obtained by ball milling. Metall Mater Trans E 2015;2:131–8.
[1352] Maeda H, Sato M, Uehara M. Fe-Zr amorphous-alloys for magnetic refrigerants near room-temperature. J Jpn Inst Met 1983;47:688–91.
[1353] Belova VM, Stolyarov VL. Temperature-dependence of magnetocaloric effect in amorphous ferromagnets. Fiz Tverd Tela 1984;26:851–3.
[1354] Franco V, Borrego JM, Conde A, Roth S. Influence of Co addition on the magnetocaloric effect of FeCoSiAlGaPCB amorphous alloys. Appl Phys Lett 2006;88:132509.
[1355] Shen TD, Schwarz RB, Coulter JY, Thompson JD. Magnetocaloric effect in bulk amorphous Pd40Ni22.5Fe17.5P20 alloy. J Appl Phys 2002;91:5240–5.
[1356] Podmiljsak B, Kim JH, McGuiness PJ, Kobe S. Influence of Ni on the magnetocaloric effect in Nanoperm-type soft-magnetic amorphous alloys. J Alloys Comp 2014;591:29–33.
[1357] Shao YZ, Lai JKL, Shek CH. Preparation of nanocomposite working substances for room-temperature magnetic refrigeration. J Magn Magn Mater 1996;163:103–8.
[1358] Ipus JJ, Blazquez JS, Lozano-Perez S, Conde A. Microstructural evolution characterization of Fe-Nb-B ternary systems processed by ball milling. Philos Mag 2009;89:1415–23.
[1359] Ipus JJ, Blazquez JS, Franco V, Conde A. Influence of Co addition on the magnetic properties and magnetocaloric effect of Nanoperm (Fe(1-x)Co(x))(75)Nb(10)B(15) type alloys prepared by mechanical alloying. J Alloys Comp 2010;496:7–12.
[1360] Blazquez JS, Franco V, Conde A. Enhancement of the magnetic refrigerant capacity in partially amorphous Fe70Zr30 powders obtained by mechanical alloying. Intermetallics 2012;26:52–6.
[1361] Ipus JJ, Blazquez JS, Franco V, Stoica M, Conde A. Milling effects on magnetic properties of melt spun Fe-Nb-B alloy. J Appl Phys 2014;115:17B518.
[1362] Moreno LM, Blazquez JS, Ipus JJ, Borrego JM, Franco V, Conde A. Magnetocaloric effect of Co62Nb6Zr2B30 amorphous alloys obtained by mechanical alloying or rapid quenching. J Appl Phys 2014;115:17A302.
[1363] Moreno-Ramirez LM, Ipus JJ, Franco V, Blazquez JS, Conde A. Analysis of magnetocaloric effect of ball milled amorphous alloys: demagnetizing factor and Curie temperature distribution. J Alloys Comp 2015;622:606–9.
[1364] Ipus JJ, Borrego JM, Blazquez JS, Stoica M, Franco V, Conde A. Influence of hot compaction on microstructure and magnetic properties of mechanically alloyed Fe(Co)-based amorphous compositions. J Alloys Comp 2015;653:546–51.
[1365] Ipus JJ, Moreno-Ramirez LM, Blazquez JS, Franco V, Conde A. A procedure to extract the magnetocaloric parameters of the single phases from experimental data of a multiphase system. Appl Phys Lett 2014;105:172405.
[1366] Franco V, Blazquez JS, Conde CF, Conde A. A Finemet-type alloy as a low-cost candidate for high-temperature magnetic refrigeration. Appl Phys Lett 2006;88:042505.
[1367] Swierczek J. Nanocrystallization and magnetocaloric effect in amorphous Fe-Mo-Cu-B alloy. J Alloys Comp 2014;615:255–62.
[1368] Thanveer T, Ramanujan RV, Thomas S. Magnetocaloric effect in amorphous and partially crystallized Fe40Ni38Mo4B18 alloys. AIP Adv 2016;6:055322.
[1369] Luo Q, Ye F, Huang C, Jiao J, Rahman A, Yu P, et al. Size-dependent structure and magnetocaloric properties of Fe-based glass-forming alloy powders. AIP Adv 2016;6:045002.
[1370] Moubah R, Boutahar A, Lassri H, Dinia A, Colis S, Hjorvarsson B, et al. Enhanced magnetocaloric properties of FeZr amorphous films by C ion implantation. Mater Lett 2016;175:5–8.
[1371] Alvarez P, Llamazares JLS, Gorria P, Blanco JA. Enhanced refrigerant capacity and magnetic entropy flattening using a two-amorphous FeZrB(Cu) composite. Appl Phys Lett 2011;99:232501.
[1372] Tian HC, Zhong XC, Liu ZW, Zheng ZG, Min JX. Achieving table-like magnetocaloric effect and large refrigerant capacity around room temperature in Fe78-xCexSi4Nb5B12Cu1 (x=0-10) composite materials. Mater Lett 2015;138:64–6.
[1373] Lai JW, Zheng ZG, Zhong XC, Franco V, Montemayor R, Liu ZW, et al. Table-like magnetocaloric effect of Fe88-xNdxCr8B4 composite materials. J Magn Magn Mater 2015;390:87–90.
[1374] Chau N, The ND, Hoa NQ, Huu CX, Tho ND, Yu SC. The discovery of the colossal magnetocaloric effect in a series of amorphous ribbons based on Finemet. Mater Sci Eng A-Struct Mater Prop Microstruct Process 2007;449:360–3.
[1375] Hoa NQ, Chau N, Yu SC, Thang TM, The ND, Tho ND. The crystallization and properties of alloys with Fe partly substituted by Cr and Cu fully substituted by Au in Finemet. Mater Sci Eng A-Struct Mater Prop Microstruct Process 2007;449:364–7.
[1376] Hoa NQ, Gam DTH, Chau N, The ND, Yu SC. The crystallization, magnetic and magnetocaloric properties in Fe76.5-xNbxSi15.5B7Au1 ribbons. J Magn Magn Mater 2007;310:2483–5.
[1377] Huu CX, Chau N, The ND, Hoa NQ. Giant magnetocaloric effect at room temperature and low-field change in Fe78-xCrxSi4Nb5B12Cu1 amorphous alloys. J Korean Phys Soc 2008;53:763–5.
[1378] Duong THG, Hai NH, Vu LV, Luong NH, Chau N. The existence of large magnetocaloric effect at low field variation and the anti-corrosion ability of Fe-rich alloy with Cr substituted for Fe. In: VanHieu N, editor. Apctp-Asean workshop on advanced materials science and nanotechnology. p. 012067.
[1379] Min SG, Ligay LG, Kim KS, Yu SC, Tho ND, Chau N. The substitution effect of Cr about large magnetocaloric effect in amorphous Fe-Si-B-Nb-Au ribbons. J Magn Magn Mater 2006;300:E385–7.
[1380] Moreno-Ramirez LM, Blazquez JS, Franco V, Conde A, Marsilius M, Budinsky V, et al. Magnetocaloric response of amorphous and nanocrystalline Cr-containing Vitroperm-type alloys. J Magn Magn Mater 2016;409:56–61.
[1381] Franco V, Gutfleisch O. Magnetic materials for energy applications. JOM 2012;64:750–1.
[1382] Liu J. Optimizing and fabricating magnetocaloric materials. Chin Phys B 2014;23:047503.
[1383] Smaili A, Chahine R. Composite materials for Ericsson-like magnetic refrigeration cycle. J Appl Phys 1997;81:824–9.
[1384] de Oliveira IG, von Ranke PJ, Nobrega EP. Understanding the table-like magnetocaloric effect. J Magn Magn Mater 2003;261:112–7.
[1385] Hashimoto T, Kuzuhara T, Sahashi M, Inomata K, Tomokiyo A, Yayama H. New application of complex magnetic-materials to the magnetic refrigerant in an ericsson magnetic refrigerator. J Appl Phys 1987;62:3873–8.
[1386] Engelbrecht K, Bahl CRH, Nielsen KK. Experimental results for a magnetic refrigerator using three different types of magnetocaloric material regenerators. Int J Refrig-Rev Int Froid 2011;34:1132–40.
[1387] Yan A, Muller KH, Gutfleisch O. Structure and magnetic entropy change of melt-spun LaFe11.57Si1.43 ribbons. J Appl Phys 2005;97:036102.
[1388] Liu J, Zhang PN, Dai FP, Yan AR. A new approach to prepare spherical La-Fe-Si-Co magnetocaloric refrigerant particles. Scr Mater 2013;69:485–8.
[1389] Katter M, Zellmann V, Reppel GW, Uestuener K. Magnetocaloric properties of La(Fe Co, Si)(13) bulk material prepared by powder metallurgy. IEEE Trans Magn 2008;44:3044–7.
[1390] Lowe K, Liu J, Skokov K, Moore JD, Sepehri-Amin H, Hono K, et al. The effect of the thermal decomposition reaction on the mechanical and magnetocaloric properties of La(Fe, Si, Co)(13). Acta Mater 2012;60:4268–76.
[1391] Franco V, Pirota KR, Prida VM, Neto A, Conde A, Knobel M, et al. Tailoring of magnetocaloric response in nanostructured materials: role of anisotropy. Phys Rev B 2008;77:104434.

[1392] Baldomir D, Rivas J, Serantes D, Pereiro M, Arias JE, Bujan-Nunez MC, et al. Magnetocaloric effects in magnetic nanoparticle systems: a Monte Carlo study. J Non-Cryst Solids 2007;353:790–2.
[1393] Skomski R, Binek C, Mukherjee T, Sahoo S, Sellmyer DJ. Temperature- and field-induced entropy changes in nanomagnets. J Appl Phys 2008;103:07B329.
[1394] Serantes D, Baldomir D, Pereiro M, Hernando B, Prida VM, Llamazares JLS, et al. Magnetocaloric effect in dipolar chains of magnetic nanoparticles with collinear anisotropy axes. Phys Rev B 2009;80:134421.
[1395] Alvarez P, Sanchez-Marcos J, Llamazares JLS, Franco V, Reiffers M, Blanco JA, et al. Magnetocaloric effect in nanostructured Pr2Fe17 and Nd2Fe17 synthesized by high-energy ball-milling. Acta Phys Pol A 2010;118:867–9.
[1396] Belova VM, Nikolaev VI, Stuchebn Vm. Magnetocaloric effect in superparamagnetic substances. Zhurnal Eksperimentalnoi Teor Fiz 1973;64:1746–9.
[1397] Bennett LH, McMichael RD, Swartzendruber LJ, Shull RD, Watson RE. Monte-Carlo and mean-field calculations of the magnetocaloric effect of ferromagnetically interacting clusters. J Magn Magn Mater 1992;104:1094–5.
[1398] Franco V, Kiss LF, Kemeny T, Vincze I, Conde CF, Conde A. High-temperature evolution of coercivity in nanocrystalline alloys. Phys Rev B 2002;66:224418.
[1399] McMichael RD, Shull RD, Swartzendruber LJ, Bennett LH, Watson RE. Magnetocaloric effect in superparamagnets. J Magn Magn Mater 1992;111:29–33.
[1400] Skorvanek I, Kovac J, Marcin J, Svec P, Janickovic D. Magnetocaloric effect in amorphous and nanocrystalline Fe81-xCrxNb7B12 (x=0 and 3.5) alloys. Mater Sci Eng A-Struct Mater Prop Microstruct Process 2007;449:460–3.
[1401] Shen HX, Xing DW, Llamazares JLS, Sanchez-Valdes CF, Belliveau H, Wang H, et al. Enhanced refrigerant capacity in Gd-Al-Co microwires with a biphase nanocrystalline/amorphous structure. Appl Phys Lett 2016;108:092403.
[1402] Thanh TD, YiKyung Y, Ho TA, Manh TV, Phan TL, Tartakovsky DM, et al. Critical behavior in double-exchange ferromagnets of $Pr_{0.6}Sr_{0.4}MnO_3$ nanoparticles. IEEE Trans Magn 2015;51:2501004.
[1403] Turcaud JA, Bez HN, Ruiz-Trejo E, Bahl CRH, Nielsen KK, Smith A, et al. Influence of manganite powder grain size and Ag-particle coating on the magnetocaloric effect and the active magnetic regenerator performance. Acta Mater 2015;97:413–8.
[1404] Wang ZM, Ni G, Che YL. Magnetocaloric effect in perovskite manganite La0.65Nd0.05Ba0.3MnO3 with double metal-insulator peaks. J Supercond Nov Magn 2012;25:533–9.
[1405] Keshri S, Biswas S, Wisniewski P. Studies on characteristic properties of superparamagnetic La0.67Sr0.33-xKxMnO3 nanoparticles. J Alloys Comp 2016;656:245–52.
[1406] Fatnassi D, Rehspringer JL, Hlil EK, Niznansky D, Ellouze M, Elhalouani F. Structural and magnetic properties of nanosized La0.8Ca0.2Mn1-xFexO3 particles (0 <= x <= 0.2) prepared by sol-gel method. J Supercond Nov Magn 2015;28:2401–8.
[1407] Gharsallah H, Bejar M, Dhahri E, Hlil EK, Sajieddine M. Effect of the annealing temperature on the structural and magnetic behaviors of 0.875La(0.6)Ca(0.4)MnO(3)/0.125La(0.6)Sr(0.4)MnO(3) composition. J Magn Magn Mater 2016;401:56–62.
[1408] Shinde KP, Oh SS, Baik SK, Kim HS, Sinha BB, Chung KC. Glycine-assisted combustion synthesis and magnetocaloric properties of polycrystalline La0.8Ca0.2MnO3. J Korean Phys Soc 2012;61:2000–4.
[1409] Poddar P, Gass J, Rebar DJ, Srinath S, Srikanth H, Morrison SA, et al. Magnetocaloric effect in ferrite nanoparticles. J Magn Magn Mater 2006;307:227–31.
[1410] Li J, Ma S, Wang H, Gong WJ, Jiang JJ, Li SJ, et al. Enhanced cryogenic magnetocaloric effect induced by small size GdNi5 nanoparticles. J Mater Sci Technol 2014;30:973–8.
[1411] Phong PT, Manh DH, Hoan LC, Ngai TV, Phuc NX, Lee IJ. Particle size effects on La0.7Ca0.3MnO3: Griffiths phase-like behavior and magnetocaloric study. J Alloys Comp 2016;662:557–65.
[1412] Hueso LE, Sande P, Miguens DR, Rivas J, Rivadulla F, Lopez-Quintela MA. Tuning of the magnetocaloric effect in La0.67Ca0.33MnO3-delta nanoparticles synthesized by sol-gel techniques. J Appl Phys 2002;91:9943–7.
[1413] Poddar P, Srinath S, Gass J, Prasad BLV, Srikanth H. Magnetic transition and large magnetocaloric effect associated with surface spin disorder in Co and CocoreAgshell nanoparticles. J Phys Chem C 2007;111:14060–6.
[1414] Franco V, Conde A, Sidhaye D, Prasad BLV, Poddar P, Srinath S, et al. Field dependence of the magnetocaloric effect in core-shell nanoparticles. J Appl Phys 2010;107:09A902.
[1415] Zeleňáková A, Hrubovčák P, Kapusta O, Zeleňák V, Franco V. Large magnetocaloric effect in fine Gd2O3 nanoparticles embedded in porous silica matrix. Appl Phys Lett 2016;109:122412.
[1416] Wang XQ, Yang SY, Wang CF, Chen L, Chen S. Multifunctional hydrogels with temperature, ion, and magnetocaloric stimuli-responsive performances. Macromol Rapid Commun 2016;37:759–68.
[1417] Yuzuak E, Dincer I, Elerman Y, Auge A, Teichert N, Hutten A. Inverse magnetocaloric effect of epitaxial Ni-Mn-Sn thin films. Appl Phys Lett 2013;103:222403.
[1418] Caballero-Flores R, Franco V, Conde A, Kiss LF, Peter L, Bakonyi I. Magnetic multilayers as a way to increase the magnetic field responsiveness of magnetocaloric materials. J Nanosci Nanotechnol 2012;12:7432–6.
[1419] Wang DH, Zhang CL, Xuan HC, Han ZD, Zhang JR, Tang SL, et al. The study of low-field positive and negative magnetic entropy changes in Ni43Mn46-xCuxSn11 alloys. J Appl Phys 2007;102:013909.
[1420] Barati MR, Selomulya C, Sandeman KG, Suzuki K. Extraordinary induction heating effect near the first order Curie transition. Appl Phys Lett 2014;105:162412.
[1421] Xuan HC, Zhang YQ, Li H, Han PD, Wang DH, Du YW. Enhancement of the martensitic transformation and magnetocaloric effect of Ni-Mn-V-Sn ribbons by annealing treatment. Phys Status Solidi A-Appl Mater 2015;212:1954–60.
[1422] Belov KP, Cherniko La, Nikitin SA, Tikhonov VV, Talalaev Ev, Kudryavt Tv, et al. Determination of exchange interaction of sublattices in gadolinium iron-garnet on basis of magnetocaloric effect. Soviet Physics Jetp-Ussr 1972;34:588–90.
[1423] Belov KP, Talalayeva EV, Chernikova LA, Ivanova TI, Ivanovsky VI, Kazakov GV. Observation of spin reorientation based on measurements of magnetocaloric effect. Zhurnal Eksperimentalnoi Teor Fiz 1977;72:586–91.
[1424] Franco V, Conde A, Provenzano V, Shull RD. Scaling analysis of the magnetocaloric effect in Gd5Si2Ge1.9X0.1 (X=Al, Cu, Ga, Mn, Fe, Co). J Magn Magn Mater 2010;322:218–23.
[1425] Kouvel JS, Fisher ME. Detailed magnetic behavior of nickel near its curie point. Phys Rev a-Gen Phys 1964;136:1626.
[1426] Sanchez-Perez M, Moreno-Ramirez LM, Franco V, Conde A, Marsilius M, Herzer G. Influence of nanocrystallization on the magnetocaloric properties of Ni-based amorphous alloys: determination of critical exponents in multiphase systems. J Alloys Comp 2016;686:717–22.
[1427] Franco V, Conde CF, Blazquez JS, Conde A, Svec P, Janickovic D, et al. A constant magnetocaloric response in FeMoCuB amorphous alloys with different Fe/B ratios. J Appl Phys 2007;101:093903.
[1428] Smith A, Nielsen KK, Bahl CRH. Scaling and universality in magnetocaloric materials. Phys Rev B 2014;90:104422.
[1429] Romero-Muñiz C, Tamura R, Tanaka S, Franco V. Applicability of scaling behavior and power laws in the analysis of the magnetocaloric effect in second-order phase transition materials. Phys Rev B 2016;94:134401.
[1430] Alvarez P, Gorria P, Llamazares JLS, Perez MJ, Franco V, Reiffers M, et al. Magneto-caloric effect in the pseudo-binary intermetallic YPrFe17 compound. Mater Chem Phys 2011;131:18–22.
[1431] Zhong XC, Min JX, Zheng ZG, Liu ZW, Zeng DC. Critical behavior and magnetocaloric effect of Gd65Mn35-xGex (x=0, 5, and 10) melt-spun ribbons. J Appl Phys 2012;112:033903.
[1432] Debnath JC, Shamba P, Strydom AM, Wang JL, Dou SX. Investigation of the critical behavior in Mn0.94Nb0.06CoGe alloy by using the field dependence of magnetic entropy change. J Appl Phys 2013;113:093902.

[1433] Pelka R, Konieczny P, Fitta M, Czapla M, Zielinski PM, Balanda M, et al. Magnetic systems at criticality: different signatures of scaling. Acta Phys Pol A 2013;124:977–89.
[1434] Mahjoub S, Baazaoui M, M'Nassri R, Boudjada NC, Oumezzine M. Critical behavior and the universal curve for magnetocaloric effect in Pr0.6Ca0.1Sr0.3Mn1-xFexO3 (x=0, 0.05 and 0.075) manganites. J Alloys Comp 2015;633:207–15.
[1435] Li RW, Kumar P, Mahendiran R. Critical behavior in polycrystalline La0.7Sr0.3CoO3 from bulk magnetization study. J Alloys Comp 2016;659:203–9.
[1436] Sattibabu B, Bhatnagar AK, Vinod K, Rayaprol S, Mani A, Siruguri V, et al. Studies on the magnetoelastic and magnetocaloric properties of Yb1-xMgxMnO3 using neutron diffraction and magnetization measurements. RSC Adv 2016;6:48636–43.
[1437] Han H, Zhang L, Zhu XD, Du HF, Ge M, Ling LS, et al. Critical phenomenon in the itinerant ferromagnet Cr11Ge19 studied by scaling of the magnetic entropy change. J Alloys Comp 2017;693:389–93.
[1438] Franco V, Caballero-Flores R, Conde A, Dong QY, Zhang HW. The influence of a minority magnetic phase on the field dependence of the magnetocaloric effect. J Magn Magn Mater 2009;321:1115–20.
[1439] Law JY, Franco V, Ramanujan RV. The magnetocaloric effect of partially crystalline Fe-B-Cr-Gd alloys. J Appl Phys 2012;111:113919.
[1440] Romero-Muniz C, Ipus JJ, Blazquez JS, Franco V, Conde A. Influence of the demagnetizing factor on the magnetocaloric effect: critical scaling and numerical simulations. Appl Phys Lett 2014;104:252405.
[1441] Banerjee BK. On a generalised approach to first and second order magnetic transitions. Phys Lett 1964;12:16–7.
[1442] Ge M, Zhang L, Menzel D, Han H, Jin CM, Zhang CJ, et al. Scaling investigation of the magnetic entropy change in helimagnet MnSi. J Alloys Comp 2015;649:46–9.
[1443] Collins SC, Zimmerman FJ. Cyclic adiabatic demagnetization. Phys Rev 1953;90:991–2.
[1444] Rosenblum SS, Sheinberg H, Steyert WA. Continuous refrigeration at 10 mK using adiabatic demagnetization. Cryogenics 1976;16:245.
[1445] Pratt Jr WP, Rosenblum SS, Steyert WA, Barclay JA. A continuous demagnetization refrigerator operating near 2 K and a study of magnetic refrigerants. Cryogenics 1977;17:689.
[1446] Steyert WA. Rotating carnot-cycle magnetic refrigerators for use near 2K. J Appl Phys 1978;49:1227–31.
[1447] Barclay JA, Moze O, Paterson L. Reciprocating magnetic refrigerator for 2-4-K operation - initial results. J Appl Phys 1979;50:5870–7.
[1448] Barclay JA. A 4-K to 20-K rotational-cooling magnetic refrigerator capable of 1 mW to greater-than 1 W operation. Cryogenics 1980;20:467–71.
[1449] Delpuech C, Beranger R, Mardion GB, Claudet G, Lacaze AA. Double acting reciprocating magnetic refrigerator - 1st experiments. Cryogenics 1981;21:579–84.
[1450] Numazawa T, Hashimoto T, Tanji N, Horigami O. The helium magnetic refrigerator. II - Liquefaction process and efficiency. Adv Cryogenics Eng 1984;29:589–96.
[1451] Mastumoto K, Ito T, Hashimoto T. An ericsson magnetic refrigerator for low temperature. Adv Cryogenics Eng 1988;33:743–50.
[1452] Nakagome H, Yasuda S. Magnetic refrigerator. Tokyo Shibaura Denki Kabushiki Kaisha; 1985.
[1453] Hakuraku Y, Ogata H. A static magnetic refrigerator for superfluid-helium with new heat switches and a superconducting pulse coil. Jpn J Appl Phys Part 1 - Regul Pap Short Notes Rev Pap 1985;24:1538–47.
[1454] Barclay JA, Stewart WF, Overton WC, Candler RJ, Harkleroad OD. Experimental results on a low-temperature magnetic refrigerator. Adv Cryogenics Eng 1986;31:743–52.
[1455] Hakuraku Y, Ogata H. A rotary magnetic refrigerator for superfluid-helium production. J Appl Phys 1986;60:3266–8.
[1456] Hakuraku Y, Ogata H. A magnetic refrigerator for superfluid-helium equipped with a rotating superconducting magnet system. Jpn J Appl Phys Part 1 - Regul Pap Short Notes Rev Pap 1986;25:140–6.
[1457] Taussig CP, Gallagher GR, Smith Jr JL, Iwasa Y. Magnetic refrigeration based on magnetically active. In: Proceedings of the fourth international cryocoolers conference.
[1458] Nakagome H, Kuriyama T, Ogiwara H, Fujita T, Yazawa T, Hashimoto T. Reciprocating magnetic refrigerator for helium liquefaction. Adv Cryogenics Eng 1986;31:753–62.
[1459] Nakagome H, Takahashi M, Ogiwara H. A parasitic magnetic refrigerator for cooling superconducting magnet. IEEE Trans Magn 1988;24:1113–6.
[1460] Kuz'min MD, Tishin AM. Magnetic refrigerants for the 4.2-20 K region: garnets or perovskites? J Phys D: Appl Phys 1991;24:2039–44.
[1461] Filin NV, Mihailov II, Dovbish AL, Ronjin PL, Keilin VE, Kovalev IA. Development and study of magnetic refrigerators of the static type. IEEE Trans Magn 1992;28:953–6.
[1462] DeGregoria AJ, Feuling LJ, Laatsch JF, Rowe JR, Trueblood JR. Modeling the active magnetic regenerator. Adv Cryogenics Eng 1992;37:867–73.
[1463] Bezaguet A, Casascubillos J, Lebrun P, Losserandmadoux R, Marquet M, Schmidtricker M, et al. Design and construction of a static magnetic refrigerator operating between 1.8-K and 4.5-K. Cryogenics 1994;34:227–30.
[1464] Jeong S, Smith JL, Iwasa Y. Tandem magnetic refrigerator for 1.8-K. Cryogenics 1994;34:263–9.
[1465] Zimm CB, Jastrab AG, Johnson JW. Design of active magnetic regenerative stage interfacing to a g-m cryocooler. New York: Plenum Press Div Plenum Publishing Corp; 1995.
[1466] Kashani A, Helvensteijn BPM, McCormack FJ, Spivak AL. Performance of a magnetic refrigerator operating between 2 K and 10 K. New York: Plenum Press Div Plenum Publishing Corp; 1996.
[1467] Kashani A, Helvenstein BPM, McCormack FJ, Spivak AL, Kittel P. Development of a magnetic refrigerator operating between 2 K and 10 K. Cryocoolers 1995;8:637–46.
[1468] Satoh T, Onishi A, Li R, Asami H, Kanazawa Y. Development of 1.5W 4K G-M cryocooler with magnetic regenerator material. New York: Plenum Press Div Plenum Publishing Corp; 1996.
[1469] Zimm CB, Johnson JW, Murphy RW. Test results on a 50K magnetic refrigerator. New York: Plenum Press Div Plenum Publishing Corp; 1996.
[1470] Ohira K, Matsuo S, Furumoto H. The characteristics of magnetic refrigeration operating at the temperature of 20 K. In: Proceedings of 16th International Cryogenic Engineering Conference/International Cryogenic Materials Conference.
[1471] Hall JL, Barclay JA. Analyzing magnetic refrigeration efficiency: a rotary AMR - Reverse Brayton case study. In: Kittel P, editor. Advances in cryogenic engineering, vol. 43 Pts a and B. New York: Plenum Press Div Plenum Publishing Corp; 1998. p. 1719–28.
[1472] Yayama H, Hatta Y, Makimoto Y, Tomokiyo A. Hybrid cryogenic refrigerator: combination of brayton magnetic-cooling and Gifford-McMahon gas-cooling system. Jpn J Appl Phys 2000;39:4220–4.
[1473] Hepburn I, Emes M, Worth LBC, Feger D. Cooling system for ultra low temperature cryogenic detector cameras. In: Smith RMAR, editor. Passive millimeter-wave imaging technology V. Bellingham: Spie-Int Soc Optical Engineering; 2001. p. 72–81.
[1474] Kamiya K, Numazawa T, Matsumoto K, Nozawa H, Yanagitani T. Design and build of magnetic refrigerator for hydrogen liquefaction. In: Weisend JG, Barclay J, Breon S, Demko J, DiPirro M, Kelley JP, et al., editors. Advances in cryogenic engineering, vol. 51A and B. Melville: Amer Inst Physics; 2006. p. 591–7.
[1475] Numazawa T, Kamiya K, Yoshioka S, Nakagome H, Matsumoto K. Development of a magnetic refirgerator for hydrogen liquefaction. In: Jgbjbsdjdmkjpkpkaljptpjr Weisend, editor. Advances in cryogenic engineering, vol. 53a and 53b. Melville: Amer Inst Physics; 2008. p. 1183–9.
[1476] Matsumoto K, Kondo T, Yoshioka S, Kamiya K, Numazawa T. Magnetic refrigerator for hydrogen liquefaction. In: Kes PJR, editor. 25th International conference on low temperature physics. Bristol: Iop Publishing Ltd; 2009. p. 012028.
[1477] Numazawa T, Kamiya K, Utaki T, Matsumoto K. Magnetic refrigerator for hydrogen liquefaction. Progr Supercond Cryogen 2013;15:1–8.
[1478] Kim Y, Park I, Jeong S. Experimental investigation of two-stage active magnetic regenerative refrigerator operating between 77 K and 20 K. Cryogenics 2013;57:113–21.
[1479] Brown GV. Magnetic heat pumping. The United States Of America As Represented By The United States National Aeronautics And Space Administration; 1978.
[1480] Steyert WA. High temperature refrigerator. The United States Of America As Represented By The United States Department Of Energy; 1978.

[1481] Kirol LD, Dacus MW. Rotary recuperative magnetic heat pump. In: Cryogenic engineering conference.
[1482] Green G, Chafe J, Stevens J, Humphrey J. A Gadolinium-Terbium Active Regenerator. Adv Cryogenics Eng 1990;35:1165–74.
[1483] Zimm C, Jastrab A, Sternberg A, Pecharsky V, Gschneidner K, Osborne M, et al. Description and performance of a near-room temperature magnetic refrigerator. In: Kittel P, editor. Advances in cryogenic engineering, vol. 43 Pts a and B. New York: Plenum Press Div Plenum Publishing Corp; 1998. p. 1759–66.
[1484] Lawton LM, Zimm CB, Jastrab AG. Reciprocating active magnetic regenerator refrigeration apparatus. Astronautics Corporation Of America; 1999.
[1485] Bohigas X, Molins E, Roig A, Tejada J, Zhang XX. Room-temperature magnetic refrigerator using permanent magnets. IEEE Trans Magn 2000;36:538–44.
[1486] Hirano N, Nagaya S, Takahashi M, Kuriyama T, Ito K, Nomura S. Development of magnetic refrigerator for room temperature application. In: Adams M, DiPirro M, Breon S, Glaister D, Hull JR, Kittel P, Pecharsky V, Radebaugh R, Theilacker J, Van Sciver S, Weisend II JG, Zeller A, editors. AIP Conference Proceedings, Advances in cryogenic engineering, vol. 47, Pts a and B. Melville: Amer Inst Physics; 2002. p. 1027–34.
[1487] Rowe AM, Barclay JA. Design of an active magnetic regenerator test apparatus. In: Adams M, DiPirro M, Breon S, Glaister D, Hull JR, Kittel P, Pecharsky V, Radebaugh R, Theilacker J, Van Sciver S, Weisend II JG, Zeller A, editors. AIP Conference Proceedings, Advances in cryogenic engineering, vol 47, Pts a and B. Melville: Amer Inst Physics; 2002. p. 995–1002.
[1488] Zimm CB, Sternberg A, Jastrab AG, Boeder AM, Lawton LM, Chell JJ. Rotating bed magnetic refrigeration apparatus. Astronautics Corporation Of America; 2003.
[1489] Zimm C, Boeder A, Chell J, Sternberg A, Fujita A, Fujieda S, et al. Design and performance of a permanent magnet rotary refrigerator. In: Egolf PW, editor. 1st International conference on magnetic refrigeration at room temperature. Paris: Int Inst Refrigeration; 2005. p. 367–73.
[1490] Zimm C, Boeder A, Chell J, Sternberg A, Fujita A, Fujieda S, et al. Design and performance of a permanent-magnet rotary refrigerator. Int J Refrig-Rev Int Froid 2006;29:1302–6.
[1491] Blumenfeld PE, Prenger FC, Sternberg A, Zimm C. High temperature superconducting magnetic refrigeration. In: Adams M, DiPirro M, Breon S, Glaister D, Hull JR, Kittel P, Pecharsky V, Radebaugh R, Theilacker J, Van Sciver S, Weisend II JG, Zeller A, editors. AIP Conference Proceedings, Advances in cryogenic engineering, vol. 47, Pts a and B. Melville: Amer Inst Physics; 2002. p. 1019–26.
[1492] Lu DW, Xu XN, Wu HB, Jin X. A permanent magnet magneto-refrigerator study on using Gd/Gd-Si-Ge/Gd-Si-Ge-Ga alloys. In: Egolf PW, editor. 1st International conference on magnetic refrigeration at room temperature. Paris: Int Inst Refrigeration; 2005. p. 291–6.
[1493] Okamura T, Yamada K, Hirano N, Nagaya S. Performance of a room-temperature rotary magnetic refrigerator. Int J Refrig-Rev Int Froid 2006;29:1327–31.
[1494] Clot P, Viallet D, Allab F, Kedous-Lebouc A, Fournier JM, Yonnet JP. A magnet-based device for active magnetic regenerative refrigeration. IEEE Trans Magn 2003;39:3349–51.
[1495] Allab F, Kedous-Lebouc A, Yonnet JP, Fournier JM. A magnetic field source system for magnetic refrigeration and its interaction with magnetocaloric material. In: Egolf PW, editor. 1st International conference on magnetic refrigeration at room temperature. Paris: Int Inst Refrigeration; 2005. p. 309–17.
[1496] Richard MA, Rowe AM, Chahine R. Magnetic refrigeration: single and multimaterial active magnetic regenerator experiments. J Appl Phys 2004;95:2146–50.
[1497] Rowe A, Tura A. Experimental investigation of a three-material layered active magnetic regenerator. Int J Refrig-Rev Int Froid 2006;29:1286–93.
[1498] Shir F, Bennett LH, Della Torre E, Mavriplis C, Shull RD. Transient response in magnetocaloric regeneration. IEEE Trans Magn 2005;41:2129–33.
[1499] Vasile C, Muller C. Innovative design of a magnetocaloric system. Int J Refrig-Rev Int Froid 2006;29:1318–26.
[1500] Yu BF, Gao Q, Wang CF, Zhang B, Yang DX, Zhang Y. Experimental investigation on refrigeration performance of a reciprocating active magnetic regenerator of room temperature magnetic refrigeration. In: Egolf PW, editor. 1st International conference on magnetic refrigeration at room temperature. Paris: Int Inst Refrigeration; 2005. p. 375–91.
[1501] Gao Q, Yu BF, Wang CF, Zhang B, Yang DX, Zhang Y. Experimental investigation on refrigeration performance of a reciprocating active magnetic regenerator of room temperature magnetic refrigeration. Int J Refrig-Rev Int Froid 2006;29:1274–85.
[1502] Kawanami T, Chiba K, Ikegawa M, Sakurai K. Optimization of a magnetic refrigerator at room temperature for air cooling systems. In: Egolf PW, editor. 1st International conference on magnetic refrigeration at room temperature. Paris: Int Inst Refrigeration; 2005. p. 275–82.
[1503] Kim S, Bethala B, Ghirlanda S, Sambandam SN, Bhansali S. ASME. Design and fabrication of a magnetocaloric microcooler. micro-electro-mechanical systems - 2005. New York: Amer Soc Mechanical Engineers; 2005. p. 763–7.
[1504] Yao GH, Gong MQ, Wu JF. Experimental study on the performance of a room temperature magnetic refrigerator using permanent magnets. Int J Refrig-Rev Int Froid 2006;29:1267–73.
[1505] Hirano N, Nagaya S, Okamura T, Kawanami T, Wada H. Development o room temperature magnetic refrigerator-overall plan. In: Proceedings of the second international conference on magnetic refrigeration at room temperature.
[1506] Okamura T, Rachi R, Hirano N, Nagaya NT. Improvement o 100 W class room temperature magnetic refrigerator. In: Proceedings of the second international conference on magnetic refrigeration at room temperature.
[1507] Egolf PW, Kitanovski A, Sari O, Derrick AC, Gendre F. Magnetic refrigerator and/or heat pump using magnetocaloric fluid and process for magnetic heating and/or cooling with such a refrigerator and/or heat pump. Haute Ecole D'ingenierie Et De Gestion Du Canton De Vaud (Heig-Vd); 2006.
[1508] Huang JH, Liu JR, Jin PY, Yan HW, Qiu JF, Xu LZ, et al. Development of permanent magnetic refrigerator at room temperature. Rare Metals 2006;25:641–4.
[1509] Huang JH, Song L, Jin PY, Yan HW, Wang Y, Tegus O, et al. Research on the magneto-caloric effect in LaFe11.17-XCo0.78Si1.05BX alloys. In: Proceedings of the second international conference on magnetic refrigeration at room temperature.
[1510] Zimm C, Auringer J, Boeder A, Chells J, Russek S, Sternberg A. Design and initial performance of a magnetic refrigerator with a rotating permanent magnet. In: Proceedings of the second international conference on magnetic refrigeration at room temperature.
[1511] Tura A, Rowe A. Design and testing of a permanent magnet magnetic refrigerator. In: Proceedings of the second international conference on magnetic refrigeration at room temperature.
[1512] Buchelnikov VD, Taskaev SV, Bychkov IV, Chernets IA, Denisovskiy AN. The prototype of effective device for magnetic refrigeration. In: Proceedings of the second international conference on magnetic refrigeration at room temperature.
[1513] Chen YG, Tang YB, Wang BM, Xue XQ, Tu MJ. A permanent magnet rotary magnetic refrigerator. In: Proceedings of the second international conference on magnetic refrigeration at room temperature.
[1514] Petersen TF, Pryds N, Smith A, Bahl CRH. A numerical analysis of a reciprocating active magnetic regenerator with a parallel-plate regenerator geometry. In: Proceedings of the second international conference on magnetic refrigeration at room temperature.
[1515] Muller C, Bour L, Vacile C. Study of a efficiency of a magnetothermal system according to the permeability of the magnetocaloric material around its Curie temperature. In: Proceedings of the second international conference on magnetic refrigeration at room temperature.
[1516] Nakamura K, Kawanami T, Hirano S, Ikegawa M, Fumoto K. Improvement of room temperature magnetic refrigerator using air as heat transfer fluid. New York: IEEE; 2008.
[1517] Bahl CRH, Petersen TF, Pryds N, Smith A. A versatile magnetic refrigeration test device. Rev Sci Instrum 2008;79:093906.
[1518] Hirano S, Kawanami T, Nakamura K, Fumoto K, Ikegawa M, Hirasawa S. A development of spherical-shaped magnetocaloric materials using power coating method. In: Proceedings of the third international conference on magnetic refrigeration at room temperature.
[1519] Zheng ZG, Yu HY, Zhong XC, Zeng DC, Liu ZW. Design and performance study of the active magnetic refrigerator for room-temperature application. Int J Refrig-Rev Int Froid 2009;32:78–86.
[1520] Bour S, Hamm J, Michot H, Muller C. Experimental and numerical analysis of a reciprocating room temperature active magnetic regenerator. In: Proceedings of the third international conference on magnetic refrigeration at room temperature.

[1521] Coelho AA, Gama S, Magnus A, Carvalho A. Prototype of a Gd-based rotaring magnetic refrigerator for work around room temperature. In: Proceedings of the third international conference on magnetic refrigeration at room temperature.
[1522] Dupuis C, Vialle AJ, Legait U, Kedous-Lebouc A, Ronchetto D. New investigations in magnetic refrigeration device, AMR cycle and refrigerant bed performance evaluation. In: Proceedings of the third international conference on magnetic refrigeration at room temperature.
[1523] Kim Y, Jeong S. Investigation on the room temperature active magnetic regenerative refrigerator with permanent magnetic array. In: Proceedings of the third international conference on magnetic refrigeration at room temperature.
[1524] Pryds N, Bahl CRH, Smith A. Do simple magnetic refrigeration test devices lead to more successful prototypes? In: Proceedings of the third international conference on magnetic refrigeration at room temperature.
[1525] Sari O, Balli M, Trottet G, Bonhote P, Egolf PW, Muller C, et al. Initial results of a tests-bed magnetic refrigeration machine with practical running conditions. In: Proceedings of the third international conference on magnetic refrigeration at room temperature.
[1526] Tagliafico LA, Scarpa F, Tagliafico G, Valsuani F, Canepa F, Cirafici S, et al. Design and assembly of a linear reciprocating magnetic refrigerator. In: Proceedings of the third international conference on magnetic refrigeration at room temperature.
[1527] Tagliafico LA, Scarpa F, Valsuani F, Tagliafico G. Preliminary experimental results from a linear reciprocating magnetic refrigerator prototype. Appl Therm Eng 2013;52:492–7.
[1528] Tura A, Rowe A. Progress in the characterization and optimization of a permanent magnet magnetic refrigerator. In: Proceedings of the third international conference on magnetic refrigeration at room temperature.
[1529] Tusek J, Zupan S, Prebil I, Poredos A. Magnetic cooling - development of magnetic refrigerator. Strojniski Vestn-J Mech Eng 2009;55:293–302.
[1530] Trevizoli PV, Barbosa JR, Ferreira RTS. Experimental evaluation of a Gd-based linear reciprocating active magnetic regenerator test apparatus. Int J Refrig-Rev Int Froid 2011;34:1518–26.
[1531] Kim Y, Jeong S. Numerical simulation and its verification for an active magnetic regenerator. Int J Refrig-Rev Int Froid 2011;34:204–15.
[1532] Balli M, Sari O, Mahmed C, Besson C, Bonhote P, Duc D, et al. A pre-industrial magnetic cooling system for room temperature application. Appl Energy 2012;98:556–61.
[1533] Tura A, Rowe A. Permanent magnet magnetic refrigerator design and experimental characterization. Int J Refrig-Rev Int Froid 2011;34:628–39.
[1534] Park I, Kim Y, Jeong S. Development of the active magnetic regenerative refrigerator for room temperature application. Progr Supercond Cryogenics 2012;14:60–4.
[1535] Engelbrecht K, Eriksen D, Bahl CRH, Bjork R, Geyti J, Lozano JA, et al. Experimental results for a novel rotary active magnetic regenerator. Int J Refrig-Rev Int Froid 2012;35:1498–505.
[1536] Arnold DS, Tura A, Ruebsaat-Trott A, Rowe A. Design improvements of a permanent magnet active magnetic refrigerator. Int J Refrig-Rev Int Froid 2014;37:99–105.
[1537] Park I, Kim Y, Jeong S. Development of the tandem reciprocating magnetic regenerative refrigerator and numerical simulation for the dead volume effect. Int J Refrig-Rev Int Froid 2013;36:1741–9.
[1538] He XN, Gong MQ, Zhang H, Dai W, Shen J, Wu JF. Design and performance of a room-temperature hybrid magnetic refrigerator combined with Stirling gas refrigeration effect. Int J Refrig-Rev Int Froid 2013;36:1465–71.
[1539] Romero Gómez J, Ferreiro Garcia R, Carbia Carril J, Romero Gómez M. Experimental analysis of a reciprocating magnetic refrigeration prototype. Int J Refrig 2013;36:1388–98.
[1540] Aprea C, Greco A, Maiorino A, Mastrullo R, Tura A. Initial experimental results from a rotary permanent magnet magnetic refrigerator. Int J Refrig-Rev Int Froid 2014;43:111–22.
[1541] Eriksen D, Engelbrecht K, Bahl CRH, Bjork R, Nielsen KK, Insinga AR, et al. Design and experimental tests of a rotary active magnetic regenerator prototype. Int J Refrig-Rev Int Froid 2015;58:14–21.
[1542] Kolano R, Kolano-Burian A, Hreczka M, Polak M, Szynowski J, Tomaka W. Magnetocaloric cooling device with reciprocating motion of the magnetic field source. Acta Phys Pol A 2016;129:1205–9.
[1543] Lozano JA, Capovilla MS, Trevizoli PV, Engelbrecht K, Bahl CRH, Barbosa JR. Development of a novel rotary magnetic refrigerator. Int J Refrig-Rev Int Froid 2016;68:187–97.
[1544] Abdelmessih AN, Bartholomae PW, Casillas ML, DeLyon RE, Flaherty JF, Goolsby BD, et al. Design of a Magnetic Cooling Device Using Gadolinium Alloy and Permanent Magnets. In: Proceedings of the ASME summer heat transfer conference.
[1545] Benedict MA, Sherif SA, Beers DG, Schroeder MG. Design and performance of a novel magnetocaloric heat pump. Sci Technol Built Environ 2016;22:520–6.
[1546] von Ranke PJ, de Oliveira NA, Plaza EJR, de Sousa VSR, Alho BP, Carvalho AMG, et al. The giant anisotropic magnetocaloric effect in DyAl2. J Appl Phys 2008;104:093906.
[1547] Lorusso G, Roubeau O, Evangelisti M. Rotating magnetocaloric effect in an anisotropic molecular dimer. Angew Chem-Int Ed 2016;55:3360–3.
[1548] Phan MH, Mandrus D. Cooling achieved by rotating an anisotropic superconductor in a constant magnetic field: a new perspective. AIP Adv 2016;6:125022.
[1549] Ujihara M, Carman GP, Lee DG. Thermal energy harvesting device using ferromagnetic materials. Appl Phys Lett 2007;91.
[1550] Kitanovski A, Egolf PW. Innovative ideas for future research on magnetocaloric technologies. Int J Refrig-Rev Int Froid 2010;33:449–64.
[1551] Moya X, Kar-Narayan S, Mathur ND. Caloric materials near ferroic phase transitions. Nat Mater 2014;13:439–50.
[1552] Gough J. A description of a property of caoutchouc or Indian rubber; with some reflections on the cause of the elasticity of this substance. Mem Lit Phil Soc Manch 1805;1:288–95.
[1553] Joule JP. On some thermo-dynamic properties of solids. Philos Trans R Soc Lond 1859;149:91–131.
[1554] Manosa L, Planes A. Materials with giant mechanocaloric effects: cooling by strength. Adv Mater 2017;29:1603607.
[1555] Scott JF. Electrocaloric materials. Annu Rev Mater Res 2011;41:229–40.
[1556] Kitanovski A, Plaznik U, Tomc U, Poredoš A. Present and future caloric refrigeration and heat-pump technologies. Int J Refrig 2015;57:288–98.
[1557] Bruederlin F, Ossmer H, Wendler F, Miyazaki S, Kohl M. SMA foil-based elastocaloric cooling: from material behavior to device engineering. J Phys D: Appl Phys 2017;50.
[1558] de Vries W, van der Meer TH. Application of Peltier thermal diodes in a magnetocaloric heat pump. Appl Therm Eng 2017;111:377–86.
[1559] Cwik J, Palewski T, Nenkov K, Lyubina J, Warchulska J, Klamut J, et al. Magnetic properties and specific heat of Dy1-xLaxNi2 compounds. J Magn Magn Mater 2009;321:2821–6.
[1560] Marcos JS, Fernandez JR, Chevalier B, Bobet JL, Etourneau J. Heat capacity and magnetocaloric effect in polycrystalline and amorphous GdMn2. J Magn Magn Mater 2004;272:579–80.
[1561] de Oliveira NA, von Ranke PJ. Magnetocaloric effect in the Laves phase pseudobinaries (Dy1-c R-c)Al-2 (R = Er and Ho). J Magn Magn Mater 2008;320:386–92.
[1562] Troper A, von Ranke PJ, de Oliveira NA. Magnetocaloric effect in the pseudobinary Ho(Co1-cRhc)(2). J Magn Magn Mater 2004;272:583–4.
[1563] Singh NK, Agarwal S, Suresh KG, Nirmala R, Nigam AK, Malik SK. Anomalous magnetocaloric effect and magnetoresistance in Ho(Ni, Fe)(2) compounds. Phys Rev B 2005;72:014452.
[1564] de Oliveira NA, von Ranke PJ, Troper A. Magnetocaloric effect in rare-earth pseudobinary Er(Co1-cNic)(2). Phys Rev B 2004;69:064421.
[1565] Gomes AM, Proveti JR, Takeuchi AY, Passamani EC, Larica C, Guimaraes AP. La(Fe1-xCox)(11.44)Al-1.56: a composite system for Ericsson-cycle-based magnetic refrigerators. J Appl Phys 2006;99:116107.
[1566] Balli M, Fruchart D, Gignoux D. Optimization of La(Fe, Co)(13-x)Si-x based compounds for magnetic refrigeration. J Phys-Condes Matter 2007;19:236230.

[1567] Shen J, Li YX, Zhang J, Gao B, Hu FX, Zhang HW, et al. Large magnetic entropy change and low hysteresis loss in the Nd- and Co-doped La(Fe, Si)(13) compounds. J Appl Phys 2008;103:07B317.
[1568] Kumar P, Lyubina J, Gutfleisch O. Magnetic and magnetocaloric effect in melt spun La1-xRxFe(13-y)Al(y)C(z) (R = Pr and Nd) compounds. J Phys D-Appl Phys 2009;42:205003.
[1569] Pathak AK, Basnyat P, Dubenko I, Stadler S, Ali N. Magnetic, magnetocaloric, and magnetoelastic properties of LaFe11.57Si1.43Bx compounds. J Appl Phys 2009;106:063917.
[1570] Sun JR, Shen BG, Hu FX. Magnetocaloric effect and materials. New York: Springer; 2009.
[1571] Balli M, Fruchart D, Gignoux D. The LaFe11.2Co0.7Si1.1Cx carbides for magnetic refrigeration close to room temperature. Appl Phys Lett 2008;92:232505.
[1572] Zeng H, Zhang JX, Kuang CJ, Yue M. Direct measurements of magneto-caloric effect of Gd5Si2Ge2 alloys in low magnetic field. J Supercond Nov Magn 2012;25:487–90.
[1573] Kumar DMR, Raja MM, Gopalan R, Balamuralikrishnan R, Singh AK, Chandrasekaran V. Microstructure and magnetocaloric effect in Gd5Si2(Ge1-xGax)(2) alloys. J Alloys Comp 2008;461:14–20.
[1574] Hou XL, Xiang J, Zeng Z, Huang J, Wang XZ, Xu H. The magentocaloric effect of Gd5Si2Ge2-xZnx alloy. In: Wang JH, Qi JG, editors. Materials and manufacturing, Pts 1 and 2. Stafa-Zurich: Trans Tech Publications Ltd; 2011. p. 525–9.
[1575] Chen X, Chen YG, Tang YB. The studies of phase relation, microstructure, magnetic transition, magnetocaloric effect in (Gd(1-x)Er(x))(5)Si(1.7)Ge (2.3) compounds. J Alloys Comp 2011;509:9604–8.
[1576] Yucel A, Elerman Y, Aksoy S. Changes in the phase structure and magnetic characteristics of Gd5Si2Ge2 when alloyed with Mn. J Alloys Comp 2006;420:182–5.
[1577] Yuzuak E, Dincer I, Elerman Y. Effects of manganese doping on magnetocaloric effect in Ge-rich Gd5Ge2.05Si1.95 alloy. J Rare Earths 2012;30:217–21.
[1578] Campoy JCP, Plaza EJR, Nascimento FC, Coelho AA, Pereira MC, Fabris JD, et al. Magnetocaloric effect and transport properties of Gd5Ge2(Si1-xSnx)(2) (x=0.23 and 0.40) compounds. J Magn Magn Mater 2007;316:368–71.
[1579] Misra S, Mozharivskyj Y, Tsokol AO, Schlagel DL, Lograsso TA, Miller GJ. Structural, magnetic, and thermal characteristics of the phase transitions in Gd5GaxGe4-x magnetocaloric materials. J Solid State Chem 2009;182:3031–40.
[1580] Ryan DH, Elouneg-Jamroz M, van Lierop J, Altounian Z, Wang HB. Field and temperature induced magnetic transition in Gd5Sn4: a giant magnetocaloric material. Phys Rev Lett 2003;90:117202.
[1581] Campoy JCP, Plaza EJR, Carvalho AMG, Coelho AA, Gama S, von Ranke PJ. Experimental study of the magnetocaloric effect in Gd5Sn2Si2 compound. J Magn Magn Mater 2004;272:2375–6.
[1582] Svitlyk V, Cheung YYJ, Mozharivskyj Y. Structural, magnetic and magnetocaloric properties of the Gd5Si4-xSbx (x=0.5-3.5) phases. J Magn Magn Mater 2010;322:2558–66.
[1583] Tegus O, Dagula O, Bruck E, Zhang L, de Boer FR, Buschow KHJ. Magnetic and magneto-caloric properties of Tb5Ge2Si2. J Appl Phys 2002;91:8534–6.
[1584] Yao JL, Wang P, Mozharivskyj Y. Tuning magnetic and structural transitions through valence electron concentration in the giant magnetocaloric Gd5-xEuxGe4 phases. Chem Mater 2012;24:552–6.
[1585] Yuzuak E, Emre B, Elerman Y, Yucel A. Giant magnetocaloric effect in Tb5Ge2-xSi2-xMn2x compounds. Chin Phys B 2010;19:057501.
[1586] Wada H, Tanabe Y, Hagiwara K, Shiga M. Magnetic phase transition and magnetocaloric effect of DyMn2Ge2. J Magn Magn Mater 2000;218:203–10.
[1587] Kumar P, Singh NK, Suresh KG, Nigam AK. Magnetic and magnetocaloric properties of SmxGd1-xMn2Si2. J Alloys Comp 2007;427:42–5.
[1588] Kumar P, Singh NK, Suresh KG, Nigam AK, Malik SK. Heat capacity and magnetocaloric effect in polycrystalline Gd1-xSmxMn2Si2. J Magn Magn Mater 2007;319:1–4.
[1589] Kumar P, Singh NK, Suresh KG, Nigam AK, Malik SK. Effect of Ge substitution for Si on the anomalous magnetocaloric and magnetoresistance properties of GdMn2Si2 compounds. J Appl Phys 2007;101:013908.
[1590] Kumar P, Singh NK, Suresh KG, Nigam AK, Malik SK. Multiple magnetic transitions and the magnetocaloric effect in Gd1-xSmxMn2Ge2 compounds. J Phys-Condes Matter 2007;19:386210.
[1591] Samanta T, Das I, Banerjee S. Contribution of energy-gap in the ferromagnetic spin-wave spectrum on magnetocaloric parameters of CeRu2Ge2. J Phys-Condes Matter 2009;21:026010.
[1592] Wang JL, Campbell SJ, Zeng R, Poh CK, Dou SX, Kennedy SJ. Re-entrant ferromagnet PrMn2Ge0.8Si1.2: magnetocaloric effect. J Appl Phys 2009;105:07A909.
[1593] Dincer I, Elerman Y. Magnetoresistance and magnetocaloric properties of the Pr0.1Gd0.9Mn2Ge2 compound. Phys Scr 2010;81:025703.
[1594] Li LW, Nishimura Y, Huo DX, Qian ZH, Nishimura K. Effect of Fe substitution on magnetic and magnetocaloric effect in Gd(Co(1-x)Fe(x))(2)B(2) compounds. J Appl Phys 2011;110:083915.
[1595] Li LW, Nishimura K, Hutchison WD, Qian ZH, Huo DX, NamiKi T. Giant reversible magnetocaloric effect in ErMn2Si2 compound with a second order magnetic phase transition. Appl Phys Lett 2012;100:152403.
[1596] Li LW, Nishimura K, Huo DX, Matsui S, Qian ZH, Namiki T. Effect of Fe substitution on magnetocaloric effect in borocarbide superconductor Dy(Ni1-xFex)(2)B2C. In: Enpuku K, Izumi T, editors. Advances in superconductivity Xxiv. Amsterdam: Elsevier Science Bv; 2012. p. 44–7.
[1597] Li LW, Nishimura K, Usui G, Huo DX, Qian ZH. Study of the magnetic properties and magnetocaloric effect in RCo2B2 (R = Tb, Dy and Ho) compounds. Intermetallics 2012;23:101–5.
[1598] Yusuf SM, Halder M, Rajarajan AK, Nigam AK, Banerjee S. Magnetic properties and magnetocaloric effect in intermetallic compounds NdMn2-xCoxSi2. J Appl Phys 2012;111:093914.
[1599] Peña A, Gutiérrez J, Campo J, Barandiarán JM, Lezama L, Gil de Muro I, et al. Structural, magnetic and magnetotransport properties of La0.7Pb0.3(Mn1–xNix)O3 ($0.1 \leq x \leq 0.3$) CMR manganites. Eur J Inorg Chem 2008;2008:2569–76.
[1600] Li LW, Nishimura K, Hutchison WD, Mori K. Large magnetocaloric effect in La2/3Ca1/3Mn1-xSixO3 (x=0.05-0.20) manganites. J Phys D-Appl Phys 2008;41:175002.
[1601] Dhahri J, Dhahri A, Oumezzine M, Dhahri E. Effect of Sn-doping on the structural, magnetic and magnetocaloric properties of La0.67Ba0.33Mn1-xSnxO3 compounds. J Magn Magn Mater 2008;320:2613–7.
[1602] Kolat VS, Gencer H, Gunes M, Atalay S. Effect of B-doping on the structural, magnetotransport and magnetocaloric properties of La0.67Ca0.33MnO3 compounds. Mater Sci Eng B-Solid State Mater Adv Technol 2007;140:212–7.
[1603] Cabeza O, Long M, Severac C, Bari MA, Muirhead CM, Francesconi MG, et al. Magnetization and resistivity in chromium doped manganites. J Phys: Condens Matter 1999;11:2569.
[1604] Cao D, Bridges F, Anderson M, Ramirez A, Olapinski M, Subramanian M, et al. Local distortions in La0.7Ca0.3Mn1-bAbO3 (A=Ti and Ga) colossal magnetoresistance samples: Correlations with magnetization and evidence for cluster formation. Phys Rev B 2001;64:184409.
[1605] Liu X, Xu X, Zhang Y. Effect of Ti dopant on the carrier density collapse in colossal magnetoresistance material La0.7Ca0.3Mn1-yTiyO3. Phys Rev B 2000;62:15112.
[1606] Rivadulla F, López-Quintela MA, Hueso LE, Sande P, Rivas J, Sánchez RD. Effect of Mn-site doping on the magnetotransport properties of the colossal magnetoresistance compound La2/3Ca1/3Mn1-xAxO3 (A=Co, Cr; x<0.1). Phys Rev B 2000;62:5678.
[1607] Sun Y, Xu X, Zhang Y. Effects of Cr doping in La0.67Ca0.33MnO3: magnetization, resistivity, and thermopower. Phys Rev B 2000;63:054404.
[1608] Turilli G, Licci F. Relationship between spin order and transport and magnetotransport properties in La0.67Ca0.33Mn1-xAlxOy compounds. Phys Rev B. 1996;54:13052.
[1609] Zhao TS, Li BH, Han G. Magnetic, transport and microstructural properties of polycrystalline samples with nominal composition of La0.7Ca0.3Mn1−xVxO3 (0<x<0.2). J Magn Magn Mater 2008;320:924–9.

[1610] Zhou XZ, Li W, Kunkel HP, Williams G, Zhang SH. Relationship between the magnetocaloric effect and sequential magnetic phase transitions in Ni-Mn-Ga alloys. J Appl Phys 2005;97:10M515.
[1611] Albertini F, Canepa F, Cirafici S, Franceschi EA, Napoletano M, Paoluzi A, et al. Composition dependence of magnetic and magnetothermal properties of Ni-Mn-Ga shape memory alloys. J Magn Magn Mater 2004;272:2111–2.
[1612] Albertini F, Paoluzi A, Pareti L, Solzi M, Righi L, Villa E, et al. Phase transitions and magnetic entropy change in Mn-rich Ni2MnGa alloys. J Appl Phys 2006;100:023908.
[1613] Khan M, Stadler S, Craig J, Mitchell J, Ali N. The overlap of first- and second-order phase transitions and related magnetic entropy changes in Ni2+xMn1-xGa Heusler alloys. IEEE Trans Magn 2006;42:3108–10.
[1614] Babita I, Raja MM, Gopalan R, Chandrasekaran V, Ram S. Phase transformation and magnetic properties in Ni-Mn-Ga Heusler alloys. J Alloys Comp 2007;432:23–9.
[1615] Muthu SE, Rao NVR, Raja MM, Kumar DMR, Radheep DM, Arumugam S. Influence of Ni/Mn concentration on the structural, magnetic and magnetocaloric properties in Ni50-xMn37+xSn13 Heusler alloys. J Phys D-Appl Phys 2010;43:425002.
[1616] Phan TL, Duc NH, Yen NH, Thanh PT, Dan NH, Zhang P, et al. Magnetocaloric effect in Ni0.5Mn0.5-xSnx alloys. IEEE Trans Magn 2012;48:1381–4.
[1617] Ma SC, Xuan HC, Zhang CL, Wang LY, Cao QQ, Wang DH, et al. Investigation of the intermediate phase and magnetocaloric properties in high-pressure annealing Ni-Mn-Co-Sn alloy. Appl Phys Lett 2010;97:052506.
[1618] Podgornykh SM, Gerasimov EG, Mushnikov NV, Kanomata T. Heat capacity of the Ni50Mn37(In0.2Sn0.8)(13) alloy. In: Takahashi M, Saito H, Yoshimura S, Takanashi K, Sahashi M, Tsunoda M, editors. 2nd International symposium on advanced magnetic materials and applications. Bristol: Iop Publishing Ltd; 2011. p. 012004.
[1619] Pathak AK, Khan M, Dubenko I, Stadler S, Ali N. Large magnetic entropy change in Ni50Mn50-xInx Heusler alloys. Appl Phys Lett 2007;90:262504.
[1620] Gao B, Hu FX, Shen J, Wang J, Sun JR, Shen BG. Tuning the magnetic entropy change of Ni50-xMn35+xIn15 alloys by varying the Mn content. J Appl Phys 2009;105:083902.
[1621] Rao NVR, Gopalan R, Chandrasekaran V, Suresh KG. Large low-field inverse magnetocaloric effect near room temperature in Ni50-x Mn37+x In-13 Heusler alloys. Appl Phys A-Mater Sci Process 2010;99:265–70.
[1622] Xuan HC, Ma SC, Cao QQ, Wang DH, Du YW. Martensitic transformation and magnetic properties in high-Mn content Mn50Ni50-xInx ferromagnetic shape memory alloys. J Alloys Comp 2011;509:5761–4.
[1623] Liu FS, Wang QB, Ao WQ, Yu YJ, Pan LC, Li JQ. Magnetocaloric effect in high Ni content Ni(52)Mn(48-x)In(x) alloys under low field change. J Magn Magn Mater 2012;324:514–8.
[1624] Pathak AK, Dubenko I, Pueblo C, Stadler S, Ali N. Magnetism and magnetocaloric effects in Ni50Mn35-xCoxIn15 Heusler alloys. J Appl Phys 2010;107:09A907.
[1625] Pathak AK, Dubenko I, Stadler S, Ali N. The effect of partial substitution of In by Si on the phase transitions and respective magnetic entropy changes of Ni50Mn35In15 Heusler alloy. J Phys D-Appl Phys 2008;41:202004.
[1626] Takeuchi AY, Guimaraes CE, Passamani EC, Larica C. Enhancement of magnetocaloric properties near room temperature in Ga-doped Ni50Mn34.5In15.5 Heusler-type alloy. J Appl Phys 2012;111:103902.
[1627] Dubenko I, Khan M, Pathak AK, Gautam BR, Stadler S, Ali N. Magnetocaloric effects in Ni-Mn-X based Heusler alloys with X = Ga, Sb, In. J Magn Magn Mater 2009;321:754–7.
[1628] Nayak AK, Rao NVR, Suresh KG, Nigam AK. Magneto-thermal and magneto-transport behavior around the martensitic transition in Ni50-xCoxMn40Sb10 (x=9, 9.5) Heusler alloys. J Alloys Comp 2010;499:140–3.
[1629] Pathak AK, Dubenko I, Xiong YM, Adams PW, Stadler S, Ali N. Effect of partial substitution of Ni by Co on the magnetic and magnetocaloric properties of Ni50Mn35In15 Heusler alloy. J Appl Phys 2011;109:07A916.
[1630] Pathak AK, Dubenko I, Pueblo C, Stadler S, Ali N. Magnetoresistance and magnetocaloric effect at a structural phase transition from a paramagnetic martensitic state to a paramagnetic austenitic state in Ni50Mn36.5In13.5 Heusler alloys. Appl Phys Lett 2010;96:172503.
[1631] Ma SC, Cao QQ, Xuan HC, Zhang CL, Shen LJ, Wang DH, et al. Magnetic and magnetocaloric properties in melt-spun and annealed Ni42 7Mn40 8Co5 2Sn113 ribbons. J Alloys Comp 2011;509:1111–4.
[1632] Bruck E, Tegus O, Li XW, de Boer FR, Buschow KHJ. Magnetic refrigeration towards room-temperature applications. Physica B 2003;327:431–7.